CINEL
EXPLORE THE CLIMATE

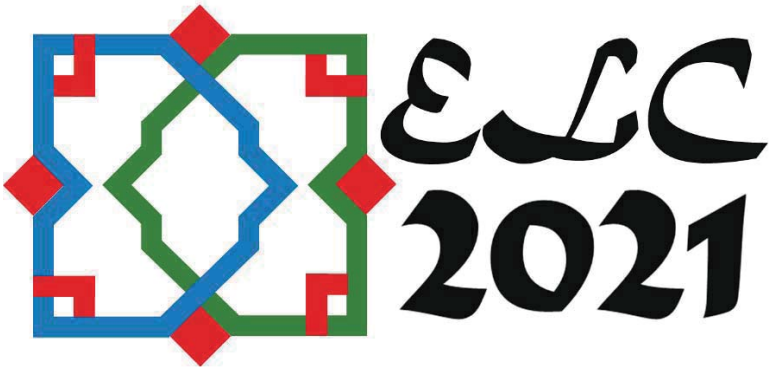

European Lidar Conference 2021

Granada

Proceedings Book

IISTA
Instituto Interuniversitario de Investigación del Sistema Tierra en Andalucía

FACULTAD DE CIENCIAS

UNIVERSIDAD DE GRANADA

raymetrics
lidar systems

EUMETSAT

GRASP
In principle, yes!

CINEL
EXPLORE THE CLIMATE

PROBE
COST ACTION

imap
INFORMÁTICA

Organized by the Atmospheric Physics Research Group
Andalusian Institute for Earth System Research (IISTA-CEAMA), University of Granada

Preface

We are pleased to invite you to the 3rd edition of the European Lidar Conference (ELC), which will take place in Granada (Spain) from the 16th to the 18th of November 2021, hosted by the University of Granada, in a hybrid format.

The European Lidar Conference is settling down in the lidar community after two successful editions. This conference is intended to be organized each two years in between ILRCs, in five different sessions covering a wid e range of state-of-the-art lidar-related topics. Each session is structured in oral and poster presentations, as well as a time slot dedicated to open discussion led by the session chairs.

ELC aims to be a friendly environment where lidarists can have a deep and open discussion. During 2.5 days, experts will have the opportunity to network, find new collaborations and develop longstanding ones, exchange ideas, create novel ones, and be inspired by top-level keynote lectures, to further improve the field of lidar research... A place where we can meet and discuss the very technical aspects of our work.

The amazing city of Granada, home of the encharming Alhambra, will be the scenery of ELC2021 that brings European groups active in lidar research, as well as researchers from many other countries worldwide. As in the previous edition, the participation of young researchers is especially encouraged.

Note that there is no board or established committee behind ELC, just a group of scientists who mobilized their resources for this experiment. As such, the involvement of the community for the continuation of this event will be needed. The whole idea is to “keep it simple” and “make it useful”.

This edition we are really looking forward to welcome you in Granada after the difficult time we all have been through.

Dr. Juan Antonio Bravo-Aranda

Marie Skłodowska-Curie

Cofund Postdoc

Dr. María J. Granados-Muñoz

Marie Skłodowska-Curie

IF Postdoc

Dr. Juan Luis Guerrero-Rascado

Tenured Professor

ELC2021 Local Organizing Committee

Committees

Conference Chairs

Lucas Alados-Arboledas (University of Granada, Spain)

Doina Nicolae (National Institute for Research and Development for Optoelectronics, Romania)

Alexandros Papayannis (National Technical University of Athens, Greece)

Local Organizing Committee

Juan Antonio Bravo-Aranda (University of Granada, Spain)

María José Granados-Muñoz (University of Granada, Spain)

Juan Luis Guerrero-Rascado (University of Granada, Spain)

Scientific Committee

Chair: Adolfo Comerón (Universitat Politècnica de Catalunya, Spain)

Session 1: Lidar technology

Paolo di Girolamo (Università degli Studi della Basilicata, Italy)

Igor Veselovskii (A.M. Prokhorov General Physics Institute, Russia)

Session 2: Lidar algorithms and data products

Ina Mattis (Deutscher Wetterdienst, Germany)

Ewan O'Connor (Finnish Meteorological Institute, Finland)

Session 3: Lidar applications

Iwona Stachlewska (University of Warsaw, Poland)

Patrick Rairoux (University of Lyon, France)

Session 4: Challenges - Atmospheric boundary layer and low altitude profiling

Romain Ceolato (ONERA, France)

Lucas Alados-Arboledas (University of Granada, Spain)

Session 5: Open topic - Synergies

Anca Nemuc (National Institute for Research and Development for Optoelectronics, INOE, Romania)

Rodanthi-Elisavet Mamouri (Cyprus University of Technology, Cyprus)

Open forum: Companies and users

Livio Belegante (National Institute for Research and Development for Optoelectronics, INOE, Romania)

Aldo Amodeo (Institute of Methodologies for Environmental Analysis, CNR-IMAA, Italy)

Technical Program Committee

Responsible for abstracts reviewing:

Holger Baars (Leibniz Institute for Tropospheric Research, TROPOS, Germany)

Antonella Boselli (Institute of Methodologies for Environmental Analysis, CNR-IMAA, Italy)

Juan Antonio Bravo-Aranda (University of Granada, Spain)

Carmen Córdoba-Jabonero (Spanish Institute for Aerospace Technology, INTA, Spain)

Maria João Costa (University of Évora, Portugal)

Ronny Engelmann (Leibniz Institute for Tropospheric Research, TROPOS, Germany)

Alexander Geiss (Meteorological Institute of the Ludwig-Maximilians-Universität Munich, Germany)

María José Granados-Muñoz (University of Granada, Spain)

Silke Gross (Geman Aerospace Center, DLR, Germany)

Juan Luis Guerrero-Rascado (University of Granada, Spain)

Birgit Heese (Leibniz Institute for Tropospheric Research, TROPOS, Germany)

Qiaoyun Hu (University of Lille, France)

Fabio J. S. Lopes (Center for Lasers and Applications, Nuclear and Energy Institute, Brasil)

Eleni Marinou (National Observatory of Athens, NOA, Greece)

Francisco Molero (Centro de Investigaciones Energéticas, Medioambientales y Tecnológicas, CIEMAT, Spain)

Anca Nemuc (National Institute for Research and Development in Optoelectronics, INOE, Romania)

Nikos Papagiannopoulos (Institute of Methodologies for Environmental Analysis, CNR-IMAA, Italy)

Rolf Rüfenacht (MeteoSwiss, Switzerland)

Michael Sicard (Universitat Politècnica de Catalunya, Spain)

Nikos Siomos (Aristotle University of Thessaloniki, Greece)

Scott Spuler (National Center for Atmospheric Research, NCAR, USA)

Kevin Strawbrigde (Environment and Climate Change Canada, Canada)

Sponsors

The organizers wish to acknowledge the support offered by the following sponsors, who made possible the "Participation Grants" for young researchers:

- EUMETSAT (https://www.eumetsat.int/)
- Raymetrics (https://www.raymetrics.com/)
- GRASP (https://www.grasp-sas.com/)
- IMAP (https://informaticaimap.es/)
- Cost Action PROBE (http://www.probe-cost.eu/)
- Atmospheric Physics Group, University of Granada (https://atmosphere.ugr.es/)
- Faculty of Sciencies, University of Granada (https://fciencias.ugr.es/)
- Andalusian Institute for Earth System Research (IISTA) (https://www.iista.es/)

And the following companies participating with a stand:

- Lumibird (https://www.lumibird.com/)
- Cimel Electronique (https://www.cimel.fr/)
- Alava Ingenieros (https://www.grupoalava.com/)

Conference Program

	ELC2021 - 3rd European Lidar Conference				
Duration	**Time**		**16-11-2021**	**17-11-2021**	**18-11-2021**
00:45	08:30	08:45	Registration		
	08:45	09:00			
	09:00	09:15			
00:15	09:15	09:30	Welcome and logistics		
00:30	09:30	09:45	Invited talk	Session 3 - oral 1	Session 5 - oral 1
	09:45	10:00		Session 3 - oral 2	Session 5 - oral 2
01:15	10:00	10:15	Session 1 - oral 1	Session 3 - oral 3	Session 5 - oral 3
	10:15	10:30	Session 1 - oral 2	Session 3 - oral 4	Session 5 - oral 4
	10:30	10:45	Session 1 - oral 3	Session 3 - oral 5	Session 5 - oral 5
	10:45	11:00	Session 1 - oral 4	Session 3 - oral 6	Session 5 - oral 6
	11:00	11:15	Session 1 - oral 5	Coffee Break	Coffee Break
01:15	11:15	11:30	Coffee Break	Session 3&4 - posters	Session 5 - posters
	11:30	11:45	Session 1&2 - posters		
	11:45	12:00			
	12:00	12:15		Open forum: companies and users	
	12:15	12:30			Session 5 - Discussion
00:45	12:30	12:45	Session 1 - Discussion		
	12:45	13:00			
	13:00	13:15			Concluding remarks & next conference
01:30	13:15	13:30	**Lunch Break**	**Lunch Break**	
	13:30	13:45			
	13:45	14:00			
	14:00	14:15			
	14:15	14:30			
	14:30	14:45			
01:15	14:45	15:00	Session 2 - oral 1	Session 4 - oral 1	
	15:00	15:15	Session 2 - oral 2	Session 4 - oral 2	
	15:15	15:30	Session 2 - oral 3	Session 4 - oral 3	
	15:30	15:45	Session 2 - oral 4	Session 4 - oral 4	
	15:45	16:00	Session 2 - oral 5	Session 4 - oral 5	
01:15	16:00	16:15	Coffee Break	Coffee Break	
	16:15	16:30	Session 1&2 - posters	Session 3&4 - posters	
	16:30	16:45			
	16:45	17:00			
	17:00	17:15			
00:45	17:15	17:30	Session 2 - Discussion	Session 3&4 - Discussion	
	17:30	17:45			
	17:45	18:00			
	20:00	-		Social dinner	

Sessions
S1 Lidar Technology
S2 Lidar Algorithms and Data Products
S3 Lidar applications
S4 ABL and low altitude profiling
S5 Open topic – Synergies
S6 Open forum – companies and users

ELC2021 Opening. Invited Talk

A wind, temperature, H_2O and CO_2 scanning lidars mobile observatory to study surface-atmosphere interaction. Application in temperate and semi-arid region.

F. Gibert[1], *D. Edouart*[1], *P. Monnier*[1], *C. Cénac*[1], *J. Lopez*[1], *J. Collignan*[1]
gibert@lmd.polytechnique.fr
(1) Laboratoire de Météorologie Dynamique (LMD/IPSL), École polytechnique, Institut polytechnique de Paris, Sorbonne Université, École normale supérieure, PSL Research University, CNRS, École des Ponts, Palaiseau, France

Introduction

The motivation for this work is to provide advanced observations of the main variables that characterize the land-atmosphere exchanges: momentum, temperature, water vapor and carbon dioxide.
There are multiple goals: (i) to address the representativeness of in situ measurements in heterogeneous landscape, especially for surface fluxes (Wulfmeyer et al. 2018) (ii) to assess the relevance of Monin-Obukhov similarity theory (MOST) which links gradient and flux close to the surface (iii) to address the issue of dissimilarity of scalar transport such as heat and water vapor or CO_2 in inhomogeneous landscape (Huang et al. 2009) (iv) to help to find advanced model parameterizations of land-surface exchange and transport processes, for both convective and stable planetary boundary layers, especially during the late afternoon transition (Lothon et al. 2014).
To do so, new observations are needed that can provide, first, a 3-D view of the atmosphere and second, that have turbulence-scale temporal and spatial resolutions in order to investigate flux-gradient relationships and estimate higher-order moments. The observations will also have to be made in different climate zones in order to study the robustness of advanced parameterizations.

In this paper we present the first measurements of two scanning lidars that were developed at Laboratoire de Météorologie Dynamique, Ecole Polytechnique during the last years (Fig.1).
First one is a temperature and water vapor Raman lidar at 355 nm (TERA). This lidar uses a diode-pumped and seeded tripled Nd :YAG laser that provides 200 mJ pulses at 100 Hz and a 50 cm diameter telescope and scanning device (Fig. 1a). The detection set-up is similar to the one developped in Radlach et al. (2008).
Second is a prototype DIAL and Doppler lidar at 2051 nm (COWI). This lidar makes use of a fiber-pumped dual wavelength seeded Ho :YLF MOPA emitter that provides 10 mJ pulses at 2 kHz (Gibert et al. 2018). The lidar has a coherent detection for wind speed measurement and a direct detection using a new HgCdTe APD and a 20 cm diameter telescope for differential absorption measurement of CO_2 (Dumas et al. 2017).

Figure 1. (a) Temperature and H_2O Raman lidar at 355 nm (b) CO_2 and wind, DIAL and Doppler lidar at 2 µm as deployed at SIRTA observatory, Palaiseau, France.

The mobile lidar observatory is completed by two in situ flux stations with sonic anemometers and gas analyzers to assess the precision of lidar data of wind speed, temperature, H_2O and CO_2 mixing ratios and to serve as a reference for flux estimates.

After a test field experiment in a temperate region at SIRTA observatory, Palaiseau, France, the mobile lidar observatory moved to the semi-arid area of Lleida, Spain in the framework of LIAISE experiment, Land surface Interactions with the Atmosphere over the Iberian Semi-arid Environment, July 2021 (Fig. 2).

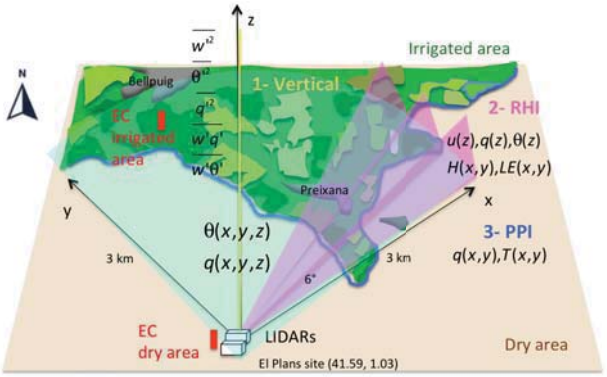

Figure 2. LIAISE experimental site (41.587, 1.0299) and lidar operation modes. EC: eddy-covariance station, RHI: range-height indicator, PPI: plane polar indicator

Main objectives are (i) to study the key natural and

anthropogenic semi-arid surface processes that modulate and govern turbulent fluxes and spatial heterogeneity (ii) to study the impact of highly heterogeneous surface (natural and anthropized due to irrigation) on boundary layer development and mesoscale circulation. To do so, the lidar is operated sequentially in three different modes:
1- vertical : troposphere characteristics, scalar profiles and moments, vertical and horizontal integral scales, vertical profiles for sensible, latent heat and CO_2 fluxes using the eddy-correlation method (Gibert et al. 2011).
2- RHI, range-height indicator : low altitude vertical profiles to test MOST method for surface fluxes estimates over the dry and irrigated area (Eichinger et al. 2000).
3- PPI, plan polar indicator : scalar field heterogeneity, low altitude wind field speed and direction an spatial integral scales for wind, temperature, H_2O and CO_2, local friction velocity u* and Moni-Obukhov length estimates (Cooper et al. 2007).

Results and discussion

Figure 3 shows the results of TERA and COWI simultaneous measurements during the morning transition of the boundary layer at SIRTA observatory, June 9, 2021.

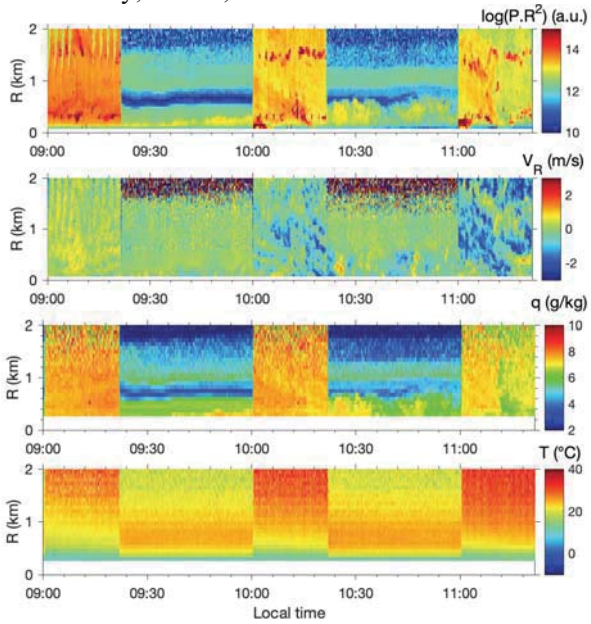

Figure 3. Lidar reflectivity and radial wind speed from COWI lidar at 2 µm and water vapor specific humidity and temperature from TERA Raman lidar.

The time serie starts with 20 minutes of RHI and PPI scanning modes. Then there is 40 min of vertical measurements. The radial wind speed RHI and PPI scans showed the emergence of turbulent strutures that becomes larger as the convective boundary layer develops. These structures are correlated with lidar reflectivity (which accounts for both particles and relative humidity flutuations), water vapor and temperature fluctuations.

Challenges

In this paper we will present preliminary analysis of the data that were collected at SIRTA observatory and during the LIAISE experiment. This may be discussed during the conference.

Acknowledgements

This work is supported by the European Space Agency (ESA), the National Space Agency (CNES), the Directorate General of Armaments (DGA), the National Centre for Scientific Research (CNRS) and the Research National Agency (ANR). We also thank Henri Salvador and Vincent Gauthier who developed the lidar scanning devices.

References

Cooper et al., An advanced method for deriving latent energy flux from a scanning Raman lidar, *Agron. J.*, 99, 272–284, 2007

Dumas et al., Evaluation of a HgCdTe e-APD based detector for 2 µm CO2 DIAL application, *Appl. Opt.*, 56 (27), 7577-7585, 2017.

Eichinger et al., Estimation of spatially distributed latent heat flux over compex terrain from a Raman lidar, *Agricultural Forest Meteor.*,105, 145-159, 2000

Gibert et al., Can CO2 turbulent flux be measured by lidar? A preliminary study, *J. Atmos. Ocean. Tech.* , 28 (3), 365-377, 2011

Gibert et al., 2-µm double-pulse single-frequency Tm:fiber laser pumped Ho:YLF laser for a space-borne CO2 lidar, *Appl. Opt.*, 57 (36), 10370-10379, 2018.

Huang et al., Dissimilarity of scalar transport in the convective boundary layer in inhomogeneous landscapes, *Boundary-Layer Meteor.*, 130, 327-345, 2009.

Lothon et al., The BLLAST field experiment: Boundary-Layer and Sunset Turbulence, *Atmos. Chem. Phys.* 14, 10931-10960, 2014

Radlach et al., Scanning rotational Raman lidar at 355 nm fort he measurement of tropospheric temperature fields, *Atmos. Chem. Phys.*, 8, 159-169, 2008.

Wulfmeyer et al., A new research approach for observing and characterizing land-atmospheric feedbacks, *BAMS*, 1639-1668, 2018

Session 1.
Lidar Technology

Picosecond Short-Range Elastic Backscatter Lidar Technique for Measuring Ultrafine Particles including Smoke

Romain Ceolato, Andres Bedoya-Velasquez, Frederic Fossard, Vincent Mouysset, Lucas Paulien, Sidonie Lefebvre, Claudio Mazzoleni, Christopher Sorensen, Matthew Berg, Jerome Yo
Romain.Ceolato@onera.fr

(1) ONERA, The French Aerospace Lab, Toulouse

Introduction

A bi-static short-range elastic backscatter micro-lidar, named Colibri, has been developed for quantitative aerosol profiling with high range and temporal resolution within the first hundred meters. The geometric (i.e., overlap) and radiometric (i.e., lidar constant) calibrations were performed along with dark current and background noise characterizations. Results of a measurement campaign have demonstrated the capability of our system to characterize aerosol plumes with high range-resolution (<10 cm) in the short-range close to their emission sources (from 10 m). To this aim, fog-oil aerosol plumes were generated in a tunnel and characterized by using an optical particle counter. A forward inverse method without boundary conditions is presented for inverting short-range lidar profiles when no reference molecular zone is available. Lastly, we report the different retrieved lidar products, namely the distribution of aerosol layers, radiative properties (i.e., backscatter profiles), and the microphysical properties (i.e., number concentration profiles). For the validation of the proposed methodology, the lidar products were compared with measurements from the optical particle counter. Finally, the impact of calibration errors on the lidar products is determined through an uncertainty analysis.

Results and discussion

The Colibri micro-lidar is a forward-pointing elastic-backscatter lidar designed to characterize aerosols plumes (e.g., cloud, fog, soot). The function of this instrument is to perform remote measurements of particulate media in the short-range within the first hundred meters with high range-resolution of 10 cm along the line of sight and high-temporal resolution up to 1 measurement per millisecond. The micro-lidar architecture is bi-static and multi-axial with scanning capability in order to ensure measurements in the short-range. The system is lightweight, compact, and suitable for a mobile platform. The instrument optical layout is depicted in Figure 1.

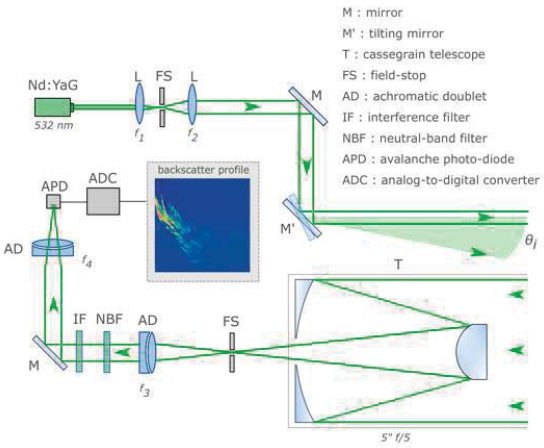

Figure 1. Optical diagram of the Colibri lidar used to measure backscatter profiles. A Nd:YaG laser along with a collimator emits a laser beam in the direction of the aerosol plume. The backscattered light is collected by a compact Cassegrain telescope then relayed by another achromatic lens to the Si-APD sensor.

Here, we report some experimental results obtained during an experimental campaign located in Toulouse (Occitanie, France) at ONERA. In this particular work, the experiments took place in a tunnel with 80 m length by 3 m height, approximately. The measurements were performed on 12 and 13 February 2020 and the same configuration was kept for both days. A fog-oil generator was located inside the tunnel to create a controlled aerosol environment for the system characterization. Fog-oil plumes are obscurant smoke screens produced by the heating of a glycol solution and are disseminated in the air as an electromagnetic obscurant for military applications, entertainments, or fire simulation. A fog-oil plume is disseminated by vaporization using a generator and then is condensed as the vapors cool in the atmosphere beyond the exhaust pipe. The efficiency of fog-oil plumes depends on the aerosol concentration and particle size distribution, which are characterized in this experiment using an optical particle counter (Palas, Fidas 200). This instrument is based on polychromatic light-scattering and provides particle size and number concentrations of aerosol particles in the size range from 0.18 to 18 µm.

One objective of the Colibri micro-lidar is to monitor the evolution and dispersion of the aerosol plumes, here fog-oil smoke particles, in the short-range with high range-resolution and temporal-resolution. Figure 2 shows an example of the Colibri micro-lidar measurements carried out on 13th February at ONERA center. The glycol fog-oil emission event was remotely and horizontally characterized from 0 to 60 m during 60 s. It was possible to study the structural properties and spatio-temporal variability of the aerosol layers in the short-range with high range and temporal resolution. Note that all range levels given in this section are meant as the horizontal distance from the lidar system. The range-corrected signal RCS measurements were converted to attenuated backscatter profiles by applying the geometric and radiometric calibration procedure. The aerosol backscatter profiles $\beta_{aer}(r)$ are retrieved from the attenuated backscatter profiles according to a forward inverse method without boundary conditions presented fully explained elsewhere [1]. The aerosol number concentration $N_p(r)$ can be retrieved from aerosol backscatter signal using ancillary information provided by the optical particle counter (Fidas 200) and reported in Ceolato et. al 2020. The backscattering cross-section and lidar ration are the key physical quantities to be evaluated using light-scattering models (e.g. Mie theory for spheres, or Rayleigh-Debye-Gans for aggregates for spheres).

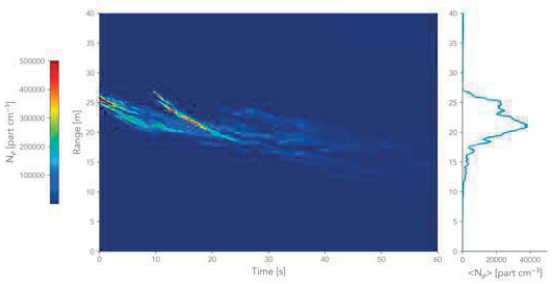

Figure 2. Spatio-temporal (left panel) and 60 s time-averaged (right panel) aerosol number concentration profiles with high range and temporal resolution of fog-oil plumes derived from aerosol backscatter profiles measured by the Colibri micro-lidar.

Figure 2 shows an example of the retrieved aerosol number concentration profiles of the fog-oil smoke event in false color. From the measurements, a high number concentration of particles was detected in the first 30 s of the measurement, reaching values up to 5.0 10^5 part cm^{-3}, and then evidencing the rapid decrease of the number of aerosol concentration over time, reaching values lower than 10^5 part cm^{-3} in less than 30 s. The time-averaged aerosol number concentration ⟨Np⟩ measured during the first 60 s of the event is represented in the right panel of Figure 3.

The present work has demonstrated the feasibility of our self-designed short-range elastic backscatter micro-lidar to provide relevant properties of aerosol plumes, including radiative and microphysical properties. An indoor measurement campaign was carried out to assess the performances of the micro-lidar under controlled environment conditions. This campaign allowed us to monitor the dynamics of aerosol plumes and to retrieve quantitative micro-lidar products, including aerosol backscatter and number concentration profiles as a result of a rigorous calibration and a dedicated inverse method without any boundary condition. In a nutshell, the following highlights can be drawn from our in-door measurement campaign using the Colibri micro-lidar: (i) short-range elastic backscatter lidar measurements were proved to measure backscattering from aerosol plumes in the short-range (within the first tens of meters) with a high range-resolution (<10 cm) and a high-temporal-resolution (1 ms); (ii) the inversion of micro-lidar signals was made possible using a forward inverse method without boundary conditions; (iii) aerosol backscatter and number concentration profiles could be retrieved using lidar-relevant parameters derived from light-scattering models and ancillary in-situ instruments.

Acknowledgements

The authors would like to thank Gilles Roy (RDDC-DRDC, Canada) for his valuable advices in the field of lidar design and inversion. The authors are grateful for helpful discussions with Nicolas Riviere (ONERA, France), Sidonie Lefebvre (ONERA, France), Lucas Paulien (ONERA, France), and Matthew J. Berg (Kansas State University, USA). We thank Guillaume Huss and Paul-Henri Pioger from Leukos (https://www.leukos-laser.com/) for developing and proving the laser source.

References

Ceolato, R.; Bedoya-Velásquez, A.E.; Mouysset, V. Short-Range Elastic Backscatter Micro-Lidar for Quantitative Aerosol Profiling with High Range and Temporal Resolution. Remote Sens., 12, 3286, 2020. https://doi.org/10.3390/rs12203286

Ceolato, R. and Berg, M. J., Aerosol light extinction and backscattering: A review with a lidar perspective", Journal of Quantitative Spectroscopy and Radiative Transfer, 262, 2021. doi:10.1016/j.jqsrt.2020.107492.

Identification of Atmospheric Aerosol Composition from Raman-Scattering and Fluorescence Spectra: Results from Laboratory Investigations

B. Tatarov [1] *and D. Müller* [1]
ƒ b.tatarov@herts.ac.uk
(1) Department of Physics, Astronomy and Mathematics, School of Physics, Engineering and Computer Science, University of Hertfordshire, College Lane, Hatfield, United Kingdom

Atmospheric aerosols such as mineral dust, bio-aerosols and volcanic ash can be transported over tens of thousands of kilometers from its source regions. Despite an abundance of observations and modelling studies, large gaps remain in our understanding of the effect of mineral dust on air quality, human health, and climate. The aim of this work is to use a Raman/fluorescence microscope to collect "optical fingerprints" of aerosol samples (i.e. pure materials and atmospheric samples collected from different source regions) in the form of Raman and fluorescence spectra. In the present work we have been mapping peaks in Raman spectra of mineral dust. Goal of this work is to see if such peaks can be used for determining the composition of mineral dust in the atmosphere from light detection and ranging (lidar) measurements (Inaba and Kobayasi, 1972).

Raman spectroscopy represents a particularly powerful tool for laser remote sensing because it allows us to both identify and quantify the chemical constituents in a complex aerosol mixture - as is often the case for atmospheric aerosol pollution. Nowadays, Raman lidar allows for an independent quantitative measurement of aerosol backscatter and extinction coefficient profiles with the use of Raman scattering from nitrogen or oxygen molecules. Previous works (Müller et al. 2010; Tatarov et al. 2012) have shown that the detection of Raman scattering by silicone dioxide in a lidar receiver can be used to infer the concentration of mineral dust in the atmosphere. In recent years we have been developing a novel multi-channel spectrometric lidar system (Tatarov and Müller 2021). This new system will be used for detecting characteristic features of Raman spectra, which subsequently can be used for inferring chemical signatures of aerosol particles. To achieve this goal, we need currently unavailable information on the Raman spectra of aerosol species commonly found in the atmosphere.

A complex inelastic lidar spectrometer has been developed at the University of Hertfordshire (Tatarov and Müller 2021). In this contribution we present experimental results of Raman and fluorescence spectra of a collection of 30 different aerosol samples. These samples are well characterized in terms of their chemical composition. The samples include, mineral dust (quartz, hematite, kaolinite, barite, calcite etc.), and bio- aerosols. We investigated these samples under laboratory conditions with a Raman microscope. The setup includes an Olympus BX51TRF-6 microscope with objective-lens magnifications x5, x10, x20, x50, and x100.The setup allow for a spatial resolution better that 1µm. The Raman and fluorescence spectra are obtained with a HORIBA 1250M Research Spectrometer that uses four different gratings. The spectral resolution thus is better that 1cm-1. Data acquisition is done by a PI-MAX4 ICCD camera, an ANDOR iXon 3 EMCCD camera, photo multiplier tubes, and Si and InGaAs detectors.

We will discuss potential applications of the data collected in this work in the context of lidar observations of atmospheric aerosols and their chemical composition. The calibration methods and quality assurance of the results will be presented. For that purpose, we compare our results to spectra that can be found in Raman- scattering databases

Acknowledgements
This work has been supported by the University of Hertfordshire through capital investment. Boyan Tatarov was supported by a Marie-Skłodowska-Curie Action Fellowship of the European Commission (CAPABLE, H2020-MSCA- IF-2015). Detlef Müller was supported by Royal Society (WM120052).

References

Inaba and Kobayasi. Laser-Raman radar -Laser-Raman scattering methods for remote detection and analysis of atmospheric pollution, *Opto-electronics*, 4, 101-123, 1972.

Müller et al., Mineral quartz concentration measurements of mixed mineral dust/urban haze pollution plumes over Korea with multiwavelength aerosol Raman-quartz lidar, *Geophys. Res. Lett.*, 37, 2010GL044633, 2010.

Tatarov et al., Record heavy mineral dust outbreaks over Korea in 2010: Two cases observed with multiwavelength aerosol/depolarization/Raman-quartz lidar, *Geophys. Res. Lett. 39*, 2012GL051972, 2012.

Tatarov and Müller, LITES: Rotational Raman Spectra of Air Molecules Measured by High-Resolution-Spectroscopy Lidar, *Opt. Letters*, 2021, DOI: 10.1364/OL.420070, accepted 25 Mar 2021.

Development of a satellite altimeter for the planetary defence program HERA

***L. Belegante*[1], *A. Nemuc*[1], *T. Sousa*[2], *V. Granadeiro*[2] *P. Gordo*[3]**
((1) National Institute of Research and Development for Optoelectronics, INOE,409 Atomistilor Str, Magurele, Romania, belegantelivio@inoe.ro
(2) Efacec Power Solutions, Apartado 1018 · 4466-952 S. Mamede de Infesta · Portugal
(3) Synopsis Planet - Advance Engineering, Unipessoal, Lda. RUA AQUILINO RIBEIRO, 16 6ºdto. 2810-174, ALMADA Portugal

Introduction

Hera is an European project contributing to an international double-spacecraft collaboration between NASA and ESA: AIDA: The Asteroid Impact Deflection Assessment cooperation, is the first planetary defence mission [ESA website].
The Hera mission aims to deploy a satellite to a binary asteroid system – the Didymos pair of near-Earth asteroids. The 780 m-diameter mountain-sized main body is orbited by a 160 m moon, called 'Didymoon'. NASA will first perform a kinetic impact on the smaller of the two bodies – called DART collision – then, two years later, Hera will follow-up with a detailed post-impact survey that will turn this grand-scale experiment into a well-understood and repeatable planetary defence technique, transforming this large-scale experiment into a technique that will divert asteroids whenever required [ESA website].
During the mission, Hera will demonstrate multiple novel technologies, such as autonomous navigation around the asteroid and gather crucial scientific data, to help scientists and future mission planners better understand asteroid compositions and structures. One of the instruments used for this task is a state-of-the-art altimeter used to collect information about the new orbit of the body after the impact.
The altimeter (PALT) developed by the current consortium will make it possible to study the asteroid orbit precisely measuring the distance to the asteroid [link]. PALT will be one of the fundamental tools for achieving Hera's objectives: the LIDAR (Light Detection And Ranging) altimeter, capable of measuring distances of up to 20 km with an accuracy of 10 cm.
The consortium of the project is composed of two Portuguese companies (EFACEC and Synopsis Planet), two Romanian members (Efacec-Romania and INOE) and a Latvian company (Eventech).
The challenges of the project rely in the size, weight and power consumption limitations – typical for all space missions. The concept design of the altimeter was based on a singular telescope and a bi-axial setup.

Optical design

Receiver:

One of the factors influencing the optical design is the size of the optical length. This length is limited by the size of the instrument. Roughly, the dimension of the altimeter enclosure will be around 100 x 120 x 100 mm. The size of the enclosure will limit both the optical length but also the size of the telescope. The initial optical design was focused on a 100 mm diameter primary mirror and optical length of 80 mm inside the altimeter box. The length of the optical path was increased to ~200 mm due to difficulties in designing an optical setup that should be able to focus the 100 mm image of the primary mirror to the sensitive area of the detector (200 microns). The design should be able to resolve an extended dynamic range: 100 m to 20 km. After several simulations and the power budget and the required overlap, the final design was based on a 70 mm telescope and a total optical path of 240 mm – Figure 1.

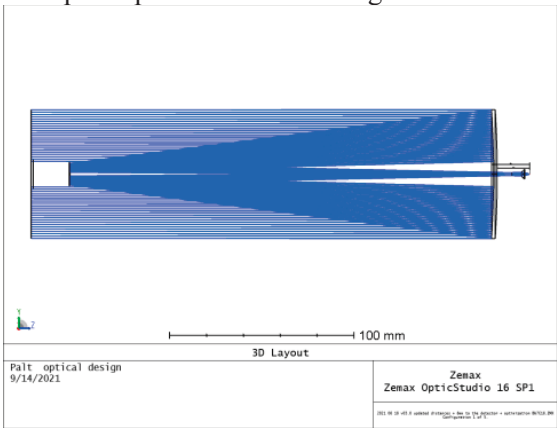

Figure 1: Overall optical design of PALT

The optical design employs a Cassegrain telescope and a condenser lens able to focus the entire image of the primary to the 200 microns detector for all distances required during the mission – Figure 2.

The main optical parameters of the altimeter

Laser divergence (after 10x expansion): 1,1 mrad
Laser diameter (after 10x expansion): 10 mm
Separation between laser and telescope: 35 mm
Telescope FoV: 1,3 mrad
Emission wavelength: 1532 nm

Primary
Concave mirror
Primary mirror diameter: 70 mm
Primary mirror interior diameter: 13 mm
Primary mirror radius = -550 mm
Secondary
Convex mirror
Secondary mirror diameter: 13 mm
Secondary mirror radius = -111 mm

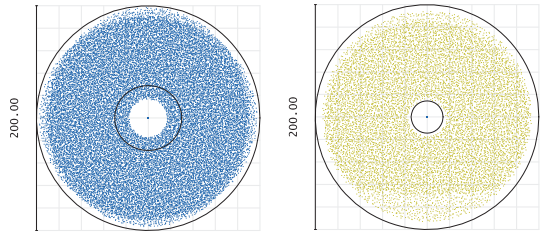

Figure 2: Field spot diagram for the 200 microns sensitive area of the detector. Left: light collected from 15 km; Right: light collected from 200 m.

In the current design, the overlap of the instrument starts around 70 m reaching the 90% limit to 500 m. The full overlap of the instrument is reached at 1280 m – Figure 3.

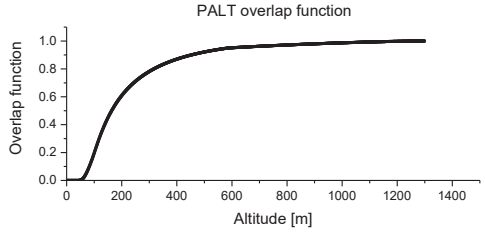

Figure 3. Overlap function of the PALT altimeter in the current design: 70 mm telescope, 1.3 mrad telescope FoV, 1.1 mrad laser divergence - full width and a 90 mm separation between emission and receiver axes.

Emission:

The emission design is based on a Galilean design made of one bi-concave lens and a plano convex lens placed 90.51 mm apart – Figure 4. The emission will expand the laser beam spot 10x, reducing the laser divergence to 1 mrad. The field spot diagram of the emitted light indicates an additional divergence of 0.1 mrad.

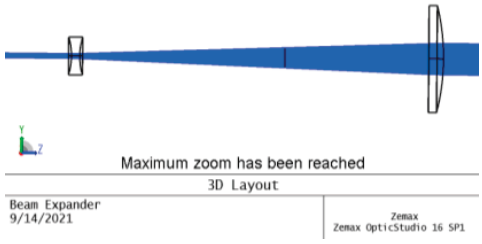

Figure 4. Emission design of PALT

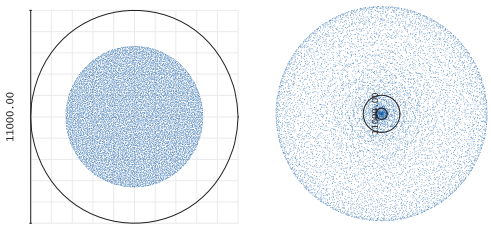

Figure 5. Field spot diagram for image Left: 1 m and Right: 10 km

Current status

Currently the first prototype of the altimeter is assembled. The altimeter will be subject to a series of quality assurance tests designed to validate the nominal performance of the unit. By the end of next year, a second space qualified prototype will be developed. This prototype will be designed to accommodate space qualified materials. The new unit will operate over a wide temperature domain (-40, 70 °C) and will include an additional baffle designed to protect the instrument for stray light and direct sun illumination.

Challenges

Main challenges of the design are related to the size, weight limitations but also to the detector size and operating range. Additional baffles were required to protect the instrument from unwanted light. Thermal constrains were also considered in the design.

Conclusions

The paper will present the current developments and test results of the first PALT prototype altimeter. The experience gained during the design and manufacturing of the PALT units will help the team develop the space qualified unit used in the HERA mission.

Acknowledgements

This research was funded by the Romanian National Core Program Contract No.18N/2019; by the European Regional Development Fund through the 306 Competitiveness Operational Programme 2014–2020, POC-A.1-A.1.1.1-F—2015, project CEO-Terra, by a grant of the Romanian Ministry of Education and Research, CCCDI - UEFISCDI, within PNCDI III, contract No.259/2020 and Helena ESA contract number 4000125526/18/NL/AR/zk

References

https://directory.eoportal.org/web/eoportal/satellite-missions/content/-/article/hera#foot1%29

https://ptspace.pt/planetary-defence-is-worth-portuguese-companies-eur-2-9-million/

Polarization lidar: a laboratory Pi-polarimeter to evaluate the lidar particles depolarization ratio of mineral dust, soot and pollens at 180.0° lidar backscattering angle

A. Miffre, D. Cholleton, P. Rairoux
Institute of Light and Matter (ILM), Université de Lyon, Université Lyon1, CNRS, UMR 5306, 10 Rue Ada Byron, 69 69622 Villeurbanne Cedex, France, alain.miffre@univ-lyon1.fr

Introduction

Lidar remote sensing observations of mineral dust, soot particles or pollens particles is an important topic worldwide and in the lidar European community especially [Haarig et al. 2018; Bravo-Aranda and Guerrero-Rascado 2015; Bohlmann et al. 2021]. This task is however challenging at least as the measured particles depolarization ratio (PDR) is nevertheless that of a particles mixture especially far from the source regions which is the most frequent observed situation. To face such a complexity, lidar partitioning algorithms have been developed allowing to retrieve the backscattering coefficient specific to mineral dust among two or three-component particle external mixtures (Tesche et al.,2009; David et al., 2013) and the algorithm by Tesche et al. is nowadays successfully widely applied. Despite this major advance, the intrinsic depolarization of mineral dust, soot or pollen particles still needs to be revealed. This task is render complicated by the complexity itself of the studied particle samples as mineral dust, soot and pollens indeed exhibit a wide range of sizes, shapes and mineralogy. For example, mineral dust is composed of highly-irregular nonspherical particles, sometimes with sharp edges. Likewise, soot particles are mostly fractal aggregates and the shape of pollen particles is itself nonspherical and even exhibits spikes or / and holes. As a result, no analytical solution of the Maxwell's equations exists for such complex-shaped particles allowing to numerically evaluate the lidar PDR of such aerosols. Numerical approximations have then been applied but the underlying assumptions must be carefully checked and for that a laboratory experiment at 180.0° lidar backscattering angle is coveted. Such an experiment is also coveted in laboratory where, up to now to our knowledge, the lidar PDR could only be obtained in limited scattering regions, ranging from 3° to 177°, different from 180°, as underscored in Huang et al., 2015. Moreover, existing interpolations to the 180°-lidar backscattering angle must be discussed, as recently underlined (Videen et al., 2018).

Results and discussion

In this context, a controlled-laboratory Pi-polarimeter at 180.0° lidar exact backscattering angle has been built at Lyon University to provide precise evaluations of the lidar PDR of aerosols at lidar exact backscattering angle (Miffre et al., 2016). The Pi-polarimeter is based on the scattering matrix formalism and the lidar PDR is measured at both 355 and 532 nm lidar wavelengths simultaneously. Hence, for the first time to our knowledge, the lidar PDR of various mineral dust samples could be accurately measured in laboratory at 180.0° lidar angle. Results concerning silica, hematite but also Arizona or Asian dust will be presented. Likewise, the lidar PDR of freshly-emitted soot aggregates could be evaluated in laboratory (Paulien et al., 2021) and more recently that of a core-shell organic sulfate (Dubois et al., 2021). Interestingly, the involved organics being among the most important secondary organic aerosol precursors in the atmosphere, this laboratory finding may be key for quantifying the direct radiative forcing of sulfates in the presence of organic compounds, thus more clearly resolving the impact of such aerosol particles on the Earth's climate.

The oral presentation will present our laboratory Pi-polarimeter at 180.0° lidar backscattering angle and details the methodology to retrieve accurate evaluations of the lidar PDR of various mineral dust samples, then soot-fractal aggregates or core-shell organic sulfates. The link between the laboratory measured intrinsic depolarization and the lidar-observed field lidar PDR will be discussed. If time is left, the lidar PDR of pollens will also be presented to go on the discussion that we had during the 2020 ELC conference. We hence believe this work may interest the European Lidar community as it may be applied to help better understanding 2λ-polarization lidars which are operated worldwide every day.

Acknowledgements
The authors acknowledge Lyon University and Centre National de la Recherche Scientifique (CNRS) for funding.

References

Bravo-Aranda and Guerrero-Rascado. Study of mineral dust entrainment in the planetary boundary layer by lidar depolarisation technique, *Tellus B,* 67 (1), 26180, 2015.

Bohlmann et al., Detection and characterization of birch pollen in the atmosphere using a multiwavelength Raman polarization lidar and Hirst-type pollen sampler in Finland *Atmos. Chem. Phys,21, 7083, 2021.*

David, G., Thomas, B., Nousiainen, T., Miffre, A. and Rairoux, P., Retrieving volcanic, desert dust, and sea-salt particle properties from two/three-component particle mixtures after long-range transport using UV-VIS polarization Lidar and T-matrix *Atmos. Chem. Phys.,* 13(14), 6757–6776, 2013.

Dubois, C., D. Cholleton, R. Gemayel, Y. Chen, J.D. Surratt, C. George, P. Rairoux, A. Miffre and M. Riva, Decrease in sulfate aerosol light backscattering due to reactive uptake of epoxydiols, *Phys. Chem. Chem. Phys,* 2021, 23, 5927-5935, 2021.

Haarig, M., A. Ansmann, H. Baars, C. Jimenez, I. Veselovskii, R. Engelmann, and D. Althausen, Depolarization and lidar ratios at 355, 532, and 1064 nm and microphysical properties of aged tropospheric and stratospheric Canadian wildfire smoke, *Atmos. Chem. Phys.,* 18, 11847–11861, 2018.

Huang X, G. Kattawar, P. Yang, K.N. Liou, Effect of mineral dust aspect ratio on polarized reflectance, *J. Quant. Spectrosc. Radiat. Transfer,* 151:97-109, 2015.

Miffre, A., T. Mehri, M. Francis and P. Rairoux, UV-VIS depolarization from Arizona Test Dust particles at exact backscattering angle, *J. Quant. Spec. Rad. Transf.*, 169, 79-90, 2016.

Paulien, L., R. Ceolato, F. Foissard, P. Rairoux and A. Miffre, Laboratory evaluation of the lidar depolarization ratio of freshly emitted soot aggregates from pool fire in ambient air at exact backscattering angle, *J. Quant. Spec. Rad. Transf., **260**, 107451,* 2021.

Tesche, M., Ansmann, A., Müller, D., Althausen, D., Engelmann, R., Freudenthaler, V. and Groß, S., Vertically resolved separation of dust and smoke over Cape Verde using multiwavelength Raman and polarization lidars during Saharan Mineral Dust Experiment 2008, *Journal of Geophysical Research,* 114(D13), D13202, 2009.

Videen G., E. Zubko, J.A. Arnold, N. McCall, AJ. Weinberger, Y. Shkuratov, O. Munoz., On the interpolation of light-scattering responses from irregularly shaped particles, *J. Quant. Spec. Rad. Transf.,* 211:123-128, 2018.

The Atmospheric Raman Temperature and Humidity Sounder, technical challenges through three years of measurements

D. Lange[1], A.Behrendt[1], V. Wulfmeyer[1]
(1) University of Hohenheim, Institute of Physics and Meteorology, Stuttgart, Germany, diego.lange@uni-hohenheim.de

Introduction

Between November 2018 and November 2021, the Atmospheric Raman Temperature and Humidity Sounder (ARTHUS) took part in several measurement campaigns and collected about one year of data, including temperature and water vapor mixing ratio with a high temporal and range resolution.

Very stable 24/7 operations on ground-based and shipborne platforms were achieved during several field campaigns and at the Land Atmosphere Feedback Observatory (LAFO, see https://lafo.uni-hohenheim.de/en) accumulating to almost a year of data and covering a huge variety of weather conditions (snow, haze, heavy rain, etc.) including seaborne operation during the EUREC4A campaign (Bony, 2017, Stevens, 2021).

ARTHUS demonstrated that is capable to observe the atmospheric boundary layer and lower free troposphere during daytime and nighttime with very high resolution up to the turbulence scale, high accuracy and precision, and very short latency. ARTHUS measurements resolve the strength of the inversion layer at the planetary boundary layer top, elevated lids in the free troposphere, and turbulent fluctuations in water vapor and temperature, simultaneously (Lange, 2019, Wulfmeyer, 2015). In addition to thermodynamic variables, ARTHUS provides also independent profiles of the particle backscatter coefficient and the particle extinction coefficient from the rotational Raman signals at 355 nm with much better resolution than a conventional vibrational Raman lidar.

We also faced different technical challenges, including operating a Nd:YAG laser 24/7 and keeping the housing conditions (temperature and humidity) under control, so they do not affect the measurements.

During the European Lidar Conference, we will focus on the technical challenges in our lidar operation, mainly the reliability of the laser performance over time and the stabilization of the system during the EUREC4A field campaign in the Atlantic Ocean.

Acknowledgements

This work was funded by the Helmholtz Association of German Research Centers within the Modular Observation Solutions for Earth Systems project.

References

Bony, S., Stevens, B., Ament, F. et al. EUREC4A: A Field Campaign to Elucidate the Couplings Between Clouds, Convection and Circulation. *Surv Geophys* 38, 1529–1568 (2017). https://doi.org/10.1007/s10712-017-9428-0

Stevens, B., et. al.(2021), EUREC4A, *Earth System Science Data Discussions*, 2021, 1–78, doi: 10.5194/essd-2021-18

Lange, D., Behrendt, A., and Wulfmeyer, V. (2019). Compact operational tropospheric water vapor and temperature Raman lidar with turbulence resolution. *Geophysical Research Letters*, 46. https://doi.org/10.1029/2019GL085774

Wulfmeyer, V., R. M. Hardesty, D. D. Turner, A. Behrendt, M. P. Cadeddu, P. Di Girolamo, P. Schlüssel, J. Van Baelen, and F. Zus (2015), A review of the remote sensing of lower tropospheric thermodynamic profiles and its indispensable role for the understanding and the simulation of water and energy cycles, *Rev. Geophys.*, 53,819–895, doi:10.1002/2014RG000476

Comparison of a dual-polarisation Raman lidar with a novel Vaisala CL61 Ceilometer with depolarisation capability

J. Buxmann[1], M. Osborne[1], D. O'Sullivan[1], R. Roininen[2]
joelle.c.buxmann@metoffice.gov.uk
(1)The Met Office, Fitzroy Rd, Exeter , United Kingdom
(2) Vaisala, Vanha Nurmijärventie 21, Helsinki , Finland

Introduction

We present the results of a comparison trial between a Vaisala CL61 and a Raymetrics depolarisation Raman lidar. The campaign was carried out at Cardington, Bedfordshire, UK.

The CL61 is a novel dual polarisation ceilometer with good potential for 24/7 aerosol monitoring and possibly even classification and quantification. The Raymetrics lidar with intermittent measurement schedule (to preserve the flashlamps) is more powerful and has the additional Raman capability.

The Vaisala CL61 operates at a wavelength of 910.55 ± 0.05 nm. The transmitter is pulsing at 9.5 kHz with an average laser power of 38 mW. The depolarisation measurement is done with single avalanche photodiode detector (APD) on the coaxial optical path. The cross- and parallel polarised signals are measured by mechanically switching flat polarising filters in alternating sequence with the same analogue receiver. Cross-talk is minimized with a specified contrast ratio of 1:10000 of the polarisation filters. The correct angular position of the filters is aligned at production. However, some uncertainty in respect to the polarisation calibration remains, as e.g. the laser polarisation purity is non-ideal (99%). The attenuated backscatter profile has been liquid water cloud calibrated according to the O'Connor et. al method (2004). The depolarisation Raman LR111-300s lidars are developed and manufactured to meet the Met Office and London volcanic ash advisory centre (VAAC) needs by Raymetrics. The instruments emit at 355 nm and have polar and cross-polar depolarisation detection channels at 355 nm and a N_2 Raman channel at 387 nm. The systems use Quantel CFR 200 Q-switch-pulsed Nd:YAG lasers, with nominal pulse energies of 50 mJ at 20 Hz. Data are acquired in both analogue and photon-counting modes and glued together during data processing. Polarisation discrimination is done via a polarisation beam splitter cube (PBS). Additional clean sheet filters are placed after the cube to eliminate crosstalk. The lidar needs to be calibrated regularly using the ±45◦ procedure (Freudenthaler, 2016; Buxmann et al., 2020). Aerosol optical properties are calculated using code developed at the Met Office (Osborne et al., 2019) which has been tested against the EARLINET Single Calculus Chain (e.g. Mattis et al., 2016).

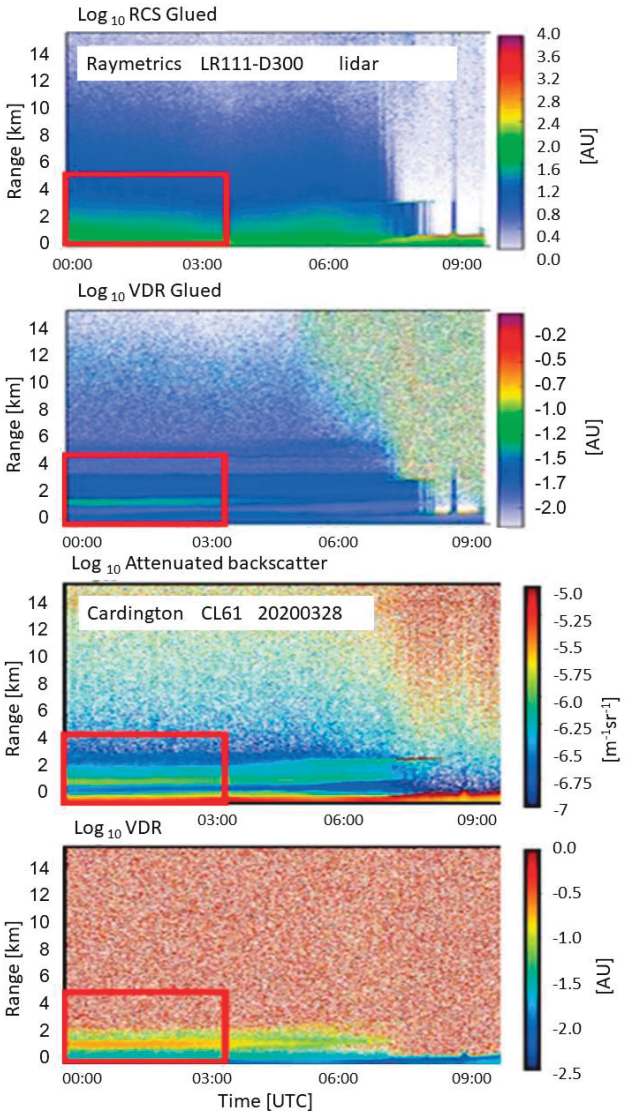

Figure 1. From top to bottom: range corrected signal (RCS) and volume depolarisation ratio (VDR) from the Raymetrics lidar; attenuated backscatter and VDR from the CL61; profiles from 28th March 2020.

Results and discussion

The signal-to-noise ratio (SNR) can be used to characterize a ceilometers ability to determine aerosol layers at different altitudes quantitatively. Photons detected in analog-mode with the CL61 do not strictly obey the Poisson statistic. Instead the highest 500 gates (at 15-15.7 km) are used to

calculate the SNR (Kotthaus et al. 2016).

The SNR of the CL61 is >1 for heights up to 6.1 km on a clear day with little aerosol content and up to 12 km for a day with cirrus clouds averaging over 2 hours. The SNR behaviour is comparable to instruments like the CHM15K (Strachlewska et. al. 2012). However, the Raymetrics lidar shows much better SNR of >10 up to 10 km for clear day and night for parallel as well as perpendicular channel.

In Figure 1 we present an example of aerosol depolarisation measurements from the CL61 and the co-located Raymetrics lidar. The Raymetrics lidar reports a range corrected signal (RCS) rather than the attenuated backscatter from the CL61.

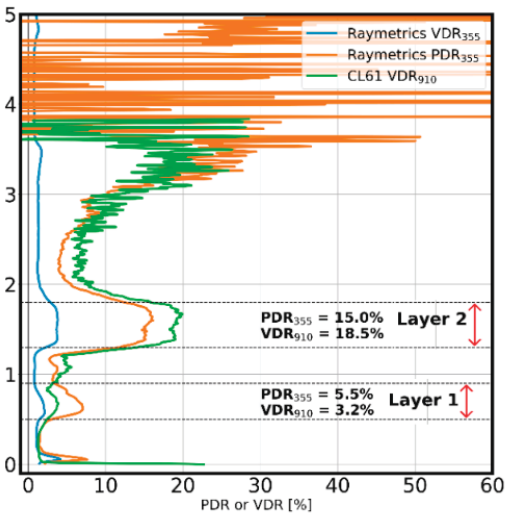

Figure 2. PDR and VDR profiles from 28th March 2020. Data is an average from midninght to 03:30 indicated by the red box in figure 1.

Figure 2 shows a comparison between vertical depolarisation ratio (VDR) and particle linear depolarisation ratio (PDR) from the Raymetrics vs VDR from the CL61. The CL61 VDR is more similar to the Raymetrics PDR, due to the lower molecular contribution in the 910 nm channel of the CL61. According to HYSPLIT backtrajectories (not shown here) the air mass corresponding to layer two has come from near the north coast of Africa and then travelled over Europe to the UK. The average PDR ~15% (weighted by backscatter) suggests some dust content in this aerosol layer. The air mass corresponding to layer one has come from Eastern Europe and has crossed much of the Balkans in the mixing layer.

Challenges & Conclusion The CL61 is capable of identifying aerosol with higher VDR such as dust shown in the example. Although PDR and VDR cannot be compared directly, their relationship at two different wavelengths may be useful for aerosol identification in the future. However, the lower power and the lack of Raman channel provide some challenges, such as lower SNR and higher uncertainties for quantitative retrievals. In addition polarisation calibration using GHK parameters (Freudenthaler, 2016) has not been applied yet. Possible calibration checks include e.g. rotation of a half wave plate and/or liquid water cloud depolarisation calibration. Overall the CL61 provides reliable attenuated backscatter and polarisation information. Lower cost and 24/7 capability is a huge benefit for the operational observing community. A longer time period of collocated CL61 and high power lidar would be beneficial in order to assess the full capacity of the instrument.

Acknowledgements

We would like to thank the team at Cardington and M.Protts for their help with the instrument. Thanks to Vaisala for the transport, set up and loan of the CL61. We are grateful to the Civil Aviation Authority and Department for Transport for funding the lidar project.

References

Freudenthaler. About the effects of polarising optics on lidar signals and the Δ90 calibration, *Atmos. Meas. Tech.*, 9, 4181–4255, 2016.

Buxmann, Osborne, Georgoussis, Freudenthaler, A Recipe to Obtain Lidar Polarisation Calibration Parameters G, H and K, *EPJ Web of Conferences* 237, 05002, 2020.

Kotthaus, O'Connor, Münkel, Charlton-Perez, Haeffelin, Gabey, Grimmond, Recommendations for processing atmospheric attenuated backscatter profiles from Vaisala CL31 ceilometers, *Atmos. Meas. Tech.*, 9(8), 3769–3791, 2016.

Mattis, D'Amico, Baars, Amodeo, Madonna, and Iarlori' EARLINET Single Calculus Chain - Technical - Part 2: Calculation of optical products, *Atmos. Meas. Tech.*, 9(7), .3009–3029, 2016.

O'Connor, Illingworth, Hogan, A technique for autocalibration of cloud lidar, *J. of Atmos. and Oceanic Tech.*, 21(5), 777–786, 2004.

Osborne, Malavelle, Adam, Buxmann, Sugier, Marenco, Haywood, Saharan dust and biomass burning aerosols during ex-hurricane Ophelia: Observations from the new UK lidar and sun-photometer network', *Atmos. Chem. Phys.*, 19, 3557–3578, 2018.

Stachlewska, Piądłowski, Migacz, Szkop, Zielińska, Swaczyna, Ceilometer Observations of the Boundary Layer over Warsaw, *Poland. Acta Geophysica*. 60, (5), 2012.

Sensitivity study for the development of a dual-channel HSRL system for aerosol and cloud studies

P. Kokkalis[1], A. Tavernarakis[2], G. Georgousis[2], G. Tskanakis[2], V. Amiridis[3], A. Papayannis[4]
panagiotis.kokkalis@ku.edu.kw
(1)Kuwait University, P.O. Box 5969, Safat 13060, Kuwait
(2) Raymetrics S.A., Spartis 32, 14452 Metamorfosi, Athens, Greece
(3) Institute for Astronomy, Astrophysics, Space Applications and Remote Sensing, National Observatory of Athens, Athens, 15236, Greece
(4) National Technical University of Athens, Department of Physics, Athens, 15780, Greece

Introduction

High spectral resolution lidars (HSRL) provide independent measurements of aerosol optical properties, namely extinction (α_{aer}) and backscatter coeffiecients (β_{aer}). Unlike to simple backscatter technique, this is done without prior assumptions about the scattering properties of the atmosphere, since HSRL readings are calibrated by reference to molecular scattering, which is measured at each height bin of the lidar profile (Eloranta et al., 2005).

Key-design features of such an instrument require: (a) strong rejection of the aerosol contribution to the molecular channel (aerosol suppression, calculated here as the ratio of the photons transmitted through each channel, namely Tr Rayleigh / Tr Mie), (b) narrow laser linewidth and (c) accurate laser locking to a specific wavelength (the I_2 absorption line 1109 is considered here). These requirements are acomplished by utilizing atomic filters (I_2 filter vapor cell) both at the emission and detection units (Piironen, et al., 1994).

Nevertheless, depending on the scientific objective (aerosol and/or cloud studies) these requirements may vary significantly, depending on the relative magnitude of the β_{aer} or β_{cloud} to β_{mol}, at various operation wavelengths. As an example here, we determine the effect of cross-talk reduction and laser linewidth to the retrieval accuracy of aerosol and cloud optical properties at 532.26 nm. Our simulations will reveal the requirements of the optical components needed for the integration & development (to be done by Raymetrics SA), of an HSRL capable of measuring aerosol and cloud optical properties (α_{aer}, β_{aer}).

Results and discussion

In our analysis we assumed two atmospheric scenes, namely (a) a lofted dust aerosol layer at 3 km with max. $\beta_{aer} = 4.5\text{x}10^{-6}$ m^{-1} sr^{-1} and (b) a dense liquid water cloud (LWC) at 5 km, with max. $\beta_{cloud} = 5.5\text{x}10^{-4}$ m^{-1} sr^{-1}. The Rayleigh and Mie detection channels considered to be noise-free signals.

Iodine absorption spectrum is composed by a set of discrete absorption lines and an absorption continuum. The length of the vapor filter affects the transmission of the detected light around the central line (Forkey et al., 1996), and consequently the aerosol suppression. For the aerosol case, even a short-length saturated I_2 filter, operating at moderate temperature of 30 °C (P=95.69 Pa), can lead to a suppression order of ~10^3, for a 60 MHz laser linewidth (Figure 1). For high β_{aer} values (LWC), such suppression order can be achieved only with longer filter, at that temperature.

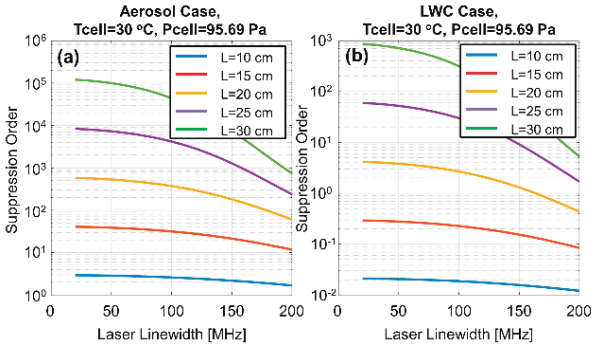

Figure 1. Suppression order achieved as a function of laser linewidth and the I_2 cell length, for (a) aerosol and (b) LWC case.

The laser linewidth deviation affects the suppression uncertainty, especially for higher linewidths (Figure 2). According to our monte carlo simulations, a laser linewidth of 60 MHz with 50% uncertainty is enough to keep the suppression uncertainty below 5%. Moreover, the laser locking line at 1109 line should be achieved with less than 2 MHz stability.

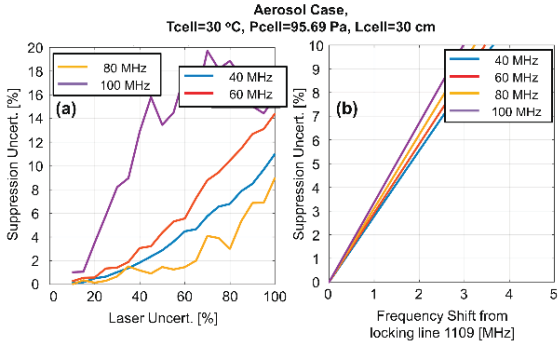

Figure 2. Suppression uncertainty as a function of: (a) laser linewidth uncertainty, and (b) frequency shift from cental line 1109, for various laser linewidths.

Finally, we estimate the cross-talk reduction that is needed to achieve α_{aer} & β_{aer} with accuracy less than 1-2% (Figure 3). For both aerosol and LWC cases we calculate the retrieval error based in the entire vertical extension of the layer. For the extinction retrieval a Savitzky-Golay filter of 110-m equivalent smoothing length, is applied.

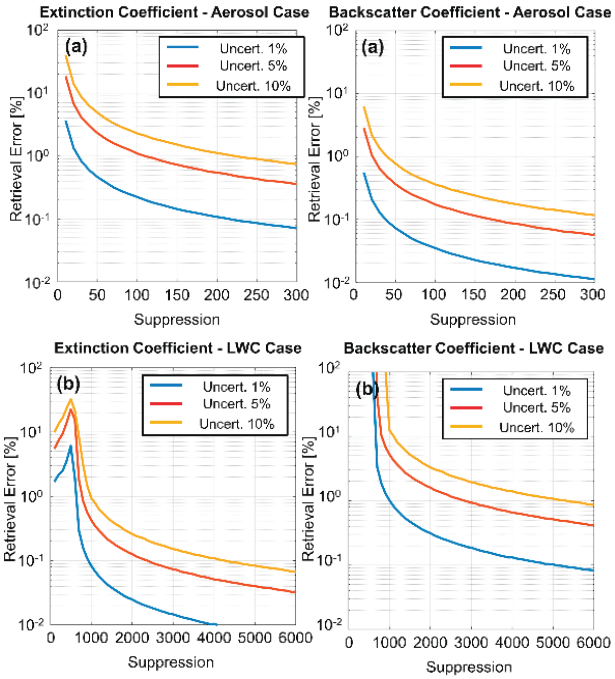

Figure 3. Retrieval error of α_{aer} & β_{aer} as a function of suppression order for various uncertainties for (a) aerosol and (b) LWC case.

The final product uncertainty depends on the accuracy of the determined suppression order. A 10% estimation accuracy of the aerosol supppression can be easily achieved, while 1% is still realistic but harder to be reached. For high enough suppression (> 6000) for the LWC, the product accuracy of 1% can be achieved even if the suppression is known with 10% uncertainty. For the aerosol case, even for high suppression uncertainty of 10%, the 1% retrieval error can be achieved with suppression order of ~250.

Overall, from our study we identified the requirements of the laser and the I_2 filter, needed for aerosol and cloud studies. Namely, for 3 to 4 orders of magnitude aerosol suppression with 5% uncertainty, a 30 to 35-cm length of I_2 cell can be installed at the Rayleigh channel, maintained at 30 ± 1 °C. A 60-MHz laser linewidth should have less than 35% jittering and the locking deviation around the 1109 I_2 absorption line should be less than 1 MHz.

Challenges

The challenges will appear during the experimental phase and the set-up period of the instrument. Briefly here, we note that the main points that will affect the complexity and concequently the cost of the instrument, are related to the following:

1. For cloud studies, a narrow optical filter (etalon) will be mandatory for sufficient solar background rejection during day-time operation (Hayman et al., 2017).
2. The laser line should be actively controlled and stabilized, by means of a feedback loop, to the minimum of the 1109 absorption I_2 line and its efficiency is crucial to the achieved suppression level. Although slow drifts can be easily compensated, the control bandwidth is limited by the laser pulse build-up time. An experimental effort will be needed in order to optimize the loop and characterize the laser frequency stability within the experimental limitations. (Hair et al., 2008)
3. The development of a calibration-scan module for the accurate estimation of the suppression order (Sroga et al., 1983).

Acknowledgements

This research has been co-financed by the European Union and Greek national funds through the Operational Program Competitiveness, Entrepreneurship and Innovation, under the call "RESEARCH-CREATE-INNOVATE" (project code: T1EΔK-03398)-CHARISM.

References

Eloranta, E. W. in Lidar: Range-Resolved Optical Remote Sensing of the Atmosphere *(ed. Weitkamp, C.)* Springer, 2005.

Forkey, J. N., Lempert, W. R. & Miles, R. B. Corrected and calibrated I_2 absorption model at frequency-doubled Nd:YAG laser wavelengths. *Applied Optics* 36, 6729 (1997).

Hayman, M., & Splurer, S., Demonstration of a diode-laser-based high sepctral resolution lidar (HSRL) for quantitative profiling of clouds and aerosols, *Optics Express*, 25, 24, 2017.

Hair, J. W., Hostelter, C.A., et al., Airborne High Spectral Resolution Lidar for profiling aerosol optical properties, *Applied Optics*, 47, 36, 2008.

Piironen, P. and E. W. Eloranta, Demonstration of a High-Spectral-Resolution Lidar based on a Iodine Absorption Filter. *Optics Letters*, 19, 3, 234-236, 1994.

Sroga, J. T., Eloranta, E.W. et al., High spectral resolution lidar to measure optical scattering properties of atmospheric aerosol. 2. Calibration and data analysis, *Applied Optics*, 22, 23, 3725-3732, 1983.

Aeronautics Application of Direct-Detection Doppler Wind Lidar: Alleviation of Airframe Structural Loads Caused by Turbulence and Gusts

P. Vrancken[1], N. Fezans[2], D. Kiehn[2], O. Kliebisch[3], Ph. Linsmayer[1], J. Thurn[3]
(1) Institute of Atmospheric Physics, German Aerospace Center (DLR), 82234 Weßling, Germany
(2) Institute of Flight Systems, German Aerospace Center (DLR), 38108 Braunschweig, Germany
(3) Institute of Technical Physics, German Aerospace Center (DLR), 70569 Stuttgart, Germany
Email: patrick.vrancken@dlr.de

Introduction

The use of lidar in the domain of aeronautics, namely in airborne operation, has been one of the earliest fields of application, endeavored shortly after the invention of the laser itself (Franken, Jenney and Rank, 1966). Such efforts, in particular aiming at turbulence in cruise flight (clear air turbulence CAT), have long been pioneered by the US (cited in Vrancken, 2016), but achievements have also been made in Japan (Inokuchi, Akiyama and Sasaki, 2018) and in Europe (AWIATOR, cf. Schmitt *et al.*, 2007; Rabadan *et al.*, 2010) where efforts have come to a halt in the early 2000s.

At DLR however, these activities have been continuously pursued. In a recently started project, we aim for the use of a Doppler Wind Lidar (DWL) as the central wind speed sensor for a real-time control scheme aboard civil passenger aircraft. This control loop shall use the wind information ahead for derivation of significant turbulent gusts and their counteraction with fast feed-forward actuation of the aircraft's control surfaces (elevators, ailerons, spoilers etc.). An exemplary maneuver could be a subtle 'nose down' pitch when detecting a vertical gust ahead. This scheme could significantly decrease the loads associated with cruise-flight turbulence encounter. Previous simulations (Fezans and Joos, 2017; Fezans, Joos and Deiler, 2019) show that the loads in the wing and fuselage structures may be reduced to a level where such a system is becoming economically attractive.

Evidently, a future commercially viable system for this type, and likewise its prior full airborne demonstration (in an R&D context), poses strong requirements on each of the ingredients of this control scheme: on the DWL laser transmitter and receiver as well as the gust identification and control function. In the presentation/poster, we give insights to the current status, latest achievements and potential of each of these crucial elements.

Activities and status

At the ELC2020 we have introduced (Vrancken and Herbst, 2020) a concept and prototype of a direct-detection DWL based on a fringe-imaging technique based on a skewed Michelson interferometer. The requirements of the described control scheme, sub-m/s precision, high data repetition rate (few to several tens of Hz), high spatial resolution (20 to 50 m), close measurement ranges (50 to 300 m) as well as sensitivity to both mixed molecular/aerosol and pure molecular backscatter (without knowledge on the ratio thereof in terms of backscatter ratio) are all adequately addressed by our design. After the general demonstration of the lidar's functionality (Vrancken and Herbst, 2019/2020) we now have identified the main drivers for absolute and relative (in terms of photon budget) improvement of the systems wind speed measurement dispersion as well as for its residual bias. The first deduced technical improvements are currently (summer 2021) counter-checked in ground-based wind measurements.

In parallel, simulation models (both a simplified analytical and a more physical end-to-end) of a realistic evolution of the lidar are used within an iterative simulation setup particularly including gust identification and the aircraft (rudder command generating) controller.

Notably, it is the module "wind reconstruction algorithm" (WRA) that significantly lowers the requirements on the lidar in a way that (direct-detection) DWL altogether may come into play with significant impact. The WRA analyzes the line-of-sight wind measurements (taken at some angle from the flight direction axis) in a maximum-likelihood estimation using a matching wind (gust) field continuously being updated. The algorithm integrates smoothing parameters in form of Tikhonov regularization terms for reducing the impact of lidar measurement noise.

The third block within the simulation ensemble is the feedforward gust load alleviation (GLA) controller itself, which is currently matched to a "generic business jet" aircraft aero-elastic model, envisioning a future demonstration on a European flight test aircraft (such as the DLR ISTAR Falcon 2000 LX or similar). The controller design is based on a new multi-channel structured discrete time H_∞ formulation (Khalil and Fezans, 2021).

The iterative analysis of this model covers the four main components of the overall system: including the lidar model, the WRA, the

feedforward GLA controller and the aircraft aeroservoelastic model. It is deemed to allow identifying a reasonable set of requirements, in particular on the lidar (with receiver, laser and scan / beam director system), all based on a reasonable and useful level of load alleviation (Fezans et al., 2020). In other words, over-specification of any sub-component is thus avoided.

Among the set of requirements, many crucial ones concern the laser transmitter. As pointed out at ELC2020, within our current ground prototype DWL we employ an existing powerful Nd:YAG UV-source (Vrancken *et al.*, 2016), however not adapted to a future GLA scenario. Previous (Herbst and Vrancken, 2016) and latest simulation results hint at low kHz laser systems as the optimum design point. For this reason, a dedicated laser development effort has been started, taking a master oscillator power amplifier (MOPA) scheme as a workhorse basis for the envisioned future airborne demonstration of the whole GLA loop. In parallel, further technology routes with lower technology readiness level (TRL), but possibly higher industrialization capability, such as fiber and semiconductor laser technology, shall be kept track of.

Challenges and discussion

Evidently, the development of such an advanced DWL system comes with many challenges and thus the authors will be pleased and eager to discuss the details, pitfalls and known unknowns of the whole scheme, in particular concerning laser, spectral analyzing receiver and scanning system. We also embrace potential future cooperations to tackle this European aeronautics domain subject.

Acknowledgements

Part of the work has been funded within the framework of the European CleanSky2 Joint Technology Initiative – Airframe (Grant Agreement Number CS2JU-AIR-GAM-2014-2015-01 Annex 1, Issue B04, October 2nd, 2015) being part of the Horizon 2020 research and innovation framework programme of the European Commission.

References

Fezans, N. *et al.* (2020) 'Designing and Maturating Doppler Lidar Sensors for Gust Load Alleviation: Progress Made Since AWIATOR', in. *Aerospace Europe Conference 2020*, Bordeaux, France.

Fezans, N. and Joos, H.-D. (2017) 'Combined Feedback and LIDAR-Based Feedforward Active Load Alleviation', in *AIAA Atmospheric Flight Mechanics Conference*. Denver, Colorado: American Institute of Aeronautics and Astronautics. doi: 10.2514/6.2017-3548.

Fezans, N., Joos, H.-D. and Deiler, C. (2019) 'Gust load alleviation for a long-range aircraft with and without anticipation', *CEAS Aeronautical Journal*, 10(4), pp. 1033–1057. doi: 10.1007/s13272-019-00362-9.

Franken, P., Jenney, J. and Rank, D. (1966) 'Airborne investigations of clear-air turbulence with laser radars', *IEEE Journal of Quantum Electronics*, 2(4), pp. 147–147. doi: 10.1109/JQE.1966.1073867.

Herbst, J. and Vrancken, P. (2016) 'Design of a monolithic Michelson interferometer for fringe imaging in a near-field, UV, direct-detection Doppler wind lidar', *Applied Optics*, 55(25), p. 6910. doi: 10.1364/AO.55.006910.

Inokuchi, H., Akiyama, T. and Sasaki, K. (2018) 'Flight demonstration of a long range onboard Doppler lidar', in *31st Congress of the International Council of the Aeronautical Sciences (ICAS 2018)*, pp. 3960–3966.

Khalil, A. and Fezans, N. (2021) 'A multi-channel H_∞ preview control approach to load alleviation design for flexible aircraft', *CEAS Aeronautical Journal*, 12(2), pp. 401–412. doi: 10.1007/s13272-021-00503-z.

Rabadan, G. J. *et al.* (2010) 'Airborne Lidar for Automatic Feedforward Control of Turbulent In-Flight Phenomena', *Journal of Aircraft*, 47(2), pp. 392–403. doi: 10.2514/1.44950.

Schmitt, N. P. *et al.* (2007) 'The AWIATOR airborne LIDAR turbulence sensor', *Aerospace Science and Technology*, 11(7–8), pp. 546–552. doi: 10.1016/j.ast.2007.03.006.

Vrancken, P. *et al.* (2016) 'Airborne forward-pointing UV Rayleigh lidar for remote clear air turbulence detection: system design and performance', *Applied Optics*, 55(32), p. 9314. doi: 10.1364/AO.55.009314.

Vrancken, P. (2016) 'Airborne remote detection of turbulence with forward-pointing LIDAR', in Sharman, R. and Lane, T. (eds) *Aviation Turbulence*. Springer International Publishing. doi: 10.1007/978-3-319-23630-8.

Vrancken, P. and Herbst, J. (2019) 'Development and Test of a Fringe-Imaging Direct-Detection Doppler Wind Lidar for Aeronautics', in *EPJ Web of Conferences. 29th International Laser Radar Conference*, Hefei, People's Republic of China.

Vrancken, P. and Herbst, J. (2020) 'A Novel Direct-Detection Doppler Wind Lidar Based on a Fringe-Imaging Michelson Interferometer as Spectral Analyzer', in *European Lidar Conference*. Granada, Spain (online).

Development of a satellite altimeter for the planetary defence program HERA

L. Belegante[1], ***A. Nemuc***[1], *T. Sousa*[2], *V. Granadeiro*[2] *P. Gordo*[3]
((1) National Institute of Research and Development for Optoelectronics, INOE,409 Atomistilor Str, Magurele, Romania, belegantelivio@inoe.ro
(2) Efacec Power Solutions, Apartado 1018 · 4466-952 S. Mamede de Infesta · Portugal
(3) Synopsis Planet - Advance Engineering, Unipessoal, Lda. RUA AQUILINO RIBEIRO, 16 6ºdto. 2810-174, ALMADA Portugal

Introduction

Hera is an European project contributing to an international double-spacecraft collaboration between NASA and ESA: AIDA: The Asteroid Impact Deflection Assessment cooperation, is the first planetary defence mission [ESA website].
The Hera mission aims to deploy a satellite to a binary asteroid system – the Didymos pair of near-Earth asteroids. The 780 m-diameter mountain-sized main body is orbited by a 160 m moon, called 'Didymoon'. NASA will first perform a kinetic impact on the smaller of the two bodies – called DART collision – then, two years later, Hera will follow-up with a detailed post-impact survey that will turn this grand-scale experiment into a well-understood and repeatable planetary defence technique, transforming this large-scale experiment into a technique that will divert asteroids whenever required [ESA website].
During the mission, Hera will demonstrate multiple novel technologies, such as autonomous navigation around the asteroid and gather crucial scientific data, to help scientists and future mission planners better understand asteroid compositions and structures. One of the instruments used for this task is a state-of-the-art altimeter used to collect information about the new orbit of the body after the impact.
The altimeter (PALT) developed by the current consortium will make it possible to study the asteroid orbit precisely measuring the distance to the asteroid [link]. PALT will be one of the fundamental tools for achieving Hera's objectives: the LIDAR (Light Detection And Ranging) altimeter, capable of measuring distances of up to 20 km with an accuracy of 10 cm.
The consortium of the project is composed of two Portuguese companies (EFACEC and Synopsis Planet), two Romanian members (Efacec-Romania and INOE) and a Latvian company (Eventech).
The challenges of the project rely in the size, weight and power consumption limitations – typical for all space missions. The concept design of the altimeter was based on a singular telescope and a bi-axial setup.

Optical design

Receiver:

One of the factors influencing the optical design is the size of the optical length. This length is limited by the size of the instrument. Roughly, the dimension of the altimeter enclosure will be around 100 x 120 x 100 mm. The size of the enclosure will limit both the optical length but also the size of the telescope. The initial optical design was focused on a 100 mm diameter primary mirror and optical length of 80 mm inside the altimeter box. The length of the optical path was increased to ~200 mm due to difficulties in designing an optical setup that should be able to focus the 100 mm image of the primary mirror to the sensitive area of the detector (200 microns). The design should be able to resolve an extended dynamic range: 100 m to 20 km. After several simulations and the power budget and the required overlap, the final design was based on a 70 mm telescope and a total optical path of 240 mm – Figure 1.

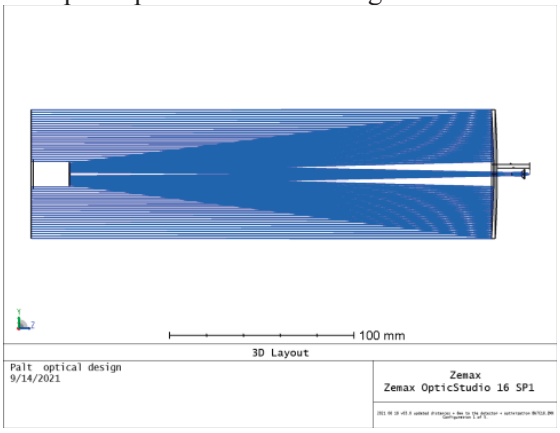

Figure 1: Overall optical design of PALT

The optical design employs a Cassegrain telescope and a condenser lens able to focus the entire image of the primary to the 200 microns detector for all distances required during the mission – Figure 2.

The main optical parameters of the altimeter

Laser divergence (after 10x expansion): 1,1 mrad
Laser diameter (after 10x expansion): 10 mm
Separation between laser and telescope: 35 mm
Telescope FoV: 1,3 mrad
Emission wavelength: 1532 nm

Primary
Concave mirror
Primary mirror diameter: 70 mm
Primary mirror interior diameter: 13 mm
Primary mirror radius = -550 mm
Secondary
Convex mirror
Secondary mirror diameter: 13 mm
Secondary mirror radius = -111 mm

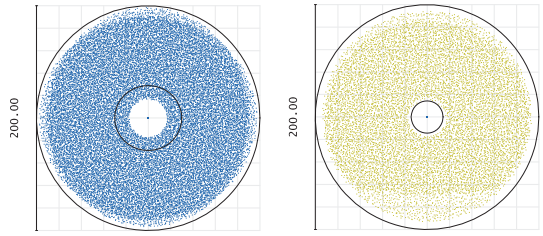

Figure 2: Field spot diagram for the 200 microns sensitive area of the detector. Left: light collected from 15 km; Right: light collected from 200 m.

In the current design, the overlap of the instrument starts around 70 m reaching the 90% limit to 500 m. The full overlap of the instrument is reached at 1280 m – Figure 3.

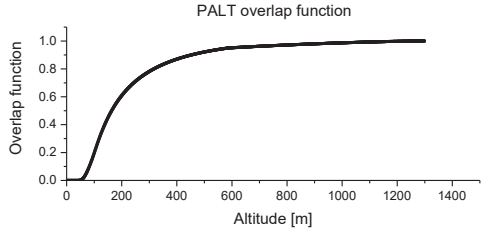

Figure 3. Overlap function of the PALT altimeter in the current design: 70 mm telescope, 1.3 mrad telescope FoV, 1.1 mrad laser divergence - full width and a 90 mm separation between emission and receiver axes.

Emission:

The emission design is based on a Galilean design made of one bi-concave lens and a plano convex lens placed 90.51 mm apart – Figure 4. The emission will expand the laser beam spot 10x, reducing the laser divergence to 1 mrad. The field spot diagram of the emitted light indicates an additional divergence of 0.1 mrad.

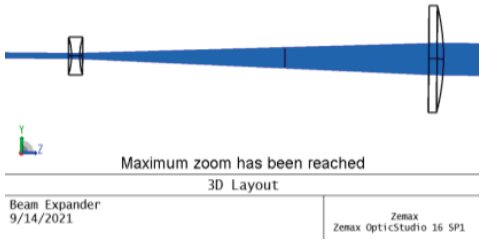

Figure 4. Emission design of PALT

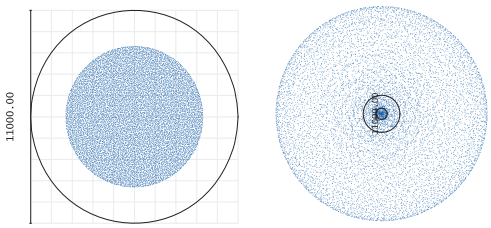

Figure 5. Field spot diagram for image Left: 1 m and Right: 10 km

Current status

Currently the first prototype of the altimeter is assembled. The altimeter will be subject to a series of quality assurance tests designed to validate the nominal performance of the unit. By the end of next year, a second space qualified prototype will be developed. This prototype will be designed to accommodate space qualified materials. The new unit will operate over a wide temperature domain (-40, 70 °C) and will include an additional baffle designed to protect the instrument for stray light and direct sun illumination.

Challenges

Main challenges of the design are related to the size, weight limitations but also to the detector size and operating range. Additional baffles were required to protect the instrument from unwanted light. Thermal constrains were also considered in the design.

Conclusions

The paper will present the current developments and test results of the first PALT prototype altimeter. The experience gained during the design and manufacturing of the PALT units will help the team develop the space qualified unit used in the HERA mission.

Acknowledgements

This research was funded by the Romanian National Core Program Contract No.18N/2019; by the European Regional Development Fund through the 306 Competitiveness Operational Programme 2014–2020, POC-A.1-A.1.1.1-F—2015, project CEO-Terra, by a grant of the Romanian Ministry of Education and Research, CCCDI - UEFISCDI, within PNCDI III, contract No.259/2020 and Helena ESA contract number 4000125526/18/NL/AR/zk

References

https://directory.eoportal.org/web/eoportal/satellite-missions/content/-/article/hera#foot1%29

https://ptspace.pt/planetary-defence-is-worth-portuguese-companies-eur-2-9-million/

Fixed and mobile Multi-wavelength Raman lidar at CNR-IMAA in Potenza in the frame of ACTRIS

***B. De Rosa*[1]**, *A. Amodeo*[1], *G. D'Amico*[1] ,*A. Giunta*[1] , *L. Mona*[1] *D. Summa*[1]
benedetto.derosa@imaa.cnr.it
Consiglio Nazionale delle Ricerche – Istituto di Metodologie per l'Analisi Ambientale CNR-IMAA, C.da S. Loja, Potenza, Italy

Introduction

The aerosol profile component of the ACTRIS (Aerosol clouds and Trace Gases Research infrastructure) has been built around the EARLINET (European Aerosol Research Lidar Network) network, the first lidar network for aerosol studies on a continental scale. Starting from very heterogeneous lidar stations in terms of system set-up and data processing, large efforts were done over the years for gaining in harmonization of the data processing and provision (1,2). Nowadays, ACTRIS/EARLINET has reached a degree of maturity that makes it suitable for near real time data provision.
The functionality of ACTRIS is based on a large number of National Facilities (NFs) distributed over Europe.
National Facilities within ACTRIS consist of Observational and Exploratory Platforms. Observational Platforms are fixed ground-based stations that heave regular measurement schedule and deliver long-term data.
Exploratory Platforms are platform laboratory, atmospheric simulation chambers, and mobile platforms that aim at investigating processes related to aerosols, clouds and reactive trace gases in dedicated experiments in specific regions, with a focus on particular scientific questions.
ACTRIS Observational Platforms must support at least one of the observational components, aerosol remote sensing, cloud remote sensing, reactive trace gases remote sensing, aerosol in situ measurements, cloud in situ measurements, and reactive trace gases in situ measurements.
The minimum setup of an ACTRIS aerosol remote-sensing station consists of a one-wavelength Raman or HSR lidar with polarization discrimination capability and a sun/sky photometer.
The IMAA CNR has recently installed two lidar systems, one fixed and one mobile. The first will be an ACTRIS Observational Platforms and the second an Exploratory Platforms available even in combination with cloud remote sensing equipment.
Both the lidars are capable of carrying out continuous measurements going well beyond the required ACTRIS/EARLINET standards.
The mobile system has the characteristics to be part of the central facility CARS (Center for Aerosol Remote Sensing), AHL-aerosol high power lidar.(3)
Furthermore the fixed system is equipped with additional measurement channels to carry out water vapour measurements, of interest for investigating the impact of water vapour on aerosol properties,
.

Systems overview

The fixed lidar is hosted in a thermally insulated container and is also equipped with a dedicated weather station. The systems can be controlled by remote access via Internet. Measurements are automatically stopped in case of rain events and restart after 10 minutes.
The fixed lidar, shown in figure 1, is based of two laser sources. One laser emits only at 1064 nm, allowing to optimize the aerosol depolarization measurement at this wavelegth.
The energy is 150 mJ with a repetition frequency of 10 Hz and a divergence < 1.2 mrad.
The second has an energy of 200 mJ at 355 and at 532 nm of 100 mJ. The repetition frequency is 10 Hz and the divergence is < 1.2 mrad for all wavelengths. The system includes two Cassegrain telescopes, one with a larger diameter (400mm) for the far range and one for the near range with a diameter of 200 mm allowing to reach a full overlap altitude at 200 m .
The calibration and the telecover measurements are motorized and therefore remotely controllable .
It is present also a CCD camera to test the alignment of all laser beams sent into the atmosphere.
This lidar has technical characteristics better than those required by ACTRIS for being a National Facility (NF).
It will be able to provide continuous measurements of aerosol backscattering at 355, 532 and 1064,

aerosol extinction coefficients at 355 and 532 nm, volume and particle depolarization ratio at 355, 532 and 1064 nm and water vapour mixing ratio in the planetary boundary layer region and in the free troposphere.

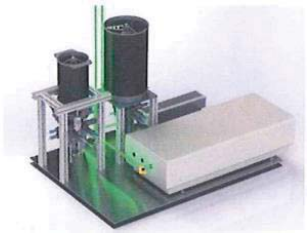

Figure 1. Fixed lidar sysrem

The mobile lidar is hosted in a container similar to the previous one, but smaller and easier to be transported. The mobile system (Fig.2) has been developed for continuous, stand-alone operation in remote environments. Also this system has two laser source. One laser emits only at 1064 nm, allowing to optimize the aerosol depolarization measurement at this wavelegth.
The first laser has an energy at 1064 nm grater than 150 mJ with a repetition frequency of 10 Hz and a divergence < 1.2 mrad. The second has an energy > of 90 mJ at 355 and at 532 nm > of 80 mJ. The repetition frequency is 10 Hz and the divergence is < 1.2 mrad for all wavelengths. The receiver is built around a telescope in Cassegrain configuration (30-cm diameter).
It will be able to provide continuous measurements of backscattering at 355, 532 and 1064 nm, extinction coefficients at 355 and 532 nm, depolarization coefficient at 355, 532 and 1064 nm.

Figure 2. Mobile lidar sysrem

In the next months, the systems will become fully operational and the fixed measurements will be integrated within the ACTRIS aerosol profile provision to CAMS. In December 2019, a contract between CNR and ECMWF was signed for a pilot ACTRIS/EARLINET data provision to the Copernicus Atmosphere Monitoring Service (CAMS). Such pilot contract (CAMS21b) aims to put in place a first data provision for a set of selected stations with the aim to demonstrate the feasibility of fully traceable and quality-controlled data provision for the whole network.
The data provision started in October 2020 at the test site of Potenza with the lidar MUSA and in January 2021 for a group of 9 stations with encouraging results.
The continuous measurements made by the described new systems will be important to improve the assimilation, near real time evaluation and re-analysis evaluation of several CAMS products, including the aerosol load over Europe for air quality issues, atmospheric composition, climate forcing and solar and UV products.
Continuous measurements allow to better understand the evolution of meteorological phenomena.
The two systems are in optimization phase and during the conference first measurements will be shown highlighting the capability of this instrument to perform continuous high-resolution measurements of aerosols and atmospheric water vapour , both in daytime and nighttime,

References

Pappalardo, G., Amodeo, A., Apituley, A., Comeron, A., Freudenthaler, V., Linné, H., Ansmann, A., Bösenberg, J., D'Amico, G., Mattis, I., Mona, L., Wandinger, U., Amiridis, V., Alados-Arboledas, L., Nicolae, D., and Wiegner, M.: EARLINET: towards an advanced sustainable European aerosol lidar network, Atmos. Meas. Tech., 7, 2389–2409, 25 doi:10.5194/amt-7-2389-2014, 2014. 7738, 7739 .

Freudenthaler, V., Groß, S., Engelmann, R., Mattis, I., Wandinger, U., Pappalardo, G., Amodeo, A., Giunta, A., D'Amico, G., Chaikovsky, A., Osipenko, F., Slesar, A., Nicolae, D., Belegante, L., Talianu, C., Serikov, I., Linne, H., Jansen, F., Wilson, K., de Graaf, M., Apituley, A., Trickl, T., Giehl, H., and Adam, M.: EARLI09 – direct intercomparison of eleven 10 EARLINET lidar systems, in: Proceedings of the 25th International Laser Radar Conference, 5–9 July 2010, St.-Petersburg, Russia, ISBN978-5-94458-109-9, 891–894, 2010. 7739.

Ulla Wandinger, Doina Nicolae, Gelsomina Pappalardo, Lucia Mona, Adolfo Comerón-ACTRIS and ist aerosol remote sensing component https://doi.org/10.1051/epjconf/202023705003 EPJ Web Conferences 237, 05003 (2020).

LinktoCAMS:http://www.ciao.imaa.cnr.it/index.php?option=com_content&view=article&layout=edit&id=248&Itemid=317.

Development and Validation of a Scanning Depolarization Lidar System for Studying Urban Aerosols in a Tropical Valley

M. Hoyos-Restrepo[1], *E. Montilla-Rosero*[1]
mhoyosr4@eafit.edu.co
(1) Applied Optics Group, Universidad EAFIT, Cra. 49 N. 7 Sur - 50, Medellín, Colombia

Introduction

The Aburra Valley, the second-largest urban agglomeration in Colombia in terms of population and economy, is located in the Colombian Central Andes between geographic coordinates 6°30'25" to 6°17'2" N and 75°40'5" to 75°13'30" W. The altitudes of the Valley vary between 1,300 and 3,100 m above sea level. The Valley is 60 km long, being the city of Medellin its wider part with 8–10 km (See Figure 1). Temperature oscillates between 16 and 29 °C, and relative humidity is about 70%. Thus, the region is characterized by a humid, tropical climate (Posada and Cadavid, 2018).

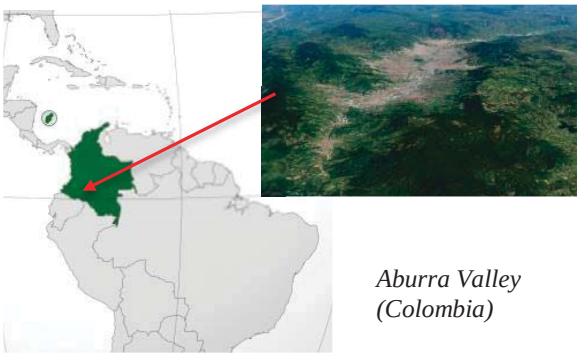

Figure 1. Measurement site location.

Due to its large population (near 4 million ihabitants), complex topographic and meteorological conditions, and the high pollution levels coming from industries and vehicle fleet, the Aburra Valley has a severe air quality problem. In fact, air pollution caused 22,922 deaths from pollution-related acute respiratory diseases in Medellin between 2012 and 2016 (Comptroller General of Medellin and Universidad Nacional de Colombia, 2019). For this reason, real-time monitoring of particulate matter to identify pollution sources is one of the main directions for environmental improvement issued by government authorities.

Lidar is an adequate technique to study these highly variable atmospheric constituents (Rascado, 2008). In addition, the depolarization lidar technique allows for retrieving the linear depolarization ratio, a primary parameter to differentiate between spherical and non-spherical particles, which, combined with other aerosol optical properties, allows aerosol-typing studies. Although there are currently existing lidars in the region, these only perform vertical measurements at ground level; the volumetric or three-dimensional information, which reflects the dynamic nature of pollution, remains a question to answer.

In this work, we have designed, developed, calibrated, and validated a scanning depolarization lidar system, which we will use to analyze the three-dimensional spatial distribution and identify fixed sources of urban pollution in the Aburra Valley by determining the optical properties of local aerosols.

Results and discussion

The developed scanning depolarization lidar system is shown in Figure 2. It can take horizontal, vertical, and volume scans of the atmosphere using elevation and azimuth stepper motors (NEMA 23, 2.8 A, 18 kg-cm) and gearboxes (1:80 for elevation and 1:30 for azimuth movement). To achieve a complete atmospheric mapping the lidar system takes 360.00 ± 0.35° azimuth and 90.00 ± 0.82° elevation scanning.

Figure 2. Photo of the developed scanning lidar.

The technical specifications of the lidar system are presented in Table 1. Our lidar system's robust and modular setup required that optical, electronic, and mechanical components were carefully selected. As a result, most parts of the mechanics and

optomechanics were produced by manual and CNC machining. This allows for cost-effective and flexible modifications of the mechanical components and mountings of optical subsystems if the system needs to be adjusted or upgraded to new scientific requirements.

Table 1. Technical specifications of the scanning depolarization lidar system.

Characteristic	Value
Laser	Q-switched Nd:YAG
Repetition rate	20 Hz
Enery per pulse	200 mJ (@532)
Pulse length	6 ns (@1064)
Divergence	<0.5 mrad
Receiver	
Telescope	Schmidt-Cassegrain (9.25")
Detectors	PMT (300 – 900 nm)
Interference filter	2.00 nm FWHM (@532)
Polarization separator	Polarizing beam splitter (PBS)
Data acquisition	LICEL, 16 bit and 40 MHz A/D converter
Range Resolution	3.75 m

The lidar system is being tested under field conditions performing quality assurance tests to characterize the performance of the hardware and to provide quality-assured data sets of products for the characterization of aerosols not only as a function of height but also of the spherical coordinates. The next results will show the scanning lidar measurements in a horizontal view at different increasing elevation angles using range corrected signals and the first result of the relative attenuated aerosol backscatter coefficient profiles at parallel and perpendicular channels, as well as linear depolarization ratio profiles, during the middle of the local dry season (July and August).

Challenges

In the upcoming months, the challenge will be to perform volume scans of the local atmosphere to analyze the three-dimensional spatial distribution and identify fixed sources of urban pollution in the Aburra Valley by determining the backscattering coefficient and linear depolarization ratio at several different spherical coordinates of local aerosols.

Acknowledgements

This work was supported by the Universidad EAFIT project 954-000003: 4DAir-MISDAM - *Estudio 3D +1 de polución atmosférica*, and the MINCIENCIAS project 1150-852-71525 - 4DAir-MOLIS.

References

Comptroller General of Medellín and Universidad Nacional de Colombia campus Medellín. Physical and economic quantification of the impact of air pollution on the health of the population of the city of Medellín (In Spanish: *Cuantificación física y económica del impacto de la contaminación atmosférica en la salud de la población de la ciudad de Medellín*). 2019.

Guerrero-Rascado.Técnica LIDAR para la caracterización atmosférica mediante dispersión elástica y Raman. PhD thesis, Universidad de Granada, 2008

Posada and Cadavid. Analysis of the temperature changes in the Aburrá Valley between 1995 and 2015 and modeling based on urban, meteorological and energetic parameters. Climate 6(2), 21, 2018.

Laboratory evaluation of the (UV,VIS) lidar depolarization ratio of pure pollen grains at exact backscattering angle

D. Cholleton[1,2], *E. Bialic*[2], *A. Dumas*[2], *P. Kaluzny*[2], *P. Rairoux*[1], *A. Miffre*[1]
danael.cholleton@univ-lyon1.fr
(1) University of Lyon, Université Claude Bernard Lyon 1, CNRS, Institut Lumière Matière, F-69622, VILLEURBANNE, France
(2) TERA Sensor, ZI Rousset, 296 Avenue Georges Vacher, 13790, Rousset, France

Introduction

Pollens are incriminated for their impact on the Earth's climate and on public health with socio-economical costs reaching 150 billion euros per year in Europe (Lake et al., 2017). Still, the detection and identification of the involved pollens taxa remains challenging, mainly due to the complexity in size and shape of these grains.

Studies have been achieved to investigate pollens using lidar remote sensing (Sassen, 2008; Noh et al., 2013; Bohlmann et al., 2019; Sicard et al., 2021), by evaluating the depolarization ratio of particle mixtures containing pollen grains. Current methods are based on assuming a zero value for the backscattering Ångström exponent of pure pollens (Shang et al., 2020) to deduce the lidar depolarization ratio of pure pollens.

In this context, a laboratory polarimeter at lidar backscattering angle has been developed which precisely evaluates the lidar depolarization ratio of several pure pollen (Cholleton et al., 2020).

Experimental set-up

The evaluation of the depolarization ratio relies on a unique laboratory polarimeter, as shown in Figure 1. The polarization state of the backscattered radiation is analysed in the framework of the Muller matrices and Stokes vectors formalism, which allows precise evaluation of the depolarization ratio, in the percent range, as detailed (Miffre et al., 2016).

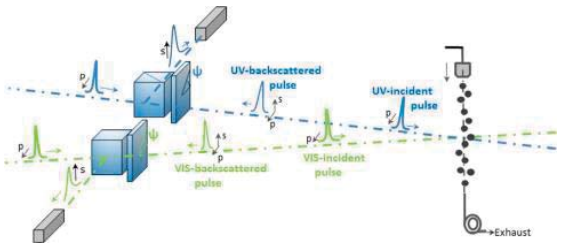

Figure 1. UV-VIS laboratory polarimeter for addressing the depolarization ratio of pure pollen grains embedded in ambient air.

The particle depolarization ratio of the following pollen taxa have hence been measured in laboratory: ragweed (*ambrosia artemisiifolia)*, ash (*fraxinus americana)*, birch (*betula pendula)*, pine (*pinus strobus)*, cypress (*cupressur sempervirens)* and spruce (*picea abies),* which are either amongst the most allergenic pollens.

Results

Figure 2 shows the backscattered (UV, VIS) intensity by ragweed pollen grains in ambient air when varying the angle of the polarization analyser. By precisely adjusting the datapoints with the scattering matrix formalism, the lidar depolarization ratio of these pollens can be retrieved. Interestingly, this methodology allows revealing the intrinsic depolarization of pure pollens and moreover their spectral dependence.

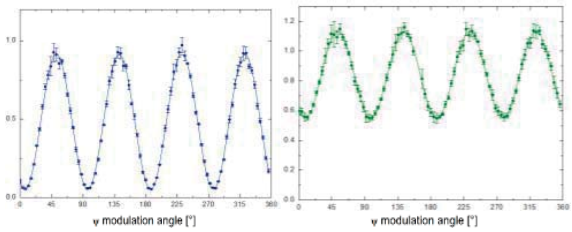

Figure 2. Detected scattered intensity by ragweed pollen grains as a function of the rotation angle of the polarization analyser at wavelength UV (left) and VIS (right). The evaluation relies on 180 measurement points, hence ensuring a precise evaluation of the particle depolarization ratio.

Following the methodology detailed in (Miffre et al., 2016), the particle depolarization ratio of ragweed pollen grains is evaluated to

$$PDR(\lambda_{UV}) = (5.3 \pm 0.2)\%$$
$$PDR(\lambda_{VIS}) = (32.5 \pm 1.5)\%$$

Similarly, the depolarization ratio of the other considered pollen taxa have been evaluated in laboratory and will be presented in the poster. The retrieved depolarization ratio at specific backscattering angle may be applied to invert multi-wavelength polarization remote sensing measurements.

References

Bohlmann, S., Shang, X., Giannakaki, E., Filioglou, M., Saarto, A., Romakkaniemi, S., and Komppula, M.: Detection and characterization of birch pollen in the atmosphere using a multiwavelength Raman polarization lidar and Hirst-type pollen sampler in Finland, Atmos. Chem. Phys., 19, 14559–14569, https://doi.org/10.5194/acp-19-14559-2019, 2019.

Cholleton, D., Bialic, E., Dumas, A., Kaluzny, P., Rairoux, P., and Miffre, A.: Laboratory evaluation of the (VIS, IR) scattering matrix of complex-shaped ragweed pollen particles, Journal of Quantitative Spectroscopy and Radiative Transfer, 254, 107223, https://doi.org/10.1016/j.jqsrt.2020.107223, 2020.

Lake, I. R., Jones, N. R., Agnew, M., Goodess, C. M., Giorgi, F., Hamaoui-Laguel, L., Semenov, M. A., Solomon, F., Storkey, J., Vautard, R., and Epstein, M. M.: Climate Change and Future Pollen Allergy in Europe, Environmental Health Perspectives, 125, 385–391, https://doi.org/10.1289/EHP173, 2017.

Miffre, A., Mehri, T., Francis, M., and Rairoux, P.: UV–VIS depolarization from Arizona Test Dust particles at exact backscattering angle, J. Quant. Spectrosc. Radiat. Transf., 169, 79–90, https://doi.org/10.1016/j.jqsrt.2015.09.016, 2016.

Noh, Y. M., Müller, D., Lee, H., and Choi, T. J.: Influence of biogenic pollen on optical properties of atmospheric aerosols observed by lidar over Gwangju, South Korea, Atmos. Environ., 69, 139–147, https://doi.org/10.1016/j.atmosenv.2012.12.018, 2013.

Sassen, K.: Boreal tree pollen sensed by polarization lidar: Depolarizing biogenic chaff, Geophys. Res. Lett., 35, https://doi.org/10.1029/2008GL035085, 2008.

Shang, X., Giannakaki, E., Bohlmann, S., Filioglou, M., Saarto, A., Ruuskanen, A., Leskinen, A., Romakkaniemi, S., and Komppula, M.: Airborne pollen observations using a multi-wavelength Ramanpolarization lidar in Finland: characterization of pure pollen types, Aerosols/Remote Sensing/Troposphere/Physics (physical properties and processes), https://doi.org/10.5194/acp-2020-794, 2020.

Sicard, M., Jorba, O., Ho, J. J., Izquierdo, R., De Linares, C., Alarcón, M., Comerón, A., and Belmonte, J.: Measurement report: Characterization of the vertical distribution of airborne Pinus pollen in the atmosphere with lidar-derived profiles: a modelling case study in the region of Barcelona, NE Spain, Aerosols/Remote Sensing/Troposphere/Physics (physical properties and processes), https://doi.org/10.5194/acp-2021-235, 2021.

Dual Comb Spectroscopy (DCS) for Atmospheric Trace Gas Detection Towards DCS in the UV range.

C.Pivard[1], S.Galtier[1], P.Rairoux[1]
sandrine.galtier@univ-lyon1.fr
1-University of Lyon, Université Claude Bernard Lyon 1, CNRS, Institut Lumière Matière, F-69622, Villeurbanne, France

Introduction

The development of more sensitive and robust instruments and new methodologies are essential to improve our understanding of the Earth's climate and air pollution. In this context, Dual comb spectroscopy method has been successfully demonstrated as a remote laser-based instrument to probe infrared absorbing species (H2O, CO2 and CH4) [Oudin2019-Rieker2014].

We here present a simulation study on the expected sensitivity of Dual-Comb spectroscopy in the UV range and an original instrumental development for Dual Comb spectroscopy in a view to monitoring the highest reactive species of the atmosphere in the UV range. The DCS methodology is presented in Figure 1. DCS is a Fourier transform spectroscopy method that takes advantage of the coherent mixing of mutually coherent two femtosecond trains of pulses. The DCS allows the acquisition of a wide spectrum (several tens of THz in the IR) with a high acquisition rate (≈1kHz), which makes it possible in particular to drastically reduce the impact of atmospheric turbulence on the sensitivity of the instrument. As demonstrated in the IR range [Rieker14], the extremely fast acquisition rate of DCS makes it particularly suitable for remote detection in the turbulent outdoor atmosphere.

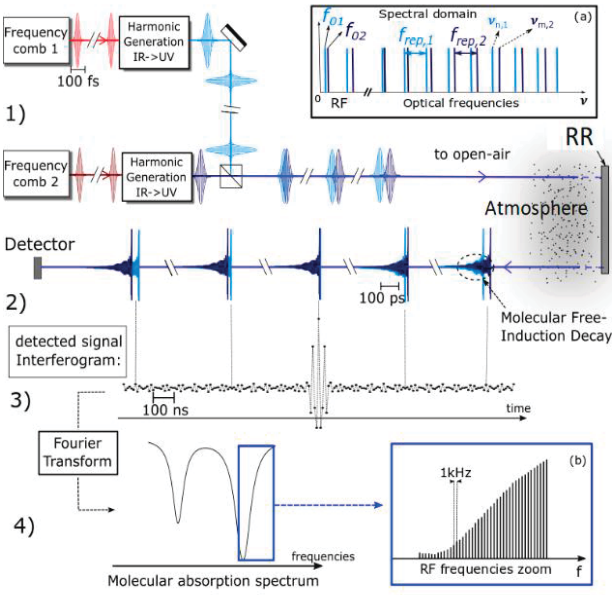

Figure 1. UV-DCS principle

Result and discussion 1: Simulation study on expected sensitivity of UV-DCS

A theoretical and numerical work has been realized to assess the feasibility of the DCS method in real atmospheric conditions [Galtier2020]. We showed that a suitable UV-DCS spectrometer must be based on Titanium:sapphire frequency combs which would provide the requested relative coherence and high enough power for an atmospheric remote application in the UV range.

The propagation of the UV femtosecond pulses into the atmosphere was assessed. The amplitude and phase fluctuations induced by atmospheric turbulence on the pulse trains were determined to be negligible for acquisition rates higher than 130 Hz, which can be easily achieved using DCS.

The minimum absorption sensitivity (MAS) of atmospheric molecules of interest OH, BrO, NO_2, OClO, HONO, CH_2O, SO_2, defined as $(\alpha_0 L)_{min}$, accessible by UV-DCS were estimated in two case studies (see Table 1). Case study 1 is centred at 308 nm (1nm wide) and case study 2 is centred at 350 nm (10 nm wide).

Table 1. Estimated sensitivity of UV-DCS.
Quality factor Q : SNR per spectral element at 1 second and corresponding to a minimum absorption sensitivity (MAS) using optimised parameters frep and Δfrep.

Case-study	Q	(frep ; Δfrep vres)	MAS
1 (308nm)	10^6	(100 MHz; 200 Hz; 2.5 GHz)	0.0021 *(OH: 0.001)
2 (350 nm)	2.10^6	(200 MHz; 200 Hz; 5 GHz)	0.031

The concentration detection limit for 2 km light path and 200 s averaging time using the UV-DCS were determined for these molecules and are given in Table 2.

The relative intensity noise (RIN) of the laser source has been identified as the main limiting source of noise of UV-DCS. We showed that UV-DCS could offer a novel remote-sensing instrument for *in situ* detection of UV absorbing trace gases, addressing the issue of the current lack of broadband remote-sensing instrument in the UV

range. We believe that this study provides a first framework for future experimental demonstrations of trace-gas remote detection in the UV range using DCS.

Table 2. Estimated concentration detection limit for 2 km light path and 200 s averaging time using UV-DCS.

Case-study	Molecule	Det limit (ppt)
1	SO2	260
	CH2O	210
	C10H8	20
	OH	0.08
2	NO2	1600
	HONO	1000
	BrO	38
	OClO	38

Result and discussion 2: The light source: Bidirectionnal TiSa laser

A homemade bidirectional Ti:sa mode-locked laser cavity was realised in our laboratory in a view to performing DCS measurements in the atmosphere in the UV range. A schema of the cavity is given in Figure 2. The main advantage of the use of a single cavity is the generation of two trains of pulses that are intrinsically mutually coherent with no need of active stabilization, as previously demonstrated [Idegushi2016]. 300 mW of averaged mode- locked output power laser was obtained in each direction (total of 600 mW) using a laser pump power of 5.5 W.

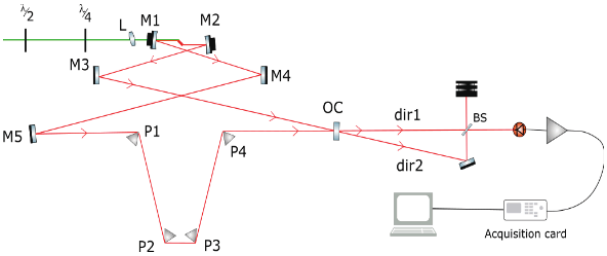

Figure 2. Home-made bidirectional Ti:sa laser cavity and DCS acquisition setup (OC: output coupler, BS: beam splitter)

Several successive interferograms were measured (Figure 3a) from the detection of the two superposed laser combs. The spectrum obtained from the FFT of one interferogram reproduces with high accuracy the spectrum obtained with a grating spectrometer (figure 3b). The spectrum obtained from the Fourier Transform of a time windows of 330 ms (composed of eight interferograms) shows the RF comb structure, which would indicate a high relative coherence of the laser source over such a duration. To our knowledge, this coherence over this length of time has never been reached with a similar Ti:sa free-running system.

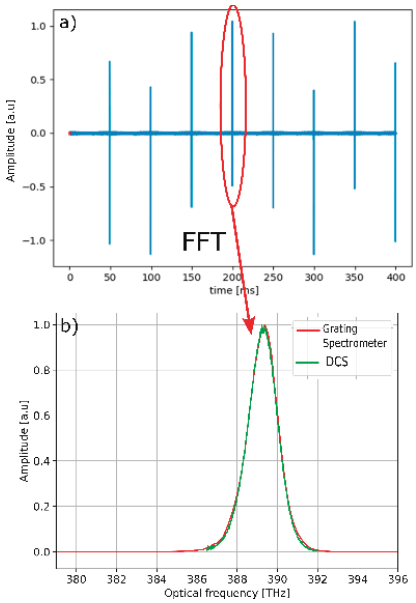

Figure 3. a) Temporal trace representing eight interferograms measured. b) Spectrum (green curve) retrieved from the FFT of one interferogram circled in panel a compared with a spectrum obtained with a grating spectrometer (red curve)

Challenges

The next challenges lie in improving the sensitivity of the home-made DCS spectrometer. Improvement of the SNR can be obtained via a dedicated laser housing, balanced detection and using *a posteriori* or *direct* correction of the residual phase noises between the two trains of pulses.

Conversion into the UV range via second harmonic and third harmonic generation in the non-linear crystal will be then realised in a view to measure atmospheric trace gas concentration in the UV range for a new UV-DCS remote-sensing instrument.

References

[Galtier2020] Galtier, S.; Pivard, C.; Rairoux, P.. Remote Sens., 12, p.3444 (2020).

[Idegushi2016] Ideguchi, T., Nakamura, T., Kobayashi, Y., & Goda, K. (2016). Optica, 3(7), 748-753.

[Oudin2019] Oudin, J.; Mohamed, A.K.; Hébert, P.J. Proc. SPIE 11180, International Conference on Space Optics (12 July 2019)

[Rieker2014] Rieker, G.B.; Giorgetta, F.R.; Swann, W.C.; Kofler, J.; Zolot, A.M.; Sinclair, L.C.; Baumann, E.; Cromer, C.;Petron, G.; Sweeney, C.; et al. Optica 1, p. 290–298 (2014)

Session 2. Lidar Algorithms and Data Products

Microphysical particle parameter retrieval from Raman lidar: Arctic case study from the MOSAiC winter

C. Böckmann[1,2], C. Ritter[1], J. Dube[1]
christine.boeckmann@awi.de
(1)Alfred Wegener Institute for Polar and Marine Research, Research Department Potsdam, 14473 Potsdam, Telegrafenberg A43, Germany
(2)University of Potsdam, Institute of Mathematics, Karl-Liebknecht-Str. 24-25, 14476 Potsdam, Germany

Introduction

The Arctic is currently warming twice as fast as the rest of the globe. This phenomenon is called "Arctic Amplification". The role of aerosol to this warming is still unclear. The annual maximum of aerosol extinction occurs in spring time; this is called the "Arctic Haze" (Quinn et. al 2007). Even if over decades the Arctic Haze may decrease (Graßl, Ritter 2019) it is still important, as in spring due to high surface albedo and solar zenith angles the aerosol may produce a warming in the Arctic, even if the same aerosol produce a cooling at lower altitudes.

The international Arctic MOSAiC campaign (2019/20) should allow, thanks to numerous additional measurements of aerosol properties and meteorology in the central Arctic, a better understanding of aerosol composition and pollution pathways into the Arctic.

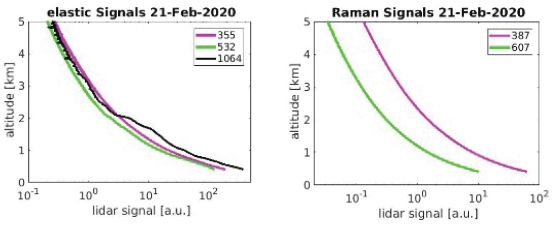

Figure 1. Lidar elastic and Raman signals from Ny-Ålesund (Spitsbergen, 78.9N, 11.9E).

Observation

In this work we report an Arctic Haze event, observed over the international research village of Ny-Ålesund on 21. Feb 2020 by the "3+2+2" Raman lidar KARL. The system consists of a spectra 290/50 laser, a 70cm telescope with about 2mrad fov and Licel electronics. It has been described by Hoffmann (2011).

The data was evaluated with 7.5m / 10min resolution according to Ansmann et al. (1992). High backscatter was found in the lowest 2km of the atmosphere. To allow a proper evaluation of the extinction (daylight conditions) the data was averaged over 1.5h. The first time refers to UT 13h40 – 15h10, while the second time is from UT 15h30 – 17h00. We selected the altitude between 1320m and 1580m a.s.l., as neither the color ratio nor the depolarization indicated any variability. Further, a local radiosonde measured moist conditions below 1km altitude, which may have led to hygroscopic growth.

Results and discussion

The lidar profiles for time 1 are shown in Figure 1. Due to the long temporal integration, the uncertainties of the extinction decreased to about 10% for 532nm and 5% for 355nm. We obtained lidar ratios (355nm / 532nm) of 38sr / 39sr for time 1 and 40sr / 45sr for time 2.

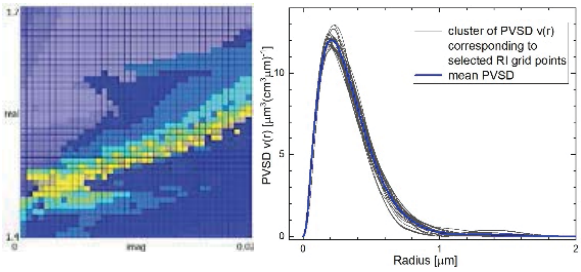

Figure 2. Layer 1 (UT 15h30 - 17h00) Left: Refractive index (RI) grid. Right: Inverted mean PVSD (blue line) mean of thin black lines, which are selected from a diagonal cluster of suitable complex RI grid points.

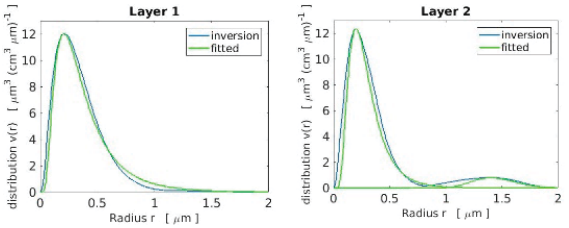

Figure 3. Layer 1(UT 15h30 - 17h00) and 2(UT 13h40 - 15h10) both same height (1320-1580m a.s.l.). Unrestricted inverted mean PVSD (blue line) and mono-modal log-normal fitted distribution (green line).

Next, the 5 independent coefficients of aerosol backscatter (355nm, 532nm, 1064nm) and extinction (355nm, 532nm) served as an input for a regularized inversion of the aerosol microphysical properties via truncated singular value decom-

position (Böckmann, 2001; Samaras et al., 2015; Müller et al., 2016).

Table 1. Retrieved microphysical parameters.[a]

Layer	1 (I)	1 (F)	2 (I)	2 (F)
RI real	1.51 ±0.03		1.52 ±0.03	
RI imag	0.014 ±0.01		0.012 ±0.01	
v_t	5.13 ±0.21		4.7 ±0.29	
s_t	70 ±1.9		67 ±1.1	
n_t		267		172
r_{eff}/r_{mod}	0.22 ±0.01	0.087	0.21 ±0.01	0.114
σ		1.92		1.68
SSA 355	0.905 ±0.06		0.921 ±0.04	
SSA 532	0.921 ±0.05		0.933 ±0.04	

[a] (I) Inverted, (F) Fitted .

The inversion of microphysical properties yielded a mono-modal particle size distribution, see Figures 2, 3, with refractive index values, and see Table 1, similar to previous long-range transported pollution and biomass-burning plumes (Stock et al., 2011; Nakoudi et al., 2020). The microphysical properties are as follows: total volume concentration v_t [$\mu m^3 cm^{-3}$], total surface area concentration s_t [$\mu m^2 cm^{-3}$], total number concentration n_t [cm^{-3}] and effective radius r_{eff} [µm] as well as single scattering albedo (SSA), see Table 1. Additionally, the median radius r_{mod} [µm] and the width σ (geometric standard deviation) of the mono-modal log-normal fits are given in Table 1. The very tiny coarse mode in layer 2 (with only n_t=0.034 cm^{-3}) is negligible and seems to be a mathematical artificial inversion effect.

In the following, we compare this event, to a case study of Arctic aerosol by Nakoudi et al (2020). In our example total volume, surface-area and number concentrations are smaller. Moreover, the fine mode particles are smaller with effective radius 0.22 and 0.21 µm against the different cases (0.19 µm to 0.49 µm) of Nakoudi et al. (2020).

However, the index of refraction of Arctic aerosol, which is generally difficult to be determined precisely, is very similar, around m= 1.5+0.01i.

As the single scattering albedo depends on m and size, this quantity is still only poorly defined – especially if possible hygroscopic growth/ shrinking acts on the aerosol.

Conclusion

Even if the inversion of lidar data is an ill-posed problem, so far we have observed stable results for Arctic Haze: the dominance of mono-modal distributions with m ≈ 1.5 +0.01i and r_{eff} ≈ 0.2µm. Therefore, lidar data should more regularly compared to in-situ measurements. Moreover, contemporary measurements between radiosondes and lidar (with strong gradients of relative humidity) may reveal any hygroscopic growth of the particles.

References

Quinn, P.K., Shaw, G., Andrews, E., Dutton, E.G., Ruoho-Airola, T. and Gong, S.L., Arctic haze: current trends and knowledge gaps, *Tellus B*, 59(1), 99-114, 2007.

Graßl, S.; Ritter, C. Properties of Arctic Aerosol Based on Sun Photometer Long-Term Measurements in Ny-Ålesund, Svalbard, *Remote Sens.* 11, 1362, 2019.

Ansmann A, Wandinger U, Riebesell M, Weitkamp C, Michaelis W. Independent measurement of extinction and backscatter profiles in cirrus clouds by using a combined Raman elastic-backscatter lidar. *Appl Opt.*, 31(33), 7113-7131, 1992.

C. Böckmann, Hybrid regularization method for the ill-posed inversion of multiwavelength lidar data to determine aerosol size distribution, *Appl. Opt.*, 40, 1329-1342, 2001.

Samaras, S., D. Nicolae, C. Böckmann, J. Vasilescu, I. Binietoglou, L. Labzovskii, F. Toanca, and A. Papayannis, Using Raman-lidar-based regularized microphysical retrievals and aerosol mass spectrometer measurements for the characterization of biomass burning aerosols, *J. Computational Physics*, 299, 156–174, 2015.

Müller, D., C. Böckmann, A. Kolgotin, L. Schneiden-bach, E. Chemyakin, J. Rosemann, P. Znak, and A. Romanov, Microphysical particle properties derived from inversion algorithms developed in the framework of EARLINET, *Atmospheric Measurement Techniques*, 9, 5007–5035, 2016.

Stock, M., Ritter, C., Herber, A., von Hoyningen-Huene, W., Baibakov, K., Graeser, J., Orgis, T., Treffeisen, R., Zinoviev, N., Makshtas, A. and Dethloff, K. Springtime Arctic aerosol: Smoke versus haze, a case study for March 2008. *Atmospheric Environment*, 52, 48-55, 2012.

K. Nakoudi, C. Ritter, C. Böckmann, D. Kunkel, O. Eppers, V. Rozanov, et al., Does the Intra-Arctic Modification of Long-Range Transported Aerosol Affect the Local Radiative Budget? (A Case Study), *Remote Sens.*,12 (13), 2112, 2020.

Statistical Intercomparison of Aeolus B10 SCA and SCAmb Backscatter Coefficient with Ground-Based Measurements of ACTRIS/EARLINET Stations in South-Western Europe

J. Abril-Gago[1,2], J.L. Guerrero-Rascado[1,2], M.J. Costa[3,4], J.A Bravo-Aranda[1,2], M. Sicard[5,6], D. Bermejo-Pantaleón[1,2], D. Bortoli[3,4], M-J. Granados-Muñoz[1,2], A. Rodríguez-Gómez[5], C. Muñoz-Porcar[5], A. Comerón[5], P. Ortiz-Amezcua[1,2,7], V. Salgueiro[3,4], M.M. Jiménez-Martín[1,2], L. Alados-Arboledas[1, 2]

jabrilgago@ugr.es

(1) Andalusian Institute for Earth System Research (IISTA-CEAMA), Granada, 18006, Spain

(2) Applied Physics Department, University of Granada, Granada, 18071, Spain

(3) Earth Remote Sensing Laboratory (EaRSLab), Évora, 7000-671, Portugal

(4) Institute of Earth Sciences (ITC) and Department of Physics, Évora, 7000-671, Portugal

(5) Department of Signal Theory and Communications, Universitat Politècnica de Catalunya, Barcelona, 08034, Spain

(6) Ciències i Tecnologies de l'Espai-Centre de Recerca de l'Aeronàutica i de l'Espai, Institut d'Estudis Espacials de Catalunya (CTE-CRAE/IEEC), Universitat Politècnica de Catalunya, Barcelona, 08034, Spain

(7) Faculty of Physics, University of Warsaw, Warsaw, 02-093, Poland

Introduction

Since 2018 the European Space Agency (ESA) is developing the Aeolus satellite mission, based on the ALADIN (Atmospheric Laser Doppler Instrument) wind lidar, encouraging large-scale dynamic studies through near real-time wind retrievals at global scale.

Besides wind profiles (L2B products), aerosol optical properties, known as L2A, are retrieved as spin-off products, such as particle backscatter and extinction coefficient profiles. Measurements are generated under specific data processing, called baselines, which are constantly being updated, and through different algorithms separately, such as SCA (Standard Correct Algorithm) and SCAmb (Standard Correct Algorithm middle bin), which differ in the way SCAmb bins are obtained (from two adjacent SCA bins, aiming to reduce noise). ALADIN emits circular-polarized radiation at 355 nm and receives the co-polar component of the signal, what will cause an underestimation of backscatter coefficients. A complete description of the instrument and the L2A products is given by Flamant et al. (2020).

In this work, we perform an intercomparison of Aeolus reprocessed B10 (baseline 10) SCA and SCAmb co-polar backscatter coefficients (β^{part}_{Aeolus}) with analogous ground-based measurements from the ACTRIS/EARLINET stations of Granada (Spain, 24 matching overpasses), Évora (Portugal, 15 overpasses) and Barcelona (Spain, 16 overpasses). Ground-based total particle backscatter coefficient is converted into Aeolus-like profiles ($\beta^{part}_{Aeolus\ like,355}$) through the linear particle depolarization ratio at 355 nm ($\delta^{part}_{linear,355}$) and a thorough bibliographic review of dual-polarization measurements for relevant aerosol types. A relation for the spectral conversion of δ^{part}_{linear} is proposed.

Results and discussion

Relevant results were obtained regarding the bibliographic review. A modest, but significant, dataset of dual-polarization measurements is obtained for different aerosol types, including mineral dust (fresh, aged, mixed), marine, mixed anthropogenic, smoke, volcanic and bioaerosol particles. For these aerosol types a linear fit is applied to estimate $\delta^{part}_{linear,355}$ from $\delta^{part}_{linear,532}$ though a factor K_δ, called the depolarization spectral conversion factor (Table 1). However, mainly mineral dust, marine and mixed anthropogenic particles are detected during Aeolus selected overpasses, so the factor $K_\delta = 0.82 \pm 0.02$ is implemented in the calculation of the Aeolus-like profiles. Additionally, bibliographic results are endorsed with analogous measurements from Barcelona (Table 1) at dust and non-dust (a mixture of marine and anthropogenic particles) conditions. The derived K_δ aims to serve as a look-up table for other stations where a depolarization channel is available only at 532 nm, which is a frequent handicap worldwide. A further explanation of the dataset used is given by Abril-Gago et al. (2021).

The statistical validation of the satellite products showed that Aeolus SCAmb retrievals presented lower RMSE values than the SCA with respect to ground-based measurements (Figure 1). SCAmb RMSE profiles are fairly similar for the three stations, providing consistency to the results. Additionally, Aeolus measurements presented a critical surface-related effect that caused the satellite to drastically overestimate the co-polar backscatter coefficients in the lowermost range. This effect was more present in the SCA retrievals than in the SCAmb. Depending on the station and the orography of the region, this effect could extend to higher altitudes.

Aeolus quality flags (QF) application entailed a strong reduction of the number of measurements available. Approximately 20 % of all the data is flagged as valid, which affected the statistical significance of the results. In addition, the statistical intercomparison was not improved after the QF application, e.g. the surface effect was not mitigated and a RMSE increase (between 40 and 65 %) was observed. Finally, SCA tends to retrieve negative and meaningless backscatter coefficient values in the free troposphere, where the concentration of aerosol is expected to be low. These negative values are avoided with the quality flag filtering.

The statistical results show the ability of the satellite to detect and characterize aerosol layers under cloud free conditions. However, a case study presented by Abril-Gago et al. (2021) shows that Aeolus is able to characterize thin cirrus clouds with an acceptable agreement. Despite the distance between the stations and the overpasses, and the fact that the products are generated by averaging horizontally over 87 km, a good agreement was found between Aeolus retrievals and ground-based lidar measurements, demonstrating its potential for the characterization of the aerosol distributions.

Challenges

A further exploration of K_δ is encouraged, as a greater dataset of dual-polarization measurements will entaill interesting and usefull results.

Regarding Aeolus cal/val activities, more stations should join in order to achieve a fully operational version of Aeolus products. In addition, Aeolus products could be improved via the quality flags application, although the surface-related effect seems to be unavoidable.

Acknowledgements

The analysis has been performed in the frame of the Aeolus Scientific Calibration & Validation Team (ACVT). The authors acknowledge the ESA project 'Aeolus L2A aerosol and cloud product validation using the European Aerosol Research Lidar Network EARLINET and Cloudnet' (ref. Aeolus AO5166). ACTRIS-2 Research Infrastructure Project and Implementation Project of the European Union's Horizon 2020 research and innovation program (grant agreement No 654109 and 871115) as well as GRASP-ACE (GA 778349) are also acknowledged.

References

Abril-Gago, J., Guerrero-Rascado, J. L., Costa, M. J., Bravo-Aranda, J. A., Sicard, M., Bermejo-Pantaleón, D., Bortoli, D., Granados-Muñoz, M. J., Rodríguez-Gómez, A., Muñoz-Porcar, C., Comerón, A., Ortiz-Amezcua, P., Salgueiro, V., Jiménez-Martín, M. M., and Alados-Arboledas, L.: Statistical validation of Aeolus L2A particle backscatter coefficient retrievals over ACTRIS/EARLINET stations in the Iberian Peninsula, Atmos. Chem. Phys. Discuss. [preprint], https://doi.org/10.5194/acp-2021-388, in review, 2021.

Flamant, P. H., Lever, V., Martinet, P., Flament, T., Cuesta, J., Dabas, A., Olivier, M., and Huber, D.: ADM-Aeolus L2A Algorithm Theoretical Baseline Document Particle spin-off products, ESA, reference: AE-TN-IPSL-GS-001, 2020.

Table 1. Factor K_δ for the different aerosol types and their Pearson correlation coefficient R

Aerosol type	K_δ	R
mineral dust, marine and mixed anthrop.	0.82 ± 0.02	0.99
biomass	1.36 ± 0.08	0.97
volcanic	0.82 ± 0.13	0.98
bioaerosol	0.46 ± 0.13	0.91
Barcelona dust and non-dust	0.76 ± 0.01	0.99

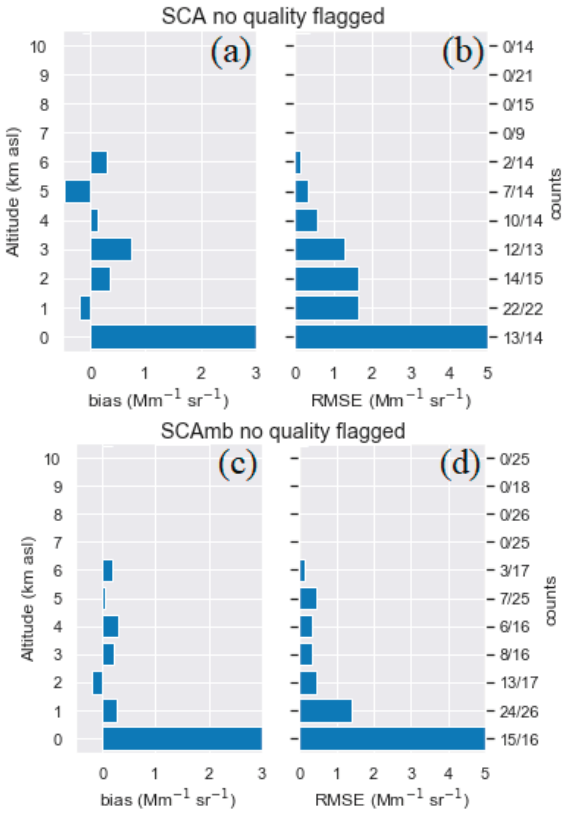

Figure 1. Statistical results for the intercomparison of Aeolus SCA and SCAmb with Barcelona ground-based measurements. The right-hand axis indicates the number of available data points included in each vertical range out of the total number of measures within that vertical range. (a) and (c) present the bias profiles calculated as $bias = \beta^{part}_{Aeolus,355} - \beta^{part}_{Aeolus\ like,355}$. (b) and (d) present the RMSE profiles. No quality flags are considered in these figures.

Retrieval of aerosol properties from lidar measurements based on the Maximum Likelihood Estimation method

Y. Chang[1], *Q. Hu*[1], *P. Goloub*[1]
yuyang.chang@univ-lille.fr
(1) Univ. Lille, CNRS, UMR 8518 – LOA – Laboratoire d'Optique Atmosphérique, 59000 Lille, France

Introduction

The inversion of height-resolved aerosol properties, such as particle size distribution (PSD), complex refractive index (CRI) and particle shape, is an important task in aerosol remote sensing. The motivation of this study is to develop an operational inversion algorithm for multi-wavelength Mie-Raman lidar systems, among which lidar LILAS (a Mie-Raman-Polarized-Fluorescent lidar (Hu et al., 2020) operated in LOA, France, in the frame of ACTRIS-EARLINET) is a good example. In the last two decades, the prevalent and well-discussed method for inverting 3β+2α measurements is the regularization method (Müller et al., 2019). Here, however, we explore the feasibility of the Maximum Likelihood Estimation (MLE) method for lidar inversion. Comparing to the regularization method, the MLE simultaneously retrieving PSD and CRI by making non-linear least-square fit, avoiding look-up tables (LUTs). By incorporating *a prior* information, retrieval parameters could be constrained and weighted properly. Besides, it could invert a variety of measurements with different sources and uncertainties by considering their variance-covariance matrix.

The MLE has been developed as the standard algorithm in the AERONET inversion scheme (Dubovik and King, 2000) and has also been used in collaborated photometer-lidar measurements (Lopatin et al., 2013). However, few studies have explored its applications to lidar stand-alone data.

The general idea of the MLE is to maximize the probability of measurements under certain state to be retrieved, which is equivalent to minimize the following cost function

$$\chi^2(\mathbf{x}) = \sum\nolimits_l [\mathbf{y}_l - \mathbf{f}_l(\mathbf{x})]^T \mathbf{S}_l^{-1} [\mathbf{y}_l - \mathbf{f}_l(\mathbf{x})]$$

where $\mathbf{x}$ is the vector of parameters to be retrieved, $\mathbf{f}_l(\mathbf{x})$ represents the quantity simulated by the forward model corresponding to the *l-th* measurements $\mathbf{y}_l$, and $\mathbf{S}_l$ is the covariance matrix of $\mathbf{y}_l$. The MLE regards *a prior* information as virtual measurements. In our cases, there are 4 independent sets of measurements: $\mathbf{y}_1$ - the real measurements made by the lidar system; $\mathbf{y}_2$ – the virtual measurements of smooth constraints on PSD; $\mathbf{y}_3$ and $\mathbf{y}_4$ – the virtual measurements of a prior information on CRI.

The minimization is achieved using the Levenberg-Marquardt method (Marquardt, 1963). Because our system is underdetermined (and so are the lidar inversions in most cases), the retrieval is performed on a reduced grids instead of a fully resolved grids used in the forward model (resampling). And for the same reason, the range of retrieval radii (the inversion window) should be chosen properly.

Results and discussion

We simulated 3β+2α optical data based on predefined aerosol properties and invert them with our algorithm. At this preliminary stage, we assume the aerosol assemble consists of spherical particles with a single wavelength-independent CRI. The volume size of the particles conforms the multi-modal log-normal distribution:

$$\frac{dV}{dlnr} = \sum_{i=f,c} \frac{V_i}{\sqrt{2\pi}\sigma_i} \exp\left[-\frac{(lnr - lnr_{Vi})^2}{2{\sigma_i}^2}\right]$$

where V_i, σ_i and r_{Vi} are the volume concentration, geometric standard deviation, and volume median radius of each mode (the subscript *c* for the coarse mode and *f* for the fine mode). The optical data are computed with the forward model proposed by Dubovik et al. (2006). Here we present the results of retrieving 4 aerosol types for which the only different quantity is the ratio of the fine mode volume to the coarse mode volume (see **Table 1** for more detail, note that $V_f/Vc = 0$ means only coarse mode and $V_f/Vc = \infty$ means only fine mode). The original integral parameters (r_{eff} – effective radius, N_t – total number concentration, V_t – total volume concentration) and the retrieved ones (together with retrieved CRIs) are listed in **Table 2** and **Table 3**, respectively. We have not introduced measurement noise yet (error-free optical data). The retrieved PSD for 2 bimodal types (type-1 and type-2) are shown in **Figure 1**.

Table 1. Parameters of the PSDs used in our test.[a]

r_{Vf}	σ_f	r_{Vc}	σ_c	V_f/V_c for each type			
				I	II	III	IV
0.15	0.4	1.7	0.6	2	0.2	0	∞

[a] The CRI is m=1.45 – i0.015 for all the cases.

Table 2. Integral parameters calculated from **Table 1**.

Type	I	II	III	IV

r_{eff}	0.78	1.72	2.03	0.16
N_t	29.75	15.65	0.17	14.79
V_t	2.39	10.46	2.06	0.16

Table 3. Retrieved integral parameters and CRI, with relative errors (shown in parentheses) for each type.[a]

Type	I	II	III	IV
r_{eff}	0.63 (-19%)	1.16 (-32%)	2.24 (10%)	0.156 (-4%)
N_t	23.98 (-19%)	11.66 (25%)	0.28 (64%)	12.05 (-18%)
V_t	1.75 (-26%)	5.51 (-47%)	2.41 (17%)	0.162 (1%)
mR	1.46 (0.7%)	1.46 (0.7%)	1.458 (0.5%)	1.466 (1.1%)
mI	0.0155 (3%)	0.0158 (5%)	0.0158 (5%)	0.0144 (-4%)

[a]*mR* and *mI* represent the real and imaginary parts of CRI, respectively.

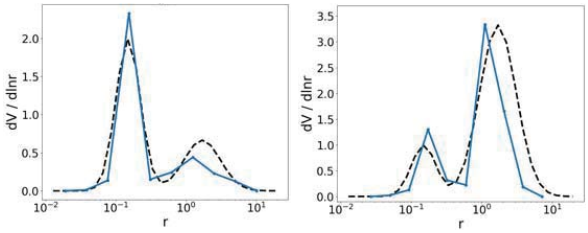

Figure 1. Volume size distribution (VSD) retrieval results for type-1 (left) and type-2 (right), along with the original VSDs in dash lines. The retrieval for the coarse mode behaves worse than that for the fine mode.

Figure 1 shows that although the two modes of bimodal aerosol could be retrieved properly, limit lidar wavelengths and error in resampling reduce the accuracy in retrieving the coarse mode. **Table 3** shows the maximum error occurs in type-3, where relative ΔN_t reaches 64%. For the monomodal retrievals, ΔN_t is much larger than ΔV_t while the situation reverses for the bimodal retrievals. We suspect it is due to the different sensitivities of the measurements to different particle sizes. The monomodal retrievals have smaller errors in effective radius than the bimodal retrievals. For monomodal aerosols retrieved from error-free optical data, our errors are comparable to those reported by Müller et al. (2019) in retrieving the N_t, V_t and r_{eff}, but are smaller in retrieving *mR* and *mI* thanks to the help of the *a prior* information.

Challenges

One main uncertainty of the MLE results from the ambiguity of *a prior* information, which refers to not only *a prior* mean and standard deviation of CRI, but also the information about the particle radius range related to the inversion window and resampling points. Improper choice of these parameters makes the cost function converges to an unrealistic local minimum.

Another challenge is the difficulty in retrieving CRI accurately, which is commonly faced in lidar inversion. In the cases above, CRIs are retrieved with good accuracy when they are close to the *a prior* value. However, in other simulation tests (not shown here) we found errors in *mR* and *mI* increase rapidly as the true *mR* and *mI* get away from their *a prior* values.

Up to now we already have several perspectives to address these challenges. We consider conducting type classification using intensive lidar parameters to provide more reliable *a prior* constraints for the retrieval. The attempt to retrieve the parameters of PSD under the assumption of bimodal log-normal distribution is also ongoing. At present, we are applying the algorithm to LILAS measurements to test its performance on real measurements with random noise.

Our inversion strategy will be implemented in the AUSTRAL (AUtomated Server for the TReatment of Atmospheric Lidars) inversion framework under development at LOA.

Acknowledgements

We thank Labex CaPPA and Région Hauts-de-France for their support.

References

Dubovik and King, A flexible inversion algorithm for retrieval of aerosol optical properties from Sun and sky radiance measurements, *Geophys. Res.*, 105(D16), 20673– 20696, 2000.

Dubovik, et al., Application of spheroid models to account for aerosol particle nonsphericity in remote sensing of desert dust, *Geophys. Res.,* 111, D11208, 2006.

Hu et al., The characterization of Taklamakan dust properties using a multiwavelength Raman polarization lidar in Kashi, China, *Atmos. Chem. Phys.,* 20, 13817–13834, 2020.

Lopatin et al., Enhancement of aerosol characterization using synergy of lidar and sun-photometer coincident observations: the GARRLiC algorithm, *Atmos. Meas. Tech.,* 6, 2065–2088, 2013.

Marquardt, An Algorithm for Least-Squares Estimation of Nonlinear Parameters, Soc. Ind. Appl. Math., 11, 431-441, 1963.

Müller et al., Automated, unsupervised inversion of multiwavelength lidar data with TiARA: assessment of retrieval performance of microphysical parameters using simulated data, *Appl. Opt*., 58(18), 4981-5008, 2019.

Robust filtering of Doppler lidar returns

M. Kayser[1], V. Lehmann[1], C. Detring[1], E. Paeschke[1], R. Leinweber[1]
Markus.Kayser@dwd.de
(1) DWD, Meteorologisches Observatorium Lindenberg-Richard Aßmann Observatorium, Lindenberg, Germany

Introduction

Fibre-optic based Doppler wind lidars (DL) are widely used for both meteorological research and in the wind energy sector. These compact systems are able to obtain vertical profiles of the mean horizontal wind vector in the atmospheric boundary layer as well as in optically thin cloud layers in the free troposphere with high spatio-temporal resolution. It is therefore likely that especially short-term forecasting would benefit from assimilating their data.

Nevertheless, a basic prerequisite for the retrieval of atmospheric quantities from Doppler lidar measurements is the robust detection of atmospheric return signals in the presence of instrumental noise. The most common approach filters the data via a fixed signal-to-noise-ratio (SNR) threshold (Pearson et al., 2009; Päschke et al. 2015). However, a conservative threshold reduces the data availability while a low threshold degrades the retrieval quality with noise. Therefore, the choice of a threshold level influences the retrieval performance (Gryning and Floors, 2019).

One way to overcome this issue is to consider a filter method, which is independent of the SNR. A well-established method that is used operationally in the mean wind retrieval of radar wind profilers is called the consensus method (CNS) (Fischler and Bolles, 1981; Frehlich and Yadlowsky, 1994). Here, we measure Doppler velocities with a velocity azimuth display (VAD) scan (Browning and Wexler, 1968). This scan geometry ensures that the atmospheric returns form a sine wave as long as the wind speed is sufficiently large and the wind field is homogenous for the measurement period of interest. Noisy data is then distributed randomly across the bandwidth of detection (Figure 1).

The CNS filter: For a measurement point (α, V) the CNS-algorithm (1) counts the number of points inside the neighbourhood ($\Delta\alpha$, ΔV) and compares it to the total number of points in the given azimuth region $\Delta\alpha$. The higher this quotient, the greater the likelihood of the measurement to be an actual atmospheric signal (Figure 1). (2) all measurements within $\Delta\alpha$ that surpass a specified consensus threshold, e.g. 60%, are included in the CNS and averaged. Thus, the CNS filter can be viewed as a density based clustering method that effectively reduces noise. But it produces satisfactory results only if the noise characteristic is approximately white and if the signal is sufficiently pronounced.

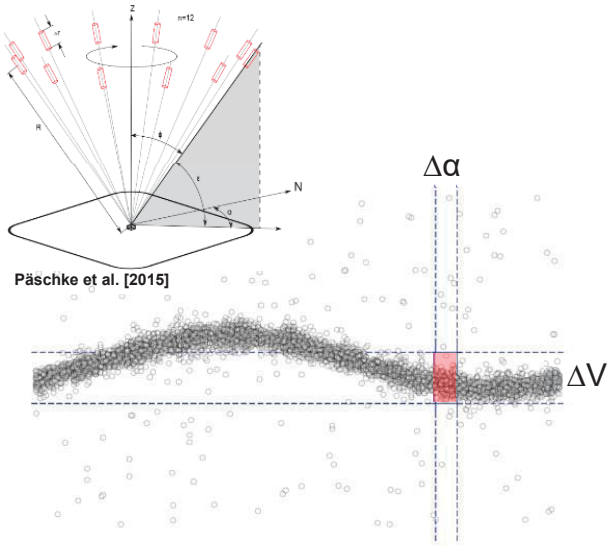

Figure 1. Schematic of the VAD scan geometry (top left, taken from Päschke et al. [2015]) and a corresponding sinusoidal distribution of radial velocities. The consensus value relates single measurement points (e.g., center of the red box) to the number of neighboring points found in a specified Δα-ΔV region (red box).

Whenever non-white noise is present, e.g., introduced through inhomogeneity of the wind field or through detector deficits, noise can pass the CNS filter.

Therefore, we introduce a new filter method based on the regular CNS that separates signal and noise, even in the presence of non-white noise. This more sensitive CNS (sCNS) is also independent of the SNR. The sCNS filter estimates the background noise, assuming that this component is independent of the azimuth direction. The necessary calculations are not considerably more expensive than the ones needed for the CNS filter.

Results and discussion

Figure 2 (top) compares the different filter methods using 30 min of measurement data from a single range gate with a large noise component around 0 ms^{-1} (n_0). The data clearly show that atmospheric returns lie on a sine wave, but the noise component has approximately the same point density.

The SNR filter performs well only for the evenly distributed random noise, but signal and n_0 pass this filter with equal amounts. Concerning the CNS filter, only a small fraction of the

measurements pass the filter and most of them are in the region, where the sine wave and n_0 overlap. On the contrary, the sCNS filter captures the signal best, even though near the 0 ms^{-1} crossing, signal and noise are indistinguishable. The histograms emphasize the improved performance of the sCNS filter compared with the other two. It reduces n_0 most effectively and keeps most of the reliable data (Figure 2, bottom).

Further, we observe that n_0 lowers the wind speed retrieved via least-square regression of the filtered data. The reduction is consistent with the amount of noise that passes the filter (Figure 2, top, solid lines). Additionally, the influence on the wind direction appears to be small.

Hence, the presented sCNS filter shows potential for operational use. It performs better than the SNR filter and the regular CNS filter and it is approximately as computationally expensive as the CNS filter. Through this approach, we hope to maximize the data availability of the mean winds while maintaining a high retrieval quality.

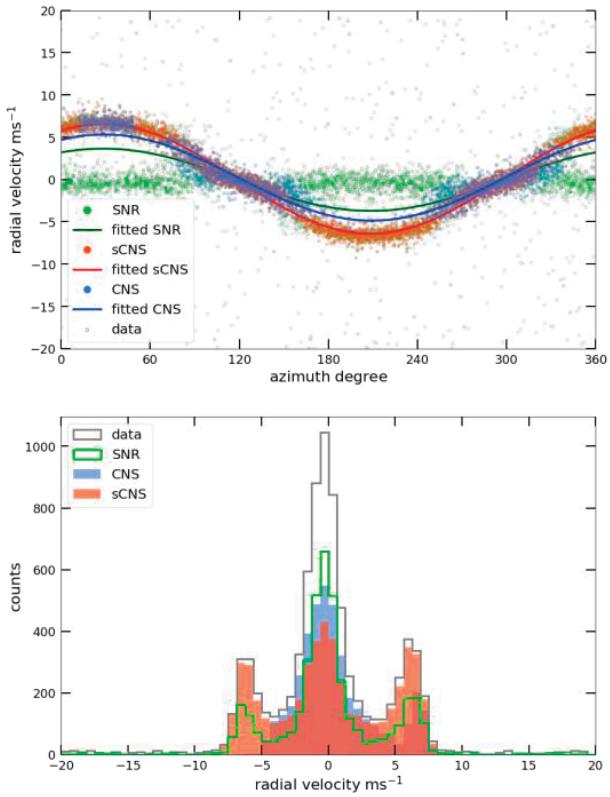

Figure 2. Example of Doppler lidar signal mixed with noise. Note that both, the SNR filter (green, -18 dB) and the regular CNS filter (blue, 60%), perform poorly, while the sCNS filter (orange, 75%) adequately captures the sine wave (top). The corresponding solid lines show the least-square fit of the filtered data points. The histogram (bottom) emphasizes that the noise around zero is most suppressed by the sCNS filter.

Challenges

It remains to show that the performance gain from the new filter approach results in a significant impact on the data availability and quality. Especially, inhomogeneous, non-stationary wind fields might still create unforeseen issues that cannot be accounted for with the presented filter method.

In addition, the authors still need to consider the benefits of this method for other scan strategies, such as continuous scanning modes (CSM) used for the retrieval of turbulence quantities or wind gusts.

For the latter scan mode, the computational efficiency is key for a near real-time retrieval and we might have to rely on computational geometry methods to achieve the desired performance.

Acknowledgements

The authors want to thank the DWD colleagues for their support in maintaining the instruments and the data archives.

References

Guy Pearson et al., An analysis of the performance of the UFAM pulsed Doppler lidar for observing the boundary layer, *Journal of Atmospheric and Oceanic Technology, 26(2):240–250, 2009.*

E. Päschke et al., An assessment of the performance of a 1.5µm Doppler lidar for operational vertical wind profiling based on a 1-year trial, *Atmospheric Measurement Techniques, 8(6):2251–2266, 2015.*

Fischler, and Bolles, Random Sample Consensus: A Paradigm for Model Fitting with Applications to Image Analysis and Automated Cartography, *Commun. Assoc. Comput. Mach., 24, 381–395, 1981.*

Frehlich, and Yadlowsky, Performance of Mean-Frequency Estimators for Doppler Radar and Lidar, J. *Atmos. Oceanic Technol., 11, 1217–1230, 1994.*

Browning and Wexler, The Determination of Kinematic Properties of a Wind Field Using Doppler Radar, *Journal of Applied Meteorology – J. Appl. Meteorol. 7. 105-113, 1968.*

Gryning and Floors, Carrier-to-Noise-Threshold Filtering on Off-Shore Wind Lidar Measurements, *Sensors 2019, 19, 592.*

Statistical Analysis Applied to Doppler Lidar Wind Profiles: Weibull, Von Misses Distributions and Complex Principal Components

P. Ortiz-Amezcua[1,2], *A. Martínez-Herrera*[3], *J.L. Guerrero-Rascado*[2,4], *L. Alados-Arboledas*[2,4]
pablo.ortiz@fuw.edu.pl
(1) Institute of Geophysics, Faculty of Physics, University of Warsaw, Warsaw, Poland
(2) Andalusian Institute for Earth System Research (IISTA-CEAMA), Granada, Spain
(3) Department of Statistics, University Carlos III, Madrid, Spain
(4) Department of Applied Physics, University of Granada, Granada, Spain

Introduction

Wind field is a key variable in understanding atmospheric processes. High resolution numerical weather forecast models require measured wind speed and direction profiles. The study of pollutant dispersion in the atmosphere is also an important field where the knowledge of wind profiles is crucial. Finally, wind power is a growing industry demanding statistical information of wind profiles, not only for determining plant location but also for determining the wind turbine power curve and, therefore, the electricity generation capability.

In this context the Doppler lidar technique represents a powerful tool to retrieve the 3D wind field with high temporal and vertical resolution. In this work we used measurements obtained with a Doppler lidar Streamline (Halo Photonics), which consists of a solid-state pulsed laser emitting at 1.5 μm and a heterodyne detector using fibre-optic technology. The signal acquisition provides a range resolution of 30 m. For this work, the instrument was operated performing conical scans in azimuth at a constant elevation of 75º every 10 min.

Wind field retrieved from Doppler lidar scans is a three dimensional quantity that is usually decomposed into zonal, meridional and vertical components. Horizontal wind vector ($\overrightarrow{U_H}$, formed by zonal and meridional components) can also be defined by wind speed (i.e., the vector modulus) and wind direction, which are linear and circular scalar quantities, respectively. Therefore, the statistical analysis of this vector requires a different approach for the components.

Scalar values of wind speed are experimentally observed to follow a Weibull distribution at any location (Stull, 2016). This distribution is commonly used in wind power industry to characterize wind regimes or to predict the production of a wind turbine. The probability density function described by the Weibull distribution with respect to wind speed depends on a scale parameter (α), proportional to mean wind speed, and a shape parameter (β) such that smaller values are given by wider spread of winds around the mean wind speed.

Wind direction measurements cannot be analyzed using linear statistics, because they are so-called *circular* data. However, they can also be fitted to certain probability distributions from circular statistics (Jammalamadaka and Sengupta, 2001). The most commonly used is the von Misses distribution, also called Circular Normal, a function of the mean direction μ and the dispersion parameter κ that measures the concentration of unimodal circular data around the mean.

Fitting wind speed and direction datasets to density distributions corresponds to a descriptive analysis of the whole time series. However, those general distributions can be the result of the combination of different wind modes or patterns, i.e., certain wind profiles that dominate the behaviour of the measurements during certain periods (e.g., seasonal pattern, diurnal pattern, etc.). In order to find such patterns, we apply here the Principal Component Analysis (PCA). This technique is commonly used in meteorology and climatology, usually to analyze single scalar fields such as temperature or pressure. To our knowledge, this is the first time that PCA is applied to wind vector profiles from Doppler lidar data. We used an adaptation of the generalized PCA method (e.g. Hardy and Walton, 1978), based on the treatment of two-dimensonal observations of horizontal wind vector as complex numbers.

With the procedures mentioned before, an interdisciplinary approach of lidar technique and data science is the primary purpose of this study.

Results and discussion

We have applied the linear and circular approaches to horizontal wind vector retrieved from Doppler lidar at the experimental observatory AGORA (Andalusian Global Observatory of the Atmosphere). In particular, the measurements were performed at the ACTRIS Granada station, at the Andalusian Institute for Earth System Research (IISTA-CEAMA) in Granada (37.16° N, 3.61° W, 680 m a.s.l.). Granada is a medium-size city in south-eastern Spain located in a natural basin delimited by Sierra Nevada mountain range, which reaches more than 3000 m a.s.l.

The whole dataset consists of two complete

years of wind measurements, from May 2016 to May 2018. The data were cleaned considering their associated signal-to-noise ratio, with a threshold of -22.2dB (Manninen et al., 2016).

The distribution of wind speeds was represented as density histograms for daytime and nighttime observations, respectively. The shape of both distributions corresponded to Weibull function (not shown here) and, therefore, a fit could be performed. From the values of α and β given by the fit the expected value (mean) and standard deviation could be computed, finding 4.4 ± 3.3 m/s for daytime and 3.3 ± 3.0 m/s for nighttime using all the available heights. It can be observed that the mean speeds are higher during daytime with also higher standard deviation.

Wind directions were analyzed and fitted to von Misses distributions for day and nighttime (Fig. 1). The circular histograms do clearly not follow unimodal von Mises distributions, and therefore a mixture of several von Mises modes was used as approach to these data. For daytime, three modes were observed with a predominance of NW wind, whereas for nighttime four equally important modes were found.

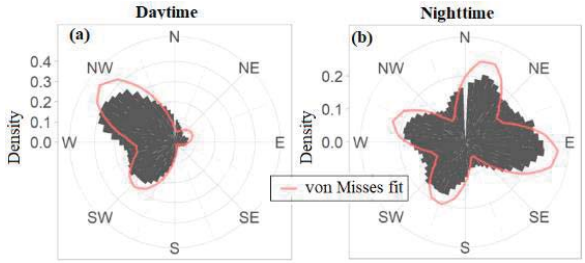

Figure 1. Density circular histograms of wind directions and fitted von Misses distributions for (a) daytime observations and (b) nighttime observations, using all available lengths.

Finally, complex PCA technique was applied to vertical profiles of horizontal wind vector. It was found that more that 95 % of the total variance was explained with the three first PCs, that are shown in Fig. 2.

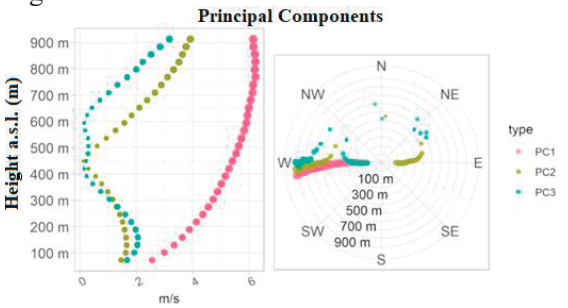

Figure 2. 1st (pink), 2nd (green) and 3rd (blue) PCs for the complete dataset. Lengths (left panel) and directions (right panel) of the vectors are plotted against height.

Challenges

Different approaches and interpretations are needed for linear, circular and vector treatment of wind data, and none of them is complete enough. By only analyzing wind speeds with linear statistics, the information about the general strenght of the wind over the measuring site is obtained, but directional behaviour is lost. On the contrary, circular analysis provides useful knowledge on clustering of wind around certain predominant directions, but light winds are considered with the same importance as strong winds.

On the other hand, the acquired experience of working with complex PCA highlighted the importance of the careful interpretation of the results. In most of the literature, the PCs are directly interpreted as the most relevant physical modes in the dataset. However, from this work it seems to be clear that the PCs do not represent any meaningful, realistic physical mode of variation in the data. Moreover, the eigenvectors obtained from complex PCA are not unique, but can be arbitrarily rotated with a constant phase shift that could be chosen, e.g., agreement with the topography of the study area. To enhance physical interpretation, a rotation of the PCs will be tested in the future.

Acknowledgements

This research has been done primarily thanks to the financial support of *Fundación Ramón Areces* through grant *Ampliación de estudios en el extranjero en Ciencias de la Vida y de la Materia. XXXII Convocatoria*. This was also partially funded by by Spanish Ministry of Economy and Competitiveness, projects CGL2016-81092- R, CGL2017-83538-C3-1-R, and CGL2017- 90884-REDT, by Horizon 2020 Framework Programme of the European Union, grant number 654109, by COST Action PROBE (CA18235), supported by COST (European Cooperation in Science and Technology), and by Programa 7 of Plan Propio of University of Granada. The authors thankfully acknowledge the FEDER program for the instrumentation used in this work and the University of Granada, which supported this study through the Excellence Units Program.

References

Manninen et al., A generalised background correction algorithm for Halo Doppler lidar and its application to data from Finland. *Atm. Meas. Tech.*, 9 (2), 817-827, 2016.

Jammalamadaka and Sengupta, Topics in Circular Statistics. Series on multivariate analysis. *World Scientific*, 2001. ISBN 9789812779267.

Stull, Practical Meteorology: an Algebra-based survey of Atmospheric Science. *BC Open Textbook Collection. AVP International*, University of British Columbia, 2016. ISBN 9780888651761.

Intense Saharan Dust Outbreak over the Iberian Peninsula in springtime 2021: Monitoring and Characterization of Transported Dust Particles

M.-Á. López-Cayuela[1], C. Córdoba-Jabonero[1], D. Bermejo-Pantaleón[2,3], M. Sicard[4,5], V. Salgueiro[6,7] F. Molero[8], C.V. Carvajal-Pérez[1], M. J. Granados-Muñoz[2,3], A. Comerón[4], M. J. Costa[6,7], R. Barragán[8], M.-P. Zorzano[9], J. A. Bravo-Aranda[2,3], C. Muñoz-Pocar[4], D. Bortoli[6,7], B. Artíñano[8], M. M. Jiménez-Martín[2,3], A. Rodríguez-Gómez[4], M. Pujadas[8], J. Abril-Gago[2,3], L. Alados-Arboledas[2,3], J. L. Guerrero-Rascado[2,3]

lopezcma@inta.es

(1) Instituto Nacional de Técnica Aeroespacial (INTA), Torrejón de Ardoz, 28850-Madrid, Spain
(2) Andalusian Institute for Earth System Research (IISTA-CEAMA), 18006-Granada, Spain
(3) University of Granada (UGR), 18071-Granada, Spain
(4) CommSensLab, Dept. of Signal Theory and Communications, Universitat Politècnica de Catalunya (UPC), 08034-Barcelona, Spain.
(5) Ciències i Tecnologies de l'Espai-Centre de Recerca de l'Aeronàutica i de l'Espai/Institut d'Estudis Espacials de Catalunya (CTE-CRAE/IEEC), Universitat Politècnica de Catalunya (UPC), 08034-Barcelona, Spain
(6) Instituto de Ciências da Terra (ICT) and EaRSLab–Earth Remote Sensing Laboratory, IIFA-EU, Évora, Portugal
(7) Departamento de Física, ECT, Universidade de Évora (UE), 7000-671, Évora, Portugal
(8) Centro de Investigaciones Energéticas, Medioambientales y Tecnológicas (CIEMAT), Madrid, Spain
(9) Centro de Astrobiología (CSIC-INTA), Torrejón de Ardoz, 28850 Madrid, Spain

Introduction

Dust particles play an important role in the frame of Earth's radiative budget and climate forcing, also affected by their interaction with clouds by acting as cloud condensation nuclei (CCN) and ice nucleating particles (INP). The retrieval of their vertically-resolved optical and microphysical properties is crucial to evaluate the aerosol radiative impact in the atmosphere (i.e., Córdoba-Jabonero et al., 2021).

In spring 2021 an intense Saharan dust outbreak reached the Iberian Peninsula (IP), lasting from 26 March until 5 April. It was monitored at six lidar stations, belonging to either MPLNET or ACTRIS/EARLINET networks, covering thus almost all the IP extension. Polarized Micro-Pulse Lidar measurements were carried out at El Arenosillo/Huelva (ARN, Spain; 37.1ºN, 6.7ºW, 40 m a.s.l.), Torrejón de Ardoz (TRJ, Spain; 40.5º N, 3.5º W, 568 m a.s.l, which is not within MPLNET yet), and Barcelona (BCN, Spain; 41.4ºN, 2.1ºE, 125 m a.s.l.); and multi-wavelength Raman lidars measurements were performed at Granada (GRA, Spain; 37.1ºN, 3.6ºW, 680 m a.s.l.), Évora (EVO, Portugal; 38.6ºN, 7.9º W, 293 m a.s.l.), and Madrid (MAD, Spain; 40.5ºN, 3.7ºW, 680 m a.s.l.).

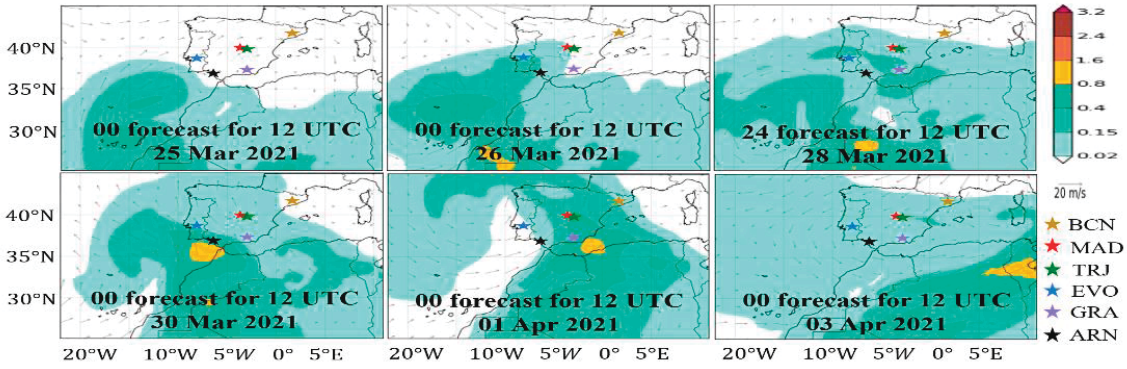

Figure 1. BSC-DREAM8b forecast images. Dust optical depth at 550 nm and 700 hPa wind field for the Saharan dust outbreak (25 March to 3 April 2021) over the IP. The six lidar stations are marked by coloured stars (see the legend).

Both particle backscatter coefficient (β_p) and particle linear depolarization ratio (δ_p) profiles at 532 nm are retrieved for all the stations under cloud-free conditions. The optical properties (backscatter and extinction coefficients at 532 nm) for both the fine (Df) and coarse (Dc) dust components are separately derived by applying the POLIPHON (POlarisation LIdar PHOtometer Networking; Mamouri and Ansmann, 2014) approach, using a lidar ratio (LR) of 55 sr and 50 sr for dust and non-dust particles, respectively. Additionally, the mass concentration profiles, the mass extinction efficiency and the height of the centre-of-mass for both fine and coarse-modes are also calculated for the overall period. Results are compared along with the evolution of the dust intrusion as it crosses the IP.

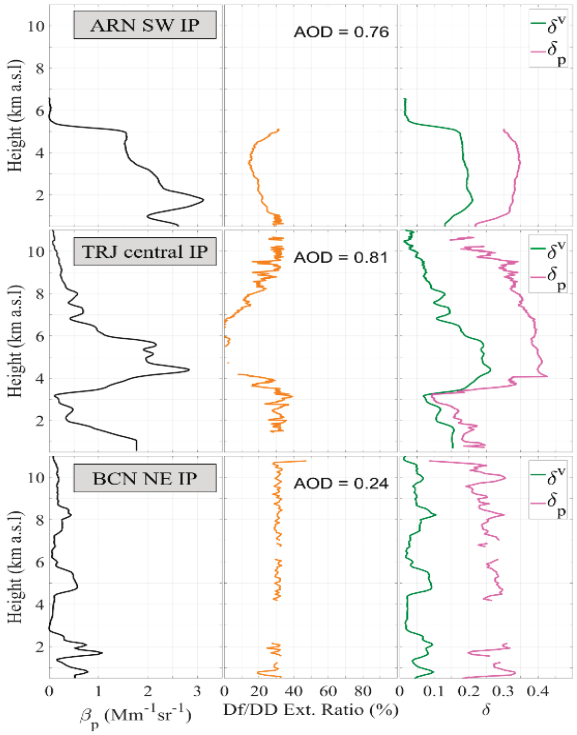

Figure 2. Vertical optical properties on 31 March at 04 UTC, as retrieved at (top) ARN, (middle) TRJ and (bottom) BCN: total β_P (black), Df/DD extinction ratio (orange), and δ^V (green) and δ_P (magenta). AERONET AOD values at 500 nm.

Results and discussion

The dust transport is analysed by combining BSC-DREAM8b and HYSPLIT modelling. Figure 1 illustrates a brief overview of the dust intrusion. The dust plume reached the South-west (SW) IP (ARN, EVO) on 26 March; a few hours later, arrived at the central IP (MAD, TRJ) and South-east (SE) IP (GRA). Finally, on 28 March, it arrived at North-east (NE) IP (BCN). The dust occurrence was below 6 km height at the southern stations, increasing the altitude as it moved northwards in the IP, reaching around 9 km height over BCN. This intense dust outbreak reached the highest incidence between 27 and 31 March, when AERONET aerosol optical depth (AOD) at 500 nm was higher than 1 at several times over the southern and central IP. The overall dust event was specially affected by the presence of clouds at altitudes just above or coincident with the dust layer, preventing the optical retrieval and generating gaps in the datasets.

In order to illustrate the dust progression from SW to NE IP, Figure 2 shows the vertical profiles of β_P, δ_P, and the volume linear depolarization ratio (δ^V) together with the Df-to-total dust (DD) extinction ratio for ARN (SW), TRJ (central) and BCN (NE) on 31 March at 04:00 UTC. β_P profiles show a vertical increase of the dust plume together with a decrease of the β_P values (and then also of dust extinction) along with the dust movement from ARN (SW IP) to BCN (NE IP). In addition, δ_P is slightly higher at ARN and TRJ with values greater than 0.3 (values of 0.4 are even found, which are rarely observed for dust, but they are within the error uncertainty in the δ_P retrieval), representing a dominance (even complete at particular layers) of coarse dust particles, whereas in BCN, δ_P is around or lower than 0.3 (fine dust contribution enhancement). Df/DD extinction ratio is height-varying at ARN and TRJ (0-35%), being almost constant (~ 30%) at BCN.

Challenges

The extreme incidence and duration of the dust outbreak provide a relevant study of dust ageing, finding a decrease of coarse dust particles during the transport of the dust plume along the Iberian Peninsula. The changes occurred in the dust optical properties due to ageing processes are expected to affect the radiative forcing. For a future work, we are interested in analysing the short-wave and long-wave radiative impact as induced by this extreme dust outbreak, as the first is modulated by the fine dust particles, and the second by the coarse dust ones. In addition, due to the high cloud coverage during this dust event, it is also specially challenging to study the cloud nucleation impact of dust by acting as CCN and/or INP. These results can be of interest for the next ESA EarthCARE validation mission.

Acknowledgements

This research was funded by the Spanish MICINN (PID2019-104205GB-C21, CGL2017-90884-REDT, CGL2017-85344-R), the Madrid Regional Government (Y2018/EMT-5177) and the EU H2020 programme (ACTRIS, GA no. 871115). EVO team is co-funded by Portuguese funds through FCT in the framework of ICT (UIDB/04683/2020, UIDP/04683/2020) and TOMAQAPA (PTDC/CTAMET/29678/2017) projects. BCN team particularly thanks E.J. Welton for providing the MPL unit in place at the Barcelona site. MALC is supported by the INTA predoctoral contract programme. The authors thank the images provided from the BSC-DREAM8b model (BSC).

References

Córdoba-Jabonero el al. Aerosol radiative impact during the summer 2019 heatwave produced partly by an inter-continental Saharan dust outbreak. Part 1: Short-wave dust direct radiative effect, *Atmos. Chem. Phys.*, 21, 6455-6479, 2021.

Mamouri and Ansmann. Fine and coarse dust separation with polarization lidar, *Atmos. Meas. Tech.*, 7, 3403-3735, 2014.

Short-wave and Long-wave Radiative Effect during the Summer 2019 Heatwave produced partly by an Inter-continental Saharan Dust Outbreak: Impact of the Fine and Coarse Dust Particles

C. Córdoba-Jabonero[1], M. Sicard[2,3], M.A. López-Cayuela[1], A. Ansmann[4], A. Comerón[2], M.-P. Zorzano[5,6], A. Rodríguez-Gómez[2], C. Muñoz-Porcar[2]

cordobajc@inta.es / msicard@tsc.upc.edu

(1) Instituto Nacional de Técnica Aeroespacial (INTA), Atmospheric Research and Instrumentation Branch, Torrejón de Ardoz, 28850 - Madrid, Spain

(2) CommSensLab, Dept. of Signal Theory and Communications, Universitat Politècnica de Catalunya (UPC), 08034-Barcelona, Spain

(3) Ciències i Tecnologies de l'Espai-Centre de Recerca de l'Aeronàutica i de l'Espai/Institut d'Estudis Espacials de Catalunya (CTE-CRAE/IEEC), Universitat Politècnica de Catalunya (UPC), 08034-Barcelona, Spain

(4) Leibniz Institute for Tropospheric Research (TROPOS), 04318 - Leipzig, Germany

Introduction

The arrival of Saharan dust intrusions over Europe is frequently observed in springtime and summertime in southern and south-eastern Europe; only in very few cases these intrusions are able to reach northern Europe. Mineral dust particles play an important role in the frame of climate forcing due to their direct effect on scattering and absorption of solar radiation as well as their indirect effect by acting as cloud condensation nuclei (CCN) and ice-nucleating particles (INP).

The aim of this work is to present the evolution of the dust direct radiative effect (DRE) during the summer 2019 heatwave over Europe. For that purpose, a case study associated with a dust intrusion observed in June 2019 is examined over two European distant stations: Barcelona (BCN, Spain; 41.4ºN, 2.1ºE, 125 m a.s.l.), where the dust plume was firstly observed on 23 June, lasting for 8 days, arriving later at Leipzig (LPZ, Germany; 51.4ºN, 12.4ºE, 125 m a.s.l.) on 29 June until 30 June. The individual short-wave (SW) and long-wave (LW) radiative contributions of both the fine and coarse dust particles is examined, as well as their net (SW+LW) DRE.

Results and discussion

Continuous polarized Micro-Pulse Lidar (P-MPL) measurements were performed in BCN and LPZ stations in order to obtain the optical and microphysical properties and the mass concentration of dust particles, separated in their fine (Df) and coarse (Dc) modes, by using the combination of P-MPL observations and POLIPHON retrievals (Córdoba-Jabonero et al., 2018). The DRE is simulated with GAME (Global Atmospheric Model) radiative transfer (RT) model (Dubuisson et al., 2004). GAME-derived radiative fluxes are calculated in several layers distributed between the surface (SRF) and the top-of-the-atmosphere (TOA). In particular, the vertical dust extinction distribution using POLIPHON outputs for both Dc and Df components is used as input parameters in the RT simulations. Results are presented in terms of instantaneous and daily DRE in both SW and LW spectral ranges in order to highlight the dominant effect of one dust mode over the other in relation with their SW, LW and net DRE. More details can be found in Córdoba-Jabonero et al. (2021) and Sicard et al. (2021).

Figures 1 and 2 show, respectively, the SW and LW DRE evolution of the particular dusty events observed at BCN (23-30 June 2019) and LPZ (29-30 June 2019) on SRF and at TOA, and in the overall atmospheric column (ATM) together with the daily-averaged Dust Optical Depth (DOD).

Despite the predominance of Dc particles under dusty conditions, the SW radiative impact of Df particles ($DRES^{W}$(Df)) can be comparable to, even higher than, that induced by the Dc ones. However, the daily $DREL^{W}$(Df) is small (< 6 % of $DRES^{W}$(Df)), which makes the $DREL^{W}$(Dc) the main driver of the total dust (Df+Dc) net DRE. The $DREL^{W}$(Dc) starts exceeding (in absolute values) the SW component in the middle of the event, which produces positive net DRE(Dc) at both SRF and TOA. Such an unusual tendency is attributed to increasing coarse-mode size and surface temperature along the dusty event. By adding the LW component, the total dust SW radiative efficiency is reduced by a factor 1.6 at both SRF and TOA. A sensitivity study performed on the surface temperature and the air temperature in the dust layer, both linked to the heatwave and upon which the DRE^{LW} strongly depends, shows that the heatwave contributed to reduce the dust net cooling effect on surface, and that it had nearly no effect at TOA. Its subsequent effect was thus to reduce the heating of the atmosphere produced by the dust particles.

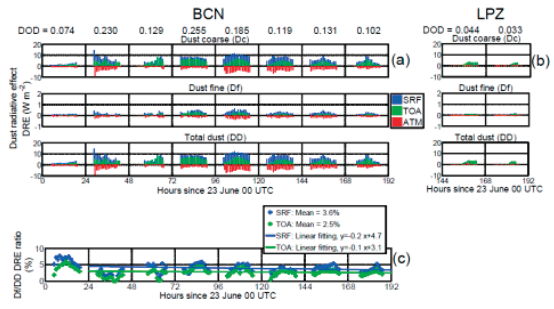

Figure 1. Instantaneous SW dust DRE (DRE^{SW}) on SRF (blue), TOA (green), and in the atmosphere (ATM, red) in (a) BCN and (b) LPZ. (c) Fine-to-total (Df/DD) ratio of DRE on SRF and at TOA in BCN. The mean values and best linear fit between 24 and 30 June were calculated. The absolute increase in Df/DD DRE^{SW} ratio on SRF (TOA) of +0.10 (+0.12) % h^{-1} is equivalent to an increase of +2.4 (+2.9) % d^{-1}. UT stands for UTC. The daily-averaged DOD is also shown at the top of the figure.

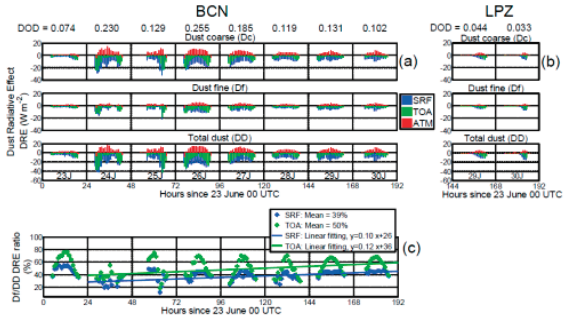

Figure 2. The same as Fig. 1, but for the instantaneous LW dust DRE ($DREL^{W}$). The absolute decrease of Df/DD $DREL^{W}$ ratio on SRF (TOA) is -0.2 (-0.1) % d^{-1}.

Results obtained in this work are especially relevant for the next ESA EarthCARE mission (launch planned in 2022), which is focused on radiation-aerosol-cloud interactions, in relation to the dust indirect radiative effect.

Challenges

Our findings show that the increase of land surface temperature (LST) and air temperature in the dust layer caused by the heatwave 1) provoked a reduction of the dust net cooling effect at SRF, 2) left unchanged the dust net cooling effect at TOA, and 3) consequently reduced the dust net heating of the atmosphere. The situation at the surface is a vicious circle: the heatwave reduces the dust cooling effect which, in turn, may increase some critical variables associated to the heatwave (e.g., LST and air temperature). The effect of the heatwave on the dust radiative effect is reverse as it contributes to cool down the atmosphere. Since recent studies have warned that mega-heatwaves such as the one studied in this work might become more frequent in the future, the novel results presented in this paper call for more research on the subject.

Acknowledgements

This research was funded by the Spanish Ministry of Science, Innovation and Universities (CGL2017-90884-REDT and PRX18/00137 "Salvador de Madariaga" programme), the Spanish Ministry of Science and Innovation (PID2019-104205GB-C21 and PID2019-103886RB-I00), the H2020 programme from the European Union (ACTRIS, GA no. 654109, 778349, and 871115), and the Unity of Excellence "María de Maeztu" (MDM-2016-0600) financed by the Spanish State Research Agency (AEI). MPZ has been partially funded by the AEI (Unity of Excellence "María de Maeztu" - Centro de Astrobiología (CSIC-INTA), MDM-2017-0737). MALC is supported by the INTA predoctoral contract programme. The MPLNET project is funded by the NASA Radiation Sciences Program and Earth Observing System. The MPLNET staff at NASA GSFC is warmly acknowledged for the continuous help in keeping the MPL systems and the data analysis up to date. We particularly thank Judd Welton for providing the MPL unit in place at the Barcelona site.

References

Córdoba-Jabonero, C., Sicard, M., Ansmann, A., del Águila, A., and Baars, H. Separation of the optical and mass features of particle components in different aerosol mixtures by using POLIPHON retrievals in synergy with continuous polarized Micro-Pulse Lidar (P-MPL) measurements. Atmos. Meas. Tech., 11(8), 4775-4795, 2018.

Córdoba-Jabonero, C., Sicard, M., López-Cayuela, M.-Á., Ansmann, A., Comerón, A., Zorzano, M.-P., Rodríguez-Gómez, A., and Muñoz-Porcar, C.: Aerosol radiative impact during the summer 2019 heatwave produced partly by an inter-continental Saharan dust outbreak – Part 1: Short-wave dust direct radiative effect, Atmos. Chem. Phys., 21, 6455–6479, https://doi.org/10.5194/acp-21-6455-2021, 2021.

Dubuisson, P., Dessailly, D., Vesperini, M., and Frouin, R. Water vapor retrieval over ocean using near-infrared radiometry, J. Geophys. Res., 109, D19106, https://doi.org/10.1029/2004JD004516, 2004.

Sicard, M., Córdoba-Jabonero, C., López-Cayuela, M.-Á., Ansmann, A., Comerón, A., Zorzano, M.-P., Rodríguez-Gómez, A., and Muñoz-Porcar, C.: Aerosol radiative impact during the summer 2019 heatwave produced partly by an inter-continental Saharan dust outbreak – Part 2: Long-wave and net dust direct radiative effect, Atmos. Chem. Phys., (in review), 2021.

Inverse methods for retrieving aerosol products from ceilometers

A.E. Bedoya-Velásquez[1], *S. Lefebvre*[2], *M. Herreras-Giralda*[3,4], *R. Román*[5], *C. Toledano*[5], *T.Huet*[1], *and R.Ceolato*[1]
andres.bedoya@onera.fr
(1)The French Aerospace Lab, Universite de Toulouse, F-31055 Toulouse, France,
(2) The French Aeorospace Lab, ONERA/DOTA, Universite Paris Saclay, F-91123 Palaiseau, France,
(3) GRASP-SAS, Remote sensing developments, Villeneuve d'Ascq, France,
(4) Laboratoire d'Optique Amosphérique, Université des Sciences et Technologies de Lille, Villeneuve d'Ascq, France,
(5) Grupo de Óptica Atmosférica, Universidad de Valladolid, Valladolid, Spain

Introduction

Atmospheric aerosols play a crucial role in atmospheric dynamics and the energy balance of the Earth. The main impact of the aerosols related-interactions is (i) the aerosol-radiation interaction (ARI), affecting the radiative fluxes of the Earth by absorbing and scattering solar and thermal radiation, and (ii) aerosol-cloud interaction (ACI) which is mainly associated with the modification of cloud properties and precipitation caused by aerosols. To quantify these impacts, the optical and microphysical properties of these atmospheric agents must be determined. In this way, different studies have been carried out over the past four decades involving in-situ and remote sensing techniques. Lidar became one of the most powerful remote sensing techniques, since aerosol properties can be obtained as height-resolved profiles.

In the lidar community, there is a latent necessity to keep testing different methods to retrieve optical and microphysical properties. Due to the nature of the atmospheric phenomena, most of the inversion approaches are ill-posed problems. In lidar, for more than two decades, the inversion problem has been mainly tackled by applying the Klett inversion method (Klett, 1985), which opened the door for having other approaches such as those presented in Bedoya-Velasquez et al. (2021a). On the other hand, non-linear regression methods have been also applied, for example Rodgers (2000), Lopatin et al., (2013), Bedoya-Velasquez et al., (2021b). In this work, we present two scenarios of the inversion problem. On one hand, a modified-Klett approach with a synergy of different instruments is presented, where some of the common assumptions to retrieve aerosol optical properties were minimized. On the other hand, we present a non-parametric nonlinear regression method, i.e. Optimal Estimation Method (OEM). The lidar instrument involved in this study is a ceilometer Vaisala CL51, highlighting the necessity to increase the use of high-level products that can be retrieved from these low-cost and widely spread instruments.

Methodology

Figure 1 shows a block diagram to clarify the procedures proposed to tackle the lidar inversion problem in two different scenarios.

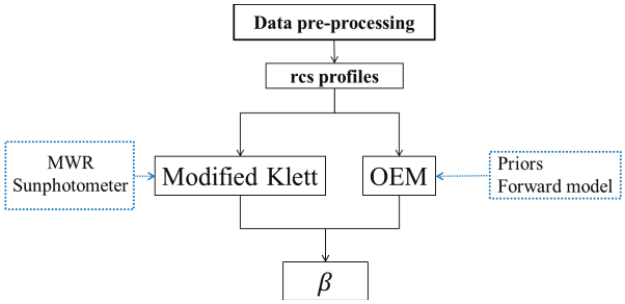

Figure 1. Block diagram of the methodology.

Since lidar instruments involved different sub-systems (i.e. emission, collection, and detection), data pre-processing is mandatory, especially in such ceilometer systems that operate in continuous mode 24/7 in most of the stations. Thus, the first block presented in Fig.1 is associated with the signal-cleaning procedure. From there, signals are split into two inversion paths, one for the Klett-like solution and the other one for the non-linear regression. Both methods need as input the range-corrected lidar signal (rcs). The block dedicated to modified Klett inversion takes atmospheric profiles from a co-located microwave radiometer (MWR) and data from the sunphotometer available at Toulouse (France); these data feed the iterative algorithm for the retrieval of the best solution of the lidar equation obtaining the backscatter and extinction coefficients, β and α, respectively, as outputs. Detailed description can be found in Bedoya-Velasquez et al. (2021a). The core of the OEM inversion block is the Forward Model (FM) and priors selected to find a Bayesian solution (Rodgers, 2000). The FM maps the state variables from the state space to measurement space, considering state and measured variables and their covariance as Gaussian distributed. A full method description is explained in Bedoya-Velasquez et al. (2021b). Nevertheless for the sake of clarity; here the state variables are the β coefficients that are used as prior information and

the rcs profiles are taken as measurement vectors.

Results and discussion

This work centers the attention on comparing the use of different approaches to solving an ill-posed problem to retrieve aerosol optical properties. The result of applying both methods is presented here to analyze qualitative and quantitative aspects such as the inputs for the algorithms and constrains requirements, error estimation, among others.

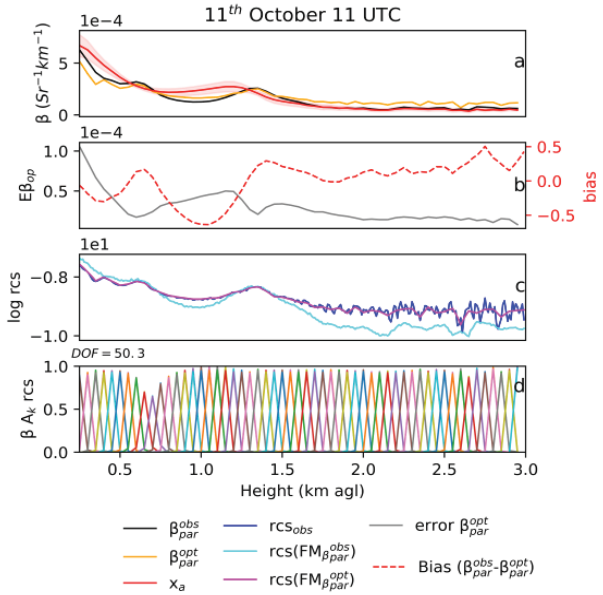

Figure 2. Example case on 11th October 2019 at 11 UTC, Toulouse. a) are presented the truth profile in black line, the optimized profile in orange, and the prior in red. In the panel b) is presented the error of the optimized profile in gray solid line, and in dotted red line, the bias between the truth and the optimized profile. In c) are presented the forward model bias results, where the blue line refers to the measured rcs profile (rcs_{obs}), in cyan is presented the rcs obtained from feeding the forward model with the truth β_{par}, and the magenta line is the rcs obtained from feeding the forward model with the optimized β_{par}. In the bottom of the figure, the rcs averaging kernels (Ak) are shown.

Figure 2 shows an example case where the ceilometer detected the atmospheric boundary layer transition up to 0.5 km agl and a particular aerosol accumulation from 1.2 to 1.5 km agl referred to a mixture of urban and dust particles. The black line refers to the β retrieved by using the modified Klett algorithm mentioned in the previous section. Particularly with Vaisala ceilometer signals, the water vapor contamination must be removed, thus atmospheric data of relative humidity and temperature were used from a co-located Microwave Radiometer (MWR). Lastly the atmospheric variables from the MWR were used for having accurate Rayleigh profiles, since the backward Klett inversion needs the molecular reference. The iterative algorithm allows to the automatic detection of these references based on the normalized rcs and Rayleigh profiles, and then the β calculation is performed until the algorithm converges to an aerosol optical depth (AOD) value close to the sunphotometer. To find the best result, the algorithm tries over a large number of lidar ratios and look after differences between AODs be lower than 0.001. The OEM retrieval presented in solid orange line in Fig. 2a has a good agreement with the Klett results mainly above 0.5 km (up to 15 %) and slightly larger errors in the first meters, reaching 25% in the worst scenario for our study cases. The red solid line in Fig. 2a indicates the prior profile used in the retrievals, nevertheless we tested with different prior configurations for evaluating the impact on the retrievals, including constant values and Gaussian profiles based on OPAC datasets. The panel's b and c in Fig.2 shows the bias profile between Klett and OEM in the red dotted line and the error of the OEM retrieval in a gray solid line, while in c the bias of the FM was calculated. In the last panel (Fig.2d), we present the averaging kernels for evaluating the model sensibility. In a nutshell, we present two ways to obtain lidar optical products allowing us to benchmark the advantages and disadvantages of facing the problem from different points of view.

Acknowledgements

This work was founded by ONERA, The French Aerospace Lab, within the framework of PROMETE Project.

References

Bedoya-Velasquez, A., Herreras-Giralda, M., Roman, R., Wiegner, M., Lefebvre, S., Toledano, C., Huet, T., Ceolato, R. Ceilometer inversion method using water-vapor correction from co-located microwave radiometer for aerosol retrievals. Atmos. Res. 250, 105379, 2021a.

Bedoya-Velásquez, A., Ceolato, R., and Lefebvre, S. Optimal estimation method applied on ceilometer aerosol retrievals. Atmospheric Environment, vol. 249, p. 118243, 2021b.

Klett, J.D. Lidar inversion with variable backscatter/extinction ratios. Appl. Optic. 24, 1638–1643, 1985.

Rodgers, C.D., 2000. Inverse Methods for Atmospheric Sounding. WORLD SCIENTIFIC.

Aeolus L2A optical product: algorithm performances and example data

A. Lacour[1], *D. Trapon*[1], *T. Flament*[1] , *A. Dabas*[1], *F. Ehlers*[2]
adrien.lacour@meteo.fr
(1) CNRM, Université de Toulouse, Météo-France, CNRS, Toulouse, France
(2) TU Delft, Geoscience and Remote Sensing Section, Delft, Netherlands

Introduction

The Aeolus satellite from the European Space Agency was launched on 22 August 2018, after a long development phase. Carrying a single instrument, the Doppler lidar ALADIN (Atmospheric LAser Doppler INstrument), Aeolus is the first satellitethat can measure vertical profiles of wind at the global scale, from the surface of the Earth up to the lower stratosphere (20 km to 25 km of altitude depending on the settings). The lidar operates in the UV at the wavelength λ= 354.8 nm. This short wavelength was chosen in order to enhance the molecular backscatter and allow measurements at high altitudes where aerosols and clouds are scarce and cannot serve as wind tracers. ALADIN implements two detection channels, a narrow-band one for the analysis of the UV light back-scattered by the particles (hydro-meteors and aerosols) that display a narrow spectrum (the full-width at half-maximum is of the order of a few tens of MHz), and a wide-band channel for the light back-scattered by the air molecules with a large spectrum (the full-width at half-maximum is several GHz) (Dabas et al., 2008). The former is called the Mie channel, and the latter the Rayleigh channel. The lidar was designed and optimized for the measurementof the wind. With its two channels, it is also what is usually called a high-spectral resolution lidar (Shipley et al., 1983).

Both channels detect a mix of photons backscattered by particles and molecules, but their sensitivity to both contributions is different. In the Rayleigh channel, the detection efficiency of molecular photons is about two-times better than for particle-backscattered photons while the Mie channel does the inverse with a sensitivity 30% better for particulate photons. With a precise calibration of the instrument, the number of photons backscattered by both types of target can thus be separated. This allows the independent measurement of the backscatter and extinction coefficients of aerosols or clouds (Flamant et al.,2008), and thus provides a direct measurement of the extinction to backscatter ratio called the "lidar ratio". This ratio gives an additional piece of information on the type of particle (Ackermann, 1998; Noh et al., 2007; Yorks et al., 2011; Illingworthet al., 2015; Shen et al., 2021).

Results and discussion

A first presentation of the L2A principles can be found in Flamant et al. (2008) and further detailed in Flament et al. (2021). The L2A original algorithm, called the Standard Correct Algorithm (SCA), does a direct retrieval of extinction and backscatter coefficient. The extinction is retrieved iteratively based on the intensity of the molecular signal. In each bin, the actual measured signal is compared to the estimated signal, based on molecular backscatter simulation and attenuation from the overlying layers. This algorithm is very sensitive to noise and an error on extinction in one bin propagates to the bins below. More precisely, the error propagates with a -1 factor from one bin to the next. If extinction is overestimated in one bin, it will be underestimated in the next one. To prevent this oscillation, the average of two adjacent bins is written into a so called „middle bin“ product. Users are advised to use this middle bin extinction product rather than the standard one. Since 12th July 2021, the L2A products described above has been released to the public.

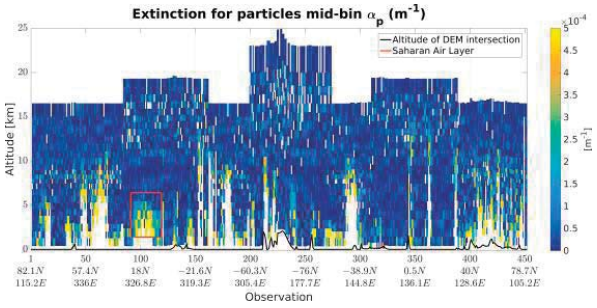

Figure 1. Middle bin extintinction from the SCA, the Saharan dust plume is visible around profile number 90 to 120, below 5 km, in the red box. Orbit file starting at 07:51 on 19 June

In the future, it is planned to implement new algorithms in the L2A. Currently, another approach is being implemented in the prototype version of the L2A (Ehlers et al. 2021). It uses a Maximum Likelihood Estimation (MLE) to determine a profile that optimally fits the signals while still checking physical contraints:

- The extinction is not allowed to be negative.
- The lidar ratio is bounded between 2 and 200 steradians.

Bounding the values for the lidar ratio ensures that backscatter and extinction occur in the same levels of the profile, but still allow the algorithm to determine an independant lidar ratio.

Example cases are given in Figure 1 and 2, during a Saharan dust emission event. The plume crossed the Altlantic in June 2020 and was well visible in Aeolus data for days.

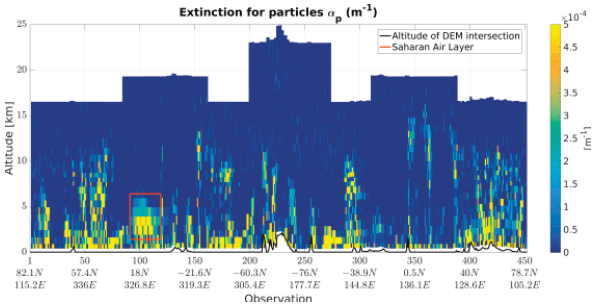

Figure 2. Extinction on the same orbit from the MLE. Observe how the noise is reduced by constraining the lidar ratio.

Finally, upcoming L2A versions will include data using the Earthcare algorithms adapted for Aeolus: AEL_PRO and AEL_FM, develloped by the KNMI.

Challenges

Aeolus was designed as a wind lidar. Thus, its characteristics are not optimized for aerosol retrieval. The high level of crosstalk between the channels and the relatively low signal to noise ratio make it more challenging to accurately retrieve particle optical properties. Yet, we show that several algorithm offer useful estimates of optical properties, either by using direct solutions as with the Standard Correct Algorithm, or by trying to compensate for the noisy signals with a maximum likelihood estimation technique. We now have to refine the algorithtms further, and promote the data towards the user community!

Acknowledgements

The auhors thanks the DISC (Data Innovation and Science Cluster) for their support and cooperation in the frame of the L2A processors development.

The L2A has been developed over more than 15 years by numerous contributor (Pierre Flamant, Marie-Laure Denneulin, Mathieu Olivier, Vincent Lever, Pauline Martinet, Hugo Stiegliz ...). Most of the development work for the L2A processor was carried out in the frame of contracts from the European Space Agency, but also benefited from the financial support of the French space agency CNES.

References

Ackermann, J.: The Extinction-to-Backscatter Ratio of Tropospheric Aerosol: A Numerical Study, Journal of Atmospheric and Oceanic Technology, 15, 1043 – 1050, https://doi.org/10.1175/1520-0426(1998)015<1043:TETBRO>2.0.CO;2, 1998.

Dabas, A., et al., Correcting winds measured with aRayleigh Doppler lidar from pressure and temperature effects, Tellus A: Dynamic Meteorology and Oceanography, 60, 206–215,https://doi.org/10.1111/j.1600-0870.2007.00284.x, 2008.

Ehlers, F, et al., Optimization of Aeolus Optical Properties Products by Maximum-Likelihood Estimation, Atmos. Meas. Tech. Discuss. [preprint], https://doi.org/10.5194/amt-2021-212, in review, 2021.

Flamant, P., et al., ADM-Aeolus retrieval algorithms for aerosol and cloud products, Tellus A: Dynamic Meteorology and Oceanography, 60, 273–286, https://doi.org/10.1111/j.1600-0870.2007.00287.x, 2008

Flament, T., et al., Aeolus L2A Aerosol Optical Properties Product: Standard Correct Algorithm and Mie Correct Algorithm, Atmos. Meas. Tech. Discuss. [preprint], https://doi.org/10.5194/amt-2021-181, in review, 2021.

Illingworth, A. J., et al., The EarthCARE Satellite: The Next Step Forward in Global Measurements of Clouds, Aerosols, Precipitation, and Radiation, Bulletin ofthe American Meteorological Society, 96, 1311 – 1332, https://doi.org/10.1175/BAMS-D-12-00227.1, 2015

Noh, Y. M., Kim, Y. J., Choi, B. C., and Murayama, T.: Aerosol lidar ratio characteristics measured by a multi-wavelength Raman lidar system at Anmyeon Island, Korea, Atmospheric Research, 86, 76–87, https://doi.org/10.1016/j.atmosres.2007.03.006, 2007

Shen, J., et al., Accurate retrieval of aerosol lidar ratio by Raman-Mie lidar in Nanjing, Optik, 227, 165 980, https://doi.org/https://doi.org/10.1016/j.ijleo.2020.165980, 2021

Shipley, S. T., et al., High spectral resolution lidar to measure optical scattering properties of atmospheric aerosols. 1: Theory and instrumentation, Appl. Opt., 22, 3716–3724, https://doi.org/10.1364/AO.22.003716, 1983

Yorks, J. E., et al., Statistics of Cloud Optical Properties from Airborne Lidar Measurements, Journal of Atmospheric and Oceanic Technology, 28, 869 – 883,https://doi.org/10.1175/2011JTECHA1507.1, 2011

Comparison between the 2D wind fields retrieved by a scanning Doppler lidar and anemometric measurements

***Jose Antonio Benavent-Oltra*[1], *Djordje Romanic*[1,2], *Milos Lompar*[3], *and Massimiliano Burlando*[1]**
jose.benavent@dicca.unige.it
(1) Department of Civil, Chemical and Environmental Engineering, University of Genoa, Genoa, Italy.
(2) Department of Atmospheric and Oceanic Sciences, McGill University, Montréal, QC H3A 0G4, Canada.
(3) Department of Meteorology, Republic Hydrometeorological Service of Serbia, Kneza Višeslava 66, Belgrade, Serbia

Introduction

In the framework of the European Project THUNDERR (Solari et al., 2020), a scanning Doppler lidar was installed in 2018 in the Port of Genoa with the aim of detecting and measuring downbursts and thunderstorm outflows that approach the Italian coast from the Ligurian Sea. As the lidar measures only the radial wind component, a procedure was needed to retrieve the two-dimensional (2D) wind fields from the raw scanning lidar data. In this work, the SingleDop software is used for the 2D wind field reconstruction and the results are compared with ultrasonic anemometric measurements. SingleDop is a software module based on the theoretical work described in Xu et al. (2006), which is intended to retrieve 2D low-level winds from either real or simulated Doppler radar data.

Instrumentation and methodology

We used the measurements of the ground-based instrumentation located at the Port of Genoa (Italy). The scanning Doppler lidar used is a WindCube 400S (Leosphere Inc.,) which scans the azimuthal range of 100º – 250º, up to a maximum distance of 14 km in the radial direction, for 4 elevations corresponding to 2.5º, 5°, 7.5° and 10º from the horizontal. The anemometer used for comparison is located about 1.3 km to the southeast of the Doppler lidar and provides the wind velocity with a sampling rate of 1 Hz. The wind speed and direction precision of the anemometer are 0.01 m/s and 1º, respectively.

The radial velocities measured by the Doppler lidar are used to retrieve 2D wind fields by the SingleDop software. The lidar dataset analyzed in this study ranges from November 2019 to July 2020. We analyzed each scan for three different de-correlation lengths (L = 1, 5 and 10 km) to evaluate the best value of L for wind field retrieval. L is a tuning parameter in the wind retrieval method. Larger values of L provide more smooth wind field, whereas the smaller values of L introduce small-scale features into the wind flow. The number of measurements available for the comparison is approximately 420 scans per day × 180 days × 4 elevations × 3 L, which results in nearly 10^6 processing cases .

Results and discussion

Figure 1 shows normalized number density plots of wind speeds retrieved by SingleDop using the lidar scans at 2.5º and compares the values to anemometer measurements. The anemometer data are averages of wind measurements over a period of ± 30 s from the lidar scanning time. Overall, the retrieved wind speeds have good correlation with anemometer measurements. The linear correlation coefficient (R) is higher than 0.9 for all values of L. The linear fit for L1 shows that SingleDop overestimates the anemometer data at high wind speeds. For L5 and L10 the linear fits are closer to 1:1 line. The RMSE for L1, L5 and L10 retrievals are 2.4, 1.6 and 1.8 m/s, respectively.

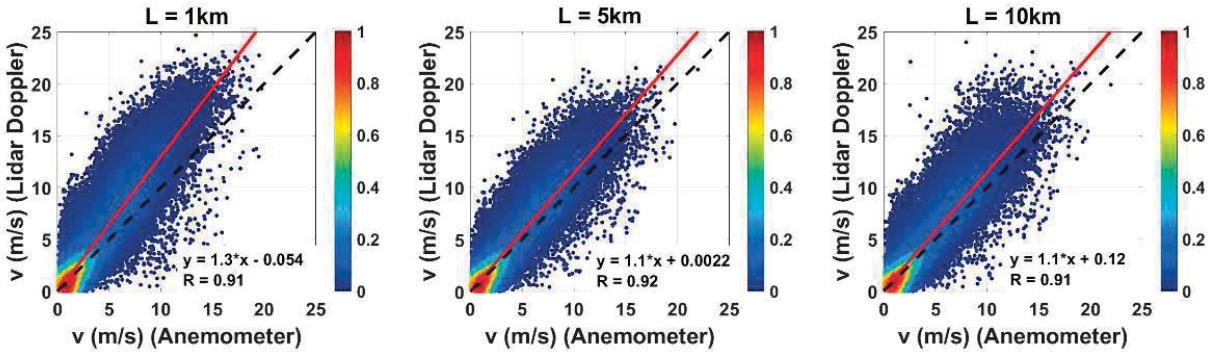

Figure 1. Wind speed retrieved by SingleDop using the Doppler lidar scans at 2.5º as a function of the anemometer measurements. Three de-correlation lengths (L) are shown: 1 km, 5 km and 10 km. The colour of points represents the relative density of points.

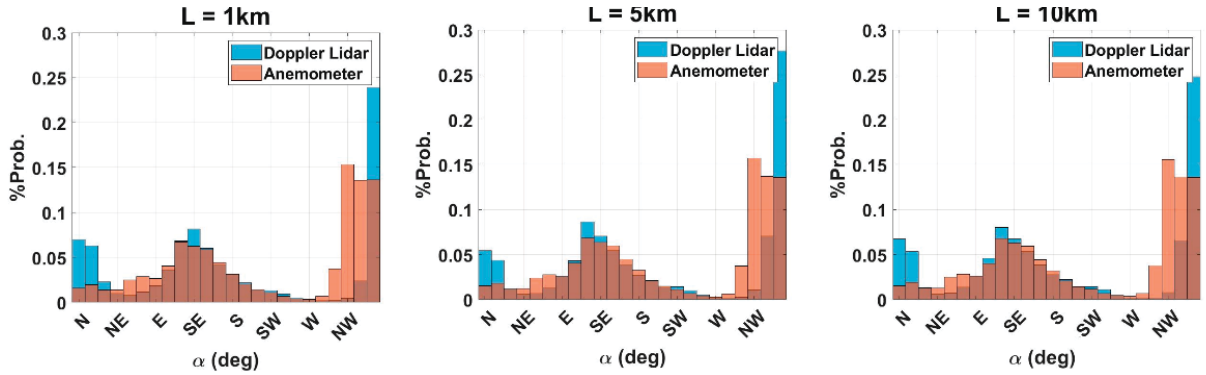

Figure 2. Distribution of wind direction measured by SingleDop and anemometer, in rectangular coordinates.

In terms of wind direction, we only considered the wind directions for which both retrieved and anemometer velocities were ≥3 m/s (~55% of data). This was done to avoid high variances in wind direction at low wind speeds. Figure 2 shows the distribution of retrieved wind direction and anemometer measurements. The circular correlation coefficient (ρ) obtained for all L's is ~0.9, thus indicating a good agreement between the retrievals and anemometer measurements. There is a predominant wind direction from NW-N with a mean value of 344 ± 12º and 330 ± 30º in both cases. The second most common wind direction was from SE (130 ± 50º).

Table 1. Regression results for wind speed and direction comparison between SingleDop L5 for 2.5°, 5°, 7.5° and 10º scans and anemometer measurements.

Wind Speed				
Elev.	**Slope**	**Offset (m/s)**	**R**	**RMSE (m/s)**
2.5º	1.1	0.002	0.92	1.6
5º	1.2	0.2	0.90	2.0
7.5	1.1	0.4	0.88	2.1
10º	1.1	0.6	0.85	2.2
Wind Direction				
Elev.	**Slope**	**Offset (º)**	**ρ**	**RMSE (º)**
2.5º	1.0	0.08	0.89	26
5º	1.0	4	0.88	29
7.5º	1.0	8	0.85	34
10º	1.0	10	0.81	37

Because the value of L5 provides the best overall correlation with anemometer measurements, Table 1 details the comparison between the L5 retrievals and anemometer data for all elevation scans The slopes are around 1 for both wind speed and direction. For wind speed, R ranges between 0.85 and 0.92, while for the wind direction ρ is higher than 0.8. The decrease of R with the elevation and the slight increase of RMSE for the values of wind speed and direction below 2.2 m/s and 37º are expected given that the difference of the altitude between the anemometer and retrievals is larger for higher scanning angles.

Acknowledgements

The contribution of Jose Antonio Benavent-Oltra, Djordje Romanic and Massimiliano Burlando to this research is funded by the European Research Council (ERC) under the European Union's Horizon 2020 Research and Innovation Program (Grant agreement No. 741273) for the project THUNDERR–Detection, simulation, modelling and loading of thunderstorm outflows to design wind-safer and cost-efficient structures–through an Advanced Grant 2016.

References

Solari et al.: Detection, simulation, modelling and loading of thunderstorm outflows to design wind-safer and cost-efficient structures. J. Wind Eng. Ind. Aerodyn., 200, 104142, 2020.

Xu et al.: Background error covariance functions for vector wind analyses using Doppler-radar radial-velocity observations. Q. J. R. Meteorol. Soc., 132, 2887-2904, 2006.

Alignment optimization and overlap function estimation in stepper motor controlled lidars

M. Di Paolantonio[1], *D. Dionisi*[1], *G. L. Liberti*[1]
marco.dipaolantonio@artov.ismar.cnr.it
(1) Institute of Marine Sciences, National Research Council, Rome, Italy

Introduction

Lidar observations are fundamental to quantitatively study the vertical distribution of atmospheric aerosols. In particular, some applications (e.g., air quality monitoring) need the description of the particulate from the ground up to the top of the atmospheric boundary layer. To correctly interpret the received lidar signal in the lowermost range, where the overlap between the telescope field of view and the laser beam is incomplete, an optimized alignment and the knowledge of the overlap function are required.

In this study we propose a new procedure as a possible solution for these two problems.

Results and discussion

The multi-wavelength multi-telescope Rayleigh-Mie-Raman "9-eyes" lidar system in Rome Tor Vergata (Congeduti et al., 1999) has the capability to move, through electronically controlled stepper motors, the orientation of the laser beams and the 3D position of the diaphragm of the receiving optical system around the focal point of the telescopes (Figure 1).

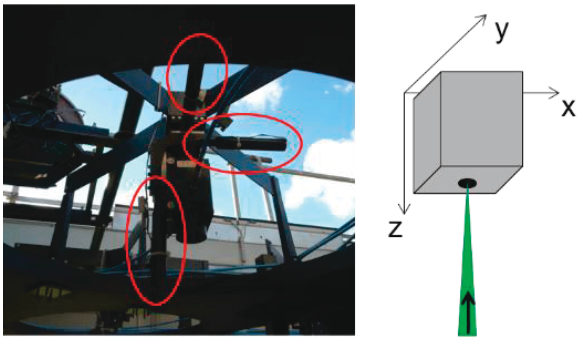

Figure 1. Receiving optical system with the 3 axis stepper motors.

Taking advantage of these instrumental characteristics, a set of semi-automated tools (the *mapping* procedure) was developed for the optimization of the telescope/beam alignment and the estimation of the overlap function. Figure 2 shows an example of results from the *mapping* procedure showing the signal at 2625 m, normalized for the maximum, as a function of a set of 9x9 discretized positions in the x-y receiving optical system plane.

By analysing the signal at different ranges as a function of the 3D position of the receiving system it is possible to optimize the position considering the specific scientific objectives of the intended measurements.

In this study the results of the *mapping* applied to a single combination of telescope (15 cm) and laser beam (532 nm) are discussed. The effectiveness of the procedure was verified by comparing the profiles of the acquired signal as well as the corresponding outcome of the telecover tests (Freudenthaler et al., 2018) before and after the *mapping*-based alignment optimization.

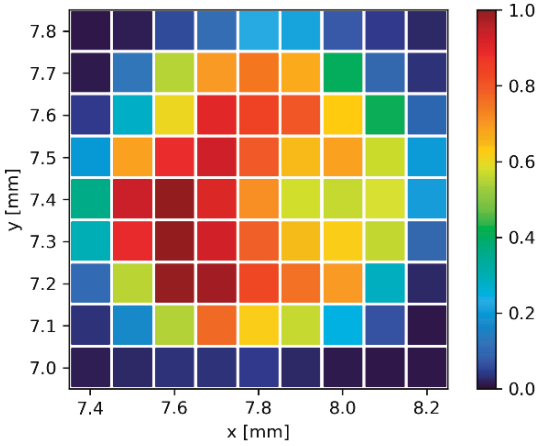

Figure 2. Example of results from the *mapping* procedure showing the signal at 2625 m, normalized for the maximum, as a function of the x-y receiving optical system position.

The additional capability, offered by the system, to also control the zenith and azimuth angles of the mirrors used to orient the laser beams, allows to implement a procedure, similar to the one described for the alignment optimization, to estimate the overlap function. Figure 3 shows the estimated overlap function using analog and photon counting data compared to the overlap function calculated from models with the assumption of a uniform/gaussian beam, diaphragm in the focal plane and tilted beam (0.3 mrad).

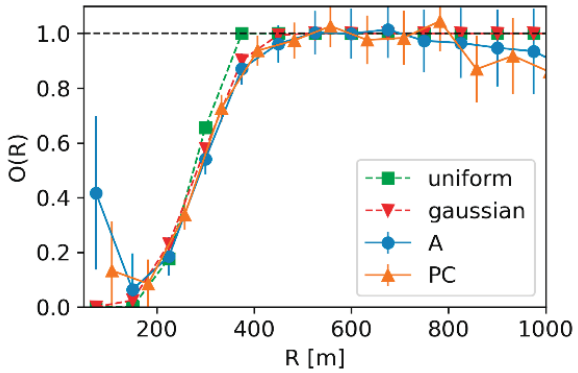

Figure 3. Estimated overlap function using analog (A) and photon counting (PC) data compared to the overlap function calculated from models with the assumption of a uniform/gaussian beam, diaphragm in the focal plane and tilted beam (0.3 mrad).

Challenges

This study applied the developed *mapping* procedure to a single combination of telescope and laser beam. As a next step, the procedure will be applied to the other available channels and the overlap function retrieval method will be validated comparing corrected middle range profiles to low range profiles.

For the "9-eyes" multi-wavelength multi-telescope system, the overall optimal alignment among telescopes and laser beams, and the resulting overlap functions, should account for the specific scientific objective(s) of the measurement sessions. This implies to introduce somehow a hierarchy among the single transmitter-receiver combinations that are not fully independent. A challenge is to translate such hierarchy in objective criteria that should, as much as possible, be valid for the relatively wide range of applications that a similar system offers.

The *mapping* procedure requires time for the movements as well as for the data acquisition. Even if movements are optimized and strategies of sampling have been implemented, to compare different measurements of a *mapping* it is necessary to account for the temporal variability of the atmosphere. Beside performing the *mapping* in the most favourable atmospheric conditions, the acquisition of a 'reference' signal, i.e., not affected by the on-going movements, has been put in place to monitor for atmospheric and emission variability. Strategies to monitor (and correct) for variability of the acquired signal should be designed for all the required *mapping* combinations.

Finally, applying the presented procedure to other lidar systems, different design characteristics could pose additional challenges. For example, inhomogeneities in the photomultiplier sensitivity will have to be considered in lidar systems that do not use optical fibers. Moreover, for non-motorized lidar systems simplified versions of the presented procedure (e.g., scan on a single axis) could be developed. With such a reduced procedure, further assumptions or controls will have to be implemented in order to compensate for the limited amount of information provided.

References

Congeduti et al., The multiple-mirror lidar "9-eyes", *J. Opt. Pure Appl. Opt.*, 1(2), 185–191, 1999.

Freudenthaler et al., EARLINET lidar quality assurance tools, *Atmospheric Meas. Tech. Discuss.*, 1–35, 2018.

Aerosol Monitoring at High Mountains Remote Station: An Example from The Yunnan Campaign At 3200 m Altitude Above Sea Level

***A. Sannino*[1]**, *A. Boselli*[2], *X. Wang*[3], *S. Amoruso*[1]
alessia.sannino@unina.it
(1) Dipartimento di Fisica "E. Pancini", Università degli Studi di Napoli Federico II, Napoli, Italy
(2) Istituto di Metodologie per l'Analisi Ambientale (IMAA) - CNR, Potenza, Italy
(3) School of Remote Sensing and Information Engineering Wuhan University, P.R. China.

Introduction

On January 2016, a monthly measurement campaign was carried out in the Chinese province of Yunnan by setting up a ground based station on the Yulong Naxi Autonomous County plateau located at an altitude of 3200 m above sea level (a.s.l.). This place is located at the ending part of a natural geographical corridor between the Himalayan chain to the North and the Indian highlands to the South. This natural corridor acts as main gate for the very long transport aerosols injection in the internal regions of China (Uno et al., 2009). The campaign was carried out within the frame of a scientific collaboration between the China Meteorological Administration (CMA), the Beijing Research Institute of Telemetry (BRIT) and the Physics Department of the University of Naples "Federico II". Among others, the primary purpose of the measurement campaign was the study of air quality at high altitudes by remote sensing lidar techniques. During the measurement campaign, various aerosol stratifications at low altitude were observed over several days. In particular, here we report the data relating to the evening of January 16 between 12.00 and 00.00 UTC when the lower aerosol layers persisted throughout the night time of acquisition.

Results and discussion

The observing station was equipped with the lidar AMPLE (A new Multi-wavelength Raman Polarization Lidar), an innovative lidar system designed and built within the homonymous program, by the "China-Italy Laser Remote Sensing Joint Research Center" between CNISM (Consorzio Nazionale Interuniversitario per le Scienze Fisiche della Materia, Italy) and BRIT (Beijing Research Institute for Telemetry, PRC).

AMPLE is a mobile lidar equipped with fast a scanning system (up to 20°/s) allowing to follow aerosol dynamics in the scanning range from -10° to 100° in the Zenith direction and from -100° to 110° in the Azimuth, with an angle accuracy of < 0.2°. Moreover, the laser source operates at a repetition rate of 1 kHz thus allowing to enhance the signal dynamic range and perform measurements of high density aerosol layers. (X.Wang et al, 2015; A.Sannino, 2017). AMPLE, in its full configuration, is able to acquire elastic channels at 355 nm (UV), 532 nm (VIS) (both with double depolarization channels) and 1064 nm (IR), as well as Raman channels at 387 (N_2), 407 nm (H_2O) and 607 nm (N_2), providing the following parameters: aerosol backscattering coefficients at 355 nm, 532 nm and 1064 nm, aerosol extinction coefficients at 355 nm and 532 nm, aerosol depolarization ratio at 355 nm and 532 nm and water vapour mixing ratio. Among collected data, we consider particularly interesting those referring to January 16th, when the LiDAR profiles evidence the presence of stratifications up to 4000 m from the base in an observational site where clean air is indeed expected. Figures 1 and 2 report the data acquired from 12:00 to 00:00 UTC on 16/01/16 in the form of RCS log of the lidar signal and the linear depolarization ratio, respectively, at a wavelength of 532 nm. The observed stratifications are characterized by very small values of the aerosol backscattering coefficient, with a maximum average value as high as $(4.6 \pm 0.5) \times 10^{-7}$ $m^{-1}sr^{-1}$, and large depolarization ratio, which reaches a maximum value of (43 ± 3)%. Moreover, these parameters display different values from layer to layer, suggesting different aerosol contributions.

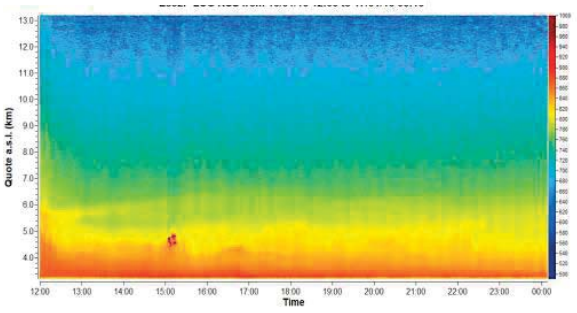

Figure 1. Log RSC of Lidar signal at 532 nm between 12:00 and 00:00 UTC on 16/01/16. Several layers and their evolution in time are visible below 6000 m. Color-scale refers to the relative variability in arbitrary units.

In order to highlight the source of these aerosols, back trajectories provided by NOAA HYSPLIT MODEL were analysed. This analysis showed that in the hours preceding the start of the acquisition, the air masses arriving at 4000 m a.s.l. (see Figure

3 a) and those at 5000 m and above, originate in two different places.

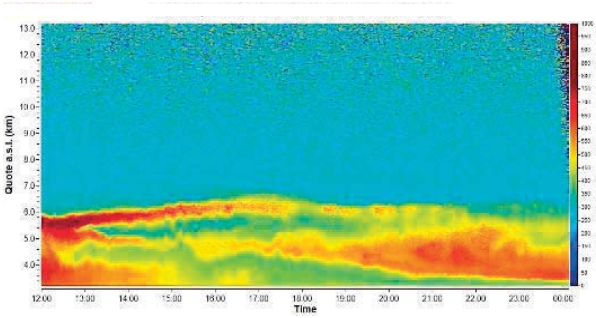

Figure 2. Lidar volume depolarization ratio signal at 532 nm between 12:00 and 00:00 UTC on 16/01/16. Several layers and their evolution in time are visible below 6000 m. Color-scale refers to the relative variability in arbitrary units.

The first (in blue colour in Figure 3 a) passes near ground in the neighbouring regions of northern Myanmar, Arunachal Pradesh and Assam typically characterized by high pollution conditions (B.Pathak et al., 2016) and reaches ground measurement point at 10.00 UTC. whereas the green line in refers to long transported air masses over the North Atlantic. Although apparently high this trajectory should be considered on its last day and a half of the whole trajectory, when happens the passage in the natural corridor created by the Himalaya mountain, whose height over the soil mountains reaches the peaks of 8800 m. During the data acquisition, as shown in Figure 3 b), the trajectories pass over the Southwest Europe and travel at same height, above 7500 m, passing also in this case in the natural corridor. They reach different altitude level only upon arrival at 16.00 UTC.

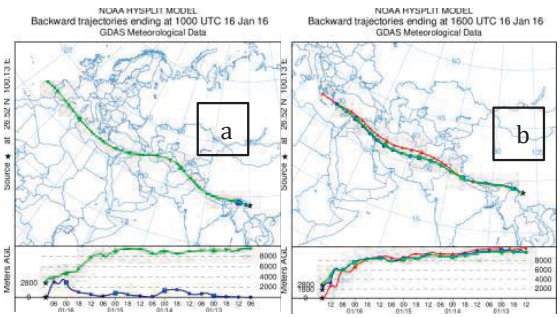

Figure 3. Models by HYSPLIT NOAA show back-trajectories referring to 16 January 2016 at a) 10:00 UTC and b) 16:00 UTC. In a) trajectory up to 4000 m a.s.l. is from north of Myanmar while those above 5000 m are long range transported over North Atlantic. In b) both trajectories are long range transport.

In this perspective, in the first half hour of acquisition the lower layers in Figures 1 and 2 can be ascribed to local particulates coming from the northern Myanmar regions, while the upper layers should contain a complex mix of mostly natural aerosols acquired during the passage in the corridor. During all time of acquisition, the upper layer continues to receive aerosols of this type. Starting from 16.00 UTC only natural aerosol continue to persist, whereas the contribution of local aerosol progressively reduces being removed from the atmosphere by relapse toward the ground. From 19.00 UTC, the lower layers are largely affected by a progressive intake of aerosols coming from higher altitudes that mix with local one as in Figures 1 and 2. In-depth analysis is currently in progress in order to give a more detailed description and an accurate optical characterization of aerosol properties.

Challenges

The observed phenomenon can be considered as an interesting case study of aerosols in high mountain, in a region that is of increasing interest due to its proximity to glaciers and their erosion due to pollutants (Rai et al,.2018) but where monitoring stations are still few and a very few are equipped with lidar systems. These systems allow coordinated and interesting characterizations of atmospheric aerosols given their portability, possibility of scanning and real-time data, an example of which has been illustrated in the present report.

Acknowledgements

We thank the China Meteorological Administration (CMA) for the hospitality at their facilities.

References

B.Pathak, et al., Aerosol characteristics in north-east India using ARFINET spectral optical depth measurements, Atmospheric Environment Volume 125, Part B, Pages 461-473, 2016

Uno, I., et al., Asian dust transported one full circuit around the globe, Nat. Geosci., 2, 557–560, 2009.

A.Sannino, 2017, Atmospheric Particles properties retrieval in China-Italy Aerosol Multi-wavelength Polarization Lidar Experiment (AMPLE) Systems, PhD diss., Università degli studi di Napoli "Federico II", online.

X.Wang et al., 2015, Calibration of Multi-wavelength Raman Polarization Lidar, EPJ Web of Conferences 89:01002.

Rai, M., Mahapatra, P.S., Gul, C., Kayastha, R.B., Panday, A.K. and Puppala, S.P. (2019). Aerosol Radiative Forcing Estimation over a Remote High-altitude Location (~4900 masl) near Yala Glacier, Nepal. *Aerosol Air Qual. Res.* 19: 1872-1891. https://doi.org/10.4209/aaqr.2018.09.0342

Cirrus Cloud Properties Over The European Arctic (Ny-Ålesund, Svalbard)

*K. Nakoudi[1, 2], M. Goldrina[2], **I. Stachlewska[3]**, C. Ritter[1]*
christoph.ritter@awi.de
(1) Alfred Wegener Institute, Telegrafenberg A45, Potsdam, Germany,
(2) University of Potsdam, Institute of Physics and Astronomy, Karl-Liebknecht Str. 24-25, Potsdam, Germany,
(3) University of Warsaw, Faculty of Physics, Institute of Geophysics, Warsaw, Poland

Introduction

Over the last decades, the rate of near-surface warming in the Arctic has been at least double than elsewhere on our planet (*Arctic amplification,* Serreze and Barry, 2011). However, the relative contribution of different feedback processes to *Arctic amplification* is a topic of ongoing research, including the role of cirrus clouds. Cirrus is the only cloud type capable of inducing daytime cooling or heating at the top of the atmosphere (TOA, Lolli et al., 2017). In order to improve the estimates of cirrus cloud radiative effect (CRE), reliable characterization of their geometrical and optical properties is needed. Over the Arctic, however, the properties of cirrus clouds are under-explored. In this work, we present the long-term properties of cirrus clouds over the research site of Ny-Ålesund, Svalbard, as derived by Raman lidar. To this end, a newly developed cirrus retrieval scheme was employed as presented in Nakoudi et al. (2021).

Cirrus retrievals with a newly developed scheme

An accurate and precise detection of cirrus cloud boundaries is of high significance as the cloud geometrical thickness (GT) is useful for the parameterization of the cirrus cloud optical depth (COD, e.g. Sassen and Comstock, 2001). Additionally, the detection of sub-visible cirrus is of special importance. More specifically, the total CRE can be negatively biased, if the contribution of sub-visible cirrus is neglected (Campbell et al., 2021).

In this work, the retrieval of cirrus geometrical and optical properties is based on a newly developed scheme, which proved sensitive to thin and faint cirrus layers (Nakoudi et al., 2021). The cirrus detection scheme extended the Wavelet Covariance Transform (WCT) method (Gamage and Hagelberg, 1993) by dynamic thresholds (*dynamic WCT*). The optical characterization scheme extended the Klett–Fernald retrieval (Klett, 1981; Fernald, 1984) by an iterative lidar ratio (LR) determination *(constrained Klett*). The iterative process was constrained by a reference value, which indicated the aerosol concentration beneath the cirrus cloud. Contrary to existing approaches, the aerosol-free assumption was not adopted, but the aerosol conditions were approximated by an initial guess. The retrieval scheme is publicly available (Nakoudi and Ritter, 2020).

Before applying the *constrained Klett* on the observations of Koldewey Aerosol Raman Lidar (KARL), a comparison to established retrievals was performed (Fig. 1). More specifically, the LR was derived from the double-ended Klett and Raman retrievals (Ansmann et al., 1992). Two reference value scenarios were applied to the double-ended Klett; one representing aerosol-free conditions (gray line) and one that approximated the aerosol conditions by an initial guess (green line) as in the *constrained Klett* (blue line).

The apparent LR values from the different retrievals displayed agreement within the range of statistical uncertainties (legend of Fig. 1). The uncertainties were higher for the Raman retrievals (applied only during night-time). When aerosol-free conditions were assumed beneath the cirrus layers, the LR was systematically overestimated because the neglected extinction was instead attributed to the cirrus layers.

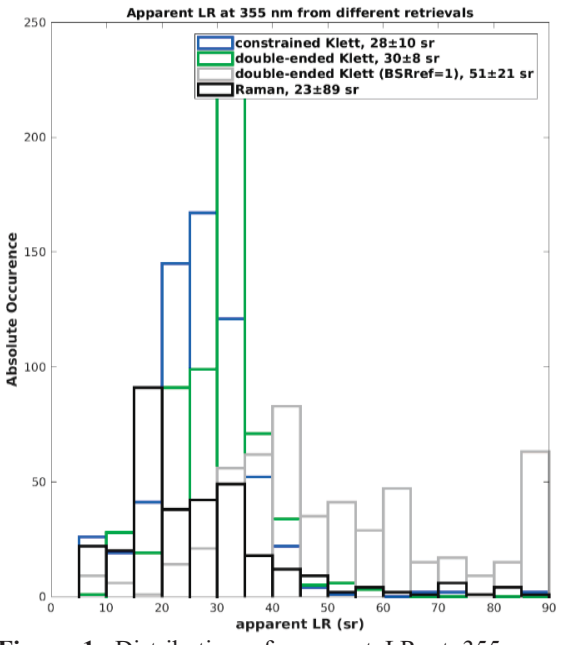

Figure 1. Distribution of apparent LR at 355 nm as derived from different retrievals.

As a next step, the LR and COD were corrected for the effect of multiple-scattering (MS). To this end, the analytical model of Eloranta (1998) was employed and it was compared to the simplified approach of Platt (1973). The latter approach (using

the assumption that the MS effect is only dependent on the COD) underestimated the MS effect in sub-visible and optically-thin layers, while an overestimation was found in opaque layers (Fig. 2). Finally, the Eloranta approach revealed that the MS correction (MSC) for the LR was equally important in all cirrus regimes.

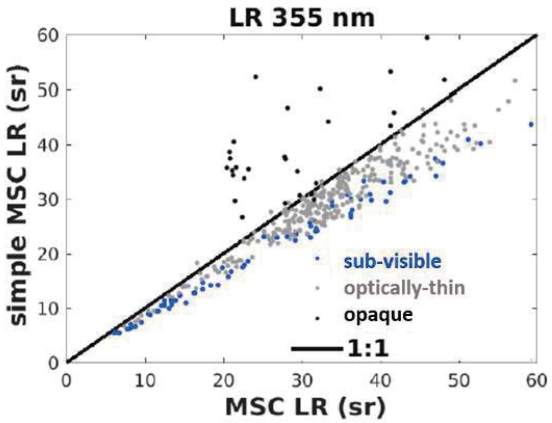

Figure 2. Simplified versus Eloranta MSC LR for different cirrus regimes.

Overview of cirrus properties: first results

Using KARL observations from 2011 to 2020, the cirrus layer geometrical properties were obtained from the *dynamic WCT* and the optical ones were retrieved from the *constrained Klett*. Collocated radiosoundings with 2 h temporal difference were used for deriving the ambient temperature. The majority of the layers fell into the optically-thin regime (73%), followed by the sub-visible one (20%). However, we should bear in mind that lidar systems have limited capabilities in probing highly opaque cirrus layers due to partial or complete attenuation of the laser beam. The properties of cirrus layers are summarized in Tab. 1.

Table 1. Median cirrus layer properties over Ny-Ålesund.

GT (km)	**C_{base} (km)**	**C_{top} (km)**
1.9 ± 0.6	7.3 ± 1.2	9.6 ± 1.2
LR_{355} (sr)	**COD_{355}**	**Temp (°C)**
33 ± 9	0.07 ± 0.24	- 57 ± 6

Summary and Outlook

For the first time, the properties of cirrus clouds were derived over an Arctic site on a long-term basis. To this end, a newly developed scheme was employed. As a next step, the seasonality and inter-relations of the different properties will be explored.

Acknowledgements

This work was partly performed during the research stay of K. Nakoudi in the Faculty of Physics, University of Warsaw, funded by the Helmholtz Graduate School for Polar and Marine Research (POLMAR). We acknowledge the support of KARL by Wilfried Ruhe and Ingo Beninga at Impres GmbH.

References

Ansmann et al., Independent measurement of extinction and backscatter profiles in cirrus clouds by using a combined Raman elastic-backscatter lidar, *Appl. Opt.*, 31.33, 7113–7131, 1992.

Campbell et al., Cirrus cloud top-of-the-atmosphere net daytime forcing in the Alaskan subarctic from ground-based MPLNET monitoring, *J. Appl. Meteorol. Climatol.* 60.1, 51–63, 2021.

Eloranta, Practical model for the calculation of multiply scattered lidar returns, *Appl. Opt.*, 37.12, 2464–2472, 1998.

Fernald, Analysis of atmospheric lidar observations: some comments, *Appl. Opt.* 23.5, 652–653, 1984.

Gamage and Hagelberg. Detection and analysis of microfronts and associated coherent events using localized transforms. *J. Atmos. Sci.* 50.5, 750–756, 1993.

Klett, Stable analytical inversion solution for processing lidar returns, *Appl. Opt.* 20.2, 211–220, 1981.

Lolli et al., Daytime top-of-the-atmosphere cirrus cloud radiative forcing properties at Singapore, *J. Appl. Meteorol. Climatol.* 56.5, 1249–1257, 2017.

Nakoudi and Ritter, AWI cirrus cloud retrieval scheme, https://doi.org/10.5281/zenodo.4265007, 2020.

Nakoudi et al., An extended lidar-based cirrus cloud retrieval scheme: first application over an Arctic site, *Opt. Express* 29.6, 8553–8580, 2021.

Platt, Lidar and radiometric observations of cirrus clouds, *J. Atmos. Sci.* 30.6, 1191–1204, 1973.

Sassen and Cho. Subvisual-thin cirrus lidar dataset for satellite verification and climatological research, *J. Appl. Meteorol.* 31.11, 1275–1285, 1992.

Sassen and Comstock. A Midlatitude Cirrus Cloud Climatology from the Facility for Atmospheric Remote Sensing. Part III: Radiative Properties, *J. Atmos. Sci.* 58.15, 2113–2127, 2001.

Serreze and Barry. Processes and impacts of Arctic amplification: A research synthesis, *Glob. Planet. Change* 77.1-2, 85–96, 2011.

ESA's Wind Lidar Mission Aeolus

J. von Bismarck[1], *T. Fehr*[2], *T. Parrinello*[1], *A. Straume-Lindner*[2], *D. Wernham*[2]
(1) European Space Agency, ESA-ESRIN, Largo Galileo Galilei, 00044 Frascati, Italy, jonas.von.bismarck@esa.int
(2) European Space Agency, ESA-ESTEC, Keplerlaan 1, 2202 AG Noordwijk, The Netherlands

The European Space Agency (ESA) wind mission, Aeolus, hosts the first space-based Doppler Wind Lidar (DWL) world-wide. The primary mission objective is to demonstrate the DWL technique for measuring wind profiles from space, intended for assimilation in Numerical Weather Prediction (NWP) models. Mission spin-off products are profiles of cloud and aerosol optical properties. Aeolus was launched on 22 August 2018, and the Atmospheric LAser Doppler INstrument (Aladin) switch-on was completed with first high-energy output in wind mode on 4 September 2018.

The on-ground data processing facility worked excellent, allowing L2 product output in near-real-time from the start of the mission. Results from the early wind profile product (L2B) assessment showed that the winds were of very high quality, with random errors in the free Troposphere slightly larger than the requirements, but still allowing significant positive impact in NWP, which remains positive while the Rayleigh SNR has decreased due to a negative trend in the return signal, observed throughout the (so far) 2 years of operation of the second laser (FM-B).

During commissioning phase and early operation phase using FM-A ESA, industry and the Aeolus Data Innovation Science Cluster (DISC) monitored particularly closely anomalies of the performance in order to prepare and support associated reactions. The DISC scientific partners from DLR, DoRIT, ECMWF, KNMI and MétéoFrance, were tasked to investigate the instrument calibration and perform product verification and validation implementing a number of corrective measures in the on-ground data processing. ESA and DISC investigations included e.g. analysis of the instrument output energy and alignment drifts, elevated dark currents on individual CCD pixels, etc. Related monitoring, performance optimization and processor improvement activities have remained on a high level throughout the 3 years since launch in order to maximize the Aeolus impact.

The product validation has also been performed by the world-wide Aeolus Scientific CAL/VAL Team (ACVT), performing collocated measurements from ground and airborne platforms around the globe and including a number of NWP centers performing impact experiment and NWP monitoring of the Aeolus winds, with several meanwhile assimilating Aeolus L2B winds operationally. After 10 months in-flight, the output energy of the first flight laser was approaching the lowest acceptable level w.r.t. instrument safety and data quality, and the redundant laser was switched on. The second flight laser has been providing a high output energy for 2 years now, interrupted by one shutdown period which did not originate from the laser. Investigations by ECMWF, which also hosts the Aeolus L2B processing facility, revealed that the Aeolus telescope thermal behavior accounts for the bulk of the currently observed wind biases. Corrections for this and other major L2B wind bias contributors have been implemented successfully in the on-ground data processing. Public release of the Aeolus L2B data product was performed in Spring 2020, while L2A follows in Summer 2021. The mission has been extended by a year to the end of 2022.

In this presentation, the latest status of the Aeolus mission and its data products will be presented together with results from the mission CAL/VAL activities and a status of the 2021 Aeolus A-TAC tropical validation campaign activities, as well as an overview of current and planned Science activities.

Databank of backscattering matrices for ice atmospheric particles with sizes of 10-100 microns for problems of laser sensing of the atmosphere

D. Timofeev[1], *I. Tkachev*[1,2], *V. Shishko*[1], *A. Konoshonkin*[1,2], *N. Kustova*[1], *A. Borovoi*[1]
tdn@iao.ru
(1)V.E. Zuev Institute of Atmospheric Optics SB RAS, 1, Academician Zuev Sq., Tomsk, 634055, Russia
(2) National Research Tomsk State University, Lenina str. 36, 634050 Tomsk, Russia

Introduction

Cirrus clouds are the object of active research by both contact and remote sensing methods. Scientific interest in cirrus clouds caused by, on the one hand, to their significant influence on the climate of our planet and on the other, to the need to take them into account when interpreting data from remote sensing (Liou, K. N., 1972). Despite the long history, the problem of light scattering on ice crystals of cirrus clouds, despite of liquid-drop clouds, has not yet been solved.

In solving the problem of light scattering by cirrus crystals, two opposite cases can be distinguished: regular hexagonal particles and particles of arbitrary shape. But these two models cannot fully describe the experimental data. More reliable results can be obtained if we assume that the cloud consists of a mixture of particles with different shapes.

Model of arbitrary oriented hexagonal particles was used to solve the problem of light scattering. The problem is solved within both the physical and geometric optics approximation, as well as by exact numerical methods. In this paper, we will focus on irregularly shaped particles. It has been proven that particles of irregular shape and particles with a rough surface are optically equivalent (Liu C. et al., 2014). This made it possible to use the physical optics method based on the beam-splitting algorithm to study the optical properties of irregular crystals using the model of arbitrarily shaped ice particles. However, the main difficulty in solving this problem is the fact that it still requires colossal computational resources (Borovoi, A. et al., 2014).

The paper presents the results of solving the light scattering problem for three types of particles: hexagonal plates, columns and arbitrarily shaped particle. The size of particles varies from 10 to 100 microns.

In the problems of laser sensing of cirrus clouds, the most often used laser wavelengths (λ) are 0.355, 0.532, and 1.064 μm. For such problems, the first data bank of the backscattering matrices of the IAO SB RAS was built (ftp://ftp.iao.ru/pub/GWDT/Physical_optics/Backscattering). However, recently the results of remote sensing of cirrus clouds in the IR region have appeared, so there is a need to fulfill the data bank with calculations at the λ of 1.55, 2, and 2.15 μm. The light scattering matrix for the case of arbitrary oriented crystals can be interpreted by two variables: the first element of the light scattering matrix (M_{11}) and the depolarization ratio (DR).

At the moment, a bank of calculations has been created for the interval 10-100 microns. This study was carried out for several reasons, firstly, to fulfill the already existing databank, and secondly, to find out the value of interference effect. The interference effect can be described by the value of the amplitude and the period of the oscillations.

Results and discussion

The results of calculations for hexagonal columns showed that for λ of 0.355, 0.532, and 1.064, the interference of M11 can be neglected since the oscillations are less than 1% of the amplitude, in the entire range of particle sizes for λ of 0.355 μm, at sizes greater than 30 μm for λ of 0.532 μm, and at sizes greater than 50 μm for λ of 1.064 μm. It is also seen that taking into account the absorption at the λ of 1.064 μm does not have a valuable effect in the entire range of particle size. The color ratio of these three wavelengths is 0.6 and 0.5. As for the solutions in the near-IR region (λ of 1.55, 2, and 2.15 μm), the oscillations become more significant (up to 5% of the amplitude for λ of 2 μm). Moreover, the influence of absorption is more noticeable, especially at λ of 2 μm.

The increase of the real part of refractive index cause a significant increase of the value of M11, but does not cause a change of the power-law dependence, which is observed for λ of 0.532 and 1.064 μm when the real part of the refractive index n changes from 1.3116 to 1.48 and from 1.3004 to 1.6, respectively. However, an increase in the imaginary part of the refractive index to 0.002i (dust aerosol) leads to a change in the size dependence of M_{11} over the entire calculation range. The DR shows that it more sensitive to the real part of the refractive index than to the wavelength of the incident radiation. In particular, for λ of 0.532 and 1.064 μm with refractive indices of ≈ 1.3, the DR is approximately 0.23 over the entire size range. In this case, an increase in the

real part of the refractive index from 1.3 to 1.48 and to 1.6 cause a significant increase in the DR to 0.27 and 0.31, respectively. However, an increase in the imaginary part of the refractive index cause an insignificant increase in the DR for small columns and to a significant decrease in the DR for large particles. This is caused by the absorption of the corner component of the scattered light and the dominance of the specular component.

An analysis of the calculation results for the plates shows that, on the one hand, for λ of 0.355 and 0.532 μm, high-frequency oscillations caused by interference effects can be neglected (their value does not exceed 1.8% in amplitude), but the oscillations caused by the waveguide effect are about 15% and have a long period, which is well traced in the depolarization relation. Moreover, all calculations, in which absorption does not have a significant effect, have a common power-law trend. It is important to note that the new refined calculations resulted in an increase in M_{11} for columns by about 10%. The value of the depolarization ratio did not change, in general.

Analysis of the results obtained for particles of arbitrary shape showed that there are no interference oscillations in the solution, since the particle has no plane-parallel faces. For wavelengths, at which there is no absorption, the power-law dependences are smooth. The color ratios for such a particle are close to 0.8 for wavelengths, at which there is no absorption. They also have a strong downtrend for wavelengths where the imaginary part of the refractive index is greater than 0.001. It is important to note that the color ratio for particles of arbitrary shape depends on the ratio of the real parts of the corresponding refractive index, rather than on the wavelength, in general. The DR is also a fairly smooth function due to the absence of interference oscillations and the waveguide effect for such particles. For wavelengths with $n \approx 1.3 + 0i$, the depolarization ratio lies in the range 0.5–0.55 for all calculated particle sizes. In this case, an increase in the real part of the refractive index to 1.48 and 1.6 cause a decrease in the depolarization ratio to 0.4 and 0.35 in the entire size range. Taking into account the influence of absorption leads to a significant decrease in the depolarization ratio, down to zero, when the value of the imaginary part of the refractive index is more than 0.002i in particle sizes of more than 100 μm. This clearly indicates the predominance of the external mirror component in the scattered radiation. Therefore, it can be concluded that the value of the depolarization ratio can be used as a criterion for creating algorithms for reconstructing the size of dust aerosol particles from the data of polarization laser sensing.

Challenges

This paper presents a solution to the problem of light scattering by arbitrarily oriented hexagonal plates and columns, as well as arbitrarily shaped particles in the size range from 10 to 100 μm for λ of 0.355; 0.532; 1.064; 1.55; 2; 2.15 μm. At λ of 0.532 and 1.064 μm, in addition to the refractive index of ice, the refractive index of the dust aerosol was used: 1.48 + 0.002i and 1.6 + 0.002i, respectively. It was found that for arbitrarily oriented hexagonal columns larger than 50 μm and arbitrarily shaped particles for λ of 0.355; 0.532 and 1.064 μm in the solution, the influence of interference oscillations can be neglected, since their value does not exceed 1%. However, for hexagonal plates, interference oscillations can exceed 5%, especially for wavelengths over 1 μm. It is shown that for particles up to 100 μm in size with an imaginary part of the refractive index greater than 0.004i, significant deviations from the power law are observed.

Acknowledgements

The calculation of the light scattering was performed with financial support of Russian Foundation for Basic Research (Grants No. 19-45-703010, 19-01-00351). The building of particle models was supported by the Ministry of Science and Higher Education of the Russian Federation (V.E. Zuev Institute of Atmospheric Optics of Siberian Branch of the Russian Academy of Sciences).

References

Liou, K. N., Light scattering by ice clouds in the visible and infrared: A theoretical study, *J. Atmos. Sci.*, 29, 524–536, 1972.

Liu C., Panetta R.L., Yang P., The effective equivalence of geometric irregularity and surface roughness in determining particle single-scattering properties, *Opt. Express*., 22 (19), 23620–23627, 2014.

Borovoi, A., Konoshonkin, A., Kustova, N., The physics optics approximation and its application to light backscattering by hexagonal ice crystals, *J. Quant. Spectrosc. Radiat. Transfer*, 146, 181–189, 2014.

Databank of backscatter matrices calculated within the framework of physical optics approximation. URL: ftp://ftp.iao.ru/pub/GWDT/Physical_optics/Backscattering

Application of Aerosol Typing to Separate Three-Component Aerosol Mixture From Raman Lidar Data Measured in West Africa, December 2015

A. Kolgotin[1], *I. Veselovskii*[1], *M. Korenskiy*[1], *P. Goloub*[2], *Q. Hu*[2], *T. Podvin*[2]
kolgotin@pic.troitsk.ru
(1) Prokhorov General Physics Institute of the Russian Academy of Sciences, Vavilov st., 38, Moscow, Russia
(2) Univ. Lille, CNRS, UMR 8518, Laboratoire d'Optique Atmospherique, 59655, Villeneuved d'Ascq , France.

Introduction

In recent study [1] we developed mathematical model and general equations describing the relationships between intensive parameters of pure aerosol components in a mixture and total intensive parameters of that mixture. The intensive parameters are characterized by particle lidar ratios, Ångström exponents and linear depolarization ratios that can be measured with Raman lidar. Here we consider particular case in which aerosol mixture may consist of 1, 2 or 3 components and apply the general equations to estimate the portions of each component from Raman lidar measurements of particle linear depolarization ratio (δ), extinction (α) and backscatter (β) coefficients (β+α+δ dataset) at 532 nm carried out in West Africa, December 2015.

Methodology

We assume aerosol external mixture may consist of 1-3 components, for example, dust (d), smoke (s) and marine (m) particles. Each component is described by unknown, non-negative, portion, or fraction $\phi_{\beta,\mathrm{d}}$, $\phi_{\beta,\mathrm{s}}$ or $\phi_{\beta,\mathrm{m}}$ of mixture backscatter coefficient β at 532 nm respectively. For that particular case the general equations developed in [1] can be simplified so that the fractions fulfill the following system of linear algebraic equations

$$\begin{cases} \phi_{\beta,\mathrm{d}}\,\Lambda_\mathrm{d} + \phi_{\beta,\mathrm{s}}\,\Lambda_\mathrm{s} + \phi_{\beta,\mathrm{m}}\,\Lambda_\mathrm{m} = \Lambda, \\ \phi_{\beta,\mathrm{d}}\,\delta_\mathrm{d}' + \phi_{\beta,\mathrm{s}}\,\delta_\mathrm{s}' + \phi_{\beta,\mathrm{m}}\,\delta_\mathrm{m}' = \delta', \\ \phi_{\beta,\mathrm{d}} + \phi_{\beta,\mathrm{s}} + \phi_{\beta,\mathrm{m}} = 1, \end{cases} \quad (1)$$

where mixture lidar ratio $\Lambda=\alpha/\beta$ and depolarization potential $\delta'=\delta(1+\delta)^{-1}$ are measured with lidar at 532 nm and Λ_p, δ_p' are respective intensive parameters of each component (p=d, s or m) we know a priori. In this study we consider, in particular, the intensive parameters of "pure" aerosol components shown in Table 1 as one of the possible scenarios [2]. Solving the system (1) permits us to express the unknown fractions in explicit form

$$\begin{cases} \phi_{\beta,\mathrm{d}} = \dfrac{\Lambda\delta_\mathrm{m}' - \Lambda\delta_\mathrm{s}' + \Lambda_\mathrm{s}\delta' - \Lambda_\mathrm{m}\delta' - \Lambda_\mathrm{s}\delta_\mathrm{m}' + \Lambda_\mathrm{m}\delta_\mathrm{s}'}{\Lambda_\mathrm{d}\delta_\mathrm{m}' - \Lambda_\mathrm{d}\delta_\mathrm{s}' + \Lambda_\mathrm{s}\delta_\mathrm{d}' - \Lambda_\mathrm{m}\delta_\mathrm{d}' - \Lambda_\mathrm{s}\delta_\mathrm{m}' + \Lambda_\mathrm{m}\delta_\mathrm{s}'} \\ \phi_{\beta,\mathrm{s}} = \dfrac{\Lambda\delta_\mathrm{d}' - \Lambda\delta_\mathrm{m}' - \Lambda_\mathrm{d}\delta' + \Lambda_\mathrm{m}\delta' + \Lambda_\mathrm{d}\delta_\mathrm{m}' - \Lambda_\mathrm{m}\delta_\mathrm{d}'}{\Lambda_\mathrm{d}\delta_\mathrm{m}' - \Lambda_\mathrm{d}\delta_\mathrm{s}' + \Lambda_\mathrm{s}\delta_\mathrm{d}' - \Lambda_\mathrm{m}\delta_\mathrm{d}' - \Lambda_\mathrm{s}\delta_\mathrm{m}' + \Lambda_\mathrm{m}\delta_\mathrm{s}'} \\ \phi_{\beta,\mathrm{m}} = \dfrac{\Lambda\delta_\mathrm{s}' - \Lambda\delta_\mathrm{d}' + \Lambda_\mathrm{d}\delta' - \Lambda_\mathrm{s}\delta' - \Lambda_\mathrm{d}\delta_\mathrm{s}' + \Lambda_\mathrm{s}\delta_\mathrm{d}'}{\Lambda_\mathrm{d}\delta_\mathrm{m}' - \Lambda_\mathrm{d}\delta_\mathrm{s}' + \Lambda_\mathrm{s}\delta_\mathrm{d}' - \Lambda_\mathrm{m}\delta_\mathrm{d}' - \Lambda_\mathrm{s}\delta_\mathrm{m}' + \Lambda_\mathrm{m}\delta_\mathrm{s}'} \end{cases} \quad (2)$$

Component extinction fractions can be found as [1]

$$\phi_{\alpha,\mathrm{p}} = \phi_{\beta,\mathrm{p}}\Lambda_\mathrm{p}\Lambda^{-1} \qquad \mathrm{p=d,s,m} \quad (3)$$

Results and discussion

We use Eqs (2)-(3) and intensive parameters of pure aerosol types (see Table 1) to separate aerosol mixture from rotation Mie-Raman lidar measurements of β+α+δ profiles at 532 nm carried out on 24 Dec 2015, 19:00-23:00, in West Africa. Detailed description of the measurement case is in Ref. [3].

Results of separation in basic scenario (at smoke lidar ratio Λ_s = 70 sr) are shown in Fig. 1. We observe that dust particles (magenta) dominate in the lower aerosol layer below 2 km whereas portion of smoke particles (gray) is largest in the upper aerosol layer above 2.5 km. Fraction of marine particles is smallest in the both aerosol layers and does not exceed $\phi_{\beta,\mathrm{m}}$=10 % in terms of backscatter coefficient if we consider the heights below 4 km. Lidar ratio at 532 nm (red, right panel) degrades from 75 sr below 4 km down to 30 sr above 4 km. As result the marine part in profile becomes prevalent in terms of backscatter coefficient at 4.25 km.

We investigate how far separation results are sensitive to the intensive parameters of pure aerosol types shown in table 1? In this regard we vary these parameters and compare derived results with basic scenario results shown in Fig. 1.

Table 1. Intensive parameters of pure aerosol types

Type	Denotation	Lidar Ratio, sr	Depolariz.
Dust	p=d	Λ_d = 58	δ_d=0.35
Smoke	p=s	Λ_s =70…80	δ_s=0.07
Marine	p=m	Λ_m = 20	δ_m=0.15

Measurements of dust intensive parameters are most robust [2-4]. Moreover, dust particles are not hygroscopic and their intensive parameters do not depend on relative humidity. In this measurement case we can admit that the lowest part of profile is represented only by dust particles because

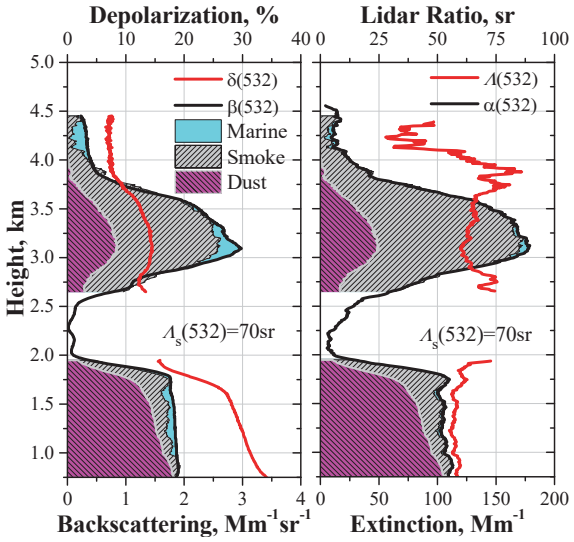

Figure 1. Separation of dust (magenta), smoke (gray) and marine (cyan) particle profiles with intensive parameters shown in Table 1 and Λ_{smoke} =70 sr from lidar measurements of backscatter (black, left panel), extinction (black, right panel) and depolarization ratio (red, left panel) at 532 nm in Senegal, 24 Dec 2015, 19:00-23:00

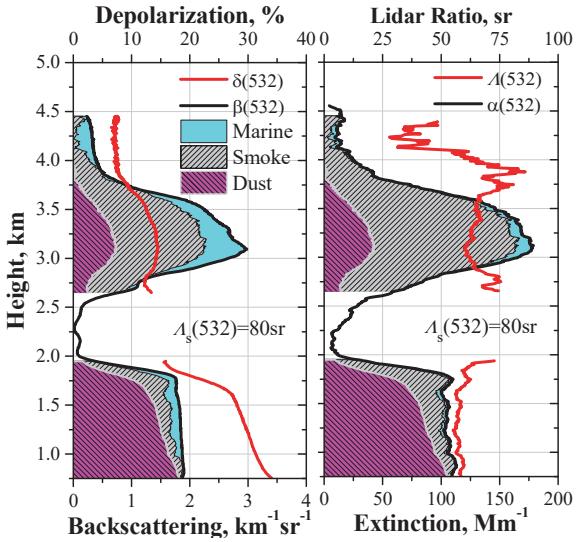

Figure 2. Same as Fig. 1 but smoke lidar ratio is equal to Λ_{smoke} =80 sr at 532 nm.

depolarization ratio is close to $\delta \approx 0.35$ at 532 nm on 750 m [2, 3]. Simultaneously, lidar ratio is $\Lambda(532) \approx 58$ sr on that height. We keep the dust intensive parameters Λ_d =58 sr and δ_d =0.35 fixed in our sensitive analysis (see Table 1).

Marine lidar and depolarization ratios usually are low and does not exceed $\Lambda_m \leq 30$ sr and $\delta_m \leq 0.05$ at 532 nm respectively. However marine particles are hygroscopic. Moreover shape of these particles becomes aspheric at dry ambient conditions and parameters δ_m may reach 0.2 and more. Therefore we considered the variation intervals $\Lambda_m \in [10;30]$ sr and $\delta_m \in [0;0.2]$ in our sensitive analysis. Results derived over these intervals and in the basic scenario do not differ significantly (not shown).

Gyroscopic properties of smoke and marine particles are similar. Variation of smoke depolarization ratio on interval $\delta_s \in [0;0.1]$ nm does not yield new solutions, too (not shown) but results of separation are sensitive to variation of smoke lidar ratio at 532 nm. Increasing the profile lidar ratio to peak values of Λ=75 sr is caused by smoke particles. Therefore we consider interval from Λ_s=70 sr in basic scenario to Λ_s=80 sr that is quite possible for smoke particles (see Table 1). Results of separation at Λ_s=80 sr are shown in Fig. 2. We see that portion of marine particles is doubled and reach $\phi_{\beta m}$=20 % in terms of backscatter coefficient at 3 km.

Challenges

Separation of complex aerosol mixture consisting of three and more components from Raman lidar data is knotty problem. The problem becomes even more complicated when the components from the mixture are characterized by high depolarization properties. So far the explicit expressions were derived just for 2 component aerosol mixture [4]. We solve this problem for arbitrary aerosol mixture that can simultaneously consist of N_{AT}=3 and even more aerosol components up to [1]

$$N_{AT} \leq 3(\beta)+2(\alpha)+3(\delta) = 8$$

References

1. A. Kolgotin et al.,Aerosol typing: how many aerosol types can be inferred from multiwavelength HSRL/Raman Lidar data?, Proceedings of the 1st ELC, July 2018, Thessaloniki, 07.

2. R. E. Mamouri and A. Ansmann, Potential of polarization/Raman lidar to separate fine dust, coarse dust, maritime, and anthropogenic aerosol profiles, *AMT*, 10, 3403–3427, 2017.

3. I. Veselovskii et al., Characterization of smoke/dust episode over West Africa: comparison of MERRA-2 modeling with multiwavelength Mie-Raman lidar observations, *AMT, 11, 949–969*, 2018.

4. M. Tesche et al., Vertically resolved separation of dust and smoke over Cape Verde using multiwavelength Raman and polarization lidars during Saharan Mineral Dust Experiment 2008, *JGR, 114*, D13202, 2009.

Algorithm to determine the aerosol pollution layers from ceilometer profiles

M. Adam[1], *V. Nicolae*[1], *M. Boldeanu*[1]
Mariana.adam@inoe.ro
(1) National Institute of Research and Development for Optoelectronics - INOE 2000, 409 Atomistilor St, Magurele, Romania

Introduction

The ceilometers were originally designed for cloud base height estimation (CBH) in order to assist the aviation. National ceilometer networks are in place, usually belonging to the national meteorological services such as Met Office and DWD (e.g., Adam et al., 2016). Over the last 10-15 years or so, the ceilometers were taken into account for scientific research and were involved in estimation of the planetary boundary layer (PBL) (e.g., Stachlewska et al., 2012; Lotteraner and Piringer, 2016; Lee et al., 2019), determination of the particles backscatter coefficient (Heese et al., 2010; Wiegner et al., 2014; Cazorla et al., 2017) or pollution monitoring (e.g., Marcos et al., 2018; Adam et al., 2020). Recently, the European automatic lidar and ceilometer network, EPROFILE, was established (https://e-profile.eu/#/cm_profile, last access 20210528) where attenuated backscatter profiles are available in near real time for 499 lidars and ceilometers.

Two Nimbus ceilometers from Lufft (https://www.lufft.com/products/cloud-height-snow-depth-sensors-288/lufft-ceilometer-chm8k-2405/, last access 20210528) were installed at INOE in 2018 and are part of EPROFILE network while one of them is part of CLOUDNET as well (https://cloudnet.fmi.fi/, last access 20210528).

The present research topic refers to the development of an algorithm, capable to estimate the tropospheric aerosol layers from ceilometer's RCS (range corrected signal). The script is written in Matlab (https://www.mathworks.com/, last access 20210528).

The main steps of the algorithm are:

- The input RCS profiles are averaged over 1 h and 60 m
- Additional smoothing is performed over 9 bins
- RCS for which SNR < 3 are dismissed
- The variance of the cumulative signal (RCS) is calculated (VCS)
- A new vector is defined as: NV=VCS(1:2:end-1).*VCS(2:2:end)
- Calculate the local maxima (islocalmax in Matlab) of NV which gives the location of the inflection points in NV
- Calculate the local minima (islocalmin in Matlab) of NV which gives the location of the minima and maxima in NV

The data for which the prominence of the inflection points and the corresponding NV values are smaller than 0.01 is dismissed

- Few other criteria are involved in order to retain the optimum number of inflection points and local minima or maxima
- The first and last 60 m from the bottom and top of the layer are dismissed.

Currently, we apply the algorithm for the profiles which do not have clouds, based on CBH information given in the raw data. However, it can be applied for clouds as well. Once mature, the algorithm will be implemented for the study on near real time alert system. We also plan to adjust it for the lidar profiles used in our research on biomass burning. See the other two presentations by Adam et al., at the conference.

Results and discussion

Figure 1 shows the layers determined on 20210410.

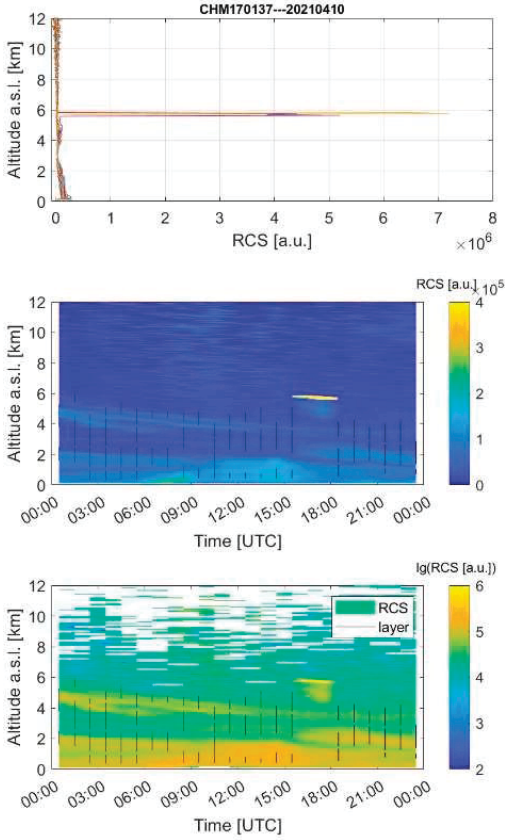

Figure 1. (upper) RCS versus altitude, (middle) RCS versus time and altitude and superimposed layers, (lower) same as middle but with RCS in log scale. Data are from 10 April 2021.

Clouds were observed between 16:00 and 18:00 UTC. We visually observe the presence of several aerosol layers. Thin layers at ~ 5 km altitude (a.s.l.) are observed at 00:00 which descend towards ~ 3.5 km at 24:00. Other layers are observed between 00:00 and 09:00 UTC around 1.5 – 2 km and between 15:00 and 24:00 around 2 km.

Figure 2 shows the profile for 05:00-06:00 UTC and the four layers detected. At a glance, the layers' delimitation looks ok. Figure 3 shown the profile for 11:00-12:00 UTC. Visually, the layers are not accurate. The first layer does not catch the whole PBL while the IInd and the IIIrd layer might have other borders.

A large variety of delicate situations will be discussed during conference while comparisons with the gradient method will be shown.

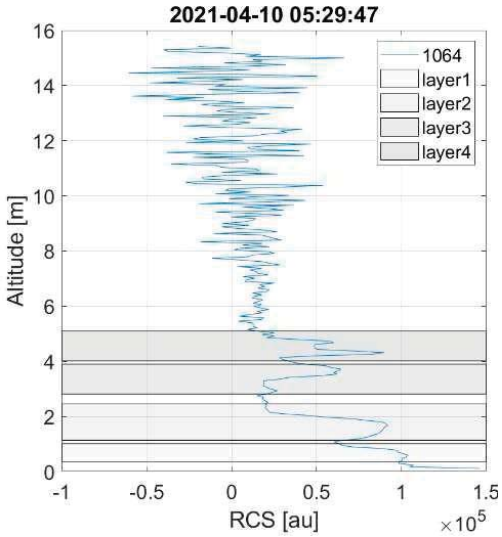

Figure 2. RCS profile for 05:00-06:00 UTC, 10 April 2021 and the estimated layers.

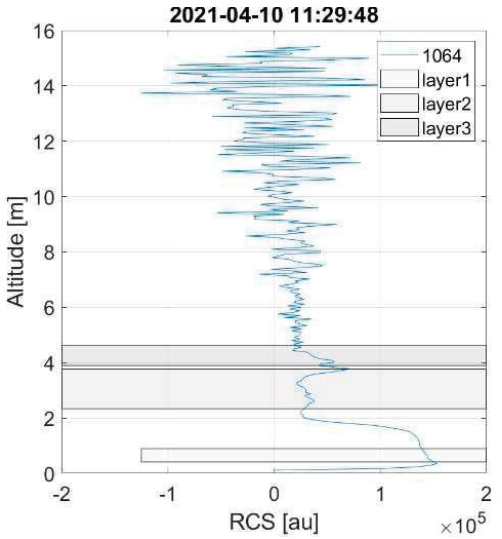

Figure 3. RCS profile for 11:00-12:00 UTC, 10 April 2021 and the estimated layers.

Challenges

The main challenges for pollution layers estimation are the following:

- Layer definition.
- How to proceed with multiple adjacent thin layers?
- Low SNR in ceilometer profiles

Acknowledgements

This work is supported by the Romanian National contracts 18N/08.02.2019, 19PFE/17.10.2018, PN-III-P2-2.1-PED-2019-1816 and partly by European Regional Development Fund through Competitiveness Operational Programme 2014-2020, Action 1.1.3 Creating synergies with H2020 Programme, project Support Centre for European project management and European promotion, MYSMIS code 107874 and European Regional Development Fund through Competitiveness Operational Programme 2014–2020, POC-A.1-A.1.1.1-F-2015, project Research Centre for environment and Earth Observation CEO-Terra".

References

Adam et al., From operational ceilometer network to operational lidar network, *EPJ Web of Conferences*,119, 27007, 2016.

Adam et al., Automatic alert system for tropospheric particulate pollution monitoring, *EPJ Web Conferences*, 237, 03004, 2020.

Cazorla et al., Near-real-time processing of a ceilometer network assisted with sun-photometer data: monitoring a dust outbreak over the Iberian Peninsula, *Atmos. Chem. Phys*., 17, 11861–11876, 2017.

Heese et al., Ceilometer lidar comparison: backscatter coefficient retrieval and signal-to-noise ratio determination, *Atmos. Meas. Tech*., 3, 1763–1770, 2010.

Wiegner et al., What is the benefit of ceilometers for aerosol remote sensing? An answer from EARLINET, *Atmos. Meas. Tech*., 7, 1979–1997, 2014.

Lee et al., Ceilometer Monitoring of Boundary - Layer Height and Its Application in Evaluating the Dilution Effect on Air Pollution, *Boundary-Layer Meteorol*., 172, 435–455, 2019.

Lotteraner and Piringer, Mixing-Height Time Series from Operational Ceilometer Aerosol-Layer Heights, *Boundary-Layer Meteorol*., 161, 265–287, 2016.

Marcos et al., Analysis of four years of ceilometer-derived aerosol backscatter profiles in a coastal site of the western Mediterranean, *Atmos. Res*., 213, 331-346, 2018.

Stachlewska et al., Ceilometer Observations of the Boundary Layer over Warsaw, Poland, *Acta Geophys*., 60, 1386-1412, 2012.

Aerosol layer identification and segmentation from lidar and ceilometer profiles using unsupervised deep learning

M. Boldeanu[1,2], *C. Manolache*[2], *H. Cucu*[2], *C. Burileanu*[2], *C. Talianu*[1],
mihai.boldeanu@inoe.ro
(1) INOE2000, National Institute for Research and Development in Optoelectronics, Măgurele, Romania
(2) ETTI, University Politehnica of Bucharest, Bucharest, Romania

Introduction

Atmospheric lidar systems are some of the most important data sources when it comes to the study of aerosols and their effect on the environment. The difficulty in using them is the huge amount of data they produce and the lack of experts that can find all the interesting events lidars capture.

In this work we focus on developing an unsupervised method to extract features from the attenuated backscatter profiles obtained from lidar and ceilometer measurements by using a deep fully-convolutional neural network architecture (Xia et al., 2017). This method will be used to select automatically interesting events that can be further analyzed by experts.

The study is performed at the Romanian Atmospheric 3D Observatory – RADO, Măgurele, Romania, covering three years (2018 - 2020) of aerosol remote sensing measurements. From this period, days with different atmospheric conditions are considered, if there were simultaneous ceilometer and lidar measurements. The attenuated backscatter profiles are computed from measurements averaged at 5 minutes and with a spatial resolution of 15 m, covering the altitude range from 0.2 km to 15.0 km.

The architecture selected makes use of un-annotated data sources and is generally used in learning image segmentations in an unsupervised manner. In this use case the architecture has two task that it is trying to learn. The first task is a segmentation of the initial four attenuated backscatter profiles (3 lidar + 1 ceilometer). The second task is to reconstruct the original input using the information stored in the segmentation. This secondary task having a regularizing effect for the first task.

In the following sections some initial results are presented and in the final section the challenges facing this approach are discussed.

Results and discussion

In Figure 1 the architecture of the neural network model is shown. It can be seen that the architecture has multiples losses that are used to train both tasks simultaneously.

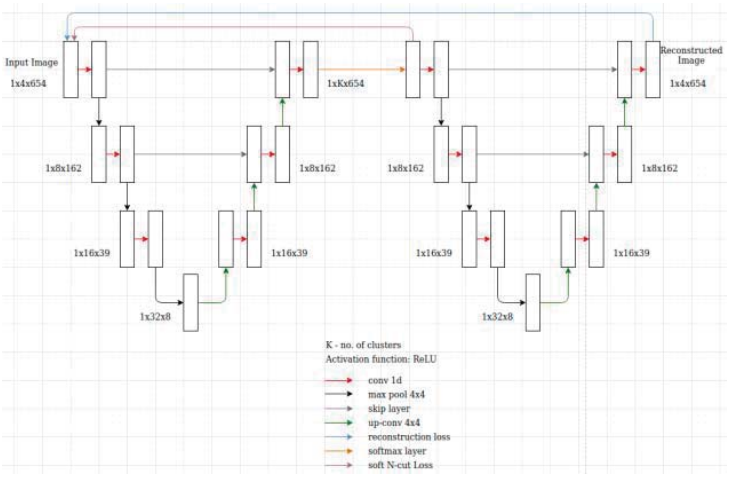

Figure 1. W-net architecture used for unsupervised aerosol layer detection.

The neural network is trained only using attenuated backscatter profiles. In Figure 2. the input signals, the reconstructions and the layer segmentations are presented. The model is trained to group together similar values that are close together in height into segmentations that minimize a normalized cut loss (Tang et al., 2018). The normalized cut loss is composed of a distance metric for the lidar bins and an intensity metric calculated from the normalized intensity of the lidar + ceilometer profiles. This type of segmentations is generally used for images but can be applied to vertical profiles with minimal modification.

The reconstruction task starts from the middle of the W-net and uses as inputs the segmentation. The network tries to recreate the original inputs using only the low dimensional segmentation made by the first part of the network. This task forces the network to learn a segmentation that keeps as much of the original information as possible.

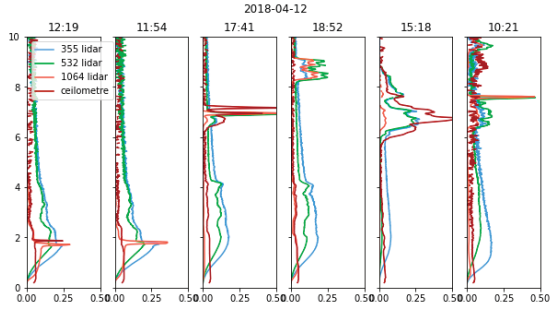

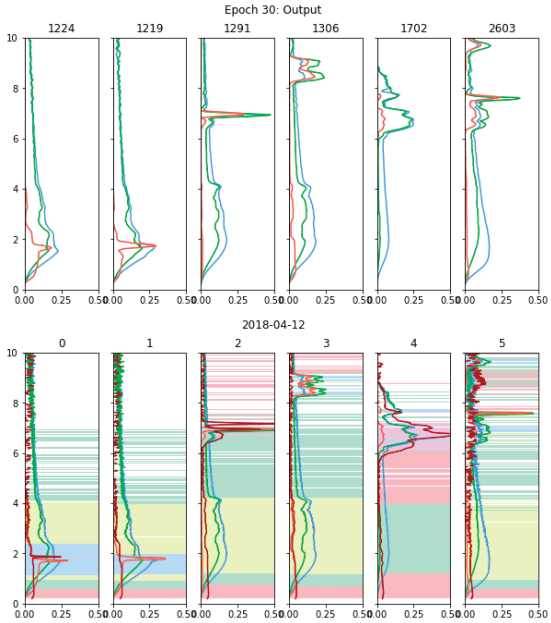

Figure 2. The top panel is a random selection of attenuated backscatter signals used as input for the network in the middle the reconstructed signals are shown and in the bottom panel the segmentation of layers made by the network.

Challenges

Previous methods for layer identification such as the gradient method (Belegante et al. 2014) and wavelet method (Cohn et al., 2000) relied on some parameters that are selected by the user. Our method allows a model to learn directly from the data without introducing human biases.
The difficult part of this study is making a correct validation of the output of neural networks. Without a database of input-output pairs the evaluation of the task is difficult. If previously developed methods are used to obtain an output for a certain input than the network will approximate that method. As such, in the near future we will create a database of input-output pairs that are identified by humans to test the algorithm against.

Acknowledgements

This work was supported by the Romanian National Core Program (Contract No. 18N/2019) and by a grant of the Romanian Ministry of Education and Research, CCCDI - UEFISCDI, project number PN-III-P2-2.1-PED-2019-2278, within PNCDI III.

References

Xide Xia, & Brian Kulis. W-Net: A Deep Model for Fully Unsupervised Image Segmentation. ArXiv, abs/1711.08506, 2017.

Meng Tang, Abdelaziz Djelouah, Federico Perazzi, Yuri Boykov, & Christopher Schroers. Normalized Cut Loss for Weakly-supervised CNN Segmentation. ArXiv, 2018.

Cohn, S. and Angevine W. M., 2000: Boundary layer height and entrainment zone thickness measured by lidars and wind-profiling radars. J. Appl. Meteor., 39, 1233–1247.

Belegante, L., Nicolae, D., Nemuc, A. et al. Retrieval of the boundary layer height from active and passive remote sensors. Comparison with a NWP model. Acta Geophys. 62, 276–289, 2014.

An end-to-end simulator and gas concentration retrieval processor applied to the MERLIN lidar mission to check its performance and study its sensitivity to geophysical parameters

V. Cassé [1], R. Armante [1], Ph. Bousquet [2], O. Chomette [1], C. Crevoisier [1], T. Delahaye [1], D. Edouart [1], F. Gibert [1], B. Millet [4], F. Nahan [3] and C. Pierangelo [4]
vincent.casse@lmd.ipsl.fr
(1) Laboratoire de Météorologie Dynamique (LMD/IPSL), École polytechnique, Institut polytechnique de Paris, Sorbonne Université, École normale supérieure, PSL Research University, CNRS, École des Ponts, Palaiseau, France
(2) Laboratoire des Sciences du Climat et de l'Environnement (LSCE/IPSL), CEA, CNRS, UVSQ, Université Paris-Saclay, Gif-sur-Yvette, France
(3) Magellium Paris, Courbevoie, France
(4) CNES, Toulouse, France

Introduction

MERLIN (MEthane Remote LIdar missioN) is a French-German space mission to monitor the atmospheric methane content (Ehret et al., 2017) using an Integrated Path Differential Absorption (IPDA) lidar (Nikolov et al., 2019). Awaiting actual space-based measurements in the second half of the decade, LIDSIM (LIDar SIMulator) simulates the digitised lidar signal. From this, PROLID (PROcessor LIDar) estimates the Differential Atmospheric Optical Depth (DAOD), the Scattering Surface Elevation (SSE) and the atmospheric methane column (XCH_4) (Cassé et al., 2021).

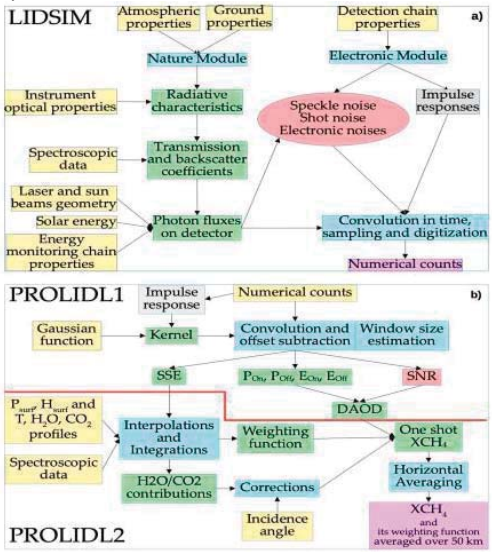

Figure 1. Flowcharts: (a) LIDSIM and (b) PROLID.

Results and discussion

Based on the atmospheric and ground properties, LIDSIM first determines the relative energy returned by the ground targets. The optical thicknesses are computed from the GEISA spectroscopic database (Jacquinet-Husson et al., 2016) including results from specific works (Delahaye et al., 2016 and 2019). Figure 2 shows the molar absorption cross sections in the passband of the filter in front of the detector.

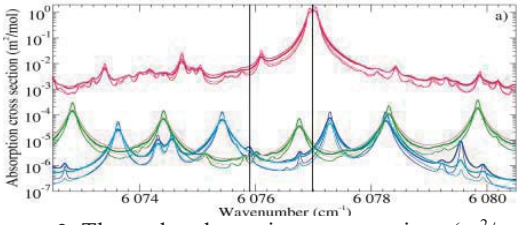

Figure 2. The molar absorption cross sections (m^2/mol) for CH_4, H_2O and CO_2. Bold curves for P = 1013.25 hPa (thin for 500 hPa), red/blue/green for T = 300 K (280 K) and magenta/cyan/brown for T = 250 K (220 K).

The detection chain that transforms the optical signal into an electrical signal is modelled, with speckle, shot and electronic noise simulated by random draws. The digitisation is done explicitly. Figure 3 shows the signals sampled at 75 MHz.

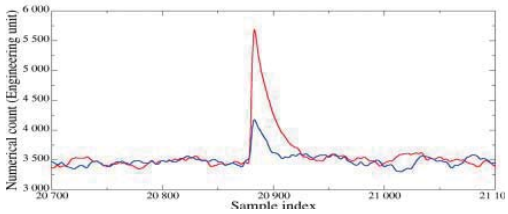

Figure 3. Simulated signals: On (blue) and Off (red).

An academic test is performed: for one atmosphere 14,000 signals are simulated with different random realisations of the noise. With a mean bias of 21 ppb and a standard deviation of 303 ppb, the shot-by-shot methane column is not useable (Figure 4). This highlights the need to average over several shots to achieve the desired accuracy (Tellier et al., 2018).

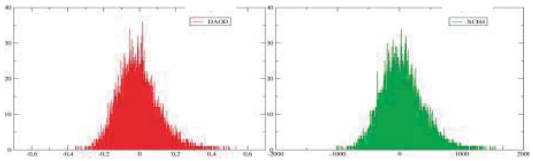

Figure 4. Error histograms for DAOD (red, with a sampling of 3.5 10-4 no unit) and methane column XCH_4 (green, with a sampling of 1 ppb).

Finally, an orbit was simulated with realistic methane, but without aerosols or clouds. The methane retrieval for each shot is almost perfect without instrumental noise, but becomes very noisy with it (Figure 5) as already seen with the academic test.

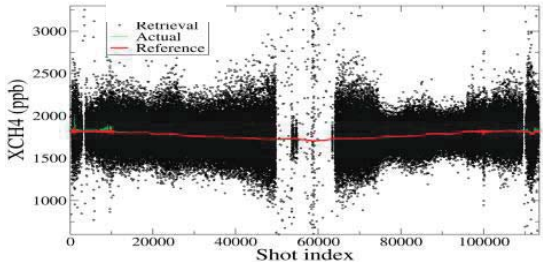

Figure 5. Retrieved XCH4 per shot with instrumental noise (in black) compared to its reference (in red).

Table 1 provides for 113 400 individual shots and for 810 cells of 50 km grouping 140 consecutive shots: the % of points for which the methane column is retrievable (sufficient reflectivity) and the corresponding SSE and XCH_4 statistics. Figure 6 shows the results per cell along the ground track.

Table 1. Mean bias and mean standard deviation.

	SSE (in m)			XCH_4 (in ppb)		
	Per shot		Per cell	Per shot		Per cell
Noise	without	with	with	without	with	with
Points	100 %	85%	83%	100 %	85%	83%
Bias	0.02	0.	0.	0.07	11.3	1.2
Sigma	0.03	1.7	0.1	0.10	250.3	16.0

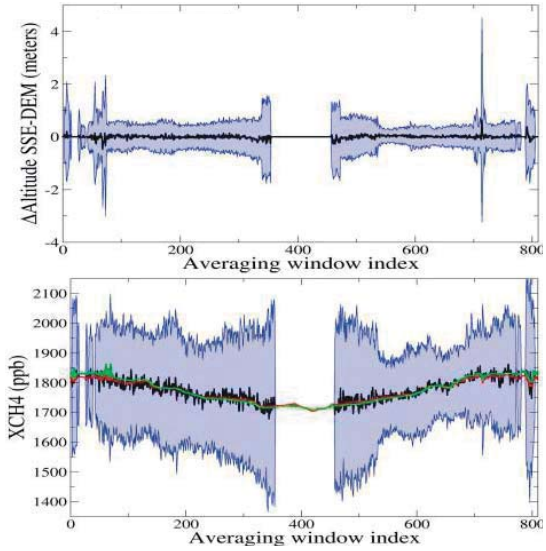

Figure 6. SSE and XCH_4 averaged over about 50 km: mean (black curve) and standard deviations (blue area).

These first full orbit simulations confirm that the MERLIN instrument design meets the required performance (Figure 7).

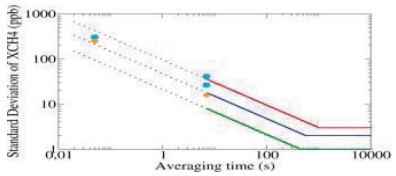

Figure 7. Results of the academic test (cyan dots) and the orbit simulation (orange dots) compared to the three performance levels set for MERLIN.

Challenges

The inclusion of aerosols and clouds will both decrease the number of cases where the methane inversion is possible and increase its uncertainty. A study is underway to quantify these effects and to confirm that they do not introduce regional biases, which are a priori lesser with active remote sensing methods.

Performance varies at first order with the square root of the averaging time. A trade-off must be made between horizontal resolution and accuracy, depending on the geophysical variability of methane and other quantities such as ground reflectance and relief.

Acknowledgements

The authors are grateful to CNES for its financial and moral support and to the whole Franco-German MERLIN project team. They dedicate their work to the memory of Pierre Flamant who initiated it in 2008.

References

Cassé et al., Development and Validation of an End-to-End Simulator and Gas Concentration Retrieval Processor Applied to the MERLIN Lidar Mission, *Remote Sens.* 13, 2679, doi:10.3390/rs13142679, 2021.

Delahaye et al., Precise methane absorption measurements in the 1.64 µm spectral region for the MERLIN mission, *JGR Atmos*., 121, 7360–7370, doi: 10.1016/j.jms.2016.06.007, 2016.

Delahaye et al., Measurement and modeling of air - broadened methane absorption in the MERLIN spectral region at low temperatures, *JGR Atmos*., 124, 3556– 3564, doi: 10.1029/2018JD028917, 2019.

Ehret et al., MERLIN: A French-German Space Lidar Mission Dedicated to Atmospheric Methane, *Remote Sens*. 9, 1052, doi:10.3390/rs9101052, 2017.

Jacquinet-Husson et al., The 2015 edition of the GEISA spectroscopic database, *J. Mol. Spectrosc*., 327, 31–72, doi: 10.1016/j.jms.2016.06.007, 2016.

Nikolov et al., MERLIN: design of an IPDA LIDAR instrument, *CEAS Space J*., 11, 437–457, doi: 10.1007/s12567-019-00267-7, 2019.

Tellier et al., Averaging bias correction for the future space-borne methane IPDA lidar mission MERLIN, *Atmos. Meas. Tech*., 11, 5865–5884, 2018.

First ever observations of mineral dust in wintertime over Warsaw, Poland

D.M. Szczepanik[1], P. Ortiz-Amezcua[1], Ł. Janicka[1], W. Kumala[1], B. Heese [2],D. Altchausen [2], G. D' Amico[3],
I.S. Stachlewska[1]
iwona.stachlewska@fuw.edu.pl
(1)University of Warsaw, Faculty of Physics, Warsaw, Poland
(2) Leibniz Institute for Tropospheric Research (TROPOS), Leipzig, Germany;
(3) Institute of methodologies for environmental analysis – Consiglio Nazionale delle Ricerche (IMAA - CNR), Potenza, Italy;

Introduction

Unique for Eastern Europe record of high temperatures during wintertime combined with clear sky conditions gave an opportunity to investigate Saharan dust aerosol inflow between noon of 24.02.2021 and sunrise on 26.02.2021 over Warsaw (52.21 N, 20.98 E, 112 m a.s.l.). Measurements were taken at the Remote Sensing Laboratory, of the Faculty of Physics at the University of Warsaw with the PollyXT lidar (Engelmann et al. 2016), operated within European Aerosol Research LIdar NETwork (EARLINET, Pappalardo et al. 2014) and the CE318 sunphotometer within Aerosol Robotic NETwork (AERONET, Holben et al., 1998). Our work aims at analysing the aerosol optical and microphysical properties of the fully developed mineral dust plume observed on 25.02.2021, when aerosol formed a very wide (in the vertical direction) layer at an altitude range of 1.0-3.5 km, with evidence of a strong depolarization (Figure 1).

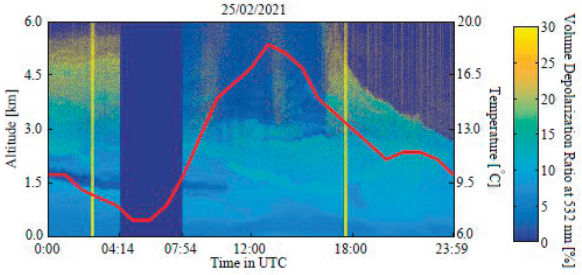

Figure 1. Volume Depolarization Ratio at 532 nm from PollyXT lidar measurements as well as diurnal cycle of air temperature (red line) at the EARLINET-ACTRIS station in Warsaw on 25.02.2021. Yellow strips denote times of depolarization calibration, while dark blue lack of data due to technical issues.

Results and discussion

Between 23-26.02.2021, unexpectedly high (nighttime minimum of 7.0°C and daytime maximum of 18.5°C) air temperatures for winter conditions were observed in Warsaw and throughout Poland. On 25.02.2021 (see Figure 1, in red), the mean temperature of +12 °C was recorded, which compared to the 20-year (2000-2020) average February temperature for Warsaw (- 0.2 ° C) indicates uniqueness of meteorological conditions. During this period the lidar data showed a high Volume Depolarization Ratio (VDR) within the boundary layer, as well as in the free troposphere, reaching the altitudes of even 3.5 km (Figure 1).

The aforementioned meteorological conditions and high VDR measured by lidar (Figure 1) together with the analyses of the backward trajectories calculated with the Hybrid Single Particle Lagrangian Integrated Trajectory model (HYSPLIT; Stein et al. 2015) depicted in Figure 2, indicate possible inflow of warm tropical air masses carrying desert dust from the Sahara. During the day, the air masses were advected from Northern Africa following stable high pressure system (meteo-maps not shown for brevity) and unlikely mixed with other aerosol sources.

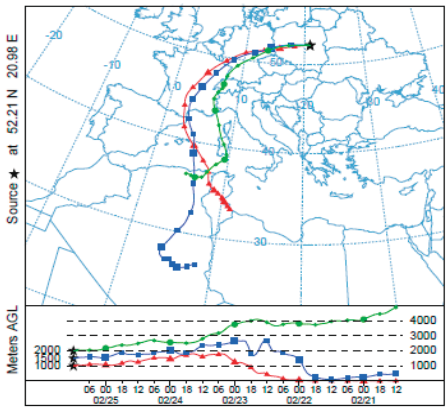

Figure 2. HYSPLIT 120h-backward trajectories ending at 12:00 UTC, 25.02.2021, calculated at 1.0, 1.5, and 2.0 km, using GDAS Meteorological Data.

Clear sky conditions allowed for obtaining 18 vertical profiles of optical properties of the atmospheric aerosol, with one hour averaging,

using the EARLINET-ACTRIS Single Calculus Chain tool (SCC, D'Amico et al. 2015, Mattis et al. 2016). Moreover, 9 almucantar scans of sunphotometer allowed to obtain the aerosol size distribution using AERONET NASA retrieval algorithm (Figure 3).

The mean values of optical properties calculated between 2.0-3.0 km from the lidar profiles coinciding in time with the sunphotometer scans are shown in Table 1. Note that the high values of Particle Depolarization Ratio δ (mean δ of 21 ± 3 %) indicate aspherical shape of the aerosol particles. Mean Lidar Ratio (LR=α/β) differs for each profile between 21 ± 5 and 66 ± 8 sr, with mean value of 39 ± 12 sr, which was reported for mineral dust mixtures within Warsaw boundary layer (Szczepanik et al. 2021).

Table 1. Mean lidar-derived optical properites within the Saharan dust layer at 2-3 km for periods coinciding with the sunphotometer measurements.

Time UTC	β 532 nm [Mm^{-1} sr^{-1}]	α 532 nm [$x10^{-4}$ m^{-1}]	δ 532 nm [%]
08:00	1.8 ± 0.5	0.84 ± 0.2	20 ± 4
09:00	2.1 ± 0.5	0.8 ± 0.2	19 ± 4
10:00	1.5 ± 0.3	1.0 ± 0.3	24 ± 2
11:00	3.3 ± 0.4	1.1 ± 0.1	20 ± 3
12:00	4.4 ± 0.8	0.9 ± 0.1	18 ± 2
13:00	2.3 ± 0.3	0.9 ± 0.2	15 ± 1
14:00	3.6 ± 0.3	1.0 ± 0.4	20 ± 2

The sunphotometer derived aerosol size distribution on 25.02.2021 was tri-modal with the coarse mode strongly dominating the inversion (see Figure 3). The difference between fine and coarse modes was increasing with time, whereby a supreme change in the values increase was observed between 9:52 and 10:52. In the previous and following periods to this time, the inversions were highly similar. The presence of middle mode of particle sizes (Figure 3, r of 0.6-0.7 µm) combined with mean value of LR (39 ± 12 sr) indicate that observed mineral dust might have been mixed with other typ of aerosol e.g. marine, pollution.

Summary

The main aim of this work was to demonstrate a first ever measured mineral dust episode during wintertime over Warsaw. The originality of this case is based on the meteorological conditions – the exceptionally high temperatures and clear sky conditions. The first results of optical properties

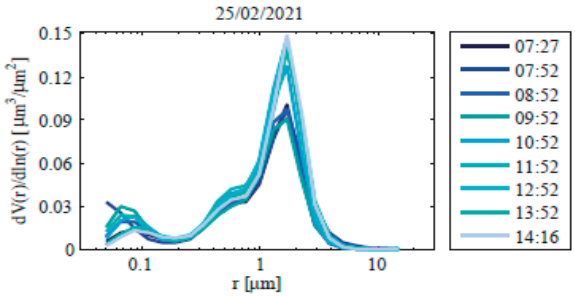

Figure 3: Aerosol size distribution obtained from the almucantar sunphotometer scans via Version 3 Inversion algorythm on 25.02.2021 calculated by the AERONET-NASA with level 1.5 data.

Acknowledgements

The EARLINET/AERONET site in Warsaw is as a part of the ACTRIS research infrastructure (https://www.actris.eu), the worldwide lidar network PollyNet (http://polly.tropos.de) and the AERONET NASA sunphotometer network. Authors acknoweledge the vital support from all those communities, especially the IMAA CNR for The Single Calculus Chain provision and development.

We gratefully acknowledge the NOAA Air Resources Laboratory (ARL) for the provision of the HYSPLIT transport and dispersion model and/or READY website (https://www.ready.noaa.gov) used in this study.

References

D'Amico et al., EARLINET Single Calculus Chain – overview on methodology and strategy, Atmos. Meas. Tech., 8, 4891-4916, 2015, doi:10.5194/amt-8-4891-2015

Mattis et al., EARLINET Single Calculus Chain – technical – Part 2: Calculation of optical products, Atmos. Meas. Tech., 9, 3009-3029, 2016, doi:10.5194/amt-9-3009-2016

Engelmann et al., The automated multiwave-length Raman polarization and water-vapor lidar PollyXT: The neXT generation., *Atmospheric Measurement Techniques*, 9. 1767-1784, doi:10.5194/amt-9-1767-2016, 2016.

Holben et al., AERONET – A federated instrument network and data archive for aerosol characterization, Remote Sens. Environ., 66, 1–16, https://doi.org/10.1016/S0034-4257(98)00031-5, 1998.

Pappalardo et al., EARLINET: towards an advanced sustainable European aerosol lidar network, Atmos. Meas. Tech., 7, 2389–2409, https://doi.org/10.5194/amt-7-2389-2014, 2014.

Stein et al., NOAA's HYSPLIT atmospheric transport and dispersion modeling system, *Bulletin of American Meteorological Society,* 96, 2059–2077. http://dx.doi.org/10.1175/BAMS-D-14-00110.1, 2015.

Szczepanik et al., Properties of Saharan Dust versus Local Urban Dust – a case study. Earth and Space Science, 2021 *accepted*

Observations of Wildfire smoke aerosols from Polly^{XT} and CL51 lidars in Finland

X. Shang[1], T. Mielonen[1], A. Lipponen[1], E. Giannakaki[1,2], A. Leskinen[1,3], V. Buchard[4,5], A. S. Darmenov[4], A. Kukkurainen[1,3], A. Arola[1], E. O'Connor[6], A. Hirsikko[6], M. Komppula[1]

xiaoxia.shang@fmi.fi
(1) Finnish Meteorological Institute, Kuopio, Finland
(2) Department of Environmental Physics and Meteorology, University of Athens, Athens, Greece
(3) Department of Applied Physics, University of Eastern Finland, Kuopio, Finland
(4) NASA/Goddard Space Flight Center, Greenbelt, MD, USA
(5) GESTAR/Universities Space Research Association, Columbia, MD, USA
(6) Finnish Meteorological Institute, Helsinki, Finland

Introduction

Wildfires release large amounts of aerosols into the atmosphere, contributing significantly to direct radiative forcing and affecting cloud optical properties by acting as cloud condensation nuclei or ice nuclei. Long-range transport of particles originating from biomass burning has been recognized as a significant source of tropospheric aerosols at northern latitudes (Generoso et al., 2003), with the most common being smoke from Russia or North America.

Several studies have investigated the properties of smoke plumes transported from Canadian wildfires to Europe (e.g., Ansmann et al., 2018), showing that biomass burning aerosols are medium- to high-absorbing particles with an almost spherical shape and small particle size, producing medium to high lidar ratios, low depolarization ratios and high Ångström exponents.

Similar observational records over Northern Europe are more scarce in the literature. On 4–6 June 2019, biomass burning aerosol layers were observed in the lower troposphere over Kuopio, Finland. These smoke particles originated from a Canadian wildfire event. In this study (Shang et al., 2021), we present observations of the smoke plume from a multi-wavelength Raman polarization lidar Polly^{XT} and a Vaisala CL51 ceilometer. A combined lidar–photometer approach is presented for estimating mass concentration.

Results and discussion

On 4–6 June 2019, aerosol layers arising from biomass burning were observed in the lower troposphere, at ~2–6 km height over Kuopio, Finland. Enhanced backscattered signals were detected by both a multi-wavelength Raman polarization lidar Polly^{XT} and a Vaisala CL51 ceilometer at the Vehmasmäki station in Kuopio (62°44'N, 27°33'E; 190 m above sea level) (Fig.1). These long-range-transported smoke particles originated from a Canadian wildfire event. An AERONET sun-photometer located in Kuopio observed enhanced AOD values in concert with high Ångström exponents (with fine-mode AOD fraction higher than 93 %), indicating the presence of fine-mode dominant aerosols in the atmospheric column.

The most pronounced smoke plume, defined as SPoI (Smoke Plume of Interest) was intensively investigated (Fig.1). Lidar ratios were derived from the Raman lidar, as 47 ± 5 sr at 355 nm and 71 ± 5 sr at 532 nm, showing that the aerosols of biomass burning origin in the SPoI were medium- to high-absorbing particles. Particle linear depolarization ratios (PDR) in this layer were measured as 0.08 ± 0.02 at 355 nm and 0.05 ± 0.01 at 532 nm.

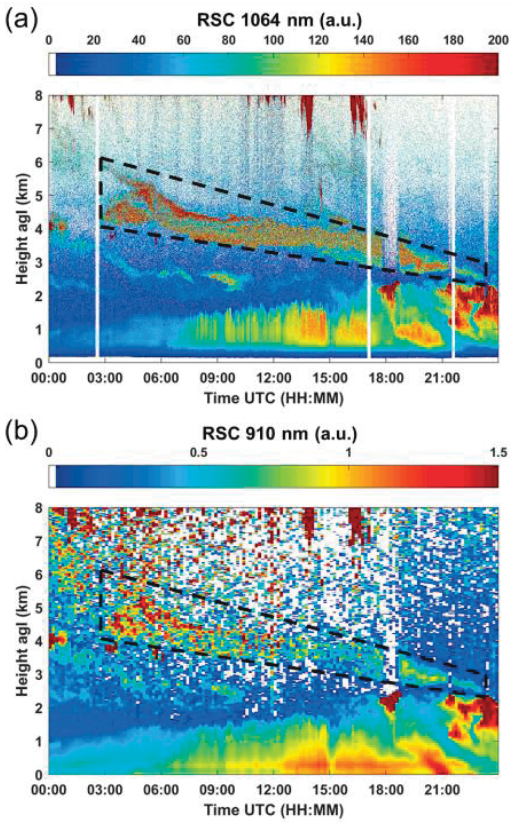

Figure 1. Range-corrected signal (RCS) (a) at 1064 nm of Polly^{XT} lidar, and (b) at 910 nm of CL51 ceilometer, on 5 June 2019 over Kuopio, Finland. The SPoI (Smoke Plume of Interest) is inside the black box with dashed lines.

A complete ceilometer data processing for a Vaisala CL51 is presented from sensor provided attenuated backscatter coefficient to particle mass concentration (including the water vapor correction for high latitude for the first time). Aerosol backscatter coefficients (BSCs) were measured at four wavelengths (355, 532, 1064 nm from Polly^{XT}, and 910 nm from CL51). Two methods, based on a combined lidar and sun-photometer approach, were applied for estimating mass concentrations: method #1, measured BSCs were converted to BSCs at 532 nm by corresponding measured backscatter-related Ångström exponent, and then be applied to estimate the mass concentrations; method #2, mass concentrations were estimated from measured BSCs at each wavelength independently. A difference of ~12 % or ~36 % was found between Polly^{XT} and CL51 estimated mass concentrations using method #1 or #2, showing that ceilometers are potential tools for mass concentration retrievals with ~50 % uncertainty, but with great spatial coverage. The mass retrievals were compared with the Modern-Era Retrospective analysis for Research and Applications, version 2 (MERRA-2) meteorological and aerosol reanalysis, where we considered and analysed two scenarios in the SPoI – 1) only smoke particles and 2) mixture of fine dust and smoke aerosols, and reported with the corresponding uncertainties.

Challenges

The retrieval methods for deriving the backscatter coefficient from ceilometers are quite mature (Wiegner and Geiß, 2012, Wiegner et al., 2014). However, the accuracy in deriving extinction coefficients (e.g. for further mass concentration estimates) is limited due to the unknown lidar ratio at 910 or 1064 nm. Characteristic lidar ratio values for aerosol types are often measured at 355 or 532 nm; it is only recently that Haarig et al. (2016) measured the lidar ratio at 1064 nm, and reported values of 80–95 sr for aged biomass burning smoke (Haarig et al., 2018). A value of 82 sr for lidar ratio, as measured at 1064 nm, was assumed as being appropriate for use at 910 nm in this study. Uncertainties in the lidar ratio at ceilometer wavelengths are much larger, compared to Raman lidars, which results in higher uncertainties in derived extinction coefficients.

An interesting feature in the MERRA-2 simulation results is the presence of dust in the SPoI. The POLIPHON (Polarization lidar photometer networking) method (Mamouri and Ansmann, 2014, 2017) was applied to separate fine dust and biomass burning aerosols for the SPoI, based on Polly^{XT} lidar data (BSC and PDR at 532 nm were used in this study). The inclusion of a dust mixture results in slightly higher estimated mass concentration values, with a difference negligible considering the uncertainties. It is not possible to perform the aerosol separation using ceilometer data alone, as no depolarization information is available at this wavelength (910 nm). For this instrument, only one aerosol type should always be assumed in the layer of interest, which then imparts an additional bias when estimating the mass concentration.

Acknowledgements

This research has been supported by the National Emergency Supply Agency (decision number 19078). Tero Mielonen's work was supported by the Academy of Finland (grant No. 308292).

References

Ansmann, A., et al., Extreme levels of Canadian wildfire smoke in the stratosphere over central Europe on 21-22 August 2017, *Atmos. Chem. Phys*., 18(16), 11831–11845, 2018.

Generoso, S., et al., Improving the seasonal cycle and interannual variations of biomass burning aerosol sources, *Atmos. Chem. Phys*., 3(4), 1211–1222, 2003.

Haarig, M., et al., 1064nm rotational Raman lidar for particle extinction and lidar-ratio profiling: Cirrus case study, *Atmos. Meas. Tech*., 9(9), 4269–4278, 2016.

Haarig, M., et al., Depolarization and lidar ratios at 355, 532, and 1064 nm and microphysical properties of aged tropospheric and stratospheric Canadian wildfire smoke, *Atmos. Chem. Phys*., 18(16), 11847–11861, 2018.

Mamouri, R. E. and Ansmann, A., Fine and coarse dust separation with polarization lidar, *Atmos. Meas. Tech*., 7(11), 3717–3735, 2014.

Mamouri, R. E. and Ansmann, A., Potential of polarization/Raman lidar to separate fine dust, coarse dust, maritime, and anthropogenic aerosol profiles, *Atmos. Meas. Tech*., 10(9), 3403–3427, 2017.

Shang, X., et al., Canadian biomass burning aerosols observations from a multi-wavelength Raman polarization lidar and a ceilometer in Finland, *Atmos. Meas. Tech. Discuss.* [preprint], in review, 2021.

Wiegner, M. and Geiß, A., Aerosol profiling with the Jenoptik ceilometer CHM15kx, *Atmos. Meas. Tech*., 5(8), 1953–1964, 2012.

Wiegner, M., et al., What is the benefit of ceilometers for aerosol remote sensing? An answer from EARLINET, *Atmos. Meas. Tech*., 7(7), 1979–1997, 2014.

End-to-end Simulation of a space-borne Raman Lidar For the thermodynamic profiling of the atmosphere

N. Franco[1], P. Di Girolamo[1], D. Summa[1,2], B. De Rosa[1,2], A. Behrendt[3], A. Comerón[4], V. Wulfmeyer[3]
noemi.franco@unibas.it
(1) Scuola di Ingegneria, Università degli Studi della Basilicata, Potenza, Italy
(2) IMAA-CNR, Tito Scalo (Pz), Italy
(3) Institut fur Physik und Meteorologie, University of Hohenheim, Stuttgart, Germany
(4) Dept. TSC., UniversitatPolitècnica de Catalunya, Barcelona, Spain

Introduction

An end-to-end model has been developed in order to simulate the expected performance of a space-borne Raman Lidar, with a specific focus on the Atmospheric Thermodynamics LidAr in Space – ATLAS proposed as a "mission concept" to the ESA in the frame of the "Earth Explorer-11 Mission Ideas" Call.

The simulator consists of a forward module and a retrieval module. The forward module simulates the interaction mechanisms of laser radiation with the atmospheric constituents and the behaviour of all the devices present in the experimental system (telescope, optical reflecting and transmitting components, avalanche photodiodes, ACCDs), which ultimatelly allows to simulate the signals collected by a space-borne Raman Lidar. The simulated signals are then fed into the retrieval module to obtain vertical profiles of water vapour mixing ratio and temperature.

The simulator finally provides statistical (RMS) and systematic (bias) uncertainties. Estimates are provided in terms of percentage (%) and absolute (g/kg) uncertainty for water vapour mixing ratio measurements and in terms of absolute uncertainty (K) for temperature measurements.

Results and discussion

The expected performance of the space-borne Raman Lidar have been analyzed under different atmospheric conditions, considering thermodynamic and optical parameters from a variety of atmospheric models (Tropical, MidLatitude Summer/Winter, Sub Arctic Summer/Winter, US Standard).

An analytical expression of the lidar equation for the water vapour and molecular nitrogen roto-vibrational Raman signals and the pure rotational Raman signals from molecular oxygen and nitrogen is used. The analytically computed signals are perturbed by simulating their shot-noise through Poisson statistics. Perturbed signals thus take into account the fluctuations in the number of photons reaching the detector over a certain time interval.

The simulator also provides an estimation of the background due to the solar contribution. Daylight background includes three distinct terms: a cloud-free atmospheric contribution, a surface contribution and a cloud contribution [1]. Background is calculated as a function of the solar zenith angle. In order to better estimate the background contribution, an integration on slant path is performed instead of a classical parallel-planes approximation. The proposed numerical model allows to better simulate solar background for high solar zenith angles, even higher than 90 degrees. Different light conditions are considered, so as to analyze the performances with both high and low background.

Based on the application of the roto-vibrational Raman lidar technique, vertical profiles of atmospheric water vapour mixing ratio are obtained from the power ratio of the water vapour to a reference signal, such as the molecular nitrogen roto-vibrational Raman signal or an alternative temperature-independent reference signal.

Vertical profiles of atmospheric temperature are then obtained from the ratio of high-to-low quantum number rotational Raman signals through the application of the pure rotational Raman lidar technique.

A background subtraction scheme is used to remove the solar contribution and vertical averaging is applied to smooth the signals.

Both atmospheric water vapour mixing ratio and temperature measurements require the determination of calibration constants, which can be obtained from the comparison with simultaneous and co-located measurements from a different sensor [2].

The simulations show that the statistical percentage error of water vapour mixing ratio is below 30% up to 2.5km for middle latitudes in Summer and below 20% up to 5km in Winter, thanks to better background conditions.

For the tropical region, the error is below 30% up to 3km with high background, while with low background conditions is below 10% up to 3km and below 30% up to 5km. In the Sub-Arctic region the statistical error is below 15% up to 3km and below 30% up to 5km in the winter period with low background.

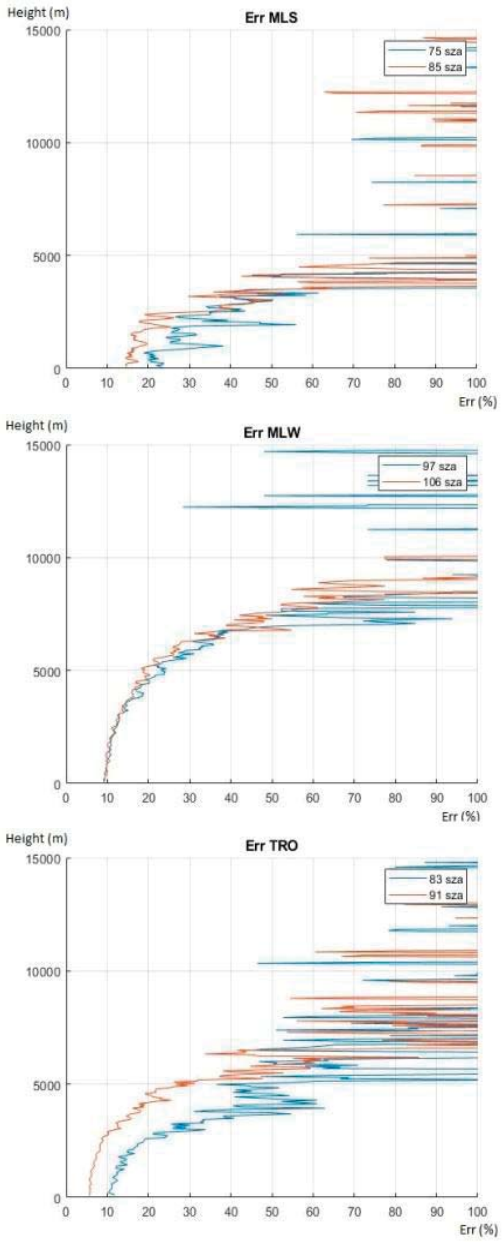

Figure 1. Statistical Error (%) of Water Vapour Mixing Ratio – Mid Latitude Summer/Winter, Tropical and Sub-Arctic Winter

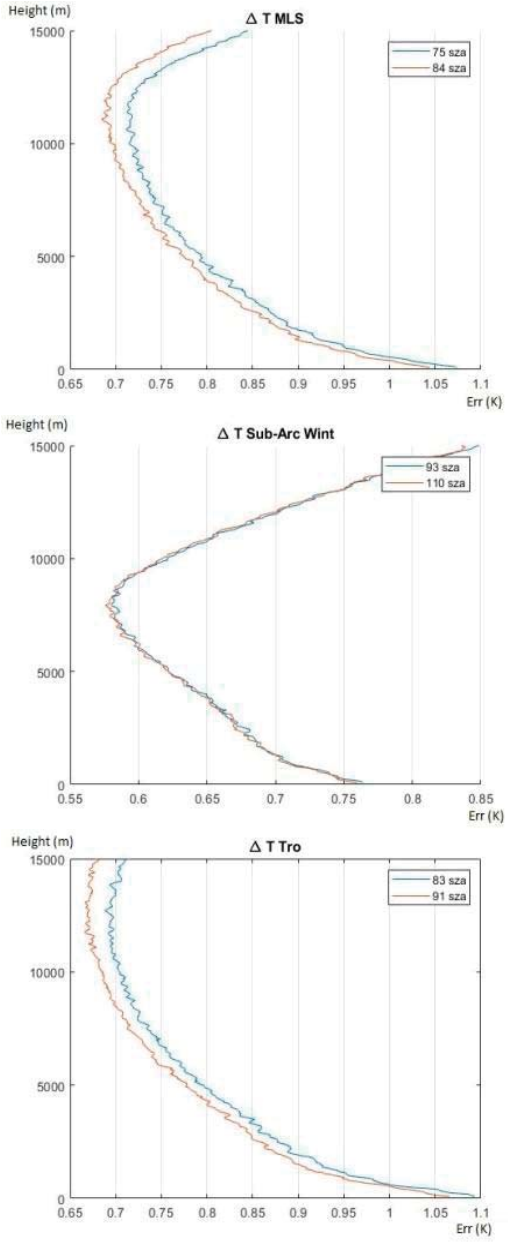

Figure2. Statistical Error of temperature (K) for Mid Latitude Summer/Winter and Tropical.

The absolute error (K) for temperature measurements is below 1K for all the latitude and background conditions up to 15km.

The next step in this research effort will be represented by the simulation of complete orbital scenes based on the use of Nasa's GEOS-5 dataset to verify the performances on a dawn-dusk orbit, with the aim to realize an OSSE to quantify the real impact of a space-borne Raman Lidar on forecasting. These encouraging results are a good starting point that could bring us to fill a gap in the observation capabilities from the surface to lower troposphere, providing measurements with high temporal and spatial resolution.

Acknowledgements

This work was supported by the Italian Ministry for Education, University and Research under the Grants"OT4CLIMA" and "FISR2019-CONCERNING".

References

[1] P. Di Girolamo et al., "Spaceborne profiling of atmospheric temperature and particle extinction with pure rotational Raman lidar and of relative humidity in combination with differential absorption lidar: performance simulations" Appl. Opt. 45, 2474-2494(2006)

[2] P. Di Girolamo et al., "Space-borne profiling of atmospheric thermodynamic variables with Raman lidar: performance simulations," Opt. Express 26, 8125-8161(2018)

Gravity wave parameters and their seasonal variations study near 120°E China based on Na LIDAR observations

X.Zou [1,2], *G. Yang* [1], *P. Batista* [3], *J.Wang* [1], *V. Andrioli* [3], *J.Jiao* [1], *and L.Du* [1]
Christian5022@163.com
(1) State Key Laboratory of Space Weather, National Space Science Center, CAS, Beijing, China
(2) College of Physics & Electronics Engineering, Hainan Normal University, Haikou, China
(3)National Institute for Space Research INPE, São José dos Campos, Brazil

Introduction

Gravity waves (GW) studies are significant for investigating the middle large-scale circulation. According to the superior temporal and spatial resolutions of Na LIDAR which reach to 3min and 100m, it is recognized as an excellent tracer of the sodium layer to study GW perturbations in the mesopause region.

And for GW seasonal distribution study, the result at different observing site are usually different due to the complex geography factor, such as Senft and Gardner and Yang et.al. reported the different GW perturbation at north America and Brazil respectively.

Despite great deal of works have focus the measurements of GW variances and their spectra, however, comprehensive comparison of seasonal variation GW spectra study at different latitudes over China are still rare until now. And due to the complex geography factor such as large dessert, ocean and mountains etc.,from north to south China it exhibits diverse geography environments, to discuss the GW source of China Main land is a considerably attracting topic indeed. Moreover, vertical detection study of mesospause of China mainland is also seldom, the OH airglow detection only cover the flat region which cannot provide the detail information of GW in vertical dimension. As a result for further understanding of generation mechanisms, resulting GW characteristics and the GW source position, starting the joint observation at different latitude will provide a long term comparable research which are necessary and full of scientific meaning.

Results and discussion

Seasonal variations of the RMS atmospheric density perturbations with their MMSE fit at Beijing (top),Hefei (middle) and Hainan (bottom) near 120°E China all indicates that the annual maxima perturbations are near the solstices while the minima are around the equinoxes as Figure 1 shows.

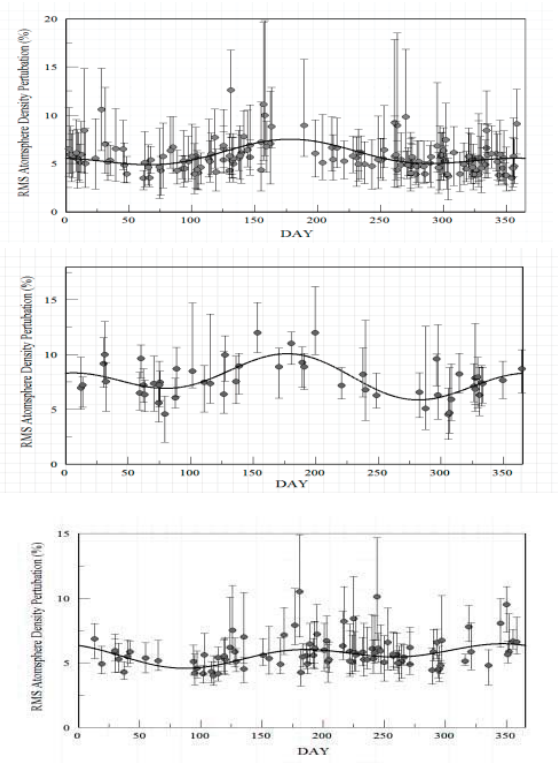

Figure 1. Seasonal variations of the RMS atmospheric density perturbations with their MMSE fit at Beijing (top)，Hefei (middle) and Hainan (bottom).

The seasonal variation RMS value of atmospheric density curves at low-middle (Hefei) and low latitude (Hainan) are also calculated as maxima are near the solstices while minimum equinox as Beijing which indicate that RMS perturbations at middle and low-middle latitude have the similar result seasonally, which could be generated from the same GW source as Tibet Plateau as the main GW source according to the previous reports.

However, obviously, at low latitude region, the atmosphere density perturbation in winter has a relative stronger activity comparing with the middle latitude region's regularity.This indicated that the perturbation in winter is still quite active at low latitude (Hainan) which means there is another abnormal GW activity. As indicated by Li et al, in winter, the GWs propagation directions at China-Qujing station (located at the strait line of Haikou and TP) are southeastward with a strong maximum value of the wind shear intensity and momentum fluxes around the southeastern edge of the TP based on (ECMWF) reanalysis wind data which may be the possible GW source at Hainan in winter.

Table 1. The calculated distances between observed site and wave source.

Distance to wave source	Hainan	Beijing	Hefei
km	1098	1132	1200

The GW source positions are roughly calculated at a distance of 1200km westward to the 120°E observing chain which the Tibet Pleau edge exist as shown in Table 1.

The vertical wave number spectral amplitudes at special frequency of three observatory shows the same annual regulations as RMS atomshpere density, and this was analyzed with mean zonal wind diagram for Northern China by open HWM93 mode (http://modelweb.gsfc.nasa.gov/) as figure 2 shows.

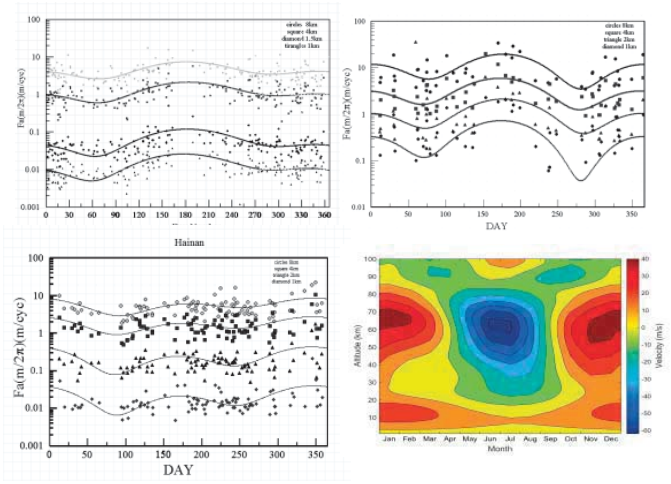

Figure 2. Seasonal variations of ertical wave number spectra with their MMSE fit at Beijing (a),Hefei (b) and Hainan (c) and Northern China zonal wind diagram (d).

Challenges

Referring to the low latitude GW source in winter , and the position of the GW source it is still need further discussed.

Acknowledgements

This work is supported by NSFC 62063005,41564006, 41264006, and 40905012 and thanks for Meridian Space Weather Monitoring Project Data support.

References

Senft and Gardner Seasonal variability of gravity wave activity and spectra in the mesopause region at Urbana *J. Geophys. Res.*, 96, 17229-17264 ,1991.

Yang-Guotao et al. Gravity wave parameters and their seasonal variations derived from Na lidar observations at 23°S, *J. Geophys. Res.*, 111, D21107 ,2006.

Li-Qinzeng et al. Characteristics of mesospheric gravity waves over the southeastern Tibetan Plateau region. *J. Geophys. Res.*, 121, 9204-9221 ,2016.

Observation of corner reflections from oriented ice crystals according to the data of the scanning lidar LOSA-M3 IAO SB RAS (Tomsk)

V. Shishko[1], G.P. Kokhanenko[1],Yu.S. Balin[1], A. Konoshonkin[1,2], N. Kustova[1], D. Timofeev[1], A. Borovoi[1]
sva@iao.ru
(1)V.E. Zuev Institute of Atmospheric Optics SB RAS, 1, Academician Zuev Sq., Tomsk, 634055, Russia
(2)National Research Tomsk State University, Lenina str. 36, 634050 Tomsk, Russia

Introduction

The numerous ground-based, aero-borne, and space-borne lidars are widely used for studying the optical and microphysical properties of cirrus clouds.

Optical properties of cirrus clouds are usually considered under the assumption that ice crystals constituting these clouds are randomly oriented. However the large ice crystals, especially if they are of plate-like habits, often reveal their quasi-horizontal orientation. Such orientations essentially change optical properties of cirrus clouds that should be taken into account in both light scattering and remote sensing problems. Well-known manifestations of the quasi-horizontal orientation of ice crystals in cirrus clouds are arcs and some halo phenomena, such as parhelion.

Earlier it is shown that the corner reflection effect inherent to the pristine hexagonal ice crystals results in sharp peaks of both the backscattering cross section and depolarization ratio at the lidar tilts of about 30° off zenith (Borovoi A.G. et al., 2018). A comparison of the theoretical data and experimental results obtained recently (Veselovskii I. et al., 2017) at the lidar tilt of 43° a partial manifestation of the corner reflection effect has been observed. It is worthwhile noting that the experimental data of (Veselovskii I. et al., 2017) obtained at the lidar tilt of 43° were not optimal for retrieving the microphysics of cirrus clouds. As was shown earlier (Borovoi A.G. et al., 2018), the optimal lidar tilt would be about 32°.

Results and discussion

Figure 1 shows the depolarization ratio for quasi-horizontally oriented hexagonal ice plates have been calculated within the framework of the physical optics approximation (Konoshonkin A.V., et al., 2016) for the case of a vertical scanning lidar. Figure 1 shows that in the calculated depolarization ratio (DR) there is a sharp increase when the lidar is tilted at an angle large than 32º.

Figure 2 shows the results of observation of the corner reflection effect on May 21, 2021 (09:45 - 09:50 local time), in location: IAO SB RAS (Tomsk). The vertical scanning of the atmosphere was conducted with the LOSA-M3 scanning polarization lidar (Kokhanenko G.P., et al., 2020), lidar wavelength was 1064 nm. The lidar tilt angle Y is shown in Fig. 2b, the scale is in arc. minutes. The angle is measured from the vertical position of radiation beam, which was set with an error of ±10 arc minutes. The scanning was carried out with the lidar axis passing through the zenith (ranging from -2° to +48°), which made it possible to control the accuracy of the lidar vertical setting. Three scan cycles were done in 10 minutes.

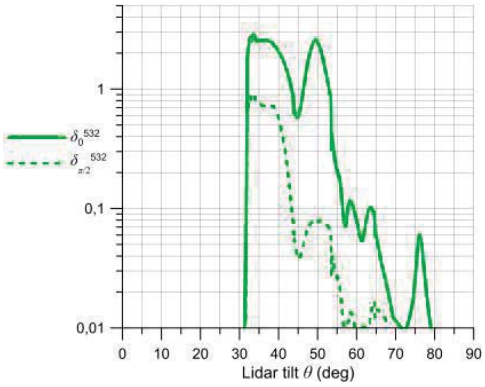

Figure 1. Linear depolarization ratios (DR) versus the lidar tilt. Index 0 and π/2 correspond to the parallel and perpendicular components. A wavelength of the incident light – 532 nm.

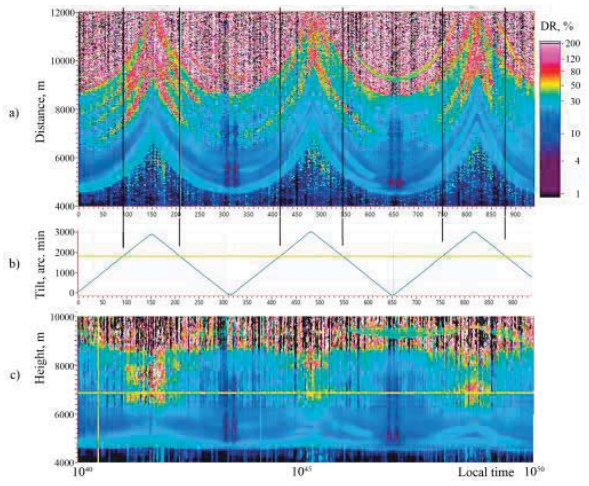

Figure 2. Dependence of the depolarization ratio vertical profile on lidar scanning angle. The upper profile (2a) is plotted according to the distance to the cloud, the lower one (2c), for convenience, according to the height of the cloud. 2b is a tilt angle in arc minutes.

Figures 2a,b demonstrates the vertical profile of the depolarization ratio (DR), the DR value is presented in a color scale as a percentage. Black vertical lines in Fig. 2a limit the range of tilt

angles to more than 32° where a sharp increase in depolarization should be observed according to Fig. 1.

When the lidar is oriented vertically (Y = 0) specular reflection areas are observed. This indicates a cloud layers consisting of quasi-horizontally oriented ice hexagonal particles. This ice cloud exhibits vertical inhomogeneity. Within the most specular cloud layer, which observed at altitudes of 4800–5800 m, DR does not change much when scanning the lidar. The cloud layer at altitudes of 6800–7200 m demonstrates the behavior of quasi-horizontally oriented particles, and DR increases with the angle of the lidar tilt. The most pronounced increase of DR is observed at the last scanning cycle, but a high level of the noise is also observed here.

The highest value of DR - more than 200% - is observed during the first cycle at altitudes of 7200-8000 m, although this layer is not characterized by minimum values of DR in the vertical position.

These results suggest a high probability of the presence of corner reflections in ice clouds. Nevertheless, it is too early to announce unambiguously the presence of this effect. It can be seen from the figures that the structure of the clouds changes during scanning. Unfortunately, the density of clouds observed at large tilt angles is significantly less than that of clouds above the lidar. Therefore, the signal-to-noise ratio is too small for reliable diagnostics of the angular dependence of backscattering. We plan to continue these observations this year.

Acknowledgements

The calculation of the linear depolarization ratios within the physical optics approximation and observation of experimental data of scanning lidar were carried out with financial support of Russian Foundation for Basic Research (Grants No. 20-35-70041, 21-55-53027). The analysis of experimental results was supported by the Ministry of Science and Higher Education of the Russian Federation (V.E. Zuev Institute of Atmospheric Optics of Siberian Branch of the Russian Academy of Sciences).

References

Borovoi A.G., Konoshonkin A.V., Kustova N.V., Veselovskii I.A. Contribution of corner reflections from oriented ice crystals to backscattering and depolarization characteristics for off-zenith lidar profiling, *JQSRT*, 212, 88–96, 2018.

Veselovskii I., Goloub P., Podvin T., Tanre D., Ansmann A., Korenskiy M., Borovoi A., Hu Q., Whiteman D.N. Spectral dependence of backscattering coefficient of mixed phase clouds over West Africa measured with two-wavelength Raman polarization lidar: features attributed to ice-crystals corner reflection, *JQSRT*, 202, 74–80, 2017.

Konoshonkin A.V., Kustova N.V., Shishko V.A., Borovoi A.G. The technique for solving the problem of light backscattering by ice crystals of cirrus clouds by the physical optics method for a lidar with zenith scanning, *Atmospheric and Oceanic Optics*, 29(3), 252–262, 2016.

Kokhanenko G.P., Balin Yu.S., Klemasheva M.G., Nasonov S.V., Novoselov M.M., Penner I.E., Samoilova S.V. Scanning Polarization Lidar LOSA-M3: Opportunity for Research of Crystalline Particle Orientation in the Clouds of Upper Layers, *Atmos. Meas. Tech.*, 13(3), 1113–1127, 2020.

Development of an automatic optimal estimation-based aerosol typing scheme

A. A. Floutsi[1], *H. Baars*[1], *M. Haarig*[1], *and U. Wandinger*[1]
floutsi@tropos.de
(1) Leibniz Institute for Tropospheric Research, Permoserstraße 15, 04318 Leipzig, Germany

Introduction

Knowledge of the spatiotemporal variability of the different aerosol types present in the atmosphere can improve our understanding of the direct and indirect aerosol effect on climate. Vertically resolved aerosol classification is of great importance for improved measurement retrievals, quantification of the anthropogenic and the natural radiative effect, radiative closure and aerosol-cloud interaction studies, as well as data assimilation and validation purposes. Since lidars are the best available instruments for vertically resolved aerosol profile measurements, an automatic typing algorithm applicable to both ground-based and spaceborne lidar systems has been developed.

The novel retrieval scheme presented here applies the optimal estimation method (OEM, Rodgers, 2000) to a combination of lidar-derived intensive aerosol properties (i.e. concentration-independent), to determine the statistically most-likely contribution per aerosol component in terms of relative volume, weighted against a priori (Wandinger et al., 2016) knowledge of the system (e.g. optical and microphysical properties of the aerosol components).

The four aerosol components considered to contribute to an aerosol mixture are two fine modes (absorbing and non-absorbing) and two coarse modes (spherical and non-spherical). These four components and their optical properties have been identified and selected from lidar-based experimental bases at 355 and 532 nm. Using an initial guess, the lidar ratio, particle linear depolarization ratio and extinction-related Ångström exponent are calculated (forward modelling for the wavelengths 355 nm, or 532 nm or both simultaneously) and then compared with the lidar measurements. If they match within an acceptable range the process stops, otherwise the iterative process continues (Levenberg – Marquardt method), adjusting the solution at each step until convergence is met. The general structure of the algorithm is presented in Fig. 1. The final product is the contribution of the four aerosol components to an aerosol mixture in terms of relative volume. Once this product meets certain quality assurance flags (Pearson's chi-squared test) it can be used to provide additional products: (a) aerosol component separated backscatter and extinction profiles, (b) aerosol optical depth per aerosol component, (c) volume concentration per component, (d) number concentration per component, (e) effective radius of the observed mixture and (f) refractive index of the mixture.

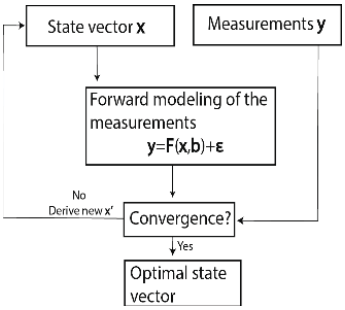

Figure 1. Generalized concept of the optimal estimation method, here used for aerosol typing.

Results and discussion

In order to demonstrate the algorithm's capabilities we have applied the OEM-based typing scheme to lidar measurements from Limassol, Cyprus. To be more specific, on 20 April 2017 a PollyXT lidar (Baars et al., 2016, Engelmann et al., 2016) (part of LACROS, Bühl et al., 2013) was located in Limassol and measured thick (optically and geometrically) dust layers. These layers originated directly from the Sahara region as indicated by the HYSPLIT backward trajectories (not shown here).

The lidar-derived optical parameters are presented in Fig. 2. Maximum extinction coefficient values of approx. 120 Mm^{-1} occurred between 3.5 and 4 km. Extinction and backscatter-related Ångström exponents of around 0.1 and 0.0, respectively were observed for this aerosol layer between 3 and 5 km height. The lidar ratio appears rather stable at the same altitudes, with values of approx. 49 sr and 44 sr for 355 and 532 nm, respectively. The particle linear depolarization ratio, is overall high, exceeding 20% above 3 km.

Table 1. Optical properties at 355 nm used as input to the OEM scheme.

Layer (km)	S (sr)	Uncertainty (sr)	δ (%)	+/- (%)
3-5	49	8	20.6	2

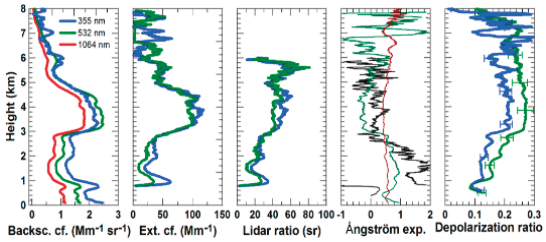

Figure 2. Vertical profiles of the particle backscatter and extinction coefficients, particle lidar ratio, Ångström exponents and particle depolarization ratio measured on 20 April 2017, over Limassol, Cyprus, between 17:00-19:00 UTC.

Layer averaged (3–5 km) lidar ratio (S) and particle linear depolarization ratio (δ) at 355 nm were used as input to the OEM scheme (Tab. 1), and a retrieval based on the 355 nm channel information was performed. The optimal solution, which was statistically significant at 95% confidence interval, confirmed the domination of the coarse, non-spherical (CNS) aerosol component to the aerosol mixture. In particular, in terms of relative volume contribution, the CNS component occupied 86±22% of the total mixture volume. The contributions of the remaining components were small and almost negligible: 10±11% of fine, spherical non-absorbing (FSNA), 4±18% of coarse, spherical (CS), and 0±8% fine, spherical absorbing (FSA) aerosol particles.

In the conference, the OEM typing scheme will be presented in detail, and in addition to the dust case presented here, another non-dust case study will be presented.

Challenges

The rather general representation of the aerosol components is in some cases restrictive, and therefore some types cannot be identified by the typing scheme at its present form (e.g. aged biomass burning aerosols). In addition, the selection of the optical and microphysical properties of these predefined aerosol components (a priori information) is challenging since modelled properties can vary significantly compared to the observed ones. For this reason, we created experimental bases, which were based on ground-based lidar measurements at 355, 532 and 1064 nm. These bases served as the source of the optical a priori information. Last but not least, meteorological conditions such as relative humidity, as well as the geographical location of the measurements should be utilised in the form of solution space constraints, leading thus to more accurate solutions.

References

Wandinger et al., HETEAC: The Aerosol Classification Model for EarthCARE. *EPJ Web of Conferences.* Vol. 119. EDP Sciences, 2016.

Rodgers, Inverse methods for atmospheric sounding: theory and practice. Vol. 2. *World scientific*, 2000.

Baars et al., An overview of the first decade of Polly NET: an emerging network of automated Raman-polarization lidars for continuous aerosol profiling. *Atmospheric Chemistry and Physics*, 2016, 16. Jg., Nr. 8, S. 5111-5137.

Engelmann et al., The automated multiwavelength Raman polarization and water-vapor lidar Polly XT: the neXT generation. *Atmospheric Measurement Techniques*, 2016, 9. Jg., Nr. 4, S. 1767-1784.

Bühl et al., LACROS: The Leipzig Aerosol and Cloud Remote Observations System. *SPIE Remote Sens.* 2013, 8890, 889002.

CALIPSO aerosol observations during an intense pollen episode in Kuopio, Finland at 2016

V. Gouliaditis[1], E. Giannakaki[1,2], M. Gatou[1], X. Shang[2], S. Bohlmann[2], M. Komppula[2]
vasgoul@gmail.com
(1) Department of Environmental Physics and Meteorology, University of Athens, Athens, Greece
(2) Finnish Meteorological Institute, Atmospheric Research Centre of Eastern Finland ,70211, Kuopio, Finland

Introduction

Pollen particles have an impact on air quality and play an important role in environmental and public health. Their concentrations are normally measured with the so-called Burkard-collectors which give the possibility to determine the pollen species and concentration with a 2-hour time resolution (Aulirantio-Lehtimäki et al., 1991). An increasing interest in pollen has arisen in the aerosol lidar community (Sassen et al., 2008). Since 2006 Cloud-Aerosol Lidar and Infrared Pathfinder Satellite Observation (CALIPSO) has been capable of providing continuous vertical profiles.

In this study we recognized a case study of pollen aerosols using a ground based Hirst-type volumetric air sampler. Next to the air sampler, ground-based multiwavelength Raman polarization lidar PollyXT performed continuous measurements and CALIPSO data was selected, to investigate the aerosol classification scheme attributed to the observed pollen type.

Methodology

Pollen collector: Hirst-type volumetric air sampler

A Hirst-type volumetric air sampler located next to the lidar, 4 m above ground, monitored the pollen concentration and type. The sampling principle is based on the design described by Hirst (1952). The pollen type was determined using characteristic features of the examined pollen grains.

Lidar: PollyXT

Lidar measurements were conducted with the multiwavelength Raman polarization lidar PollyXT (Bohlmann et al., 2021). PollyXT has three emission wavelengths (355, 532 and 1064 nm) and seven detection channels. In addition to the three emitted wavelengths, the backscattered signals at the inelastic Raman-shifted wavelengths (387, 407 and 607 nm) and the cross-polarized signal at 532 nm are detected.

CALIPSO

CALIOP provides information on the vertical distribution of aerosols and clouds and their optical and physical properties. The CALIPSO Aerosol Profile Products report profiles of particle extinction (532 Mm-1), backscatter 532 nm and 1064 nm), depolarization ratio (532 nm), color ratio while the fundamental data product provided by the layer products is the vertical location of cloud and aerosol layer boundaries.

Results and Discussion

Our experimental campaign took place at Vehmasmaki, Kuopio between May and August 2016. During the campaign the largest pollen concentration with a value of 2333.76 no/m^3 was observed on 6th of May 2016 and was attributed to Birch pollen type. Ground based lidar observations were performed with a PollyXT system at the same day between 00:00 and 02:00 UTC, while CALIPSO overpassed the station at a distance of 64.60 km, at 00:01 UTC.

The Wavelet Covariance method (Whitcher et al., 2000) has been used to identify the geometrical boundaries for the lower layer. This layer was attributed to pollen aerosols. Backward trajectory analysis, MODIS fire data and Dust model were used to exclude other possible sources of aerosols. Geometrical analysis was performed both for PollyXT lidar measurements and CALIOP using the backscatter profile. For comparison, the geometrical boundaries of CALIOP measurements were also taken from the Aerosol Layer Product. The layer was extended from 0.17 km to 1.6 km according to the CALIOP profile, while the ground based lidar layer identification resulted in a slightly thinner layer (0.63 km to 1.99 km), basically because of a higher base. This is due to the overlap problem of the ground-based system and the weakness to retrieve reliable optical properties in heights lower than 600 m.

The optical properties (Backscatter coefficient, Depolarization Ratio, extinction coefficient and Color Ratio) on this layer are calculated and presented in Table 1, where depolarization ratio at 532 nm of pollen particles was assessed, resulting in 24 ± 3 % for birch pollen.

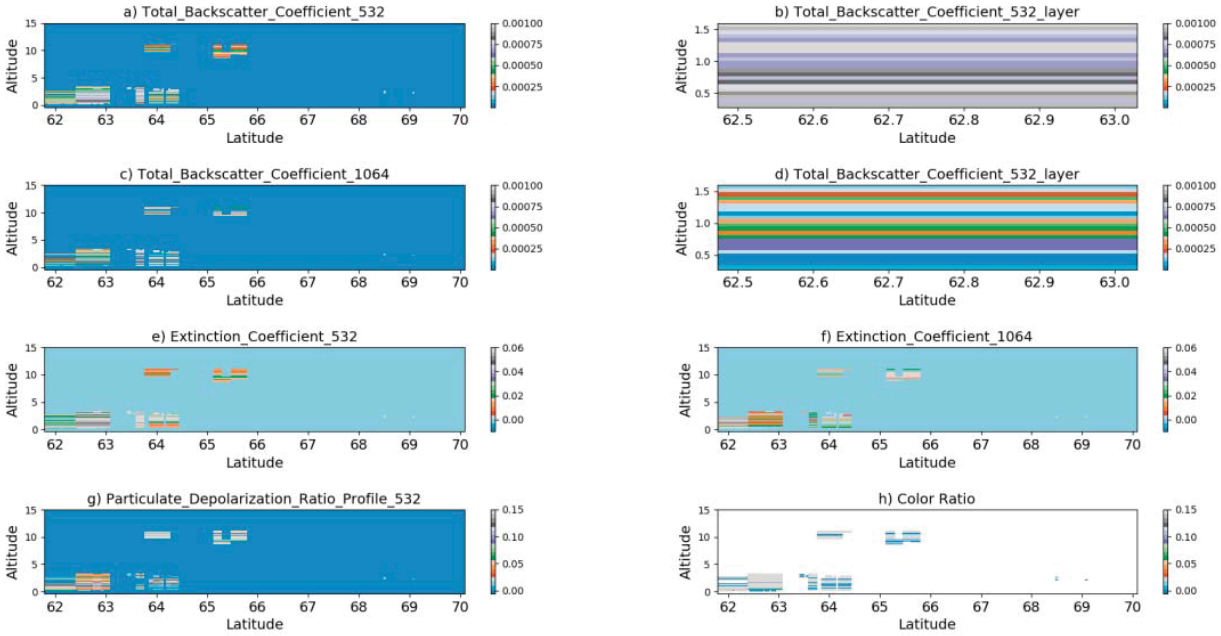

Figure 1. a) Backscatter coefficient 532 nm, b) Backscatter coefficient 532 nm focused between the first layer and the second layer, c) Backscatter coefficient 1064 nm, d) Backscatter coefficient 1064 nm focused between the first layer. e) Extinction coefficient 532nm, f) Extinction coefficient 1064 nm, g) Depolarization Ratio, h) Color Ratio.

Table 1. Mean value of space borne and ground-based lidar derived pollen aerosol properties on 6th of May 2016.

Parameter	CALIOP (profile)	CALIOP (layer)	FMI
Base (km)	0.172	0.172	0.636
Top (km)	1.60	1.60	1.68
Bsc. Coef. 532 nm (Mm^{-1} sr^{-1})	8.5e-07 ± 8.03e-09	6.9e-07 ± 23.56e-08	2.83e-07 ± 4.33e-08
Bsc Coef. 1064 nm (Mm^{-1} sr^{-1})	2.75e-07 ± 4.68e-09	3.98e-07 ± 7.324 e-08	2.20e-07 ± 1.1691 7e-08
Ext. Coef. 532 nm (Mm^{-1})	59.6 ± 1.07	-	1.54 ± 1.16e-08
Depolarization ratio 532 nm	0.052 ± 3.1e-04	0.043 ± 0.015	0.095 ± 0.022
Color ratio	0.3481 ± 1.7e-03	0.416 ± 0.022	0.7911 ± 0.095

Acknowledgements

The research work was supported by the Hellenic Foundation for Research and Innovation (H.F.R.I.) under the "First Call for H.F.R.I. Research Projects to support Faculty members and Researchers and the procurement of high-cost research equipment grant" (Project Number: 16645).

References

Aulirantio-Lehtimäki, Helander, M.L. & Pessi, AM. Circadian periodicity of airborne pollen and spores; significance of sampling height, *Aerobiologia*, 7, 129–135, 1991.

Bohlmann et.al., Lidar depolarization ratio of atmospheric pollen at multiple wavelengths, *Atmospheric Chemistry and Physics*, 21, 7083-7097, 2021.

Sassen et al., Boreal tree pollen sensed by polarization lidar: Depolarizing biogenic chaff. *Geophysical Research Letters*, 35, 10.1029/2008GL035085, 2008.

Whitcher et al., Wavelet analysis of covariance with application to atmospheric time series, *American Geophysical Union (AGU), 105*, 14941-14962, 2000.

Session 3.
Lidar applications

Vertically highly resolved climatology of cloud base heights and the Covid-19 induced anomaly in cloud occurrence in spring 2020

I. Mattis[1], *W. Thomas*[1], *A. Mödl*[2]
Ina.mattis@dwd.de
(1) Deutscher Wetterdienst, Meteorologisches Observatorium Hohenpeißenberg, Germany
(2) Technische Hochschule Nürnberg, Germany

Introduction

The Deutscher Wetterdinest (DWD) operates a network of Lufft CHM15k ceilometers at about 170 synoptic stations all over Germany, see Figure 1. Those instruments provide measurements of up to three simultaneous cloud layers with temporal and vertical resolution of 15 seconds and 15 meters, respectively. Cloud layers are reported up to 15 km above ground. They are characterized in terms of cloud base height and cloud depth (in case of transparent clouds) or vertical optical range (in case of non-transparent clouds). Nevertheless, this very detailed information is typically compressed into only three values (degree of coverage of low level, mid level, and high level clouds) with a temporal resolution of 30 minutes in SYNOP messages for weather forecast and climatological applications.

Methodology

This study is based on the data of the DWD ceilometer network of the years 2015 - 2020. The climatology of cloud occurences is retrieved from

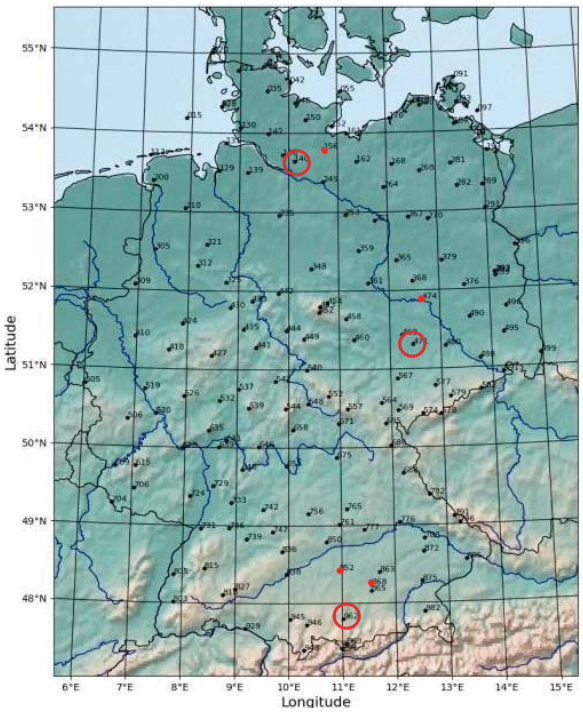

Figure 1. DWD ceilometer network. Red circles indicate stations Hamburg, Leipzig, and Hohenpeißenberg; red dots are Lübeck, Wittenberg, Augsburg, and Oberschleißheim (all from north to south).

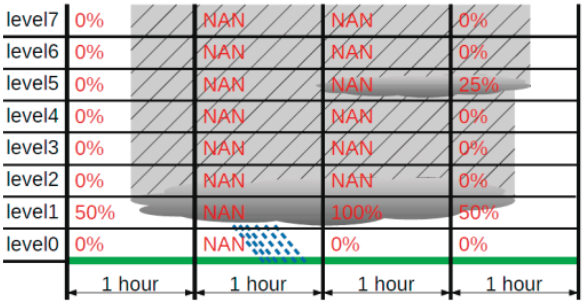

Figure 2. Schematics of cloud coverage retrieval.

cloud base height provided by the firmware algorithm (0.719 to 1.040).

We obtain the cloud coverage with a temporal and vertical resolution of 1 hour and 500 m, respectively. Figure 2 illustrates the retrieval procedure. Only the lowermost cloud layer of each 15-seconds profile is considered. Any data above a cloud are omitted (grey shaded areas). Hours with precipitation or missing raw data are excluded. If a cloud layer with less than 100% coverage is present below a second cloud, the coverage of this second cloud layer is calculated relative to the time fraction of the hour without any cloud underneath. E.g. in hour 4, the cloud in level1 lasts 30 minutes wich corresponds to 50%. If all data above this cloud are omitted, the second cloud in level5 can be seen for 7.5 minutes which corresponds to 25% of the time without a cloud underneath level5.

Climatology of cloud base heights

The year 2019 and stations Hamburg, Leipzig,

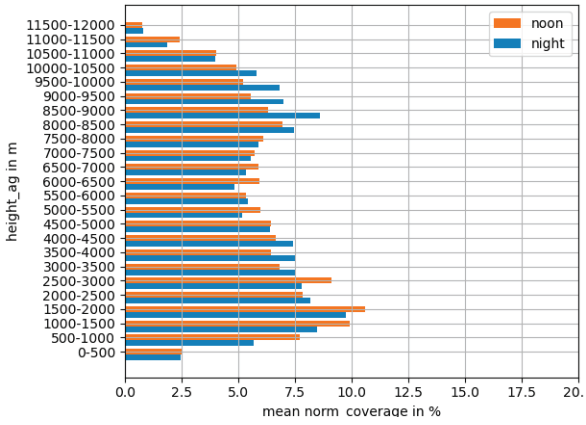

Figure 3. Mean cloud coverage at Hohenpeißenberg in 2019. Orange a blue bars correspond to measurements between 10 and 16 UTC and between sunset and sunrise, respectively.

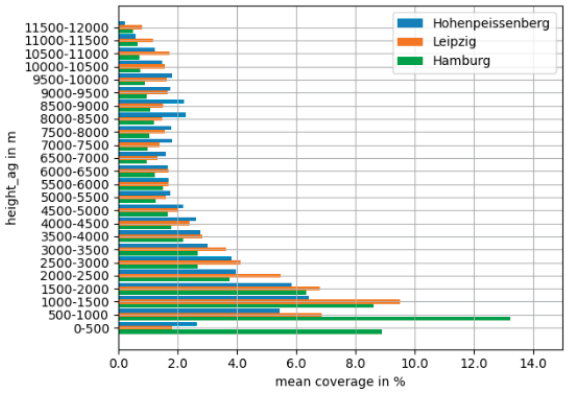

Figure 4. Regional differences of cloud coverages. Shown are the data of 2019 at Hohenpeißenberg, Leipzig, and Hamburg.

and Hohenpeißenberg have been analyzed for general features of cloud base height statistics.

Figure 3 shows a comparison between observations around noon and during nighttime. Noon is considered to be the six hours around 12 local time (lt). In Germany, 12lt ±3h corresponds to 10-16 UTC. More low and high clouds are observed around noon and during night, respectively. This pattern pattern occurs at other stations and in other years as well. It could be assumed that optically thin cirrus clouds at high altitudes might be below detection limit in daytime conditions due to higher solar background signal. But, the signal-to-noise ratio and maximum detection heights do not show significant differences between noon and night-time periods.

Figure 4 shows a comparison between the three sites Hohenpeißenberg, Leipzig, and Hamburg. Hamburg, which is characterized by a maritime climate has the maximum of cloud occurrence below 1km whereas the maximum of cloud occurrence at the more continental stations Hohenpeißenberg and Leipzig is in the 1-1.5km level. The latter two sites have also more clouds at altitudes above 6km than Hamburg. The reason for this behavior needs to be investigated in more detail.

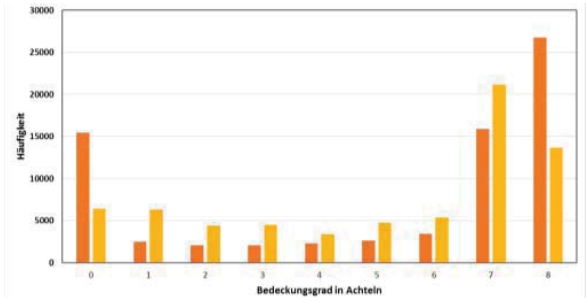

Figure 5. Total frequency of overall cloud coverage (all heights) from ceilometer (orange) vs. eye observations (yellow) in Hohenpeißenberg 2009-2018, in octa.

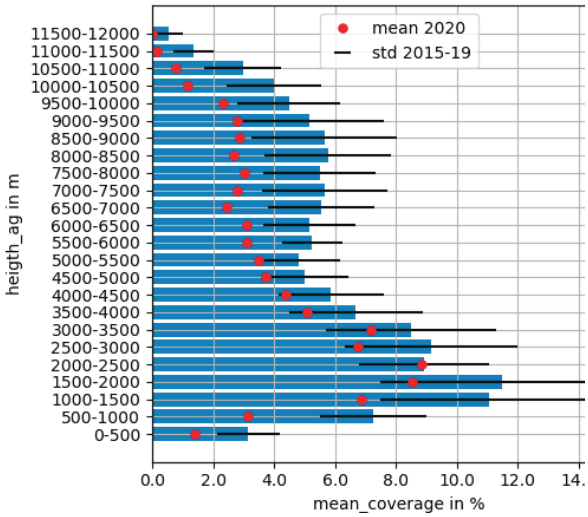

Figure 6. Vertically resolved frequency of cloud coverages at Hohenpeißenberg. Average and standard deviation spring moths of 2015-2019 (blue bars and black lines) vs. spring 2020 (red dots).

Figure 5 illustrates the challenge of combining time series of cloud coverages obtained from traditional eye observations which integrate the whole hemisphere with those from measurements with vertically pointing ceilometers and lidars. Parallel observations with both methods at Hohenpeißenberg show a significantly higher frequency of cloud free (0 octa) and overcast (8 octa) conditions in ceilometer data. The reason for the discrepancy lies in different observations strategies.

Covid-19 induced anomaly in cloud occurrence

Figure 6 shows a comparison between cloud frequency at Hohenpeißenberg in spring 2020 and spring months (March, April, May) of 2015-2019. There are clearly less clouds above 5.5.km in 2020 than the year-to-year variability of 2015-2019. Air traffic over Germany was reduced due to the Covid-19 pandemy by about 70% in the beginning of March 2020 (LIZ Bulletin 30/2020). The altitude of strongest reduction corresponds to cruising altitudes of regional and long-distance flights. A similar behavior was found at several other sites, e.g. Oberschleißheim and Augsburg (close to Hohenpeißenberg) and Hamburg. The reduction of cloud coverage at Leipzig and nearby Wittenberg is not as strong as in the other areas, but air traffic at Leipzig airport was reduced by only 20% because it is used mainly by cargo flights.

References

LIZ Bulletin 30/2020: https://www.dfs.de/dfs_homepage/de/Unternehmen/Zahlen und Daten/Statistiken/LIZBu_30_2020.pdf

Aerosol hygroscopic properties from Raman lidar measurements

***F. Navas-Guzmán*[1,2]**, *G. Martucci*[1], *M. Collaud Coen*[1], *M. Hervo*[1], *A. Barreto*[3], *J. López-Solano*[3], *J. A. Ruiz-Arias*[4], *H. Lyamani*[4], *C. Hüglin*[5], *D. Pérez-Ramírez*[2], *G. Titos*[2], *M. Alonso*[2], *L. Alados-Arboledas*[2], *B. T. Brem*[6], *M. Gysel-Beer*[6], *and A. Haefele*[1]

fguzman@ugr.es

(1) Federal Office of Meteorology and Climatology MeteoSwiss, Payerne, 1530, Switzerland

(2) Andalusian Institute for Earth System Research, University of Granada, Granada, 18006, Spain

(3) Izaña Atmospheric Research Center, Meteorological State Agency of Spain (AEMET), Spain

(4) Department of Applied Physics I, University of Málaga, Málaga, 29071, Spain

(5) Empa, Swiss Federal Laboratories for Materials Science and Technology, Dübendorf, 8600, Switzerland

(6) Laboratory of Atmospheric Chemistry, Paul Scherrer Institute, Villigen, 5232, Switzerland

Atmospheric aerosol particles scatter and absorb solar radiation, thus exerting significant impacts on the atmospheric environment and climate change. The swelling of aerosols due to water vapor uptake enhances their ability to scatter solar radiation, and is strongly dependent on the ambient relative humidity (RH). In this way, aerosol hygroscopic growth plays an important role in the earth's radiation budget. The understanding of aerosol hygroscopic processes and its quantification is crucial to improve weather and climate predictions. Despite its importance, aerosol hygroscopic properties have not been properly characterized yet using remote sensing techniques (non-invasive method). The major limitation comes from the lack of simultaneous observations of vertically resolved profiles of RH and aerosol properties.

The Swiss RAman Lidar for Meteorological Observations (Ralmo) operated at the aerological station of MeteoSwiss at Payerne (Switzerland) provides continuous profiles of aerosol properties (backscatter and extinction) and RH. These measurements allow us to monitor any change in aerosol properties that could occur as result of the water uptake by the particle under high RH (aerosol hygroscopic growth). Ralmo has shown its capability to monitor aerosol hygroscopic processes in time and in altitude for different aerosol types (Navas-Guzmán et al., 2019).

In this study, a unique statistical analysis of aerosol hygroscopic properties based on 3-year data set of Ralmo lidar has been addressed. A total of 401 layers were identified as layers that underwent hygroscopic growth following the criteria presented in Navas-Guzmán et al. (2019). Backscatter enhancement factors (f_β) at 355 nm and hygroscopic growth parameters (γ) from Hänel model (Hänel, 1976) were obtained to characterize the aerosol hygroscopicity. Figure 1 shows the occurrence distribution of γ for all the layers. In average, the layers are characterized with values of γ = 0.6±0.3 and $f_\beta(85\%) = 2.4 \pm 1.4$, evidencing a relatively strong hygroscopic behavior of the predominant aerosol over Payerne.

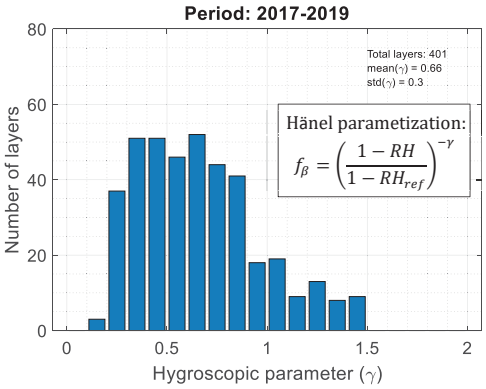

Figure 1. Occurrence distribution of the hygroscopic growth parameter (γ) for all the layers.

In-situ and remote sensing instrumentation along with model information (Flextra, CAMS, NAAPS) has allowed to identify the aerosol properties and types and the air mass origin of the hygroscopic layers. The analysis of the vertical information from the lidar showed that, in general, the aerosol present within the Planetary Boundary Layer (PBL) was less hygroscopic than in the Free Trosposhere (FT) (γ^{PBL} = 0.5±0.2; γ^{FT} = 0.7±0.3). A weak anti-correlation was also found between the hygroscopic parameter and the aerosol size. Different hygroscopic behaviour were observed depending on the air mass origin, in which the Atlantic air masses presented the most hygroscopic aerosol. Finally, the hygroscopic parameters were also characterized for several aerosol types, being the layers with high concentration of sulphates the most hygroscopic (γ = 0.8±0.3; f_β (85%) = 2.7±1.6).

Acknowledgements

This work was supported by the Swiss National Science Foundation under grant PZ00P2_168114 and by the Ramón y Cajal program (ref. RYC2019-027519-I) of the Spanish Ministry of Science and Innovation.

References

Hänel, G., The properties of atmospheric aerosol particles as func- tions of the relative humidity at thermodynamic equilibrium with the surrounding moist air, Elsevier, *Adv. Geophys.*, 19, 73-188, 1976.

Navas-Guzmán, et al., Characterization of aerosol hygroscopicity using Raman lidar measurements at the EARLINET station of Payerne, *Atmospheric Chemistry and Physics*, 19 (18), 11651-11668, 2019.

Application of fluorescence lidar for characterization of smoke particles in upper troposphere and inside cirrus clouds

Veselovskii[1], *Q. Hu*[2], *P. Goloub*[2], *T. Podvin*[2], *A. Ansmann*[3], *M. Korenskiy*[1]
igorv@pic.troitsk.ru
(1) Prokhorov General Physics Institute of the Russian Academy of Sciences, Moscow, Russia,
(2) Univ. Lille, CNRS, UMR 8518, Laboratoire d'Optique Atmospherique, 59655, Villeneuved d'Ascq , France.
(3) Leibniz Institute for Tropospheric Research, Leipzig, Germany

Introduction

Aerosol particles in high troposphere (HT) play important role in ice clouds formation. The main sources of aerosol in HT include volcanic eruption as well as intensive wildfires. Today it is well accepted that products of the fires can reach the tropopause due to self-lifting processes caused by absorption of solar radiation and heating. The smoke particles are capable to act as ice nucleating particles (INP) if the temperature is low enough, however the influence of smoke on the process of ice formation is not well understood (Ansmann et al., 2020).

Fluorescence technique provides unique opportunity to monitor smoke particles inside the cirrus clouds. Smoke possesses high fluorescence cross section, allowing to discriminate it from other types of aerosol. In our presentation we demonstrate that combining the fluorescence measurements with capabilities of multiwavelength Raman lidar observations, it is possible to estimate the key smoke characteristics, such as volume, surface and number density in cirrus clouds. The results reported were obtained during 2020 – 2021 period at Laboratoire d'Optique Atmospherique, University of Lille.

The measurements were performed with multiwavelength Mie-Raman lidar (LILAS), based on a tripled Nd:YAG laser of a 20 Hz repetition rate and pulse energy of 70 mJ at 355 nm. The backscattered light is collected by a 40 cm aperture Newtonian telescope. The system allows detection of so called 3β+2α+3δ data set. A part of fluorescence spectrum is selected by an interference filter of 44 nm width, centered at 466 nm (Veselovskii et al., 2020). The fluorescence backscattering coefficient β_F is calculated from the ratio of fluorescence and nitrogen Raman backscattering, as described in Veselovskii et al. (2020). Efficiency of the fluorescence in respect to elastic scattering is characterized by the fluorescence capacity $G_F=\beta_F/\beta_{532}$, where β_{532} is the particle backscattering coefficient at 532 nm. Sensitivity of the fluorescence technique can be limited by the fluorescence of optical elements in a lidar receiver. The minimal value of G_F obtained during clouds sounding was 1.2×10^{-8}, thus observations with G_F exceeding this value should be free of optics fluorescence contribution.

Results and discussion

Fig.1. shows results of the measurements on the night 4-5 November 2020. After the midnight the smoke layer provides strong fluorescence at approximately 12 km height. The fluorescence capacity G_F in the center of this layer for this episode was 5.3×10^{-4}. The value of G_F in our observations for different episodes in HT varied in $(4.0\text{-}6.0)\times10^{-4}$ range, thus fluorescence properties of smoke particles in UT for different episodes are quite similar. If value of G_F is known, the contribution of smoke backscattering at 532 nm (βs) to the total backscattering of aerosol mixture can be estimated. Moreover, it allows to estimate the smoke backscattering inside the cirrus clouds.

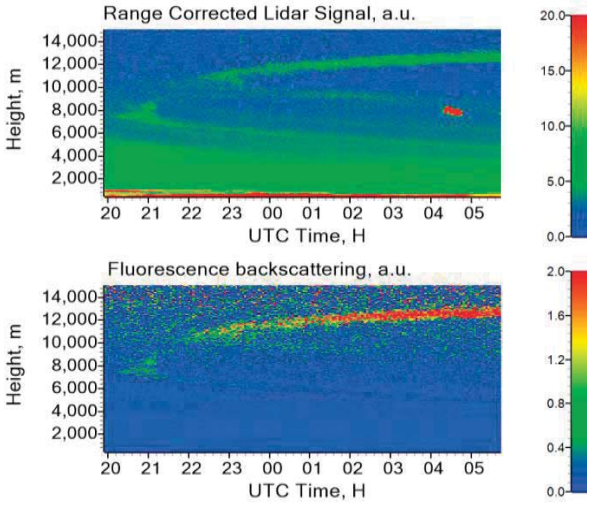

Fig.1. Range corrected lidar signal at 1064 nm, volume depolarization ratio at 1064 nm and fluorescence backscattering coefficient on 4-5 November 2020.

Results of the measurements in the presence of clouds are shown in Fig.2. Cirrus clouds were observed during the whole night. The fluorescence backscattering (plot a) was about 0.05×10^{-4} $Mm^{-1}sr^{-1}$ at 9 km and it increased up to 0.3×10^{-4} $Mm^{-1}sr^{-1}$ above the tropopause. The tropopause height was determined from the radiosonde temperature profile (Herstmonceux, UK). Plot b in Fig.2 shows smoke backscattering at 532 nm, calculated as

$\beta_s=\beta_F/G_F$. The value $G_F=5.0\times10^{-4}$ was used in all computations. Above the tropopause (~11 km) the β_{532} and β_s coincide, indicating that smoke particles are predominant.

Several examples of evaluation of smoke backscattering β_s inside the cirrus clouds and above the tropopause are shown in Fig.3. Comparing β_{532} and β_s we conclude, that on 22 October 2020 the smoke is predominant in 4 km – 6 km range and above the tropopause, while on February 3 2021, in 8 km – 10 km range the particles other than smoke may significantly contribute to β_{532}.

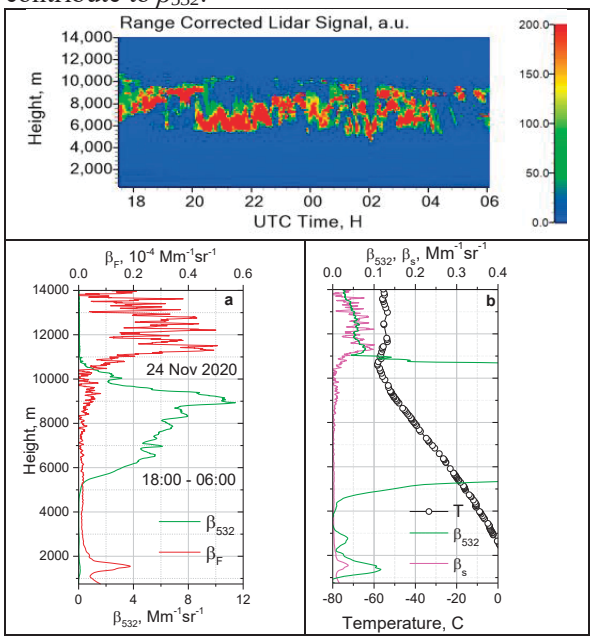

Fig.2. Height temporal distribution of the range corrected lidar signal at 1064 nm on 24-25 November 2020 (upper panel). (a) Profiles of elastic β_{532} and fluorescence β_F backscattering. (b) Profiles of β_{532} and β_s together with temperature profile from radiosonse.

The 3β+2α observations can be inverted to the particle microphysical parameters, such as number (N), surface (S) and volume (V) density (Veselovskii et al., 2002). Thus conversion factors (C_N, C_S, C_V) allowing estimation of N, S, V from fluorescence backscattering as $N=C_N\times\beta_F$, $S=C_S\times\beta_F$, $V=C_V\times\beta_F$. In June - September 2020 we observed several strong smoke layers in HT, from which we estimated conversion factors as: $G_N=100\times10^4$ cm^{-3}/Mm^{-1}sr^{-1}, $C_S=30\times10^4$ μm^{2}cm^{-3}/Mm^{-1}sr^{-1}, $C_V=1.9\times10^4$ μm^{3}cm^{-3}/Mm^{-1}sr^{-1}. These values were used to estimate the particles concentration inside the cirrus clouds. Corresponding results are summarized in Table.1. Concentration of smoke particles in the cirrus clouds is low (N is below 10 cm^{-3}), still it is detectable with fluorescence technique. As follows from Table 1, G_F is about two orders higher than possible contribution of optics fluorescence.

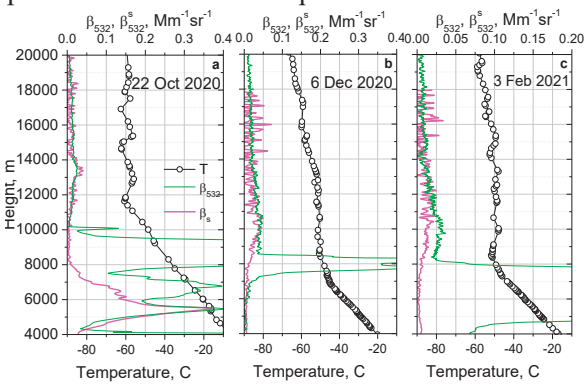

Fig.3. Vertical profiles of β_{532} and smoke backscattering β_s together with temperature profiles from radiosonde on 22-23 October (18:00–03:30), 6 December (17:30-21:00) 2020 and 3-4 February (19:00-06:00) 2021.

Table 1. Backscatterings β_{532} and β_s together with smoke number and volume density inside cirrus clouds.

Date	H, km	β_{532} Mm^{-1} sr^{-1}	G_F $\times10^{-6}$	N cm^{-3}	V, μm^3 cm^{-3}
22 Oct	9.0	1.7	2.1	3.4	0.07
24 Nov	9.0	8.0	0.6	4.9	0.1
6 Dec	8.1	1.4	5.7	7.8	0.15
3 Feb	6.0	3.0	0.3	1.0	0.02

Conclusions

In our study we have demonstrated that synergy of Mie-Raman and fluorescence lidar measurements allows to monitor content of smoke particles up to the tropopause and to estimate the concentration of smoke inside the cirrus clouds.

Acknowledgements

We thank Labexl CaPPA, OBS4CLIM, SNO PHOTONS, ESA/IDEAS+ and Russian Science Foundation (project 21-17-00114) for their grateful support.

References

Ansmann, A., Ohneiser, K., Mamouri, R.-E., Knopf, D. A., Veselovskii, I., Baars, H., Engelmann, R., Foth, A., Jimenez, C., Seifert, P., Barja, B.: Tropospheric and stratospheric wildfire smoke profiling with lidar: Mass, surface area, CCN and INP retrieval, Atmos. Chem. Phys. Discuss., https://doi.org/10.5194/acp-2020-1093, 2020.

Veselovskii I., Kolgotin, A., Griaznov, V., Müller, D., Wandinger, U., Whiteman, D.: Inversion with regularization for the retrieval of tropospheric aerosol parameters from multi-wavelength lidar sounding, Appl.Opt. 41, 3685-3699, 2002.

Veselovskii, I., Hu, Q., Goloub, P., Podvin, T., Korenskiy, M., Pujol, O., Dubovik, O., Lopatin, A.: Combined use of Mie-Raman and fluorescence lidar observations for improving aerosol characterization: feasibility experiment, Atm. Meas. Tech., 13, 6691–6701, 2020.

CALIPSO lidar observations of changes in cirrus cloud properties over the European Mid-Latitudes during the COVID-19 related air traffic reduction

S. Groß[1], *Q. Li*[1]
silke.gross@dlr.de
(1) German Aerospace Center (DLR), Institute of Atmospheric Physics, Münchener Str. 20, Oberpfaffenhofen, Germany

Introduction

Cirrus clouds have a wide global coverage and influence on the Earth's radiation budget. Overall, they are supposed to have a warming effect, but their radiative effect is strongly determined by their microphysical properties, e.g. size and shape of the ice particles as well as the ice particle concentration. Those properties, however, depend on the environmental conditions (Heymsfield and Miloshevich, 1995) as well as on the stage of evolution of the ice cloud. The forming mechanism as well as the presence of aerosols might further affect the ice cloud properties. Condensation trails induced by air traffic may, under favorable conditions, add to the natural coverage of cirrus clouds. They can furthermore cause a significant increase in cirrus cloud optical thickness (Tesche et al., 2016). Besides the effect caused by contrails, also an indirect effect was discussed over the last years. For the first time, Urbanek et al. (2018) showed an observational indication that enhanced aerosol load caused by air traffic might has an influence on naturally formed cirrus cloud properties in the European mid-latitudes. Cirrus clouds formed in regions influenced by air traffic showed significantly larger particle linear depolarization ratios (PLDR) than those cirrus clouds formed in rather pristine regions.

In spring 2020 air traffic over the European mid-latitudes were reduced by about 80% due to the COVID-19 pandemic. This reduction offers the unique opportunity to study cirrus clouds in situations that are less affected by air traffic, and how their properties change compared to former years. We use CALIPSO satellite lidar observations In addition, we are looking at the occurrence frequency of cirrus clouds with defined geometrical thicknesses. We find a clear reduction in the OR for thin cirrus clouds with a vertical extend of up to 1.0 km. Those shallow cirrus clouds might have a contribution from condensation trails that form, under favorable conditions, into persistent cirrus clouds. However, comparing with the OR in 2016 one can see, that not only the aviation effects but also the meteorological conditions have a large influence on the cirrus cloud coverage.

(Winker et al., 2010) to study changes in the cirrus cloud occurrence as well as optical properties over the European mid-latitudes. For this study we use a similar region as was used in the study by Urbanek et al. (2017) where a first indication of this indirect effect could be shown.

Results and discussion

To exclude possible influences on the ice cloud occurrence and properties caused by different meteorological conditions we analyzed the meteorological data for the different considered years to verify that 2020 was well within the year-to-year variability. As an indication of the meteorological situation the climate composites of the geopotential height at 500 hPa is shown in Figure 1 for 2020 and for a multi-year mean of 2014-2019. Although differences are found for the year to year variability of the meteorological conditions. Those analyses show that the conditions for 2020 are well with in the overall variability.

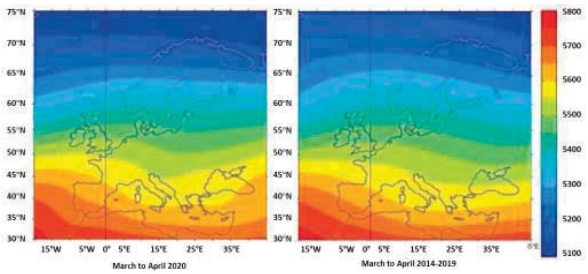

Figure 1. 500 hPa geopotential height composite over Europe for March and April for 2020 (right) and for 2014-2019 (left). The plots are reproduced based on NCEP/NCAR Reanalysis provided by Physical Sciences Laboratory, NOAA, Boulder (https://psl.noaa.gov/).

Looking at the cirrus cloud occurrence for the different years (Figure 2) we find that 2020 showed a reduced cirrus cloud occurrence rate (OR) in the temperature range between about -45°C and -55°C compared to the former years. Only 2016 showed an even lower OR due to exceptional meteorological conditions in spring 2016 (warmer and less humid). While the OR in the former, reference years was about 11% to 12% in this temperature range, the OR in 2020 was only about 8% at about -55°C and about 10% at about -45°C.

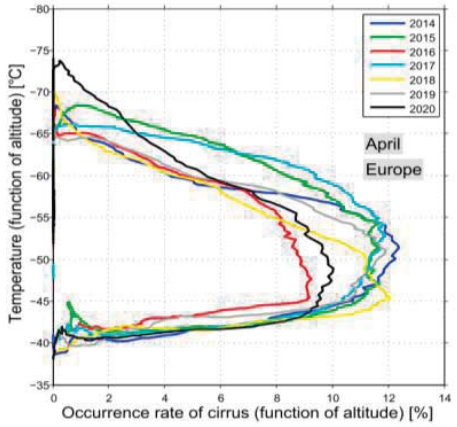

Figure 2. Mean profiles of cirrus cloud occurrence rate derived from CALIPSO lidar for April 2014-2020 (left) and histograms of cirrus cloud occurrence ratios for clouds with defined geometrical thicknesses (right).

Urbanek et al. (2018) have shown, however, that aviation might not only influence the occurrence rate of cirrus clouds by adding e.g. persistent contrail cirrus to the natural cirrus cloud cover, but they might also affect the optical and microphysical properties by acting as ice nuclei. Following their example, we analyze the particle linear depolarization ratio (PLDR) of the cirrus clouds observed over the European mid-latitudes (Figure 3).

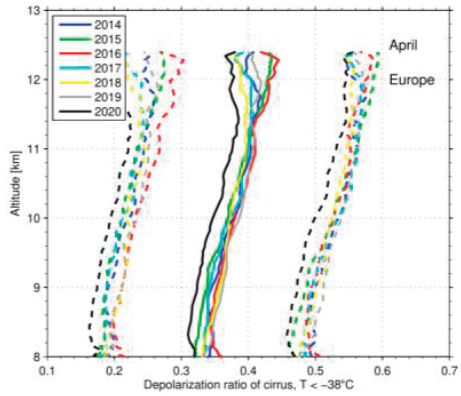

Figure 3. Profiles of the median cirrus PLDR (solid lines) and their corresponding 20th and 80th percentiles derived from CALIPSO observations for April.

The profiles of the PLDR show a well-known increase of the PLDR with increasing altitude (Urbanek et al., 2018) for all considered years. However, the median values of the PLDR for 2020 are about 0.03 smaller throughout all height ranges compared to the former years considered in this study. The higher values are an indication of more heterogeneous ice formation due to enhanced aerosol caused by aviation exhaust (Urbanek et al., 2018), which might also have an effect of the microphysical properties of the cirrus cloud particles (Groß et al., 2020).

Challenges

The reduction of aviation due to the COVID-19 pandemic in spring 2020 offered a unique opportunity to study aviation effects on cirrus cloud occurrence and cirrus cloud properties. Changes in the frequency as well as in the intense optical properties of the cirrus clouds over the European mid-latitudes were found from CALIPSO lidar observations in March and April 2020.

Changes of the occurrence rate of cirrus clouds as well as on the intensive optical (and thus microphysical) properties might have a large impact on the radiative effect. However, this study only shows a limited time period in which the largest changes in the frequency of civil aviation occurred. Long-term analysis is needed to investigate how this effect depends on the general aviation frequency, which has increased over the last years, and if the different meteorological conditions within one year might have an effect as well. And finally those measurements have to be connected to the microphysical properties which is crucial to estimate the radiative impact of the indirect aviation effect on cirrus clouds.

Acknowledgements

The authors acknowledge support from the DLR-project MABAK. We thank the NASA Langley Research Center Atmospheric Science Data Center (ASDC) and CALIPSO science team for making the data available for research.

References

Heymsfield A. J. and L. M. Miloshevich, Relative Humidity and Temperature Influences on Cirrus Formation and Evolution: Observations from Wave Clouds and FIRE II, *JAS*, 1995.

Tesche, M., P. Achtert, P. Glantz, et al. Aviation effects on already-existing cirrus clouds. *Nature Com.*7, 12016, 2016.

Urbanek, B., S. Groß, M. Wirth, C. Rolf, M. Krämer, and C. Voigt, High depolarization ratios of naturally occurring cirrus clouds near air traffic regions over Europe, *GRL*, 45(23), 2018.

Winker, D. M., Pelon, J., Coakley Jr, J. A., Ackerman, S. A., Charlson, R. J., Colarco, P. R., ... & Wielicki, B. A., The CALIPSO mission: A global 3D view of aerosols and clouds. *BAMS*, 91(9), 1211-1230, 2010.

Groß, S., Urbanek, B., Wirth, M., Ewald, F., Marinou, E., Gausa, C., Jurkat-Withschas, T., and Voigt, C., Identification of an indirect aviation effect on natural evolving cirrus clouds using airborne and space borne depolarization lidar measurements, *2. European lidar conference*, 2020.

Sensitivity Analysis of a Ground-Based Lidar System for Detecting Ultrafine Particles in the Amazon Upper Troposphere

***M.T.Silva*[1]**, *D. A. Gouveia*[1,2], *J. L Guerrero-Rascado*[3,4] , *A. L. Correia*[1] *and H. M. J Barbosa*[1,5]
matolentino.silva@gmail.com
(1) Physics Institute, University of Sao Paulo, Sao Paulo-SP, Brazil
(2) Royal Netherlands Meteorological Institute (KNMI), De Bilt, Netherlands
(3) Department of Applied Physics, University of Granada, Granada 18071, Spain
(4) Andalusian Institute for Earth System Research (IISTA-CEAMA), Granada 18006, Spain
(5) Physics Department, University of Maryland Baltimore County, Baltimore, USA

Introduction

Recent aircraft campaigns reported high number concentration of ultrafine particles in the Amazon rainforest upper troposphere (UT). These particles have diameters ranging from 20 to 90 nm and their number concentration is 1 or 2 orders of magnitude larger than in the atmospheric boundary layer (ABL), as reported by Andreae et al., 2018. These measurements suggest that biogenic volatile organic compounds, produced by the rainforest biosphere, are carried by clouds into the UT, where they condense due low temperatures forming new organic particles. These particles grow as they are transported downwards to the ABL, by large-scale subsidence or downdrafts, reaching a size range where they can act as cloud condensation nuclei. This process finally explains how the Amazon boundary layer, where new particle formation is rarely observed, can sustain the particle population necessary to feed the "green ocean" clouds. However, aircraft measurements are only available in short-term campaigns, and hence cannot provide systematic observations of these UT aerosols. Continuous measurements from the ground could fill this gap. In this work, we use numerical simulations to evaluate whether a tropospheric elastic lidar at 355 nm could detect the presence of ultrafine particles in the UT. We perform simulations of the lidar signal for different amounts of aerosol and increasing system efficiency.

Methods

Intrinsic optical properties of UT aerosols were simulated using a Mie code assuming spherical particles with refractive indexes based on AERONET measurements in the Amazon region, and an Aitken log-normal size distribution (Dg = 47 nm and σ = 1.6). Intensive optical properties, namely extinction and backscatter, are then calculated for a range of different aerosol number concentrations in the UT (N_0, $4N_0$ and $16N_0$, where N_0=1.25x10^3 cm^{-3} is the median value reported by the Andreae et al., 2018). For simplicity, we assume a layer of constant concentration from 9-15 km, as shown in Figure 1. The elastic backscatter signal was computed for each profile of optical properties, corresponding to a different aerosol optical depth (AOD), by direct application of the lidar equation and by adding Poisson noise. The simulation was calibrated to give a similar number of photons from aerosols in the ABL as measured by our ground-based lidar (Barbosa et al., 2014). The simulation was then repeated for increasing system efficiencies. This could be achieved by either improving the instrument (i.e. laser power) or the acquisition (i.e. time-averaging), as both increase the number of detected photons and the signal-to-noise ratio (S/N) in an undistinguishable manner.

For each simulated signal, the aerosol extinction profile was obtained with the Klett-Fernanld-Sasano method as implemented for Lalinet (Barbosa et al., 2014b). The molecular reference is chosen between 20 and 25 km. It is important to mention that the inversion assumes the gas profiles and lidar-ratio used for the simulations. For each aerosol amount, we determined how the probability of detecting the UT aerosol layer varies with system efficiency.

Results and discussion

Even at high concentrations, the small size of the newly formed particles in the UT makes them hard to measure with a ground-based lidar optimized for measurements in the lower troposphere. Our system has a S/N of about 2-4 at the altitudes of the UT aerosol layer, which has an AOD of 10^{-3}. To understand how much S/N ratio we need to detect this thin layer confidently, we performed simulations of our lidar signal varying the aerosol and instrument properties.

Figure 1 shows the extinction profile obtained by the inversion algorithm (in magenta) and it's true value (in black) for κ = 1, 100 and 10,000, a factor that multiplies the efficiency of our system. In these simulations we used a mean lidar signal profile of 50 min (with 100 profiles of 30 s, each one with Poisson noise) and the number concentration in the UT was fixed at N_{UT}=16N_0.

We can say our system detected the aerosol layer between 9 and 15 km if the extinction is not null, with statistical significance. For $\kappa = 1$, the noise in the extinction profile, due to the low S/N, allows for positive and negative values, in and out of the aerosol layer. Moreover, the retrieved optical depth ($\tau = 0.015$) is different from its true value ($\tau_0 = 0.013$). However, as the efficiency grows by a factor of 100 and 10,000, the S/N grows by a factor of 10 and 100. As a result, the aerosol layer stands out (with $\langle\alpha\rangle/\sigma_\alpha \sim 10, 100$ for κ=100, 10,000), and the layer was clearly detected. The retrieved optical depth is equal to the true value.

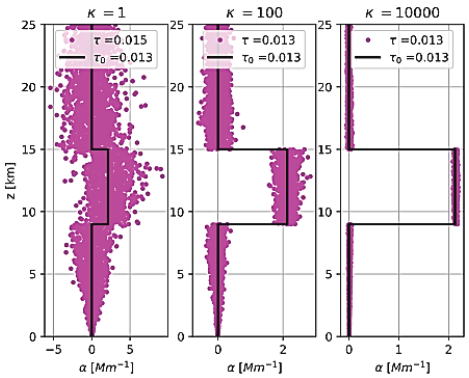

Figure 1. Retrieved (magenta) and true (black) extinction profiles for a system efficiency of κ = 1, 100 and 10,000 as indicated, and aerosol concentration of $N_{UT}=16N_0$. The legend gives the retrieved and true optical depths in each case.

The same analysis was made but now considering changes in the number concentration in the UT, for a fixed κ=100. Figure 2 shows the results for $N_{UT}=N_0=1.25\text{x}10^3$ cm^{-3}, the median values reported by Andreae et a., 2018, and for $4N_0$, and $16N_0$. This result shows that even for a system efficiency 100 times larger than ours, the ultrafine aerosols in the UT are still difficult to be detected. For $N_{UT}=N_0$, the noise in the extinction profiles does not allow discarding the null hypothesis. The retrieved optical depth is also different from its true value. However, for larger concentrations, the number of backscattered photons increases, and so does the S/N. One clearly see the aerosol layer in the middle and right panels, and the retrieved optical depths agree with the true values.

Our analysis reveals two important parameters to detect ultrafine particle layers in the UT, the system efficiency and the aerosol optical depth. Both increases the number of photons detected by the lidar system, increasing significantly the S/N. Next steps are: (1) estimating the errors of the retrieved extinction profiles; (2) applying an objective method to determine whether the layer is detected or not; (3) varying the AOD and system efficiency in finer steps; and (4) including the ABL accumulation mode aerosol. With that, we will calculate the probability of detection as a function of AOD and efficiency, to establish how much we need to improve our lidar to actually measure these UT aerosols.

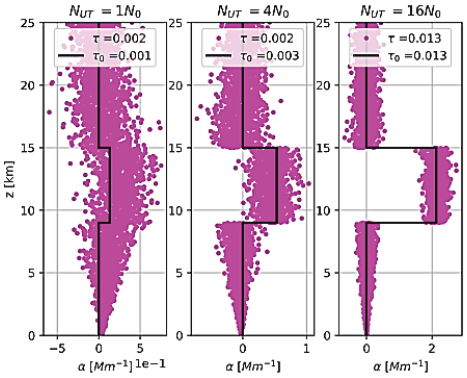

Figure 2. As figure 1, but for an aerosol concentration of N_0, $4N_0$ and $16N_0$, as indicated, and fixed system efficiency of κ=100.

Challenges

Detecting Aitken mode particles in the UT is not an easy task, especially for a lidar instrument optimized for detecting lower tropospheric aerosols. Our simulation approach allows estimating how we could improve our detection probability. However, we still need to access how the uncertainty in the lidar ratio and gases profiles could limit our detection skill.

Moreover, once we have defined the necessary increase in the system's efficiency to allow detecting these tiny particles, the question is what could be changed in our lidar system to achieve the required efficiency?

Acknowledgements

M.S. thanks to the Brazilian National Research Council (CNPq) for their financial support. H.B. and J.R. were supported by Fundación Carolina and by research grant 2018/08934-6, São Paulo Research Foundation (FAPESP).

References

Andreae et al., Aerosol characteristics and particle production in the upper troposphere over the amazon basin, Atmos. Chem. Phys., 18 (2), 921–961, 2018.

Barbosa et al., The first ALINE measurements and intercomparison exercise on lidar inversion algorithms, Óptica Pura y Aplicada, 47 (2) 99-108, 2014.

Barbosa et al., A permanent raman lidar station in the Amazon: description, characterization and first results, Atmos. Meas. Tech., 5 (7), 1745-1762, 2014.

Airborne lidar observations of seasonal differences in transatlantic Saharan dust transport towards the Caribbean

***M. Gutleben*[1,2]**, *S. Groß*[1], *M. Wirth*[1]
manuel.gutleben@dlr.de
(1) Deutsches Zentrum für Luft- und Raumfahrt, Institut für Physik der Atmosphäre, Oberpfaffenhofen, Germany
(2) Ludwig-Maximilians-Universität München, Meteorologisches Institut, Theresienstraße 37, Munich, Germany

Introduction

Saharan mineral dust particles represent a major contributor to the global aerosol mass burden. They are emitted into the atmosphere throughout the whole year and can be transported far away from their source regions. The main transportation route of the dust particles leads westwards over the Atlantic Ocean towards America and the Caribbean.

Transatlantic dust transportation routes are known to vary throughout the year. During the summer months the particles are usually transported in elevated Saharan Air Layers (SALs; Carlson and Prospero, 1972) in altitudes of up to 6 km. By analyzing lidar measurements in 2016 we found that SALs over the Caribbean come along with an enhanced amount of water vapor ($\approx$ 4 gkg^{-1}) compared to the dry free troposphere. We could also show that not the aerosol itself, but the water vapor is the main driver for radiative heating. As a consequence, water vapor has the potential to modify the atmospheric stability and the evolution of clouds in the dust-laden trades. This can explain why SALs are neutrally stratified in their interior and are confined by two inversions at the top and at the bottom. It should facilitate a turbulent regime that helps particles to stay aloft during their transport over the Atlantic Ocean.

Water vapor advection in wintertime dust plumes has never been investigated. During that time of the year dust advection is known to occur at lower altitudes (<3.5 km) and lower latitudes. As a consequence of the low altitudinal and latitudinal transportation, the dust particles are often mixed with other aerosol types, e.g. marine aerosol or biomass burning aerosol. In this study we investigate, if water vapor advection in dust plumes is also evident during winter time and whether this would have a similar radiative impact as during summer. We also study the potential of water vapor radiative heating for inducing mixing processes and turbulence inside the dust plumes and for helping the dust particles to stay aloft during transport.

Methods

To do so, airborne lidar measurements from the combined water vapor differential absorption and polarization-sensitive high spectral resolution lidar instrument WALES (Water Vapor Lidar Experiment in Space; Wirth, 2009) during the NARVAL-II field campaign (Next-Generation Aircraft Remote Sensing for Validation Studies II) in August 2016 and the EUREC^{4}A project (Elucidating the Role of Cloud-Circulation Coupling in Climate) in January/February 2020 are analyzed in detail.

During both campaigns WALES measurements of 532 nm backscatter ratio, particle linear depolarization ratio and lidar ratio as well as water vapor mixing ratio were conducted aboard the high-flying German research aircraft HALO east the Caribbean island of Barbados. In the course of these research flights several long-range-transported Saharan mineral dust plumes, both in winter and summer, were observed.

Results

Figure 1 shows a representative lidar-measurement example of a mineral dust plume observed during summer 2016. The elevated SAL with typical

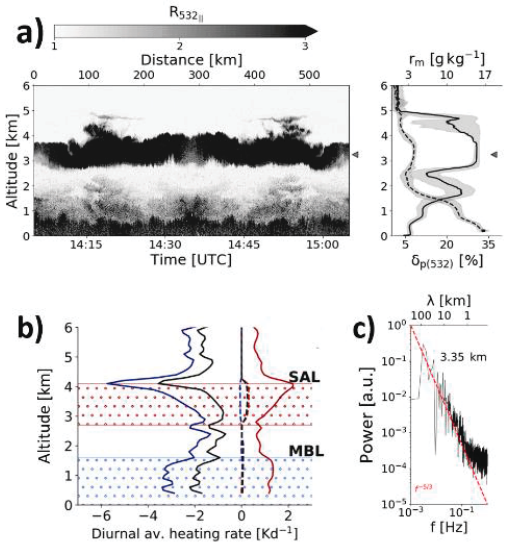

Figure 1. a) Exemplary measurement of an elevated SAL during NARVAL-II (left: backscatter ratio $R_{532||}$; right: mean profiles with standard deviation of particle linear depolarization ratio $\delta_{p(532)}$ (solid) and water vapor mass mixing ratio r_m (dashed)). **b)** Vertical profiles of radiative heating (blue: long-wave; red: short-wave, black: net; adapted from Gutleben et al. 2020). The dashed lines indicate the contributions of aerosol to the heating rate profile. **c)** Power spectrum derived from backscatter data in **a)** at 3.35 km altitude. The red line indicates the -5/3 slope for reference.

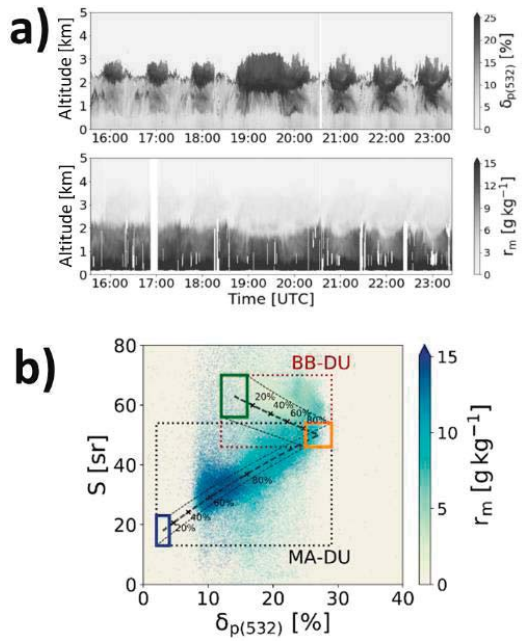

Figure 2. a) Exemplary lidar curtains of a dust plume observed in the winter season 2020 (top: particle linear depolarization ratio $\delta_{p(532)}$; bottom: water vapor mass mixing ratio r_m). **b)** Distribution of measured r_m in a space of lidar ratio (S) vs. $\delta_{p(532)}$ for measured wintertime dust plumes. Solid rectangles mark the typical positions of the pure aerosol regimes: marine aerosol (blue), transported Saharan mineral dust (orange) and biomass burning aerosol (green). Grey lines indicate the calculated mixing lines between biomass burning aerosols with transported Saharan dust aerosols (BB-DU) as well as marine aerosols (MA-DU).

particle linear depolarization ratios of 30% can clearly be detected in altitudes from 3 to 5 km. The vertical water vapor profile indicates that the SAL comes along with water vapor concentrations of approximately 4 gkg^{-1}. This has an impact on the calculated radiative heating profile (Figure 1 (b)). SAL-water vapor induces a net radiative cooling with altitude, which can be associated with the production of mixing processes inside the SAL.

When looking at the derived power spectrum of measured lidar backscatter inside the SAL (Figure 1 (c)), one can identify that the derived mesoscale turbulence cascades (using the Lomb-Scargle Algorithm (Lomb, 1976)) follow the predicted slope for turbulence of -5/3 (Lilly, 1983). This promotes the hypothesis that the radiative effect of water vapor in SALs helps to maintain the turbulent characteristics of the SAL as well as to counteract gravitational settling of dust particles along the transportation route. Small Richardson numbers from dropsonde measurements (not shown) also point towards turbulence and a well-mixed regime.

During the EUREC^{4}A project embedded water vapor in wintertime dust plumes could be recorded. Already when looking at the exemplary lidar curtain of a wintertime dust-measurement during EUREC^{4}A (Figure 2 (a)), one can identify regions of slightly enhanced water vapor in altitudes from 2 to 3 km. However, no clear separation of the dust layer from the even moister subjacent marine boundary layer is observed. During the campaign, mineral dust was never observed in altitudes greater than 3 km. As a consequence, it was always mixed with biomass burning and marine aerosol (Figure 2 (b)). The joint distribution of measured lidar ratios and particle linear depolarization ratios follows the mixing lines between marine aerosol, mineral dust and biomass burning aerosol that can be calculated from theory.

Discussion and Challenges

Similar to dust transport in the summer season, also during the winter season water vapor was observed to be transported within the dust plume. However, no clear separation between the moist dust plume and the moist marine boundary layer could be identified.

In contrast to the radiative effect of elevated SALs, the radiative effect of wintertime dust plumes could lead to high reaching convection, as the well-mixed marine boundary layer would be topped by another well mixed dust-regime. Additionally, the low-level winter-transport of the aerosol particles (i.e. biomass burning aerosol and mineral dust aerosol) may impact the evolution of clouds, since the particles can act as cloud condensation nuclei or ice nucleating particles. Future studies should investigate the radiative effect of wintertime dust plumes together with their impact on cloud development, using for example a combination of radiative transport models with lidar and radar techniques.

References

Carlson and Prospero, The large-scale movement of Saharan air outbreaks over the northern equatorial Atlantic, *J. Appl. Meteorol.*, 11, 283-297, 1972.

Gutleben et al., Radiative effects of long-range-transported Saharan air layers as determined from airborne lidar measurements, *Atmos. Chem. Phys.*, 20(20), 2020.

Lilly, Stratified turbulence and the mesoscale variability of the atmosphere, *J. Atmos. Sci.*, 40(3), 749-761, 1983.

Lomb, Least-squares frequency analysis of unequally spaced data, *Astrophys. Space Sci.*, 29(2), 447-462, 1976.

Wirth et al., The airborne multi-wavelength water vapor differential absorption lidar WALES: system design and performance, *Appl. Phys. B*, 96,201-213, 2009.

Observations and analysis of California smoke in Lille (France) with a Mie-Raman-polarization-fluorescence lidar

Q. Hu[1], P. Goloub[1], I. Veselovskii[2], T. Podvin[1]
Qiaoyun.hu@univ-lille.fr
(1) Univ. Lille, CNRS, UMR 8518 - LOA - Laboratoire d'Optique Atmosphérique, F-59000 Lille, France
(2) Prokhorov General Physics Institute of the Russian Academy of Sciences, Moscow, Russia

Introduction

In recent years, the striking wildfires in Canada (2017), Australia (2020) and California (2020) have given the media and scientific community an impression that large-scale wildfires are growing in both the intensity and occurrence. Large quantities of wildfire emissions cause increasingly concerns about the climatic and health-related impacts. Wildfire smoke is a mixture of gases and aerosol particles. Black carbon (BC) and Brown carbon (BrC) which is composed of various organic compounds, ex. hydrocarbon species, are two important aerosol components in smoke. Because of the variety of burning materials, combustion conditions and aging process, the observed smoke particles are ranging in different sizes, shapes, morphologies and properties. The characterization of smoke optical, microphysical and chemical properties, especially aged smoke after long-transport, is very limited and requires more attention of the scientific community.

From July 2020, record-breaking wildfires started in California, USA and emitted tremendous smoke plumes over the northern hemisphere. In September-November 2020, the smoke plumes originated from California wildfires were detected by lidar LILAS operated in Lille France. The most intense plumes are observed in September. LILAS is a multiwavelength Mie-Raman-polarization lidar equipped with an experimental fluorescence channel and affiliated to the ACTRIS/EARLINET (Hu et al., 2019). During the smoke episodes, LILAS was updated by replacing the water vapor channel at 408 nm by a fluorescence channel centered at 466 nm (Veselovskii et al., 2021). The fluorescence channel provides us 2 extra parameters: the fluorescence backscattering coefficient β_F and the fluorescence capacity G_F. G_F represents the capacity of the aerosols in producing fluorescence signals and it is linked to the concentration of fluorophores in aerosols. The optical parameters ($2\alpha+3\beta+3\delta+\varphi$, φ: fluorescence properties) in California smoke event help to better characterize smoke properties and to study the interaction of smoke and ice clouds.

Results and discussion

The lidar observations of smoke episodes during 10-18 Sep are shown in Figure 1. According to the back trajectory, the smoke on 11 Sep 2020 was originated from the Creek fire, which started on 04 September and that on 17 Sep was from Oregon fire, which started on 08 September.

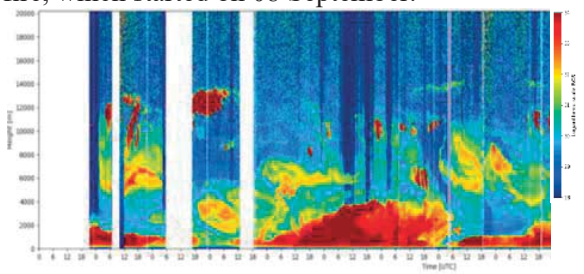

Figure 1. Lidar observations (range corrected lidar signal at 1064 nm) on 10-18 Sep 2020. Layers in yellow and green represent Californian smoke.

In Figure 2, the extinction coefficients peak at 6000 m with 200 Mm^{-1} at 355 nm and 150 Mm^{-1} at 532 nm. The linear particle depolarization ratios (PLDRs) increase versus height, with ~0.02 at 5500 nm and ~0.05 above 7000 m for 532 nm. The PLDR at 1064 nm stays at about 0.01 throughout the whole layer. The lidar ratio (LR) is about 35 sr at 355 nm and 55-75 sr at 532 nm. The fluorescence capacity is about 3.8×10^{-4}.

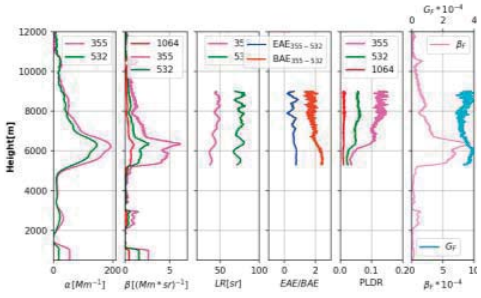

Figure 2. Case1: Averaged profiles of optical parameters at 22:00, 11 Sep--02:00, 12 Sep, 2020. The panels from left to right represent extinction, backscatter coefficient, LR, extinction and backscatter related Angström exponent (EAE/BAE), PLDR, β_F and G_F.

Observations on 17-18 Sep (Figure 3) show a weaker spectral dependence of extinction (EAE~0.0), lower lidar ratios (25 sr at 355 and 50 sr at 532 nm) and increased depolarization ratios at 355 and 532 nm. The depolarization ratio at 1064 nm is low and comparable in both cases. G_F in Case 2 is 20-40% lower than in Case 1, but still stronger than other typical aerosols (Veselovskii et al.,

2021). Variations of G_F are expectable even in the same smoke plume, because in aging process, the oxidation, evaporation and coagulation are complex and not geometrically homogenous through the smoke layer. In highly diluted smoke or at the edge of smoke, G_F could decrease due to the enhancement of evaporation of (semi)versatile organic compounds (Hodshire et al., 2021).

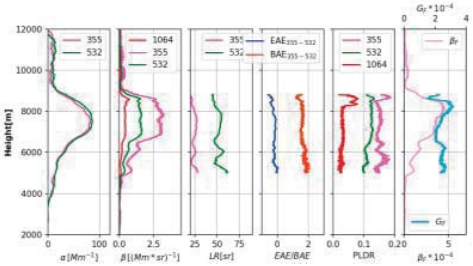

Figure 3. Case 2: Same plots with Figure 2 but at 22:00, 17 Sep-03:00, 18 Sep, 2020. Ice formation (possibly through deposition freezing) observed at 8000-9000 m.

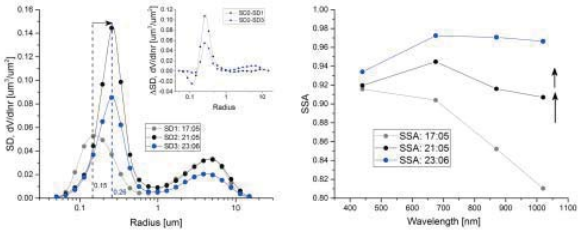

Figure 4. The change of size distribution (left) and SSA (right) when smoke from Oregon fire arrived at site PNNL on 11 Sep 2020. Results for other sites are not shown.

AERONET observations (and retrievals) near the fire places reveal similar features: when Oregon smoke coming after Creek smoke in a site, AE and LR decreases, PLDR increases and single scattering albedo (SSA) becomes dust-like. For example, Oregon smoke of 1-3 days old reached site PNNL (Figure 4) on 11 September at about 21:00 UTC, the mean radius of fine mode shifts to bigger sizes and the SSA increases, especially at longer wavelengths. CALIPSO observations also show that smoke plumes from Oregon fire and Creek fire with similar age have different PLDRs, giving 0.02-0.05 for Creek smoke and 0.10-0.15 for Oregon smoke at 532 nm, which are close to the observations LILAS. Such characteristics indicated aerosols from Oregon might be bigger in size and contain more BrC components compared to Creek smoke after 1-3 days aging, which could be resulted from the combustion process or aging in the first 1-3 days.

Figure 3 shows the presence of ice crystals at in smoke layer, which is likely a demonstration of ice nucleating (IN) upon smoke particles. The profiles of β_F and PLDR confirm the simultaneous existence of smoke and ice crystals. The impacts of burning materials, conditions and aging process on the propensity of IN and how they impact the IN regimes are not yet well revealed. Studies reported that aging process could increase the abilities of smoke in IN. Apart from the growth of particle size, oxidation of soot and OC components, the amorphous morphology of organic matter, recent study claim that the uncovering of minerals preexisting in the biomass during aging could also facilitate IN (Knopf et al., 2018, Jahl et al., 2021).

Challenges

The physical and chemical processes in smoke aging, especially during long transport, are not adequately understood and characterized, as well as their impacts on light scattering behaviors and IN abilities. Such work requires more observations and laboratory simulations with extended datasets.

Conclusions

In this study, we reported the optical characteristics $2\alpha+3\beta+3\delta+\varphi$ and their variations in transported California smoke based on Mie-Raman-polarization-fluorescence lidar data in LOA. The results reveal that the variations of smoke properties, such as size, PLDRs, fluorescence capacity and IN abilities, are strongly correlated to the combustion and aging process. Additionally, the fluorescence channel in lidar brings new information for aerosol characterization, classification and cloud study. A new lidar (**LIFE**: **L**aser **I**nduced Fluorescence Explorer) dedicated to fluorescence measurements, will be built and operated at LOA in the near future, in the frame of OBS4CLIM project and will be companion of LILAS for enhancing aerosol characterization in various situation.

Acknowledgements

We thank Labex CaPPA, SNO PHOTONS (ACTRIS-FRANCE), ESA/IDEAS+ and GPI RAS (Russia) for their support.

References

Hu et al.: Long-range-transported Canadian smoke plumes in the lower stratosphere over northern France, *Atmos. Chem. Phys.*, 19, 1173–1193, 2019.

Veselovskii et al.: Mie–Raman–fluorescence lidar observations of aerosols during pollen season in the north of France. *Atmospheric Measurement Techniques*, 14(7), 4773-4786, 2021.

Hodshire et al.: Dilution impacts on smoke aging: evidence in Biomass Burning Observation Project (BBOP) data. *Atmos. Chem. Phys*, 21(9), 6839-6855, 2021.

Jahl et al.: Atmospheric aging enhances the ice nucleation ability of biomass-burning aerosol. *Science Advances*, 7(9), eabd3440, 2021.

Knopf et al.: The role of organic aerosol in atmospheric ice nucleation: a review. *ACS Earth and Space Chemistry*, 2(3), 168-202, 2018.

COLOR: *C*DOM-proxy retrieval from ae*OL*us *O*bse*R*vations

***D. Dionisi*[1]**, *S. Bucci*[2], *C. Cesarini*[1], *S. Colella*[1], *D. D'Alimonte*[3], *L. Di Ciolo*[2], *P. Di Girolamo*[4], *M. Di Paolantonio*[1], *N. Franco*[4], *G. Gostinicchi*[2], *T. Kajiyama*[3], *G. L. Liberti*[1], *E. Organelli*[1], *R. Santoleri*[1]**

davide.dionisi@cnr.it

(1) Institute of Marine Sciences, Italian National Research Council,Rome, Italy

(2) Serco Italia S.p.A., Frascati, Italy

(3) AEQUORA, Lisbon, Portugal

(4) School of Engineering, University of Basilicata, Potenza, Italy

Introduction

The ESA Earth Explorer Wind Mission ADM-Aeolus (Atmospheric Dynamics Mission, ESA, 2008), successfully launched on 22 August 2018, has the aim to provide global observations of wind profiles, demonstrating the impact of wind profile data on operational weather forecasting and on climate research. Within the Aeolus+ Innovation program, ESA has launched an Invitation To Tender (ITT, ESA AO/1-9544/20/I/NS) to carry out studies aimed at exploring, developing and validating innovative products and applications and exploiting the novel nature of Aeolus data.

Although Aeolus's mission primary objectives and subsequent instrumental and sampling characteristics are not ideal for monitoring ocean sub-surface properties, the unprecedented type of measurements from this mission are expected to contain important and original information in terms of optical properties of the sensed ocean volume. Being the first HSRL (High Spectral Resolution Lidar) launched in space, ALADIN (Atmospheric LAser Doppler Instrument) of ADM-Aeolus gives an unprecedented new opportunity to investigate the information content of the 355 nm signal backscattered by the ocean sub-surface components.

Based on the above considerations, COLOR (CDOM-proxy retrieval from aeOLus ObseRvations), a selected Aeolus+ Innovation ITT project, aims to evaluate and document the feasibility of deriving an in-water AEOLUS prototype product from the analysis of the ocean sub-surface backscattered component of the 355 nm signal acquired by the ALADIN. An overview of the project and some preliminary results are presented.

Proposed approach

COLOR project, which started on the 10th of March 2021, focuses on the AEOLUS potential retrieval of the ocean optical properties at 355 nm: diffuse attenuation coefficient for downwelling irradiance, K_d [m-1], and sub-surface hemispheric particulate backscatter coefficient, b_{bp} [m-1]. In particular, being dominated by the absorption due to CDOM (Chromophoric Dissolved Organic Matter), K_d coefficient at 355 nm, $K_d(355)$, can be used as a proxy to describe spatial and temporal variability of this variable, which contributes to regulating the Earth's climate.

To reach COLOR objectives, the work is organized in three phases: Consolidation of the scientific requirements; Implementation and assessment of AEOLUS COLOR prototype product; Scientific roadmap.

The core activity of the project is the characterization of the signal from the AEOLUS ground bin (Δr_{grd}). In principle, the ground bin backscattered radiation signal is generated by the interaction of the emitted laser pulse radiation with two media (atmosphere and ocean, B_{grd_atm} and B_{grd_wat}, respectively) and their interface (B_{grd_surf}, see Figure 1).

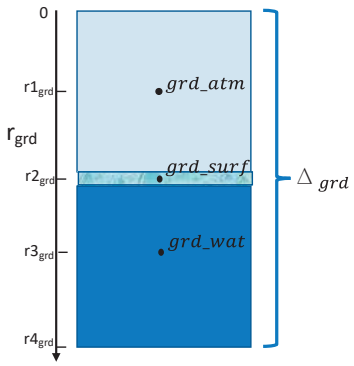

Figure 1. Schematic geometry description of the AEOLUS ground bin.

To evaluate the feasibility of an AEOLUS in-water product, COLOR proposes to develop a retrieval algorithm that is structured in three independent and consecutive phases:

1) Pre-processing analysis: aimed to identify suitable measurements to be inverted;
2) Estimation of the in-water ground bin signal contribution: aimed to remove contributions to the measured signal from variables other that the in-water ones;
3) Retrieval of in-water ground bin optical properties: aimed to estimate the targeted in-

water optical properties.

Two parallel and strongly interacting activities are associated with each step of these phases:

a) Radiative transfer numerical modelling. This tool will be essential to simulate the relevant radiative processes expected to be responsible for the generation of AEOLUS surface bin signal.
b) AEOLUS data analysis. The objective of this activity will be to verify the information content of the AEOLUS ground bin signals and the assumptions for data product retrieval.

The potential AEOLUS in-water product will be then validated through the comparison of statistical properties obtained by analyzing the whole set of data from AEOLUS (at least one year of processed measurements) and the selected reference datasets: Biogeochemical-Argo floats, oceanographic cruises and ocean-colour satellites.
The preliminary results about the above-mentioned activities will be here presented. In particular, the sea-surface backscattering and the in-water contribution of the AEOLUS ground bin have been estimated through numerical modeling. Furthermore, the preliminary experimental data analysis suggests that the observed excess of signal in the AEOLUS ground bin could be related to the signal coming from the marine layers. Further analyses are planned in the second phase of these activities to disentangle atmospheric and oceanic signal contribution in the AEOLUS ground bin.

Challenges

Recently, new applications using CALIOP (Cloud-Aerosol Lidar with Orthogonal Polarization) instrument on-board CALIPSO (Cloud-Aerosol Lidar and Infrared Pathfinder Satellite Observation) demonstrated that satellite-borne lidar can give valuable information about ocean optical properties (Behrenfeld et al., 2019; Dionisi et al., 2020). Similarly, the potential application of AEOLUS observations to ocean color studies could bring benefits to the oceanographic community. In principle, through these observations, it will be possible to study the diurnal variability of CDOM light absorption properties, the knowledge of which is up to now very scarce. However, this capability is limited partly by the spatio-temporal sampling of AEOLUS and by the actual accuracy of the AEOLUS products, which, in turn, depends on the signal-to-noise ratio that is a function of the solar illumination conditions.

A future challenge is the definition of improved instrumental requirements for satellite missions designed to optimally provide information both on relevant atmospheric and oceanic variables. Within this frame, a strong interaction between ocean color and lidar communities needs to be developed.

References

European Space Agency: ADM-Aeolus Science Report, ESA SP-1311, 2008.

Behrenfeld M., et al.: Global satellite-observed daily vertical migrations of ocean animals, *Nature*, vol. 576, n. 7786, Art. n. 7786, doi: 10.1038/s41586-019-1796-9, 2019.

Dionisi D. et al.: Seasonal distributions of ocean particulate optical properties from spaceborne lidar measurements in Mediterranean and Black sea, *Remote Sens. Environ.*, vol. 247, pag. 111889, doi: 10.1016/j.rse.2020.111889, 2020.

Triple-wavelength depolarization and lidar ratio observations in Saharan dust and comparison to AERONET retrievals

M. Haarig[1], *R. Engelmann*[1], *A. Ansmann*[1], *H. Baars*[1], *D. Althausen*[1], *and U. Wandinger*[1]
haarig@tropos.de
(1) Leibniz Institute for Tropospheric Research, Leipzig, Germany

Introduction

The non-spherical shape of mineral dust particles challenges a correct representation in scattering models. By extending the observation space towards the near infrared (NIR) in terms of depolarization and extinction measurements, a better characterization of the coarse-mode dominated dust layers will be possible. The measurements of the depolarization ratio at 1064 nm showed already, that this wavelength is sensitive to the size of the dust particles (e.g., Haarig et al., 2017). In contrast, non-spherical stratospheric smoke particles, which are fine-mode dominated show a completely different spectral slope of the particle linear depolarization ratio (Haarig et al., 2018, Hu et al., 2019). To obtain even more information about the mineral dust particles, we present the first measurements of lidar ratio at 1064 nm to cover the wavelength range from UV till NIR. The lidar ratio conveys information about the absorption linked to mineralogy and the size of the dust particles. The rotational Raman technique applied to 1064 nm allows us to measure directly the extinction as demonstrated already in Haarig et al., 2016.

From our 3+3+3 measurements (3 backscatter, 3 extinction coefficients, 3 depolarization ratios) of Saharan dust, we present one case study and compare the results to the AERONET v3 inversions (Sinyuk et al., 2020), which deliver lidar ratios and particle linear depolarization ratios at 440, 675, 870 and 1020 nm.

Results and discussion

On 22 February 2021, an enormous Saharan dust outbreak reached central Europe. The dust layer extended from the ground up to 8 km height above Leipzig, Germany. The fast transport (< 36 hours) prevented mixing-in of pollution aerosol and led to rather pure dust conditions.

Two lidar systems were operated: BERTHA (Backscatter, Extinction, lidar-Ratio, Temperature, Humidity profiling Apparatus, Haarig et al., 2017) and the Polly^{XT} Arielle (Engelmann et al., 2016). BERTHA provided the measurements at 532 and 1064 nm and Arielle at 355 nm, because the BERTHA' s signal at 355 nm was very weak that night. The depolarization ratio at 1064 nm was measured during the first 20 minutes, then the setup was changed to extinction measurement at 1064 nm during the next 2h15min. The time-height plot of the measurements is shown in Fig. 1, where the strong dust layer is clearly visible. The intensive optical properties of the main dust layer are summarized in Table 1.

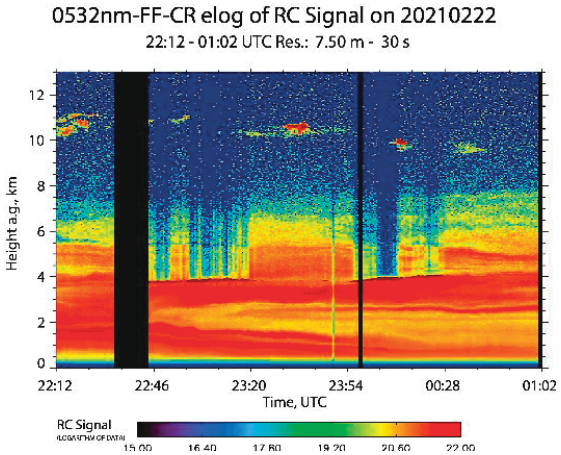

Figure 1. 22 February 2021, 22:12 – 01:02 UTC: Time-height plot of the range-corrected cross-polarized signal at 532 nm. The dust layer up to 8 km height is clearly visible.

The spectral slope of the particle linear depolarization ratio shows a typical behaviour for dust with a maximum at 532 nm and a decrease towards the UV and the NIR (see Haarig et al., 2017, Burton et al., 2015).

The spectral slope of the lidar ratio shows very similar values at 355 and 532 nm and an increase towards the 1064 nm. The lidar ratio at 1064 nm was measured for the first time for Saharan dust and was found to around 26% higher than at 532 nm.

Table 1. Optical properties of the strongest layer (3 – 4 km height) at all three wavelengths.

Wvl. (nm)	S (sr)	δ (%)
355	47 ± 8	25.6 ± 2.5
532	50 ± 5	29.8 ± 1.7
1064	63 ± 13	21.4 ± 2.5

The intensive optical properties could be compared to AERONET v3 inversions performed in the same dust layer on the next morning. The results are shown in Fig. 2 and 3.

AERONET v3 inversions are available at 440, 675. 870 and 1020 nm. The increase of the lidar ratio from the VIS towards the NIR is well covered by the AERONET inversions (Fig. 2). Towards the

UV AERONET tends to overestimate the lidar ratio. However, AERONET measures columnar values including the polluted boundary layer and not just the pure dust layer.

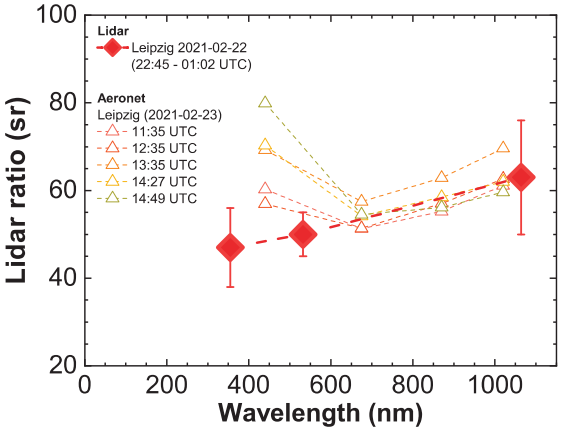

Figure 2. The spectral slope of the lidar ratio of the Saharan dust layer observed on 22 February 2021 compared to AERONET sun photometer retrievals of the lidar ratio on 23 February 2021 (5 scans at indicated times).

The spectral slope of the particle linear depolarization ratio (Fig. 3) could not be reproduced with AERONET inversions, which show a monotonic increase with wavelength. The maximum in the range around 532 nm is missing in the AERONET results and the depolarization ratio at 1064 nm is overestimated.

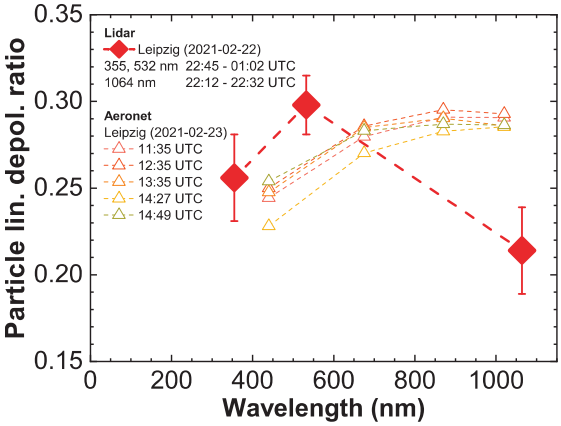

Figure 3. The spectral slope of the particle linear depolarization ratio of the Saharan dust layer observed on 22 February 2021 compared to AERONET sun photometer retrievals of the particle linear depolarization ratio on 23 February 2021 (5 scans at indicated times).

Conclusion

We present the first measurements of the lidar ratio at 1064 nm for dust particles and provide the complete 3+3+3 data set for a selected pure Saharan dust event.

The comparison to AERONET v3 inversion results show an acceptable agreement for the lidar ratio in the VIS – NIR wavelength range. The spectral slope of the particle linear depolarization ratio could not be reproduced by AERONET inversions. A similar result has been found by Shin et al., 2018 comparing lidar and sun photometer observations. In case of non-spherical dust particles, it is probably not advised to use the spheroidal particle shape implemented in AERONET inversions (Dubovik et al., 2006) for the retrieval of the linear depolarization ratio. A more complicated particle shape model would be needed to calculate the depolarization ratio at 180° backscatter direction.

We are on the way to perform more observations of the lidar ratio and depolarization ratio at all three wavelengths in Saharan dust layers.

References

Burton et al., Observations of the spectral dependence of linear particle depolarization ratio of aerosols using NASA Langley airborne High Spectral Resolution Lidar, *Atmos. Chem. Phys*., 15, 13 453–13 473, 2015.

Dubovik et al., Application of spheroid models to account for aerosol particle nonsphericity in remote sensing of desert dust, *J. Geophys. Res.: Atmospheres*, 111, D11 208, 2006.

Engelmann et al., The automated multiwavelength Raman polarization and water-vapor lidar PollyXT: the neXT generation, *Atmos. Meas. Tech*., 9, 1767–1784, 2016.

Haarig et al., 1064 nm rotational Raman lidar for particle extinction and lidar-ratio profiling: cirrus case study, *Atmos. Meas. Tech*., 9, 4269–4278, 2016.

Haarig et al., Triple-wavelength depolarization-ratio profiling of Saharan dust over Barbados during SALTRACE in 2013 and 2014, *Atmos. Chem. Phys*., 17, 10 767–10 794, 2017.

Haarig et al., Depolarization and lidar ratios at 355, 532, and 1064 nm and microphysical properties of aged tropospheric and stratospheric Canadian wildfire smoke, *Atmos. Chem. Phys.*, 18, 11 847–11 861, 2018.

Hu et al., Long-range-transported Canadian smoke plumes in the lower stratosphere over northern France", *Atmos. Chem. Phys*., 19, 1173–1193, 2019.

Shin et al., On the spectral depolarisation and lidar ratio of mineral dust provided in the AERONET version 3 inversion product, *Atmos. Chem. Phys.*, 18, 12 735–12 746, 2018.

Sinyuk et al., The AERONET Version 3 aerosol retrieval algorithm, associated uncertainties and comparisons to Version 2, *Atmos. Meas. Tech.*, 13, 3375–3411, 2020.

Lidar depolarization ratio of atmospheric pollen at multiple wavelengths

*S. Bohlmann[1,2], X. Shang[1], V. Vakkari[3,4], E. Giannakaki[1,5], A. Leskinen[1,2], K.E.J. Lehtinen[1,2], S. Pätsi[6], **M. Komppula[1]***
mika.komppula@fmi.fi
(1) Finnish Meteorological Institute, Kuopio, Finland
(2) Department of Applied Physics, University of Eastern Finland, Kuopio, Finland
(3) Finnish Meteorological Institute, Helsinki, Finland
(4) Atmospheric Chemistry Research Group, Chemical Resource Beneficiation, North-West University, Potchefstroom, South Africa
(5) Department of Environmental Physics and Meteorology, University of Athens, Athens, Greece
(6) Biodiversity Unit, University of Turku, Turku, Finland

Introduction

Pollen is an essential part of plant reproduction as they store and transport genetic information of the plant. Because of the immobility of plants, pollen grains need to be transferred by other means for example wind or animals. Most grasses (Poaceae), conifers and around 10-20 % of flowering plants are wind-pollinated (Ackerman, 2000). Typical sizes of such pollen grains range from 20-60 µm (Shukla et al., 1998), but also large pollen grains like pine (Pinus) or spruce (Picea) pollen with diameters around 100 µm are transported by wind. Pollen has various effects on climate and human health.

Pollen can be lifted up to several kilometers by turbulent mixing within the boundary layer (Mandrioli et al., 1984) and can be transported by wind over thousands of kilometers (e.g. Rousseau et al., 2008). While dispersed in the atmosphere, they can also promote the formation of clouds by acting as ice nucleating particle (e.g. von Blohn et al., 2005). Furthermore, pollen grains can rupture and lead to a high number of smaller particles, which are efficient cloud condensation nuclei (Steiner et al., 2015). An enhanced number of ice and cloud condensation nuclei can furthermore increase the cloud albedo and cloud lifetime and reduce precipitation.

It is of high importance to study the pollen distribution and transport mechanisms in the atmosphere. To further improve pollen transport and forecast models, validation measurements are needed. Previously, we have shown that in the absence of other non-spherical particles, lidar measurements and especially the particle depolarization ratio (PDR) can be used to investigate pollen grains in the atmosphere (Bohlmann et al., 2019). We have estimated the PDR at 532 nm for pure birch (Betula) and pine pollen under certain assumptions as 0.24 ± 0.01 and 0.36 ± 0.01, respectively (Shang et al., 2020).

In this study, we operated a multiwavelength Raman lidar PollyXT (Engelmann et al., 2016) with four newly added near-range channels and depolarization measurements at two wavelenghts (355 and 532 nm). To further improve the investigation of pollen depolarization properties, we assessed the depolarization measurements of a co-located Halo Doppler lidar, which provides information at 1565 nm (Vakkari et al., 2021). The measurement of the depolarization ratio at multiple wavelengths allows us to investigate its wavelength dependence. This could enable the distinction of pollen from other depolarizing aerosols, as the depolarization ratio at single wavelengths can be similar for different aerosol types.

Results and discussion

During the pollen campaign in 2019 at the EARLINET station in Vehmasmäki (Kuopio), Finland, we were able to expand the dataset of birch and spruce pollen observations with improved lidar measurements down to around 350 m. Very high depolarization ratios were detected during a 4-day period (16-20 May 2019) of birch and spruce pollen with an increasing amount of spruce pollen towards the end (Figure 1).

In-situ aerosol measurements and meteorological data have been considered to characterize the aerosol load and the air masses at the site. Ruptured pollen could affect the observed depolarization ratio as the smaller fragments of ruptured pollen are highly non-spherical. We detected a slightly higher number of particles in the diameter range from 3-10 µm on the day with high depolarization, which could be partly caused by pollen fragments. However, more research on the impact of pollen fragments is needed and the amount of pollen fragments should be recorded in future studies. Also the possible impact of the pollen surface structure on the measured depolarization ratios needs to be investigated, as the rough type-specific surface of certain pollen types can cause higher depolarization ratios.

The investigation of lidar-retrieved optical properties in detected pollen layers revealed a wavelength dependence of the depolarization ratio

especially in the presence of spruce pollen. On a day with a spruce pollen share of the total pollen number concentration of about 22%, high PDR values of 0.46 ± 0.26 and 0.30 ± 0.09 were detected at 532 and 1565 nm, respectively, in pollen layers down to around 350 m. The PDR at 355 nm could only be detected down to 900 m. In those layers, mean PDR values were 0.10 ± 0.02, 0.38 ± 0.23 and 0.29 ± 0.10 at 355, 532 and 1565 nm, respectively. The wavelength dependency could be explained with the higher sensitivity of the longer lidar wavelengths to big pollen particles (~ 100 µm) and characteristic surface pattern of those pollen. This wavelength dependence could be characteristic for large, non-spherical spruce pollen. Furthermore, negative backscatter-related Ångström exponents have been detected when the spruce pollen share was high. Negative Ångström exponents have previously been detected for dust but could also be a characteristic feature of spruce pollen. A novel method introduced by Shang et al. (2020) was applied to the measurement data and pollen depolarization ratio values of 0.44 at 532 nm and 0.16 at 355 nm were determined for the birch-spruce pollen mixture. Furthermore, a limitation of the Ångström exponent at the lidar wavelengths 355/532 nm for the characterization of very large pollen particles like spruce was found.

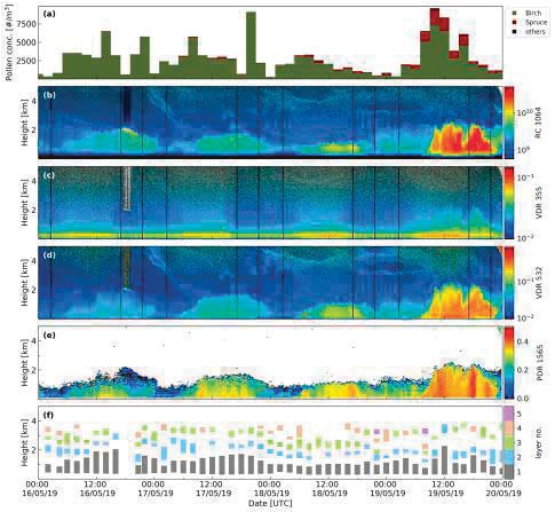

Figure 1. Overview of the 16–20 May 2019 period. Pollen concentration detect by Hirst-type spore trap at 4 m height (a), range-corrected signal at 1064 nm (b), linear volume depolarization ratio at 355 (c) and 532 nm (d) by PollyXT Raman polarization lidar, Halo Doppler lidar depolarization ratio at 1565 nm (e) and automatic layer detection (f).

To determine values and characteristics of pure pollen, more cases with high concentrations of only one pollen type are necessary. Nevertheless, our study shows the spectral dependence of the depolarization ratio for pollen, especially spruce, in the atmosphere.

Challenges

Optical properties of pure pollen types in atmospheric conditions are needed. The share ruptured pollen and their effect on optical properties need to be explored.

Acknowledgements

This work was supported by the Academy of Finland (project no. 310312).

References

Ackerman, Abiotic pollen and pollination: ecological, functional, and evolutionary perspectives, in: Plant Systematics and Evolution, edited by: Dafni, A., Hesse, M., and Pacini, E., Springer Vienna, Vienna, 167–185, 2000.

von Blohn et al., The ice nucleating ability of pollen: Part III: New laboratory studies in immersion and contact freezing modes including more pollen types, Atmos. Res., 78, 182–189, https://doi.org/10.1016/j.atmosres.2005.03.008, 2005.

Bohlmann et al., Detection and characterization of birch pollen in the atmosphere using a multiwavelength Raman polarization lidar and Hirst-type pollen sampler in Finland, Atmos. Chem. Phys., 19, 14559–14569, https://doi.org/10.5194/acp-19-14559-2019, 2019.

Engelmann et al., The automated multiwavelength Raman polarization and water-vapor lidar PollyXT: the neXT generation, Atmos. Meas. Tech., 9, 1767–1784, https://doi.org/10.5194/amt-9-1767-2016, 2016.

Mandrioli et al., Evidence for long range transport of biological and anthropogenic aerosol particles in the atmosphere, Grana, 23, 43–53, https://doi.org/10.1080/00173138409428876, 1984.

Rousseau et al., Long-distance pollen transport from North America to Greenland in spring, J. Geophys. Res.-Biogeo., 113, G02013, https://doi.org/10.1029/2007JG000456, 2008.

Shang et al., Optical characterization of pure pollen types using a multi-wavelength Raman polarization lidar, Atmos. Chem. Phys., 20, 15323–15339, https://doi.org/10.5194/acp-20-15323-2020, 2020.

Shukla et al., Biology of Pollen, APH Publishing Corporation, 133 pp., ISBN 9788170249245, 1998.

Steiner et al., Pollen as atmospheric cloud condensation nuclei, Geophys. Res. Lett., 42, 3596–3602, https://doi.org/10.1002/2015GL064060, 2015.

Vakkari et al., Aerosol particle depolarization ratio at 1565 nm measured with a Halo Doppler lidar, Atmos. Chem. Phys., 21, 5807–5820, https://doi.org/10.5194/acp-21-5807-2021, 2021.

The ERATOSTHENES CoE part of PollyNET, First observations of the PollyXT-CYP in the complex atmosphere over the Eastern Mediterranean

R. E. Mamouri[1,2], A. Nisantzi[1,2], R. Engelman[3], J. Bühl[3], P. Seifert[3], H. Baars[3], Z. Yin[3], D. Hadjimitsis[1,2], and A. Asmann[3]
rodanthi.mamouri@cut.ac.cy
(1) Cyprus University of Technology, Department of Civil Engineering and Geomatics, Limassol, Cyprus
(2) ERATOSTHENES Centre of Excellence, Limassol, Cyprus
(3) Leibniz Institut für Troposphärenforschung, Leipzig, Germany

Introduction

The permanent PollyXT lidar system started the continuous operation on 27th of October 2020, at Limassol, Cyprus. The lidar system will become a key component within the EXCELSIOR H2020 EU Teaming project. The mission of the EXCELSIOR project is to upgrade the Remote Sensing & Geo-Environment Lab, established within the Faculty of Engineering & Technology of the Cyprus University of Technology, into a sustainable, viable and autonomous Centre of Excellence, called the ERATOSTHENES Center of Excellence (ECoE). The PollyXT-CYP is hosted by the ERATOSTHENES CoE aiming to link the Centre to ACTRIS and PollyNet. Its task will document the complex mixture of the different aerosol species and clouds over the Eastern Mediterranean. The system is continuously running and since the first observations in Limassol, PollyXT-CYP (fig. 1) demostrates the complex aerosol conditions over Cyprus.

The PollyXT-CYP will be a key research infrastructure of the Cyprus Atmospheric Remote Sensing Observatory (CARO). CARO will consist of two high-tech containers housing the PollyXT-CYP lidar and state-of-the art doppler lidar, cloud radar and radiometric equipment which will be used to measure the air quality, the dust transport, and the cloud properties over Cyprus. The CARO is planned to become National Facility of the Republic of Cyprus for Aerosol and Cloud Remote Sensing Observations participating to the ACTRIS Aerosol and Cloud Remote Sensing Platforms.

In this study we present selected cases of the unique atmospheric structure from the first months of continuous operation over Cyprus as well as optical and geometrical properties of the aerosol layers.

Figure 1. PollyXT-CYP, Limassol, Cyprus

Results and discussion

Through the analysis of PollyXT-CYP data since October 2020 we have selected three case studies.

Between the 27th of October to the 1st of November 2020, the lidar observed smoke plumes from the extreme wildfires on the west coast of the U.S. The smoke travelled over the Atlantic Ocean and triggered the heterogenous ice formation at the height of 10km. Saharan dust was also detected between 2-5km and liquid clouds were formed on the top of the dust layer.

On 13th of March 2021 the Etna volcanic ash layer detected between 6 and 7km, with the characteristic value of mean lidar ratio at 71± 17sr and 65± 19 sr at 355 and 532nm respectively. The 532 nm layer-integrated particulate depolarization ratios observed for the Etna layer (PDLR= 0.24 ± 0.02) were much larger than those found for the volcanic aerosol layers produced by other eruptions (Prata et al., 2017).

On 9th of March 2021 an extreme Saharan dust event influenced the atmosphere of Limassol up to 5km (fig. 2). A well-structured dust layer from 2.5 to 4km depicts the typical values of optical properties for the Saharan dust observed in Cyprus (Nisantzi et al., 2015). The LR values for 355 and 532 nm are 59±2sr and 50±2sr and the PDLR and the PDLR are 0.30±0.01 and 0.26±0.01 respectively (fig. 3).

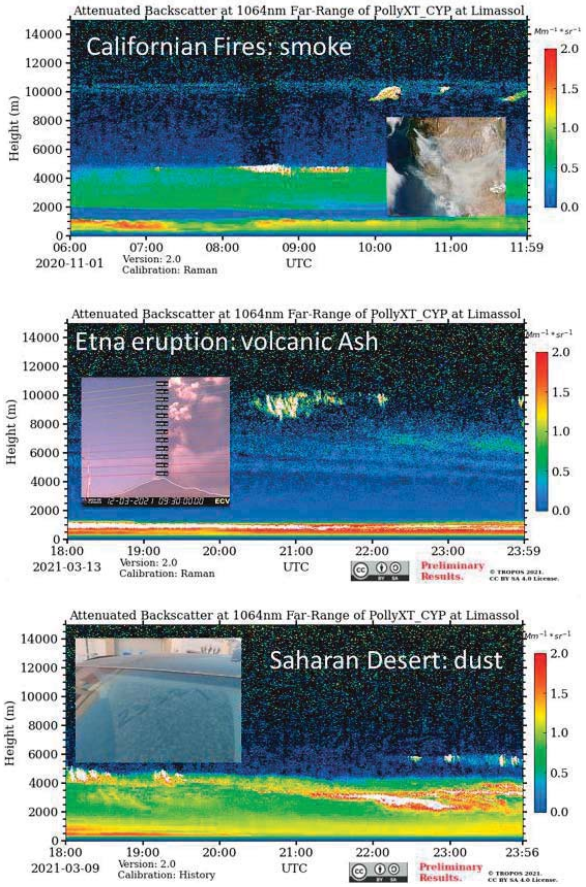

Figure 2. Smoke, Volcanic ash and Saharan dust layers observed over Polly-NET station of Limassol on 1st November 2020, 13th March 2021 and 9th March 2021 respectively. Time-height cross section of the range-corrected 1064 nm backscatter signals (log-scale, a.u.) are shown.

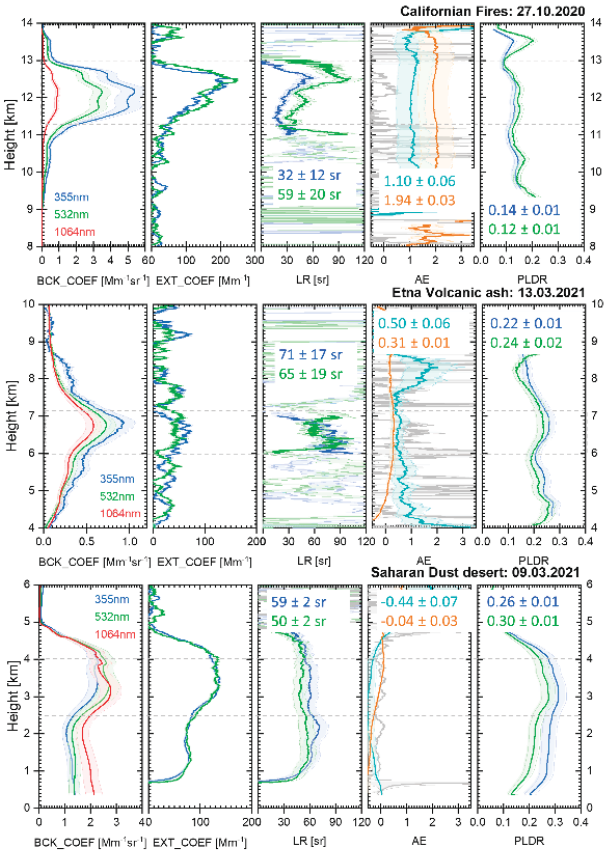

Figure 3. Vertical profiles of aerosol optical properties for California fires (upper panel), Etna volcano ash (middle panel) and Sahara dust desert (lower panel), Limassol, Cyprus, (a) Backscatter coefficient at 532 nm, (b) Extinction coefficient, (c) Lidar ratio, (d) Ångström exponent (e) Particle Depolarization Ratio, the frames identify the aerosol layers

Acknowledgements

The authors acknowledge the EXCELSIOR project that received funding from the European Union [H2020-WIDESPREAD-04-2017:Teaming Phase2] project under grant agreement no. 857510, and from the Republic of Cyprus. CUT team acknowledge the Research and Innovation Foundation of Cyprus for the financial support through the SIROCCO (EXCELLENCE/1216/0217) and AQ-SERVE (INTERGRATED/0916/0016) projects. The PollyXT-CYP was funded by the German Federal Ministry of Education and Research (BMBF) via the PoLiCyTa project.

References

Baars et al., An overview of the first decade of PollyNET: an emerging network of automated Raman-polarization lidars for continuous aerosol profiling, *Atmos. Chem. Phys.*, 16, 5111–5137, 2016.

Engelmann et al., The automated multiwavelength Raman polarization and water-vapor lidar PollyXT: The neXT generation, *Atmos. Meas. Tech.*, 9, 1767-1784

Nisantzi et al., Middle East versus Saharan dust extinction-to-backscatter ratios, *Atmos. Chem. Phys.*, 15, 7071–7084, 2015.

Prata et al., Lidar ratios of stratospheric volcanic ash and sulfate aerosols retrieved from CALIOP measurements, *Atmos. Chem. Phys.*, 17, 8599–8618, 2017.

Aerosol typing over Europe during the COVID-19 campaign: Possible changes in the dominant aerosol types during the lockdown

K.A. Voudouri[1], *D. Nicolae*[2], *L. Mona*[3], *G. D'Amico*[3], *V. Amiridis*[4], *E. Marinou*[4], *A. Gialitaki*[1,4], *A. Kampouri*[4], *A. Tsekeri*[4], *M. Sicard*[5], *A. Rodriguez*[5], *S. Romano*[6], *M. R. Perrone*[6], *A. Floutsi*[7], *X. Shang*[8], *S. Bohlmann*[8,9], *N. Papagiannopoulos*[3], *N. Siomos*[4], *C. Talianu*[2], *I. Stachlewska*[10], *R. Fortuna*[10], *M. Mylonaki*[11], *and D. Balis*[1]
kavoudou@physics.auth.gr
(1) Laboratory of Atmospheric Physics, Physics Department, Aristotle University of Thessaloniki, Thessaloniki, Greece
(2) National Institute of R&D for Optoelectronics (INOE2000), Magurele, Romania
(3) Consiglio Nazionale delle Ricerche, Istituto di Metodologie per l'Analisi Ambientale (CNR-IMAA), Potenza, Italy
(4) National Observatory of Athens ISAARS, Athens, Greece
(5) CommSensLab, Dept. of Signal Theory and Communications, Universitat Politècnica de Catalunya (UPC), Barcelona, Spain
*(6) University of Sale*nto, Physics Department, Lecce, Italy
(7) Leibniz Institute for Tropospheric Research, Leipzig, Germany
(8) Finnish Meteorological Institute (FMI), Kuopio, Finland
(9) Department of Applied Physics, University of Eastern Finland, 70211, Kuopio, Finland
(10) University of Warsaw, Faculty of Physics, Warsaw, Poland
(11) National Technical University of Athens, Physics Department

Introduction

During the first quarter of 2020, the coronavirus disease (COVID-19) spread around the world. The intense respiratory syndrome outbreak severely impacted a number of European countries, leading to fully imposed restrictions of the population movements and strict stay-at-home mandates, starting from March 2020 till end of May 2020. The question about possible changes of the aerosol components during the lockdown period arose, leading to coordinated network activities i.e., an intensive observation campaign during May 2020 (1 - 31 May 2020) organized within the European Aerosol Research Lidar Network (EARLINET), part of the ACTRIS (Aerosols, Clouds and Trace gases Research Infrastructure). The initiative was to study the aerosol type changes in the atmosphere during the COVID-19 lockdown (https://www.earlinet.org/index.php?id=covid-19).
In a community effort, coordinated by CARS and ARES, demonstrated the near-real time capability of the EARLINET-ACTRIS contribution, providing comprehensive information on the atmospheric structure, its dynamics, and its optical properties. The scope of this campaign was primarily to monitor the atmosphere's structure during the lockdown and early relaxation period within European countries and secondly to identify possible changes due to decreased emissions, by comparison with the existing aerosol climatology. The aim of the current work is part of an extended study related to the potential changes of the aerosol load over Europe, due to the COVID-19 lockdown and relaxation period, relative to a reference period (2015-2019).

Methodology – Results from the near-real time campaign in May 2020

The 21 participating EARLINET stations performed measurements at least twice per day (minimum two hours at noon, and minimum two hours after sunset) from 1st of May till 31 of May. These stations are located in regions where a complete or a partial lockdown was imposed.
Out of the 1302 scheduled observations, 693 were performed (53%). In 27% of the cases, measurements could not be performed due to meteorological conditions (rain/very low clouds). Access to the laboratory and lack of personnel made the measurements impossible in 12% of the cases, whilst only 8% of the measurements could not be performed due to technical issues, or instrument setting and check-ups.
All measurements were processed in a centralized way using the Single Calculus Chain [1], with specific configurations and settings, and were made publicly available in the near-real time (NRT). After the closure of the campaign, a re-analysis was made in order to improve the quality of the final products (Level 2), taking into consideration the results of the quality assurance tests and the model reanalysis. The re-analyzed data are publicly available on the EARLINET/ACTRIS database (https://www.earlinet.org/index.php?id=125).
In this paper, the goal is the identification of the predominant aerosol type during the COVID-19 lockdown and relaxation period, from the combination of the mean-intensive optical parameters within an identified layer in the measured aerosol backscatter (β), extinction coefficient profiles (α) and linear particle depolarization ratio (δ). The nighttime 3b+2a+1s were selected to be analyzed and processed with the Neural Network Aerosol Typing Algorithm Based on Lidar Data automatic algorithm –

NATALI [2]. The predominant aerosol type for each detected aerosol layer (in total 223 layers) from the set of multispectral lidar information (e.g., Ångström exponent, color ratios, color indexes, and lidar ratios) was derived. For statistical representativeness of the aerosol content in the lower troposphere over the European continent, the investigation was done at geographical cluster level. Five clusters were identified: (i) Western Mediterranean (WM), (ii) Eastern Mediterranean (EM), (iii) Central Europe (CE), (iv) Eastern Europe (EE) and (v) Northern Europe (NE). Figure 2 shows the pie charts with the predominant aerosol types percentages for each geographical cluster for the period May 2020 for the low troposphere (up to 3 km altitude) (Fig. 1a) and for the upper troposphere (from 3 km up to 7 km) (Fig. 1b) from the NRT campaign results.

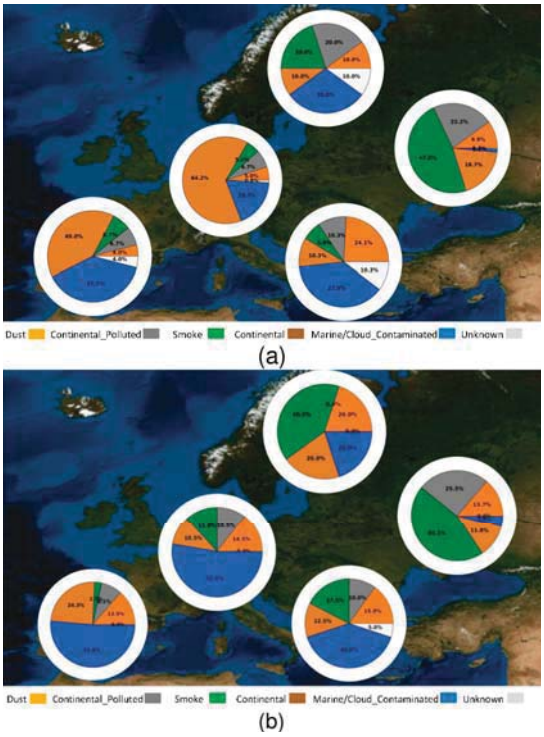

Figure 2. Pie charts with the predominant aerosol types percentages for each geographical cluster for the period May 2020 for the low troposphere (a) and for the upper troposphere (b).

Generally, WM and CE show a prevalence of clean continental aerosols below 3km. Clean continental percentages are also significant for EE and EM. Biomass burning percentages are significant above 3km for most of the geographical clusters. Marine/Cloud Contaminated percentages above 3km are expected to be lower after finalizing the dataset. Note that pollen and dust particles were not separated and are indicated in the same category.

Conclusions – Challenges

The EARLINET community demonstrated it's near-real time capability and the coordinated activity during the COVID-19 lockdown and relaxation period, providing a comprehensive information on the atmospheric structure. This work is the following work of a statistical paper focused on optical and intensive properties for EARLINET products (climatology vs May 2020). The finalized dataset (Level 2) and the layering properties from the above analysis, will be used for the aerosol typing and characterization in this work. Comparison on the predominant types within the period May 2020 with (i) the aerosol types derived the period January - May 2020 and (ii) the aerosol types derived the reference period between 2015 and 2019 (avoiding the inclusion of potential trends in the pollution content on the long term) is planned, with different typing schemes developed within EARLINET [2-3].

Since the restrictive measures were imposed at different time periods within Europe, the effect of the lock-down (if any) has manifested at different times in the different regions. For example, in Eastern Mediterranean lower values of the aerosol backscatter coefficient at 532 nm were observed starting in February, while in Central and Eastern Europe such decrease started in March. The amplitude is also different in various regions, being related to the intensity of the activity that was affected by the lockdown. Thus, the interpretation of the overall aerosol scene should be made in correlation with meteorological conditions, past observations and models.

Acknowledgements

"ACTRIS (www.actris.eu) has received funding from the European Union's Horizon 2020 research and innovation programme under grant agreement numbers: 654109 (ACTRIS-2), 759530 (ACTRIS-PPP), 871115 (ACTRIS-IMP), 824068 (ENVRI-FAIR). KAV acknowledges support by the project "PANhellenic infrastructure for Atmospheric Composition and ClimatE change" (MIS5021516).

References

[1] D'Amico, G., et al., EARLINET Single Calculus Chain – overview on methodology and strategy, Atmos. Meas. Tech., 8, 4891–4916, https://doi.org/10.5194/amt-8-4891-2015, 2015.

[2] Nicolae, D., et al., A neural network aerosol-typing algorithm based on lidar data, Atmos. Chem. Phys., 18, 14511–14537, https://doi.org/10.5194/acp-18-14511-2018, 2018.

[3] Papagiannopoulos, N., et al., An automatic observation-based aerosol typing method for EARLINET, Atmos. Chem. Phys., 18, 15879–15901, https://doi.org/10.5194/acp-18-15879-2018, 2018.

Early seasonal dust intrusions over Central and Eastern Europe observed using ground based lidar systems and satellite products

A. Mereuta[1], *H. Stefanie*[1,2], *C. Botezan*[1], *A. Ozunu*[1], *L. Deaconu*[1], *A. Radovici*[1], *N. Ajtai*[1]
alexandru.mereuta@ubbcluj.ro
(1) Babeș-Bolyai University- Faculty of Environmental Science and Engineering, Fântânele 30, Cluj-Napoca, Romania
(2) Faculty of Physics, University of Warsaw, Pasteura 5, 02-093 Warsaw, Poland

Introduction

In this paper we present case studies regarding desert dust intrusions over Central and Eastern Europe in spring of 2021, observed using a multi-wavelength Raman and depolarization LIDAR system operated in Cluj-Napoca, Romania (Stefanie et al, 2019). This type of system meets the requirements of the European Aerosol Research Lidar Network – EARLINET and is suitable to provide reliable data on optical parameters for aerosol characterization. These findings were supported by Cloud-Aerosol LIDAR Infrared Pathfinder Satellite Observations (CALIPSO) aerosol products.

While mineral aerosols are the second largest source of aerosol and are the subject of long range transport, their observations are of utmost importance for improving the understanding of climate, weather, particle transport and air quality. Other studies focusing on dust intrusions over the territory of Romania have been published in the past years (Cazacu et al., 2016) however these studies were limited to southern and eastern part of the country. Recent studies such as (Ajtai et al., 2020) suggest a cyclical pattern of Saharan dust intrusions in the first quarter of the year. The first episode presented in this study was observed earlier than the previous years, as early as February. The second episode of dust intrusion was observed in early April.

Instruments and method

We analyzed data measured in Cluj-Napoca, Romania using a series of ground based remote sensing instruments like multi-wavelength Raman depolarization lidar, part of the EARLINET and a sun-photometer, part of the Aerosol Robotic Network (AERONET). Currently, the two networks are part of the Aerosols, Clouds, and Trace gases Research InfraStructure (ACTRIS).

The Cluj-Napoca ACTRIS station is considered representative for the whole Transylvanian territory and also for the Pannonia basin given the limited coverage of AERONET and EARLINET in Hungary, Austria and south-western Ukraine. Ground-based observations from research sites located in Slovakia and Poland were also used to determine and better characterize the optical and microphysical properties of the same Saharan dust outbreak. Besides the ground based instruments, remote sensing data from Moderate Resolution Imaging Spectroradiometer (MODIS) sensors on Terra and Aqua satellites were used in this analysis. CALIPSO aerosol data was used for feature detection and layer height estimations while also aiding in aerosol typing.

In order to estimate the source of the long-range transported aerosol we used the Hybrid Single-Particle Lagrangian Integrated Trajectory (HYSPLIT) and Barcelona Supercomputing Center (BSC DREAM) models.

Results

Preliminary results processed using Single Calculus Chain (SCC) (D'Amico et al., 2015) indicate the presence of dust particles in the upper troposphere (between 5500 – 8000 m) as seen in Figure 1.

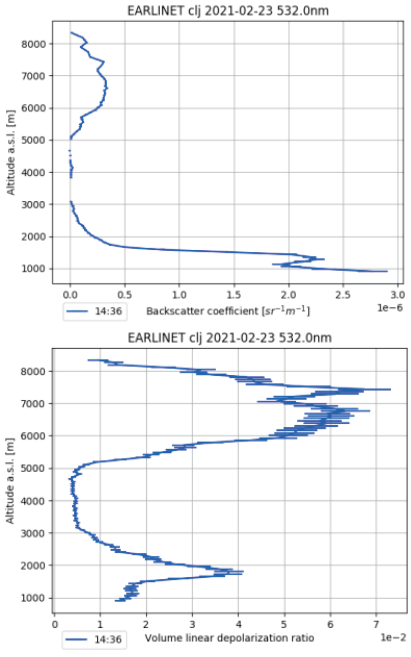

Figure 1. Backscatter coefficient and volume depolarization ratio at 532nm from Cluj Napoca lidar system (CLOP) on February 23rd, 2021, processed using Single Calculus Chain (SCC)

This dust layer was detected at higher altitudes in comparison with the CALIPSO observations due to different sampling time intervals and slight collocation mismatch, as suggested in figure 2.

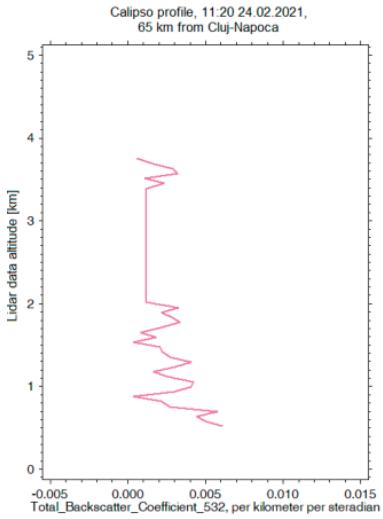

Figure 2. Backscatter coefficient at 532nm from CALIPSO on February 24rd, 2021, at 65 km from Cluj-Napoca

The HYSPLIT modelled data is in good agreement with the MODIS observations, displaying the dust intrusion, with saharan desert origin, in a recognizable trajectory circulating over the Eastern parts of Europe, as shown in Figure 3.

The results, based on the synergy of multiple ground-based and satellite sensors, confirmed the presence of a Saharan dust intrusion over the mentioned area.

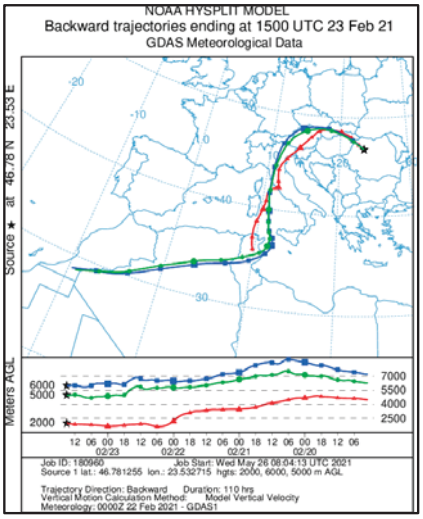

Figure 3. HYSPLIT backwards trajectories model depicting the possible origin of dust particles in the upper atmospheric layers

Acknowledgements

This work was supported by the Project entitled "Development of ACTRIS-UBB infrastructure with the aim of contributing to pan-European research on atmospheric composition and climate change" SMIS CODE 126436, co-financed by the European Union through the Competitiveness Operational Programme 2014 – 2020.

Financed by European Regional Development Fund through Competitiveness Operational Programme 2014-2020, Action 1.1.3 Creating synergies with H2020 Programme, project Strengthen the participation of the ACTRIS-RO consortium in the pan-European research infrastructure ACTRIS, MYSMIS code 107596.

The authors gratefully acknowledge the NOAA Air Resources Laboratory (ARL) for the provision of the HYSPLIT transport and dispersion model and READY website (http://www.ready.noaa.gov) used in this publication.

Images from the BSC DREAM8b-Dust model, operated by the Barcelona Supercomputing Center (http://www.bsc.es/ess/bsc-dust-daily-forecast/) were used in this study.

Satellite aerosol products from MODIS (http://dx.doi.org/10.5067/MODIS/MOD04_L2.006) and CALIPSO (https://doi.org/10.5067/CALIOP/CALIPSO/CAL_LID_L2_05kmAPro-Standard-V4-21) were used in this study.

References

Stefanie H et al., Assessing the Long Term Stability of the Depolarization Constant for the Cluj Station, 29TH International Laser Radar Conference (ILRC 29), EPJ Web of Conferences, Vol. 237, 08006, 2020.

Marius Cazacu et al., A case study of the behavior of aerosol optical properties under the incidence of a saharan dust intrusion event, Applied Ecology and Environmental Research, 14, 3, 183-194, 2016.

Nicolae Ajtai et al., Multi-Sensor Observation of a Saharan Dust Outbreak over Transylvania, Romania in April 2019, Atmosphere, 11 (4), 364, 2020.

D'Amico, G., Amodeo, A., Baars, H., Binietoglou, I., Freudenthaler, V., Mattis, I., Wandinger, U., and Pappalardo, G.: EARLINET Single Calculus Chain – overview on methodology and strategy, Atmos. Meas. Tech., 8, 4891-4916, doi:10.5194/amt-8-4891-2015, 2015

Aerosol vertical hygroscopic growth from multi-wavelength lidar measurements in Barcelona, NE Spain: a spectral analysis

***D.C.F.S Oliveira*[1]**, *C. Muñoz-Porcar*[1], *A. Comerón*[1], *A. Rodríguez-Gómez*[1], *M. Sicard*[1,2]

daniel.camilo.fortunato@upc.edu
(1) CommSensLab, Dept. of Signal Theory and Communications, Universitat Politècnica de Catalunya (UPC), 08034-Barcelona, Spain
(2) Ciències i Tecnologies de l'Espai-Centre de Recerca de l'Aeronàutica i de l'Espai/Institut d'Estudis Espacials de Catalunya (CTE-CRAE/IEEC), Universitat Politècnica de Catalunya (UPC), 08034-Barcelona, Spain

Introduction

Atmospheric aerosols and water vapor are important components of the Earth's atmosphere and can affect Earth's energy balance by means of direct, semi-direct, and indirect effects. Some of these effects are a consequence of the increase in aerosol size by the water uptake, hence, modifying also their optical properties (Hänel, 1976) (Granados-Muñoz et al., 2015). This growth process is called hygroscopic growth (Hänel, 1976).

The enhancement factor is an aerosol response to the hygroscopic growth (Carrico et al., 2013). In this study, it is calculated for the particle backscatter coefficient, β_{aer}, retrieved with a multi-wavelength lidar system in a coastal, humid area (Barcelona, Spain), and so-called particle backscatter coefficient enhancement factor, f_β, and calculated by the following equation:

$$f_\beta(RH) = \beta(RH)/\beta(RH_{min}) \quad (1)$$

where β increases from a reference relative humidity, RH_{min}, to RH in the analyzed layer.

To identify the hygroscopic growth cases, the first criterion of our methodology was analyzing a simultaneous increase between the profiles of β derived from lidar together with profiles of relative humidity from radiosoundings. These profiles were treated as potential cases of hygroscopic growth. After that, a series of conditions were applied on the profiles such as monotonicity of the profiles, potential temperature (± 2º K), wind speed (± 2 m/s), wind direction (15 deg.), water vapor mixing ratio (± 1 g/kg) that are indicative of a well-mixed condition inside the layer. Such criteria have been applied by other authors (Granados-Muñoz et al., 2015; Navas-Guzman et al., 2019). Back trajectories are also used to check whether the aerosols are of the same type, that means, the base and top of the layers have the same origin. Subsequently, the potential cases were selected as hygroscopic growth at three wavelengths (355, 532, and 1064 nm).

The database consists of measurements made between 2010 and 2018 with the Barcelona European Aerosol Lidar Network (EARLINET) lidar. Then, the Hänel parametrization (Hänel, 1976) was chosen and applied to obtain the indicator of the hygroscopicity, γ. The particle backscatter enhancement factor chosen here as f_β (RH = 85%) to compare with other studies, forcing all cases to RH_{ref} = 40%, i.e., f_β (RH = 40%) =1 in order to homogenize the relationship for all cases.

$$f_\beta(RH_{ref}) = f_\beta(RH_{min})((1-RH_{min}/100)/(1-RH_{ref}/100))^{-\gamma} \quad (2)$$

Note that the term on the right-hand side multiplying f_β (RH_{min}) allows to convert f_β (RH_{min}) into f_β (RH_{ref}).

Results and discussion

Figure 1 shows the resulting spectral Hänel fits and enhancement factors at 355, 532, and 1064 nm. They are those scaled in order to start at RH_{ref}=40%. In all those plots the Hänel fits are calculated considering all points. The spectral values of f_β (RH = 85%) and γ are summed up in Tab. 1 which also includes the correlation coefficient of the Hänel fit. The particle backscatter coefficient enhancement factor has a clear spectral behavior, f_β (RH = 85%) (γ) is 3.08 (0.73 ± 0.05), 2.65 (0.69 ± 0.03) and 2.00 (0.49 ± 0.03) at 355, 532 and 1064 nm, respectively. This singular behavior implies that the water uptake by the particles modifies the particle backscatter coefficient more strongly at shorter wavelengths than at larger wavelengths, suggesting a stronger increase in backscattered radiation at shorter wavelengths when RH increases for small particles, and it was reported by Navas-Guzmán et al. (2019) and Pérez-Ramírez et al. (2021). Based on these hygroscopic characteristics, Navas-Guzmán et al. (2019) classified the aerosols as a mixture of rural aerosol and smoke particles. Despite their aerosols are less hygroscopic than ours, low f_β and γ values, Pérez-Ramírez et al. (2021) explained the large effect of aerosol hygroscopicity on aerosol properties by the aerosol total mass in which sulfate and water-soluble organic are the hydrophilic predominant species. Qualitatively and in order to demonstrate the

influence of marine aerosol in Barcelona as well, we compared our results with the following studies, Granados-Muñoz et al. (2015) found f_β(RH=80%)=3.0 ± 1.0 and f_β(RH=85%)=3.9 ± 1.5 at 532 nm, Titos at al. (2014) which values of f_β(RH=80%) are from 1.4 to 3.4 with influence of marine aerosol, and our results also agree with Haarig et al. (2017) that found f_β(RH=80%)=3.01 at 355 nm. It is important to mention that the results of Haarig et al. (2017) have a different spectral dependence when analyzing the other wavelengths, i.e. shorter wavelengths are less hygroscopic than larger ones, however we have only compared 355 nm.

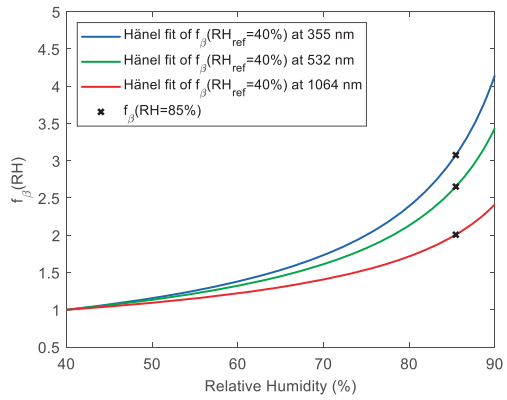

Figure 1. Particle backscatter coefficient enhancement factors with RH_{ref}=40% and Hänel fits by Eq. (4) at 355, 532, and 1064 nm. Blue, green, and red curves correspond to f_{355}, f_{532}, and f_{1064}, respectively. Black Xs are f_β (RH = 85%) at each wavelength.

Table 1. The outputs from Hänel parametrization calculated by Eq. (4), and their statistical parameters

λ	f_β (RH = 85%)	γ ± σ	R^2
355	3.08	0.73±0.05	0.57
532	2.65	0.69±0.03	0.74
1064	2.00	0.49±0.03	0.61

The analysis of back trajectories modelled by HYSPLIT model (Stein et al. 2015) confirmed that more than half of the air mass origins come from continental zones followed by the Atlantic and Mediterranean contribution, and there are three episodes of dust with origins from Sahara. In agreement with the air masses, the wind directions coming most often between north-northwest and south-southwest, Spain inland, blowing stronger from west. There is also a contribution between northeast and east-northeast directions, Mediterranean influence.

The hygroscopic growth cases in Barcelona have higher values of f_β and γ for shorter wavelengths. This singular behavior is attributed to small particles from a mixture of continental and polluted aerosol with a slightly contribution of marine aerosol and mineral dust. These aerosol types agree with the aerosol sources from air masses and wind directions.

Acknowledgements
We thank EARLINET network, Universitat Politècnica de Catalunya, and the Meteorological Service of Catalonia, Meteocat for the radiosoundings.

References

Carrico et al., Mixtures of pollution, dust, sea salt, and volcanic aerosol during ACE-Asia: Radiative properties as a function of relative humidity, *J. Geophys. Res.*, 108, NO. D23, 8650, 2003.

Granados-Muñoz et al., Hygroscopic growth of atmospheric aerosol particles based on active remote sensing and radiosounding measurements: selected cases in southeastern Spain, *Atmos. Meas. Tech.*, 8, 705–718, 2015.

Haarig et al., Dry versus wet marine particle optical properties: RH dependence of depolarization ratio, backscatter, and extinction from multiwavelength lidar measurements during SALTRACE, *Atmos. Chem. Phys.*, 17, 14199–14217, 2017.

Hänel. The properties of atmospheric aerosol particles as functions of the relative humidity at thermodynamic equilibrium with the surrounding moist air, in: Advances in Geophysics, edited by: Landsberg, H. E. and Mieghem, J. V., 73–188, *Elsevier*, 1976.

Navas-Guzmán et al., Characterization of aerosol hygroscopicity using Raman lidar measurements at the EARLINET station of Payerne, *Atmos. Chem. Phys.*, 19, 11651–11668, 2019.

Pérez-Ramírez et al., Spatiotemporal changes in aerosol properties by hygroscopic growth and impacts on radiative forcing and heating rates during DISCOVER-AQ 2011, *Atmos. Chem. Phys.*, 2021.

Stein et al., NOAA's HYSPLIT atmospheric transport and dispersion modeling system. *Am. Meteorol Soc.*, 96 (12), 2059–2077, 2015.

Titos et al., Aerosol light-scattering enhancement due to water uptake during the TCAP campaign, Atmos. Chem. Phys., 14, 7031–7043, 2014.

Aerosol typing from remote sensing techniques and in situ data over Thessaloniki, Greece

K.A. Voudouri[1], N. Siomos[1,2], K. Michailidis[1], A. Chatzopoulou[1], A. Natsis[1], I. Fountoulakis[1,3], A. Karanikolas[4], G. Kouvarakis[5], K. Garane[1], A. Bais[1] and D. Balis[1]*
kavoudou@physics.auth.gr
(1) Laboratory of atmospheric physics, Physics Department, Aristotle University of Thessaloniki, Greece
(2) IAASARS, National Observatory of Athens, Athens, Greece
(3) Aosta Valley Regional Environmental Protection Agency (ARPA), 11020 Saint-Christophe, Italy
(4) Physikalisch-Meteorologisches Observatorium Davos, (PMOD/WRC) Dorfstrasse 33, 7260 Davos Dorf, Switzerland
(5) Environmental Chemical Processes Laboratory, Department of Chemistry, University of Crete, P.O. Box 2208, 71003, Voutes, Heraklion, Greece

Introduction

Operational monitoring of aerosol properties are performed routinely at the Laboratory of Atmospheric Physics (LAP) in Thessaloniki (40.63°, 22.95°, 60m asl), Greece. A combination of different ground-based instruments are measuring including both a single and double Brewer spectrophotometer, a multiwavelength depolarization Raman Lidar, and a CIMEL photometer, among others. During the two PANACEA campaigns (PANhellenic infrastructure for Atmospheric Composition and climatE chAnge, https://panacea-ri.gr/), LAP was further equipped with in situ instruments, including an Aethalometer, a GRIMM, a PurpleAir sensor and a TE-1000 PUF Poly-Urethane Foam High Volume Air Sampler and a Leckel Sampler (Figure 1). Taking advantage of the multispectral information and the high temporal and vertical resolution acquired with all the instrumentation, synergetic techniques that deploy spectrophotometer data, lidar data and sunphotometer data are applied, in order to provide the characterization of the aerosol load over Thessaloniki, including the aerosol typing. The results are analyzed along with the in-situ observations for the common measuring period.

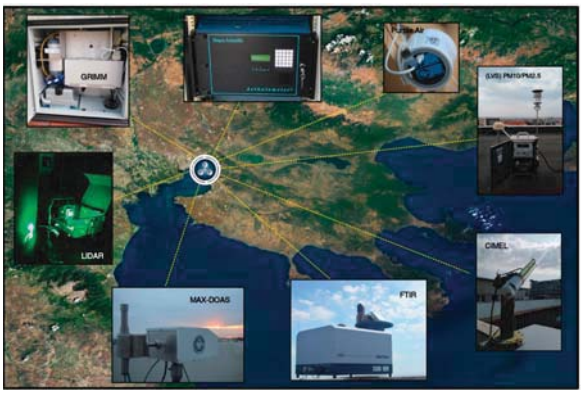

Figure 1. Instrumentation deployed routinely and during the two PANACEA campaigns in Thessaloniki station.

Methodology and Results

The aerosol typing technique used in this study, is based on the Mahalanobis distance metric [1], a common approach in cluster analysis. This metric has already been applied for the classification of columnar aerosol data acquired by sunphotometers and spectrophotometer [2], and of aerosol layers derived by lidar systems, based on the lidar-derived aerosol-intensive properties [3]. By providing a training dataset that consists of pre-classified lidar/Brewer cases, any case can be assigned to one of these clusters based on a number of threshold criteria applied. Full description of the above procedure can be found in [2, 3].

The identification of the most probable aerosol type from the lidar measurements is made using a combination of mean-layer-intensive optical parameters (i.e., lidar ratio at 532nm, backscatter Ångström exponent at 355/1064, ratio of lidar ratios) from the provided aerosol backscatter and extinction coefficient profiles. From the lidar analysis, four main aerosol types have been discriminated corresponding to: (i) large particles with medium lidar ratios (Dust), (ii) large particles with low lidar ratios (i.e., Maritime), (iii) small particles with high lidar ratios (PollutedSmoke - PSmoke) and (iv) small particles with medium lidar ratios (i.e., Clean Continental - Ccontinental).

Whilst the identification of the aerosol type in individual layers is possible with lidars, this is not the case for spectrophotometric measurements that see the whole atmospheric column. However, the predominant aerosol type in the whole column can be derived. The selected intensive aerosol optical properties for typing from the Brewer spectrophotometer, are the Extinction Ångström Exponent at 320/360 nm and the Single Scattering Albedo at 340 nm. By applying the Mahalanobis distance algorithm to the Brewer timeseries, measurements were automatically assigned in one of the following clusters: Fine Non Absorbing Mixtures (FNA), Black Carbon Mixtures (BC), Dust Mixtures (DUST) and Mixed type aerosols.

The aerosol typing from the columnar analysis,

showed that the FNA cluster is encountered far more often (87.5%) in Thessaloniki, during the summer campaign (10 July to 10 August, 2019). The BC cluster comes next with occurrence ratio 6.2%, followed by Dust (3.1%) and Mixtures (3.1%). During the winter period (10 January to 10 February, 2020), the occurrence ratio of BC particles is generally higher (50%), probably associated with the increased emissions from domestic heating. The prevalence of the black carbon (BC) dominated particles is in agreement with the Aethalometer and the lidar observations, where the biomass burning particles have occurrence ratio of 54%. From the other hand, pure dust cases are the most rare (4.5%) since mixing with urban particles usually takes place, while FNA and Mixtures correspond to 27.3% and 18.2% respectively.

The majority of the detected layers from the lidar system during the summer campaign are attributed to biomass burning aerosols (Smoke category, highly absorbing particles) from remote sources (e.g. wildfires and agricultural fires). Dust particles come next with occurrence ratio 36%, followed by Clean Continental particles (14%). The biomass burning category is the most predominant one during the winter campaign, mainly attributed to the increasing use of wood.

Generally, the biomass burning aerosols are also confirmed by the high percentage of wood burning particles measured by the Aethalometer (>15%), while the Clean Continental category is linked to lower percentages.

Figure 2 presents the common observations typed from the lidar system and the BREWER during the PANACEA summer campaign. The lidar profiles were typed per observed layer, whilst typing from Brewer corresponds to the total column. The typing scores (per cent) are calculated with respect to the total number of cases.

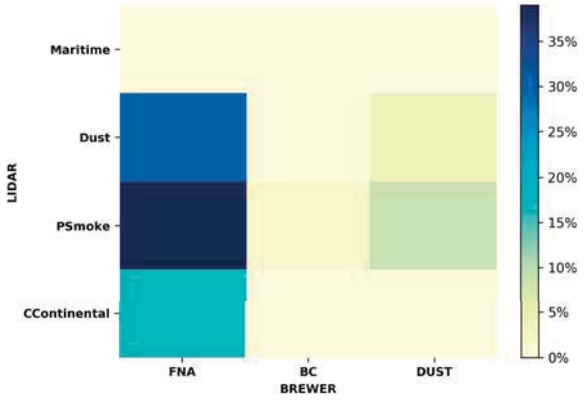

Figure 2. Percentages of matches per aerosol type derived by BREWER (x-axis) and LIDAR measurements (y-axis) for the common days of measurement during the summer PANACEA campaign (23 layers).

Figure 2 shows that, FNA cases from BREWER tend to correspond to PSmoke and DUST layers typed from lidar. Generally, isolating FNA cases (FNA columnar cluster) is quite challenging as black carbon can still be present to a certain degree in continental profiles. It is worthwhile mentioning that the particle linear depolarization ratio could effectively discriminate spherical and non-spherical particles. However, this quantity was not available in the aerosol typing presented here.

Conclusions

This is the first time that a number of collocated in situ and remote sensing instruments are deployed in Thessaloniki. In this work we identified the shortcomings of columnar instruments to provide aerosol typing especially when aerosol layers of different origin and type are observed with a collocated lidar instrument. This aerosol typing will be further analyzed and discussed, taking into account the intensive and extensive aerosol optical properties from the lidar determined aerosol layers. Thessaloniki is a coastal metropolitan area, with urban aerosols affecting the lower layers and desert dust and biomass burning particles transported from remote sources (and affecting mainly higher layers in the troposphere). In situ measurements, show that BC is linked mainly to traffic, while the domestic wood burning percentages to the total BC are higher during the winter period.

Acknowledgements

We acknowledge support of this work by the project “PANhellenic infrastructure for Atmospheric Composition and ClimatE change” (MIS5021516) which is implemented under the Action “Reinforcement of the Research and Innovation Infrastructure”, funded by the Operational Programme "Competitiveness, Entrepreneurship and Innovation" (NSRF 2014-2020) and co-financed by Greece and the European Union (European Regional Development Fund). This project has received funding from the European Union’s Horizon 2020 research and innovation programme under grant agreement No 654109.

References

[1] Mahalanobis, P.C. On the Generalized Distance in Statistics; National Institute of Science of India: Odisha, India, 1936; Volume 12, pp. 49–55.

[2] Siomos, N., et. al., Automated Aerosol Classification from Spectral UV Measurements Using Machine Learning Clustering. Remote Sens., 12, 965, 2020.

[3] Papagiannopoulos, N., et al., An automatic observation-based aerosol typing method for EARLINET, Atmos. Chem. Phys., 18, 15879–15901, https://doi.org/10.5194/acp-18-15879-2018, 2018.

Synoptic Environment Associated With a Large Wildfire and a Dust Outbreak Affecting Portugal

***Flavio T. Couto*[1,2]**, *Vanda Salgueiro*[1,2], *Nuno Andrade*[4], *Maria J. Costa*[1,2,3], *Rui Salgado*[1,2,3], *Daniele Bortoli*[1,2,3], *Juan L. Guerrero-Rascado*[5]
fcouto@uevora.pt
(1) Instituto de Ciências da Terra – ICT (Polo de Évora), Universidade de Évora, Évora, Portugal
(2) Earth Remote Sensing Laboratory (EaRS Lab), Universidade de Évora, Évora, Portugal
(3) Departamento de Física, Escola de Ciências e Tecnologia, Universidade de Évora, Évora, Portugal
(4) Escola de Ciências Sociais, Universidade de Évora, Évora, Portugal
(5) Instituto de Investigación del Sistema Tierra en Andalucía (IISTA-CEAMA). Universidad de Granada, Departamento de Física Aplicada, Granada, Spain

Introduction

In the last decades, the atmospheric models have achieved a high degree of sophistication and realism, and are powerful tools to examine the physical and dynamic mechanisms involved in the development of extreme atmospheric phenomena. The Meso-NH (Lac et al., 2018) is one of these models and it is used in the study. It is implemented with a rather complete parametrization package of sub-grid scale physical processes in the atmosphere, such as convection, cloud microphysics, cloud electricity, turbulence, surface processes, among others. In Portugal, it has been successfully used in several research fields, in particular in the understanding of fire weather conditions (Couto et al., 2020, 2021a) and dynamics of dust outbreaks (Couto et al., 2021b). However, forecasting the atmospheric conditions associated with large wildfires and dust outbreaks is still an operational problem worldwide.

The present study concentrates on the efforts to understand the meteorological environments that favour the evolution of significantly large wildfires, namely in the context of the Iberian Centre for Research and Forest Firefighting (CILIFO, www.cilifo.eu). Moreover, the main factors associated with a desert dust outbreak that occurred in the same period are also examined.

Methodology

The observations available from the Cloud-Aerosol LIdar with Orthogonal Polarization (CALIOP), a space-borne two-wavelength polarization lidar on board CALIPSO satellite are used. The CALIPSO's orbit track was identified crossing the Southern Portugal on 7th August 2018, where the Monchique wildfires burned an area of about 27000 ha. Figure 1a shows the presence of a forest fire smoke layer in southern Portugal, below 2 km altitude, and mineral dust southward extending up to the middle troposphere. Such a lidar observation was crucial for the development of the study by confirming the presence of the different types of aerosols.

Furthermore, the dust episode is also identified through the satellite observation on 2nd August 2018 (Figure 1b). The AERONET aerosol columnar properties measured at the ACTRIS Évora (38.5ºN, 7.91ºW, 293 m above sea level) confirmed the dust outbreak in early August (not shown) and helped to design the numerical experiment.

In order to explore the large mesoscale environment associated with the dust episode and the fire weather in Southern Portugal, the Meso-NH model was configured in a single domain at 10 km horizontal resolution and 270×360 grid points (Figure 1c). The vertical grid was configured with 50 stretched levels following the terrain. The simulation was initialized and forced with the European Centre for Medium-Range Weather Forecasts (ECMWF) analysis, updated every 6 hours. The physical configuration is quite similar to those used by Couto et al. (2021b), with dust emission computed using the Dust Entrainment And Deposition – DEAD model, which was incorporated in SURFEX and modified to better account for the size distribution of erodible material. On the other hand, the interactions between the wildfire and the atmosphere were not taken into account in the simulation. The experiment started on 28th July 2018 at 0000 UTC and finished at 0000 UTC on August 10, 2018.

Results and discussion

The Monchique wildfire started on 3rd August and burned up to August 10, 2018. In the first day of the episode, the model simulated air temperature values above 35ºC, relative humidity below 20 %, and wind gusts around 10 m/s (not shown), factors that favoured wildfire occurrence and propagation.

The simulation that included dust emission allowed to understand how the atmospheric dynamics affects the mobilization of Saharan dust and its transport outward from North Africa. The simulation showed that the dust observed in Évora

had origin over the Sahara Desert and was mobilized in late July. The dust transport was favoured by the circulation at around 2 km altitude from the western side of the Atlas Mountains and over the Atlantic Ocean (Figure 1c). The simulation is qualitatively in good agreement with the satellite observation (Figure 1b).

Observational and numerical approaches have been extensively used to study extreme events. Here, a wildfire event and a dust outbreak were selected and analysed thanks to the lidar observations and numerical simulations. The present study is ongoing, but already demonstrates the importance of the use of atmospheric models to complement the observations in order to better understand large scale atmospheric processes behind them. Remote sensing was used as a baseline for detecting the wildfire smoke in Southern Portugal and dust outbreak. The next steps of the study include exploring the main characteristics of the smoke and dust identified by the lidar, as well as validating the model results.

Challenges

The scientific challenges are also related to better represent this event numerically, improving the simulation, aiming to explore and understand the interactions of smoke and dust and their effects in the atmosphere.

Acknowledgements

This research was funded by the European Union through the European Regional Development Fund in the framework of the Interreg V A Spain – Portugal program (POCTEP) through the CILIFO project (Ref.: 0753_CILIFO_5_E), FIREPOCTEP project (0756_FIREPOCTEP_6_E), and also by national funds through FCT - Foundation for Science and Technology, I.P. under the PyroC.pt project (Refs. PCIF/MPG/0175/2019), ICT project (Refs. UIDB/04683/2020 and UIDP/04683/2020), and TOMAQAPA (PTDC/CTAMET/ 29678/2017).

References

Couto et al., Lightning modelling for the research of forest fire ignition in Portugal. *Atmos. Res*. 242, 104993, 2020.

Couto et al., Forest fires in Madeira island and the fire weather created by orographic effects. *Atmosphere*, 12, 827. 2021a.

Couto et al., How a mesoscale cyclonic vortex over Sahara leads to a dust outbreak in South-western Iberia, *Atmos Res*, 249:1–13.2021b.

Lac et al., Overview of the Meso-NH model version 5.4 and its applications. *Geosci. Model Dev.*, 11, 1929-1969. 2018.

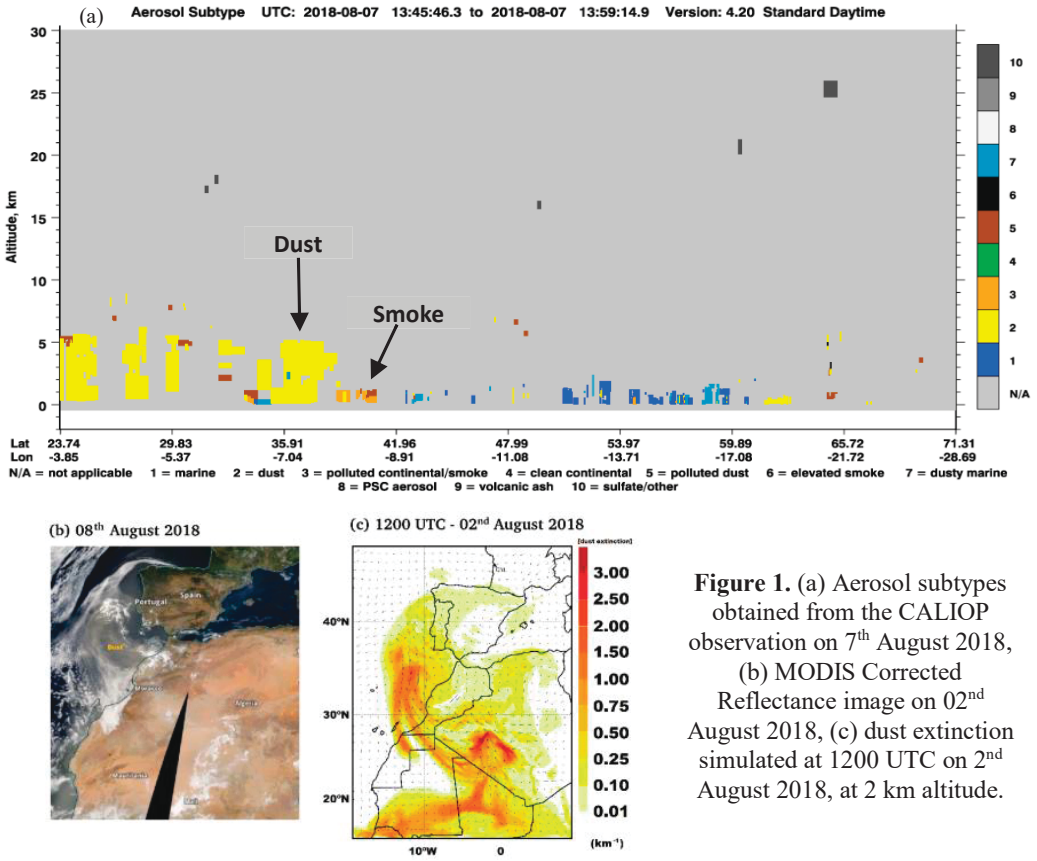

Figure 1. (a) Aerosol subtypes obtained from the CALIOP observation on 7th August 2018, (b) MODIS Corrected Reflectance image on 02nd August 2018, (c) dust extinction simulated at 1200 UTC on 2nd August 2018, at 2 km altitude.

Radiative forcing of marine and dust aerosols over the Eastern Mediterranean

M. Tsichla[1,2*], *A. Tsekeri*[1], *V. Amiridis*[1], *A. Nersesian*[3,1], *S. Kazadzis*[4], *A. Gialitaki*[1,5], *E. Marinou*[1,5], *I. Tsikoudi*[1,6], *N. Kalivitis*[2], *and N. Mihalopoulos*[2,7]

[1]*Institute for Astronomy, Astrophysics, Space Applications and Remote Sensing, National Observatory of Athens, Greece*
[2]*Environmental Chemical Processes Laboratory, Department of Chemistry, University of Crete, Greece*
[3]*Sterrenkundig Observatorium Universiteit Gent, Belgium*
[4]*Physikalisch-Meteorologisches Observatorium Davos and World Radiation Center PMOD/WRC*
[5]*Laboratory of Atmospheric Physics, Aristotle University of Thessaloniki, Thessaloniki, Greece*
[6]*Department of Environmental Physics and Meteorology, University of Athens, Athens Greece*
[7]*Institute for Environmental Research & Sustainable Development, National Observatory of Athens, Greece*

*Contact: *mtsichla@noa.gr*

Introduction

Marine and dust aerosols are two of the most abundant types of natural aerosols in the atmosphere. They interact with light either by scattering or absorption, leading to changes in the Earth-Atmosphere radiative balance. This is important to investigate in order to quantify the contribution of natural aerosols to their total (natural & anthropogenic) radiative forcing and its climate implications. Many related studies have been conducted (Kok et al., 2017; Gutleben et al., 2020) in order to understand whether these aerosols have warming or cooling efects on the planet.

Methodology and Data

In this study, radiative transfer simulations are performed with the vector radiative transfer code "Monte carlo code for the phYSically correct Tracing of photons In Cloudy atmospheres" (MYSTIC), (Mayer and Kylling, 2005). MYSTIC simulates the photon's random path through the atmosphere and calculates the spectral irradiances and the polarization of the light at any given height, along with the heating rates associated with its absorption.

The optical properties of the aerosol particles that are used as input to MYSTIC are provided by the sun-photometer and lidar measurements at the Panhellenic Observatory of Antikythera (PANGEA) of the National Observatory of Athens (NOA). The CIMEL sun-photometer is part of the Aerosol Robotic Network (AERONET) and the Polly^{XT} lidar of NOA is part of the European Aerosol Research Lidar Network (EARLINET). The sun-photometer provides products of the size distribution and refractive index, which are used to derive the optical properties of the marine and dust particles, using the "Modeled optical properties of ensembles of aerosol particles" scattering database (MOPSMAP),(Gasteiger and Wiegner, 2018). The lidar measurements provide the profile of the aerosol extinction coefficient. In order to separate the marine and dust components we used the "polarization-lidar photometer networking (POLIPHON) method" (Mamouri and Ansmann, 2017). Moreover, the concentration profiles of the dust and marine particles can be provided by the combination of the sun-photometer and lidar measurements, using the Lidar-Radiometer Inversion Code (LIRIC) algorithm (Chaikovskii et al, 2016, Tsekeri at el., 2017).

For this work we use measurements of dust and marine particles above the PANGEA observatory during the summer of 2020. Figure 1 shows an example, with marine and dust aerosols. The source of the particles in the atmospheric column is investigated with air mass back-trajectory analysis (Fig. 1).

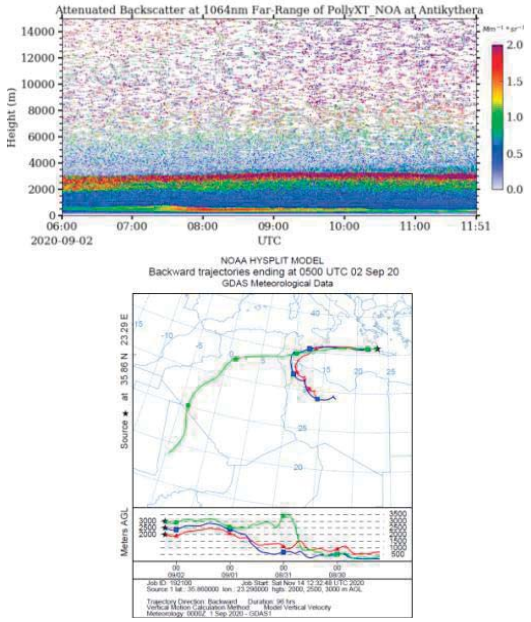

Figure 1. (top-panel) Attenuated backscatter at 1064 nm from PANGEA Polly-XT lidar measurements, at 6:00-12:00 UTC, on 2 September 2020. (bottom-panel) 96-

hour backward trajectories ending at PANGEA observatory, at 5:00 UTC, on 2 September 2020.

Results

Spectral (Fig.2) and integrated irradiances and heating rates (Fig.3) are calculated in order to quantify the impact of the marine and dust particles to the atmospheric equilibrium in the PANGEA observatory, at a region which is representative of the eastern Mediterranean. The figures below indicate that dust particles for example, absorb the solar radiation causing heating in the atmosphere.

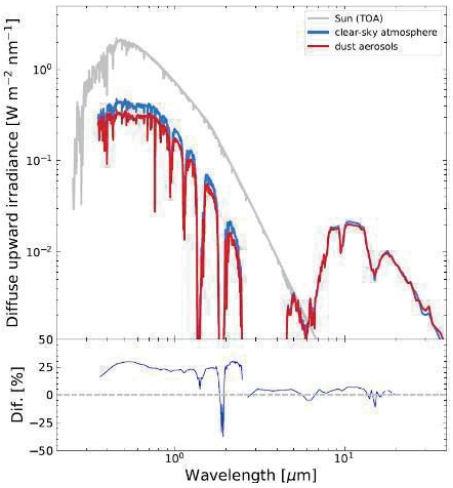

Figure 2. (top-panel) Diffuse upward spectral irradiance calculated at the top of the atmosphere for clear-sky (blue line) and dust aerosol conditions (red line). (bottom-panel) Percentage difference of clear minus dust aerosol MYSTIC spectra.

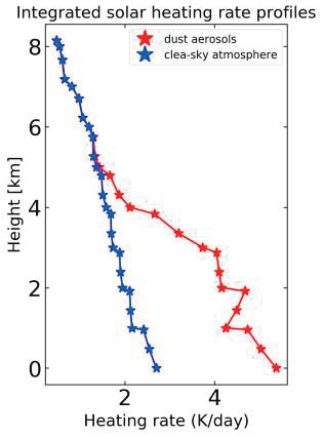

Figure 3. Integrated solar heating rate profiles of clear-sky (black line) and dust aerosol conditions (green line).

Challenges

The challenges of this work include the derivation of the optical and microphysical properties for the marine and dust particles in the environment of the PANGEA observatory, where these components co-exist. As described extensively in Tsekeri et al. (2017), this is not an easy task, mainly due to their similar sizes for their larger particles.

Moreover, the calculation of the optical properties of the dust particles is an ongoing research, with many challenging aspects, as for example the irregular shape and size of the dust particles (e.g. Gasteiger et al., 2011). In our work, we use the spheroidal shape for the particles, used in the MOPSMAP scattering database for the size range considered. This aerosol shape assumption can introduce uncertainties, related especially with the reproduction of the backscattered light measured by the lidar instrument.

Acknowledgements

This research was supported by data and services obtained from the PANhellenic GEophysical Observatory of Antikythera (PANGEA) of the National Observatory of Athens (NOA). We acknowledge support of this work by the ERC D-TECT project (Grant Agreement 725698), the project "PANhellenic infrastructure for Atmospheric Composition and climatE change" (MIS 5021516), the Stavros Niarchos Foundation and the "National Network on Climate Change and its Impacts (CLIMPACT)" which is funded by the Public Investment Program of Greece, General Secretary of Research and Technology/Ministry of Development and Investments.

References

Chaikovsky, A., et al, *Atmos. Meas. Tech*., 9, 1181–1205, https://doi.org/10.5194/amt-9-1181-2016, 2016.

Gasteiger, J., et al., Tellus B, 63, 725–741, https://doi.org/10.1111/j.1600-0889.2011.00559.x, 2011.

Gasteiger, J. and Wiegner, M., *Geosci. Model Dev*., 11, 2739–2762, https://doi.org/10.5194/gmd-11-2739-2018, 2018.

Gutleben, M., et al., Atmos. Chem. Phys., 20, 12313–12327, https://doi.org/10.5194/acp-20-12313-2020, 2020.

Kok, J.F., et al., *Nat. Geosci*., 10, no. 4, 274-278, doi:10.1038/ngeo2912, 2017.

Mamouri, R.-E. and Ansmann, A.: Potential of polarization/Raman lidar to separate fine dust, coarse dust, maritime, and anthropogenic aerosol profiles, *Atmos. Meas. Tech*., 10, 3403–3427, https://doi.org/10.5194/amt-10-3403-2017, 2017.

Mayer, B. and Kylling, A., *Atmos. Chem. Phys*., 5, 1855–1877, https://doi.org/10.5194/acp-5-1855-2005, 2005.

Tsekeri, A., et al., Atmos. Meas. Tech., 10, 4995–5016, https://doi.org/10.5194/amt-10-4995-2017, 2017.

Aerosol typing using AERONET data products

E. Giannakaki[1,2], *G. Giagkogiakis*[1], *M. Gatou*,[1], *M. Komppula*[2]
elina@phys.uoa.gr
(1) Department of Environmental Physics and Meteorology, University of Athens, Athens, Greece
(2) Finnish Meteorological Institute, Atmospheric Research Centre of Eastern Finland ,70211, Kuopio, Finland

Introduction

Atmospheric aerosols play a central role in influencing the Earth's climate by direct, indirect, and semi-direct effects. In attempts to quantify these effects, the main difficulties arise from the very high variability in time and space of the aerosol concentration and related physical, optical, and chemical properties.

The Ångstrom exponent that is calculated from the spectral dependence of the aerosol optical thickness (AOT) is commonly used as a good indicator of the dominant size of the atmospheric particles determining the AOT. Values of å≤1 indicate size distributions dominated by coarse-mode aerosols (radii≥0.5μm) that are typically associated with dust and sea salt particles, and values of å≥1.5 indicate size distributions dominated by fine-mode aerosols (radii<0.5μm) that are usually associated with urban pollution and biomass burning particles.

A simple graphical method to visually convert å and its spectral curvature (1å) to both the fine-mode aerosol radius and the contribution of the fine-mode aerosol to the AOT was proposed by Gobbi [2]. In this study AERONET level 3 data of depolarazation and lidar ratio to investigate the potential of aerosol typing through this simply graphical method. Seven AERONET stations were used and the case of Thessaloniki were selected for demonstration of the method. In the future we will apply the graphical method to lidar derived data.

Methodology

Measurement sites and Data-

The graphical method was applied in seven stations as presented in Table 1.

Thessaloniki station was selected for demonstration since is well suited for aerosol typing studies and for the investigation of the performances of different aerosol typing algorithms. The CIMEL multiband sun-sky photometer was installed in Thessaloniki in 2003 as part of the AERONET Global Network. It performs direct solar irradiance and sky radiance measurements at 340, 380, 440, 500, 670, 870, and 1020nm automatically during the day. Measurements are automatically performed every 15 minutes or less, depending on the sun's zenith angle[5],[6]. The AERONET inversion algorithms[6],[7] are applied automatically to the raw data.

Table 1. AERONET stations used for graphical representation

Station	Start	End	N
Beijing	2/2010	3/2019	1734
Tamanrasset	10/2006	6/2018	1072
Thessaloniki	1/2010	11/2018	762
Kanpur	1/2010	9/2019	7283
Alta Floresta	7/1993	10/2018	869
Mongu	6/1997	10/2009	1568
Ispra	7/1997	9/2018	1128

Quality assured direct-sun data in the 440–870nm wavelength range retrieved from sun photometers operating within AERONET were used by Gobbi [2] to demonstrate the feasibility of the introduced classification scheme. Considering the operating wavelengths of AERONET sun photometers, å was derived for the wavelength pairs of 440–870nm, and its spectral curvature was represented by the difference 1å=å(440, 675) – å(675, 870). The graphical method was applied by Gobbi [2] to the analysis of daily records. The version 3 inversion products were also used that provide the spectral particle linear depolarization ratios and lidar ratios.

Results

In the first attemp the data were devided in classes of different AOT. Different colours are used for intervals of 0.05 AOT (Figure 1, top). The different AOTs are occupy different part of the plot, indicating that the same Aerosol Optical Depth could be result of different aerosol size and different fraction of fine to coarse aerosols. Thus, we use clusters of single scattering albedo (SSA) of 0.1 intervals for the graphical display. In this second attempt it is more clear that different colors occupy certain areas of the figure. This indicate that the smaller the SSA the lower the percentage that fine particles contributes to AOT.

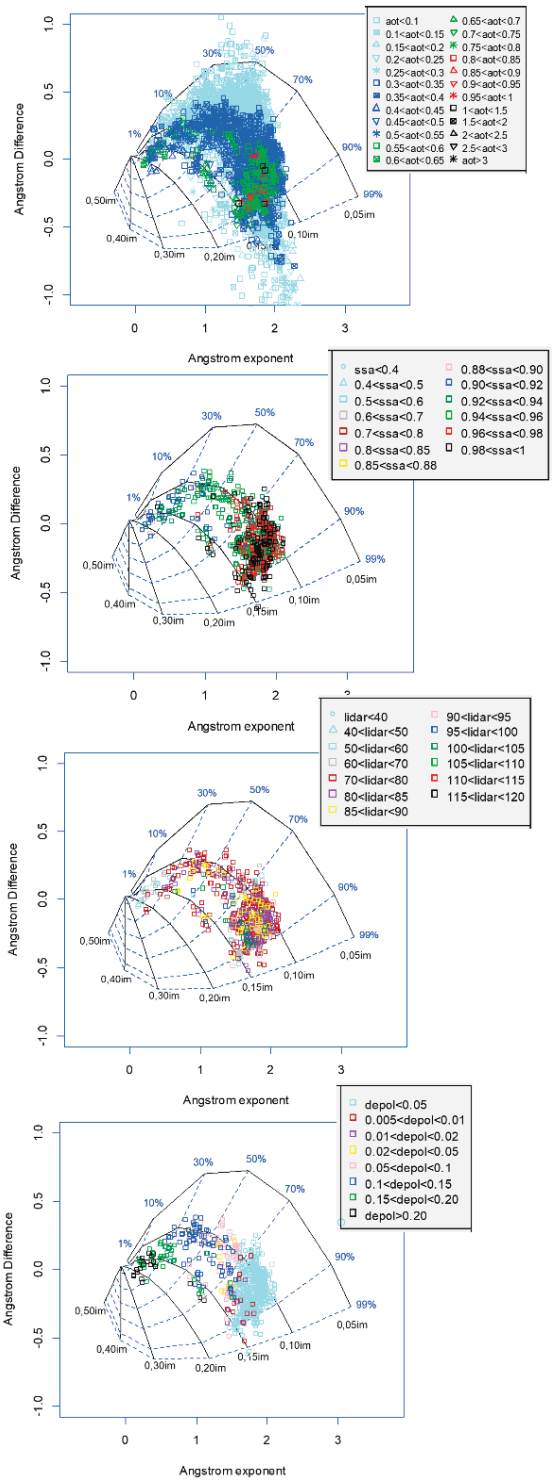

Figure 1. Gobbi graphical display of Thessaloniki AERONET data for different classes of AOT, SSA, LR and Depolarazation ratio

In the third attempt the classification is performed using the lidar ratio (LR) parameter in intervals of 10 sr. The different colors again are not attributed in certain areas of the graph. Thus the contribution of fine particles to the total optical depth is not directly correlated to the LR parameter.

In the fourth and last attempt we use different intervals of the depolarization ratio parameter. The contribution of fine particles to the total optical depth is directly correlated with different values of depolarization values. The more unspherical the particles are, the larger the depolarization ratio and the lower the contribution of fine particles to the total optical depth but with larger fine particles.

Future plans include the use of pure and mixed AERONET stations with capabilities of Lidar-depolarization measurements.

Acknowledgements

The research work was supported by the Hellenic Foundation for Research and Innovation (H.F.R.I.) under the "First Call for H.F.R.I. Research Projects to support Faculty members and Researchers and the procurement of high-cost research equipment grant" (Project Number:16645).

Authors want to thank the following PIs Investigators of AERONET Sites used in this study for maintaining their instruments and providing their data to the community: Hong-Bin Chen (Beijing), Emilio Cuevas-Agullo (Tamanrasset), Alkiviadis Bais (Thessaloniki), Brent Holben (Kanpur, Alta Floresta, Mongu), Giuseppe Zibordi (Ispra).

References

[1] Schuster, G. L., *et al.* (2006). Angstrom exponent and bimodal aerosol size distributions. Journal of Geophysical Research: Atmospheres, 111(D7).

[2] Gobbi, G. P., *et al.* (2007). Classification of aerosol properties derived from AERONET direct sun data. Atmospheric Chemistry and Physics, 7(2), 453-458.

[3] O'neill, N. T., *et al.* (2003). Spectral discrimination of coarse and fine mode optical depth. Journal of Geophysical Research: Atmospheres, 108(D17).

[4] Kaufman, Y. J. (1993). Aerosol optical thickness and atmospheric path radiance. Journal of Geophysical Research: Atmospheres, 98(D2), 2677-2692.

[5] Holben, B. N., *et al.* (1998). AERONET—A federated instrument network and data archive for aerosol characterization. Remote sensing of environment, 66(1), 1-16.

[6] Dubovik, O., & King, M. D. (2000). A flexible inversion algorithm for retrieval of aerosol optical properties from Sun and sky radiance measurements. Journal of Geophysical Research: Atmospheres, 105(D16), 20673-20696.

[7] Dubovik, O., *et al.* (2006). Application of spheroid models to account for aerosol particle nonsphericity in remote sensing of desert dust. Journal of Geophysical Research: Atmospheres, 111(D11).

Highlights of Aerosols Multiwavelength Lidar Measurements over Athens, Greece (2020-2021)

***M. Gidarakou*[1]**, *A. Papayannis*[1], *D. Anagnou*[1], *M. Mylonaki*[1], *O. Soupiona*[1], *C. A. Papanikolaou*[1], *R. Foskinis*[1], *E. Kralli*[1], *P. Kokkalis*[2]
marilena.98@hotmail.com
(1) Laser Remote Sensing Unit, Physics Department, National Technical University of Athens, Zografou, Greece,
(2) Physics Department, Kuwait University, Safat 13060, Kuwait

Introduction

After the industrial revolution, aerosol concentrations have been significantly increasing and the response of the Earth's climatic system to this sharp increase of anthropogenic emissions is still not well assessed and needs to be further investigated (IPPC, 2013). Consequently, we need to improve our understanding of the role of aerosols and cloud droplets in the climate system (both direct and indirect effects).

According to IPCC (IPCC, 2013), the total direct aerosol radiative forcing combined across all aerosol types is -0.5 Wm^{-2} , with a 5 to 95 % confidence range of -0.1 to -0.9 Wm^{-2} and with a medium-low level of scientific understanding. This is especially true for the Eastern Mediterranean region, where insufficient knowledge of the microphysical properties of aerosol particles as well as their spatial distribution remains a key issue to evaluate their effect on global climate.

To further understand the effects of aerosols on the Earth's climate, the vertical profiles of their optical and microphysical properties are required with high spatio-temporal resolution. The light detection and ranging (lidar) technique is the ideal tool for such studies from which the vertical profiles of the aerosol backscatter (b_{aer}), and extinction coefficients (a_{aer}), as well as the lidar ratio (LR), the Ångström exponent (AE) and the particle linear depolarization ratio (pldr) can be extracted.

The aim of this study, is to present the optical properties of the various aerosol types and their mixtures observed over the city of Athens by the EOLE lidar system during in the time period 2020-2021. The aerosol characterization was based on the airmass trajectory analysis provided by the Hybrid Single-Particle Lagrangian Integrated Trajectory model (HYSPLIT; Draxler, 1998) and the corresponding fire spots information was provided by the Fire Information for Resource Management System (FIRMS).

The vertical profiles of the aerosol optical properties were retrieved by using the Single Calculus Chain (SCC) described by D'Amico et al. (2016) and Mattis et al. (2016). The aerosol stratifications (layering) were derived by a recently published method based on image processing of lidar signals (Maroufidis et al., 2020).

Results and discussion

In total, we studied 24 cases of aerosol layers of which we present, here, the case of 12th of April 2021, which was characterized by a Saharan dust transport over Athens. Figure 1 presents the air mass 192-hours back-trajectories arriving over Athens on 12 April 2021 (16:00 UTC). The red dots refer to fire hot spots derived from MODIS data. We see that the air masses originating from the Saharan desert, overpassed the Mediterranean Sea and arrived over Athens through Italy and Albania, where fire hot spots were detected.

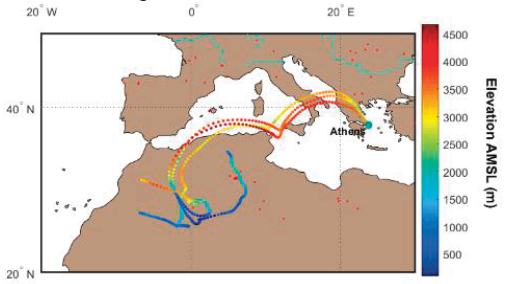

Figure 1. 192-hours airmass backward trajectories arriving over Athens at 2, 2.5 and 3 km asl. on 12.04.21 (16:00 UTC). The red dots represent active fires retrieved by MODIS (confidence level>80%).

In Figure 2 (top) we present the spatio-temporal evolution of the range-corrected lidar signal obtained at 1064 nm on 12 April 2021 (09:00-18:10 UTC). In this case a discrete aerosol layer was observed in the height region ~2.5-3.5 km (09:00-10:00 UTC) which extended later from 1.9-3.3 km height, finally, showing 4 discrete aerosol layers at 2, 2.4, 2.9 and 3.3 km height amsl. (17:22-18:10 UTC).

The retrieved optical properties of b_{aer}, AE, pldr and b_{aer}, a_{aer}, LR, AE, are shown in Fig. 2 (bottom-left: 16:00-17:00 UTC and bottom-right: 17:22-18:10 UTC, respectively). The high value of the pldr (~20-23%) inside the aerosol layer (2-2.5 km height) corroborates the presence of dust particles, probably mixed with biomass burning (BB) ones through their passage over Italy and Albania.

Table 1 summarizes the mean values of $A_{b355/532}$, $A_{b532/1064}$, LR_{355} and LR_{532} for 3 detected aerosol layers (daytime L_1, L_2; nighttime L_3).

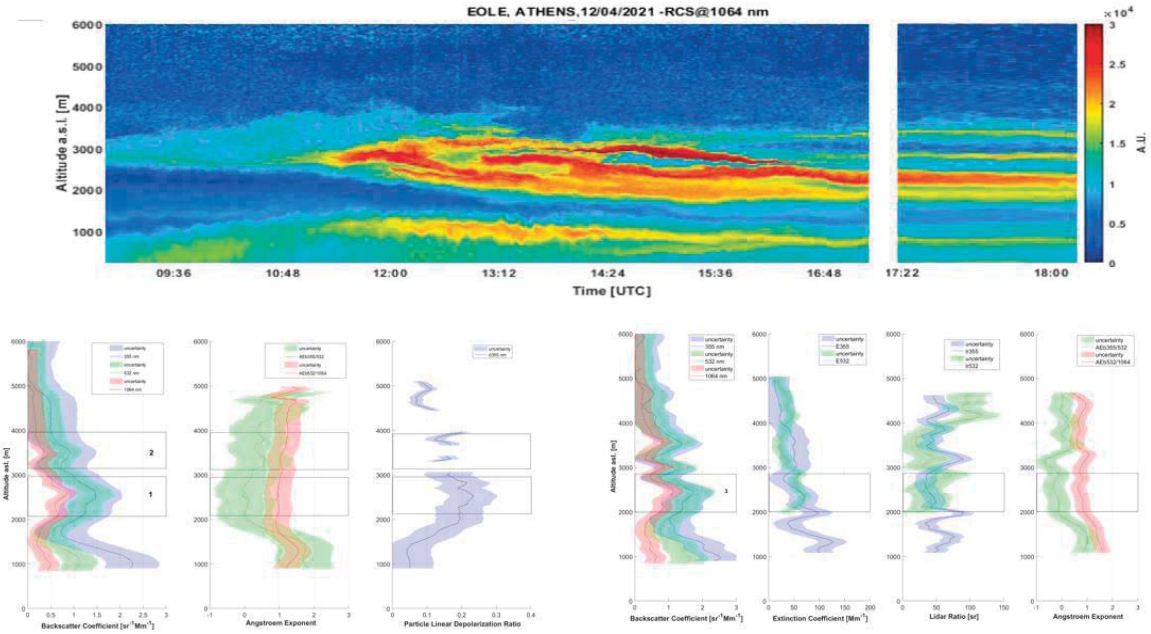

Figure 2. (*top*) Spatio-temporal evolution of the range-corrected lidar signal obtained by the EOLE lidar at 1064 nm (09:00-18:10 UTC); retrieved aerosol optical properties (*bottom left*: 16:00-17:00 UTC and *bottom right*: 17:22-18:10 UTC) on 12 April 2021.

Table 1. Mean value and standard deviation for 3 observed aerosol layers (L) detected by the EOLE lidar over Athens on 12 April 2021 (daytime L_1, L_2; nighttime L_3).

L	$A_{b355/b532}$	$A_{b532/b1064}$	LR_{355} [sr]	LR_{532} [sr]
1	0.04±0.08	0.97±0.03	-	-
2	0.45±0.12	1.12±0.08	-	-
3	-0.21±0.09	0.76±0.07	45±11	40±7

The next step, regarding the analyzed aerosol layers, will be to calculate their relevant microphysical and radiative properties and estimate their climatic contribution in our area.

Acknowledgements

This work has been supported by the Action titled "National Network on Climate Change and its Impacts (CLIMPACT)" which is implemented under the sub-project 3 of the project "Infrastructure of national research networks in the fields of Precision Medicine, Quantum Technology and Climate Change", funded by the Public Investment Program of Greece, General Secretary of Research and Technology/Ministry of Development and Investments. The authors gratefully acknowledge the NOAA Air Resources Laboratory (ARL) for the provision of the HYSPLIT transport and dispersion model and/or READY website (http://www.ready.noaa.gov) used in this publication.

We acknowledge the use of data products or imagery from the Land, Atmosphere Near real-time Capability for EOS (LANCE) system operated by NASA's Earth Science Data and Information System (ESDIS) with funding provided by NASA Headquarters.

References

D'Amico et al., EARLINET Single Calculus Chain – technical – Part 1: Pre-processing of raw lidar data, *Atmos. Meas. Techn.*, 9, 491-507, 2016.

Draxler, R. and Hess, G. An Overview of the HYSPLIT_4 Modelling System for Trajectories, Dispersion, and Deposition, *Australian Meteor. Magazine*, 47(4), 295-308, 1998.

IPCC, 2013: Climate Change 2013: The Physical Science Basis. Contribution of Working Group I to the Fifth Assessment Report of the Intergovernmental Panel on Climate Change [Stocker, T.F., D. Qin, G.-K. Plattner, M. Tignor, S.K. Allen, J. Boschung, A. Nauels, Y. Xia, V. Bex and P.M. Midgley (eds.)]. Cambridge University Press, Cambridge, United Kingdom and New York, NY, USA, 1535 pp.

Mamouri, R.E. et al., Multi-wavelength Raman lidar, sun photometric and aircraft measurements in combination with inversion models for the estimation of the aerosol optical and physico-chemical properties over Athens, Greece, Atmos. Meas. Tech., 5, 1793–1808, https://doi.org/10.5194/amt-5-1793-2012, 2012.

Mattis, I. et al., EARLINET Single Calculus Chain – Technical – Part 2: Calculation of optical products, *Atmos. Meas. Techn.*, 9(7), 3009-3029, 2016.

Long-term characterization of the vertical impact of the Saharan Air layer in the North Atlantic subtropical atmosphere

A. Barreto[1,2], *E. Cuevas*[1], *R. D. García*[3,1], *J. Carrillo*[4], *J. M. Prospero*[5], *L. Illic*[6], *S. Basart*[7], *A. Berjón*[3,1], *C. L. Marrero*[1], *Y. Hernández*[8,1], *J. J. Bustos*[1], *S. Nickovic*[6] *and M. Yela*[9]
firts_author_email@adress: abarretov@aemet.es
(1) Izaña Atmospheric Research Center (IARC), Agencia Estatal de Meteorología (AEMET), Santa Cruz de Tenerife, Spain
(2) Atmospheric Optics Group, University of Valladolid, Valladolid, Spain
(3) TRAGSATEC, Madrid, Spain
(4) Departamento de Física, Universidad de La Laguna (ULL), La Laguna, Canary Islands, Spain
(5) Rosenstiel School of Marine and Atmospheric Science, Univ. of Miami, Miami, USA
(6) Republic Hydrometeorological Service of Serbia, Belgrade, Serbia
(7) Barcelona Supercomputing Centre, Barcelona, Spain
(8) Consejería de Educación, Universidades y Sostenibilidad, Gobierno de Canarias, Spain
(9) Instrumentation and Atmospheric Research Department, National Institute for Aerospace Technology (INTA), Madrid, Spain

Introduction

The interaction between atmospheric aerosols and the climate system is nowadays the dominant source of uncertainty in radiative forcing and climate studies (IPCC, 2013). Therefore many questions remain unanswered about their physical, chemical or optical properties, as well as the vertical distribution of aerosols in the atmosphere. The latter constitutes valuable information to assess their radiative effect (Myhre et al., 2013) since aerosol vertical distribution may certainly influence the Earth's radiation budget in a rather complex way. Dust is one of the most important atmospheric aerosol, representing about 75% of the global aerosols injected into the atmosphere (Kinne et al, 2006; Mona et al., 2012), with half of these global dust emissions coming from the Sahara and surrounding regions (IPCC, 2013).

Many studies in the literature confirm that mineral dust plays an important role significantly affecting the solar and terrestrial radiative balance mainly by means of massive dust ejections (IPCC, 2013) or affecting the properties of clouds and their impact on climate (Sassen et al., 2003).

While African desert dust is transported westwards to the North Atlantic throughout the year, most of the descriptions of the Saharan layer published in the literature are restricted to summer, when dust outbreaks are mostly confined to an elevated mixed layer, often called the Saharan Air Layer (SAL) (Prospero and Carlson, 1980). Comparatively very few studies have been conducted on the long-term description of the different seasonal features this prevalent westward transport of dust experiments in the North Atlantic region (Prospero and Carlson, 1980, among others). Since the altitude at which aerosols are lifted and therefore transported have a strong influence on the aerosol lifetime and radiative effect (Generoso et al., 2008), systematic ground-based mineral dust observations by lidar and thermodynamic soundings in key regions are critical to enhancing our understanding of the dust climatology and the radiative role played by desert dust.

The radiative effect that the small amount of water vapour carried on the elevated SAL in summer is also under study. This amount, although really small, is significantly higher than that present in the clean free troposphere (FT). Therefore, as shown by other authors in some case studies (Gutleben et al., 2019, 2020), this low amount of water vapour could represent an important radiative driver for the dust layer in summer.

In this study, the long-term seasonal evolution of the vertical atmospheric parameters and aerosol distribution over a subtropical region located in the North Atlantic (Tenerife, Canary Island), is carried out by means of 12-years of observations (2007-2018) from two types of instruments: Micropulse Lidar (MPL-3) data to analyze the vertical distribution of aerosols, and vertical information from radiosondes to characterize the vertical thermodynamical structure of the atmosphere. The synergy of lidar/sunphotometer has been used to minimize the uncertainties involved in aerosol extinction retrieval using such elastic backscatter system (Berjón et al., 2019).

Results and discussion

In this work, the summer-SAL appears as a well-stratified layer, relatively dry at lower levels but more humid at higher levels. Aerosol extinction (α) peaks at $\sim$ 2.5 km, but dust can be observed up to $\sim$ 6.0 km. This altitude has been defined as the SAL's top or STI (SAL's temperature inversion), according to the temperature inversion from thermodynamic soundings. The winter-SAL layer appears as a confined dust layer, compressed in the

first 2 km. The most significant features of this layer in winter are the dry anomaly observed at lower levels, the α peak at ~ 1.3 km height, and the STI observed at 2.3 km. Clean FT (CFT) conditions were found above this level.

The SAL radiative impact of the summer-SAL has been also studied in this work, revealing that both dust and water vapour play an important role in the radiative balance. Our results revealed the dominant dust-induced shortwave (SW) radiative warming in summer (heating rates up to 0.7 K day^{-1}) below the dust peak. A net SW warming within the SAL (3.5 K day^{-1}), as well as a strong cold anomaly due to longwave (LW) adiabatic cooling near the SAL's top (-0.6 K day^{-1}) are observed as a result of the combined effect of dust and water vapour. Radiative processes are found to dominate in the marine boundary layer (heating), between 2.5 km and 6 km (heating), and above 6 km (cooling), while thermal advection processes play a dominant role in summer from 800 m to 2.5 km height.

Finally, a higher occurrence of moderately supercooled mid-level clouds near its top (5-7 km) under the presence of the summer-SAL could point to a possible impact of the SAL on heterogeneous ice nucleation.

Acknowledgements

This work has been developed within the framework of the activities of the World Meteorological Organization (WMO) Commission for Instruments and Methods of Observations (CIMO) Izaña Testbed for Aerosols and Water Vapour Remote Sensing Instruments. AERONET sun photometers at Izaña have been calibrated within the AERONET Europe TNA, supported by the European Community Research Infrastructure Action under the FP7 ACTRIS grant, agreement no. 262254. The LibRadtran Radiative Transfer Model has been used to estimate the heating rates. The authors also want to acknowledges F. Molero for his useful tips on the atmospheric heating rates retrieval and the funding provided by the Institute of Physics Belgrade, through the grant by the Ministry of Education, Science, and Technological Development of the Republic of Serbia. AEMET and BSC authors have participated in this study to contribute to the WMO Sand and Dust Storm Warning Advisory System (SDS-WAS) Regional Center for Northern Africa, Middle East, and Europe.

References

Berjón, A., Barreto, A., Hernández, Y., Yela, M., Toledano, C., and Cuevas, E.: A 10-year characterization of the Saharan Air Layer lidar ratio in the subtropical North Atlantic, Atmos. Chem. Phys., 19, 6331-6349, https://doi.org/10.5194/acp-19-6331-2019, 2019.

Generoso, S., Bey, I., Labonne, M., and Bréon, F.-M.: Aerosol vertical distribution in dust outflow over the Atlantic: Comparisons between GEOS-Chem and Cloud-Aerosol Lidar and Infrared Pathfinder Satellite Observation (CALIPSO), J. Geophys. Res., 113, D24209, doi: 10.1029/2008JD010154, 2008.

Gong W., Min, Q., Li, R., Teller, A., Joseph, E., and Morris, V.: Detailed cloud resolving model simulations of the impacts of Saharan air layer dust on tropical deep convection - Part 1: Dust acts as ice nuclei, Atmos. Chem. Phys. Discuss., 10, 12907–12952, doi:10.5194/acpd-10-12907-2010, 2010.

Gutleben, M., Groß, S., Wirth, M., Emde, C., & Mayer, B.: Impacts of water vapor on Saharan air layer radiative heating, Geophys. Res. Lett., 46, 14,854–14,86, https://doi.org/10.1029/2019GL085344, 2019.

Gutleben, M., Groß, S., Wirth, M., and Mayer, B.: Radiative effects of long-range-transported Saharan air layers as determined from airborne lidar measurements, Atmos. Chem. Phys., 20, 12313–12327, https://doi.org/10.5194/acp-20-12313-2020, 2020.

IPCC: Climate Change 2013: The Physical Science Basis. Contribution of Working Group I to the Fifth Assessment Report of the Intergov- ernmental Panel on Climate Change, edited by: Stocker, T. F. Et al., Cambridge University Press, Cambridge, UK and New York, NY, USA, 1535 p., 2013.Granados-Muñoz et al., Retrieving aerosol microphysical properties by Lidar-Radiometer Inversion Code (LIRIC) for different aerosol types, *J. Geophys. Res.,* 119 (8), 4836-4858, 2014.

Kinne, S., Schulz, M., Textor, C., Guibert, S., Balkanski, Y., Bauer, S. E., Berntsen, T., Berglen, T. F., Boucher, O., Chin, M., Collins, W., Dentener, F., Diehl, T., Easter, R., Feichter, J., Fillmore, D., Ghan, S., Ginoux, P., Gong, S., Grini, A., Hendricks, J., Herzog, M., Horowitz,L., Isaksen, I., Iversen, T., Kirkevag, A., Kloster, S., Koch, D., Kristjansson, J. E., Krol, M., Lauer, A., Lamarque, J. F., Lesins, G., Liu, X., Lohmann, U., Montanaro, V., Myhre, G., Penner, J., Pitari, G., Reddy, S., Seland, O., Stier, P., Takemura, T., and Tie, X.: An AeroCom initial assessment-optical properties in aerosol component modules of global models, Atmos. Chem. Phys., 6, 1815–1834, 2006.

Mona, L., Liu, Z., Müller, D., Omar, A., Papayannis, A., Pappalardo, G., Sugimoto, N., and Vaughan, M.: Lidar measurements for desert dust characterization: An overview, Advances in Mateorology, vol. 2012, Article ID 356265, doi: 10.1155/2012/356265, 2012.

Myhre, G., Samset, B. H., Schulz, M., Balkanski, Y., Bauer, S. and co-authors: Radiative forcing of the direct aerosol effect from AeroCom Phase II simulations. Atmos. Chem. Phys. 13, 1853-1877, 2013.

Prospero, J. M. and Carlson, T.: Saharan air outbreaks over the Tropical North Atlantic, Pure Appl. Geophys., 119, 677-691, 1980.

Sassen, K., P. J. DeMott, J. M. Prospero and M. R. Poellot, Saharan dust storms and indirect aerosol effects on clouds: CRYSTAL-FACE results, Geophys. Res. Lett.,30, 1633, 2003.

Optical and Microphysical Properties of Biomass Burning Aerosols and Mixtures Lidar Observations in Athens, Greece (2011-2019)

Maria Mylonaki[1], Alexandros Papayannis[1], Dimitra Anagnou[1], Igor Veselovskii[2], Christina-Anna Papanikolaou[1], Panagiotis Kokkalis[3], Ourania Soupiona[1], Romanos Foskinis[1], Marilena Gidarakou[1], Eleni Kralli[1]*

**mylonaki.mari@gmail.com*

(1) Laser Remote Sensing Unit, Department of Physics, National and Technical University of Athens, Zo-grafou, 15780, Greece;

(2) Prokhorov General Physics Institute of the Russian Academy of Sciences, Moscow, Russia;

(3) Physics Department, Kuwait University, P.O. Box 5969, 13060 Safat, Kuwait;

Introduction

Biomass Burning (BB) aerosols are estimated to contribute ~62 % to the global particulate Organic Carbon (OC) and ~27 % to the Black Carbon (BC) emissions annually (Wiedinmyer et al., 2011). In fact, BC and OC aerosols, when embedded in permanent ice, can reduce its reflectance leading to the glacial melting (Mahowald et al., 2011) and affect the cloud formation, acting as Cloud Condensation Nuclei (CCN) or Ice Nuclei (IN) and changing their optical properties and lifetime (Rosenfeld et al., 2014).

The total industrial era climate forcing of BC is estimated to be +1.1 Wm^{-2} with ~90% uncertainty bounds of 0.11 Wm^{-2} to 2.1 Wm^{-2}. Of the total estimate of 1.1 Wm^{-2}, up to 0.18 Wm^{-2} (with a large uncertainty range) is derived from effects on cloud thermodynamic phase alone. Towards the elimination of this uncertainty range, it is important the enhancement of the existing literature with relative studies.

Thus, to better understand the BB aerosol effects on the Earth's climate, their optical - Backscatter Coefficient (b_{aer}), Extinction Coefficient (a_{aer}), Lidar Ratio (LR) and Ångström Exponent (AE) - and microphysical properties - Effective Radius (reff), Volume Density (vd), real part (mR) and imaginary part (mI) of the Refractive Index and Single Scattering Albedo (SSA) - are urgently needed to be measured with the LIght Detection and Ranging (lidar) technique from which vertical profiles of the aerosol properties can be extracted.

In this paper, we present for the first time a comprehensive study of 9-years multi-wavelength Raman lidar measurements, obtained over Athens, Greece. We retrieved the vertical profiles of the optical and the microphysical properties of aged BB aerosols and mixtures, providing a narrower range of mean values for the 3 aerosol categories. On top of that, we propose a new method of how to distinguish between the pure smoke and layers mixed with continental polluted aerosols. These aerosol layers are frequently observed over Europe due to the presence of anthropogenic pollution and are difficult to be discriminated due to their aerosol optical properties overlapping values. Finally, the results derived from this study provide typical values of the BB aerosol properties over Europe, which may be useful in global climatic models, in reducing the currently large uncertainty in climate forcing due to this kind of aerosols.

Results and discussion

In total, we studied 34 aerosol layers which were characterized as: 1) smoke (s), 2) smoke + continental polluted (s+cp) and 3) smoke + mixed dust (s+md). The resident time (i.e. number of hours) of a HYSPLIT backward trajectory above a burned area versus the variable LR532/LR355 for each aerosol layer of s and s+cp categories is presented in Figure 1.

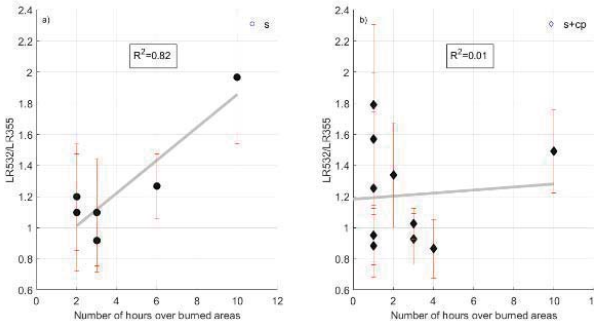

Figure 1. Correlation between the variables LR532/LR355 and Number of hours over burned areas for a) the s aerosol layers, b) the s+cp aerosol layers.

Concerning the s aerosol category, the LR532/LR355 variable increases as the number of hours over the burned areas increase, resulting in a high correlation between these two variables (correlation coefficient R^2=0.82). On the other hand, the corresponding correlation coefficient for the s+cp category is extremely low (equal to 0.01), thus, showing no correlation at all between the two variables for this aerosol category.

Table 1. Mean values along with their standard deviation of s, s+cp and s+md aerosol categories for aerosol optical and microphysical properties presented in this study.

Aerosol category

		s	s+cp	s+md
Optical properties				
LR 355 nm [sr]	this study	57±10	51±5*	39±5
	literature	21-67		35-92
LR 532 nm [sr]	this study	73±11	59±10*	62±12
	literature	26-80		32-75
AE ext 355/532	this study	0.90±0.52	1.13±0.44*	0.49±0.88
	literature	0.64-2.3		0.50-1.70
AE bsc 355/532	this study	1.43±0.27	1.35±0.09*	1.56±0.21
	literature	~1.90		0.44-1.50
AE bsc 532/1064	this study	1.67±0.15	1.70±0.09*	1.58±0.14
	literature	~1.90		0.44-1.50
LR532/LR355	this study	1.27±0.36	1.17±0.34*	1.39±0.57
	literature	0.9-1.4		0.7-1.0
Microphysical properties				
reff [μm]	this study	0.24±0.14	0.24±0.13*	0.24±0.11
	literature	0.13-0.44		0.17-0.45
mR	this study	1.49±0.06	1.50±0.07*	1.53±0.07
	literature	1.37-1.6		1.37-1.50
mI	this study	0.013±0.004i	0.011±0.005i*	0.011±0.005i
	literature	0.001i-0.053i		0.004i-0.007i
vd [$\mu m^{-3}cm^{-3}$]	this study	8.6±3.2	20.7±14.1*	9.7±6.1
	literature	8-50		7.4-24.0
SSA 355 nm	this study	0.916±0.042	0.929±0.036*	0.928±0.037
	literature	0.760-0.890		0.948-0.964
SSA 532 nm	this study	0.932±0.023	0.936±0.024*	0.933±0.025
	literature	0.790-0.997		0.937-0.958
SSA 1064 nm	this study	0.918±0.008	0.923±0.031*	0.915±0.045*
	literature	0.740-0.980		

*introduced in the literature within this study.

Mean LR values of 57±10 sr and 73±11 are observed for the s category, at 355 nm and 532 nm, respectively. The corresponding LR values of the s+cp category is 51±5 sr and 59±10 sr, respectively while for the s+md category they are equal to 39±5 sr and 62±12 sr, respectively. The AE backscatter-related mean values are all higher than 1.4. On the other hand, the AE extinction-related especially of s+md category has significant low mean value (0.49±0.88). The ratio of the LRs (LR532/LR355) was found >1 for all cases.

The mean values of the aerosol microphysical properties have no noticeable difference between the various aerosol categories, except the vd property (20.7±14.1 $\mu m^{-3}cm^{-3}$) for the s+cp category which found to be ~100% greater than the corresponding mean val-ues for the s and s+md categories (8.6±3.2 $\mu m^{-3}cm^{-3}$ and 9.7±6.1 $\mu m^{-3}cm^{-3}$, respectively). On the other hand, the mean value of reff was found to be 0.24±0.14 μm for all aerosol categories, the mean value of mR ranged between 1.49±0.06 and 1.53±0.07, while the mI value ranged between 0.0108i±0.0048i and 0.0126i±0.0043i. Finally, the mean value of SSA (at all 3 wavelengths 355, 532, 1064 nm) ranged between 0.915±0.045 and 0.936±0.024.

Acknowledgements

The research work was supported by the Hellenic Foundation for Research and Innovation (HFRI) under the HFRI PhD Fellowship grant (Fellowship Number: 669). We also acknowledge the support of this work by the project "PANhellenic infrastructure for Atmospheric Composition and climatE change" (MIS 5021516) which is implemented under the Action "Reinforcement of the Research and Innovation Infrastructure", funded by the Operational Programme "Competitive-ness, Entrepreneurship and Innovation" (NSRF 2014-2020) and co-financed by Greece and the European Union (European Regional Development Fund). Moreover, the authors acknowledge support through ACTRIS under grand agreement no. 262 254 of the European Commission Seventh Framework Programme (FP7/2007-2013) and ACTRIS-2 under grant agreement no. 654109 from Horizon 2020 research and innovation program of the European Commission. The authors gratefully acknowledge the NOAA Air Resources Laboratory (ARL) for the provision of the HYSPLIT transport and dispersion model and/or READY website (http://www.ready.noaa.gov) used in this publication. We acknowledge the use of data products or imagery from the Land, Atmosphere Near real-time Capability for EOS (LANCE) system operated by NASA's Earth Science Data and Information System (ESDIS) with funding provided by NASA Headquarters. Develop-ment of lidar retrieval algorithm was supported by Russian Science Foundation under project 21-17-00114.

References

Mahowald, N., Ward, D. S., Kloster, S., Flanner, M. G., Heald, C. L., Heavens, N. G., Hess, P. G., Lamarque, J. F. and Chuang, P. Y., Aerosol impacts on climate and biogeochemistry, *Ann. Rev. Environ. Resour.*, 36, 45–74, 2011.

Rosenfeld, D., Sherwood, S., Wood, R. and Donner, L., Climate effects of aerosol-cloud interactions, *Science*, 343, 379–380, 2014.

Wiedinmyer, C., Akagi, S. K., Yokelson, R. J., Emmons, L. K., Al-Saadi, J. A., Orlando, J. J. and Soja, A. J., The Fire INventory from NCAR (FINN): A high resolution global model to estimate the emissions from open burning, *Geosci. Model Dev.*, 4(3), 625–641, 2011.

Statistics over three years of near real time alert system for tropospheric aerosol pollution using ceilometer, photometer and backtrajectory analysis

M. Adam[1], K. Fragkos[1], I. Binietoglou[1,2], D. Wang[3], I. S. Stachlewska[3]
mariana.adam@inoe.ro
(1) National Institute of Research and Development for Optoelectronics - INOE 2000, 409 Atomistilor St, Magurele, Romania
(2) Institute for Astronomy, Astrophysics, Space Applications and Remote Sensing, National Observatory of Athens, Athens, Greece
(3) Faculty of Physics, University of Warsaw, 02-093, Warsaw, Poland

Introduction

The detection of the aerosol pollution layers in near real time is beneficial for society in order to prevent various undesirable implications which vary from human health to airspace safety.

In the current research, we employ the use of low-cost instruments which can operate continuously and unattended, i.e., a Lufft ceilometer (https://www.lufft.com/products/cloud-height-snow-depth-sensors-288/lufft-ceilometer-chm8k-2405/, last access 20/05/2021) and a Cimel solar/sky/lunar photometer (https://www.cimel.fr/?instrument=sun-sky-lunar-multiband-photometer, last access 20/05/2021), to detect aerosol pollution layers in the free troposphere and generate a near real time alert system (Adam et al., 2020). In addition, in order to identify the aerosol pollution source, the HYSPLIT backtrajectory is used (Stein et al, 2015).

This alert system was initiated by February 2018 (when two Lufft ceilometers were acquired by INOE) and became operational in May 2018. The method was described by Adam et al. (2020) while examples were shown. Briefly, the main steps are the following. A quick look of RCS (range corrected signal) is updated each 15 min (http://liverali.inoe.ro/Ceilometer/). We search for aerosol layers by identifying the ALH (aerosol layer height) for the second (ALH2) and third (ALH3) layers detected by ceilometer and provided by manufacturer's algorithm in the raw data file. Once these ALH are identified, the HYSPLIT backtrajectory is performed for these altitudes. Next, we look for available Aeronet data for our photometer (Holben et al, 2011). The current values are compared with the climatological monthly values (Carstea et al, 2019). If one of the current values for aerosol optical depth (AOD), Angstrom Exponent (AE), fine mode fraction (FMF) and associated AOD are outside the 90th percentile or AE is below 10th percentile we label the pollution event as "outside climatological limits". The alert sent by email (at all times when we find an ALH) specifies in this case this label. This alert is meant to warn the scientists and take further actions such as the start of the non-operational instruments (e.g., multi-wavelength Raman lidar and in-situ instruments when the pollution reaches the PBL and the ground) which can bring additional information about the aerosol pollution. All the alerts are also saved in a logfile.

Results and discussion

Over three years period (11/05/2018 – 11/05/2021) we recorded a number of 5167 alerts (ALH2 and ALH3 detected above 2500 m a.g.l.). Note that the Lufft's algorithm detects three layers from the surface up to 4000-5000 m altitude. Thus, upper tropospheric layers are not considered. For 4036 events, Aeronet data was available. For the other 1131 events with Aeronet data, we have 556 events labelled as "within climatological limits" while the rest 575 were labelled "outside climatological limits". The most common errors which occur and thus we fail to get information about lofted aerosol layers are:

- Aeronet data is not available. Most of the cases occur due to unfavourable weather. Sporadically we encountered technical issues such as failure to transmit the data from photometer towards Photons (Lille, France).
- The HYSPLIT backtrajectory could not be performed. In most cases, error messages indicate the lack of the meteorological fields.
- Local issues with power failures or internet disruptions.

The source is considered where the distance between terrain altitude and airmass trajectory altitude is minimum. The pollution sources for the 5167 events are shown in Figure 1. A simple classification of the sources assumes three groups as: dust, marine and continental aerosol (including biomass burning, urban, industrial). We counted the following numbers: 1208 cases of marine aerosol, 389 dust (Africa and Arabian Desert) and 3570 continental aerosol. From the latter, 175 events represent long range transport from America. Most of the sources are located close to the measurement site, in the southern part of Romania. The

histograms of the travel time and travel distance are shown in Figures 2 and 3. The highest number of occurrences is for travel time within 0.5 days and within 100 km travel distance. The number of events (ALH2 and ALH3) recorded by month is shown in Figure 4. The lower plot represents a normalization to the total number of 15 min intervals over the three years of measurements. There is a limited number of events during winter time as the most of the aerosol pollution events occur during summer (e.g., biomass burning or dust). On the other hand, most of the ALH2 and ALH3 provided are recorded below 2500 m.

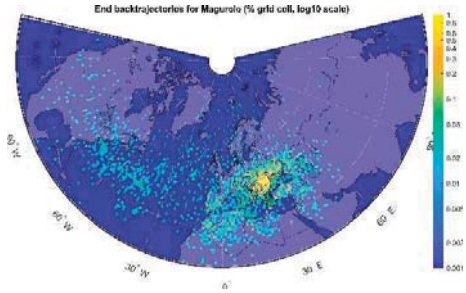

Figure 1. The aerosol pollution sources for 5167 pollution events detected over May 2018 – May 2021.

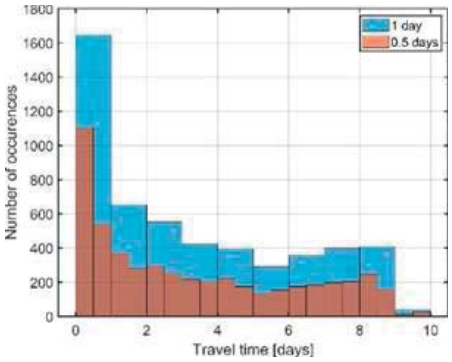

Figure 2. The histogram of the travel time of the air mass from the measurement site to the source.

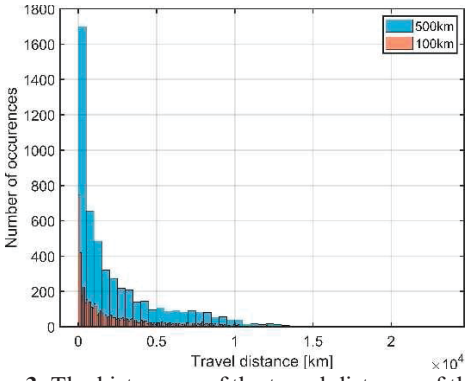

Figure 3. The histogram of the travel distance of the air mass from the measurement site to the source.

Latest edit: the aerosol pollution source was reconsidered following Radenz et al (2021). More results will be presented during conference.

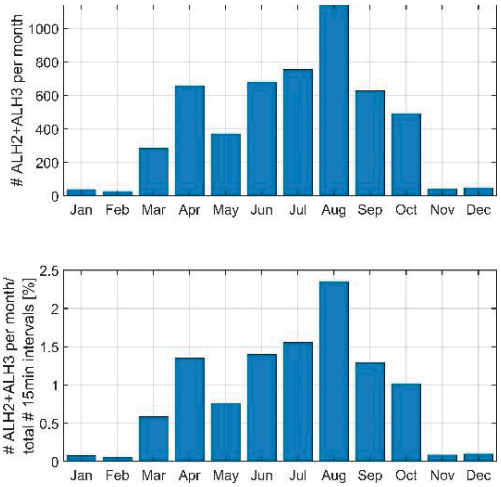

Figure 4. The number of events (ALH2+ALH3) recorded by month, in absolute values (upper) and normalized to the total number of 15 min intervals over the three years of measurements (lower).

Challenges

To be discussed:

- The accuracy of detecting aerosol layers in the ceilometer RCS profile (low SNR).
- The accuracy of estimating the source of the aerosol pollution.
- The methodology does not work when no photometer data is available.
- New criteria in defining the degree of pollution in the layer as compared with the whole atmospheric column.

Acknowledgements

This work was supported by the Romanian National contracts 18N/08.02.2019, 19PFE/17.10.2018, European Regional Development Fund through Competitiveness Operational Programme 2014-2020, Action 1.1.3 Creating synergies with H2020 Programme, project H2020 Support Centre for European project management and European promotion, MYSMIS code 107874.

References

Adam et al., Automatic alert system for tropospheric particulate pollution monitoring, ILRC 29, *EPJ Web Conferences* 237, 03004, 2020.

Carstea et al., Columnar aerosol measurements in a continental southeastern Europe site: climatology and trends, *Theor. Appl. Climatol.* 137, 3149-3159, 2019.

Holben et al, AERONET: a federated instrument network and data archive for aerosol characterization, *Remote Sens Environ*, 66, 1–16, 1998.

Radenz et al., Automated time–height-resolved air mass source attribution for profiling remote sensing applications, *Atmos. Chem. Phys.*, 21, 3015–3033, 2021.

Stein et al., *Bull. Amer. Meteor. Soc.*, 96, 2059-2077, http://dx.doi.org/10.1175/BAMS-D-14-00110.1, 2015.

Estimation of cloud base and top using 3D Lidar measurements the frame of SAFE-TRANS project

O. Soupiona[1], *H.X. Delastic*[1], *A. Papayannis* [1] *G. Georgoussis*[2], *V. Kostopoulos*[2]
soupiona.rania@gmail.com
(1) Laser Remote Sensing Unit, Physics Department, National Technical University of Athens, Zografou, Greece
(2) Raymetrics S.A., Spartis 32, Metamorphosis, Greece

Introduction

The present study lays on the project named "Development of an innovative operational 3D Scanning LIDAR system for real-time meteorological and atmospheric measurements in order to increase safety and efficiency in the aviation and transportation industry (SAFE-TRANS)". In this project, the innovative lidar system will be able to provide critical information on the state of the atmosphere in the surrounding area of an airport and to provide measurements and data in three dimensions of the cloud base, Slant Visual Range Vertical Optical Range Runway Visibility (Werner et al., 2005), as well as an early warning data for incoming phenomena such as fog, rain, etc.

Within the frame of the present study we will focus on the use of the advanced lidar system developed in the frame of SAFETRAN to estimate the cloud base and top height, not only in vertical but also in slant configuration. Herewith, we present the methodology and basic results of the field measurements performed in a test airport site.

Instrumentation

Table 1 presents the basic technical characteristics of the 3D Lidar, developed by Raymetrics S.A. in the frame of the SAFE-TRANS project. Moreover, a SKYVUETM8 [CS136] lidar ceilometer was additionally operating and its data were used for a measurement intercomparison.

Table 1. 3D Lidar technical specifications

Description of the 3D Lidar:	
Wavelength	355 nm
Repetition rate	20 Hz
Detection wavelength	355p / 355s
Spatial resolution	3.75 m
Scanning range angle	Zenith: 6° to -90° Azimuth: 0° to 360°
Max reporting range (vetrically)	12 km

A SKYVUE^{TM}8 [CS136] lidar ceilometer was additionally operating and its data were used for a measurement comparison and its basic specification characteristics are shown in Table 2.

Table 2. Ceilometer technical specifications

Description of the SKYVUE^{TM}8**:**	
Wavelength	912 nm
Pulse frequency	10 kHz
Spatial resolution	5 m
Max reporting range (vetrically)	8 km

The working procedure of the ceilometer's automatic cloud algorithm is to investigate the shape of the backscattered profile, discard maxima originating from signal noise or falling precipitation, and generate a data message provifing the cloud base height(s) and the instrument status information. Additional parameters reported include the vertical meteorological visibility and the amount of precipitation.

Methodology

Our cloud detection algorithm is based on the method presented by Zhao et al., (2014). In this methodology, the key point is how to minimize the impact of noise from the scatterer (cloud or aerosols) so that aerosol and cloud signatures can be distinguished. By using Mie thoery, we calculate the mean value and the standard deviation of the lidar signals in the farest signal range and we apply the atmospheric background correction, as well as moving average filtering techniques for a further denoising of the lidar signals. Then, a Value Distribution Equalization (VDE) process is applied. The main idea of the VDE process is the calculation of a reference baseline. Afterwards, the lidar signals are reordered based on the signal intensity and are placed in descending order into a slant line in agreement with the baseline. In this way, the peaks of the lidar returns due cloud or aerosol layers cause signals to move away from this line.

In this way, the SAFETRANS system is able to identify cloud layers, having a vertical growth of at least 45 m (empirically estimated threshold value) up to 12 km heights. Consecutive loud layers having a vertical distance equal or smaller than 45 km (empirically estimated) are merged and considered as one continuous layer.

Airport filed measurements

In the case of SAFETRANS three airports were selected to deploy our instrument, in the folloing locations in Greece (cf. Fig. 1): Chania (Crete), Elefsina (Athens) and Thessaloniki, under different time periods of the year: spring, summer and winter under different meteorological conditions: for example during spring, several dust transport events usually occur over south Greece affecting visibility and air quality (Soupiona et al., 2020). During spring, except dust trasnport events, cloud formation and early morning fog are usual events in the seaside airport of Elefsina, while during winter, heavy fog events and rain are the main problems of visibility reduction at Thessaloniki airport.

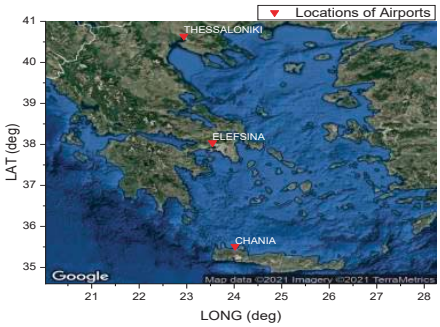

Figure 1: Locations of field measurements.

Results and discussion

A typical example of a cloudy case was observed at 10/05/2020, over the Chania airport, where scattered clouds in the free upper troposphere were present.

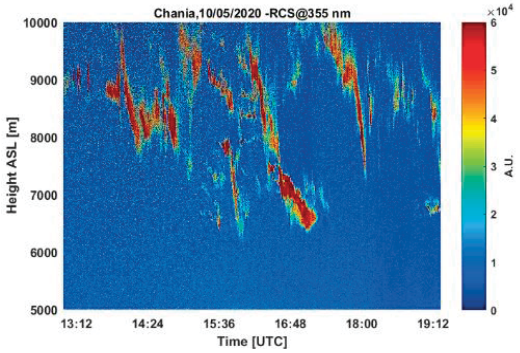

Figure 2: Spatio-temporal evolution (vertical direction) of the RCS at 355 nm observed by the 3D lidar over Chania (10 May 2020, 13:12-19:12 UTC).

Figure 2 presents the spatio-temporal evolution of the range-corrected lidar signal (RCS) at 355 nm, (vertical direction, 90º). In the period 13:12-19:12 UTC, clouds are present between 6 and 10 km. For this case, the cloud identification technique was applied and the results are depicted in Fig. 3. The clouds bottom (green points) as well as clouds top (red points) are successfully recorded, even for clouds with several layers. For the same day, ceilometer data were also available (blue points) and therefore an interocomparison between the two measurements was performed. However, it is important to mention here that the two instruments technical specifications differ and such comparison should be handled with care.

Through this comparison it becomes clear that the 3D Lidar can give estimations not only for the base, but also for the top of each cloud layer, even up to heights greater than 8 km, which is the maximum reporting range of the ceilometer. For altitudes lower than 8 km, the 3D lidar has identified existing clouds that have been ignored by the ceilometer due to non fullfillment of the applied cretiria by the latter. On the other hand, we notice that the clouds identified by the ceilometer (blue dots) also appear in the SAFETRANS time series and the results are in good agreement after 16:50 UTC (Fig. 3), where the cloud base and top are shown by the green and red points, respectively.

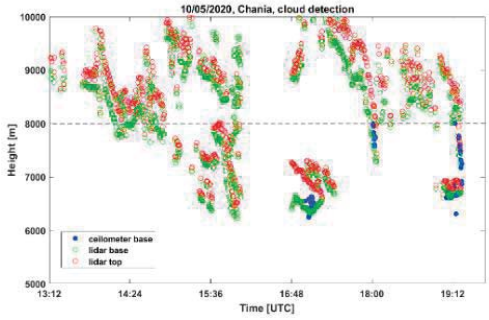

Figure 3: Cloud identification technique from the 3D Lidar (Chania airport 10/05/2020). The Ceilometer data for cloud base heights are presented with blue points.

Acknowledgements

This research has been co-financed by the European Union and Greek national funds through the Operational Program Competitiveness, Entrepreneurship and Innovation, under the call "RESEARCH-CREATE-INNOVATE" (project code: T1EΔK-03147)-SAFE TRANS.

References

Soupiona O., et al., EARLINET observations of Saharan dust intrusions over the northern Mediterranean region (2014–2017): properties and impact on radiative forcing, Atmos. Chem. Phys., 20, 15147–15166, 2020, https://doi.org/10.5194/acp-20-15147-2020

Werner C., et al., Visibility and Cloud Lidar. In: Weitkamp C. (eds) Lidar. Springer Series in Optical Sciences, vol 102. Springer, New York, NY., 2005 https://doi.org/10.1007/0-387-25101-4_6

Zhao, C., et al., A new cloudand aerosol layer detection method based on micropulse lidar measurements, J. Geophys. Res. Atmos.,119,6788–6802, 2014. doi:10.1002/2014JD021760.

Long-range transport of aerosols over Athens, Greece during Autumn 2020

C. A. Papanikolaou[1], A. Papayannis[1], M. Mylonaki[1], O. Soupiona[1], E. Kralli[1], P. Kokkalis[2], R. Foskinis[1], D. Anagnou[1], M. Gidarakou[1]
papanikolaouca@mail.ntua.gr
(1) Laser Remote Sensing Unit, Department of Physics, National and Technical University of Athens, Zografou, 15780, Greece
(2) Physics Department, Kuwait University, P.O. Box 5969, 13060 Safat, Kuwait

Introduction

The long-range transport of atmospheric aerosols can influence the air quality worldwide in local, regional or even intercontinental levels. It presents long residence times in the atmosphere and may contribute to the increase of air pollution (Martins *et al.*, 2018).

For instance, aerosols produced in wildfires in North America once they are embedded in the free troposphere or stratosphere, can travel over great distances and reach Europe (Ortiz-Amezcua et al., 2017; Baars et al., 2019; Papanikolaou et al., 2020). Under specific meteorological conditions their optical and chemical properties can be kept unaltered throughout their joutney, or they can be changed through mixing processes with other aerosol types, for instance desert dust, especially during lower free tropospheric transport (Papanikolaou et al., 2020).

Greece is an important cross-road of tropospheric aerosols originating from natural sources (deserts, volcanoes, wildfires, etc.) mostly within the European and the African continent (Soupiona *et al.*, 2020; Mylonaki *et al.*, 2021), while the intercontinental transport (e.g. North America) of aerosols over our area has not been studied in a systematic way. In this work we present three cases of intercontinental transportation of aerosols reaching Athens based on the DEPOLarization lidar systEm (DEPOLE) (Papayannis *et al.*, 2020) located at the Laser Remote Sensing Unit (LRSU of National Technical University of Athens (NTUA, (37.97° N, 23.78° E, elev. 212 m a.s.l.), in terms of aerosol backscatter coefficient (b_{aer}) and particle linear depolarization ratio (PLDR) at 355 nm.

Results and discussion

The cases presented here concern long-range aerosol transport which occurred on 14 and 30 September and on 1 October 2020. The first case (14 September 2020) concerns a long-range transport of biomass burning aerosols over Athens. In Figure 1 (a) we present the spatio-temporal evolution of the range-corrected lidar signal at 355 nm between 17:00 and 18:22 UTC. In that figure we can see the presence of a free tropospheric filamented aerosol layer located at 8.13±0.18 km height. The vertical profiles of the aerosol optical properties (b_{aer}, PLDR) were retrieved by using the Single Calculus Chain (SCC; D 'amico *et al.*, 2015) in the time period 17:19-18:19 UTC (Fig. 1a, orange rectangle) and are shown in Figure 1b. Regarding the optical properties of that layer (blue colored) we found a mean value of b_{aer} of 0.40±0.16 $Mm^{-1}sr^{-1}$ and of PLDR of 0.19±0.01.

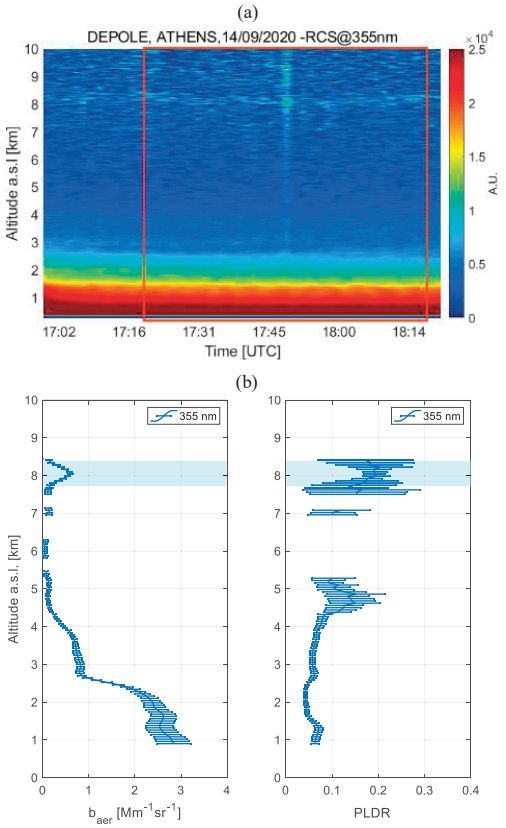

Figure 1. (a) Spatio-temporal evolution of the range-corrected lidar signal at 355 nm; (b) vertical distribution of b_{aer} [$Mm^{-1}sr^{-1}$] and PLDR at 355 nm, as observed by the DEPOLE lidar system on 14 September 2020 (17:19 –18:19 UTC) over Athens. The blue-shadowed rectangle represents the geometrical boundaries of the studied aerosol layer.

In Figure 2 we present the air mass backward trajectory ending after 144 hours over the city of Athens at 17:00 UTC, based on the results of the HYSPLIT model along with the active fires obtained by MODIS. In this case the air mass originated over the North American continent on 9-10 September, while at the same time period an extreme wildfire event was taking place in the State of California.

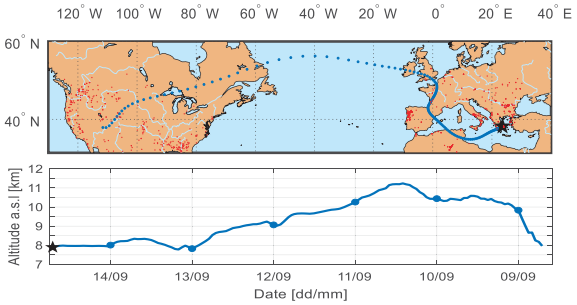

Figure 2. The HYSPLIT air mass backward trajectory for the aerosols arriving over Athens between 7.86-8.40 km a.s.l. along with the MODIS active fires (red spots).

In total 6 aerosol layers were observed and are presented in Table 1 along with the mean values of the aerosol optical properties: one layer on 14 September 2020, 2 layers on 30 September 2020 and 3 layers on 1 October 2020.

Table 1. Geometrical (top, bottom, mean altitude) and optical (mean b_{aer} and PLDR) properties of the studied aerosol layers, as observed by the DEPOLE lidar system at 355 nm over Athens on 14 and 30 September 2020 and 01 October 2020.

	Date [dd/mm/yy]		
Parameter	**14/09/20**	**30/09/20**	**01/10/20**
Bottom [km]	7.86	4.08 4.86	2.88 3.96 4.92
Top [km]	8.40	4.50 5.22	3.96 4.50 6.18
Mean altitude [km]	8.13±0.18	4.29±0.15 5.04±0.13	3.42±0.34 4.23±0.18 5.55±0.39
b_{aer} [$Mm^{-1}sr^{-1}$]	0.40±0.16	0.56±0.31 0.54±0.20	0.83±0.19 0.66±0.19 0.58±0.20
PLDR	0.19±0.01	0.16±0.05 0.22±0.02	0.07±0.03 0.08±0.01 0.06±0.01

Acknowledgements

We acknowledge support of this work by the project "PANhellenic infrastructure for Atmospheric Composition and climatE change-PANACEA" (MIS 5021516) which is implemented under the Action "Reinforcement of the Research and Innovation Infrastructure", funded by the Operational Programme "Competitiveness, Entrepreneurship and Innovation" (NSRF 2014- 2020) and co-financed by Greece and the European Union (European Regional Development Fund). The authors gratefully acknowledge the NOAA Air Resources Laboratory (ARL) for the provision of the HYSPLIT transport and dispersion model and/or READY website (https://www.ready.noaa.gov). *We also acknowledge the use of data and/or imagery from NASA's Fire Information for Resource Management System (FIRMS) (https://earthdata.nasa.gov/firms), part of NASA's Earth Observing System Data and Information System (EOSDIS)* used in this work.

References

Martins, L. D. *et al.*, Long-range Transport of Aerosols from Biomass Burning over Southeastern South America and their Implications on Air Quality, AAQR, 1734–1745, 2018.

Ortiz-Amezcua, P. *et al.*, Microphysical characterization of long-range transported biomass burning particles from North America at three EARLINET stations, *Atmos. Chem. Phys.*, 17(9), 5931–5946, 2017.

Baars, H. *et al.* (2019) 'The unprecedented 2017 – 2018 stratospheric smoke event : decay phase and aerosol properties observed with the EARLINET', pp. 15183–15198.

Papanikolaou, C. A. *et al.* (2020) 'Canadian biomass burning aerosol properties modification during a long-ranged event on August 2018', *Sensors (Switzerland)*, 20(18), pp. 1–19. doi: 10.3390/s20185442.

Soupiona, O. *et al.* (2020) 'EARLINET observations of Saharan dust intrusions over the northern Mediterranean region (2014-2017): Properties and impact on radiative forcing', *Atmospheric Chemistry and Physics*, 20(23), pp. 15147–15166. doi: 10.5194/acp-20-15147-2020.

Mylonaki, M. *et al.* (2021) 'Tropospheric vertical profiling of the aerosol backscatter coefficient and the particle linear depolarization ratio for different aerosol mixtures during the PANACEA campaign in July 2019 at Volos, Greece', *Atmospheric Environment*, 247, p. 118184. doi: https://doi.org/10.1016/j.atmosenv.2021.118184.

Papayannis, A. *et al.* (2020) 'Recent upgrades of the EOLE and AIAS lidar systems of the National Technical University of Athens operating since 2000 in Athens , Greece', 02030, pp. 4–7.

D 'amico, G. *et al.* (2015) 'EARLINET Single Calculus Chain – overview on methodology and strategy', *Atmos. Meas. Tech*, 8, pp. 4891–4916. doi: 10.5194/amt-8-4891-2015.

An intercomparison study of the retrieval algorithm for Water Vapour Mixing Ratio profiles using the Raman lidar technique and the ERA5 model

E. Kralli[1], *R. Foskinis*[1], *A. Papayannis*[1], *O. Soupiona*[1], *H.–X. de Lastic*[1], *M. Mylonaki*[1], *C.A. Papanikolaou*[1], *D. Anagnou*[1], *M. Gidarakou*[1]
elkralli@mail.ntua.gr
[1]*Laser Remote Sensing Unit, Physics Department, National Technical University of Athens, Zografou, Greece .*

Introduction

This study presents an intercomparison of the water vapour mixing ratio (WVMR) derived from a multi-wavelength Raman lidar and the reanalysis 5th generation meteorological reanalysis dataset (ERA5), as provided by the European Centre for Medium-range Weather Forecasts (ECMWF).

The WVMR profiles were obrtained by the EOLE Raman lidar system of the National Technical University of Athens (NTUA), for the case study of 18 May 2014, within the European Aerosol Research LIdar NETwork (EARLINET).

The water vapour is the most important variable constituent of the atmosphere (Ambaum, 2010), which has a major key role on the Earth's radiation budget, as it has the ability to absorb and transfer huge amounts of energy throught the atmosphere. For this reason, it is essential to improve and validate the current water vapour mixing ratio (WVMR) measurement techniques.

Results and discussion

The water vapour can be derived by the use of a multi-wavelength Raman lidar, providing vertical profiles with great accuracy during nighttime under cloud-free conditions. The vertical profiles of the water vapour can be expressed as mass mixing ratio profiles of water vapour to dry air masses (WVMR). The retrieving algorithm of water vapour mixing ratio (WVMR) (cf. Eq. 1) is based on the ratio of the inelastic backscattered lidar signals of 407 and 387nm channels, respectively (Whiteman, 2003). Also, the ambient temperature (T_{amb}) and pressure (P_{amb}) has to be considered to estimate the relevant extinction of the lidar signals.

$$WVMR(z) = C_0\, \rho_{air}(z)\, \frac{e^{-\int_0^z c_{\lambda_1} \frac{P_{amb}(z)}{T_{amb}(z)} dz}}{e^{-\int_0^z c_{\lambda_2} \frac{P_{amb}(z)}{T_{amb}(z)} dz}} \frac{RCS(\lambda_2,z)}{RCS(\lambda_1,z)} \quad (1)$$

where C_0=23.99 is the Raman lidar calibration constant, ρ_{air} is the atmospheric density, λ_1 = 387 nm and λ_2 = 407 nm, $c_{\lambda 1}$ = 1.1202 10^{-5} and $c_{\lambda 2}$ = 1.3942 10^{-5} the molecular extinction constants, z is the reference height, while range corrected signal (RCS) is the range-corrected background subtracted lidar signal at each channel, respectively (Freudenthaler et al., 2016).

The tropospheric water vapour profiles were also provided by the Copernicus site through the specific humidity product of ERA5, expressed at pressure levels in a hourly base (https://cds.climate.copernicus.eu/cdsapp#!/dataset/reanalysis-era5-pressure-levels?tab=overview).

Moreover, the P_{amb} and T_{amb}, as well as the ambient relative humidity (RH) vertical profiles, were also provided by ERA5 model and were used to estimate the ambient air density profile.

The C_0 value has been validated during the Hygroscopic Aerosols to Cloud Droplets (HygrA-CD) experimental campaign which took place in the Greater Athens Area (Papayannis et al., 2017; Labzovskii et al., 2018).

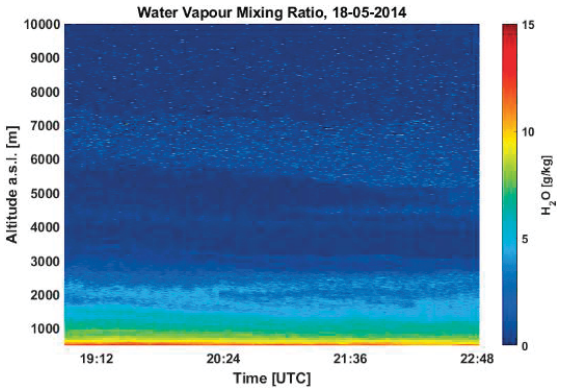

Fig. 1: The spatio-temporal evolution of water vapour mixing ratio (WVMR) as observed by the EOLE lidar on 18th May 2014 (19:08-20:37 UTC) over Athens, Greece.

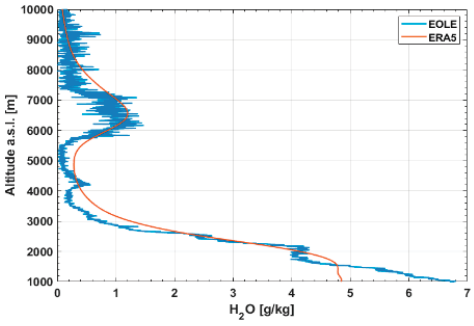

Fig. 2: The retrieved water vapour mixing ratio (WVMR) vertical profile by the EOLE lidar system for the 18 May 2014 (19:08-20:37 UTC) compared to ERA5 specific humidity profile (20:00 UTC), of the same day.

In this study, we will show how the use of ERA5 data can improve the retrieval algorithm of the

vertical profiles of water vapour mixing ratio (WVMR) including the profiles of P_{amb} and $T_{amb.}$

As an example we show the water vapour vertical profile (cf. Fig. 1) obtained over Athens by EOLE on the 18th May 2014 (19:08-22:48 UTC). The water vapour mixing ratio (WVMR) has been retrieved based on the Eq. 1. In this Figure we see a nearly dry water vapor layer between 3 and 5.5 km height. More humid air masses are observed below 2 km height, with even more humid layers inside the PBL height ranging from ground to 1.8 km height. Between between 5.5-7.5 km asl. a well-stratified humid layer is observed.

In Fig. 2 we present the water vapor profiles retrieved from both methods from 1 to 10 km height asl. In general, we observe a good agreement between the two methods, mainly over 1.5 km height. We observe within the PBL (below 1.8 km height) increased values of water vapour mixing ratio (WVMR) mainly over 5 gr/kg dry air, while between 6 and 8 km we observe a wet layer, which is linked to cirrus presence observed during the measurement.

In Fig. 3 we show the difference (%) of the vertical profile of the lidar-based water vapour mixing ratio (WVMR) on the 18th May 2014 (19:08-20:37 UTC) compared to the derived one from the ERA5 (20:00 UTC), in the height range 0.8-10 km (cf. color bar in Fig. 3).

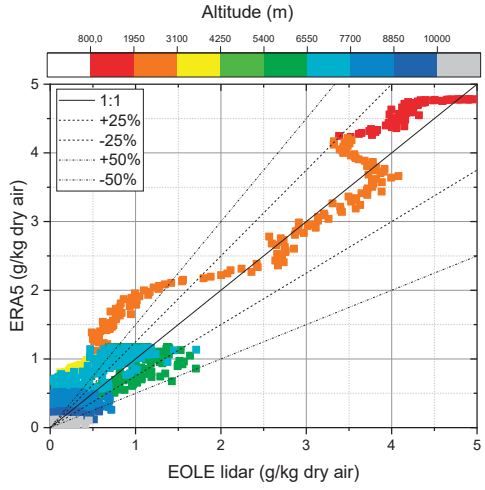

Fig. 3: The percentage difference of the lidar-based WVMR vertical profile on 18 May 2014 (19:08-20:37 UTC) compared to ERA5 specific humidity profile (20:00 UTC).

The percentage difference of the water vapour mixing ratio (WVMR) compared to ERA5 specific humidity profile presented in Fig. 3 showed that the difference remains below ±25% under 3 km height, while the best fit between the two methods is strongest for WVMRs ranging between 2.5 and 4 g/kg.

As a conclusion, we showed that both techniques are almost equivalent and are able to retrieve similar water vapor patterns, while the Raman lidar presents an additional of much higher spatio-temporal resolution against the ERA 5 assimilation model.

In future work, we are going to collect more case studies for further investigation on the performance of ERA5 against real measurements.

Acknowledgements

We acknowledge support by the project "PANhellenic infrastructure for Atmospheric Composition and climatE change" (MIS 5021516) which is implemented under the Action "Reinforcement of the Research and Innovation Infrastructure", funded by the Operational Programme "Competitiveness, Entrepreneurship and Innovation" (NSRF 2014-2020) and co-financed by Greece and the European Union (European Regional Development Fund).

References

Ambaum, M. H. P.: Water in the Atmosphere, in thermal physics of the atmosphere, pp. 93–107, John Wiley and Sons, Ltd., 2010.

Freudenthaler, V. About the effects of polarising optics on lidar signals and the Δ90 calibration. Atmos. Meas. Techn., 9, 4181‑4255. https://doi.org/10.5194/amt - 9 - 4181 - 2016.

Labzovskii, L. D., Papayannis, A., Binietoglou, I., Banks, R. F., Baldasano, J. M., Toanca, F., Tzanis, C. G. and Christodoulakis, J.: Relative humidity vertical profiling using lidar-based synergistic methods in the framework of the Hygra-CD campaign. Ann. Geophys, 36, 213–229, doi:10.5194/angeo-36-213-2018, 2018.

Papayannis, A., Argyrouli, A., Bougiatioti, A., Remoundaki, E., Vratolis, S., Nenes, A., Solomos, S., Komppula, M., Giannakaki, E., Kalogiros, J., Banks, R., Eleftheriadis, K., Mantas, E., Diapouli, E., Tzanis, C. G., Kazadzis, S., Binietoglou, I., Labzovskii, L., Vande Hey, J. and Zerefos, C. S.: From hygroscopic aerosols to cloud droplets: The HygrA-CD campaign in the Athens basin - An overview. Sci. Total Environ., 574, 216–233, doi:10.1016/j.scitotenv.2016.09.054, 2017.

Whiteman, D. N.: Examination of the traditional Raman lidar technique. II. Evaluating the ratios for water vapor and aerosols. Appl. Opt., 42, 2593-2608, doi:10.1364/ao.42.002593, 2003.

Long-term lidar measurements of Australian wildfire smoke layer in the stratosphere over southern South America in 2020-2021: Potential influence on ozone reduction?

K. Ohneiser[1], *A. Ansmann*[1], *B. Kaifler*[2], *A. Chudnovsky*[3], *B. Barja*[4], *H. Baars*[1], *P. Seifert*[1], *C. Jimenez*[1], *M. Radenz*[1], *R. Engelmann*[1]

ohneiser@tropos.de

(1) Leibniz Institute for Tropospheric Research, Leipzig, Germany

(2) Deutsches Zentrum für Luft- und Raumfahrt, Institut für Physik der Atmosphäre, Oberpfaffenhofen, Germany

(3) Tel Aviv University, Porter School of Earth Sciences and Environment, Tel Aviv, Israel

(4) Atmospheric Research Laboratory, University of Magallanes, Punta Arenas, Chile

Introduction

Record-breaking wildfires with an unprecedentedly strong pyroconvection series were raging in Australia in late December 2019 and early January 2020. These fires injected never observed amounts of biomass burning smoke into the stratosphere (Kablick et al., GRL, 2020; Khaykin et al., Nature, 2020; Ohneiser et al., ACP, 2020). We show multiwavelength polarization Raman lidar measurements performed at Punta Arenas (53.2°S, 70.9°W), Chile, at the southernmost tip of South America, over 18 months from January 2020 to June 2021. The decay of the stratospheric perturbation is discussed based on optical properties such as the smoke extinction coefficient, optical thickness, Ångström exponent, extinction-to-backscatter ratio (lidar ratio), and particle linear depolarization ratio as well as the smoke fraction and layer geometrical properties (top and base heights). The maximum smoke optical thickness was almost two orders of magnitude above stratospheric background level. Lidar ratios of 69sr, 91sr, and 120sr were obtained at 355nm, 532nm, and 1064nm, respectively.

During the decay phase of the stratospheric aerosol perturbation a record-breaking ozone hole occurred in the southern hemispheric spring of 2020. We will discuss the potential link between the smoke and the strong ozone depletion based on our long-term smoke observations and ozone profiles downloaded from the NDACC network web page (NDACC, 2021).

Results and discussion

Lidar observations in Punta Arenas (53.2°S, 70.9°W; 9m above sea level, a.s.l.), Chile, were conducted in the framework of the long-term DACAPO-PESO (Dynamics, Aerosol, Cloud And Precipitation Observations in the Pristine Environment of the Southern Ocean) campaign lasting from November 2018 to the end of 2021 (Radenz et al., ACPD, 2021). A multiwavelength polarization Raman lidar (Polly-XT, Engelmann et al., AMT 2016) was run continuously (with some short irregular measurement gaps) at the University of Magallanes (UMAG) in Punta Arenas and observed the upper tropospheric and lower stratospheric (UTLS) biomass burning smoke layer originating from the strong Australian bushfires since January 2020.

Results in Fig. 1 provide an overview of the lidar measurements of the UTLS smoke layer over southern South America. The first smoke plumes arrived at Punta Arenas on 5 Jan 2020. Initial smoke layers were optically thick and showed ascending features. After some months, smoke layers appeared blurrier and were usually found between 7-26 km height. UTLS layer mean extinction coefficients decreased exponentially with time.

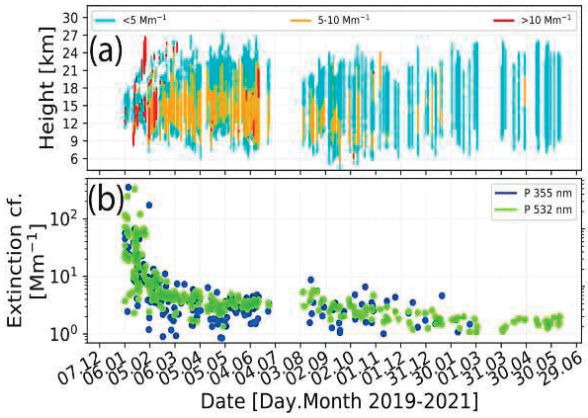

Figure 1. (a) Overview of Polly lidar observations of UTLS smoke layers (colored bars from bottom to top, one bar per day) from January 2020 to June 2021. The colors in each bar indicate different extinction coefficient levels (see legend in the panel). (b) Layer mean 355 and 532 nm particle extinction coefficient (layer mean particle backscatter coefficient values multiplied by a lidar ratio of 60sr and 95sr).

Figure 2 provides an impression of the ozone conditions over the southern part of the southern hemisphere. The shown deviation of the ozone partial pressure from the long-term mean is strongly negative in spring 2020 (especially in October 2020). The record-breaking ozone depletion occurred in the smoke layer. Base (grey) and top

(black) heights of the smoke layer are indicated in Figure 2.

There are two pathways to influence ozone depletion by aerosol pollution. The smoke particles can influence the nucleation of particles of polar stratospheric clouds (PSCs) and therefore the number and size of the PSC particles (and particle surface area concentration available for heterogeneous chemical reactions). PSCs are a major factor in chlorine activation and ozone depletion. Furthermore, the smoke particles can be directly involved in heterogeneous chemical processes that convert nonreactive chlorine components into reactive forms. Lidar is able to provide valuable information on the optical and microphysical characteristics of these smoke layers (Ansmann, et al., 2020) in which strong ozone depletion was found.

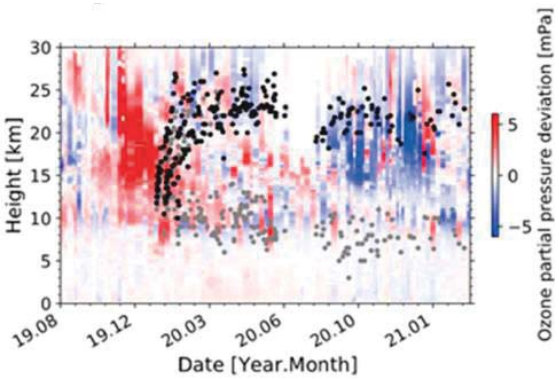

Figure 2. Ozone partial pressure deviation (with respect to 2000-2020) at Neumayer (data from NDACC (2021)) with smoke layer boundary data from Punta Arenas lidar. The gray dots show the smoke layer bottom, the black dots show the smoke layer top.

Figure 3 shows these microphysical characteristics of the smoke layers above Punta Arenas in terms of estimated surface area (SA) concentration using the retrieval method in Ansmann et al. (ACPD, 2020). Between approximately 8 and 25 km clearly increased SA conc. values were found in the range between 0.3 and 8.0 µm-2 cm3. In the same height range negative relative ozone partial pressure deviations were found at all heights. The data shown are averaged ozone sonde data of Lauder, Neumayer, and South Pole (NDACC, 2021) between September 2020 and November 2020 with respect to the mean values of September to November between 2000-2020. Especially between 14 and 22 km height the negative deviations were in the range between 15 and 25%. To what extent the enhanced Australian smoke aerosol burden influenced the record-breaking southern hemispheric ozone hole will have to be further investigated. Sophisticated lab studies and modelling efforts are needed to clarify the detailed influence of the organic wildfire particles on ozone depletion.

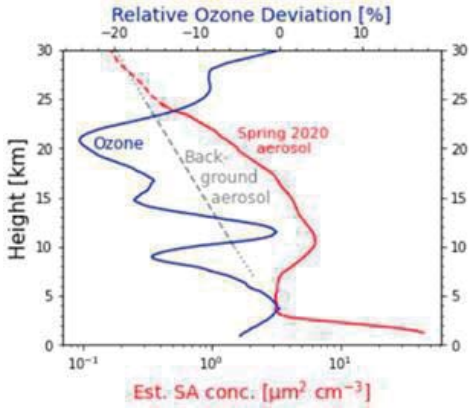

Figure 3. Blue: Ozone partial pressure relative deviation September to November 2020 (with respect to 2000-2020) at Neumayer (data from NDACC (2021)). Red: Estimated surface area (SA) concentration of the biomass burning aerosol between August and November 2020. Gray: Estimated surface area (SA) concentration of the background aerosol 1996-2008 found in Sakai 2016.

References

Ansmann et al., Tropospheric and stratospheric wildfire smoke profiling with lidar: mass, surface area, CCN, and INP retrieval, *Atmos. Chem. Phys*., 21, 9779–9807, 2021.

Engelmann et al., The automated multiwavelength Raman polarization and water-vapor lidar PollyXT: the neXT generation, *Atmos. Meas. Tech*., 9, 1767–1784, 2016.

Kablick et al., Australian PyroCb Smoke Generates Synoptic-Scale Stratospheric Anticyclones, *Geophysical Research Letters*, 47, e2020GL088101, 2020.

Khaykin et al., The 2019/20 Australian wildfires generated a persistent smoke-charged vortex rising up to 35 km altitude, *Commun Earth Environ* 1, 22, 2020.

NDACC, Network for the Detection of Atmospheric Composition Change, available at: http://www.ndaccdemo.org/, last access: 29 June, 2021.

Ohneiser et al., Smoke of extreme Australian bushfires observed in the stratosphere over Punta Arenas, Chile, in January 2020: optical thickness, lidar ratios, and depolarization ratios at 355 and 532 nm, *Atmos. Chem. Phys.*, 20, 8003–8015, 2020.

Radenz et al., Hemispheric contrasts in ice formation in stratiform mixed-phase clouds: Disentangling the role of aerosol and dynamics with ground-based remote sensing, *Atmos. Chem. Phys. Discuss*., in review, 2021.

Sakai et al., Long-term variation of stratospheric aerosols observed with lidars over Tsukuba, Japan, from 1982 and Lauder, New Zealand, from 1992 to 2015, *J. Geoph. Research: Atmospheres*, 121, 10,283–10,293, 2016.

First Results on the Aeolus L2A Validation During ASKOS Campaign

***P. Paschou*[1,2], *N. Siomos*[1,2], *G. Georgoussis*[3], *E. Marinou*[1], *A. Gkikas*[1], *V. Freudenthaler*[4], *J. Von Bismarck*[5], *Thorsten Fehr*[6] *and V. Amiridis*[1]**

pepaschou@noa.gr

(1) National Observatory of Athens, Athens, Greece

(2) Aristotle University of Thessaloniki, Thessaloniki, Greece

(3) Raymetrics S.A., Athens Greece

(4) Ludwig Maximilians University, Munich, Germany

(5) European Space Agency (ESA-ESRIN), Frascati, Italy

(6) European Space Agency (ESA-ESTEC), Noordwijk, The Netherlands

Introduction

Aeolus constitutes a core satellite mission of the European Space Agency (ESA) Earth Explorers, flying in a polar orbit since August 2018 (Reitebuch, 2012). The only payload onboard the platform is the Atmospheric Laser Doppler Instrument (ALADIN), a Doppler Wind Lidar (Lolli et al., 2013) providing vertical profiles of the Horizontal Line-of-Sight (HLOS) wind component at global scale (Stoffelen et al., 2006). ALADIN is also a High Spectral Resolution Lidar (Shipley et al., 1983) that provides as Level-2A (L2A) products the particle backscatter coefficient, the particle extinction coefficient and backscatter-to-extinction ratio (Flamant et al., 2007, 2008). The system emits circularly polarised light at 355 nm, 35o off nadir in a transceiver configuration and detects only the co-polar component of the backscattered lidar signal (Flamant et al., 2007). When the undetected cross-polar component of the backscattered signal is not negligible under the presence of depolarising non-spherical particles such as volcanic ash, desert dust, or stratospheric smoke (Ansmann et al., 2010; Freudenthaler et al., 2009; Gialitaki et al., 2020), the measured particle backscatter coefficient from Aeolus is underestimated (Flamant et al., 2007). A first attempt to assess the performance of Aeolus and validate the L2A products will take place in the framework of the forthcoming ASKOS campaign (https://askos.space.noa.gr/). ASKOS is an Aeolus calibration and validation (Cal/Val) tropical campaign which is held on Mindelo, Cape Verde between 2021 to 2022 with 3 intense phases on July and September 2021 and May/June 2022.

The ground-based lidar

The ground based lidar system that will be used in the ASKOS campaign as reference for the Aeolus L2A products is a novel polarisation lidar system, the Enhancement and Validation of ESA products (eVe) lidar system (Figure 1). The eVe lidar is a combined linear/circular polarisation lidar system with Raman and scanning capabilities that utilises a dual-laser/dual-telescope configuration. This dual configuration enables the system to mimic the performance of both ALADIN and the polarisation lidar systems with linearly polarised emission.

Two Nd-Yag lasers are used for the interleaved emission of linearly and circularly polarised light at 355 nm with a repetition rate of 20 Hz for each laser. In the receiver unit, the backscattered signals are collected from two Dall-Kirkham type telescopes. At the first telescope, the collected elastically backscattered signal from the linearly polarised emission is optically separated with a linear polarisation analyser in parallel and cross polarised components which are measured in two channels. An additional channel is deployed for the interleaved detection of the inelastic backscattering at 387 nm from both linearly and circularly polarised emission. At the second telescope, the collected elastically backscattered signal from the circularly polarised emission is optically separated with a circular polarisation analyser in co- and cross-polar polarised components which are measured in two channels. Thus, the system retrieves the particle backscatter and extinction coefficients from linear and circular emission, the volume and particle linear depolarisation ratios, and the volume and particle circular depolarisation ratios at 355 nm.

Figure 1. The eVe lidar

The system was developed to support Aeolus Cal/Val via the acquisition of well characterized reference measurements of particles (aerosol and cloud particles) optical properties from ground. In

Figure 2, a first attempt to validate the Aeolus backscatter coefficient against the eVe lidar is presented as an example. The collocated measurement was performed on 1st July 2020 when Aeolus flew near Athens (~85 km northwest from the eVe position). The presented Aeolus profile of the particle backscatter coefficient and its error was retrieved using the standard correct algorithm (Flamant et al., 2007). The retrieved eVe profile of particle backscatter coefficient using the circularly polarised emission was converted to the profile that the Aeolus would measure from ground (Mimic Aeolus) in order to be comparable with the Aeolus profile. The two days backward trajectories analysis (not shown here) indicate that different air masses were sampled by the two systems highlighting the need of eVe measurements closer to the Aeolus overpass.

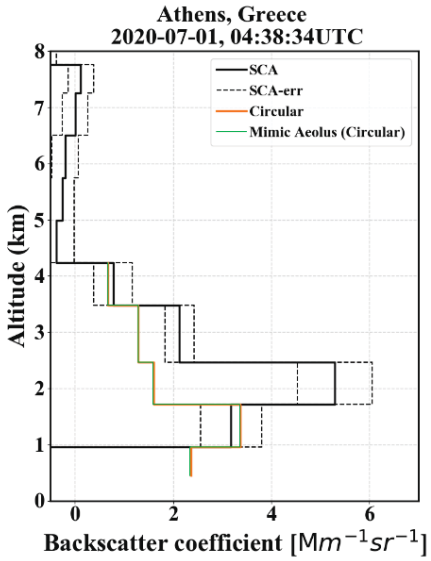

Figure 2. Profiles of the particle backscatter coefficients retrieved from Aeolus (black) and eVe lidar (green and orange) on 01-07-2020 over Athens.The eVe profiles were retrieved using the Klett inversion method and the assumed aerosol-free reference height was selected at 4 km. After the inversion the eVe profiles were resampled with the Aeolus vertical resolution.

Methodology

During the ASKOS campaign the eVe lidar will be located in Mindelo, Cape Verde and it will perform collocated measurements with Aeolus every Friday afternoon during the closest Aeolus overpass over the site (~5 km). The measurement angle of the eVe lidar will be 35° off-zenith and the measurement interval will be 1.5 hour before and after the overpass time in order to fulfil the Cal/Val requirements for the L2A products. First results from this comparison will be presented in the ELC conference.

Acknowledgements

eVe lidar was developed under an ESA project (No. 4000127438/19/I-BG) by Raymetrics S.A. in collaboration with the National Observatory of Athens and the Ludwig-Maximilians University. The work is supported by the European Space Agency project ASKOS (4000131861/20/NL/IA); the European Research Council under the European Community's Horizon 2020 research and innovation frame-work program/ERC Grant Agreement 725698 (D-TECT); the project "PANhellenic infrastructure for Atmospheric Composition and climatE change" (MIS 5021516), implemented under the Action "Reinforcement of the Research and Innovation Infrastructure", funded by the Operational Programme "Competitiveness, Entrepreneurship and Innovation" (NSRF 2014-2020) and co-financed by Greece and the European Union (Euro-pean Regional Development Fund), and the Stavros Niarchos Foundation.

References

Ansmann et al., The 16 April 2010 major volcanic ash plume over central Europe: EARLINET lidar and AERONET photometer observations at Leipzig and Munich, Germany, Geophys. Res. Lett., 37 (13), 2010.

Flamant et al., ADM-Aeolus L2A Algorithm Theoretical Baseline Document, [online] Available from: https://earth.esa.int/pi/esa?type=file&table=aotarget&cmd=image&alias=Aeolus_L2A_Algorithm_TBD, 2007.

Flamant et al., ADM-Aeolus retrieval algorithms for aerosol and cloud products, Tellus A, 60 (2), 273–288, 2008.

Freudenthaler et al., Depolarization ratio profiling at several wavelengths in pure Saharan dust during SAMUM 2006, Tellus B, 61 (1), 165–179, 2009.

Gialitaki et al., Is the near-spherical shape the "new black" for smoke?, Atmos. Chem. Phys., 20 (22), 2020.

Lolli et al., 0.355-micrometer direct detection wind lidar under testing during a field campaign in consideration of ESA's ADM-Aeolus mission, Atmos. Meas. Tech., 6(12), 3349–3358, 2013.

Reitebuch, The Spaceborne Wind Lidar Mission ADM-Aeolus, edited by U. Schumann, pp. 815–827, Springer Berlin Heidelberg, Berlin, Heidelberg., 2012.

Shipley et al., High spectral resolution lidar to measure optical scattering properties of atmospheric aerosols 1: Theory and instrumentation, Appl. Opt., 22(23), 3716, 1983.

Stoffelen et al., ADM-Aeolus Doppler wind lidar Observing System Simulation Experiment, Q. J. R. Meteorol. Soc., 132(619), 1927–1947, 2006.

Optical properties of fresh smoke: a case study from PANGEA observatory

A. Gialitaki[1,2], A. Tsekeri[1], A. Kampouri[1,3], M. Tsichla[1,4], I. Tsikoudi[1,5], E. Marinou[1], V. Amiridis[1] and D. Balis[2]
Contact: togialitaki@noa.gr
(1) National Observatory of Athens, Athens, Greece
(2) Laboratory of Atmospheric Physics, Aristotle University of Thessaloniki, Thessaloniki, Greece
(3) Department of Meteorology and Climatology, School of Geology, Aristotle University of Thessaloniki, Thessaloniki, Greece
(4) Department of Environmental Physics and Meteorology, National and Kapodistrian of Athens, Athens, Greece
(5) Environmental Chemical Processes Laboratory, Department of Chemistry, University of Crete, Heraklion, Greece

Introduction

Biomass burning particles tend to alter their properties significantly as they evolve with time in the atmoshere. This particularity originates from their hydrophylic nature, as the complex shaped soot aggregates originally emitted, gather weakly absording materials around them (i.e. sulfates) during what we call atmospheric aging. The coatings formed onto the particles modify their shape and composition and subsequently their optical properties (i.e. Amiridis et al. 2009, Ishimoto et al., 2019). A property that is mostly sensitive to the particle morphhology is the particle linear depolarization ratio (PLDR) which can be measured by a polarization lidar. However, ground-based lidar measurements are usually performed away from the fire source and correspond to aged smoke, which has been observed to differentiate from freshly emitted smoke in terms of PLDR (i.e. Burton et al., 2012). This finding is also supported by scattering models simulating smoke optical properties (Ishimoto et al., 2019). What is more, multiwavength polarization lidar measurements for smoke were not so frequently reported in lidar literature up to recently. Thus, the investigation on smoke PLDR spectral dependence is still a subject of fruitfull discussion.

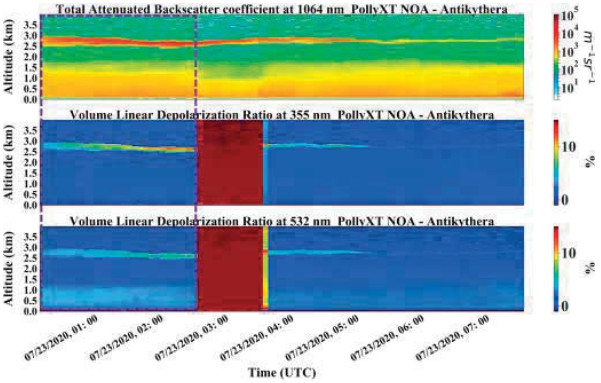

Figure 1. Time-height displays of the (a) attenuated backscatter coefficient at 1064nm, (b) volume linear depolarization ratio at 355nm and (c) at 532nm on 23 July, 2020. Measurement gap during 02:35 – 02:45 UTC corresponds to the time interval used for the Δ90 depolarization calibration (Freudenthaler, 2016).

Herein, we present a case study of freshly emitted (less than a day old) smoke originating from wildfires in the area of Korinth (37.85N, 22.93E, Peloponesse, Greece), and measured with the PollyXT-NOA multi-wavelength polarization lidar in PANGEA observatory (Antikythera; 35.86N, 23.31E, 193m a.s.l.). Over the course of two days, optically thick smoke layers were observed between 2 and 3km above the station (Fig. 1). Trajectory analysis and atmosheric models (Fig. 2) indicate that below 4km there is no contribution of known depolarizing aerosols (i.e. dust particles), and yet PLDR values exceed 13% at 355nm for the fresh smoke layer, while there is a steep decrease towards 532nm.

Optical properties

To derive the smoke optical properties lidar profiles were averaged between 00:00 and 02:30UTC. During this time a distinct smoke layer was located between 2.5 and 3km above Antikythera station as shown in Fig.1. The bottom and top smoke layer heights were determined from the gradient of the particle backscatter coefficient at 1064nm. Lidar profiles are shown in Fig. 3 and the layer-integrated mean values of smoke intensive optical properties in Table 1.

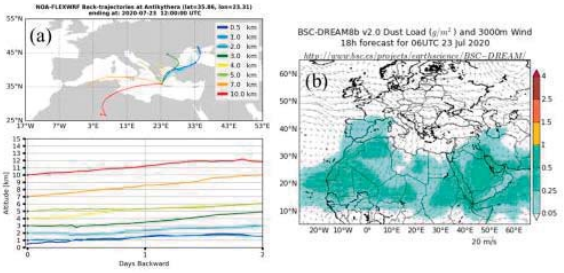

Figure 2. (a) 2-day Backward trajectory analysis for the air masses above Antikythera and (b) dust load from BSC-DREAM model on 23 July, 2020.

Results and Discussion

The lidar ratio (S) varies between ~80-109sr at 355nm and between ~65-89sr at 532nm, indicating the absording nature of the particles. This has already been observed in the past for fresh smoke, while the opposite behavior is reported for aged smoke (i.e. Burton et al., 2012; Illingworth et al., 2015). The large Angstrom exponent values could

be also characterized as typical for smoke particles which are expected to be quite small.

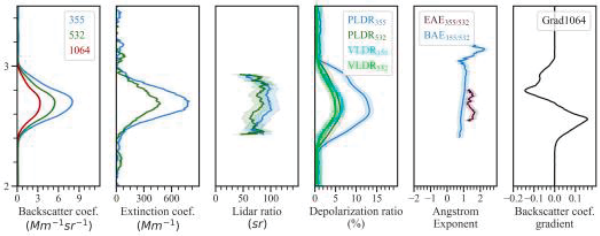

Figure 3. Lidar profiles of (left to right) particle backscatter and particle extinction coefficient, lidar ratio (S), PLDR, Angstrom exponent and gradient of particle backscatter coefficient at 1064nm.

Table 1. Lidar derived optical properties for the layer between 2.5 and 3km.

	Mean value ± standard deviation (max value)
S_{355} (sr)	94.5 ± 14.2
S_{532} (sr)	76.9 ± 11.6
$PLDR_{355}$ (%)	12.3 ± 0.01 (13.7)
$PLDR_{532}$ (%)	5.9 ± 0.1 (6.5)
Ang. exp.	1.45 ± 0.05

The key finding of our analysis lies in PLDR values: while at 532nm PLDR does not exceed 7%, at 355nm it reaches almost 14%. The latter is already large, in terms of absolute values, compared to what is usually observed for smoke in the lower troposphere. Recent findings utilizing multiwavelenght polarization lidar measurements have shown that PLDR of smoke particles found in the upper troposphere/lower stratosphere (UTLS) may reach up to ~25% and ~20% at 355 and 532nm respectively, and thus exhibiting a noticeable spectral dependence (Haarig et al., 2018; Hu et al., 2019; Gialitaki et al., 2020; Ohneiser et al., 2020). In our case the decrease in PLDR is more prominent with the increasing wavelength, and to the best of our knowledge, has not been reported before for smoke found in the lower troposphere.

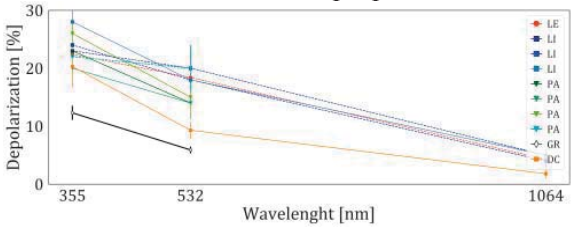

Figure 4. PLDR spectral dependence for recent case studies found in the literature.

Figure 4 presents an overview of multi-wavelength PLDR measurements from Leipzig (LE; Canadian stratospheric smoke), Lille (LI; Canadian stratospheric smoke), Punta Arenas (PA; Australian stratospheric smoke), PANGEA observatory (GR; Peloponnese lower tropospheric smoke) and airborne lidar measurements above Denver, Colorado (DC; Canadian upper tropospheric smoke). The spectral dependence of PLDR for the case of GR is more closely resembling those of DC and of PA. This may be related to the type of burning material (PA and GR) or the fact that smoke is found in the troposphere (DC and GR) and is part of our ongoing research.

Acknowledgements

This research was supported by data and services obtained from the PANhellenic Geophysical Observatory of Antikythera (PANGEA) of the National Observatory of Athens (NOA). We acnowledge support from the ERC Grand D-TECT (Grant Agreement 725698), the PANACEA project (MIS 5021516), and the Stavros Niarchos Foundation.

References

Amiridis et al., Optical characteristics of biomass burning aerosols over Southeastern Europe determined from UV-Raman lidar measurements, Atmos. Chem. Phys., 9, 2431–2440, 2009.

Burton et al., Aerosol classification using airborne High Spectral Resolution Lidar measurements – methodology and examples, Atmos. Meas. Tech., 5, 73–98, 2012.

Freudenthaler, About the effects of polarising optics on lidar signals and the Δ90 calibration, Atmos. Meas. Tech., 9, 4181–4255, 2016.

Gialitaki, A., et al.: Is the near-spherical shape the "new black" for smoke?, Atmos. Chem. Phys., 20, 14005–14021, 2020.

Haarig et al., Depolarization and lidar ratios at 355, 532, and 1064 nm and microphysical properties of aged tropospheric and stratospheric Canadian wildfire smoke, *Atmos. Chem. Phys., 18, 11847–11861, 2018.*

Hu et al., Long-range-transported Canadian smoke plumes in the lower stratosphere over northern France, Atmos. Chem. Phys., 19, 1173–1193, 2019.

Illingworth et al., The earthcare satellite: The next step forward in global measurements of clouds, aerosols, precipitation, and radiation, Bulletin of the American Meteorological Society, 96 (8), pp. 1311-1332, 2015.

Ishimoto et al., A shape model of internally mixed soot particles derived from artificial surface tension, Atmos. Meas. Tech., 12, 107–118, 2019.

Ohneiser et al., Smoke of extreme Australian bushfires observed in the stratosphere over Punta Arenas, Chile, in January 2020: optical thickness, lidar ratios, and depolarization ratios at 355 and 532 nm, Atmos. Chem. Phys., 20, 8003–8015, 2020.

Evaluation of the AEOLUS L2A Aerosol Product over Europe using ground based lidar data from EARLINET

N. Siomos[1,2], A.Gkikas[1], H. Baars[2], U. Wandinger[2], V. Amiridis[1], P. Paschou[1], and the EARLINET consortium

nsiomos@noa.gr
(1) IAASARS, National Observatory of Athens, Athens, Greece
(2) Leibniz Institute for Tropospheric Research, Leipzig, Germany

Introduction

In this study, we identify systematic and statistical uncertainties in the L2A aerosol product of the AEOLUS satellite. AEOLUS, a core mission of the European Space Agency, was launched on August 2018 and is operating since in a polar orbit (Reitebuch et al., 2012). The system is capable of measuring aerosol optical properties such as the co-polar backscatter and the extinction coefficient profiles (Flamant et al., 2008). Prior to launch, ESA encouraged multiple networks to contribute to the validation of the satellite products (Straume et al., 2019). The European Aerosol Research Lidar Network (EARLINET) (Papalardo et al., 2004), part the European Research Infrastructure for the observation of Aerosol, Clouds and Trace Gases (ACTRIS) that numbers 29 active European lidar stations, actively participated in the Cal/Val activities since the beginning of the mission. The collected lidar profiles have been analyzed in order to quantify the discrepancies between AEOLUS and the European ground based systems.

Methodology

While AEOLUS was launched in 2018, the timeseries deployed here covers the period 06/2019 - 05/2021 that correspond to the best available versions of the satellite L2A processing algorithms (baseline 10 and baseline 11 products).
We harvest the collocations using the following spacio-temporal criteria. Only overpasses that fall within a radius less than 100km around the station are included. To isolate collocated data we reject all AEOLUS data with a time interval between the overpass and the central time of the ground-based measurement that is greater than 3 hours. Furthermore, we handle multiple AEOLUS profiles within the overpass as follows. The closest overpass (Clo) is identified as the AEOLUS profiles closest to the station. The average overpass (Avg) is also calculated by averaging all available AEOLUS profiles. Moreover, the EARLINET data are also re-scaled to match the AEOLUS bins. This conversion is performed case-wise as the altitude limits of each bin slightly change per profile.
AEOLUS L2A products include the aerosol extinction and co-polar backscatter coefficient profiles at 355nm from circularly polarized light emission. While the extinction profiles are directly comparable with the ground-based lidars, this is not the case for the backscatter profiles since AEOLUS cannot measure the cross polar component of the aerosol backscatter (Flamant et al., 2008). The co-polar backscatter is close to the total backscatter only in the absence of highly depolarizing scatterers such as dust, pollen, volcanic ash, and cirrus ice crystals. Ground-based measurements are divided in two categories for the evaluation depending on whether aerosol depolarization measurements have been performed. If the particle linear depolarization ratio (PLDR) is available, it can be applied to convert the lidar total backscatter to an AOLUS-like co-polar backscatter coefficient. This category is applied for the direct evaluation of the satellite product, the number of such data is however limited as the majority of the EARLINET stations do not perform PLDR measurements at 355nm. Cases that lack PLDR information assist to quantify the uncertainties introduced by using the AEOLUS co-polar backscatter as a substitute for the total backscatter.
The optical profiles calculated from the Standard Correct Aglorithm (SCA) come in two different vertical scales. The Rayleigh bin scale (Ray Bin) maintains the original bins of the Rayleigh channels. The middle bin scale is designed to compensate an error propagation in the extinction. The products are derived from the average over two vertical bins. The value is affected to a mid-bin ranging from the middle of the upper bin to the middle of the lower one (Stieglitz et al., 2020).

Results and discussion

In the analysis below we will have focused on the backscatter product. The comparison between the co-polar backscatter values of EARLINET and AEOLUS is presented in Fig. 1. More information is summarized in Tables 1 and 2. Apart from the correlation coefficients, statistical metrics of the bias distribution (AEOLUS – EARLINET) of the total and co-polar backscatter profiles are included in two atmospheric region, below 2km (near

range) and above 2km (far range). The correlation generally increases when switching to the co-polar backscatter but the number of bins decreases due to the lower data availability. Higher values are observed for the Mid rather than the Ray Bin products and also for the closest rather than the average overpass. Absolute mean biases are generally below 0.6 Mm^{-1} sr^{-1}. Bias spread (standard deviation) values are lower for the Mid rather than the Ray bin product. In addition, the bias spread is generally larger in the near range.

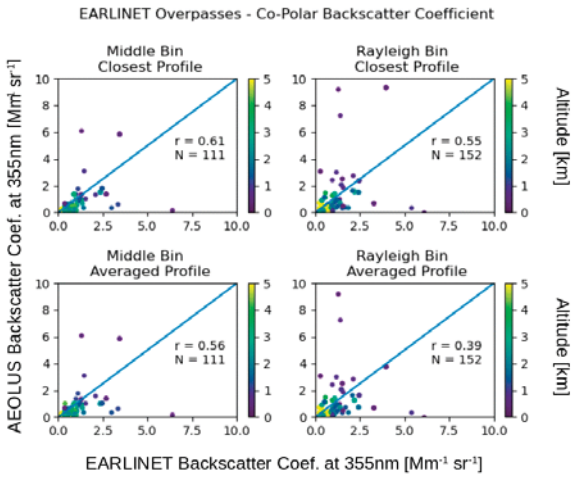

Figure 1. Scatterplot of the EARLINET total vs AEOLUS co-polar backscatter values per vertical bin. The total number of bins (N) and Person's r are also displayed.

Table 1. EARLINET vs AEOLUS bin wise comparison – Backscatter Coefficient

Product	μ nr	σ nr	μ fr	σ fr	r
Mid Bin Clo	0.04	1.59	-0.08	0.37	0.49
Mid Bin Avg	0.01	1.61	-0.09	0.40	0.46
Ray Bin Clo	-0.30	2.30	-0.18	0.52	0.47
Ray Bin Avg	-0.55	2.04	-0.20	0.51	0.41

[a] Where **μ** is the mean bias, **σ** the standard deviation, and **r** the Pearson's r, while **nr** and **fr** stand for near (<2km) and far range (>2km), respectively.

Table 2. EARLINET vs AEOLUS bin wise comparison – Co-polar Backscatter Coefficient

Product	μ nr	σ nr	μ fr	σ fr	r
Mid Bin Clo	-0.04	1.74	-0.27	0.36	0.61
Mid Bin Avg	-0.15	1.79	-0.33	0.42	0.56
Ray Bin Clo	0.02	2.58	-0.32	0.44	0.55
Ray Bin Avg	0.57	2.00	-0.34	0.45	0.39

[a] Where **μ** is the mean bias, **σ** the standard deviation, and **r** the Pearson's r, while **nr** and **fr** stand for near (<2km) and far range (>2km), respectively.

Challenges and future Work

An underestimation when using the total EARLINET backscatter is visible only for the Rayleigh bin products. When switching to the co-polar backscatter there is no unanimous improvement for all four products. The reduced number of bins certainly affects the co-polar metrics. Enriching the current dataset is rather important for the statistical analysis. AEOLUS overpass measurements are still ongoing within EARLINET so the representativity of these metrics is expected to improve in the future.

In addition, most EARLINET stations are located in European urban areas, where highly depolarizing aerosols are rare with the exception of transported events. In the future we will apply an aerosol classification scheme to isolate dust cases. by utilizing both the lidar PLDR and also sunphotometer fine mode fraction measurements when they are available. A total against co-polar backscatter comparison for dust cases will give us a clearer image of the decree of systematic biases introduced due to AEOLUS relying on the co-polar instead of the total aerosol backscatter coefficient.

Acknowledgements

The work is supported by the European Space Agency project ASKOS (4000131861/20/NL/IA); the European Research Council under the European Community's Horizon 2020 research and innovation frame-work program/ERC Grant Agreement 725698 (D-TECT); the European Union's Horizon 2020 research and innovation programme under grant agreement No 654109 and previously from the European Union Seventh Framework Programme (FP7/2007-2013) under grant agreement n° 262254. The authors acknowledge EARLINET for providing aerosol LIDAR profiles available at https://data.earlinet.org.

References

Flamant P., et al., ADM-Aeolus retrieval algorithms for aerosol and cloud products, Tellus A, 60(2), 273–288, doi:10.1111/j.1600-0870.2007.00287.x, 2008.

Pappalardo G., et al., EARLINET: towards an advanced sustainable European aerosol lidar network, Atmos. Meas. Tech., 7, 2389–2409, https://doi.org/10.5194/amt-7-2389-2014, 2014.

Reitebuch, The Spaceborne Wind Lidar Mission ADM-Aeolus, edited by U. Schumann, pp. 815–827, Springer Berlin Heidelberg, Berlin, Heidelberg., 2012

Stieglitz, H., et al. L2A user guide, Aeolus Data Innovation Science Cluster, DISC, 2020

Straume, A. G., et al., Aeolus Scientific Calibration and Validation Implementation Plan, 2019

Identification and tracking of a desert dust plume detected at Ny-Ålesund, Svalbard

*S. **Herrero-Anta**[1], D. Mateos[1], R. Román[1], D. González-Fernández[1], C. Toledano[1], R. González[1], V. E. Cachorro[1], A. Calle[1], Ángel M. de Frutos[1]*

sara@goa.uva.es

(1) Grupo de Óptica Atmosférica, Departamento de Física Teórica, Atómica y Óptica, Facultad de Ciencias, Universidad de Valladolid, Paseo Belén 7, 47011 Valladolid, Spain

Introduction

Atmospheric aerosols consist of small solid or liquid particles floating in the air. Public analysis released by the Intergovernmental Panel on Climate Change (IPCC) point out that, nowadays, atmospheric aerosols are the biggest source of uncertainty in the assessment of Climate Change. In addition, the presence of aerosols in polar regions could possibly be more significant due to the extreme sensibility presented by these regions to external changes.

Polar regions, in addition, represent a difficult area to be monitored because of the high reflectance of the surface, but also due to the difficult access to these remote places.

In this context, lidar instrumentation can provide a strong support to aerosol analysis and characterization. The vertically-resolved data provided by lidar technology determine the vertical distribution of aerosols, along with some of their properties. In addition, lidar is capable to provide data also during polar night, when other instruments like sun-photometers cannot take measurements. Hence, the aim of this work is to use lidar instrumentation to detect aerosol plumes in polar regions and to identify their origin.

Results and discussion

In the case of study of this work, several types of lidar instruments were employed to assess the presence of an aerosol plume in the super-site of Ny-Ålesund (78.92ºN, 11.92ºE), Svalbard, in the Norwegian region of the Arctic Circle. The different types of lidar employed in the study included two ground-based instruments: a multi-wavelength Raman lidar (KARL) and a Multi-Pulse Lidar (MPL). In addition, Cloud-Aerosol LIdar with Orthogonal Polarization (CALIOP), onboard the CALIPSO satellite, has also been used.

The backscatter signal provided by these instruments (at 532 nm for the MPL, 532 and 1064 nm for CALIOP, and 355 nm in addition to these two wavelengths for KARL) supplied information about the vertical profile of the atmosphere. Also, the study of the depolarization of the backscattered laser beam and the color ratio allowed to retrieve some properties of the aerosols suspended in the atmosphere.

Finally, the lidar CALIOP was employed in conjunction with the airmass trajectory model HYSPLIT (Hybrid Single-Particle Lagrangian Integrated Trajectory model) to identify the possible origin of the detected aerosol plume. Because CALIOP is on board a satellite platform, it was possible to follow the aerosol plume trajectory along the globe.

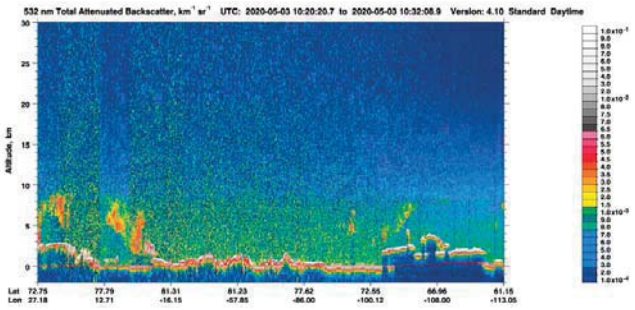

Figure 1. Backscatter profile at 532 nm from CALIOP lidar the 3rd of May 2020.

An aerosol outbreak was initially detected with a sun-photometer belonging to the Aerosol Robotic Network (AERONET), which registered an unusual load of aerosol in the atmosphere on the 3rd and 5th of May 2020.

Data collected from ground-based instruments (MPL and KARL) showed that the aerosol outbreak took place at about 8-9 km asl. This information was in line with the information provided by CALIOP (see Figure 1). The study of the depolarization and the color ratio indicated that the aerosol was composed mainly of non-spherical big particles.

Then, the combination of the HYSPLIT model with the observations taken from CALIOP traced the aerosol origin back to the Gobi and Taklamakan deserts. Hence, the present case of study has, as source area, the tropical parts of the Earth.

Challenges

Lidar technology can be used to retrieve aerosol properties also in the North Pole and to identify its origin. Moreover, the good correlation between different instruments was tested throughout this study.

This work shows the effectiveness of lidar instruments in the study of atmospheric aerosols. Then, the implementation of this kind of instrument around the globe or on board satellites would represent an improvement in the study of aerosols. For a better understanding about the properties of aerosols, more aerosol plumes should be monitored to stablish typical values for different parameters retrieved by lidars.

Acknowledgements

The authors acknowledge the “Ministerio de Ciencia, Innovación e Universidades” the support obtained with the ePOLAAR (RTI2018-097864-B-I00) project, and the “Junta de Castilla y León” for the AEROCyL (VA227P20) project. The authors also acknowledged the contributions from C. Ritter, R. Neuber and the staff from AWIPEV station in Ny-Ålesund.

Monitoring and characterization of clouds and aerosols in real homogeneous and dust-induced cloud nucleation scenarios

C. V. Carvajal-Pérez[1], *C. Córdoba-Jabonero*[1], *M.-Á. López-Cayuela*[1], *M.-P. Zorzano*[2], *M. Sicard*[3,4]
ccarper@inta.es
(1) Instituto Nacional de Técnica Aeroespacial (INTA), Torrejón de Ardoz, 28850-Madrid, Spain
(2) Centro de Astrobiología (CSIC-INTA), Torrejón de Ardoz, 28850-Madrid, Spain
(3) Dep. Signal Theory and Communications, Universitat Politècnica de Catalunya (UPC), 08034-Barcelona, Spain
(4) Ciències i Tecnologies de l'Espai-Centre de Recerca de l'Aeronàutica i de l'Espai/Institut d'Estudis Espacials de Catalunya (CTE-CRAE/IEEC), Universitat Politècnica de Catalunya (UPC), 08034-Barcelona, Spain

Introduction

The impact of clouds on the climate is one of the most important research fields in atmospheric sciences, since their radiative forcing is still estimated with large uncertainties (Myhre et al., 2013). In particular, the indirect radiative forcing produced by aerosol-cloud interactions (ACI) is still poorly characterized. In fact, the next ESA EarthCARE mission (planned launch in 2023) has as a primary objective the study of the aerosol-cloud-radiation interactions to determine their effect on the energy balance of the atmosphere, and therefore their impact on the climate.

Atmospheric aerosol can influence the formation and evolution of clouds, their lifetime and precipitation ability, and their microphysical properties in two ways. First, it is the particle reservoir that favours the formation of ice clouds through heterogeneous nucleation processes (INP, Ice-Nucleating Particles). Second, they can serve as the reservoir of cloud condensation nuclei (CCN) for liquid droplet nucleation (water clouds formation). Among the diverse aerosol types, mineral dust is one of the most active particles efficiently acting as INP (DeMott et al., 2003) and CCN (Karydis et al., 2011).

Polarized lidar observations are used to determine cloud-relevant parameters: 1) profiles of dust-induced INP and/or CCN concentrations (e.g. Mamouri and Ansmann, 2016), by separating the dust contribution from the total aerosol extinction (e.g. Córdoba-Jabonero et al., 2018), and 2) the thermodynamic phase (ice, mixed, liquid) of homogeneous clouds using the cloud phase diagnosis (CPD) method (Lewis et al., 2020). These two methodologies are used in this work to investigate the evolution of clouds under actual homogeneous and heterogeneous nucleation conditions.

For that purpose, a case study of high (cirrus) and middle clouds and dust-induced CCN concentrations is selected for illustration. This case study is observed at the MPLNET/AERONET El Arenosillo station near the Huelva city (Huelva/ARN, 37.1ºN 3.7ºW, 40 m asl) on 26-27 May 2021. A polarized Micro-Pulse Lidar (P-MPL) is used for cloud and aerosol monitoring. P-MPL measurements are used for deriving: 1) the dust extinction coefficient as required to derive CCN concentrations (Mamouri and Ansmann, 2016); and 2) the volume linear depolarization ratio (VLDR), together with the temperature field, for determining the thermodynamic phase of clouds (CPD, Lewis et al., 2020) and the nucleation signature. Temperature and relative humidity profiles are obtained from the Global Data Assimilation System (GDAS).

The aim of this work is to show the potential of P-MPL observations under real aerosol-cloud scenarios to determine both the thermodynamic phase of homogeneous clouds and the CCN (or INP) concentration related to dust-induced nucleation processes.

Results and discussion

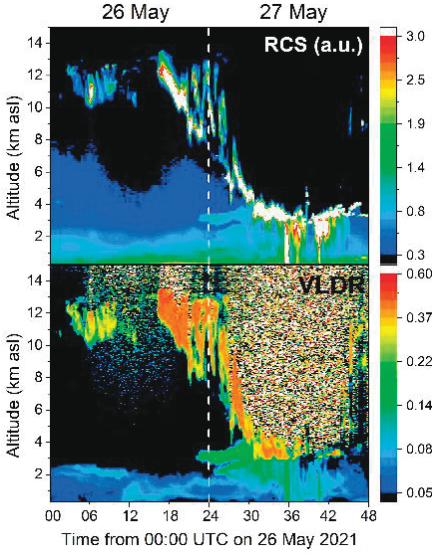

Figure 1. Aerosol-cloud scenario as observed at Huelva/ARN site during 26-27 May 2021 in terms of the P-MPL measurements: (Top panel) RCS, and (Bottom panel) VLDR.

The aerosol-cloud scenario observed along 26-27 May 2021 at the Huelva/ARN station is illustrated in terms of P-MPL measurements in Figure 1: the

range-corrected signal (RCS) (top panel) and the VLDR (bottom panel).

Several features are highlighted along the two-day scenario: high ice clouds (cirrus), the arrival of dust particles and potential water cloud nucleation. On 26 May, cirrus clouds are observed almost all day long between 7 and 13 km height. They are totally decoupled from the dust intrusion coming at around 22UTC. On 27 May, middle clouds appear at lower altitudes, spreading down to 4 km height, where the top of the dust layer is found. The dust-induced nucleation begins at around 05UTC (no aerosol inversion possible). Dust optical depths of 0.2-0.3 were derived.

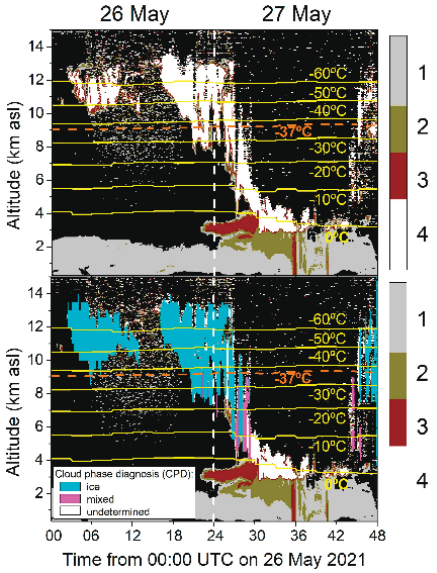

Figure 2. (Top) Aerosol/cloud discrimination: background aerosol (1, grey), mixed-dust/non-dust (2, dark green) and pure dust (3, brown), together with cloud signature (4, white). (Bottom) The CPD where the cloud signature was detected (in white at the top panel): ice (blue) and mixed (magenta), no liquid; the potential cloud nucleation region is also shown (undetermined, in white). Isotherms are also marked by yellow lines (that for -37ºC in orange).

Figure 2 (top) shows the aerosol typing: pure dust, 'mixed' dust/non-dust (differing from pure dust), and background aerosol, as discriminated from the clouds. The temperature field is also shown as isotherm yellow lines, highlighting the -37ºC-isotherm (homogeneous ice nucleation threshold) in orange. The CPD for clouds is included Fig. 2 (bottom panel), where the potential cloud nucleation signature (as an additional phase) is also shown.

Clouds are recognised in this particular aerosol-cloud scenario as ice and mixed (no liquid), in the basis of the VLDR and its uncertainty, and the temperature (at the top of the cloud) (Lewis et al., 2020). Looking at the temperatures regimes in the nucleation region, the dust particles could be most likely acting as CCN. Vertical CCN concentrations were also estimated from the dust extinction profiles (when inversion possible), deriving values of 200-250 cm^{-3}.

Challenges

The reliable potential of the P-MPL observations for cloud and aerosol monitoring and characterization is revealed. The synergetic use of the different P-MPL-based methodologies used in this work shows the suitable determination of the cloud thermodynamic phase, the aerosol typing and the nucleation region, in addition to the retrieval of the dust-induced CCN concentrations. Moreover, it will be especially interesting to study the cloud nucleation impact of dust by also acting as INP. Therefore, the challenge is addressed to the application of the same methodologies in other real aerosol-cloud interaction scenarios. All these results can be of interest for the next ESA EarthCARE mission.

Acknowledgements

This research was funded by the Spanish MICINN (PID2019-104205GB-C21, PID2019-103886RB-I00, CGL2017-90884-REDT), and the EU H2020 programme (ACTRIS, GA n. 654109, 871115). Authors thank the El Arenosillo technical staff for the P-MPL maintenance and operation support. CVC-P and M-ÁL-C are supported by the INTA predoctoral contract programme. The MPLNET project is funded by the NASA Radiation Sciences Program and Earth Observing System. Authors also thank the NOAA/READY system for providing the GDAS meteorological profiles.

References

Córdoba-Jabonero et al., Separation of the optical and mass features of particle components in different aerosol mixtures by using POLIPHON retrievals in synergy with continuous polarized Micro-Pulse Lidar (P-MPL) measurements, *Atmos. Meas. Tech*., 11, 4775-4795, 2018.
DeMott et al., African dust aerosols as atmospheric ice nuclei, Geophys. Res. Lett., 30 (14), 1732-1735, 2003.

Karydis et al., On the effect of dust particles on global cloud condensation nuclei and cloud droplet number, *J. Geophys. Res*., 116, D23204, 2011.

Lewis et al., Determining cloud thermodynamic phase from the polarized Micro Pulse Lidar, *Atmos. Meas. Tech*., 13, 6901-6913, 2020.

Mamouri and Ansmann, Potential of polarization lidar to provide profiles of CCN- and INP-relevant aerosol parameters, *Atmos. Chem. Phys*., 16, 5905-5931, 2016.

Myhre et al., Anthropogenic and natural radiative forcing, in: Climate Change 2013, *Fifth Assessment Report of the IPCC*, Cambridge University Press, NY, USA, 2013.

Tracking with Aeolus the Californian wildfire smoke transported over Atlantic

D. Trapon[1], *A. Lacour*[1], *T. Flament*[1], *A. Dabas*[1], *F. Ehlers*[2]
dimitri.trapon@meteo.fr
(1) CNRM, Université de Toulouse, Météo-France, CNRS, Toulouse, France
(2) ESA/ESTEC, Keplerlaan, Noordwijk, Netherlands

Introduction

In early September 2020, massive smoke plumes from Californian wildfires were transported east accross the United States and observed by various instruments such as NASA Suomi NPP VIIRS 330 (Jakson et al, 2013), NASA CALIPSO CALIOP (Winker et al, 2009) or Copernicus Sentinel-5p TROPOMI (Zweers and al, 2018). Smoke residuals were also compared to ground based lidar above West of Europe (Baars et al, 2021), confirming the long range transport above the Atlantic. The Aeolus satellite from the European Space Agency is operating since 2018 a Doppler lidar instrument ALADIN (Atmospheric LAser Doppler Instrument). It is the first High Spectral Resolution Lidar (HSRL) operating in Ultraviolet (UV) in space and it observed directly the Californian smoke through several orbits. Despite being designed for wind profile measurement the Rayleigh and Mie channels of ALADIN can be used to directly retrieve the particle only co-polar extinction to backscatter ratio (Flamant et al, 2008). Using UV Aerosol Index (AI) from TROPOMI L2 pre-operational data, multiple Aeolus orbits colocated with the biomass burning (BB) smoke layer over time have been selected to illustrate the observing capabilities of Aeolus with L2A Aerosol Optical Properties Product.

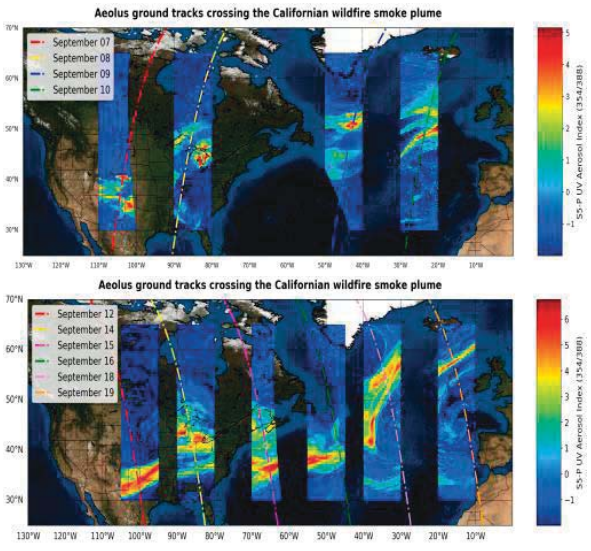

Figure 1. Aeolus orbits crossing two distinct smoke plumes transported over the Atlantic and overlaid with AI and Worldmap (ESRI, 2021)

The poster study will show the output of the main L2A algorithms and underline observations made on the smoke plume optical characteristics. The particle extinction and backscatter coefficients calculated by the Standard Correct Algorithm (SCA) (Flament et al, 2021), are then compared with denoised signals (e.g., Figure 2) given by a newly developed scheme based on physically constrained minimization named Maximum Likelihood Estimation (MLE) (Ehlers et al, 2021).

Results and discussion

Aerosol index products such as TROPOMI L2 and OMPS-NPP L2 NM (Omar et al, 2019) have been used to proxy the UV absorbing particles following Californian wildfires. Multiple Aeolus descending and ascending orbits crossing two distinct BB layers have been selected (e.g., Figure 1). Co-polar extinction to backscatter ratio are illustrated and allowed the following observations:

- A relatively constant SCA co-polar lidar ratio ~80-120sr is observed for the plume.
- The MLE co-polar lidar ratio produces closer values to total lidar ratio measured by other instruments for such smoke (i.e., ~40-70sr).
- The highest SCA and MLE co-polar lidar ratio correspond to smoke filaments far from the emission source. A direct role of black carbon (BC) particles in « fresh smoke » could then be highlighted waiting for further analysis.
- The plume is reaching rapidly the low stratosphere up to 10-12km and appears to be staying at this altitude over a very large distance before colapsing. This provides further evidence of the tropopause limit, i.e. the elevated aerosol layer being locked at the corresponding altitude and partially injected into the stratosphere.
- Additional work using Auxiliary Meteorological Data showed an increasing cloud contamination for the aging plume, illustrating the Ice Nucleating Particles (INP) role in cloud formation.
- A first look at CALIOP depolarization ratio showed an increase of depolarizing particles for the core plume. This is in line with Aeolus retrievals, i.e. observing increasing lidar ratio.

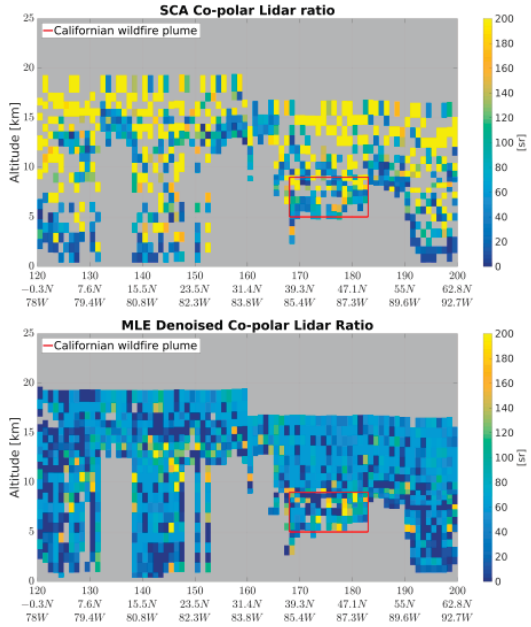

Figure 2. SCA and MLE co-polar lidar ratio with applied quality flag showing smoke plume evidence in red box above United States on September 14, 2020

Challenges

The complex role of aerosols and BC in climate and cloud chemistry is still a major unknown, especially during aging of smoke plumes. The tendency of localized aerosol layers to collapse and the cloud contamination make ground based measurements difficult. The present case study focuses on two BB smoke generated from Californian wildfires. The smoke layers have drifted from South West United States to East Atlantic Ocean allowing week-long observations by Aeolus satellite. Due to sufficient heat the smoke convection column riched the top troposphere hence the smoke plumes were observable with an accepetable Signal to Noise Ratio (SNR). Therefore this has offered an opportunity to analyze the optical properties of such BB aerosols and their evolution in time. Useful estimates of the co-polar lidar ratio for particles measured by ALADIN have been seen increasing as the plumes rise and get far from emission source. The use of external informations also helped assess the validity of Aeolus observations, e.g., showing higher depolarization ratio for mature layer.

Acknowledgements

The authors thanks the DISC (Data Innovation and Science Cluster) for their support and cooperation in the frame of the L2A processors development. The L2A has been developed over more than 15 years by numerous contributors (Pierre Flamant, Marie-Laure Denneulin, Mathieu Olivier, Vincent Lever, Pauline Martinet, Hugo Stiegliz ...). Most of the development work for the L2A processor was carried out in the frame of contracts from the European Space Agency, but also benefited from the financial support of the French space agency CNES. We acknowledge the use of Sentinel-5P L2 pre-operational data from the Sentinel-5P Pre-Operations Data Hub and the NASA Earth Observing System Data and Information System (EOSDIS).

References

Baars, H., Radenz, M., Floutsi, A. A., Engelmann, R., Althausen, D., Heese,B., et al. (2021). Californian wildfire smoke over Europe: A first example of the aerosol observing capabilities of Aeolus compared to ground-based lidar. Geophysical Research Letters, 48, e2020GL092194. https://doi.org/10.1029/2020GL092194

Ehlers, F, et al., Optimization of Aeolus Optical Properties Products by Maximum-Likelihood Estimation, Atmos. Meas. Tech. Discuss. [preprint], https://doi.org/10.5194/amt-2021-212, in review, 2021.

Esri, DigitalGlobe, GeoEye, i cubed, FSA, U., USGS, AEX, Getmapping, Aerogrid, IGN, IGP, swisstopo, and the GIS User Community: Http://server.arcgisonline.com/arcgis/services/World_Imagery/MapServer, downloaded on 25 Mar. 2021, 2021.

Flament, T., et al., Aeolus L2A Aerosol Optical Properties Product: Standard Correct Algorithm and Mie Correct Algorithm, Atmos. Meas. Tech. Discuss. [preprint], https://doi.org/10.5194/amt-2021-181, in review, 2021.

Jackson, J. M., Liu, H., Laszlo, I., Kondragunta, S., Remer, L. A., Huang, J., and Huang, H.-C.: Suomi-NPP VIIRS aerosol algorithms and data products: SUOMI-NPP VIIRS AEROSOL ALGORITHMS, Journal of Geophysical Research: Atmospheres, 118, 12,673–12,689, https://doi.org/10.1002/2013JD020449, http://doi.wiley.com/10.1002/2013JD020449, 2013.

Omar Torres (2019), OMPS-NPP L2 NM Aerosol Index swath orbital V2, Greenbelt, MD, USA, Goddard Earth Sciences Data and Information Services Center (GES DISC), Accessed: [04 Oct. 2021], 10.5067/40L92G8144IV

Winker, David & Vaughan, Mark & Omar, Ali & Hu, Yongxiang & Powell, Kathleen & Liu, Zhaoyan & Hunt, William & Young, Stuart. (2009). Overview of the CALIPSO mission and CALIOP data processing algorithms. Journal of Atmospheric and Oceanic Technology. 26. 2310-2323. 10.1175/2009JTECHA1281.1.

Zweers, D. S.: TROPOMI ATBD of the UV aerosol index, KNMI and ESA, https://sentinels.copernicus.eu/documents/247904/2476257/Sentinel-5P-TROPOMI-ATBD-UV-Aerosol-Index, 2018.

Investigating the relationship between ice crystals clouds and the source of underlying aerosols

K.A. Voudouri[1,3], *Britta Schäfer*[2], *Martin Flügge*[3], *Ingrid Hanssen*[3], *and Michael Gausa*[3]
kavoudou@physics.auth.gr

(1) Laboratory of Atmospheric Physics, Physics Department, Aristotle University of Thessaloniki, Thessaloniki, Greece
(2) Department of Geosciences, University of Oslo, Oslo, Norway
(3) Andøya Space AS , Bleiksveien 46, 8480 Andenes, Norway

Introduction

Cirrus clouds, which predominantly consist of ice crystals, are challenging components in atmospheric and global climatological research as they affect the global radiation budget [1]. Their formation highly depends on the presence of aerosol particles which are efficient ice-nucleating particles (INPs). Knowledge about the interaction of aerosol particles with clouds as well as the formation of cirrus clouds due to aerosol particles is crucial for improving our current understanding of the climate system. This study uses a novel dataset of cirrus clouds observations at a sub-arctic station to investigate possible connections between the amount and type of aerosols and the formation of cirrus clouds.

Instrumentation and methods

Aerosol and cloud measurements were performed with the 'tropospheric' lidar system situated at Andøya (69.2780 N, 16.0080 E, 380m), Northern Norway. The lidar is part of the Arctic Lidar Observatory for Middle Atmosphere Research (ALOMAR), operating since 2005, and member of the European Aerosol Research Lidar Network (EARLINET, [3]). If weather conditions allow measurements are performed both for the climatological weekly EARLINET schedule as well as for validation activities for satellite missions such as the Atmospheric Dynamics Mission Aeolus (ADM-Aeolus).

The lidar configuration is a monostatic, biaxial system, operating with a pulsed Nd:YAG solid state laser. The first (1064 nm), second (532 nm), and third harmonic (355 nm) frequency are emitted with a 30 Hz repetition rate. The laser beam is pointed into the atmosphere at an off-zenith angle of 3° so that the impact of the specular reflection by ice crystals into cirrus layers on the backscattered signals is negligible.

The set-up of the system includes three elastic channels at 355, 532 and 1064nm, one Raman channel at 387 nm and one depolarization channel at 532 nm. The vertical resolution of the signal profiles is equal to 7.5 m and the temporal resolution is 67 s. A detailed technical description of the instrument can be found in Frioud et al. [4].

In the following case study, the EARLINET Single Calculus Chain (SCC) algorithm was used for the processing of the optical products. All products are publicly available at https://www.earlinet.org/.

Case Study: 1 April 2011

On 1 April 2011, the lidar system observed a cirrus cloud layer between 9.7 and 11.5 km altitude between 09:53 to 11:20 UTC. On that day, the coast in Northern-Norway was located between a low-pressure system west of Iceland and a high-pressure center over Svalbard. The observed cirrus clouds were located in a region between a warm front to the north, which passed Andøya a day before, and a vanishing occluded front that spanned over the Atlantic from east of Greenland to Southern Norway [5].

The range corrected signal at 1064 nm from the ground based lidar is shown in Figure 1. The temperature values (http://weather.uwyo.edu) between the cloud base and the cloud top ranged between -62.5°C to -69.5°C. The linear volume depolarization ratio (not shown here) ranged from 0.2 to 0.3 within the cloud layer, indicating the presence of non – spherical ice particles.

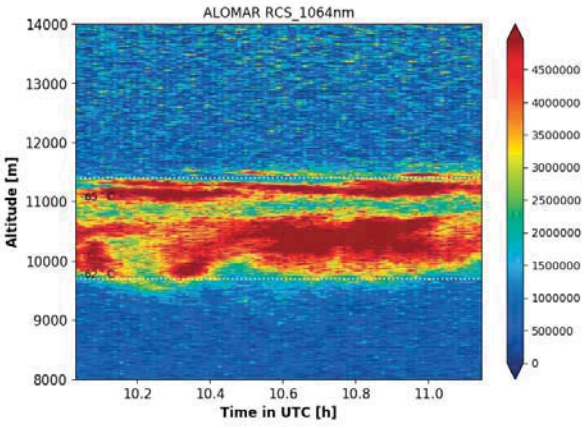

Figure 1. Range corrected signal from the ALOMAR lidar at 1064nm on 1 April 2011. The vertical and temporal resolution of the ALOMAR lidar are 7.5 m and 67 s, respectively.

The optical product analysis revealed an aerosol layers below the cirrus clouds, at altitudes between

6.5 and 7.5 km (Figure 2). The temperature values within this altitude range varied between -33°C and -48°C (http://weather.uwyo.edu) .

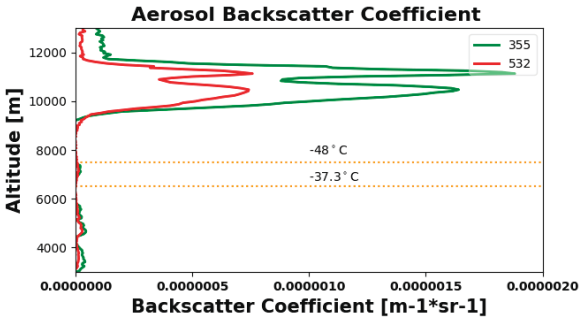

Figure 2. Backscatter coefficient profiles at 532 and 1064 nm from the ALOMAR lidar on 1 April 2011. Temperature values are marked along with the height of the aerosol layer underlying the cirrus cloud.

As mineral aerosols and non-spherical smoke particles can act as effective ice nuclei particles (INPs) in low temperatures, the source of the aerosol particles below the cirus cloud layer was further investigated. For this purpose, air mass backward trajectories were calculated using the Hybrid Single- Particle Lagrangian Integrated Trajectory model (HYSPLIT, [6]).

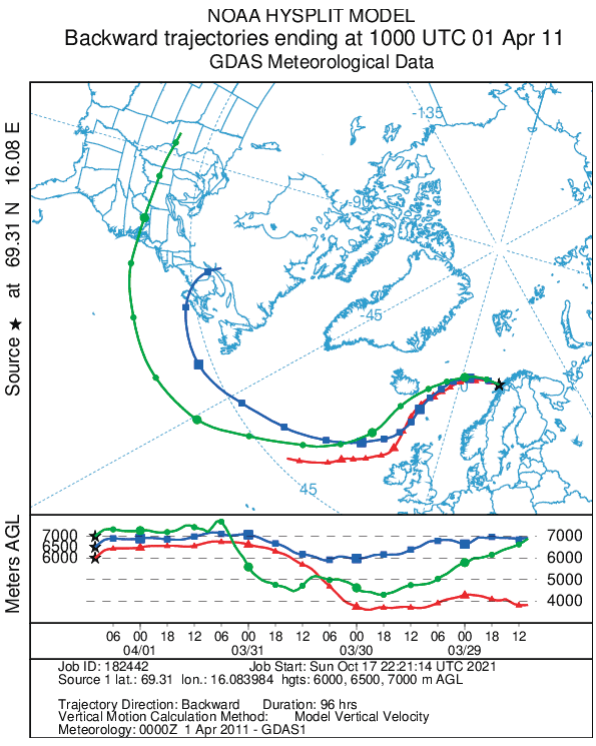

Figure 3. 4-day backward trajectories arriving at ALOMAR at height altitudes below the cirrus cloud.

In this case study, the aerosol particles were found to have been transported from North America and the North Atlantic at altitudes below the cirrus cloud layer. Further investigation on the origin of these particles and their link to biomass burning eventsand/or the Eyjafjallajökull volcano activity is going to be discussed.
Additionally, the spectral dependence of the cirrus optical properties in terms of the ice particles shape is also addressed

Conclusions – Challenges

The potential of soot particles to serve as INPs and the potential impact on ice formation on a cirrus cloud formed above ALOMAR station is going to be analyzed.

Acknowledgements

We gratefully acknowledge the donation of lasers for the tropospheric lidar system at ALOMAR by the Leibniz-Institute of Atmospheric Physics at the University of Rostock.

References

[1] Campbell, J., Lolli, S., Lewis, J., Gu, Y., and Welton, E.: Daytime Cirrus Cloud Top-of-the-Atmosphere Radiative Forcing Properties at a Midlatitude Site and Their Global Consequences, J. Appl. Meteorol. Clim., 55, 1667–1679, https://doi.org/10.1175/JAMC-D-15-0217.1, 2016.
[2] Marinou, E., Tesche, M., Nenes, A., Ansmann, A., Schrod, J., Mamali, D., Tsekeri, A., Pikridas, M., Baars, H., Engelmann, R., Voudouri, K. A., Solomos, S., Sciare, J., Groß, S., Ewald, F., and Amiridis, V.: Retrieval of ice-nucleating particle concentrations from lidar observations and comparison with UAV in situ measurements, Atmos. Chem. Phys., 19, 11315–11342, https://doi.org/10.5194/acp-19-11315-2019, 2019.
[3] Pappalardo, G.; et al. EARLINET. Atmospheric Measurement Techniques 2014, pp. 2389–2409. doi:10.5194/amt-7-2389-2014.
[2] Skatteboe, R. ALOMAR: atmospheric science using lidars, radars and ground based instruments. Journal of Atmospheric and Terrestrial Physics 1996, 58, 1823–1826.
[4] Frioud, M.; Gausa, M.; Baumgarten, G.; Kristjansson, J.E.; Føre, I. New tropospheric lidar system in operation at ALOMAR (69°N, 16°E). Reviewed and Revised Papers of the 23rd International Laser Radar Conference (ILRC), 2006, pp. 24–28.
[5] Digital Library and Archive, Forecast Data and Analysis. Crown Copyright [2011,2017]. Information provided by the National Meteorological Library and Archive - Met Office, UK. https://digital.nmla·metoffice.gov.uk/SO_a3062731-4abc-43b4-8a8a-477c76231d31/.
[6] Stein, A. F., Draxler, R. R., Rolph, G. D., Stunder, B. J. B., Cohen, M. D., and Ngan, F.: NOAA's HYSPLIT atmospheric transport and dispersion modeling system, B. Am. Meteorol. Soc., 96, 2059–2077, https://doi.org/10.1175/BAMS-D-14-00110.1, 2015

Comparison between lidar observations and reanalysis simulations of dust layer evolution over three EARLINET sites across the Mediterranean region in July 2012

***M. Mytilinaios*[1]**, *L. Mona*[1], *S. Basart*[2], *E. Di Tomaso*[2]
michalis.mytilinaios@imaa.cnr.it
(1) National Research Council of Italy - Institute of Methodologies for Environmental Analysis (CNR-IMAA), C.da S. Loja, 85050 Tito Scalo (PZ), Italy
(2) Barcelona Supercomputing Center (BSC), Barcelona, Spain

Introduction

In this study we compare the dust extinction coefficient (DEC) profiles produced by the MONARCH dust regional reanalysis (Di Tomaso et al., 2021a), against dust profiles retrieved from particle backscatter measurements provided by the EARLINET network, in order to evaluate the ability of the reanalysis to reproduce desert dust intrusions over specific locations, at a sub-daily temporal scale. The regional dust reanalysis used in this study is based on the MONARCH chemical weather system (Klose et al., 2021) and covers the region of Northern Africa, the Middle East and Europe (NAMEE) for a 10-year period from 2007 to 2016 (Di Tomaso et al., 2021b). The vertical distribution of dust in the atmosphere is represented by three-dimensional dust mass concentrations as well as by DEC profiles at 550 nm, provided at a 3-hour temporal resolution and 40 hybrid pressure-sigma vertical levels from the surface up to ~20 km.

In a companion work (Mytilinaios et al., 2021) we provide a thorough evaluation of the reanalysis DEC profiles over the NAMEE region using lidar observations from CALIPSO and EARLINET. In such study, the comparison is performed at annual and seasonal scales, because of the coarse temporal resolution of the observations, which additionally differs from site to site (e.g. there are 1-3 CALIPSO measurements available on a monthly basis, depending on the grid cell). Here instead, we provide an insight into the reanalysis performance at the shortest temporal scale the reanalysis resolution allows (i.e. 3 hours), using a special EARLINET dataset which provides 1-hourly lidar products for 72 consecutive hours, produced during the EARLINET 72h campaign. In particular, the EARLINET 72h dataset provides coordinated and continuous measurements performed by eleven EARLINET stations in the Mediterranean area, between 9 July 2012 at 06:00 UTC and 12 July at 06:00 UTC.

The EARLINET dust profiles at 532 nm were obtained by separating the pure dust from the total aerosol backscatter coefficient, using the particle depolarization ratio to distinguish dust from spherical particles (Tesche et al., 2009). Then the DEC profiles were retrieved by assuming a typical lidar ratio at 532 nm equal to 55 sr referring to pure dust particles observed by EARLINET in the past (Papagiannopoulos et al., 2018). Finally, the EARLINET DEC profiles were averaged around the 40 vertical levels of the reanalysis and within ± 1.5 hour from the 3-hourly output times, in order to achieve the spatio-temporal collocation of the two datasets.

The EARLINET DEC were produced over three stations which provide simultaneous particle backscatter coefficient and depolarization ratio measurements at 532 nm during the campaign: Granada (latitude: 37.2°N, longitude: -3.6°E), Potenza (latitude: 40.6°N, longitude: 15.7°E) and Bucharest (latitude: 44.3°N, longitude: 26.0°E). In this manuscript we present the results obtained over Potenza EARLINET station, while the overall results from the three stations will be presented in the poster session of the ELC2021 conference.

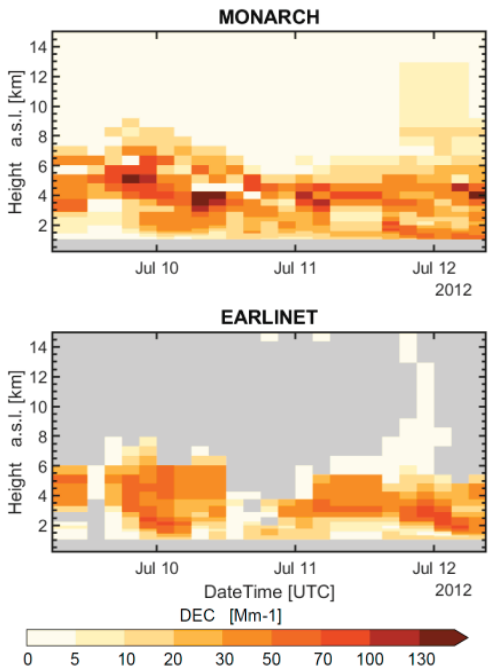

Figure 1. Sequence of the 3-hourly MONARCH (up) and EARLINET (down) DEC profiles between 9/7/2012 at 6 UTC and 12/7/2012 at 6 UTC, over Potenza station.

Results and discussion

Figure 1 depicts the sequence of the simulated and the observed DEC profiles over Potenza station.

MONARCH identifies quite well the spatio-temporal evolution of the dust layer, i.e. in terms of altitude and of time, although the model overestimates the observed DEC values. As Figure 2 shows, both mean profiles locate a dust layer between 2 and 6 km, while the spatial correlation (SC) between the two profiles along the height axis is significantly high (0.87); however, the mean bias (MB) profile, defined as the difference between the two mean DEC profiles, indicates that MONARCH overestimates DEC by more than 10 Mm^{-1} between 3 and 7 km. Lastly, the temporal correlation (TC) between modelled and observed DEC at different altitude levels, shows a near zero TC between 2 and 4 km, whereas TC increases constantly above that and up to 7.5 km.

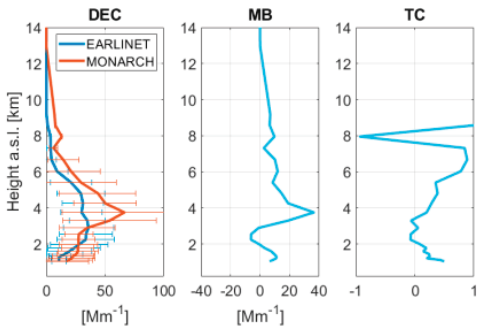

Figure 2. Mean 72-hour MONARCH and EARLINET DEC profiles (left), MB (middle) and TC profile (left).

Moreover, for each 3-hourly DEC profile we computed the altitude of the center of mass (COM) of the dust layer (Equation 1 of Mona et al., 2006) and the dust optical depth (DOD) by integrating the DEC profiles over the altitude, obtaining a time-series for each parameter (Fig. 3). Comparison scores presented in Table 1 show that the reanalysis reproduces very well the temporal evolution of the COM with high TC (0.79) and a relatively low mean overestimation (MB = 280 m) compared to the COM values which are resulted higher than 2.5 km, in most cases (Fig. 3), while the vertical resolution of the reanalysis profiles exceeds 400 m around those levels. Similarly, the DOD comparison shows a high TC (0.74) since the reanalysis reproduces correctly the temporal changes of DOD during the study period, and a relatively low mean overestimation (MB = 0.06).

In conclusion, the MONARCH reanalysis captures very well the spatio-temporal evolution of the dust vertical distribution; however, overestimates the intensity of the dust event observed over Potenza during the EARLINET 72h campaign.

Challenges

The present work demonstrates the lidars' capability to provide dust profiles and their application for model and reanalysis evaluation. It highlights the importance for such studies to be conducted more often and in various sites. This calls for more open data of lidar measurements, including depolarization ratio, at more locations, and potentially their use for NRT evaluation purposes.

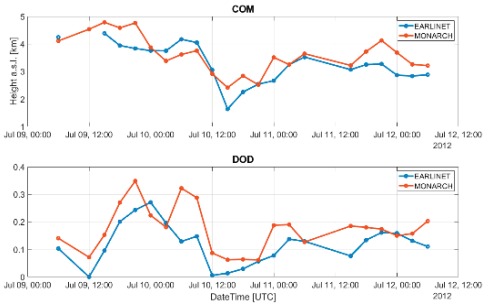

Figure 3. MONARCH (blue line) and EARLINET (orange line) COM (up) and DOD (down) time-series.

Table 1. MB and TC of COM and DOD

Parameter	MB	TC
COM	0.28 km	0.79
DOD	0.06	0.74

References

Di Tomaso et al., MONARCH high-resolution reanalysis data set of desert dust aerosol over Northern Africa, the Middle East and Europe, *BSC*, *THREDDS*, 2021a.

Di Tomaso et al., The MONARCH high-resolution reanalysis of desert dust aerosol over Northern Africa, the Middle East and Europe (2007-2016), *submitted to ESSD* 2021b.

Klose et al., Mineral dust cycle in the Multiscale Online Nonhydrostatic AtmospheRe CHemistry model (MONARCH) Version 2.0, *Geosci. Model Dev. Discuss. [preprint], in review*, 2021.

Mona et al., Saharan dust intrusions in the Mediterranean area: Three years of Raman lidar measurements, *J. Geophys. Res.*, 111, D16203, 2006.

Mytilinaios et al., Evaluation of the MONARCH reanalysis dust extinction profiles over Northern Africa, Middle East and Europe, using CALIPSO, IASI and EARLINET observations, *in preparation*, 2021.

Papagiannopoulos et al., An automatic observation-based aerosol typing method for EARLINET, *Atmos. Chem. Phys.*, 18, 15879-15901, 2018.

Tesche et al., Vertically resolved separation of dust and smoke over Cape Verde using multiwavelength Raman and polarization lidars during Saharan Mineral Dust Experiment 2008, *J. Geophys. Res.*,114, D13202, 2009.

Session 4. Challenges: Atmospheric Boundary Layer and low altitude profiling

Comparison in the estimation of mixing layer height from ceilometer profiles using the STRATfinder algorithm with IFS and WRF model predictions

R. Barragán[1], F. Molero[1], M. R. Theobald[1], M. García Vivanco[1], A. Rodríguez-Sánchez[1] V. Gil[1], J. L. Garrido[1], M. Pujadas[1], B. Artíñano[1]

(1)CIEMAT, Avda Complutense, 40. 28040, Madrid, Spain ruben.barragan@ciemat.es

Introduction

It is well known that anthropogenic aerosols are one of the main factors that contribute to poor air quality, constituting a public health risk and therefore, their characterization is a priority. However, this characterization is hampered by the fact that aerosols present a heterogeneous distribution in the atmosphere, being mostly concentrated within the atmospheric boundary layer (ABL). The ABL extends from ground level up to a variable height that usually coincides with the presence of a temperature inversion, limiting the vertical mixing of air pollutants emitted near the surface. Therefore, it can be assumed that the ABL is directly affected by the radiation emitted by the surface and its variability throughout the day.

In order to study the ABL, the main instrument used in this work is a ceilometer Lufft CHM15k-Nimbus (Heese et al., 2010), which operates at 1064nm providing data related to atmospheric aerosols, with a repetition frequency of 6.5 kHz and a maximum height of 15.36 km a.g.l. The ceilometer is deployed next to the MDR-CIEMAT ACTRIS station (40.4565ºN, 3.7257ºW, 669 m a.s.l.) (Molero et al., 2014), which is located in the North-West outskirts of the city of Madrid. This city is located in the center of the Iberian Peninsula and its metropolitan area has a population of nearly 6 million inhabitants and a car fleet of almost 3 million vehicles. All the available ceilometer profiles, retrieved every 15 seconds for a total of 344 days of the year 2020, stored in the Madrid database, covering different synoptic situations, such as long-range transport of aerosols or clean atmospheric conditions are used in the present work

Since typical techniques, such as the wavelet and the gradient methods are unable to detect the ABL in cases with presence of low clouds or residual layers, the STRATfinder algorithm (Kotthaus et al., 2020) is used in the present work. By means of this algorithm, the ABL height is estimated together with the mixing layer height (MLH), which is defined as the lowest atmospheric layer in which aerosols and moisture are dispersed by recent mixing processes. The STRATfinder algorithm tracks ML and ABL heights to provide values every 10 minutes during a 24-hour period. These heights were compared with the values obtained from two different atmospheric models: ECMWF-IFS (three-hourly interpolated to hourly) and WRF (hourly).

Outputs from the IFS model (Integrated Forecasting System, European Centre for Medium-Range Weather Forecasts (ECMWF); www.ecmwf.int) were obtained from the MARS archive (access facilitated by AEMET for research projects). In particular, the high resolution product, HRES, was used, with a horizontal resolution of approximately 0.1º (or 9 km) and 137 vertical levels. The Weather Research and Forecasting model (WRF; Skamarock et al., 2005) was executed for the whole year of 2020 for 2 "two-way" nested domains. The coarser domain covers a large area of Europe with a horizontal spatial resolution of 15 x 15 km^2 and the finer one was centered on Spain at a resolution of 5 x 5 km^2. Information for the initial and boundary conditions was taken from the global GFS (Global Forecast System) model. The Bougeault-Lacarrere Scheme was chosen for the PBL parameterization.

The main objective of this research is the assessment of the MLH by means of the STRATfinder algorithm using ceilometer signals, during the whole 2020 and the comparison of the results with different model estimations in order to establish the similarities for different meteorological conditions.

Results and discussion

Our very preliminary results show that the MLH estimated by the IFS and WRF models are in good agreement with the heights estimated by STRATfinder during summer months, reaching correlation coefficients (R^2) about 0.92. The mean R^2 found for winter and fall months are about 0.37 and 0.38 respectively, while for spring and summer months the mean R^2 values are larger (about 0.55 and 0.63). The presence of low clouds coupled to the ML and the low surface temperatures during winter and fall may be reason for the lower correlation. A more detailed study was made by selecting 46 cases throughout 2020, covering different synoptic situations, such as Saharan dust intrusions. Fig. 1a shows one of the 46 selected cases, specifically July 4th. The presence of the ABL is evident, above 2km height, from 00 to 12 UTC, when the estimations MLH and ABLH coincide. Then from 12 to 20 UTC the presence of

a convective boundary layer is clear, reaching a height of approximately 2.5 km. However, between 18 and 20 UTC the MLHs estimated by both, models and STRATfinder, suddenly decrease. This behavior shows that the estimates depend strongly on solar radiation. It is clear, therefore, that the solar radiation needs to be parameterized correctly in the models to provide reliable estimates of the MLH. Figs 1b and 1c, monthly and hourly normalized mean bias (NMB), clearly show the aforementioned relation between the solar radiation and the estimation of the MLH. During summer months and central hours of the day the differences between the values estimated by the models and STRATfinder are lower than in months and hours with less solar radiation.

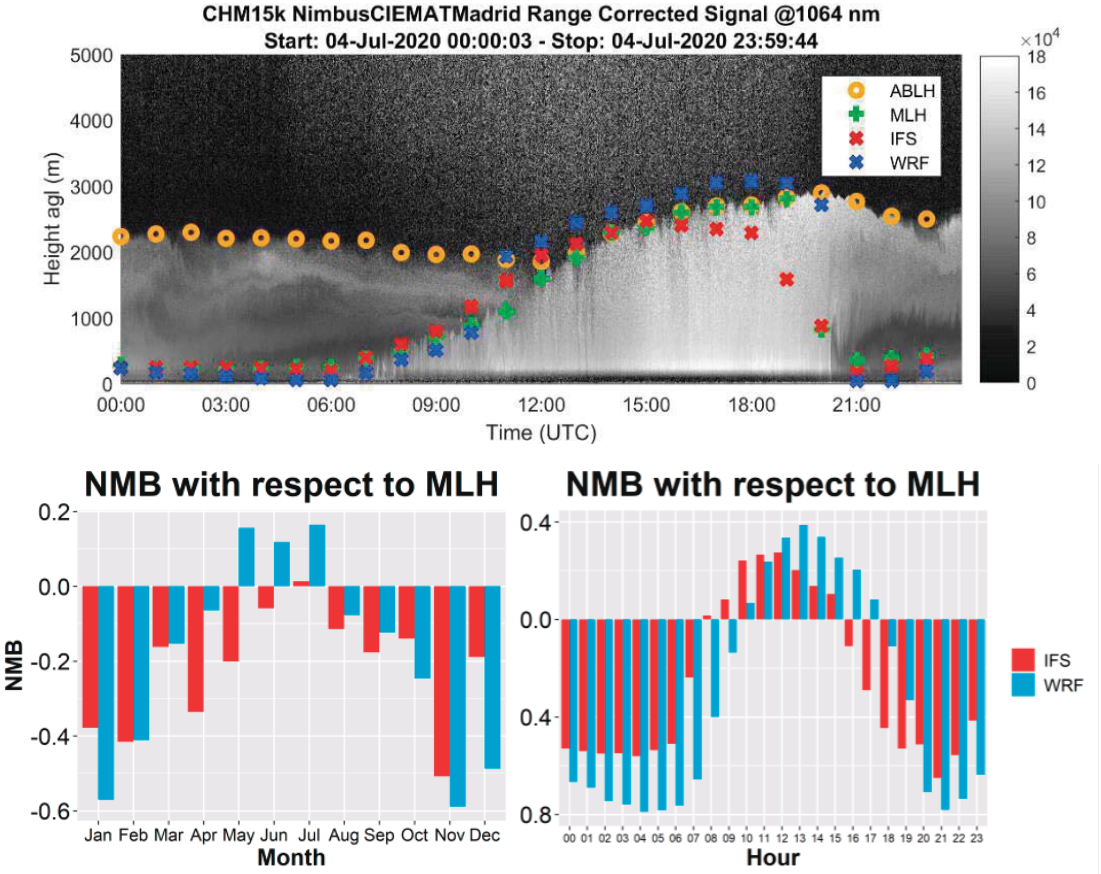

Figure 1. Ceilometer range-corrected backscatter signal (a) for July 4th, where orange circles and green crosses represent the ABLH and MLH, both estimated by the STRATfinder algorithm and red and blue crosses represent the MLH estimated by the IFS and WRF models, respectively. Monthly (b) and hourly (c) normalized mean bias, red and blue bars represent the IFS and WRF models, respectively.

Acknowledgements

This work was supported by H2020 programme from the European Union (grant 654109, ACTRIS-2 project), the Spanish Ministry of Economy and Competitivity (CRISOL, CGL2017-85344-R; Retos-AIRE, RTI2018-099138-B-100) and Madrid Regional Government (TIGAS-CM, Y2018/EMT-5177). Thanks to AEMET for the access to the ECMWF MARS archive.

References

Heese, B., Flentje, H., Althausen, D., Ansmann, A., Frey, S. Ceilometer lidar comparison: backscatter coefficient retrieval and signal-to-noise ratio determination, *Atmos. Meas. Tech., 3*, 1763–1770. https://doi.org/10.5194/amt-3-1763-2010. 2010.

Molero, F.; et al. Study of vertically resolved aerosol properties over an urban background site in Madrid (Spain). Int. J. *Rem Sensing 35(6)*, 2311-2326. http://dx.doi.org/10.1080/01431161.2014.894664. 2014.

Kotthaus, S.; Haeffelin, M.; Drouin, M.-A.; Dupont, J.-C.; Grimmond, S.; Haefele, A.; Hervo, M.; Poltera, Y.; Wiegner, M. Tailored Algorithms for the Detection of the Atmospheric Boundary Layer Height from Common Automatic Lidars and Ceilometers (ALC). *Remote Sens. 12*, 3259. https://doi.org/10.3390/rs12193259. 2020.

Skamarock, W. C., Klemp, J. B., Dudhia, J., Gill, D. O., Barker, D. M., Wang, W. and Powers, J. G.: A description of the advanced research WRF version 2, NCAR Technical Note: NCAR/TN-468+STR https://doi.org/10.5065/D6DZ069T, 2005.

The Role of Dry Layers and Cold Pools in the Activation of Mesoscale Convective Systems: A Characterization Study based on the Combined Use of Raman Lidar and DIAL Measurements and MESO-NH Model Simulations

Paolo Di Girolamo[1*], *Marie-Noelle Bouin*[2], *Cyrille Flamant*[3], *Donato Summa*[1,4], *Benedetto De Rosa*[1,4], *Noemi Franco*[1]
(1) Scuola di Ingegneria, Università della Basilicata, Potenza, Italy,
email: paolo.digirolamo@unibas.it
(2) Météo-France /CNRM, 29280 Plouzané, France
(3) LATMOS/IPSL, UPMC Univ. Paris 06 Sorbonne Universités, UVSQ, CNRS, Paris, France
(4) IMAA-CNR, Tito Scalo (Pz), Italy

Introduction

As part of the Cevennes-Vivarais site, the University of Basilicata Raman lidar system BASIL (Di Girolamo *et al.*, 2009, 2012, 2916) was deployed in Candillargues (Cévennes-Vivarais Southern France Lat: 43°37′ N; Long: 04°04′ E; Elev: 1 m) and operated throughout the duration of HyMeX-SOP 1 (September-November 2region, 012, Ducrocq et al., 2014), providing high-resolution and accurate measurements, both in daytime and night-time, of atmospheric temperature, water vapour mixing ratio and particle backscattering and extinction coefficient at three wavelengths.

Measurements carried out by BASIL on 28 September 2012 reveal a water vapour field characterized by a quite complex vertical structure. Reported measurements were run in the time interval between two consecutive heavy precipitation events, from 15:30 UTC on 28 September to 03:30 UTC on 29 September 2012. Throughout most of this observation period, lidar measurements reveal the presence of four distinct humidity layers.

In this research work we try to identify the presence of dry layers and cold pools and assess their role in the genesis of the mesoscale convective systems and the heavy precipitation events (HPEs) observed on 29 September 2012 based on the combined use of water vapour mixing ratio and temperature profile measurements from BASIL and water vapour mixing ratio profile measurements from LEANDRE 2, supported by MESO-NH simulations. LEANDRE 2, which stands for „Lidar Embarque pour l''etude des Aerosols et des Nuages, de l'interaction Dynamique–Rayonnement et du cycle de l'Eau", is an airborne differential absorption lidar (DIAL) system capable to measure nadir profiles of water vapour number density and particle backscattering at 730 nm.

Results and discussion

Figure 1 illustrates the time evolution of the water vapour mixing ratio as measured by BASIL (upper panel) and simulated by the Mesoscale Non-Hydrostatic model (MESO-NH, lower panel) over the 6-hour time interval from 15:30 to 23:30 UTC on 28 September 2012. MESO-NH is non-hydrostatic cloud-resolving research model developed by Laboratoire d'Aérologie and CNRM-GAME (Lafore *et al.*, 1998).

Based on the combined use of BASIL and LEANDRE 2 observations and MESO-NH back-trajectory analyses, we determined that humid air masses feeding the precipitation system were originated in the North Atlantic (2-3 days earlier), Tropical Atlantic (4-5 days earlier) and Tropical Africa (10 days earlier) and were transported in the lower troposphere for 3-4 days, finally subsiding upon reaching the Mediterranean 12-40 hours before HPEs.

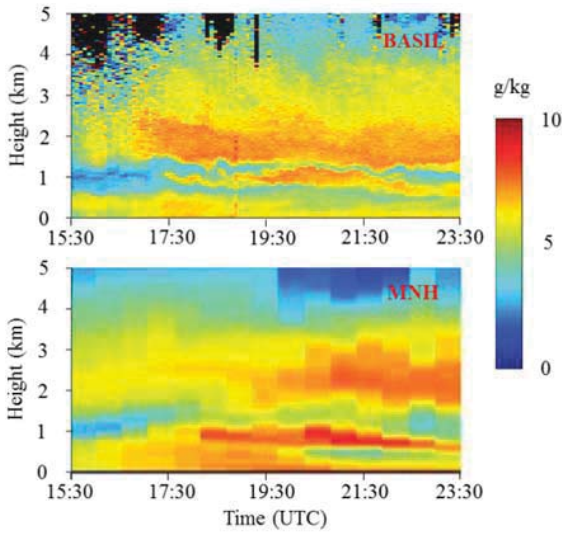

Figure 1: Time evolution of the water vapour mixing ratio as measured by BASIL (upper panel) and simulated by MESO-NH (lower panel) over the 6-hour time interval from 15:30 to 23:30 UTC on 28 September 2012.

Low-level cold pools are found to play a fundamental role in the genesis and development of deep convection and heavy precipitation events, especially in the north-western Mediterranean coasts especially in autumn (Ducrocq *et al.*, 2008). Two different prognostic variables are typically

used to identify cold pools (Bouin *et al*., 2017), namely virtual potential temperature and equivalent potential temperature. Virtual potential temperature, directly related to the air masses density, is defined as (e.g. Ducrocq *et al*., 2008; Bresson *et al*., 2012):

$$\theta_v(z) = T(z)\left(\frac{p_0}{p(z)}\right)^{R/cp}\left(1 - x_{H_2O}\ (z)\right)$$

with *p(z)* and *T(z)* being the atmospheric pressure, temperature and water vapour mixing ratio, respectively, p_0 being the reference pressure, and *R* and c_p being the dry air gas constant and the specific heat at constant pressure, respectively. Equivalent potential temperature, which characterizes the heat and moisture content of the inflow, is defined as:

$$\theta_e(z) = T(z)\left(\frac{p_0}{p(z)}\right)^{R/cp} exp\left(\frac{Lw_s[T(z), p(z)]}{c_p T(z)}\right)$$

with *L* and w_s being the latent heat of condensation and the saturation mixing ratio, respectively. Cold pools are identified by virtual potential temperature values below 23 ^{0}C (or 296 K) and equivalent potential temperature values below 52 ^{0}C (or 325 K). Figure 2 illustrates the time evolution of the virtual potential temperature as measured by BASIL over the 12-hour time interval from 15:30 to 03:30 UTC on 28-29 September 2012. The red ellipse within the figure identifies an elevated cold pool, characterized by virtual potential temperature values lower than 296 K. More results from this study, including comparisons with mesoscale modeling, will be illustrated and discussed at the Conference.

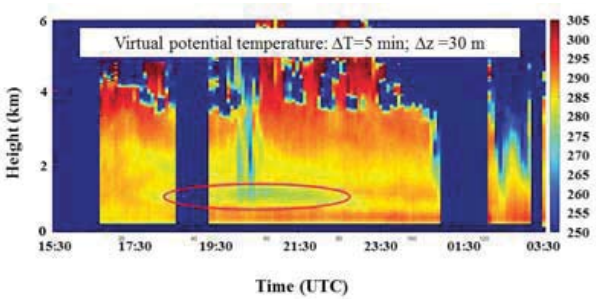

Figure 2: Time evolution of the virtual potential temperature as measured by BASIL over the 12-hour time interval from 15:30 to 03:30 UTC on 28-29 September 2012

Acknowledgements

This work was supported by the Italian Ministry for Education, University and Research under the Grants "OT4CLIMA" and "FISR2019-CONCERNING".

References

Bouin, M.-N., Redelsperger, J.-L. and Lebeaupin Brossier, C. (2017), Processes leading to deep convection and sensitivity to sea-state representation during HyMeX IOP8 heavy precipitation event. Q.J.R. Meteorol. Soc, 143: 2600-2615. https://doi.org/10.1002/qj.3111

Bresson, E., Ducrocq, V., Nuissier, O., Ricard, D. and de Saint-Aubin, C. (2012), Idealized numerical simulations of quasi-stationary convective systems over the Northwestern Mediterranean complex terrain. Q.J.R. Meteorol. Soc., 138: 1751-1763. https://doi.org/10.1002/qj.1911

Di Girolamo, P., Summa, D., Ferretti, R.: Multiparameter Raman lidar measurements for the characterization of a dry stratospheric intrusion event. *J. Atmos. Oceanic Technol*., **26,** 1742–1762, doi: 10.1175/2009JTECHA1253.1, 2009.

Di Girolamo, P., Summa, D., Bhawar, R., Di Iorio, T., Cacciani, M., Veselovskii, I., Dubovik, O., and Kolgotin, A.: Raman Lidar observations of a Saharan dust outbreak event: Characterization of the dust optical properties and determination of particle size and microphysical parameters. *Atmospheric Environment*, **50**, 66-78, 2012.

Di Girolamo, P., Flamant, C., Cacciani, M., Richard, E., Ducrocq, V., Summa, D., Stelitano, D., Fourrié, N., and Saïd, F.: Observation of low-level wind reversals in the Gulf of Lion area and their impact on the water vapour variability, *Q. J. Roy. Meteor. Soc*., **142**, 153–172, https://doi.org/10.1002/qj.2767, 2016.

Ducrocq, V., *et al*., HyMeX-SOP1, the field campaign dedicated to heavy precipitation and flash-flooding in northwestern Mediterranean. Bull. Am. Meteorol. Soc., **95**, 1083–1100, doi: 10.1175/BAMS-D-12-00244.1, 2014.

Lafore JP, Stein J, Asencio N, Bougeault P, Ducrocq V, Duron J, Fischer C, H´ereil P, Mascart P, Masson V, Pinty JP, Redelsperger JL, Richard E, Vilà-Guerau de Arellano J. TheM´eso-NH atmospheric simulation system. Part I: Adiabatic formulation and control simulations. *Ann. Geophys.* **16**: 90–109, 1998.

Exploring The Application Boundaries Of Stochastic Theories Regarding Turbulent Atmospheric Ceilometer Data

***I. A. Roșu*[1,2], *M. M. Cazacu*[2], *A. Timofte*[3], *M. Agop*[2,4]**
alin.iulian.rosu@gmail.com
(1) Faculty of Physics, Alexandru Ioan Cuza" University of Iasi, Bulevardul Carol I 11, 700506 Iasi, Romania
(2) Department of Physics, „Gheorghe Asachi" Technical University of Iasi, 700050 Iasi, Romania
(3) National Meteorological Administration Regional Forecasting Center, 600234 Bacau, Romania
(4)Romanian Scientists Academy, 050094 Bucharest, Romania

Introduction

The notion of the structure function of a parameter in a turbulent flow can be expanded so as to connect various equations regarding the structure and inhomogeneity of that parameter field in a turbulent flow; central to this theory is the notion that many of these parameters are conservative passive additives. This assumption is found to be reasonable for reduced spatial shifts and small fluctuations (Tatarski, 1961; Roșu et al., 2019).

In order to connect equations regarding the evolution of the mean and the fluctuations of the chosen additives, the inhomogeneity of the additive field is considered to be stationary, thus the production and dissipation of inhomogeneity in the given atmospheric column are considered to be equal and of opposite sign. This balance of production and dissipation shall be named the "Tatarski hypothesis" (Tatarski, 1961). The atmospheric refractive index n and atmospheric temperature T can then be connected through a series of equations and equation systems. These formulas can be solved with RCS data obtained via ceilometer or elastic lidar data.

Finally, it is possible to approximate a temperature profile in a limited altitude interval using this data. The advantages and disadvantages of this method are discussed, including certain theoretical limits. Suggestions towards improving the method in the future are given – many improvements would have to be of a technical nature, given the theoretical limits of this method, and would be useful with calculating other atmospheric turbulence characteristics as well. The results are compared with a standard lapse-rate temperature profile, a novel temperature profile employing an approximation of the connection between atmospheric multifractality and temperature, and aerosonde profiles (Roșu et al., 2021).

Results and discussion

From a technical perspective, the platform utilized in this study is a CHM15k ceilometer platform operating at a wavelegth of 1064nm – it is positioned in Bucharest, Romania, at the „Măgurele Center for Atmosphere and Radiation Studies", which is a part of the National Institute for Research and Development in Optoelectronics "INOE 2000", at an altitude of 93m ASL (Stachlewska et al., 2014). The aerosonde profiles were obtained through nearby profiling.

First, standard timeseries profiles of RCS and the coefficient of the refractive index structure function C2N are exemplified (Figs. 1, 2). A relatively-calm cold-season scenario was chosen for the analysis, one in which the PBL is visible and the temperature evolution at higher altitudes throughout time can be observed (Fig. 3). The necessary calculations are performed through software developed in Python 3.6.

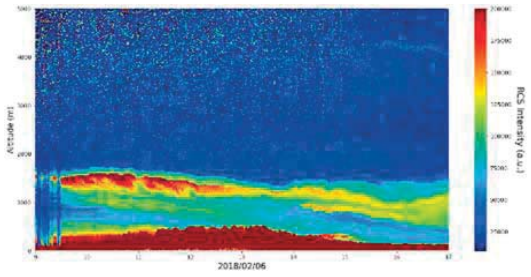

Figure 1. RCS timeseries, 2018/02/06.

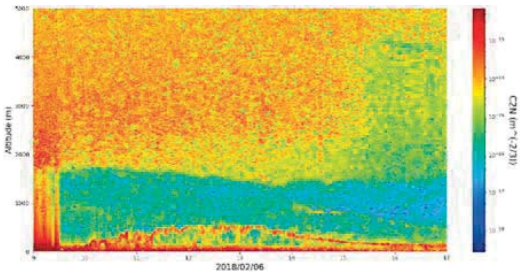

Figure 2. C2N timeseries, 2018/02/06.

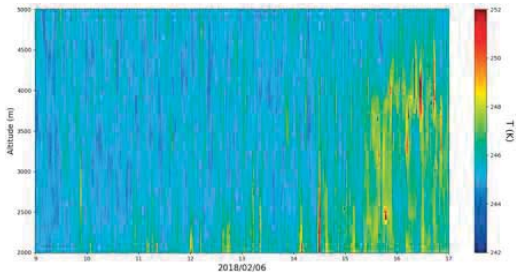

Figure 3. T timeseries (Tatarski hypothesis method), 2018/02/06.

It is found that multifractal dimension of atmospheric turbulent entities is proportional to the inverse of the square root of temperature; this is then used to approximate temperature profiles at low altitudes in what is named the "multifractal method" (Fig. 4). At higher altitudes, the previously-presented Tatarski hypothesis is used to construct temperature profiles (Fig. 5). While the first method is only effective at low altitudes because it is inferred and calibrated by ground-level temperature measurement, the second method is only effective at higher altitudes because of its approximative nature and because of its high sensitivity to aerosol variation. These methods are then compared with a standard lapse-rate temperature profile and aerosonde temperature profile (Figs. 4, 5).

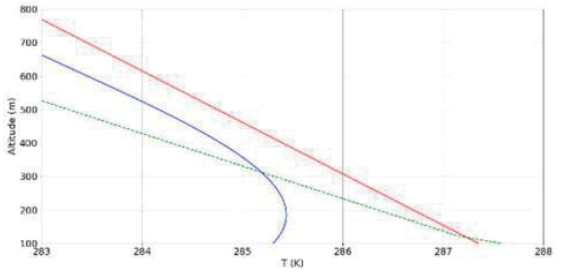

Figure 4. T profile (multifractal method), 2018/02/02, 12:00.

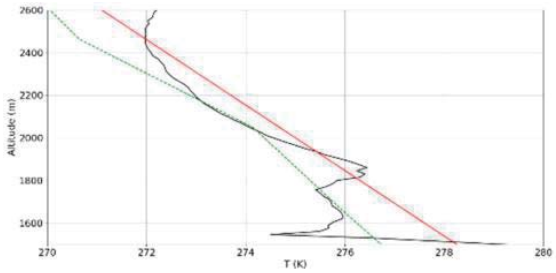

Figure 5. T profile (Tatarski hypothesis method), 2018/02/02, 12:00.

Challenges

The obtained results are strongly influenced by the conditions employed in the theory; at the forefront of these conditions lies the fact that additive inhomogeneity is considered to be constant throughout the measurement intervals used in the calculations. The theoretical consequences of this assumption must be considered.

It is possible to infer a connection between homogeneity and entropy from the very definition of entropy itself – this connection, combined with the Kolmogorov-Sinai interpretation of chaos and entropy, implies that the Tatarski hypothesis is fully valid, instead of approximately valid, only for temporal scales short enough that the various turbulent transport phenomena taking place in the given atmospheric profile are no longer chaotic and irreversible (Rodewald, 1990).

This troubling conclusion means that, in order to avoid any and all errors associated with this method, data profiled at Lyapunov time increments must be used – thus, one should ideally employ data taken at intervals of approximately a hundreth of a second. Unfortunately, this data collecting frequency is beyond what most telemetric platforms can reasonably achieve, although this frequency is feasible for some meteorological instruments – however, if this technical and theoretical avenue is explored, the benefits of temperature profiling with elastic lidar data would be tremendous.

Acknowledgements

The authors would like to thank the National Institude for Research and Development in Optoelectronics „INOE 2000" for providing access to the experimental platform used in this study and to the associated data. This work was supported by a grant of the Romanian Ministry of Education and Research, CNCS – UEFISCDI, project number PN-III-P1-1.1-TE-2019-1921, within PNCDI III.

References

Rodewald. Entropy And Homogenity, *American Journal of Physics*, 58 (2), 164-168, 1990.

Roșu et. al., A Turbulence-Oriented Approach To Retrieve Various Atmospheric Parameters Using Advanced Lidar Data Processing Techniques, *Atmosphere*, 10 (1), 38, 2019.

Roșu et. al., Multifractal Model of Atmospheric Turbulence Applied to Elastic Lidar Data, *Atmosphere*, 12 (2), 226, 2021.

Stachlewska et. al., Evaluation of the Boundary Layer Morning Transition Using the CL-31 Ceilometer Signals, *Acta Geophysica*, 62 (2), 367-380, 2014.

Tatarski, Wave Propagation in a Turbulent Medium, Institute of Atmospheric Physics Academy of Sciences of the USSR, Translated from Russian by R.A. Silverman, Dover Publications Inc.: New York, 1961.

Planetary Boundary Layer Height retrievals using Remote Sensing Observational datasets

I. Tsikoudi[1,2], E. Marinou[1,3], A. Gialitaki[1,4], M. Tsichla[1,5], V. Amiridis[1], E. Giannakaki[2,6], M. Tombrou[2], V. Vakkari[7,8], M. Komppula[6] and H. Flocas[2]

Contact: jtsik@noa.gr

(1) Institute for Astronomy, Astrophysics, Space Applications and Remote Sensing, National Observatory of Athens, Vas. Pavlou & I. Metaxa, 15236 Penteli, Greece
(2) Department of Environmental Physics and Meteorology, National and Kapodistrian University of Athens, 15784 Athens, Greece
(3) Institute of Atmospheric Physics, German Aerospace Center (DLR), Oberpfaffenhofen, Germany
(4) Laboratory of Atmospheric Physics, Aristotle University of Thessaloniki (APTH), Thessaloniki, Greece
(5) Environmental Chemical Processes Laboratory, Department of Chemistry, University of Crete, Heraklion, Greece
(6) Finnish Meteorological Institute, Atmospheric Research Centre of Eastern Finland, Kuopio, Finland
(7) Unit for Environmental Sciences and Management, North-West University, ZA-2520 Potchefstroom, South Africa
(8) Finnish Meteorological Institute, FI-00101 Helsinki, Finland

Introduction

The Planetary boundary layer (PBL), is directly affected and formed by the interaction of the Earth surface-atmosphere system. Frictional drag, evaporation and transpiration, vertical fluxes of latent and sensible heat have a strong impact on the formation of the boundary layer. Therefore, estimation of the PBL top height, provide useful information on the available air volume above the Earth's surface into which emitted air pollutants are diluted and thus constitutes a fundamental parameter regarding air quality and weather or dispersion forecasting models.

In this study, active remote sensing of meteorological parameters and aerosols by means of Lidars, are used to detect PBL height. The measurements were collected in the frame of the Pre-TECT Campaign that took place in Finokalia (35.34°N, 25.67°E, 250 m a.s.l.), Crete, during the period 1-30 April 2017, organized by the National Observatory of Athens (NOA). Moreover, continuous ground-based lidar observations from an experimental campaign (1-30 April 2016) at Nicosia Cyprus (35.08°N, 33.22°E, 181 m a.s.l.), are presented.

For the retrievals of PBL Height (PBLH), wavelet covariance transform method is applied on backscatter and water vapor mixing ratio profiles acquired with a Raman Lidar the type of Polly-XT. Water Vapor Mixing ratio retrievals are only available during Raman Scattering times (00:00-04:00UTC and 18:00-24:00UTC). Collocated Halo Wind Doppler Lidar provides wind speed-direction and PBLH, using flat threshold method from 15-min averaged turbulent dissipation rate.

Results and discussion

In Figure 1, a case-study from Nicosia (02 April 2016) is presented. The diurnal evolution of the PBLH is well-captured by the WCT method implied on the backscatter 15-minute averaged profiles (cyan triangles). The well-mixed, convective layer during local noon reaches the height of 2.25km and the nocturnal stable layer, ranges from 400 to 700m. On the other hand, WCT on the water vapor mixing ratio (purple circles), results in a lower values of PBLH, which possibly corresponds to a surface layer rich in water vapor, reserving a significant difference between the two parameters.

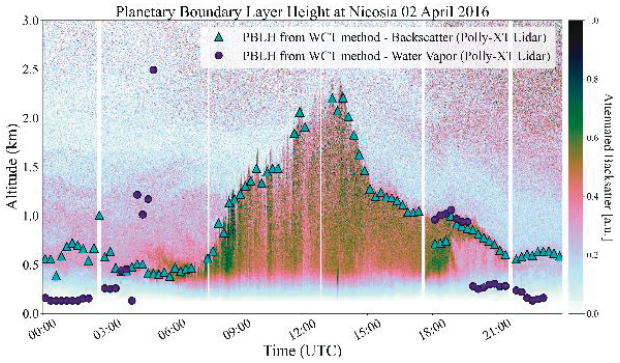

Figure 1. Time-height plot of the Overlap Corrected Attenuated backscatter from Polly-XT Lidar and PBLH: from WCT applied on 15-minute averaged profiles of backscatter (cyan triangles) and water vapor mixing ratio (purple circles) – 02 April 2016 Nicosia, Cyprus

In Figure 2, a case-study from the PreTECT Campaign (02 April 2017), includes measurements from PollyXT Raman Lidar (cyan and purple points) and Halo Wind Doppler Lidar (red hexagons). In this case, the diurnal evolution is not well represented, possibly due to the presence of dust aerosols. However, there is a good accordance between the water vapor and the backscatter retrievals, that detect a well-mixed aerosol residual

(0-4UTC) and nocturnal (18-24UTC) layer. Finally, concerning the layer detected by using threshold method from 15-min averaged Turbulent Kinetic Energy dissipation rate, it is noteworthy that Halo Wind Doppler Lidar and PollyXT Raman Lidar are in good agreement during 6:00-9:00UTC, when turbulent air motion starts, and a mixing layer begins to be formed. The lower mixing layers that Halo estimates, represent low turbulence during afternoon and night (16:00- 24:00), in the absence of powerful winds.

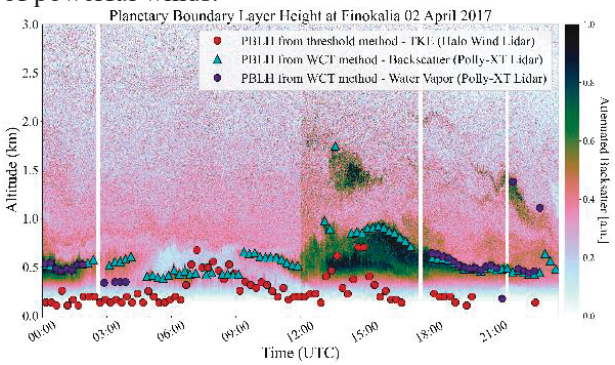

Figure 2. Time-height plot of the Overlap Corrected Attenuated backscatter from Polly-XT Lidar and PBLH: from WCT applied on 15-minute averaged profiles of backscatter (cyan triangles) and water vapor mixing ratio (purple circles). The red hexagons correspond to the PBLH from Halo Doppler Wind Lidar threshold method – 02 April 2017 Finokalia, Crete.

Concerning the weather conditions, the wind speed and direction measured from Halo Wind Lidar, is presented in Figure 3. The first half of the day, strong north winds occured, resulting in an almost stable layer (00:00-09:00UTC). After 12:00UTC, south winds contribute to the change of the atmospheric circulation with calm south winds that are possibly related with dust aerosols transport, and low TKE values.

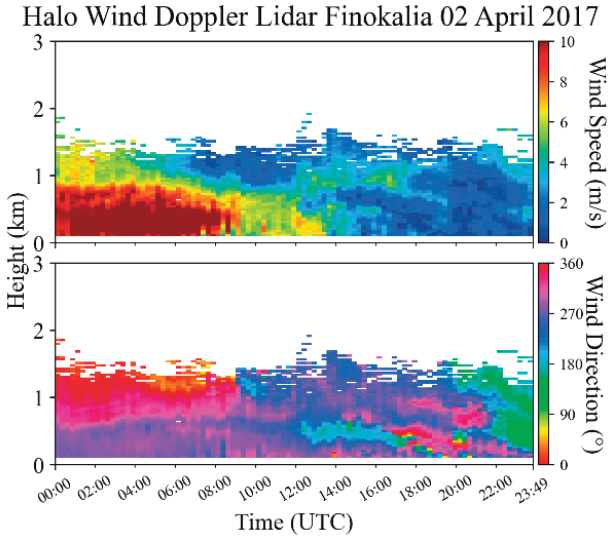

Figure 3. Top: Wind Speed from Halo Wind Doppler Lidar, Bottom: Wind Direction from Halo Wind Doppler Lidar – 02 April 2017, Finokalia, Crete.

Challenges

Wavelet covariance transform method is a multidimensional topic for the detection of PBL Height. The right choice of the dillation and threshold, as well as the atmospheric conditions (wind, aerosol concentration) constitute a challenging procedure and directly affects the reliability of the results. Furthermore, each parameter (e.g. backscatter, water vapor, TKE), might represent different layer (convective, redisual, nocturnal). The combination of these information can describe adequately the diurnal evolution of the PBL Height.

Acknowledgements

We acknowledge support of this work by the project "PANhellenic infrastructure for Atmospheric Composition and climatE change" (MIS 5021516) which is implemented under the Action "Reinforcement of the Research and Innovation Infrastructure", funded by the Operational Programme "Competitiveness, Entrepreneurship and Innovation" (NSRF 2014-2020) and co-financed by Greece and the European Union (European Regional Development Fund).

References

Stull Ronald B., An Introduction to Boundary Layer Meteorology, Springer, (1988).

Baars Holger et al., Continuous monitoring of the boundary-layer top with lidar, *Atmos. Chem. Phys.* 8, 7281–7296, 2008.

Brooks, Ian M., Finding boundary layer top: Application of a wavelet covariance transform to lidar backscatter profiles, *Journal of Atmospheric and Oceanic Technology*, 20.8, 1092-1105, 2003.

Vakkari Ville et al., Low-level mixing height detection in coastal locations with a scanning Doppler lidar, *Atmos. Meas. Tech.*, 8, 1875–1885, 2015.

The characteristics of planetary boundary layer over Măgurele, Romania investigated using a synergy between Doppler wind lidar, cloud radar, and radiometer

***R. Pîrloagă*[1], *F. Țoancă*[1], *S. Andrei*[1], *C. Marin*[1], *D. Ene*[1], *B. Antonescu*[1], *D. Nicolae*[1]**
razvan.pirloagă@inoe.ro
(1) Remote Sensing Department, National Institute of Research and Development for Optoelectronics INOE 2000, Str. Atomiştilor 409, Măgurele, RO077125 Ilfov, Romania

Introduction

The air pollution costs in Bucharest the capital of Romania is one of the highest in Europe. A study published in 2020 estimated that the air pollution cost (mainly due to PM 2.5 and PM10) per in 2018 in Bucharest were of approximately 3,000 euro being the highest in Europe (CE Delft 2020).

To better understand the mechanisms that enhance the pollution in Bucharest and surrounding areas it is necessary to understand both local characteristics of the planetary boundary layer (PBL) and the large-scale circulation. Thus, the aim of this research is two folds. First, to characterize the dynamic and thermodynamic structure of the PBL using a synergy between Doppler wind lidar, cloud radar, and radiometer. Second, to study the synoptic scale circulation in which the PBL evolves. This will provide a detailed understanding of the local and large-scale circulations in the transport, accumulation, and the dispersion of pollutants.

Data and methods

The remote sensing instruments used in this study are a Doppler lidar scanning system, a 94 GHz cloud radar and a radiometer, located at a newly developed Măgurele Center for Atmosphere and Radiation Studies (MARS). MARS is a research infrastructure that provides detailed observations for the study of clouds, precipitation, aerosols, and radiation. It is situated at Măgurele (44.34°N, 26.01°E, 71 m MSL) approximately 12.5 km from the centre Bucharest, Romania (Figure 1). MARS is situated in the Romanian Plain, a region characterized by hot summer and humid continental climate with no significant difference in precipitation between seasons. The data were collected between Dec 2019 and May 2021.

The *Doppler-Lidar scanning system* (manufactured by Metek, Germany in association with Halo, UK) measures both the optical characteristics of the constituents in the atmosphere layers, their direction and speed. The instrument is operated continuously in vertical Stare mode (400 gates with a 30m gate length) and every 15 minutes 2 consecutive VAD scans are scheduled (30° and 70° fixed elevations, and 12 azimuthal beams-30° difference).

The *94 GHz frequency modulated continuous-wave Doppler cloud radar* (manufactured by RPG, Germany) is an essential instrument for characterizing micro- and macrophysiscal properties of clouds (Figure 1). The radar operates on a 4-chirp sequence in the 100–15,000 m height interval. Profiles of reflectivity and radial Doppler speed are produced continuously with a 2.97 s temporal resolution and a variable spatial resolution from 27.1 m between 100–1,100 to 51.1 m between 10000–15,000.

The *14-channels humidity and temperature microwave profiler* (HATPRO G5 series, RPG, Germany) provides profiles of temperature, humidity, integrated water vapor content (IWV) and liquid water path (LWP) during the study period. The profiles of temperature were obtained with 10 min resolution and those of humidity with 1 min resolution. IWV and LWP are retrieved every second. The vertical resolution of the profiles varies from 30 m below 520 m to 300 m between 6,000–10,000 m.

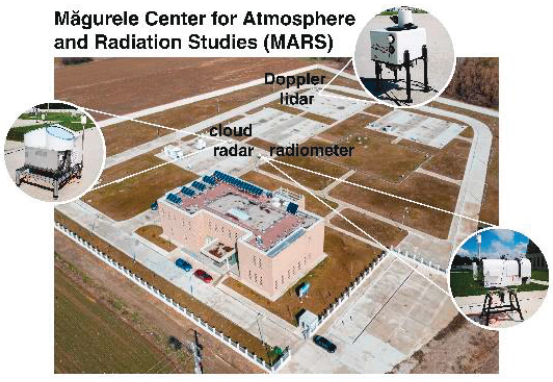

Figure 1. The Măgurele Center for Atmosphere and Radiation Studied (MARS) showing the position of the remote sensing instruments used in this study.

Meteorological data for the characterization of synoptic scale circulations were obtained from the ERA5 hourly dataset (https://cds.climate.copernicus.eu, i.e., wind, divergence, vertical velocity) and from surface weather stations.

These data were used to understand the impact of synoptic scale circulation on pollution over Bucharest. The circulations were classified using the Lamb–Jenkinson (Lamb, 1972; Jenkinson and Collison, 1977) weather types. This type of analysis was recently applied by Jiang et al. (2021) to dynamic-thermal structures of the PBL dominated by synoptic circulations and the regular effect on air pollution in Beijing.

The hourly PM10 concentrations in the Bucharest-Ilfov area are acquired from the National Air Quality Monitoring Network Platform (https://www.calitateaer.ro/), under the coordination of the National Environmental Agency. Bucharest- Ilfov area has eight air quality monitoring stations from which 1 for urban background, 3 industrial, 1 suburban, 2 traffic, and one rural background. PM 2.5 is measured just in three of these locations.

Results and discussion

The results show (1) the dynamic and thermodynamic characteristics of PBL observed at MARS under different Lamb–Jenkinson weather types and (2) the distribution of pollutants (i.e., PM2.5 and PM10) in the Bucharest area.

Challenges

Current challenges that we are trying to address:

- Can we establish the characteristics of PBL using a synergy of remote sensing instruments?
- What are the mechanisms that enhance the pollution in Bucharest and surrounding areas?

Acknowledgements

Part of the work performed for this study was funded by the Romanian Ministery of Research and Innovation, CCCDI - UEFISCDI, project number PN-III-P1-1.2-87PCCDI/2018, within PNCDI III and COST Action "PROfiling the atmspheric Boundary layer at European scale" (PROBE) CA18235 www.cost.eu, by the Romanian National Core Program (Contract No. 18N/2019) and by a grant of the Romanian Ministry of Education and Research, CNCS-UEFISCDI (Project No. PN-III-P1-1.1-TE-2019-0649) within PNCDI III, and by the European Regional Development Fund through Competitiveness Operational Programme 2014-20020, Action 1.1.3 Creating synergies with H2020 Programme, project Strengthen the participation of the ACTRIS-RO consortium in the pan-European research infrastructure ACTRIS, MYSMIS code 107596.

References

CE Delft. *Health costs of air pollution in European cities and the linkage with transport*. Delft, October 2020.

Jenkinson, A.F. and Collison, F.P. An initial climatology of gales over the North Sea. *Synoptic Climatology Branch Memorandum No 62*, p.18, Meteorological Office, Bracknell, 1977.

Jiang, Y. Et al. The thermodynamic structures of the planetary boundary layer dominated by synoptic circulations and the regular effect on air pollution in Beijing, *Atmos. Chem. Phys.*, **21**, 6111–6128.

Lamb, H.H. British Isles weather types and a register of the daily sequence of circulation patterns. *Geophysical Memoirs 116*, London: HMSO, 1972.

Raman lidar profiling of optical properties of urban winter smog

*K.Borek [1], **Iwona S. Stachlewska [1]**, Ronny Engelmann [2]*
iwona.stachlewska@fuw.edu.pl
(1)University of Warsaw, Faculty of Physics, (UW), Warsaw, Poland;
(2) Leibniz Institute for Tropospheric Research (TROPOS), Leipzig, Germany;

Introduction

Smog is considered one of the most significant anthropogenic pollution types. To monitor smog conditions in the cities typically in-situ surface measurements are used. In our study we aim at exploring the use of the near-range lidar signals for smog monitoring within boundary layer. We reckon this method could be well exploited within the EARLINET-ACTRIS community in the future, especially for the lidars capable of near-range quasi-continuous observations.

Methodology

EARLINET/ACTRIS site located in city-center of Warsaw, performs 24/7 lidar observations with PollyXT and NARLa lidars. The 12–channel NeXT Generation PollyXT Lidar [7] uses a single Nd–YAG laser as a light source that is sending simultaneously and co-axially into the atmosphere high-power laser pulses (180/110/60 mJ) at 1064/532/355 nm emitted with 20 Hz frequency. The backward scattered light is collected onto two Newtonian–type telescopes. The large telescope measures the elastic Mie and Rayleigh scattering at 355, 532 and 1064 nm, the elastic cross–polarized scattering at 355 and 532 nm, and the Raman scattering at three wavelengths (for N2 at 387 and 607 nm, for H2O at 407 nm). The small telescope measures backward elastic scattering at 532 and 355 nm and N2 Raman scattering at 607 and 387 nm. With the large telescope we can obtain signals that can be evaluated from an altitude of about 300–500 m above the ground. The NARLa is designed to enhance the lowermost range of signals from an altitude of about 30–50 m above the ground. An incomplete geometrical overlap range between the emitted laser beam and the full field of view of the telescope affects the measured signals and can be partly corrected using the combination of the signals.

Both lidars applied together, comprise unique capabilities allowing for daytime near-range wavelength-dependent Raman polarization and water vapor retrieval. It is a first report on added value of such lidar combination for low-troposphere sensing, as demonstrated on a case study for an urban smog episode, which occurred on 20-22 February 2018 in Warsaw, Poland.
From lidar signals we derived sets of optical properties that captured the evolution of the spatio-temporal variability of smog on a scale of 3 days. Lidar products were compared with particulate matter measurements of particulate matter ($PM_{2.5}$ and PM_{10}) measured by the Warsaw WIOŚ monitoring network (data available via http://powietrze.gios.gov.pl/pjp/archives).

Results

An example of the results obtained is given in Figure 1. It has been found, that fine particle fraction (size < 2.5 µm) during smog episode was significant, whereby the fine-to-coarse mass ratio (FCR of 1.3-3.5) obtained for the dry-smog (40-70%) was indicating less domination of fine particles than for the wet-smog (65-85%) measured on 09-11 January 2017.
In general, the highly and positively correlated RH and FCR at the surface was observed; the higher the fine particle fraction (FCR) the higher the relative humidity (RH). No clear relationship between the RH nor FCR and the AE_{BL}(355/532) nor LR (at 355 and 532 nm) was found. The higher the AOD_{BL}(at 355 and 532 nm) the higher the FCR and RH but no clear relation with AE_{BL}(355/532). For the higher AE_{BL}(355/532) the lower LR were obtained (at both corresponding wavelengths).
In the FCR, the fine particle fraction dominated but it was constrained with AE values of 1-2, which means that the smaller in size of particles (< 500 nm) derived within boundary layer must have significantly contributed to the fine particle fraction.

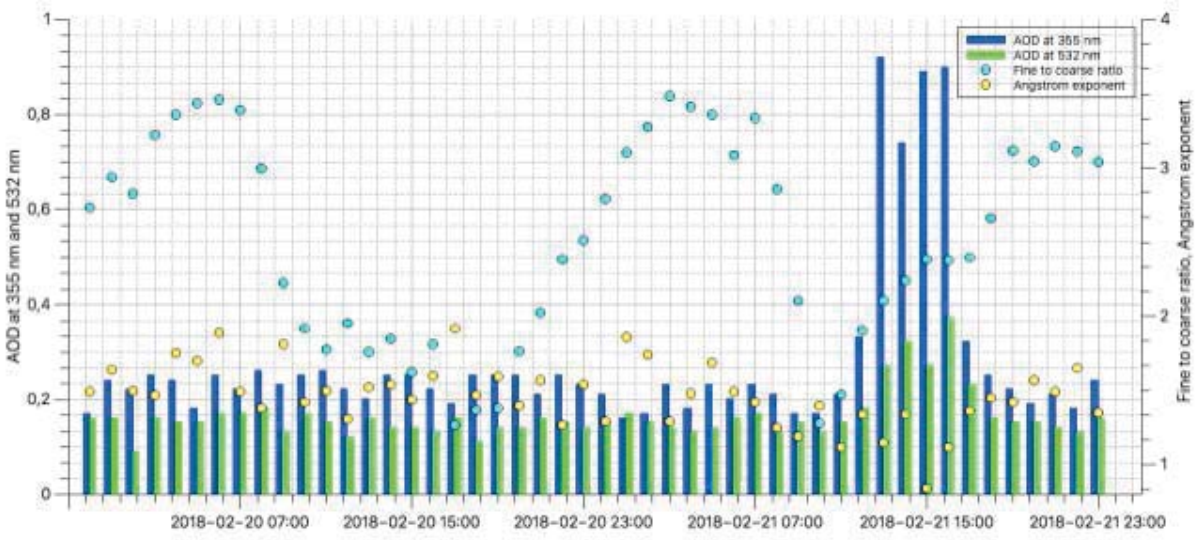

Figure 1 *Evolution of AOD along with AE, RH and FCR on 20-22 February 2017 over Wrasaw; in general, decrease/increase of FCR (blue dots) occurred with decrease/increase of AE (yellow dots).*

Conclusions

Smog was observed by the means of lidar and in-situ sensors. Meteorological measurements indicated prevailing conditions of dry-smog (RH < 80%) for which PM_{10} 120, $PM_{2.5}$ 70, AE 1.7±0.3 was observed and some indication of wet-smog (RH 80-95%) for which PM_{10} 160, $PM_{2.5}$ 120 and AE 1.5±0.4 was observed.

For both smog types higher AOD was related to higher AE and lower LRs within boundary layer, as related to higher RH and FCR at surface. This means that more humid particles tend to have smaller size (< 2.5 um) at surface, and smaller size also in boundary layer (< 500 nm), what could explain higher optical depth and lower visibility in such conditions.

FCR and RH follow similar trends of diurnal changes, with characteristic increase at nighttime. However, for the wet-smog FCR and AE seem to be strongly anti-correlated, which mean that very high humidity contributes significantly to dominating fine-particles fraction at surface but the effect is weaker within boundary layer. Moreover the diurnal cycle of FCR and RH is disappearing in wet-smog.

Acknowledgements

This work would not be possible without involvement of technical staff, especially Rafał Fortuna and Wojciech Kumala at University of Warsaw.

References:

Stachlewska, I.S.; Costa-Suros, M.; Althausen, D. (2017a) Raman Lidar water vapor profiling over Warsaw, Poland. Atmos. Res. 194, 258–267.

Stachlewska, I.S.; Zawadzka O; Engelmann R. (2017b) Effect of Heat Wave Conditions on Aerosol Optical Properties Derived from Satellite and Ground-Based Remote Sensing over Poland Remote Sens. 9, 1199; doi:10.3390/rs911119

Comparison of spatial aerosol distributions measured in situ and by a scanning LIDAR

H. Zhang[1], *H. Saathoff*[1], *C. Rolf*[2], *R. Tillmann*[3], *F. Wagner*[4], *F. Wienhold*[5],*T. Leisner*[1]
Hengheng.zhang@kit.edu
(1) Institute of Meteorology and Climate Research, Karlsruhe Institute of Technology, Eggenstein-Leopoldshafen, Karlsruhe, Germany
(2) Institute of Energy and Climate Research - Stratosphere (IEK-7), Forschungszentrum Jülich GmbH, Wilhelm-Johnen-Straße, Jülich, Germany
(3) Institute of Energy and Climate Research - Troposphere (IEK-8), Forschungszentrum Jülich GmbH, Wilhelm-Johnen-Straße,Jülich, Germany
(4) Deutscher Wetterdienst (DWD), Frankfurter Str. 135, Offenbach am Main, Frankfurt,Germany
(5) Institute for Atmospheric and Climate Science, ETH Zurich, Universitätstrasse 16, Zürich, Switzerland

Introduction

The distribution and temporal evolution of atmospheric aerosol particles has great impact on human health and climate. To investigate the horizontal and vertical distribution within and above boundary layer, we collected a comprehensive dataset by remote sensing and in situ measurements combining measurements with a scanning LIDAR, an optical particle counter (OPC) on an unmanned aerial vehicle (UAV) and a backscatter-sonde on a balloon. The UAV measurements provide vertical profiles of atmospheric parameters from ground to around 1.2 km above ground level whereas the balloon reached an altitude of 30 km. These datasets contain information on particle backscatter and size but also on atmospheric temperature, pressure and humidity. In this work, we will discuss the uncertainties and advantages of the different methods as well as the evolution of the atmospheric boundary layer.

Results and discussion

The measurements were conducted at the Jülich Research Center (FZJ) (6.4131 °E, 50.9084 °N, 110 m above sea level) near the city of Jülich with support of the Modular Observation Solution for Earth System (MOSES) project. A 3-D scanning LIDAR (LR111-ESS-D200, Raymetrics Inc.), a UAV platform (eBee, sensefly) carrying meteorological sensors and an OPC (N3, alphasense), as well as a radiosonde carrying the Compact Optical Backscatter Aerosol Detector (COBALD, ETH Zürich) and meteorological sensors were used to study the vertical distribution and evolution of aerosol particles.

The UAV was launched from early morning to the late afternoon to study the evolution of the boundary layer. Figure 1 shows an example measured at 8:30, on July 9th, 2018. The backscatter coefficients and particulate matter (PM_1) concentrations calculated from the OPC size distributions are shown. The LIDAR performed scanning measurements using elevation angles from 90° to 5° with steps of 5°. The thin gray line shows the backscatter coefficients for each scanning angle and the thick red line is the average of them. The vertical distribution of the aerosol particles in the well-mixed boundary layer is reflected well in both, LIDAR and OPC measurements. Furthermore, the backscatter coefficients from both methods seem to agree as well. In addition, the vertical layered number size distribution is shown at the right side of Figure 1. Larger particles were detected only below 300 m altitude.

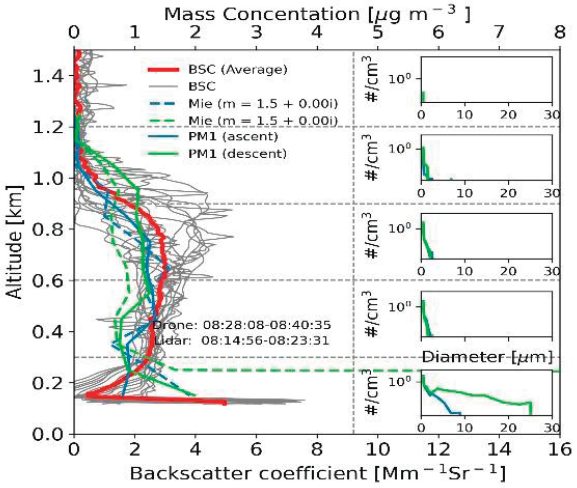

Figure 1. LIDAR backscatter coefficients and backscatter coefficients, mass concentration, and particle size distribution calculated from UAV-borne OPC on July 9th, 2018.

The balloon-borne COBALD sensor provided backscatter ratios from ground to around 30 km at two wavelengths (455 nm & 940 nm).

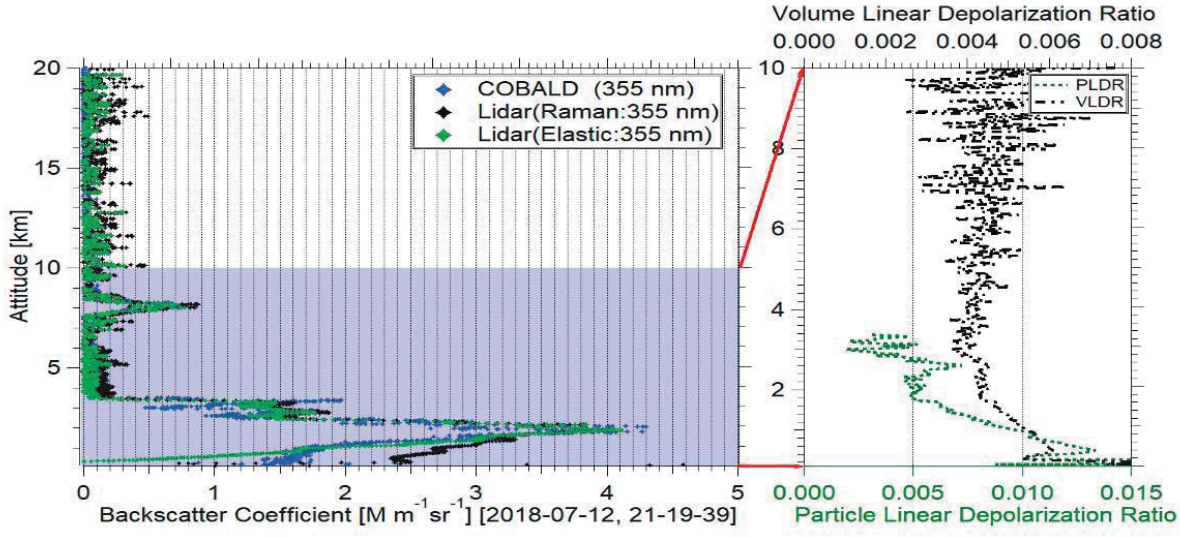

Figure 2. Backscatter coefficients measured by balloon-borne COBALD and LIDAR (left) as well as aerosol volume and particle depolarization ratio measured by LIDAR. (right) on night time of July 12th of 2018.

Figure 2 shows the backscatter coefficients from COBALD and LIDAR measurement for a LIDAR integration time of 1 hour. Here the backscatter coefficients from COBALD have been corrected for the field of view (Brunamonti et al., 2020) and by wavelength conversion. We find a good agreement between backscatter coefficients from LIDAR and COBALD measurement except for the attitudes below 2 km. This discrepancy is due to the temporal evolution of aerosol particles in the boundary layer as can be seen from LIDAR data with higher temporal resolution (e.g. 5 min). In addition, the volume and particle depolarization ratios measured by LIDAR are shown in the right side of Figure 2. The low depolarization ratios support our assumption that the particles are spherical and that we can use Mie calculations for the field of view correction.

Conclusions

The evolution of the spatial distribution of aerosol particles was investigated using a scanning LIDAR, an UAV platform, and balloon measurements. UAV-borne OPC measurements and LIDAR measurements show similar vertical aerosol distributions and a good aerosol mixing within the boundary layer. The Balloon-borne COBALD backscatter coefficients show good agreement with LIDAR measurement. Both types of in suit measurements confirm our LIDAR analysis. At the conference, more details of the uncertainties and advantages of the different measurement methods will be discussed.

Acknowledgements

Support by the staff of the Institutes of Meteorology and Climate Research (KIT) and the Institute of Energy and Climate Research (FZJ) as well as, financial support by the project Modular Observation Solutions for Earth Systems (MOSES) of the Helmholtz Association (HGF) are gratefully acknowledged.

References

Brunamonti, S., Martucci, G., Romanens, G., Poltera, Y., Wienhold, F. G., Haefele, A., and Navas-Guzmán, F.: Validation of aerosol backscatter profiles from Raman lidar and ceil-ometer using balloon-borne measurements, 2020.

Liu, C., Huang, J., Wang, Y., Tao, X., Hu, C., Deng, L., Xu, J., Xiao, H.-W., Luo, L., and Xiao, H.-Y.: Vertical distribution of PM2.5 and interactions with the atmospheric boundary layer during the development stage of a heavy haze pollution event, Science of the Total Environment, 704, 135329, 2020.

Marinou, E., Tesche, M., Nenes, A., Ansmann, A., Schrod, J., Mamali, D., Tsekeri, A., Pikridas, M., Baars, H., and Engelmann, R.: Retrieval of ice-nucleating particle concentrations from lidar observations and comparison with UAV in situ measurements, Atmos. Chem. Phys., 19, 11315-11342, 2019.

Zhang, K., Wang, D., Bian, Q., Duan, Y., Zhao, M., Fei, D., Xiu, G., and Fu, Q.: Tethered balloon-based particle number concentration, and size distribution vertical profiles within the lower troposphere of Shanghai, Atmos. Environ., 2017.

ABL determination by Raman lidar and comparison with different approaches in the frame of HyMeX SOP1

D.Summa[1,2], P.Di Girolamo[2], G.Vivone[1], G.D'Amico[1], and N.Franco[2]
Donato Summa donato.summa@imaa.cnr.it
(1)CNR-IMAA C.Santa Loja Tito Scalo (Potenza), Italy
(2) University of Basilicata, via Ateneo Lucano, Potenza Italy

Introduction

The atmospheric planetary boundary layer (ABL) is the lower region of the atmosphere directly in contact with the earth's surface and strongly influenced by this surface. In this layer physical quantities such as flow velocity, temperature and moisture display rapid fluctuations associated with turbulent motion and vertical mixing.

The characterization of the planetary boundary layer is of primary importance in a variety of fields such as weather forecasting, climate change modeling and air quality prediction .

The structure of the PBL can be complex and highly variable. The PBL height is commonly used to characterize the vertical extent of mixing within the boundary layer and the height at which exchange with the free troposphere takes place (Seibert et al., 2000).

An alternative lidar approach is based on the application of a Haar wavelet covariance transform to the lidar backscatter signals. Based on this approach the boundary layer top is automatically detected by locating the covariance maximum. In this paper we compare different independent methods for the determination of the ABL height. Retrievals are obtained with different techniques applied to different instruments operating during used during HyMeX-SOP1, Wind Profiler, the Raman lidars system BASIL, and from different models, the ECMWF global model and the MESO-MH mesoscale model. In the present work we compute the ABL in the period of measurements from 16th to 21th october 2012.

Results and discussion

The lidar system BASIL makes use of a Nd:YAG laser source, equipped with second and third harmonic generation crystals, capable to emit pulses at 1064, 532 and 355 nm. Laser pulses at these three wavelengths are simultaneously transmitted in the atmosphere along the zenith. The shortest of these wavelengths (355 nm) is used to stimulate vibrational and rotational Raman scattering from water vapour, nitrogen and oxygen molecules. These scattering processes, and the corresponding lidar echoes, are exploited to ultimately measure the vertical profiles of water vapour temperature and multi-wavelength particle backscatter and extinction. The use of the 355 nm wavelength maximizes lidar performance, as in fact Rayleigh and Raman scattering cross-sections are proportional to the fourth negative power of the wavelength.

For the specific operation of HyMeX-SOP1, the laser source was upgraded to generate a single pulse energy power at 355 nm of 500 mJ (corresponding to an average power of 10 W at a pulse repetition frequency of 20Hz). The received is developed around a Newtonian telescope, with a primary mirror diameter of 0.45 m. The receiver also includes two small lenses, with a diameter of 0.05 m, these latter two used for the collection of the 532 and 1064 nm elastic signals. The key feature of BASIL is represented by its capability to perform daytime and night-time high-resolution and accurate measurements of atmospheric temperature and water vapour based on the application of the rotational and vibrational Raman lidar technique, respectively.(Di Girolamo et al., 2016)

Figure 1 Supersite in Candillargues, Southern France were was located Basil system (Maps Data: Google, @2021)

Throughout the duration of HyMeX-SOP1, the University of BASILicata ground-based Raman Lidar system (BASIL) was deployed in the Ceveninnes-Vivres site (Candillargues, Southern France, Lat: 43°37' N, Long: 4° 4' E, Elev: 1 m, see figure 1) and operated between 5 September

and 5 November 2012, collecting more than 600 hours of measurements, distributed over 51 measurement days and 19 intensive observation periods (IOPs).

Rotational Raman signals can potentially be used to infer both the mixed layer and the residual layer height. In this respect, we need to recall that temperature measurements are performed by BASIL through the application of the rotational Raman lidar technique in the UV. These same rotational signals can be used to determine the ABL height (Summa *et al.*, 2013).

Rotational lines fall within two narrow spectral bands in the proximity of the laser wavelength: one including lines characterized by low quantum rotational numbers, P_{LoJ} (z), and the other including lines characterized by high quantum rotational numbers, P_{HiJ} (z). In this case we consider the ratio between two signals

$R(z)= P_{HiJ}(z)/ P_{LoJ}(z)$

The ratio $R(z)$ is characterized by a strong sensitivity to temperature variations, therefore we can analyze minimum of the derivative for the range corrected signals $RCS(z)=R(z)z^2$ in the follow algorithm to determine the height of the ABL:

$$ABL = \frac{d}{dz}\{\log RCS(z)\}$$

The results from the Raman lidar are compared with a Wind Profiler, with ECMWF-ERA5 reanalysis, with MESO-MH mesoscale forecasts, and also with the MIPA methodology (Vivone et al.2021) (see Figure 2), while figure 3 reports the percentage deviations between BASIL and the other methodologies/sensors/models, which are found to always be within ±50%.

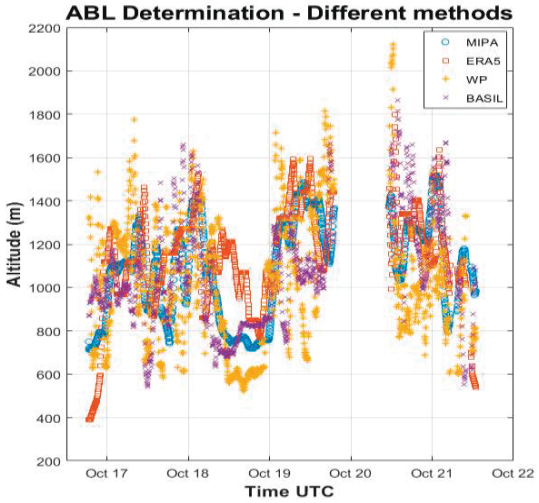

Figure 2. ABL Comparison in terms of ABL estimates from different approach during the period 16-21 October 2012

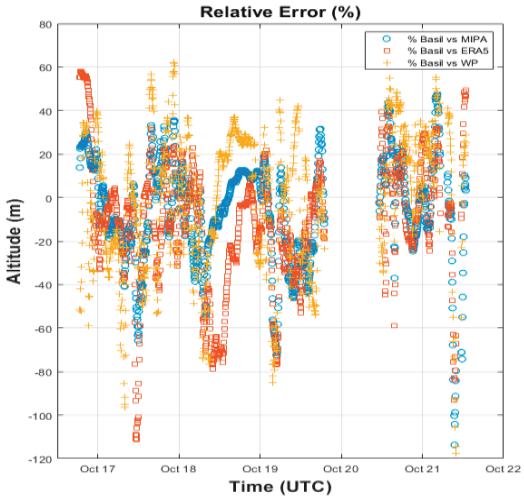

Figure 3. Percentage deviations between BASIL and the other methodologies/sensors/models during the period16-21 October 2012

Other result will be presented and discuss during the conference.

Acknowledgements

Wind Profiler dataset were extracted from the HyMeX database (Contact person: Said Frèdèrique Laboratoire d'Aérologie, Université de Toulouse, UMR CNRS 5560). This work was possible based on the support from the Italian Ministry for Education, University and Research under the Grants OT4CLIMA and FISR2019-Concerning, and the support of the Italian Space Agency, under the Grant As-ATLAS.

References

P. Seibert, F. Beyrich, S.-E. Gryning, S. Joffre, A. Rasmussen, P. Tercier, Review and intercomparison of operational methods for the determination of the mixing height, *Atmospheric Environment, Volume 34*, Issue 7, Pages 1001-1027, ISSN 1352-2310, 2000.

P. Di Girolamo, C. Flamant, M. Cacciani, E. Richard, V. Ducrocq, D. Summa, D. Stelitano, N. Fourrié and F. Saïd, Observation of low-level wind reversals in the Gulf of Lion area and their impact on the water vapour variability, *Quarterly Journal of the Royal Meteorological Society,142 (Suppl 1):* 153–172, doi: 10.1002/qj.2767, 2016.

D. Summa, P. Di Girolamo, D. Stelitano, and M. Cacciani Characterization of the planetary boundary layer height and structure by Raman lidar: comparison of different approaches *Atmos. Meas. Tech.*, 6, 3515–3525, 2013

G.Vivone, G.D'Amico, D.Summa, S.Lolli, A.Amodeo, D. Bortoli, and G. Pappalardo. Atmospheric boundary layer height estimation from aerosol lidar: a new approach based on morphological image processing techniques *Atmos. Chem. Phys.*, 21, 4249–4265, 2021

Combining Ceilometer and Surface Meteorological Data with Machine Learning to Estimate the Atmospheric Boundary Layer Height at the ACTRIS Granada station

G. de Arruda Moreira[1,2,3], G. Sánchez-Hernandez[1,4], J.L. Guerrero-Rascado[1,2], A. Cazorla[1,2], L. Alados-Arboledas[1,2]
gregori.moreira@ifsp.edu.br.br
(1) Andalusian Institute for Earth System Research (IISTA-CEAMA), Granada, Spain
(2) Dpt. Applied Physics, University of Granada, Granada, Spain
(3) Federal Institute of São Paulo (IFSP), São Paulo, Brazil
(4) Dpt. of Physics, University of Jaén, Jaén, Spain

Introduction

The Atmospheric Boundary Layer (ABL) is the region of the troposphere directly influenced by the presence of the Earth's surface, and responds to surface forcings with a timescale of about an hour or less (Stull, 1988). The characteristics of the ABL, and particularly, the ABL height (ABLH), play a fundamental role in numerous atmospheric areas such as weather forecasting, air quality and/or numerical modeling.

The estimation of the ABLH with high temporal resolution is not an easy task, due mainly to the variability of its daily cycle. In the last years numerous remote sensing systems, such as elastic lidars, ceilometers, Doppler lidars and microwave radiometers have been widely used to characterize the ABLH. Ceilometers have the advantage to be a low-cost and low-maintenance systems that monitors aerosol and clouds layers. Such characteristics have favored the creation of numerous worldwide networks, such as E-PROFILE and ICENET, and the use of ceilometer for ABLH detection.

However, there are important limitations in the use of ceilometers for ABLH monitoring, particularly in complex cases such as rainy situations, presence of low clouds, and dust outbreaks. In these situations, the abrupt changes of the aerosol vertical profile notably affect to the gradient method used to estimate the ABLH with the ceilometer. Another drawback in the application of ceilometers to obtain ABLH is the difficulty for discriminating between the RL top height (RLH) and SBL height (SBLH) during stable periods.

Recent studies have applied Machine Learning Techniques to estimate the ABLH. Thus, Jiang et al. (2021) applied Machine Learning combined GPS radio occultation technology to build a simulation model to estimate the ABLH, while Krishnamurthy et al. (2021) proposes a method based on Random Forest algorithm to estimate the ABLH from meteorological and Doppler lidar data. In this framework, the main objective of this study is to propose a Machine Learning algorithm to improve the ABLH estimations obtained from the combination of a ceilometer and surface meteorological data, i.e. the typical dataset available at common ceilometer stations worldwide.

Model and dataset

The Gradient Boosting Regression Trees (GBRT) is a supervised non-parametric Machine Learning technique widely applied in classification and regression problems. The idea behind *boosting* is to sequentially fit multiple 'weak learners', that is, simple models that perform relatively poorly with low accuracy (Fig. 1). In each iteration, a new model is proposed using information from the previous model trying to learn from its mistakes and improving iteration by iteration. In the case of GBRT, the 'weak learners' are decision tree models with very few branches.

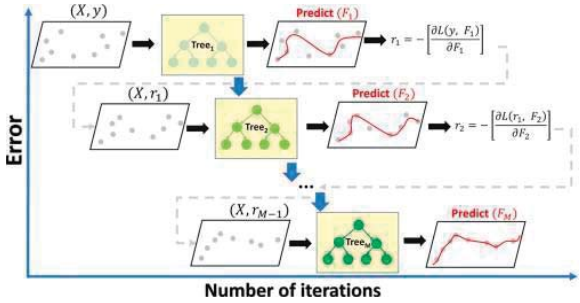

Figure 1. Example of GBRT algorithm

The GBRT algorithm proposed in this study uses as features (independent variables) estimations of the ABLH derived applying the gradient method to a ceilometer signal ($ABLH_{CEIL}$) and several surface meteorological variables, while the target (reference) ABLH values in this study have been those estimated from a microwave radiometer ($ABLH_{MWR}$). A detailed study of the features and the hyperparameters involved in the model set-up have been developed in order to avoid the model overfitting and guarantee its good performance during the training stage. The GBRT have been trained and tested using the entire years of 2015 and 2016.

The measurements analyzed in this study were

recorded at the ACTRIS Granada station located on the roof of the Andalusian Institute of Earth System Research (IISTA-CEAMA) at Granada (37.164 ºN, 3.605 ºW, 680 m a.s.l.). The analysis has been performed in terms of the Mean Relative Error (MRE) estimated as:

$$MRE_{GBRT}(\%) = sum\left(\frac{ABLH_{GBRT} - ABLH_{MRW}}{ABLH_{MRW}}\right).100$$

Results and discussion

The new algorithm has been validated using the entire year 2017. The model performance analysis has shown a daily pattern in the MRE_{GBRT} values (Fig. 2), with their highest values during the night-time (stable situations) and their lower values along the day-time (convective situations). Minimum differences between $ABLH_{GBRT}$ and $ABLH_{MWR}$ appears, during the central hours of the day and first hours in the afternoon, when the ABL presents is higher height. This pattern has been observed for all seasons with MRE_{GBRT} ranging between -5% and 35%. A remarkable improvement is observed with respect to the MRE_{CEIL} values, which show similar daily patterns but range between 36% and 190%.

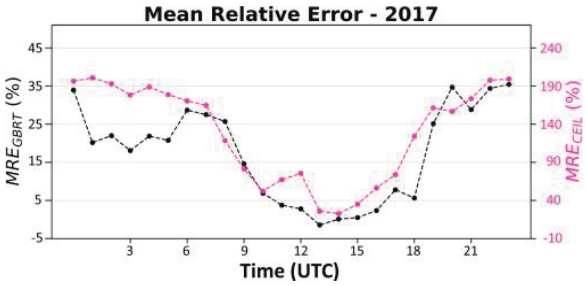

Figure 2. MRE for all cases

The proposed model has been analyzed under different atmospheric conditions revealing no dependence on cloudiness conditions. Small differences have been observed between stable and convective situations. Thus, while MRE_{GBRT} is around 11% in convective situations, these values increase up to 28% in the case of stable situations. Nevertheless, for both cases R^2 values are above 0.75 for stable and convective atmospheres and take a value of 0.91 when all conditions are considered. These results confirm the robustness of the GBRT algorithm presented in this study.

Three particular cases: 1) a clear-sky day, 2) a day with presence of low-clouds (Fig. 3A), and 3) a dust outbreak event (Fig. 3B), have been chosen to deeply analyze the GBRT. In general, in these three particular situations $ABLH_{GBRT}$ shows very similar values and behaviour than the $ABLH_{MWR}$, confirming the good model performance and a remarkable improvement with respect to the $ABLH_{CEIL}$ in these complex situations. Additionally, the new model allows enables the detection of SBLH, CBLH and RLH from ceilometer data and surface meteorological information.

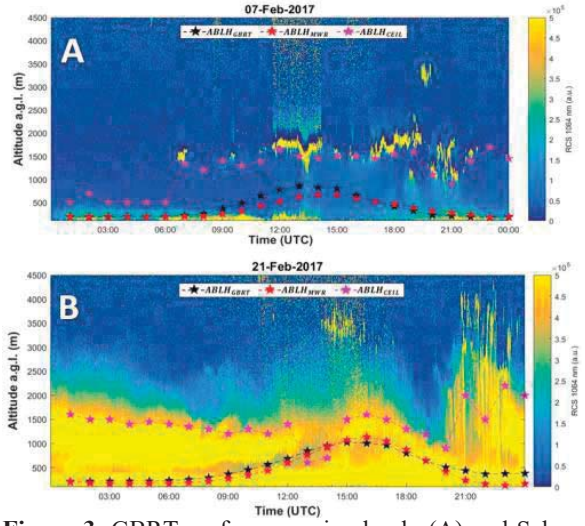

Figure 3. GBRT performance in cloudy (A) and Sahara dust outbreak (B) situations.

Challenges

Although this algorithm has been generated good results and made possible an expansion in the ABLH studies from ceilometer data, a great challenge will be the propagation of it to other ceilometer stations and networks. Although the necessary database is not complex, adaptations will probably be necessary to the peculiarities of each station.

Acknowledgements

This work was also supported by the Spanish Ministry of Economy and Competitiveness through the project CGL2017-83538-C3-1-R and the Spanish Ministry of Science and Innovation through the project PID2020-117825GB-C21. The authors thankfully acknowledge the FEDER program for the instrumentation used in this work and the University of Granada that supported this study through the Excellence Units Program. This work is related to activities within the COST Action PROBE (CA18235) and InDust (CA16202). Guadalupe Sanchez-Hernandez: Ministerio de Ciencia, Innovación y Universidades, programa Juan de la Cierva-Formación (FJCI-2017-33923)

References

Jiang et al., Analysis of differences between thermodynamic and material boundary layer structure: Comparison of detection by ceilometer and microwave radiometer. *Atmospheric Research,* 248, 105179, 2021.

Krishnamurthy et al., On the estimation of boundary layer heights: A machine learning approach, *Atmos. Meas. Tech. Discuss.*, 2021

Stull, R. B., An Introduction to Boundary Layer Meteorology, 666 pp., *Kluwer Acad., Dordrecht*, Netherlands, 1988.

Performances and evolution of CIMEL CE376 micro-pulse LIDAR

I. Popovici[1,2], S. Victori[1], L. Proniewski[1], M. F. Sanchez Barrero[1,2], T. Podvin[2], P. Goloub[2], Y. Gonzalez Ramos[1,3], P. Augustin[4]

i-popovici@cimel.fr
(1) CIMEL Electronique, R&D Department, 75011, Paris, France
(2) Univ. Lille, CNRS, UMR8518 – LOA – Laboratoire d'Optique Atmosphérique, 59000 Lille, France
(3) Izaña Atmospheric Research Centre, Santa Cruz de Tenerife, 38001, Spain
(4) Université du Littoral Côte d'Opale (ULCO), Laboratoire de Physico-Chimie de l'Atmosphère (LPCA), Dunkerque, France

Introduction

Continuous monitoring of aerosol vertical distribution is necessary for many applications: detection of aerosols intrusions in the altitude, clouds and rain occurrence and aerosols dynamics in the Planetary Boundary Layer (PBL). Continuous lidar data is thus important for both aerosols and clouds research community and helps better understand the processes that impact the surface and air quality. An automatic lidar system is useful for monitoring the atmospheric events that can be missed by other systems that operate only on defined schedules. During unexpected situations like the Covid-19 lockdowns, such automatic lidar instruments that do not require any human intervention are especially valuable. The CIMEL CE376 micro-pulse lidar provides long time series of continuous lidar data from which the PBL variability can be derived and allows to study the impact of such exceptional events like the Covid-19 lockdowns on air quality.

CE376 Lidar system

The Cimel CE376 lidar (Figure 1) is a biaxial system with small FOV for emission (50 μrad) and reception (120 μrad) making it suitable for aerosol profiling in the lowest altitude range. The technical characteristics are described in Table 1.
The CE376 is suitable for continuous measurements in an aerosol observation network, as standardized lidars of same model are preferable for a network. Several sites with a CE376 lidar are part of ACTRIS-FR (Lille, Paris, OHP) and four new will be setup on challenging environments, such as a high altitude site at 5230 m in Chacaltaya, Bolivia, a high temperature site on Ivory Coast (Lamto, Africa) and one remote, difficult to reach, marine environment site on Amsterdam Island. All these sites highlight the difficulty of maintenance, so an automatic system is the best candidate for such network operation. This work will be done in the frame of the OBS4CLIM (Observation for Climate) national project contributing to ACTRIS-FR and ICOS infrastructures.

Figure 1. CIMEL CE376 micro-pulse LIDAR set up at Observatoire de Haute Provence (OHP), France

The CE376 lidar was deployed in two field campaigns, for stationary measurements of background and transported aerosols at a rural site during COBIACC (Campagne d'Observation Intensive des Aérosols et précurseurs à Caillouël-Crépigny), a joint CLIMIBIO/CaPPA campaign in June-July 2019 in France, and for mobile on-road measurements of wildfires smoke at the sources during the FIREX-AQ (Fire Influence on Regional to Global Environments and Air Quality) July-August 2019 in the northwestern US (Popovici et al., 2020)

Table 1. Technical specifications of the CE376 lidar

λ	532 nm (G) 808 nm (NIR)	**Detector**	APD
Laser	Nd:YAG (G) laser diode (NIR)	**Config.**	Biaxial
Pulse energy	6 μJ/12 μJ (G) 2-4 μJ (NIR)	**Eye-safe**	Yes/No
Rep. rate	4.7 kHz	**Weight**	40 kg

Performances

The typical maximum range for a standard CE376 lidar is 5-6 km altitude by day and 18-20 km by night for 532 nm and 2-3 km by day and 10-12 km

by night for 808 nm (Figure 2; example for maximum AOD of 0.4 at 532 nm and 0.2 at 808 nm). The full overlap of the 532 nm and 808 nm channels is 1300 m and 700 m, respectively. Below this altitude we correct the incomplete lidar signal by the overlap function (Kunz and de Leeuw, 1993). We check the performances of the CE376 lidar by following the standard EARLINET procedures (Freudenthaler et al., 2018), namely the Rayleigh fit (5-10% relative deviations from molecular) and we perform telecover measurements using a 3D-printed telecover system. For the polarization calibration, we use the ±45° method. The results of both Rayleigh fit and depolarization are very comparable to the LILAS Raman multi-wavelength lidar in operation, at Lille, in ACTRIS/EARLINET (Hu et al., 2019) (Figure 2).

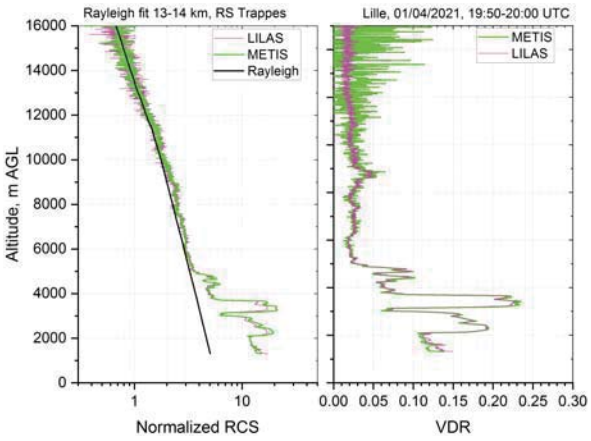

Figure 2. Rayleigh fit and Volume Depolarization Ratio (VDR) profiles at 532 nm of CE376 METIS lidar and LILAS ACTRIS/EARLINET lidar at Lille, 1 April 2021

Results

Figure 3 shows continuous time series of lidar Range Corrected Signals (RCS) at 532 nm and 808 nm measured during a heat wave event at a rural site in France, end of June 2019, during the COBIACC campaign. The PBL height was determined using the 808 nm channel, which has a low complete overlap (700 m). The profiles are corrected for the overlap function, describing the aerosol variability as close to the surface. The PBL height from the lidar is used in synergy with the anemometer data, to deduce the mixing time scale and complement the in-situ data and understand the chemical processes at the surface. The depolarization measurements allowed identifying a Saharan dust event coinciding with the heat wave, event which transported mineral dust into the PBL.

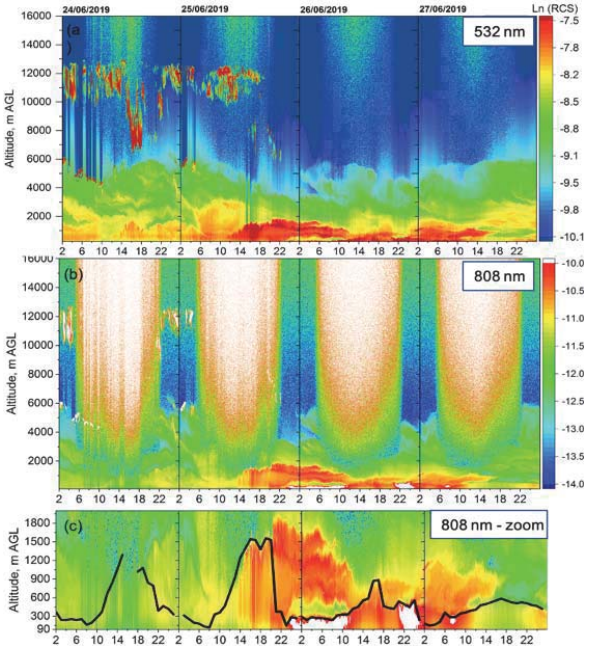

Figure 3. Lidar Range Corrected Signal (RCS) at (a) 532 nm, (b) 808 nm and (c) zoom at 808 nm with the PBL top overlaid; COBIACC campaign, Caillouel, France.

Evolution and perspectives

The evolutions of the CE376 lidar consist in the automation of the polarization calibration procedure using a motorized mount, adding linear polarizers to clean the cross-talk and optimizing the stability, robustness and temperature control of the lidar system. Also, we plan to evaluate the CE376 lidar by the CARS ACTRIS Facility.

References

Freudenthaler et al., EARLINET lidar quality assurance tools, *Atmos. Meas. Tech. Discuss.*, 1–35, doi:10.5194/amt-2017-395, 2018.

Hu et al., Long-range-transported Canadian smoke plumes in the lower stratosphere over northern France, *Atmos. Chem. Phys.*, 19(2), 1173–1193, doi:10.5194/acp-19-1173-2019, 2019.

Kunz, G. J. and de Leeuw, G.: Inversion of lidar signals with the slope method, *Appl. Opt.*, 32(18), 3249–3256, doi:10.1364/AO.32.003249, 1993.

Popovici et al., Smoke observations by lidar and sun photometer mobile measurements during FIREX-AQ camapign in summer 2019, *European Lidar Conference (ELC)*, 2020.

Method to retrieve aerosol extinction profiles and aerosol scattering phase functions with a modified CCD laser atmospheric detection system

***Y. Bian*[1,*], *C. Zhao*[2]**
bianyx@cma.gov.cn
(1) State Key Laboratory of Severe Weather, Chinese Academy of Meteorological Sciences, 100081 Beijing, China
(2) Department of Atmospheric and Oceanic Sciences, School of Physics, Peking University, 100871 Beijing, China
** now at: IMK-AAF, Karlsruhe Institute of Technology, 76344 Eggenstein-Leopoldshafen, Germany*

Introduction

Aerosols play an important role in air pollution and climate change. Many instruments were developed to measure ground level aerosol physical and chemical properties under dry state conditions. However, the vertical distribution of ambient aerosols might be of higher importance for the assessment of their climate impacts. A charged couple device camera-laser atmospheric detection system (CLADS) was developed to measure the vertical distribution of aerosol optical characteristics, especially under 1 km altitude, however, lacking direct measurements of ambient aerosol phase function, which is an important parameter in the CLADS retrieval algorithm.

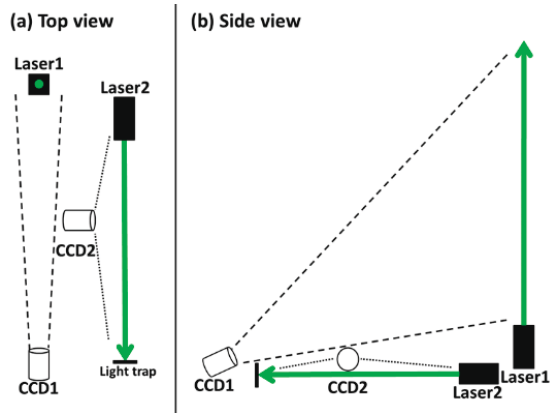

Figure 1. Sketch map of the geometric structure of modified CLADS: a. top view of the CLADS; b. side view of the CLADS.

In this work, a modified CLADS based on the camera imaging principle and the optical structure of the fisheye lens is developed to measure ambient scattering aerosol phase functions simultaneously with aerosol extinction coefficient vertical profiles (Figure 1). An improved retrieval method was setup to obtain the vertical profiles of aerosol extinction coefficients using simultaneously obtained phase functions, highly lowering afore-mentioned uncertainties of assumed phase functions, improving the accuracy of retrieved results. The advantage of this modified CLADS is that it can accomplish these aerosol measurements independent of other supplementary instruments. Benefiting from its low cost and high spatial resolution (~1 m on average) in the boundary layer, this measurement system can play an important role in the research of aerosol vertical distributions and its impacts on environmental and climatic studies.

Results and discussion

During January 2016, a comprehensive field campaign focused on wintertime air pollution in the North China Plain (NCP) was conducted on the Yanqi campus of the University of Chinese Academy of Sciences (UCAS, 40° 24′ N, 116° 40′ E, 91 m a.s.l.) located in Huairou district, Beijing, China. This site is 60 km northeast of downtown Beijing and is at the edge of the NCP, which makes it suitable for the study of regional pollution properties. In this campaign,

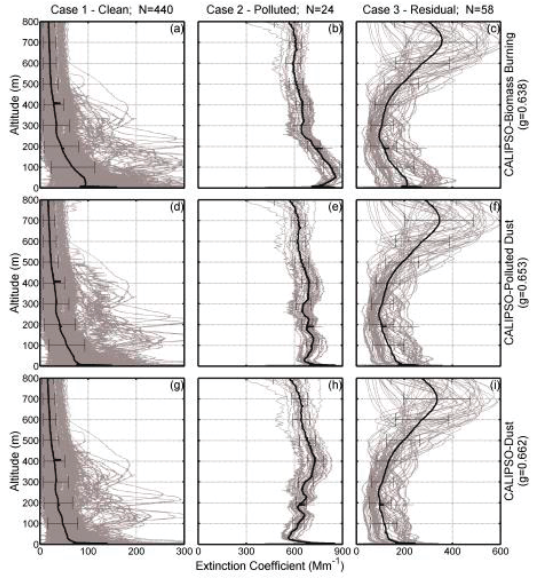

Figure 2. Aerosol extinction coefficient profiles retrieved with three different aerosol phase functions.

Following the methodology, the aerosol extinction coefficient profile can be retrieved with aerosol scattering function profile and aerosol phase function. To evaluate the influence of aerosol phase function to the retrieval results, three kinds of aerosol phase functions from CALIPSO aerosol classification were used to retrieve the aerosol extinction coefficient.

Results are displayed in Figure 2, which shows the

retrieved aerosol extinction coefficient profiles (gray lines) and the average extinction coefficients profiles and their standard deviation at various altitudes. In all the three cases, significant differences were detected in the vertical profiles retrieved with different aerosol phase functions, especially in case 2. Differences were typically larger in the near surface layer. The relative differences between the results using these two assumptions are 20.07% and 15.45% near the ground, 44.25% and 39.52% at 100m altitude for Case 1 and Case 3, respectively. For the "polluted" case, even the vertical distribution pattern changed remarkably with aerosol phase function. This sensitivity study shows that, if ambient aerosol phase function changed from CALIPSO "biomass burning" to "dust" aerosol phase function, using a constant aerosol phase function would result in large uncertainties.

To further evaluate the retrieval method of modified CLADS, a comparison between remote sensing retrieved and in-situ measured aerosol extinction coefficients was made. Note that these instruments measured dry state aerosol properties in the laboratory. However, due to the relatively low ambient relative humidity in this campaign, the in-situ measurement can be used to compare with ambient aerosol observations.

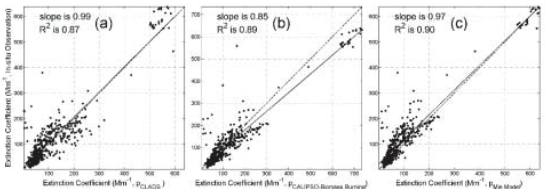

Figure 3. Comparison results between extinction coefficients measured by CLADS and in-situ instruments with different aerosol phase functions.

Figure 3 shows the comparison results. Here, aerosol phase function retrieved with real time modified CLADS, aerosol phase function of "biomass burning" aerosol introduced in the CALIPSO aerosol classification and aerosol phase function simulated with Mie model and aerosol size distribution measurements are used to retrieve the aerosol extinction coefficient profiles and compared to in-situ measurements. The slope of the fitting lines reached 0.99, 0.85 and 0.97, respectively. Results obtained using measured and modelled aerosol phase function were closer to in-situ measurements than those retrieved using "biomass burning" aerosol phase function. The coefficients of determination (R^2 in Figure 3) were 0.87, 0.89 and 0.90, respectively. However, the modelled aerosol phase function was only applicable because the relative humidity during this campaign remained mostly below 50%.

Performance of the improved retrieval method with modified CLADS was evaluated in a comprehensive field campaign on wintertime air pollution in the North China Plain during January 2016. 522 aerosol scattering function profiles were obtained by the vertical CLADS, which were classified into three case categories ("clean", "polluted" and "residual") according to their vertical distribution characteristics. Different aerosol phase functions provided in the CALIPSO aerosol classification were used to retrieve aerosol extinction coefficient profiles. Results show that time-resolved aerosol phase functions are necessary in retrieval of aerosol extinction coefficient profiles. Assuming constant aerosol phase functions would lead to significant uncertainties. Real-time measured ambient aerosol phase function by the horizontal CLADS and Mie code modelled ones were also used to retrieve the aerosol extinction coefficient profiles, which both agreed better with in-situ measurements than those retrieved with a constant CALIPSO aerosol phase function assumption, again emphasizing the importance to use time-resolved phase functions. However, the Mie model approach is only applicable to low humidity conditions and depends on aerosol size distribution and aerosol absorption property measurements, whereas the modified CLADS can derive ambient aerosol phase functions with relatively high accuracy and use them to simultaneously retrieve vertical profiles of aerosol extinction coefficients with low uncertainties and independent of other measurement instruments.

Acknowledgements

We thank Dr. Harald Saathoff for his support of Yuxuan's participating in ELC2021.

References

Barnes, J. E. et al.: Boundary Layer Scattering Measurements with a Charge-Coupled Device Camera Lidar, *Appl. Opt.*, 42(15), 2647–2652, 2003.

Bian, Y. et al.: A novel method to retrieve the nocturnal boundary layer structure based on CCD laser aerosol detection system measurements, *Remote Sensing of Environment*, 211, 38-47, 2018.

Bian, Y. et al.: Method to retrieve aerosol extinction profiles and aerosol scattering phase functions with a modified CCD laser atmospheric detection system, *Opt. Express*, 28, 6631-6647, 2020.

Session 5.
Open topic - Synergies

Aerosol Layer Height from ground based active remote sensing and satellite ALH product of S5P/TROPOMI

***A.Nemuc*[1]**, *M.Boldeanu*[1,2], *A.Dandocsi*[3] ,*M.Adam*[1], *V. Nicolae*[1,4]
(1) National Institute of R&D for Optoelectronics, INOE, 409 Atomistilor Street, Magurele, Romania, ***anca@inoe.ro***
(2) Faculty of Electronics, „Politechnica“ University of Bucharest, 1-3 Iuliu Maniu Bvd, Bucharest, Romania
(3) Directorate of Earth Observation Programmes, European Space Agency (ESA), ESRIN, 00044 Frascati, Italy
(4) Faculty of Physics, University of Bucharest, Atomistilor 405, Magurele, Romania.

Introduction

The aim of this study is to find a suitable method of validation for the satellite product ALH (Aerosol Layer Height) derived from passive remote sensing observation from S5P/TROPOMI, using ground based ceilometer measurements.

At present, daily global observations of aerosol height are not available on an operational basis. However, passive sensors on board satellites can scan the entire earth in a single day. On 13 October 2017 the Copernicus Sentinel 5 Precursor (S5P), the first of the European Sentinel satellites dedicated to monitoring of atmospheric composition, was launched with a single payload of TROPOspheric Monitoring Instrument (TROPOMI), a nadir viewing shortwave spectrometer that measures in the UV-visible wavelength range (270 – 500 nm), the near infrared (710 – 770 nm) and the shortwave infrared (2314 – 2382 nm). The ALH product is derived from measurements of the oxygen A-band in the near infrared region between 758 nm and 770 nm. It is focused on retrieval of vertically localized aerosol layers in the free troposphere, such as desert dust, biomass burning aerosol, or volcanic ash plumes (Nanda et al., 2020). Pixel size before August 2019 is 7 km x 3.5 km while after is 5.5 km x 3.5 km. Data are available through Copernicus hub (s5phub.copernicus.eu). S5P overpasses daily at around 12 UTC over mid latitude locations. Satellite data were selected based on quality flags of the available Level 2 data.

Active remote sensing techniques (such as ceilometers) can provide vertical profiles of the aerosol attenuated backscatter with vertical resolution of a few meters from ground up to 15 km. They are part of the coordinated European Network **e-profile**: (https://www.eumetnet.eu/activities/observations-programme/current-activities/e-profile/) and provide continuous vertical information for the aerosol load over Europe, but an operational algorithm for aerosol layer height assessment hasn't been implemented at the network level.

First ground based validation of satellite ALH but retrieved from GOME-2/MetOp observations was done using EARLINET lidar observations by Michailidis et al., 2021. They applied wavelet covariance transform to the lidar data in order extract geometrical characteristics (lofted layers and clouds). The method was able to obtain a significant number of collocated and coincident ground and satellite measurements due to long term satellite data based (12 years). S5P is orbiting only since 2017, therefore our study is focused on ceilometer measurements due to their continuous operation, near real time data availability and spread across Europe. Two methods were tested for aerosol layer detection: gradient method (Nicolae et al., 2018), and local minimum/maximum method (Adam et al.2020). The target requirement on the accuracy and precision of retrieved ALH is 0.5 km.

Results and discussion

Preliminary results of about 15 overpass-coincidences of S5P over Magurele, Romania (44.35N, 26.03E) during October 2017- April 2021 showed high variability of altitudes of the layers detected in a 50 km circle above Magurele for some scenes. The ALH retrieval algorithm implements a pixel selection scheme before committing to retrieving ALH satellite's estimates. The number of pixels varies from 10 to 127 for a particular scene.

Similar results were obtained when applying the two abovementioned methods to ceilometer data for aerosol heights, but there is a wide range of feature locations and backscatter intensities that can be encountered during a single day of measurements. Figure 1 is an example: three aerosol layer heights derived from ceilometer measurements in Magurele (blue, yellow, green) during 2 hours before and after the satellite overpass on 30.08.2018. The spatially averaged (in a 50 km circle above Magurele) S5P ALH is represented in black, with the error bar indicating the variability of the values. The question is now how to interpret this scene. Are these layers dust, biomass burning or volcanic ash? Using Hysplit backtrajectories (https://www.arl.noaa.gov/hysplit), dust modelling DREAM BSC (https://ess.bsc.es/bsc-dust-daily-forecast) and FIRMS (https://firms.modaps.eosdis.nasa.gov/) we were not able to specifically determine the source of these layers.

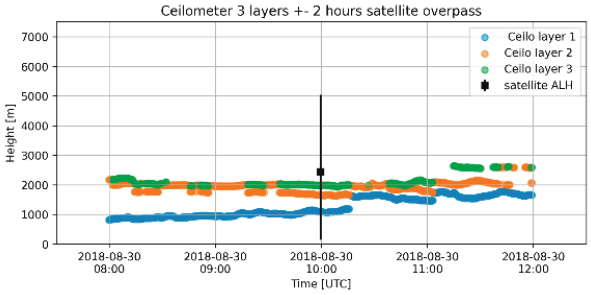

Figure 1. Aerosol layer heights derived from ceilometer measurements in Magurele (blue, yellow, green) during 30.08.2018 and derived from S5P(black)-spatially averaged (in a 50 km circle above Magurele)

On other days with similar scenes, we could identify that some layers were long range transported from Africa (e.g. a layer at 3.8 km on 5.10.2020; layers represented in Figure 2) and we could confirm as a validation case. When there is a well-developed and spatially well-spread aerosol layer then only questions related to how to average the satellite data are taken into account. On 5.10.2020 there were two satellite overpasses represented in Figure 2 in black, with error bars highlighting the variability of the satellite data.
The averaged satellite value for the first overpass it is very close the one derived from ceilometer and confirmed to be long range transported dust. For the second overpass only one pixel got a close value (3838m).

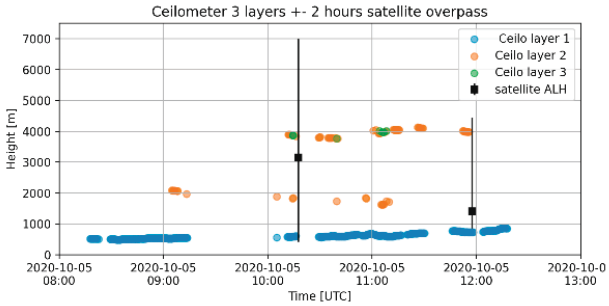

Figure 2. Aerosol layer heights derived from ceilometer measurements in Magurele (blue, yellow, green) during 05.10.2020 and derived from S5P(black)-spatially averaged (in a 50 km circle above Magurele)

The difference between the satellite pixel size and the point view of the ground-based observations is definitely a challenging issue in top of the ones related to different retrieving techniques. Several sensitivity studies have been performed but a lot of questions still remains:

- What is the best way to temporally average the ceilometer information to compare with a satellite overpassing once or twice per day?
- How to better choose which layer to take into consideration for comparison in a complex scene? Can this be done unsupervised by an automated algorithm?
- Can the satellite scene be considered as a proven case of existing layer?

.

Challenges

The reported satellite ALH is the height of a single aerosol layer (Dust, Biomass burning or volcanic ash) for the entire atmospheric column within the scene measured by TROPOMI. During our study we have encountered several cases where distinctly separated elevated and boundary layer aerosols are present in the same scene.
Open questions: What could be the best approach in comparing aerosol layer heights from satellite passive remote sensing measurements and the ones from ground based active remote sensing data? Several specific cases will be brought to the community attention during the conference.

Acknowledgements

This research was partially funded by the Romanian National Core Program Contract No.18N/2019; by a grant of the Romanian Ministry of Education and Research, CCCDI - UEFISCDI, within PNCDI III, contract No.259/2020 and by the EU and ESA through the Contract No. 4000132151/20/NL/FF/ab, SVANTE.
The work is related to activities within the COST Action CA18235 PROBE (PROfiling the atmospheric Boundary layer at European scale).

References

Adam, M., Nicolae, D., Stachlewska, I. S., Papayannis, A., and Balis, D.: Biomass burning events measured by lidars in EARLINET – Part 1: Data analysis methodology, Supplement section 3, Atmos. Chem. Phys., 20, 13905–13927, https://doi.org/10.5194/acp-20-13905-2020, 2020.

Michailidis, K., Koukouli, M.-E., Siomos, N., Balis, D., Tuinder, O., Tilstra, L. G., Mona, L., Pappalardo, G., and Bortoli, D.: First validation of GOME-2/MetOp absorbing aerosol height using EARLINET lidar observations, Atmos. Chem. Phys., 21, 3193–3213, https://doi.org/10.5194/acp-21-3193-2021, 2021

Nanda, S., de Graaf, M., Veefkind, J. P., Sneep, M., ter Linden, M., Sun, J., and Levelt, P. F.: A first comparison of TROPOMI aerosol layer height (ALH) to CALIOP data, Atmos. Meas. Tech., 13, 3043–3059, https://doi.org/10.5194/amt-13-3043-2020, 2020.

Nicolae, D., Vasilescu, J., Talianu, C., Binietoglou, I., Nicolae, V., Andrei, S., Antonescu, B. A neural network aerosol-typing algorithm based on lidar data. *Atmos. Chem. Phys.* 2018, 18, 14511-14537, https://doi.org/10.5194/acp-18-14511-2018

Statistical analysis of the atmospheric aerosol radiative properties over a year in Granada

E. Bazo, *M.J. Granados-Muñoz[1,2], J.A. Bravo-Aranda[1,2] , R. Román[3]*
elebazgon@correo.ugr.es
(1) Andalusian Inter-University Institute for Earth System Research (IISTA-CEAMA), Spain
(2) Department of Applied Physics, University of Granada, , Spain
(3) Group of Atmospheric Optics (GOA-UVa), Universidad de Valladolid, Spain

Introduction

Atmospheric aerosol have a major impact on the Earth's climate. According to the Fifth Assesment (AR5) of the Intergovernnamental Panel on Climate Change (IPCC, 2013) atmospheric aerosols and its interactions with both radiation and clouds are the principal source of uncertainty in the quantification of the total anthropogenic radiative forcing. In order to properly quantify the effects of the aerosol in the Earth's climate, not only it is necessary to estimate the radiative effects in the shortwave (SW) range, but also in the longwave (LW). The LW range has an important contribution; however it is usually neglected.

It is for this purpose that in the present work, we examine the radiative properties, in the SW and LW spectra, of the atmospheric aerosol in the city of Granada (37.2ºN, 3.6ºW, 680 m a.s.l.) in 2017.

The optical and microphysical properties, both vertical and column-integrated, are necessary to obtain the radiative properties. These properties have been obtained in this work using the GRASP (Generalized Retrieval of Aerosol and Surface Properties) algorithm (Duvobik et al., 2014; Benavent-Oltra et al., 2017), following the method proposed by Román et al. (2018), based on the use of data measured by a sun-sky photometer and by a ceilometer as input. These instrumentation is available at the Andalusian Institute for Earth System Research (IISTA-CEAMA), where the sun-sky photometer belongs to AERONET (Aerosol Robotic NETwork; Holben et al., 1996) and the ceilometer is part of the ICENET (Iberian CEilometer NETwork; Cazorla et al., 2017).

To calculate the radiative forcing (RF) of the aerosols we have used the GAME (Global Atmospheric Model) radiative transfer model (Dubuisson, 2004), which allows to calculate upward and downward fluxes at different vertical levels. Specifically, in this study we have established 80 vertical levels with decreasing vertical resolution, covering altitudes from the surface up to 20 km. The solar and thermal fluxes have been calculated in two adjustable spectral ranges, 0.297-3.1 µm for the SW and 4.5-100 µm for the LW.

Results and discussion

The aerosol RF profiles obtained with GAME are presented in Fig. 1. On the left, the annual mean profiles of the RF in SW and in LW are shown, along with the standard deviation as errorbars. Time series of the RF profiles, AOD at 1064nm, the RF at the surface level and the fine mode fracion (FMF) are represented on the right pannels.

In the SW spectral range, the annual mean RF on the surface is -20 Wm^{-2}, showing decreasing values (in absolute value) with height. It is also noticeable that the main values in which the RF_{SW} ranges, for most of the data, along the year are 0 and -30 Wm^{-2}. The maximum values of the RF_{SW} are found in February and July. In the first case, the RF_{SW} reaches up to -150 Wm^{-2} along the entire vertical profile, whereas in July the RF_{SW} is around -100 Wm^{-2}. The RF_{SW} on the surface correlates very well with the time series of the AOD in 1064 nm, with a correlation coefficent for of 0.84 (note that the absolute value of RF_{SW} has been used), indicating a strong dependence of the RF_{SW} with the aerosol load. This dependence has been confirmed in previous studies (e.g. Granados-Muñoz et al., 2019).

The extreme events observed in February and July correspond to an extreme dust event in the city of Granada in February, which is described in Fernández et al. (2019), and a biomass burning transport event from Portugal in July. The dust event in February presented high AOD, being around 1.5, while the AOD in July it is only is 0.24, but particles observed are much more absorbing increasing the RF_{SW} values. An additional dust event in April is observed, with the RF_{SW} on the surface reaching up to -80 Wm^{-2}, for an AOD of 1.33. Aditionally, the entire month of August presents high values of the RF_{SW} along the vertical profile, with its maximum in the end of the month: -50 Wm^{-2}, caused by high concentrations of mineral dust particles.

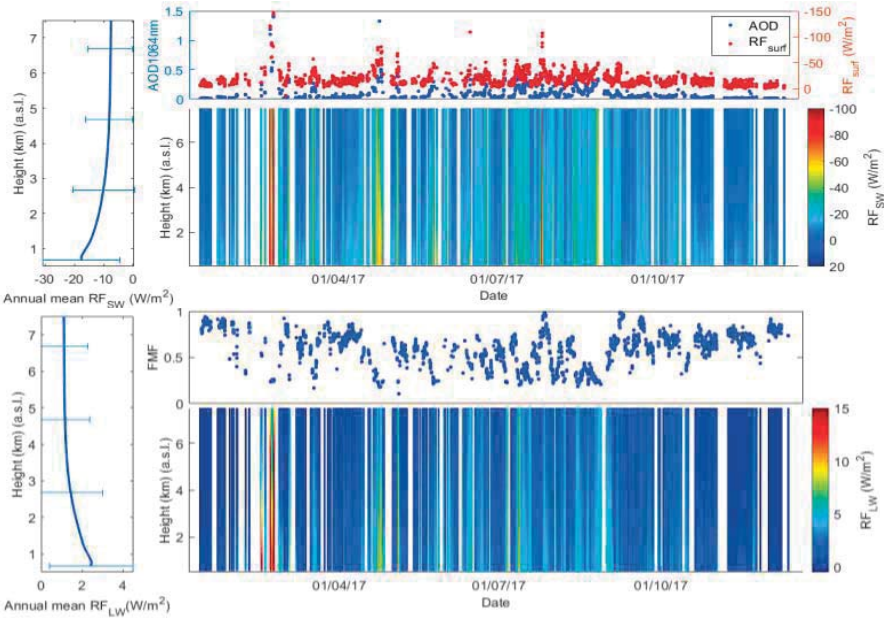

Figure 1. a) Time series of the AOD_{1064nm} and the RF_{SW} on the surface (top). Time series of the vertical profiles of RF_{SW} (down). Annual mean profile of RF_{SW} with its standard deviation as errorbars (left). b) Time series of the FMF (top). Time series of the vertical profiles of RF_{LW} (down). Annual mean profile of RF_{LW} with its standard deviation as errorbars (left).

In the LW spectral range, the RF is positive. The annual mean RF_{LW} on the surface is 2 Wm^{-2}, showing decreasing values with height. The range of the RF_{LW} is smaller than in the SW regime, the majority of the data being in the range 0-5 Wm^{-2}. The maximum values are found in February, when the dust outbreak took place. The radiative effects of the aerosol in the LW regime are stronger for large particles, thus, when the FMF is close to 0. It is clear that in the events of February and April, where the values of RF_{LW} are large, the FMF is very small: the aerosol type is mineral dust. In case of mineral dust, the RF_{LW} is about 20% of the RF_{SW} (Granados-Muñoz et al., 2019). In February, the RF_{LW} is 20 Wm^{-2} on the surface, decreasing up to 5 Wm^{-2} at 4 km a.s.l. This RF_{LW} represents a 13% of the SW component. Aditionally on April a RF_{LW} of 7 Wm^{-2} is found at heights near the surface, which is a 9% of the RF_{SW}. On the other hand, the RF_{LW} of the events in July is small, of about 3.5 Wm^{-2}, agreeing with the large values of FMF, close to 1. Thus, the aerosol in July belongs to the fine mode.

In this work, we have examined the radiative properties of the aerosol in the city of Granada, during 2017. We have developed a method that allows to obtain the aerosol radiative effects automatically from the GRASP output data. This methodology can easily be applied to different stations and in the near future research it is planned to to determine the radiative properties in different stations of ICENET performing a multiyear analysis.

Challenges

The main challenge found in the development of this work was the lack of aerosol data available in the LW, which implies the use of a Mie code to retrieve optical properties, thus amplifying the errors in the calculations of the radiative forcings.

Acknowledgements

Maria J. Granados-Muñoz was funded by a Marie Sklodowska-Curie IF under grant agreement no. 796539. Juan Antonio Bravo-Aranda received funding from the Marie Sklodowska-Curie Action Cofund 2016 EU project – Athenea3i under grant agreement no. 754446.

References

Benavent-Oltra et al., (2017). *Atmos. Meas. Tech.* 10:4439-4457.10.5194/amt-10-4439-2017.

Cazorla et al., (2017). *Atmos. Chem. Phys.* 17(9):11861-11876. 10.5194/acp-17-11861-2017.

Dubovik et al., (2014). *SPIE Newsroom.* 10.1117/2.1201408.005558.

Dubuisson et al., (2004), *J. Geophys. Res.* 109, D19106, doi:10.1029/2004JD004516.

Fernández et al., (2019). *Atmospheric Research*. 228. 10.1016/j.atmosres.2019.06.007.

Granados-Muñoz et al., (2019). *Atmos. Chem. Phys.* 19,:13157-13173. 10.5194/acp-19-13157-2019

Holben et al., (1998). *Remote Sens. Environ.* 66, 1–16, 1998.

IPCC, 2013: Cambridge University Press, Cambridge, United Kingdom and New York, NY, USA, 1535 pp, doi:10.1017/CBO9781107415324.

Román et al., (2018). *Atmospheric Research.* 204(11):161-177. 10.1016/j.atmosres.2018.01.021.

Aerosol Properties retrieved from LIDAR and Photometer Mobile measurements during FIREX-AQ Campaign in 2019

M. F. Sanchez-Barrero[1,2], *I. Popovici*[1,2], *P. Goloub*[2], *S. Victori*[1], *T. Podvin*[2], *L. Blarel*[2], *G. Dubois*[2], *A. Lapionak*[2], *L. Proniewski*[1], *B. Holben*[3], *D. Giles*[3,4], *A. LaRosa*[3,4], *T. Eck*[3,5], *M. Sorokin*[3,4], *J. Schafer*[3,4], *A. Smirnov*[3,4], *A. Sinyuk*[3,4], *I. Slutsker*[3,4], *J. Kraft*[3,4], *B. Torres*[2]

mariafernanda.sanchezbarrero@univ-lille.fr

(1) R&D Department, Cimel Electronique, 75011 Paris, France

(2) Univ. Lille, CNRS, UMR8518 – LOA – Laboratoire d'Optique Atmosphérique, 59000 Lille, France

(3) NASA Goddard Space Flight Center, Greenbelt, MD, USA

(4) Science Systems and Applications, Inc., Lanham, MD, USA

(5) Universities Space Research Association, Columbia, MD, USA

Introduction

In the last decades, extreme wildfire seasons and isolated wildfire events have hit North America. Particularly in the Northwest states of US, air quality is getting worse in contrast to other states of the country. Hence, an extensive field campaign FIREX-AQ (Fire Influence on Regional to Global Environments and Air Quality) has been organized over this specific region. The campaign was focused on investigating the chemistry and transport of smoke from wildfires and agricultural burning (FIREX White Paper, 2019).

One of the broad scientific targets of the FIREX-AQ campaign was to evaluate and study smoke properties at the source and its transport on a local and regional scale. Remote sensing instruments such as LIDAR systems and photometers are suitable to asses this particular target. Nevertheless, measurements of both ground-based instruments are limited by their location with respect to the fire source and wind patterns. Thus, two mobile platforms called DMU-1 and DMU-2 (Dragon Mobile Unit) equipped with remote sensing instruments performed on-road mobile measurements. The mobile component made possible to follow the smoke plumes closer to their source. The installation of remote sensing instruments in both DMUs followed the design of MAMS (Mobile Aerosol Monitoring System) platform (Popovici et al., 2018) and were equipped with CIMEL micro-pulse LIDARs (CE376 and CE370 systems) and automatic photometers (CIMEL CE318-T and PLASMA). With the synergetic mobile measurements, we were able to obtain height resolved and column integrated optical properties of smoke aerosols at different ageing states.

Results and discussion

During the campaign, the DMUs were performing mobile measurements all day, at night mostly at a fixed location. During the day along the roads around the major fire sources with occasionally stationary measurements in between. The continuous measurements performed by CIMEL CE318-T photometer in DMU-1 and PLASMA sun-photometer in DMU-2 provided us a general overview of the column-integrated optical properties during the campaign. With Angstrom Exponent (AE) values always higher than 1.4, we confirmed the strong presence of fine mode aerosols (expected for fresh smoke) at a regional level. The measured AOD showed a non-homogeneous distribution of aerosols in the fire areas, where the complexity of the mountainous terrain plays an important role in the local to regional transport of smoke.

We have measurements from the CIMEL CE376 micro-pulse LIDAR (532 and 808 nm, polarized) on DMU-1 and CIMEL CE370 micro-pulse LIDAR (532 nm, unpolarized) on DMU-2. The LIDAR data coupled with the photometer allow us to apply the AOD constrained Klett inversion method using BASIC code (Mortier, 2013). We obtained extinction profiles and column-integrated Lidar Ratio (LR) at 532 nm with both systems and also at 808 nm with CE376 LIDAR. Therefore, we could calculate the AE.

In addition, we derived Volume Depolarization Ratio (VDR) profiles, providing qualitative information of the shape and type of aerosols thanks to the depolarization channels at 532 and 808 nm of CE376 LIDAR. Especially for night-time measurements when the signal to noise ratio (SNR) in all 4 channels is higher.

With the data obtained during the campaign and retrieved aerosol properties, we saw the limitations and capabilities of both systems. The laser was attenuated by thick smoke layers, and the harsh environmental (topography and high temperatures) played a role in these limits. However, both lidars were able to retrieve aerosols information close to the source of smoke, which has never been done before.

In order to show the ongoing investigation on aerosols properties during the FIREX-AQ campaign we present a case study of mobile measurements performed by DMU-1. We illustrate the temporal variability of some of the retrieved optical

properties from CIMEL CE376 LIDAR and CIMEL CE318-T photometer.

DMU-1 case study: August 5th, 2019

For this particular day, DMU-1 performed mobile measurements around William Flats Fire during daytime. The quicklook in Figure 1 shows the temporal variability of PR2 (RCS) profiles at 532 nm for DMU-1 approaching the fire (14 – 20 h UTC). Below the RCS, the temporal variation of column integrated LR retrieved at 532 and 808 nm are shown, as well as AOD at 532 and 808 nm, and AE (532/808) retrieved from the coupled photometer.

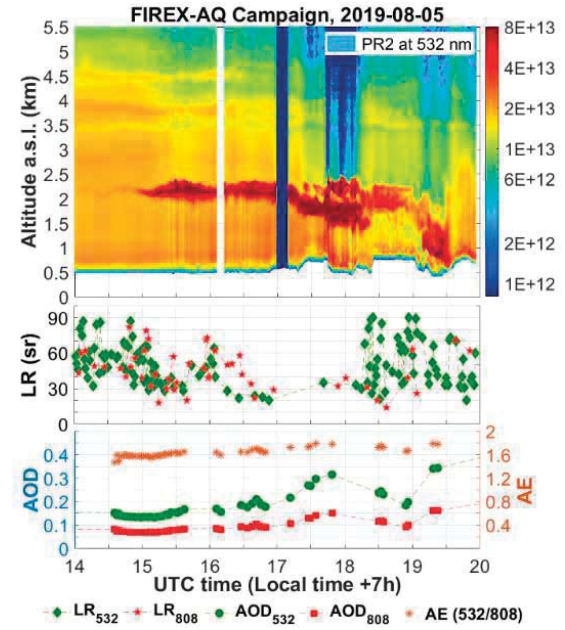

Figure 1. PR2 Quicklook at 532 nm from DMU-1 with its respective time series of LR and AOD at 532 and 808 nm, as well as AE (532/808).

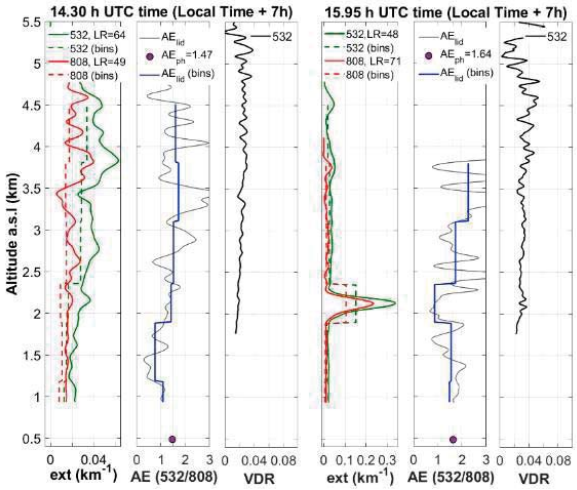

Figure 2. Extinction profiles at 532 and 808 nm and AE, and VDR profiles at 532 nm. AE_{ph} calculated from photometer.

We observe LR varying from 30 to 90 sr at 532 nm and 808 nm, with lower values (20-40 sr) when the smoke plume is thicker. Previous studies of fresh smoke transported one day far from source reported LR of 60-85 sr for 532 nm (Alados-Arboledas, 2011; Tesche et al., 2011).

Even though the SNR for 808 nm is low by day, we were able to get some extinction profiles and calculate the AE vertical variation (Figure 2) inside and outside the smoke plume. We observe the decrease of AE (from 1.5 to 0.8) in the thick smoke layer at ~2 km, indicating a higher presence of coarse particles. For both cases VDR values at 532 nm are below 0.04.

Challenges and Future Work

The selection of an adequate reference zone for the inversion of LIDAR signals turns out to be difficult in presence of thick smoke layers, which is a common scenario close to their source. Also, the LR values for smoke at different ageing states are influenced by a wide-range of parameters, including the type of soil, fuel, state of the fire and chemical mixing (Nicolae et al., 2013). Simply assuming a LR based on literature can lead to inaccurate results. Additional investigation and validation of the retrievals obtained is needed. For future studies we plan to introduce the 2-wavelength joint inversion looking for improvements on LIDAR retrievals. Throughout the campaign we also detected during night-time high-altitude aerosol plumes (~17 km a.s.l.) injected by the Raikoke and Ulawun volcanic eruptions (Vaughan et al., 2021) which are interesting to investigate.

References

Alados-Arboledas et al., Optical and microphysical properties of fresh biomass burning aerosol retrieved by Raman lidar, and star-and sun-photometry. *Geophys. Res. Letters*, 38 (1), 2011.

FIREX-AQ White Paper, 2019, available at www.esrl.noaa.gov/csl/projects/firex-aq/whitepaper.pdf

Mortier, Tendances et variabilites de l'aerosol atmospherique a l'aide du couplage Lidar/Photometer sur les sites de Lille et Dakar (Doctoral dissertation, Lille 1, 2013).

Nicolae et al., Characterization of fresh and aged biomass burning events using multiwavelength Raman lidar and mass spectrometry, *J. Geophys. Res.: Atmos.*, *118*(7), 2956-2965, 2013.

Popovici et al., Description and applications of a mobile system performing on-road aerosol remote sensing and in situ measurements. *Atmos. Meas. Techniques*, 11(8), 4671-4691, 2018.

Tesche et al., Profiling of Saharan dust and biomass-burning smoke with multiwavelength polarization Raman lidar at Cape Verde. Tellus B: *Chem. and Phys. Meteo.*, 63(4), 649-676, 2011.

Vaughan et al., Measurement Report: Lidar measurements of stratospheric aerosol following the 2019 Raikoke and Ulawun volcanic eruptions, *Atmos. Chem. Phys.*, 21, 5597–5604, 2021.

Synergy processing of diverse ground-based remote sensing and in situ data using the GRASP algorithm: applications to radiometer, lidar and radiosonde observations

A. Lopatin[1], *O. Dubovik*[2], *D. Fuertes*[1], *G. Stenchikov*[3], *T. Lapyonok*[2], *I. Veselovskii*[4], *F. G. Wienhold*[5], *I. Shevchenko*[3], *Q. Hu*[2], *S. Parajuli*[3]
Anton.lopatin@grasp-sas.com
(1) GRASP SAS, Villeneuve-d'Ascq, 59650, France
(2) Laboratoire d'Optique Atmosphérique, CNRS/Université de Lille, Villeneuve-d'Ascq, 59650, France
(3) Physical Science and Engineering Division, King Abdullah University of Science and Technology, Thuwal, 23955-6900, Kingdom of Saudi Arabia
(4) Prokhorov General Physics Institute of the Russian Academy of Sciences, Moscow, 117942, Russia
(5) Eidgenössische Technische Hochschule, Zurich, 8092, Switzerland

Introduction

Ground-based remote sensing is widely recognized as a valuable source of information about the details of the optical properties of atmospheric aerosols. The passive ground-based remote sensing including spectral observations of the direct- and multi-angular diffuse Sun radiation have significant sensitivity to the atmospheric aerosol amount, its particles size, shape and morphology; but almost no sensitivity to its vertical variability. On the other hand, the active lidar observation techniques that are usually used to obtain the information about vertical distribution of aerosol are lacking information content with respect to the detailed properties of aerosols. Therefore, information from collocated photometric measurements is always desirable for the interpretation of lidar observations and the complementarity of the passive and active measurement remains important even if the advanced lidar systems that include inelastic and depolarisation observations are used.

There are many suggestions for joint processing of coincident photometric and lidar ground-based observations, which provide complementary information. For example, Lidar and Radiometer Inversion Code (LiRIC) (Chaikovsky et al., 2016) and Generalized Aerosol Retrieval from Radiometer and Lidar Combination/Generalized Retrieval of Atmosphere and Surface Properties (GARRLiC/GRASP) (Lopatin et al., 2013, 2021) algorithms use the joint data from a multi-wavelength lidar and an Aerosol Robotic Network (AERONET) Sun–sky-scanning radiometer to derive vertical profiles of fine and coarse aerosol components as well as extra parameters of the column-integrated properties of aerosols. Here we discuss the evolution of GRASP (Dubovik et al., 2011, 2014) approach and demonstrate a wide spectrum of the possibilities for realizing the processing ground-based observations. Several potentially fruitful aspects of observation synergy were considered.

First, a set of passive and active ground-based observations collected during both day- and nighttime was inverted simultaneously under the assumption of temporal continuity of aerosol properties. Such an approach explores the complementarity of the information in different observations and results in robust and consistent processing of all observations. For example, the interpretation of the nighttime active observations usually suffers from the lack of information about aerosol particles sizes, shapes and complex refractive index. In the realized synergy retrievals, the information propagating from the nearby Sun-photometric observations provides sufficient constraints for reliable interpretation of both day- and nighttime lidar observations.

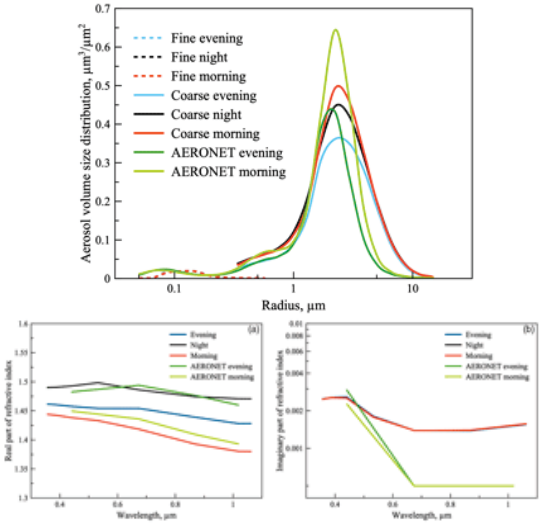

Figure 1. Aerosol volume size distributions (top) and complex refractive indices (bottom) for fine (dashed) and coarse (solid) aerosol components retrieved on 15–16 April 2015. Distributions retrieved before and after the advanced lidar observation in a combination with Sun-photometer data are shown in blue, and those retrieved by AERONET are in dark and light green, respectively.

Second, the synergetic processing of such complementary observations with enhanced information content allows for optimizing the

aerosol model used in the retrieval. Specifically, the external mixture of several aerosol components with predetermined sizes, shapes and composition has been identified as an efficient approach for achieving reliable retrieval of aerosol properties in several situations. This approach allows for achieving consistent and accurate aerosol retrievals from processing stand-alone advanced lidar observations with reduced information content about aerosol columnar properties. The observations of LIlle Lidar AtmosphereS (LILAS) – an advanced lidar system with multi-wavelength volume depolarization observations and several Raman channels (Veselovskii et al., 2015) were used for demonstration of such approach.

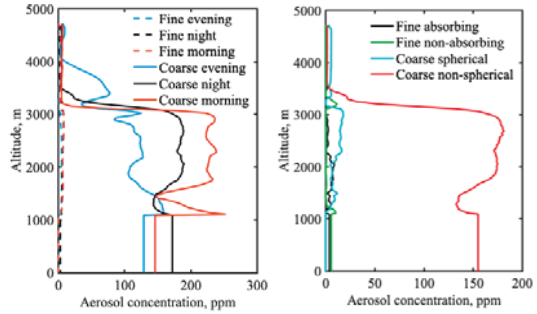

Figure 2. Aerosol vertical distributions retrieved from for fine (dashed) and coarse (solid) aerosol components retrieved on 15–16 April 2015 from multi-temporal (left) and stand-alone (right) LILAS observations. Distributions retrieved before and after the LILAS observation in combination with photometer data are shown in blue and red, respectively.

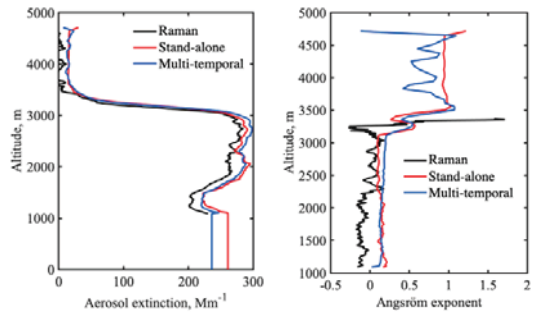

Figure 3. Vertical profile of the aerosol extinction at 355 nm (left) and Ångström exponent at 355/532 nm (right) retrieved from LILAS observations using stand-alone (red) and multi-temporal approaches (blue) performed on 16 April 2015 in comparison with estimation from 355/532 nm inelastic backscatter measurements (black).

Third, the potential of synergy processing of the ground-based Sun-photometric and lidar observations, with the in-situ backscatter sonde measurements was explored using the data from KAUST.15 and KAUST.16 field campaigns held at King Abdullah University of Science and Technology (KAUST) in the August of 2015 and 2016. The inclusion of the Compact Optical Backscatter Aerosol Detector (COBALD, Vernier et al., 2015) radiosonde data has been demonstrated to provide significant additional constraints to validate and improve the accuracy and scope of aerosol profiling.

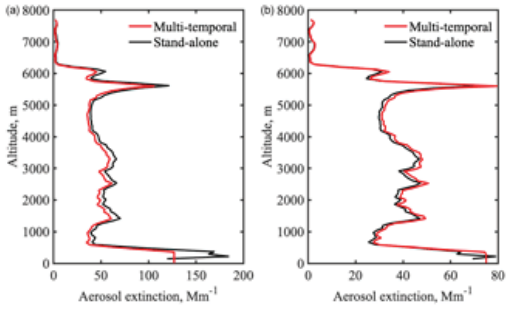

Figure 4. Aerosol extinction profiles at 455 nm (left) and 940 nm (right) estimated from COBALD profiles acquired on 11 August 2015 using a stand-alone (black) and multi-temporal (red) retrieval schemes.

Acknowledgements
We are thankful to the teams of AERONET, MPL, IRD, LOA and KAUST that made the operation of field campaigns used in this study possible.

References

Chaikovsky et al., Lidar-Radiometer Inversion Code (LIRIC) for the retrieval of vertical aerosol properties from combined lidar/radiometer data: development and distribution in EARLINET, *Atmos. Meas. Tech.*, 9, 1181–1205, 2016.

Dubovik, et al., Statistically optimized inversion algorithm for enhanced retrieval of aerosol properties from spectral multi-angle polarimetric satellite observations, *Atmos. Meas. Tech.*, 4, 975–1018, 2011.

Dubovik, et al., GRASP: a versatile algorithm for characterizing the atmosphere, *SPIE Newsroom*, 2-1201408, 2014.

Lopatin, et al., Enhancement of aerosol characterization using synergy of lidar and sun-photometer coincident observations: the GARRLiC algorithm, *Atmos. Meas. Tech.*, 6, 2065–2088, 3, 2013.

Lopatin, et al., Synergy processing of diverse ground-based remote sensing and in situ data using the GRASP algorithm: applications to radiometer, lidar and radiosonde observations, *Atmos. Meas. Tech.*, 14, 2575–2614, 2021.

Vernier, et al., Increase in upper tropospheric and lower stratospheric aerosol levels and its potential connection with Asian pollution, *J. Geophys. Res.-Atmos.*, 120, 1608–1619, 2015.

Veselovskii, et al., Use of rotational Raman measurements in multiwavelength aerosol lidar for evaluation of particle backscattering and extinction, *Atmos. Meas. Tech.*, 8, 4111–4122, 2015.

Presenting ASSA: An Aerosol Species Separation Algorithm based on the synergy of lidars and spectrophotometers

N. Siomos[1,2], *I. Fountoulakis*[1,3], *F. Gkertsi*[2], *K. A. Voudouri*[2], *K. Michailidis*[2], *K. Garane*[2], *D. Karagkiozidis*[2], *A. Karanikolas*[2,4], *A. Natsis*[2], *A. F. Bais*[2], *D. Balis*[2]

nsiomos@noa.gr
(1) IAASARS, National Observatory of Athens, Athens, Greece
(2)Laboratory of atmospheric physics, Physics Department, Aristotle University of Thessaloniki, Greece
(3) Aosta Valley Regional Environmental Protection Agency (ARPA), 11020 Saint-Christophe, Italy
(4) Physikalisch-Meteorologisches Observatorium Davos, World Radiation Center (PMOD/WRC) Dorfstrasse 33, 7260 Davos Dorf, Switzerland

Introduction

In this study, the concept of a synergistic algorithm to retrieve the vertical concentration profiles of individual aerosol species is presented based on lidar and spectrophotometer measurements from the Laboratory of Atmospheric Physics (LAP) in Thessaloniki, Greece. The optical properties per species is provided by the raw species of the Optical Properties of Aerosols and Clouds (OPAC, Koepke et al., 2018). Currently, a lookup table of mixtures is compiled and an ensemble of mixture/mass concentration combinations that best describe the lidar attenuated backscatter profiles are identified. In the next step, we will import these profiles to a radiative transfer model in order to isolate the combination that best reproduces ratios between the direct solar radiance, sky radiance, and global irradiance spectra measured by the spectrophotometers.

The Data

The proposed technique for the retrieval of aerosol species profiles relies on vertically resolved lidar signals and columnar spectrophotomer data from the LAP (40.5°N, 22.9°E; 50 m). Synergies among the following instruments will be deployed: a multiwavelength depolarization Raman lidar, a double monochromator Brewer and a DOAS/MAX-DOAS spectrophotometer. LAP is a member station of the PANhellenic infrastructure for Atmospheric Composition and climatE chAnge (PANACEA, https://panacea-ri.gr/). The testing dataset is based on 14 collocated lidar and spectrophotometer measurements that were performed in the station during the first PANACEA summer campaign (10th of July - 10th of August 2019).

Methodology

The Aerosol Species Separation Algorithm (ASSA) relies on a lookup table (LUT) of mixtures generated from pure aerosol species modeled by the OPAC database (Hess et al. 1998, Koepke et al. 2015). We produce 792 external mixtures for up to eight aerosol modes: water solubles, insolubles, soot, accumulation and coarse mode sea salt, and nucleation, accumulation and coarse mode mineral dust. Mineral dust species are modeled as spheroids (Koepke et al. 2015) and depolarize the backscattered light accordingly. The other species are assumed to be spherical. A depolarization ratio value of 0.01 at 532nm is used instead of 0 (perfect spheres) similar to Hara et al. 2018 in order to get more realistic retrievals. Hygroscopic growth calculations are included in OPAC for 8 relative humidity classes (0%, 50%, 70%, 80%, 90%, 95%, 98%, 99%) for the water soluble and sea salt species. Modification of the sea salt depolarization based on humidity according to Haarig et al., 2018 is planned but not yet applied.

By iterating over a number of predefined mass concentration levels and mixture entry of the LUT, the algorithm reconstructs the available lidar attenuated backscatter and volume depolarization profiles. Currently, 200 equidistant levels are assumed in a logarithmic scale ranging from 10^{-2} to 10^{3} μgr m^{-3}. Reconstruction begins from the end of the profile (reference height) and proceeds downwards by forward-modeling the elastic lidar equation (e.g. Weitkamp et al., 2005). All molecular profiles are calculated using radiosonde temperature and pressure profiles. The residuals of the constructed versus measured lidar values are calculated for each vertical level per concentration-mixture combination. The combinations are sorted in ascending residual order and the first N (currently 20) are marked as the most probable solutions.

Results and discussion

An sample case on 29th of July 2019 is presented below. Fig. 1 depicts the constructed attenuated backscatter and volume depolarization profiles of ASSA that correspond to the first 20 mixtures per vertical level that show the best agreement with the measured profiles.

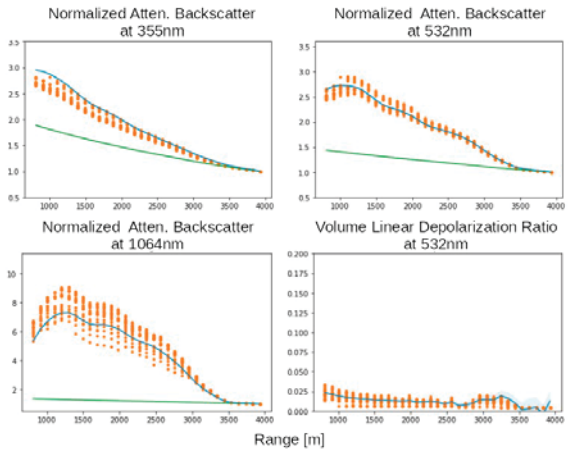

Figure 1: Measured (blue) and fitted (orange) attenuated backscatter values. The respective molecular attenuated backscatter profiles are also included (green).

Fig. 2 includes the respective solutions, that is, the mass concentration values per vertical level species that correspond to the minimum residuals. For this specific case, ASSA indicates mixing among water solubles, accumulation mode sea salt, soot, and/or fine dust.

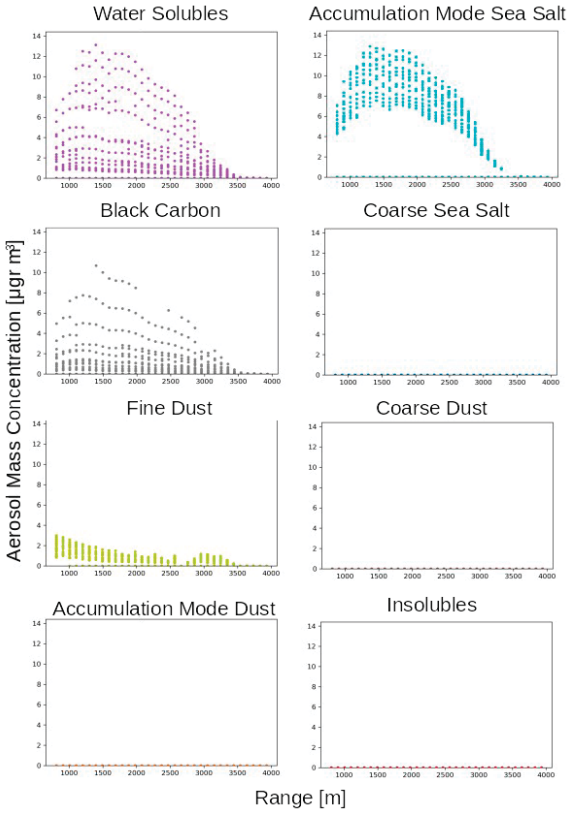

Figure 2: Ensemble potential mass concentration solutions per aerosol species and per vertical level. The first 20 solutions that best reproduced the measured profiles are displayed.

LAP is an urban station less than 1km away from the sea. Mixing polluted continental aerosols with local marine salt is rather common. A small quantity of fine dust is also retrieved but it is probably an artifact as ASSA tries to reconstruct volume depolarization values above 0.01 (spherical species). We expect this to change after implementing the sea salt depolarization modification scheme of Haarig et al. 2018.

We highlight here that no final solution profile is yet retrieved. From Fig. 1, it is obvious that four independent lidar optical properties are not sufficient to for a certain retrieval as some combinations can produce similar results. They can provide, however, indications of the aerosol mixing state and the concentration level margins per aerosol species. In the next step, the potential solutions from ASSA will be imported in a radiative transfer model to compare the forward modeled radiance spectra with the ones measured from the spectrophotometers. Then, the profile that corresponds to the lowermost residuals will be selected as the final solution that best satisfies both the lidar and the spectrophotomer measurements.

Acknowledgments

N. S. is co-financed by Greece and the European Union (European Social Fund- ESF) through the Operational Programme «Human Resources Development, Education and Lifelong Learning» in the context of the project “Reinforcement of Postdoctoral Researchers - 2nd Cycle” (MIS-5033021), implemented by the State Scholarships Foundation (IKY); by the project "PANhellenic infrastructure for Atmospheric Composition and climatE change" (MIS 5021516) which is implemented under the Action "Reinforcement of the Research and Innovation Infrastructure", funded by the Operational Programme "Competitiveness, Entrepreneurship and Innovation" (NSRF 2014-2020) and co-financed by Greece and the European Union (European Regional Development Fund).

References

Haarig, M., et al., Dry versus wet marine particle optical properties: RH dependence of depolarization ratio, backscatter, and extinction from multiwavelength lidar measurements during SALTRACE, Atmos. Chem. Phys., 2017

Hara, Y. et al., Retrieval of Aerosol Components Using Multi-Wavelength Mie-Raman Lidar and Comparison with Ground Aerosol Sampling, Remote Sensing, 2018

Hess, M. et al., Optical Properties of Aerosols and Clouds: The Software Package OPAC, Bulletin of the American Meteorological Society, 1998

Koepke, P. et al., Technical Note: Optical properties of desert aerosol with non-spherical mineral particles: data incorporated to OPAC, Atmos. Chem. Phys., 2015

Weitkamp, C. (Ed.), Lidar Range-Resolved Optical Remote Sensing of the Atmosphere Springer, New York, 2005

Dealing with the vertical dimension of extreme pollution episodes

L. Alados-Arboledas, J. Abril-Gago, D. Bermejo-Pantaleón, J. A. BravoAranda, A. Casans-Gabasa, J. A. Casquero-Vera, S. Castillo, A. Cazorla, I. Foyo, M. J. Granados-Muñoz, J. L. Guerrero-Rascado, M.M. JiménezMartín, I. López-Lozano, H. Lyamani, F. Navas-Guzmán, F.J. Olmo, D. Pérez-Ramírez, F. Rejano, G. Sánchez-Hernández, G. Titos, A. Valenzuela

(1) Andalusian Institute for Earth System Research (IISTA-CEAMA), Granada, Spain _ alados@ugr.es

(2) Dpt. Applied Physics, University of Granada, Granada, Spain.

Introduction

Urban areas present high number of pollutants continuously emitted into the atmosphere, with great chemical variety of compounds and complex atmospheric processes. This situation could be aggravated by the meteorological conditions and the geographical situations of this urban areas. The urban agglomerations located in mountainous areas are affected by local meteorological situations influenced by the elevation, constraining the dispersion of air pollutants, and therefore having a negative influence in air quality. In addition to these local factors, the urban areas could be also affected by external emissions, as natural emissions, that constrain the atmospheric situation. Both, local and external emissions, have impact in the particulate matter (PM) concentrations at surface level, increasing their concentrations. The differences could be observed in the vertical profile of the troposphere. Whereas along the local pollution events, the PM concentration is observed in the low troposphere, during the dust events, high PM concentration could be observed from few metres to several kilometres in the vertical.

The city of Granada (south eastern Spain, 680 m a.s.l.) is located in a valley surrounded by mountains with high elevations ranging from 1000 to more than 3300 m.a.s.l. The location and the position of the city favour marked seasonal meteorological conditions, with a winter period characterized by low temperatures, frequently stagnation episodes due to high pressure systems located in Western Europe and North Africa, and the dominance of very weak wind speeds and a dry summer period with elevated temperatures. In both periods, large diurnal temperature variations are typical. The mountainous topography of Granada favours, mostly in winter, the development of thermal inversions (Lyamani et al., 2010). These situations affect the atmospheric boundary layer growth, making the height of this layer (ABLH) an important factor controlling the dilution of pollutants emitted near the surface. On the other hand, the city, due to its geographical position close to Sahara Desert, is around the 35% of the days under African dust air masses influence. These events increase the PM levels in the city exceeding the annual and daily limit values of PM10.

In this context, the main objective of the present work is the multi-instrumental and synergetic analysis, at surface level and in the vertical, of an extreme local pollution event registered in Granada in January 2021. The concentration of PM10 have been obtained from the air quality monitoring station Palacio de Congresos (PAL, urban background station) located in Granada, belonging to the Andalusian government (http://juntadeandalucia.es/medioambiente). The rest of information, both fron in-situ measurements and remote sensing, have been gathered at AGORA station, that operates in the framework of ACTRIS and will be proposed as one of the future National Facilities in the frame of ACTRIS-ERIC.

Results and discussion

We focus our attention on the day 18th of January. In this sense, Figure 1 evidences de evolution of PM10 over the daily evolution of the 532nm backscattered signal gathered by MULHACEN, multispectral Raman Lidar and the Atmospheric Boundary Layer Height, ABLH, retrieved from Halo Streamline wind Doppler Lidar by the algorithm described in Moreira et al. (2018; 2019) and Manninen et al. (2018).

Figure 1 suggest an anticorrelation between PM10 and ABLH while the 532nm backscattered signal offers some insight on the evolution of the aerosol load on the vertical column.

Figure 2, showing the Klett-Fernald retrieval of the aerosol backscttering coefficient at 532nm evidences that along the day the load of scatterers in the low troposphere presents a clear evolution related to the decrease of aerosol load at surface level. This aspect has been investigated using GRASP code (Lopatin et al., 2013) for the retrieval of aerosol volume concentration profiles, from the combinaion of MULHACEN lidar three channels and the use of the CIMEL radiometer operated at AGORA, in the framework of AERONET. This procedure has been succesfully applied at our station in previous studies. The results evidence that the combination of Remote Sensing measuremenst

with GRASP code contributes to offer information on the vertical profile during the extreme episode, although it is clear that there is room for improving the retrieval close to the surface, for example by improving the overlap features of the lidar, something that will be acomplished in brief.

Additionaly to this approach, we have used the scheme proposed by Roman et al, (2018), where GRASP is used with backscattered signal provided by a NIMBUS ceilometer in combination with the CIMEL radiometer data, to retieve the volume concentration profiles, without splitting it in fine and coarse particles. The retieval offers promising results that could be useful taking advantages of extended networks of ceilomters collocated with CIMEL radiometers.

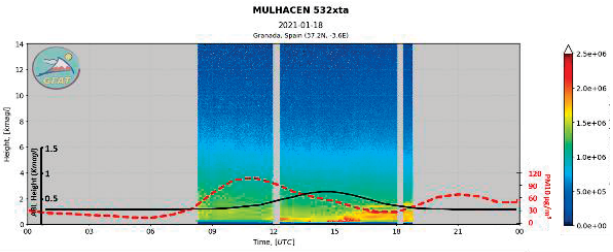

Figure 1. Extreme pollution event showing: PM10 evolution, clearly exceeding the EU AQ threshold; 532nm backscattered signal from Mulhacen and ABLH derived from wind Doppler lidar. The colour slots are related to Figure 2 retrieved backscatter coefficient profiles.

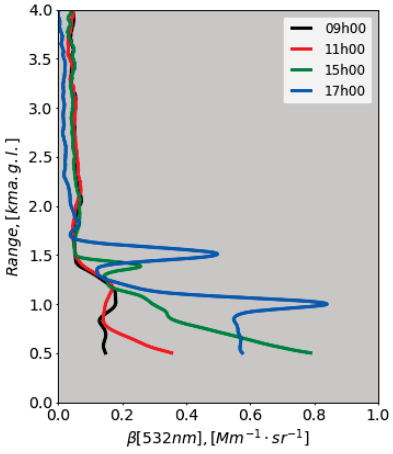

Figure 2. Vertical backscatter coefficient profiles at 532 nm retrieved at the different times of the day marked in figure 1.

Challenges

The results shown in this work evidence the potenciality of ground based active and passive remote sensing for the generation of vertical information during severe pollution events. Nevertheles, the main challenge is improving the retieval of information in the lower part of the profile, something that requires improving the overlap of the lidar systems, for example by the inclusion of close range telescopes. Another relevant issue for pollution events is the concentration of pollutant gases, in that case the vertical profile could be retieved by DOAS systems, thus, providing a 3D information on these events by synergetically combining in-situ and remote sensing techniques in the core of ACTRIS.

Acknowledgements

This work was supported by the Spanish Ministry of Economy and Competitiveness trough CGL2015-73250-JIN, CGL2016-81092-R and CGL2017-90884-REDT, by the UE H2020 through ACTRIS-2 (Ref. 654109) and by the University of Granada through the Excellence Units Program and through Plan Propio 2019, Programa 8.

References

Lyamani, H., Olmo, F. J., and Alados-Arboledas, L. Physical and optical properties of aerosols over an urban location in Spain: seasonal and diurnal variability, *Atmospheric Chemistry and Physics*, 10, 239-254, 2010.

Manninen, A. J., Marke, T., Tuononen, M. J., and O'Connor, E. J. Atmospheric boundary layer classification with Doppler lidar, *Journal of Geophysical Research: Atmospheres*, 123, 8172–8189, 2018.

de Arruda Moreira, G., Guerrero-Rascado, J. L., Bravo-Aranda, J. A., Benavent-Oltra, J. A., Ortiz-Amezcua, P., Róman, R., Bedoya-Velásquez, A. E., Landulfo, E., Alados-Arboledas, L. Study of the planetary boundary layer by microwave radiometer, elastic lidar and Doppler lidar estimations in Southern Iberian Peninsula, *Atmospheric Research*, 213, 185-195, 2018.

de Arruda Moreira, G., Guerrero-Rascado, J. L., Benavent-Oltra, J. A., Ortiz-Amezcua, P., Román, R., E. Bedoya-Velásquez, A., Bravo-Aranda, J. A., Olmo Reyes, F. J., Landulfo, E., and Alados-Arboledas, L. Analyzing the turbulent planetary boundary layer by remote sensing systems: the Doppler wind lidar, aerosol elastic lidar and microwave radiometer, *Atmospheric Chemistry and Physics*, 19, 1263–1280, 2019.

Lopatin, A., et al. "Enhancement of aerosol characterization using synergy of lidar and sun-photometer coincident observations: the GARRLiC algorithm." Atmospheric Measurement Techniques 6.8 (2013): 2065-2088.

Román, Roberto, et al. "Retrieval of aerosol profiles combining sunphotometer and ceilometer measurements in GRASP code." Atmospheric Research 204 (2018): 161-177.

Analysis of a heavy African dust event in South Europe: synergies between lidar and in-situ measurements

F. Mirza-Montoro[1], S. Castillo[2,3], J.A. Bravo-Aranda[2,3], M.J. Granados-Muñoz[2,3], D. Bermejo-Pantaleón[2,3], J. Abril-Gago[2,3], J. L. Guerrero-Rascado [2,3], L. Alados-Arboledas[2,3] , I.S. Stachlewska[1]
fmirza@fuw.edu.pl
(1) Institute of Geophysics, Faculty of Physics, University of Warsaw, Warsaw, Poland
(2) Andalusian Institute for Earth System Research (IISTA-CEAMA), Granada, Spain.
(3) Dpt. Applied Physics, University of Granada, Granada, Spain

Introduction

A very strong Saharan dust episode hit Europe between 16th February and 10th March, 2021, presenting several specific days with high values in PM10 concentration. Due to its proximity to the African continent, this dust outbreak affected mainly Southern and Central Europe but it reached as far as Scandinavia.

In the Andalusian Institute for Earth System Research (IISTA-CEAMA, ACTRIS-UGR station), located in Granada (37,164° N, -3,605° E, 680 m a.s.l.), a medium size city in the south-eastern of Spain, remote sensing instruments such as the lidar system MULHACEN measured vertically-resolved aerosol optical properties for this specific episode. These profiles were analysed together with in situ aerosol observations carried out at the same experimental station, being able to quantify the PM10 concentration by gravimetric method as in EN1234-1 reference method, as well as with data obtained at the Andalusia Government air quality monitoring stations at various locations in Granada (http://juntadeandalucia.es/medioambiente).

Saharan dust intrusions can cause brownish skies, limited visibility and a significant deterioration in the air quality in the affected regions. The direct input of dust over the area typically increases the concentrations of coarse particulate matter (PM10) (Alastuey et al., 2005) causing also a higher value for the aerosol optical depth (AOD) (Cazorla et al., 2017). On the other hand, sharp decreases in the Angström exponent (AE), used tipically as a indicative for particles sizes, also correspond with the arrival of the dust plumes (Guerrero-Rascado et al., 2008).

In this context, the main objective of the present work is the multi-instrumental and synergetic analysis of this extreme Saharan dust event over Granada.

Results and discussion

Values of AOD and AE Between 12th February and 10th March, 2021, obtained from the Aerosol Robotic Network - AERONET retrieval (Version 3, level 1.5 at 500 nm), in consecutive days for Granada, are given in Table 1. The increase of the AOD values with a maximum on 1st to 4th March can be seen, as well as the decrease of columnar AE, presenting a minimum for the same period.

Table 1. Mean and standard deviation of AOD at 500 nm and AE (440-870nm) over Granada obtained from AERONET (level 1.5) during Saharan dust event.

Date		AOD(500)		AE (440-870)	
		mean	S.D.	mean	S.D.
Feb	12-15	0.048	0.015	1.271	0.138
	16-19	0.065	0.023	1.198	0.048
	20-23	0.081	0.037	1.003	0.471
	24-28	0.307	0.075	0.385	0.171
Mar	1-4	0.633	0.150	0.336	0.105
	5-8	0.268	0.023	0.875	0.191
	9-10	0.153	0.018	1.477	0.238

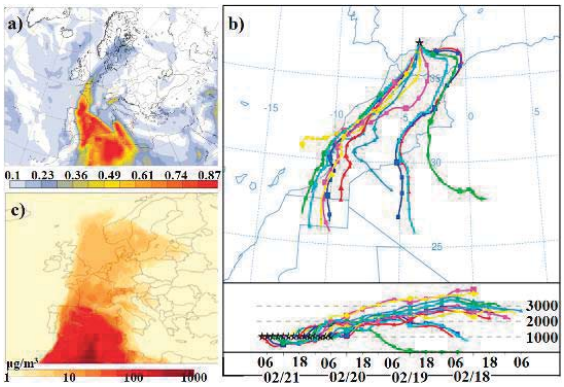

Figure 1. a) CAMS global AOD (550nm) forecast from 19th to 21st February 2021 **b)** CAMS PM dust concentrations from 19th to 21st, February 2021. **c)** Backwards trajectories obtained with the HYSPLIT model for 21st February 2021.

The comparison of the AERONET AODs with the maps of global AOD forecast (Figure 1a) and PM concentrations (Figure 1b) of the Copernicus Atmosphere Monitoring Service (CAMS) from 19th to 21st February, shows how the Saharan dust plume reached the Iberian Peninsula. The backward trayectories calculated with the HYSPLIT (Hybrid Single-Particle Lagrangian Integrated Trajectory)

model (Draxler and Rolph, 2003) show different back trajectories over Granada between days 20th and 21st, February, calculated with a difference of two hours between each other. Figure 1c shows that all these air masses are coming from the Sahara desert

Figure 2 shows lidar range corrected signals (RCS) measured at ACTRIS-UGR station on 4th March, carried out with the multi-wavelength Raman lidar system MULHACEN (LR331-D400, Raymetrics Inc.). It shows a persistent thick layer of Saharan dust between 3-6 km altitude during the whole day. Apart from this decoupled layer, a significant signal increase was also observed within the ABL. Thus, dust particles were likely mixed with the other pollutants at the surface. This episode presents a center of mass concentrated in the first kilometer, which makes it different from most of these types of events, where the center of mass is usually much higher.

With the aim to characterize the intensity of this Saharan dust event, PM10 concentrations, AOD and columnar AE are represented between 12th Febrary and 14th March (Figure 3).

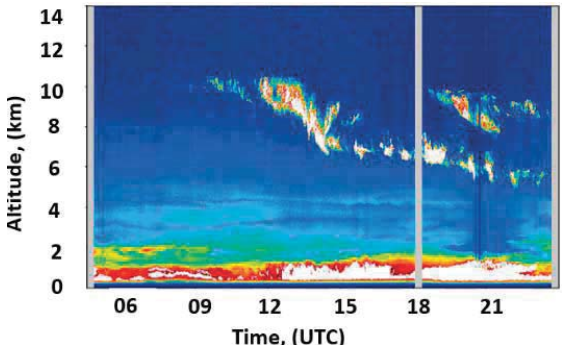

Figure 2. RCS at 532 nm obtained from MULHACEN in the UGR station for 4th March, 2021.

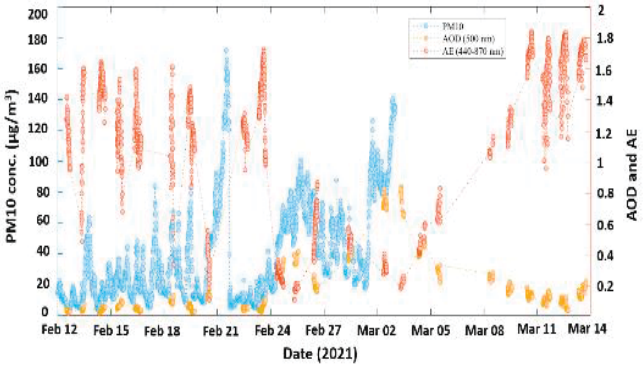

Figure 3. PM10 concentrations at the air quality monitoring station Palacio de Congresos close to UGR station (blue), and AOD (yellow) and AE (red) values at UGR station from 12th February to 4th March 2021.

Regarding PM10 concentration, the first peak is registered from 22nd to 23rd February. The second period with high concentrations is registered from 26th February to the beginning of March, reaching PM10 concentration ~150 µg/m^3, a notable increase with respect to the first days of February (~20 µg/m^3). In the Figure it is possible to see the opposite behaviour for AE values, as expected.

Challenges

In this work we show how the combination of lidar technique, providing information about optical properties of aerosols above the full overlap height, and in situ measurements at ground level leads to a more complete understanding of Saharan dust events. The next step of this work is to combine the above mentioned techniques with an in situ chemical analysis of the pollutants with the aim to get an entire analysis of this episode.

The main challenge we face in this kind of synergetic analysis is the comparison and combination of lidar and insitu measurements at the same heights, e.g., having information at different heights within the dust layer using instrumentation on board an aircraft or in a complementary high-altitude station.

Finally, another challenging analysis would be the effect of the dust layer in the radiative forcing, depending on the optical properties, on the measured PM, the chemical composition and the altitdue and thickness of the layer

Acknowledgements

This research is being done in the framework of the Erasmus PLUS internship enabling the accomplishment of this work.

This abstract is based upon work from COST Action 18235 PROBE, supported by COST (European Cooperation in Science and Technology).

Juan Antonio Bravo-Aranda received funding from theMarie Sklodowska-Curie Action Cofund 2016 EU project – Athe-nea3i under grant agreement no. 754446

References

Alastuey et al., Characterisation of TSP and PM2.5 at Izaña and Sta. Cruz de Tenerife (Canary Islands, Spain) during a Saharan Dust Episode (July 2002), *Atmos. Environ.*, 39, 4715–4728, 2005

Cazorla et al., Near-real-time processing of a ceilometer network assisted with sun-photometer data: monitoring a dust outbreak over the Iberian Peninsula., *Atmos. Chem. Phys.*, 17, 11861–11876, 2017

Guerrero-Rascado et al., Multi-spectral Lidar characterization of the vertical structure of Saharan dust aerosol over southern Spain, *Atmos. Environ.*, 42, 2668–2681, 2008

Draxler, R.R., Rolph, G.D., HYSPLIT (HYbrid Single Particle Lagrangian Integrated Trajectory) Model access via NOAA ARL READY Website /http://www.arl.noaa.gov/ ready/hysplit4.htmlS. NOAA Air Resources Laboratory, Silver Spring, MD., 2003

Algorithm and software package LIRIC-2 for retrieving aerosol parameters from combined CALIOP and AERONET Sun-radiometer measurements

V. Peshcharankou[1], *A. Chaikovsky*[1], *A. Bril*[1]
vlad.pescherenkov@gmail.com
(1) B.I. Stepanov Institute of Physics of the National Academy of Sciences of Belarus, Nezavisimosti Ave. 68-2, Minsk, Belarus

Introduction

Methodology of combined lidar and radiometer sounding of aerosol (LRS) has been successfully tested for joint processing of collocated observations by ground-based radiometers (AERONET) and spaced-based lidar (CALIOP) (Chaikovsky et al, 2018).

We present the latest versions of the algorithm and software package that implement LRS approach for spaced-based lidar. This version (LIRIC-2) is based on the previously developed code LIRIC (Chaikovsky et al, 2016) retaining the main advantages of this code, namely, stable solutions of incorrect inverse problems, which is of importance at a low level of signal to noise ratio of CALIOP daytime lidar data. The presentation includes several case studies demonstrating the potential of the LIRIC-2 code.

Algorithm background

Unlike basic ground based lidar systems, CALIOP lacks a 355 nm channel. However, the absence of lidar data at a wavelength of 355 nm does not significantly affect the error in determining the aerosol parameters. (Chaikovsky et al, 2016).

Similarly to LIRIC, atmospheric aerosol is represented as a mixture of spherical particles and randomly oriented spheroids. Aerosol model consist of two or three modes, which use depending on the specifics of studying object and the number of well-recorded CALIOP signals: 2 modes when the intensity of 2 backscatter signals (532 and 1064 nm) are processed, or 3 modes for additional availability of the cross-polarized component.

Software package modification

Software package LIRIC-2 for the CALIOP lidar data includes several procedures from previous code version (LIRIC) for ground-based lidars:

- parametrization of the altitude-dependent aerosol layer as well as development of a model of the aerosol layer model;
- “forward task” formulation;
- retrievals of the target parameters of the aerosol model.

However, the specificity of satellite lidar data requires additional software products to provide of the data samples that are collocated with available radiometric observations (data selection); filtering of the lidar data that are contaminated by the cloud effects; preliminary signal averaging, interpolation and smoothing. Figure 1 shows the flowchart of the data selection algorithm.

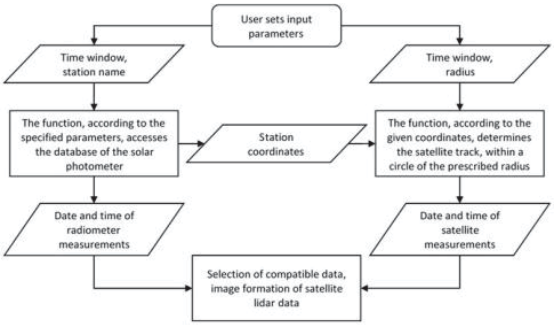

Figure 1. Flowchart of the selection algorithm of CALIOP lidar data.

The presented software package allows us to retrieve the key optical and microphysical parameters of atmospheric aerosol (scattering matrices, scattering indices, attenuation indices, absorption indices, forms of aerosol particles, profiles of concentrations of aerosol fractions, the number of aerosol fractions) parameters required for the analysis of aerosol pollution of the atmosphere, aerosol radiative forcing and other practically important tasks.

Case studies

Algorithm and software package LIRIC-2 were tested by processing combined lidar and radiometer data, measured in different geographical regions to evaluate the optimal setting parameters of code LIRIC-2 for different types of aerosol events.

Dust event

When CALIOP sounds the aerosol layer with an increased concentration of large non-spherical particles, the signal-to-noise ratio of the recorded backscatter signals, including the cross-polarized component of the lidar signal, becomes relatively large. A three-component aerosol model can be used. Figure 2 (a) shows a diagram with concentration profiles of fine, coarse spherical (Coarse 1) and coarse non-spherical (Coarse 2) particles retrieved from data of CALIOP and

AERONET radiometer site ”Dakar”. In this example, the coarse spherical fraction is present in trace concentrations.

Wildfires smoke event

Figure 2(b) shows the aerosol concentration profiles with dominant fine mode in the region of AERONET site “Yakutsk”, Siberia, Russia, 24-06-2020, during fire smoke event.

Antarctic aerosol

Because of the satellite orbit inclination about 98 degree, the outer part of Antarctica is only accessible to CALIOP observations. The main problem is the low aerosol load of the cloudless atmosphere in Antarctica and, as a consequence, the low level of the signal-to-noise ratio. Increasing the length of the satellite orbit segment observed, spatial smoothing and special settings for the software package are applied to obtain satisfactory results.

Figure 2 (c) gives an example of aerosol concentration profiles retrieved in the area of the AERIONET site “Vechernaya_Hill“; 67.660 S, 46.158 E.

Conclusions

Synergy of AERONET and CALIOP data enables multipoint retrievals of aerosol optical and microphysical parameters at ≈ 400 AERONET sites all over the world. We have presented software package LIRIC-2 to implement these retrievals.

Acknowledgements

We acknowledge the AERONET community and Atmospheric Science Data Center for the provision of the radiometer and CALIPSO data what made this project possible. We thank principal investigators and co-investigators of the “Yakutsk“ site Prof. Brent Holben, Prof. Sergey_Sakerin, Prof. Mikhail_Panchenko and “Dakar“ site Prof. Didier Tanre, and their staff for establishing and maintaining the sites which data are used in this investigation.

References

Chaikovsky et al, Lidar&radiometer inversion code (LIRIC) for synergetic processing of EARLINET, AERONET and CALIPSO lidar data, *EDJ Web of Conferences* 176, 08007, 2018.

Chaikovsky et al, Lidar-Radiometer Inversion Code (LIRIC) for the retrieval of vertical aerosol properties from combined lidar/radiometer data: development and distribution in EARLINET, Atmos. Meas. Tech., 9 (3), 1181–1205, 2016.

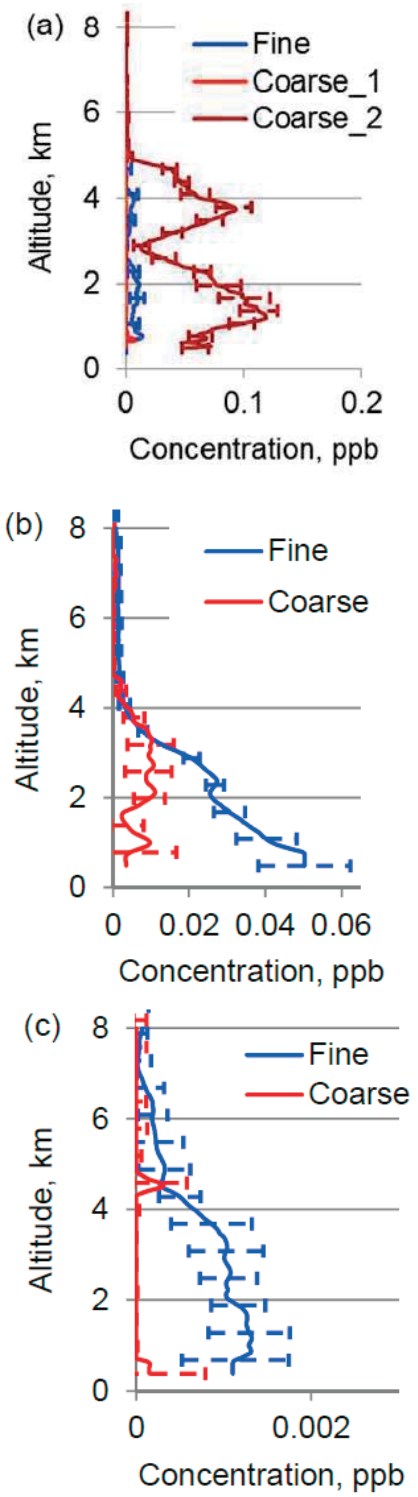

Figure 2. Aerosol mode concentration profiles: a – dust event, Dakar, 14-05-2017; b – forest fire smoke, Yakutsk, 29-06-2020; c – Antarctic, Vechernaya Hill, 24-01-2020.

First Characterization of Aerosol Profiles Retrieved from Ceilometer and Sun-photometer by the GRASP Algorithm at the Rural Guadiana-UGR Station

A. Bereinkua[1], D. Pérez-Ramírez[1,2], H. Lyamani[1,3], A. Cazorla[1,2], R. Román[4], R. González[4], D. Bermejo-Pantaleón[1,2], S. D. Aguirre-García[1,5], S. Aranda[1,5], P. Cariñanos[1,6], M. J. Granados-Muñoz[1,2], J. A. Bravo-Aranda[1,2], J. Abril -Gago[1,2], L. Alados-Arboledas[1,2] and J. L. Guerrero-Rascado[1,2]

aitorbereinkua@correo.ugr.es

(1) Andalusian Institute for Earth System Research (IISTA-CEAMA), Av. del Mediterráneo, 18006, Granada, Spain
(2) Dpt. Applied Physics, University of Granada, Fuentenueva, 18071, Granada, Spain
(3) Dpt. Applied Physics I, University of Málaga, Bulevar Louis Pasteur, 29010, Málaga, Spain
(4) Grupo de Óptica Atmosférica (GOA), Universidad de Valladolid, Paseo Belén, 47011, Valladolid, Spain
(5) Dpt. Ecology, University of Granada, Fuentenueva, 18071, Granada, Spain
(6) Dpt. Botany, University of Granada, Fuentenueva, 18071, Granada, Spain

Introduction

Aerosols are a key component in the Earth's climate system due to its influence on the radiative balance through the scattering and absorption of solar and/or thermal radiation. Following the 5th IPCC report, aerosol properties are known within a high confidence level; however, more studies are needed regarding its vertical distribution.

The place of study is an olive crop situated in Jaén (Spain, 37º 54' 39.30"N, 3º 13' 42.4"W, 370 m asl). This station is representative of the Mediterranean drylands, in a rural area surrounded by olive plantations with spontaneous weed cover, remote from sources of industrial pollution. Therefore, it is a station of special interest for monitoring autochthonous aerosols (mainly pollen grains, mineral dust from soil and aerosols from fertilizers) and allochthonous aerosols from mid- and long-range transport (such as those originated in Iberian Forest fires, Saharan desert and North American forest fires, among others).

In this work, we focus on the full dataset acquired between the 14th January and 31st May 2021. The mentioned station is equipped by a ceilometer Nimbus CHM15K (Lufft) and an AERONET Sun-sky photometer CE318 (Cimel Electronique SAS). The vertical and columnar aerosol properties in this area were obtained combining the measurements of both instruments following the method proposed by Román et al. (2018), which uses the GRASP algorithm. For the sake of completeness, a bioaerosol particle sampler Lanzoni VPPS 1000, was used starting at noon (12-14 h UTC) to sporadically acquire pollen samples every 10-15 days. In addition, atmospheric models such as HYSPLIT (air masses trajectory model), BSCDream8b (dust), NAAPS (dust, smoke, sulphates) and SILAM (pollen) were employed to contextualize the atmospheric scenarios. Finally, the aerosol classification proposed by Lee et al. (2010), focusing on column integrated physical properties, was used. This classification considers thresholds based on the Fine Mode Fraction at 500 nm (FMF_{500}) and the Single Scattering Albedo at 440 nm (SSA_{440}), to distinguish among dust, mixture, non-absorbing, slightly-absorbent, moderately-absorbent and highly-absorbent aerosols. In order to take into account pollen grains in this classification, which are potentially predominant during the main pollen season, and to separate pollen particles from other aerosol types, the Mann-Whitney U Test was performed to identify the column-integrated aerosol properties that can help us to distinguish between pollen and other aerosols.

Results and discussion

Modified Lee's classification

As the place of study is an olive orchard crop, the presence of *Olea* pollen-type was expected mainly from middle April to middle July. According to the information given by the bioaerosol particle sampler, the maximum pollen grain count was on 6th May 2021, with a concentration of 17187 grains/m^3 in 1 hour at surface level. To guarantee that the atmospheric scenario was dominated by pollen grains, a data temporal window of ±7 days around the peak day was selected. This data-period shows that pollen particles have a FMF_{500} slightly above 0.6, overlapping with the absorbent aerosols category in the traditional Lee's classification.

From this statistical test, taking the period 30th of April – 13th of May as a pollen dominated period, we found that the SSA_{440}, SSA_{1020}, FMF_{500}, real and imaginary refraction index (at 440 and 1020 nm) and columnar lidar ratio at 1020 nm have different values for each aerosol type (pollen, dust, absorption aerosols and mixture) during the whole period analysed, i.e. 14th of January and 31st May 2021. Nevertheless, the second derivative of the aerosol optical depth (AOD) with respect to the wavelength ($AOD''=d^2LnAOD/dLn\lambda^2$) is a good columnar property to separate pollen particles from absorbent aerosols. As a result, and as a modification in the Lee´s classification, the AOD'' was found a good columnar property to

discriminate between pollen grains and absorbent aerosols, with AOD'' being generally negative for pollen grains and positive for absorbent aerosols. As a result, we proposed a modification in the Lee's classification, classifying pollen grains when FMF_{500}>0.60 and AOD'' <0.

Case study: an intense Saharan dust event

As an illustration of the experimental design, an intense Saharan mineral dust event, occurring on 26th March – 2nd April, 2021 is presented. According to the HYSPLIT backtrajectories analysis, the first days air masses came from the South-West, near the Moroccan coast and as the days went on, changed coming across the Northern Sahara (Morocco and Algeria). BSC-Dream8b and NAAPS models properly forecasted this dust intrusion. Dust particles entered the Iberian Peninsula by the South-West on the 26th March and went across all of Spain between the 30th March and the 2nd April. AOD was large, especially between 29th March and 1st April with an AOD_{440} of 0.60-0.70, low Ansgtröm Exponent ($AE_{440-870}$) of 0.1-0.2 and FMF_{500} below 0.40. Thus, according to modified Lee's classification it was a mineral dust event. The columnar particle size distribution presented a monomodal distribution with predominance of coarse mode particles. Figure 1 shows the mineral dust vertical profiles retrieved in the morning of 31st March by GRASP. Aerosols extended from surface up to 6 km asl, with a maximum presence of particles between 2.0 and 3.5 km asl. Maximum values of particle extinction and backscatter coefficients were 317 Mm^{-1} and 4.6 $Mm^{-1}sr^{-1}$ at 440 nm, respectively, registered at 2.3 km asl. At this altitude, volume concentrations above 150 $\mu m^3/cm^3$ were found.

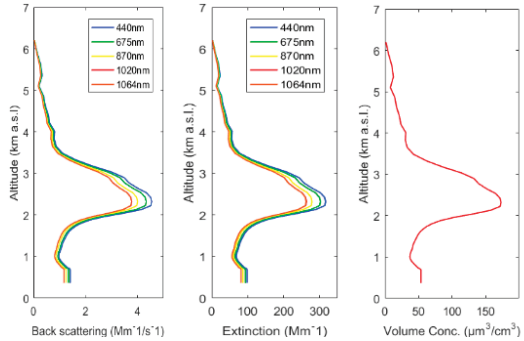

Figure 1. Vertical profiles for a case of mineral dust on 31st March 2021 at 09:15 UTC.

Statistical analysis

In addition to the characterization of specific events, a statistical analysis in terms of their vertical distribution considering the predominant aerosol type was performed. Figure 2 shows the statistics for the volume concentration for each aerosol type within 500-m bins. Note the lack of pollen category, because of low AODs and/or cloud presence prevented the retrieval of pollen-related profiles. Because absorbent and highly-absorbent particles corresponds to fine mode, the influence on the total volume concentrations is rather low. These particles remained at low altitudes, mainly confined below 2.5 km asl. Mixture particles are composed by some dust and other particles, so the volume concentration is larger compared to the absorbent particle category and they can reach higher altitudes. Finally, mineral dust particles have much more larger volume concentration as they are coarse mode particles and values remain nearly constant from the surface to around 3 km asl, and with a lesser concentration up to roughly 5 km asl.

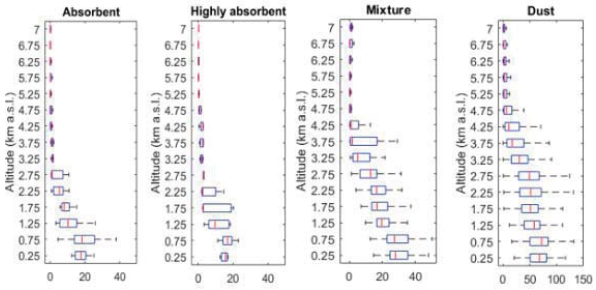

Figure 2. Volume concentration's boxplots for absorbent aerosol, highly absorbent, mixture and dust.

Challenges

Two challenges have been identified in this work. On one hand, the need of long-term data series of particle optical properties (both column-integrated and vertically-resolved) with co-located aerobiological information, in order to precisely characterize the pollen optical properties during the main pollen season of the predominant taxa at a given location. On the other hand, it is highly encouraged to spread the use of ceilometers and Sun-photometers with depolarization capabilities.

Acknowledgements

This work was also supported by the Spanish projects CGL2017-83538-C3-1-R and PID2020-117825GB-C21, and by the University of Granada through the Excellence Units Program. The authors thankfully acknowledge the FEDER program for the instrumentation used in this work. This work is related to activities within the COST Action PROBE (CA18235) and InDust (CA16202).

References

Lee et al., Characteristics of aerosol types from AERONET sun-photometer measurements. *Atmos. Env.* 44, 3110-3117, 2010.

Román et al., Retrieval of aerosol profiles combining Sunphotometer and ceilometer measurements in GRASP code. *Atmos. Res.*, 204, 161–177, 2018.

Expanding the national facilities for aerosol, clouds and trace gases research infrastructure (ACTRIS-UBB) in Cluj-Napoca, Romania

A. Radovici[1], *A.Ozunu*[1], *H. Stefanie*[1], *L. Deaconu*[1], *C. Botezan*[1], *A. Mereuta*[1], *N. Ajtai*[1]
andrei.radovici@ubbcluj.ro
(1) Babeș-Bolyai University- Faculty of Environmental Science and Engineering, Fântânele 30, Cluj-Napoca, Romania

Introduction

Babeș-Bolyai University (UBB) started developing its aerosol remote sensing infrastructure in 2009 within several national (ROLINET - *ROLINET, Romanian Lidar NETwork – PN II – Partnership 31-002/2007*, MADECIP - *Development of research infrastructure for disaster management based on high performance computing, POS CCE Funding, ID 1862 / SMIS 48801*) and international (RADO - *Romanian Atmospheric Research 3D Observatory, Innovation Norway Research Programme, no. 115266/2008*) projects.

A Cimel CE 318 sun photometer is operational on site since 2010 with data available via the NASA-AERONET website (https://aeronet.gsfc.nasa.gov). A single wavelength (532β) LIDAR prototype was operational since 2009, and further upgraded in 2015 to a multiwavelegth Raman and depolarization system (3α+2β+1δ) followed by its integration in EARLINET (www.earlinet.org) and it's Single Calculus Chain (SCC) processing system (D'Amico et al., 2015).
UBB was part of the Research Infrastructure (RI) proposal submited and accepted for the 2016 ESFRI Roadmap, as part of the ACTRIS-RO community (www.actris.ro) represented by the National Institute for R&D in Optoelectronics (INOE2000). Duringthepreparatory and implementation phases of the ACTRIS-RI (www.actris.eu), UBB has made efforts to improve its aerosol remote sensing infrastructure and to extend its research interest and capacities on cloud remote sensing (Ajtai et al., 2020).

In this context, UBB submitted in 2019 a Large Research Infrastructures project proposal for accessing EU regional development funds. The contract was signed in 2020, completion and start of operations is foreseen for 2024.

UBB plans to develop a high level infrastructure for the observation and characterization of the atmosphere, by using advanced remote sensing techniques complemented by in-situ methods, in order to fulfil 2 national facility criteria for integration within ACTRIS-RI.

UBB will develop an international level atmospheric observatory that will host the ACTRIS-RI national facilities for aerosol and cloud remote sensing (ARS & CRS) by acquiring specific equipment and R&D software. Furthermore, a data center will be developed, for efficient and secure storage and pre-processing of measurements made.

Results and discussion

A new atmospheric observatory (CARO - Cluj Atmospheric Remote sensing Observatory) will be built in Cluj-Napoca to house the ACTRIS aerosol and clouds remote sensing national facilities. The observatory will have dedicated laboratories, offices, conference room, and housing capabilities for campaigns. The rendering of the envisaged building is shown in Figure 1.

Figure 1. 3D rendering of the CARO facility

The equipment to be installed within CARO was planned according to the labelling process agreed within the ACTRIS Preparatory Phase Project (ACTRIS-PPP).

1) For aerosol remote sensing (ARS NF):

- Multiwavelegth Raman and depolarization LIDAR system (3α+2β+1δ) – fixed, not eye safe, not continuous operation;
- Solar+lunar+polarized photometer;
- Van + 355nm with Raman and depolarization LIDAR system (1β+1α+1δ) – mobile, eye safe, continuous operation;

2) For cloud remote sensing (CRS NF):

- Dual-frequency microwave radiometer;
- Cloud radar with Doppler capability;
- Ceilometer;
- Doppler Wind profiling LIDAR.

In-situ instrumentation:

- Aerosol Chemical Speciation Monitor (ACSM);
- Condensation Particle Counter (NF);
- Inductively coupled plasma mass spectrometer – triple-qurdupole (ICPMS);
- Gas monitoring system (CO, NO, NOx, CO2, CH4, O3, SO2, PM);

Added-value equipment:

- All-sky camera;
- Weather station;
- Radiation sensors.

Acknowledgements

This work was supported by the Project entitled "Development of ACTRIS-UBB infrastructure with the aim of contributing to pan-European research on atmospheric composition and climate change" SMIS CODE 126436, co-financed by the European Union through the Competitiveness Operational Programme 2014 – 2020.

Financed by European Regional Development Fund through Competitiveness Operational Programme 2014-2020, Action 1.1.3 Creating synergies with H2020 Programme, project Strengthen the participation of the ACTRIS-RO consortium in the pan-European research infrastructure ACTRIS, MYSMIS code 107596.

References

Ajtai et al., Multi-Sensor Observation of a Saharan Dust Outbreak over Transylvania, Romania in April 2019, Atmosphere, 11 (4), 364, 2020.

D'Amico et al., EARLINET Single Calculus Chain – overview on methodology and strategy, Atmos. Meas. Tech., 8, 4891–4916, 2015.

The TROPOMI/Sentinel-5P Aerosol Layer Height product: A validation approach using the EARLINET database

Michailidis K.[1] Koukouli M. E.[1] , Mamouri R. E.[2], de Graaf, M.[3], Veefkind, J. P.[3], Balis D.[1]*
komichai@physics.auth.gr
(1) Laboratory of Atmospheric Physics, Aristotle University of Thessaloniki, Thessaloniki, Greece
(2) Cyprus University of Technology, Dep. of Civil Engineering and Geomatics, Limassol, Cyprus
(3) Royal Netherlands Meteorological Institute (KNMI), De Bilt

Introduction

The aim of this study is to investigate the potential of the TROPOMI instrument, on board the Sentinel5-P satellite platform, to deliver accurate geometrical features of lofted aerosol layers over the Mediterranean basin. For this purpose, we use ground-based lidar data from lidar stations belonging to the European Aerosol Research Lidar Network (EARLINET). Knowledge of the aerosol layer height (ALH) is essential for understanding the impact of aerosols on the climate system. Ground- based observations are important to verify the accuracy and validity of satellite observations as well as model-based results. We present a dust case event originating from the Sahara desert, on the 27th of March 2020, over Cyprus. This dust event was well-captured by multiple instruments with satisfactory co-location points, namely the S5P/TROPOMI, the Limassol EARLINET station (CUT-TEPAK) as well as with the spaceborne lidar, CALIOP/CALIPSO.

Data and Methodology

EARLINET Data

Lidar instruments can provide aerosol profile information, such as the backscatter and extinction coefficients at different wavelengths, which are representative of the aerosol load with a vertical resolution of a few meters. The European Aerosol Research Lidar Network (EARLINET) database covers a large collection of ground-based data of the vertical aerosol distribution on a continental scale (Pappalardo et al., 2014). Moreover, EARLINET consists of quite different lidar systems regarding the number of measured wavelengths and signal channels. The lidar station of the Cyprus University of Technology (CUT) at Limassol (33.04°E/34.67°N), part of EARLINET, is equipped with a 532 nm polarization/Raman lidar (additional channel at 1064 nm) and measures the N_2 Raman signal profiles at 607 nm.

TROPOMI Data

TROPOMI is the single payload on the Copernicus Sentinel-5P satellite that was launched on the 13th of October 2017. TROPOMI maps the global atmosphere daily with a spatial resolution of 7km × 3.5km (5.5×3.5 after August 2019) with a local overpass time of around 13:30 (Veefkind et al., 2012). The TROPOMI Aerosol Layer Height (ALH) product focuses on the retrieval of vertically localised aerosol layers in the free troposphere, such as desert dust, biomass burning aerosol, or volcanic ash plumes. The height of such layers is retrieved for cloud-free conditions. The TROPOMI ALH algorithm was developed by the Royal Netherlands Meteorological Institute (KNMI) and utilizes the absorption in the oxygen *A* band of the spectrum between 759-770 nm. A detailed description of the TROPOMI aerosol layer height product can be found in Nanda et al., 2020.

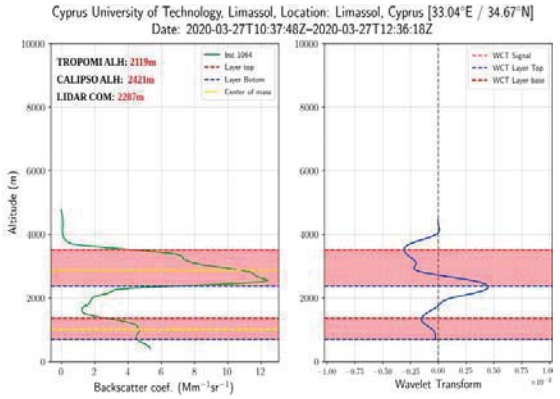

Figure 1. Limassol lidar station (CUT-TEPAK): (left) lidar backscatter profile at 1064 nm and (right) resulting WCT profile on 27 March 2020. The horizontal dashed red line represents the detected aerosol layer top applying the WCT methodology.

Validation methodology

Our analysis is based on the method of Baars et al. (2008) that applies the wavelet covariance transform (WCT) to lidar data in order to extract aerosol layer features. The method detects geometrical features in the lidar signal, such as the planetary boundary layer (PBL), the lofted aerosol and cloud boundaries. More details about the methodology can be found in work of Michaildis et al. (2020). An example of lidar backscatter profile with resulting WCT profile from the Limassol lidar station on March 27, 2020 is presented in Figure 1. The optimum search radius around the EARLINET station for TROPOMI, considering the high spatial resolution of instrument but also the low availability of S5P observations is set to 150km. The lidar measurements closest to the TROPOMI overpass

time within a 3h temporal interval were selected. We highlight that the satellite detects the centroid of aerosol layer, rather than the geometric top of the aerosol layer. For this, we calculate the aerosol profile center of mass for each lidar backscatter profile.

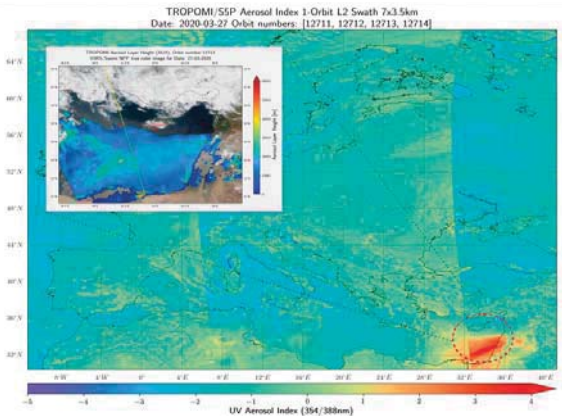

Figure 2. The outer map show the TROPOMI Aerosol index at 354/388nm over Europe on the 27th of March 2020. The inset map illustrates the Suomi/NPP VIIRS image on 27 March 2020, overlain with TROPOMI layer height pixels in colour and the CALIPSO orbit in yellow. VIIRS images are obtained from NASA Worldview, https://wvs.earthdata.nasa.gov/.

Results and discussion

Over the eastern Mediterranean region, the 27th of March 2020 was selected for as a case study for examining the ALH from TROPOMI/S5P, the Limassol (CUT-TEPAK) lidar observations and the CALIOP/CALIPSO sensing. Figure 1 shows the backscatter coefficient, derived from the Single Calculus Chain algorithm (SCC), and calculated WCT profile (right) at 1064nm observed from the CUT-TEPAK Raymetrics lidar at Limassol. As can be seen, a lofted thick layer is detected above Limassol, ranging between 2 and 4km. In Figure 2, the observed TROPOMI Aerosol layer height ranging from 1.8-2.2km, in most of the region. Also, The TROPOMI UV aerosol index is illustrated, showing high positive values (>1.0) corresponding to a heavy absorbing aerosol load. The agreement between TROPOMI and Lidar aerosol height is better than 0.5km for this strong dust event. Comparing the retrieval to co-located CALIPSO data in Figure 3, there are aerosols observed up to the 4km altitude, possibly in a two-layered structure. According to the CALIPSO dataset, the predominant aerosol type is dust.

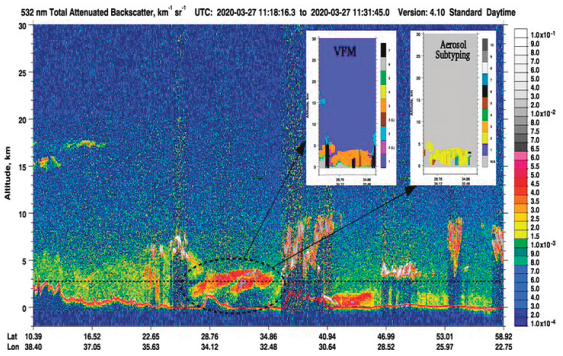

Figure 3. CALIPSO total attenuated backscatter at 532nm, on 27 March 2020 between 11:18:16 and 11:31:45 UTC. The black dashed ellipse shows the elevated aerosol plume. The inset maps illustrate the CALIOP VFM and aerosol subtyping plots.

Challenges and Outlook

The biggest challenge of the TROPOMI's ALH validation is to find collocations both in time and space for both instruments. The discussed methodology can be applied to EARLINET stations with at least one elastically resolved backscatter profile. The results of this study encourages the operational usage of the WCT-based algorithms in validation processes, providing valuable validation results for the ALH.

Acknowledgements

We acknowledge support of this work by the project "PANhellenic infrastructure for Atmospheric Composition and climatE change" (MIS 5021516) which is implemented under the Action "Reinforcement of the Research and Innovation Infrastructure", funded by the Operational Programme "Competitiveness, Entrepreneurship and Innovation" (NSRF 2014-2020) and co-financed by Greece and the European Union (European Regional Development Fund).

References

Baars, H., Ansmann, A., Engelmann, R., and Althausen, D.: Continuous monitoring of the boundary-layer top with lidar, Atmos. Chem. Phys., 8, 7281–7296, https://doi.org/10.5194/acp-8-7281-2008, 2008.

Michailidis, K. et al.,.: First validation of GOME-2/MetOp absorbing aerosol height using EARLINET lidar observations, Atmos. Chem. Phys., 21, 3193–3213, https://doi.org/10.5194/acp-21-3193-2021, 2021.

Pappalardo, G. et al. .: EARLINET: towards an advanced sustainable European aerosol lidar network,Atmos. Meas. Tech., 7, 2389–2409, https://doi.org/10.5194/amt-7-2389-2014 , 2014.

Nanda, S., de Graaf, M., Veefkind, J. P., Sneep, M., ter Linden, M., Sun, J., and Levelt, P. F.: A first comparison of TROPOMI aerosol layer height (ALH) to CALIOP data, Atmos. Meas. Tech., 13, 3043–3059, https://doi.org/10.5194/amt-13-3043-2020, 2020.

Veefkind, J. et al.: TROPOMI on the ESA Sentinel-5 Precursor: A GMES mission for global observations of the atmospheric composition for climate, air quality and ozone layer applications, Remote Sens. Environ., 120, 70–83,https://doi.org/10.1016/j.rse.2011.09.027, 2012.

Profiling of the anthropogenic aerosols in Europe during the ACTRIS/EARLINET COVID-19 campaign

A. Tsekeri[1], *A. Gialitaki*[1,2], *M. Di Paolantonio*[3], *D. Dionisi*[3], *G. L. Liberti*[3], *A. Fernandes*[4], *A. Szkop*[4], *A. Pietruczuk*[4], *D. Pérez-Ramírez*[5,6], *M. J. Granados Muñoz*[5,6], *J. L. Guerrero-Rascado*[5,6], *L. Alados-Arboledas*[5,6], *D. Bermejo-Pantaleón*[5,6], *J. A. Bravo-Aranda*[5,6], *E. Marinou*[1,2], *V. Amiridis*[1], *A. Comerón*[7], *C. Muñoz-Porcar*[7], *A. Rodríguez-Gómez*[7], *M. Sicard*[7], *S. Romano*[8], *M.R. Perrone*[8], *X. Shang*[9], *M. Komppula*[9], *R. E. Mamouri*[10,11], *A. Nisantzi*[10,11], *D. Hadjimitsis*[10,11], *F. Navas-Guzmán*[12,6], *A. Haefele*[12], *I.S. Stachlewska*[13], *D. Szczepanik*[13], *R. Fortuna*[13], *B. Livio*[14], *D. Nicolae*[14], *P. Fréville*[15], *J. L. Baray*[15,16], *K. Eswaran*[16], *K. A. Voudouri*[2], *D. Balis*[2], *A. Floutsi*[17], *H. Baars*[17], *L. Miladi*[18], *N. Pascal*[18], *Q. Hu*[19], *P. Goloub*[19], *O. Dubovik*[19], *and A. Lopatin*[20]

atsekeri@noa.gr

(1) IAASARS, National Observatory of Athens, Athens, Greece
(2) Laboratory of Atmospheric Physics, Physics Department, AUTH, Thessaloniki, Greece
(3) CNR-ISMAR, Rome, Italy
(4) Institute of Geophysics, Polish Academy of Sciences, Warsaw, Poland
(5) Applied Physics Department, University of Granada, Granada, Spain,
(6) Andalusian Institute for Earth System Research (IISTA-CEAMA), Granada, Spain
(7) CommSensLab, Dept. of Signal Theory and Communications, UPC, Barcelona, Spain
(8) Mathematics and Physics Department, University of Salento, Lecce, Italy
(9) Finnish Meteorological Institute, Kuopio, Finland
(10) Cyprus University of Technology, Dep. of Civil Engineering and Geomatics, Limassol, Cyprus
(11) ERATOSTHENES Centre of Excellence, Limassol, Cyprus
(12) Federal Office of Meteorology and Climatology, MeteoSwiss, Payerne, Switzerland
(13) University of Warsaw, Faculty of Physics, Warsaw, Poland
(14) National Institute of R&D for Optoelectronics, Magurele, Romania
(15) Observatoire de Physique du Globe de Clermont Ferrand, CNRS, Université Clermont Auvergne, Aubière, France
(16) Laboratoire de Météorologie Physique, CNRS, Université Clermont Auvergne, Aubière, France
(17) Leibniz Institute for Tropospheric Research, Leipzig, Germany
(18) AERIS/ICARE Data and Services Center Villeneuve d'Ascq, France
(19) Laboratoire d'Optique Atmosphérique, Lille 1 Université de Lille - Science and Technology, Lille, France
(20) GRASP SAS, Villeneuve-d'Ascq, France

Introduction

The lockdown due to the COVID-19 pandemic during spring 2020 in Europe, minimized anthropogenic activities in the continent and thus, possibly affected the load and characteristics of the anthropogenic aerosol particles in the atmosphere. Our work focuses on the characterization of the anthropogenic aerosols during the relaxation period after the lockdown (May 2020), using a combination of active and passive ground-based remote sensing measurements performed by the European Aerosol Research Lidar Network (EARLINET) and the Aerosol Robotic Network (AERONET).

Data and methodology

We analyzed more than thirty cases along the wide spatial coverage of the EARLINET sites participating in the campaign, shown in Fig. 1. For deriving the microphysical properties of the particles we used the GARRLiC/GRASP retrieval algorithm (Lopatin et al., 2013), which combines the lidar and sun-photometer measurements to provide columnar size distribution and refractive index for fine and coarse particles, along with their concentration profiles (e.g., Fig. 2).

Figure 1. The spatial distribution of the active and passive ground-based remote sensing measurements of EARLINET and AERONET used in the study.

For this study, we consider that the anthropogenic component is composed of fine particles only. Our results are augmented by backward-trajectory analysis (e.g. Fig. 3) for verifying the anthropogenic source of the fine particles, and thus, excluding the measurements related to the long-range transported smoke or fine dust particles.

Results and discussion

The retrievals were quite challenging due to the low aerosol loads observed during the relaxation period,

with AOD in the range of ~0.05-0.15 at 500nm for the fine particles.

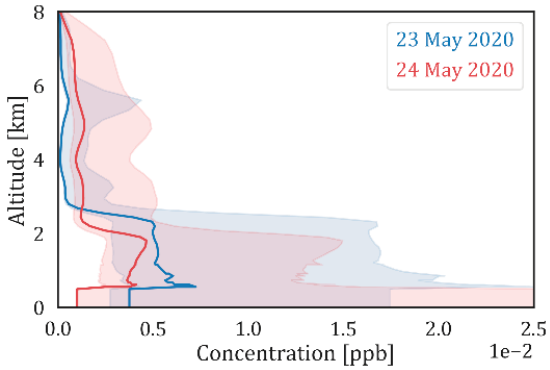

Figure 2. The anthropogenic aerosol concentration at Kuopio EARLINET station, on 23 and 24 May, 2020 (two days during the relaxation period of COVID-19 pandemic lockdown).

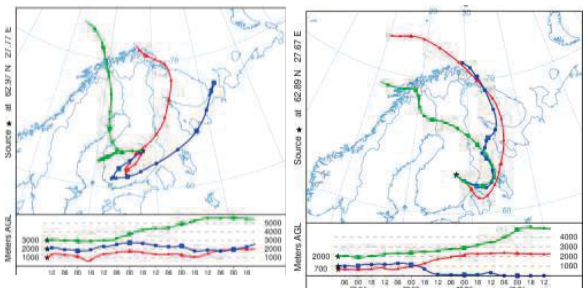

Figure 3. The back-trajectory analysis for Kuopio EARLINET station, on 23 (left) and 24 (right) May 2020, corresponding to the profiles shown in Fi. 2.

Overall, our analysis verifies the low concentrations of the anthropogenic component. The particles are found mainly up to 2-4km a.g.l. (e.g., as shown in the example depicted in Fig. 2). Further characterization (and typing) based on the derived refractive index is challenging, due to the low AOD and correspondingly high retrieval uncertainties.
This work shows the potential of combining the lidar with sun-photometer measurements from the EARLINET and AERONET networks, for the derivation of the size, abundance and vertical distribution of the anthropogenic aerosols in Europe, even during a period with low aerosol loads, as the lockdown and relaxation period of the COVID-19 pandemic.

Challenges

The microphysical retrievals presented in this work are quite challenging, due to the low aerosol loads (AOD of 0.05-0.15 at 500nm). Although the size, abundance and vertical distribution of the anthropogenic component are derived from the combination of the lidar with the sun-photometer measurements with sufficient accuracy, this is not the case for the refractive index of the anthropogenic component at these low loads.

Acknowledgements

We thank EARLINET (https://www.earlinet.org/), ACTRIS (https://www.actris.eu), AERONET (https://aeronet.gsfc.nasa.gov/) and AERONET-Europe for the data collection, calibration, processing and dissemination.

References

Lopatin, A., et al., *Atmos. Meas. Tech.*, 6, 2065–2088, 2013.

Geometrical and microphysical properties of clouds formed in dust presence above the Eastern Mediterranean

Marinou E.[1,2,3], Voudouri K. A.[1], Tsikoudi I.[2], Rosoldi, M.[4], Ene D.[5] and Meleti C.[1]*
elmarinou@noa.gr
(1) Laboratory of Atmospheric Physics, Aristotle University of Thessaloniki, Thessaloniki, Greece
(2) IAASARS, National Observatory of Athens, Athens, Greece
(3) Institute of Atmospheric Physics, German Aerospace Center, Oberpfaffenhofen, Germany
(4) Institute of Methodologies for Environmental Analysis, National Research Council of Italy , Potenza, Italy
(5) National Research & Development Institute Optoelectronics INOE 2000, Rumania

Introduction

Clouds play a vital role for our weather and climate, affecting precipitation and the Earth's radiation budget. The processes governing their formation, evolution, geometrical and microphysical properties, as well as their radiative effects are far from being well understood from the community. The inability to correctly describe the ice content in clouds globally is one of the main limitations in Global Climate Models (GCMs) inducing climate prediction uncertainties. The uncertainty is higher for the quantification of ice and/or water content in Mixed Phase Clouds (MPC; clouds consisting of water vapor, ice particles, and supercooled liquid droplets). These limitations affect significantly the estimation of the cloud albedo in GCMs, altering the equilibrium climate sensitivity up to 2°C (Tan et al., 2016). High resolution/accuracy vertical profiles of cloud microphysics in different regions and aerosol conditions could help fill these gaps.

In this study, we use collocated lidar/radar observations to retrieve high-resolution vertical profiles of cloud properties above the Eastern Mediterranean. Specific focus is given to clouds formed in the presence of dust particles. The study is based on measurements collected during the Pre-TECT experiment (http://pre-tect.space.noa.gr/; 1 - 30 April 2017) at the Greek atmospheric observatory of Finokalia, Crete (University of Crete).

During Pre-TECT, continuous observations of aerosols and clouds were performed with high vertical and temporal resolution, using collocated measurements from the PollyXT-NOA lidar system (Engelmann et al., 2016) and the MIRA36 cloud Doppler radar system of CNR-IMMA (Madonna et al., 2011). The lidar and radar measurements were processed with the target classification algorithm of Cloudnet (https://cloudnet.fmi.fi/) (Hogan and O'Connor, 2004). The algorithm combines the vertical profiles of the lidar attenuated backscatter coefficient at 1064 nm, the radar reflectivity and Doppler velocity and ECMWF thermodynamic variables (temperature, pressure, humidity and horizontal wind) to provide information on the phase of clouds (e.g. ice, cloud droplets only, ice and supercooled droplets). The time evolution of the clouds observed is inspected using the MSG-Seviri cloud top temperature product over the Mediterranean.

Results and discussion

On 19 and 20 of April 2017, the circulation due to a deep low-pressure system over central Europe led to Saharan advection from Africa towards Finokalia. From the instantaneous MSG-Seviri plots we see that clouds were formed on top of the Saharan layers with the support of weakened frontal activity (Fig. 1).

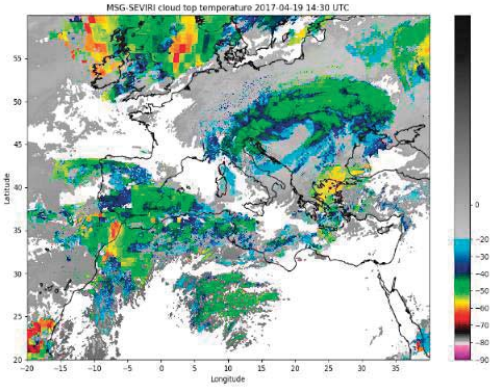

Figure 1. MSG-Seviri cloud top temperature on 19th of April 2017 at 14:30 UTC.

Figure 2 shows the observations above Finokalia from the lidar and the radar, along with the outputs of the Cloudnet algorithm, on 20th of April. The time evolution of the dust advection above the station and the characteristics of the clouds that were formed on top of the dust layer can be seen. At the beginning of the event, clouds formed at altitudes between 3 and 6 km and at temperatures from 0 °C to -20 °C. Later on, the cloud formation continued, extending up to higher latitudes, above 6 km, and at temperatures lower than -20 °C. Some rainfall in Finokalia was observed. Significant presence of mixed phase layers is observed from the cloud classification.

Analyzing the Cloudnet target classification retrievals for this day , statistics for each modeled temperature level (with vertical resolution of 1 °C) was derived. The results are shown in Figure 3 (left panel: number of observations for all-target

categories, right panel: percentage of observations for only-cloud categories).

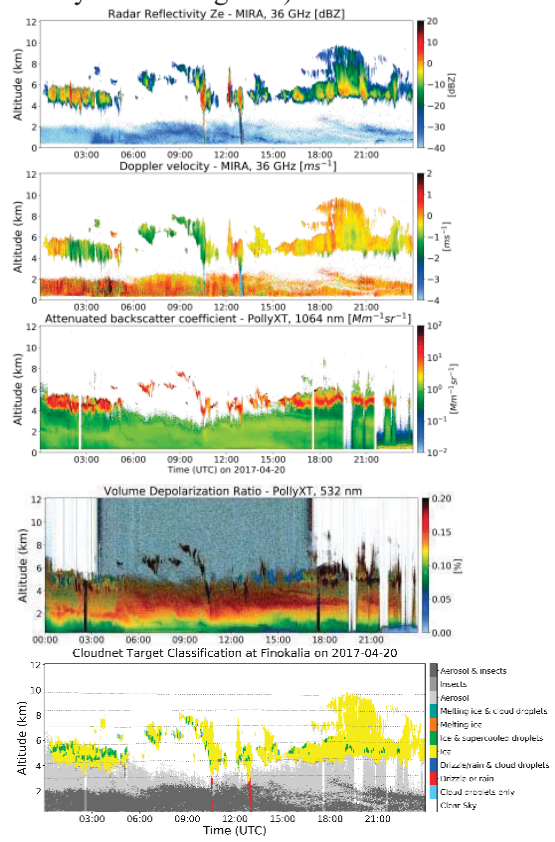

Figure 2. From top to bottom: Observations of the radar reflectivity, the radar Doppler velocity, the lidar attenuated backscatter coefficient and the lidar volume depolarization ratio on 20 April 2017 above Finokalia, Crete. Bottom plot: Cloudnet target classification retrieval on the same day. The dotted lines in the Cloudnet target classification plot are the modeled temperature levels of 0, -10, -20, -30, -40 and -50°C.

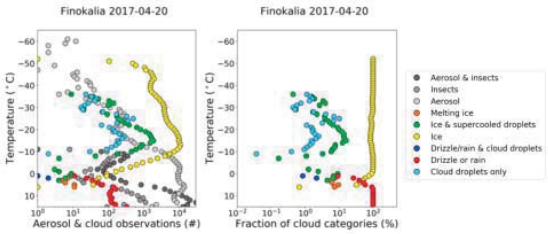

Figure 3. Cloudnet target classification statistics (left) and statistics of the cloud phase (right) per 1 °C as observed during the dust event on 20 April 2017 above Finokalia.

We find that the clouds observed at altitudes with temperatures below 0°C are dominated by pure ice phase, with frequent observations of thin layers of (a) ice coexisting with supercool droplets and (b) supercool droplets. Hereon (a) and (b) are referred as mixed phase layers/targets. The majority of temperatures of the observed mixed phase layers were between -8 to -17 °C, and up to -26 °C. The mixed phase targets represent the 21% (at – 16 °C) of the total cloud observations in this day, with a significant contribution (10% at -16 °C) of "supercooled droplets"-only.

Analyzing all cloud observations during PreTECT, we found that the ice coexisting with supercool water layers had maximum abundance at temperatures in the ranges [-10, 0] °C and [-20, -10] °C, representing the 14% and 7% of the cloud observations at -3 °C and -15 °C respectively. During dusty cases, the abundance of the mixed phase targets was by 4% higher to the mean conditions observed.

Challenges

In order to quantify the effect of dust particles on the clouds formed above the Eastern Mediterranean, long-term lidar/radar collocated observations, geostationary satellite observations and models outputs are needed. The upcoming cloudnet stations in the Pangea observatory (PANGEA "PANhellenic GEophysical observatory of Antikythera) and in Cyprus will fill this gap.

Acknowledgements

This research is co-financed by Greece and the European Union (European Social Fund-ESF) through the Operational Programme «Human Resources Development, Education and Lifelong Learning 2014 - 2020» in the context of the project "Μελέτη της αλληλεπίδρασης των Αερολυμάτων και των Νεφών στην περιοχή της Ανατολικής Μεσογείου με τη συνεργιστική χρήση δεδομένων από επίγεια και δορυφορικά συστήματα ενεργής τηλεπισκόπησης" (MIS 5047913). The authors would like to acknowledge EARLINET, Cloudnet, PollyNET and ACTRIS for the data collection, calibration, processing and dissemination. We thank the Pre-TECT team for providing us access to the pre-TECT datasets. We acknowledge support from the ERC Grand D-TECT (Grant Agreement 725698).

References

Engelmann R. et al., The automated multiwavelength Raman polarization and water-vapor lidarPollyXT: the neXT generation, Atmos. Meas. Tech., 9, 1767–1784, 2016.

Hogan and O'Connor, Facilitating cloud radar and lidar algorithms: the Cloudnet Instrument Synergy/Target Categorization product, Dept. of Meteorol. Univ. of Reading, UK, 2004.

Madonna F. et al., CIAO: the CNR-IMAA advanced observatory for atmospheric research, Atmos. Meas. Tech., 4, 1191–1208, 2011.

Tan I. et al., Observational constraints on mixed-phase clouds imply higher climate sensitivity, Science, 352 (6282), pp. 224-227, 2016.

Lidar-photometer combined retrieval of the aerosol layer types

***D. Nicolae*[1]**, *J. Vasilescu*[1], *C. Talianu*[1], *M. Boldeanu*[1,2], *V. Nicolae*[1,3], *I. Binietoglou*[1],
nnicol@inoe.ro
(1)National Institute of R&D for Optoelectronics, 409 Atomistilor Str., Magurele, Romania
(2) Faculty of Electronics, „Politechnica" University of Bucharest, 1-3 Iuliu Maniu Bvd, Bucharest, Romania
(3) Faculty of Physics, University of Bucharest, 405 Atomistilor Str., Magurele, Romania

Introduction

An improved approach of the aerosol typing algorithm NATALI (Nicolae et al., 2018) was developed in the frame of the ESA funded contract 4000121773/17/I-EF, DIVA. This version of the typing algorithm is named **NATALI+**.

The typing process within the previous NATALI software is based on artificial neural networks (ANN), the intensive optical lidar parameters being the ANN input and the aerosol types the outputs. A comprehensive set of optical parameters are presented to several ANNs, after the algorithms for layering are applied and these intensive optical products retrieved. NATALI algorithm requires as input at least 3 backscatter and 2 extinction coefficients in order to resolve 5 main aerosol types (and up to 14 aerosol mixtures if the linear particle depolarization ratio is provided). With the current vibrational Raman technology, the extinction coefficient profile cannot be accurately retrieved during daytime, which makes the algorithm usable only for nighttime measurements for most of the EARLINET/ACTRIS operating stations.

The new algorithm NATALI+ also relies on ANNs but it uses as input the full information (Angstrom exponent, color ratios, lidar ratios and linear particle depolarization ratio) provided by GRASP (Generalized Retrieval of Aerosol and Surface Properties) (Dubovik et al., 2011), taking advantage of the synergy between the aerosol high-power lidar and the photometer. GRASP was developed for enhanced characterization of the properties of both aerosol and land surface from diverse remote sensing observations. It embeds but is not limited to GARRLiC (Generalized Aerosol Retrieval from Radiometer and Lidar Combined data) which was developed by Lopatin et al. (2013) in the frame of ACTRIS for inversion of coincident multi-spectral lidar and radiometer observations. With this approach, both nighttime (NATALI) and daytime (NATALI+) measurements can be accommodated.

The NATALI+ code is developed in Python and currently is embedded into the DIVA platform (https://hub.grasp-cloud.com/diva) which also accommodates the most recent version of GRASP.

When re-programming the ANNs in an open source environment, we took the opportunity to also revise the aerosol types provided initially by NATALI, i.e. we considered separately the fine and the coarse dust. The mixture of 3 aerosol types was no longer considered, being too difficult to differentiate from a spectroscopically poor content of the data.

Table 1. Aerosol types retrieved by NATALI+ software

NATALI+ retrieved type	**Aerosol mixture**	**Correspon-ding type in NATALI**
Continental	Continental	Continental
Marine	Marine	**New**, partially in Marine / Cloud Corrupted
Smoke	Smoke	Smoke
Fine Dust	Fine Dust	**New**, partially in Dust
Coarse Dust	Coarse Dust	**New**, partially in Dust and Volcanic
Continental polluted	Continental Polluted	Continental Polluted
Marine Polluted	Continental Polluted + Marine	Coastal Polluted
Coastal	Continental + Marine	Coastal
Dust	Fine Dust + Coarse Dust	Dust
Continental Smoke	Continental + Smoke	Continental Smoke
Continental Dust	Continental + Fine Dust + Coarse Dust	Continental Dust
Marine Dust	Marine + Fine Dust + Coarse Dust	Marine mineral
Smoke Dust	Smoke + Fine Dust + Coarse Dust	Dust Polluted

Results and discussion

The model developed for aerosol classification is a feed-forward neural network trained using a synthetic database created while developing NATALI. The main improvement is the use of an open-source, platform independent library (Tensorflow) for developing and training the

model. This allows the trained models to be ran on any hardware. In figure 1 the performance of the trained model can be evaluated by comparing the label predicted by the network with the ground-truth.

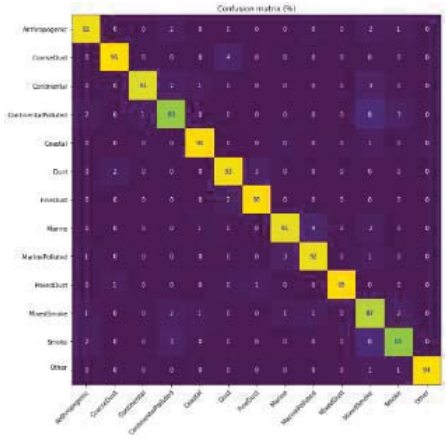

Figure 1. Confusion matrix for the best model.

DIVA platform integrates the pre-trained NATALI+ model, ready to be used by the users. Within the DIVA platform, all collocated lidar / photometer measurements are automatically inverted using GRASP to produce aerosol microphysical properties, and calculate optical property profiles (extinction, backscatter, depolarization coefficients).

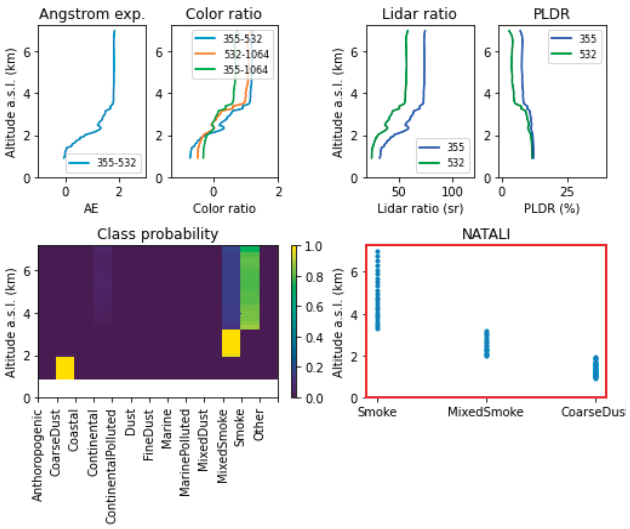

Figure 2. Example NATALI+ retrieval based on INOE measurements on 12th July 2017. Top: Input aerosol properties profiles calculates through GRASP. Bottom left: Profiles of class probabilities. Bottom right: NATALI+ output of most probable aerosol class per height

NATALI+ uses these data to produce aerosol type estimates for each altitude. The demonstration script is implemented in a Jupyter notebook environment, to allow easy interaction for new users. Figure 2 shows an example retrieval for 12th July 2017.

The results indicate the presence of dust particles in the lowest two kilometers and a transition first to mixed smoke and then to pure smoke in higher altitudes. Note that the GRAPS/NATALI+ retrieval will assign an aerosol type even in altitudes with low aerosol load.

Challenges

The presence of clouds in the averaged lidar profiles has proven to be a difficulty in separating Marine aerosols and sometime even large dust particles. Broken clouds or very thin clouds may still pass the SCC cloud masking automatic procedure, and can be embedded in the average inputs for GRASP. A general threshold to separate aerosol and clouds has not been found. The most efficient way to identify cloud corrupted profiles and/or regions with activated aerosols relies on the calculated intensive optical parameters, therefore on GRASP output products which are used as inputs for the aerosol typing. As such, in the near future we will implement an algorithm based on ratios of intensive optical lidar parameters to differentiate Cloud corrupted and Smog from the rest of aerosol types.

Acknowledgements

This work was supported by ESA under contract 4000121773/17/I-EF (DIVA) and by the Ministry of Research, Innovation and Digitization through Romanian National Core Program contract no.18N/2019.

References

Nicolae et al. A neural network aerosol-typing algorithm based on lidar data. *Atmos. Chem. Phys.* 2018, 18, 14511-14537, 2018.

Dubovik et al., Statistically optimized inversion algorithm for enhanced retrieval of aerosol properties from spectral multi-angle polarimetric satellite observations, *Atmos. Meas. Tech.*, 4, 975-1018, 2011.

Lopatin et al. Enhancement of aerosol characterization using synergy of lidar and sun-photometer coincident observations: the GARRLiC algorithm, *Atmos. Meas. Tech.*, 6, 2065–2088, 2013.

Updates on biomass burning in relationship with vegetation type

M. Adam[1], K. Fragkos[1], S. Solomos[2], L. Belegante[1], D. Ene1, V. Nicolae1, L. Janicka3, V. Amiridis4
mariana.adam@inoe.ro
(1) National Institute of Research and Development for Optoelectronics - INOE 2000, 409 Atomistilor St, Magurele, Romania
(2) Research Centre for Atmospheric Physics and Climatology, Academy of Athens, Athens, Greece
(3) Faculty of Physics, University of Warsaw, 02-093, Warsaw, Poland
(4) Institute of Astronomy, Astrophysics, Space Applications & Remote Sensing, National Observatory of Athens, Athens, Greece

Introduction

In a recent study by Adam et al. (2020a), the biomass burning measurements at 13 stations in EARLINET over 2008-2017 were analysed by the means of intensive parameters, with focus on biomass burning events measured by two stations, long range transport from North America and statistical analysis for four chosen geographical regions (while the sources were roughly associated with a continent). One of the outcomes of the previous study was that we usually measure "mixed smoke", i.e., a mixture of smoke originating from many different sources.

Currently, we focus on the lidar measurements in Magurele (Romania, latitude 44.3448 N, longitude 26.0123 E) over 2008-2020 period. The data are reprocessed using the latest version of Single Calculus Chain (SCC; v5.2.2) issued in May 2021. The main purpose of the study is to investigate the relationships between the optical properties retrieved from lidar measurements (in particular, intensive parameters) and the vegetation type of the biomass burning. Overall, the data analysis follows the methodology presented by Adam et al. (2020a). Briefly, the biomass burning sources are identified based on the HYSPLIT backtrajectory (https://www.ready.noaa.gov/hypub-bin/trajtype.pl?runtype=archive, last access 20/05/2021), considering as a source the fire/s found within 100 km and +/- 1 h from the airmass trajectory. The fires' locations are provided by FIRMS (https://firms.modaps.eosdis.nasa.gov/, last access 20/05/2021). However, a few improvements have now been added. The most important one is that the injection height is now computed based on the fire radiative power provided by FIRMS, following Amiridis et al. (2010) and Solomos et al. (2019) in order to assess the altitude of the smoke injected in the atmosphere and verify if it reaches the airmass trajectory. As mentioned in a previous presentation (Adam et al., 2020b), the land cover data is provided by MODIS (https://lpdaac.usgs.gov/products/mcd12c1v006/, last access 20/05/2021).

Results and discussion

During 2008 – 2020 a total number of 1702 files were recorded over Magurele, representing 373 time stamps over 116 days. The EARLINET QC rejected 17 files. From 373 time stamps (datasets) we chose 108, representing 3+2+1 measurements. For those, the first QC was visually performed. We have chosen 38 datasets (35%) for which we have 64 layers. The second QC was performed over the optical properties, following Adam et al. (2020). There were 26 datasets (39 layers) passing the criteria (24 % of initial set).

In Fig. 1 we show an example of ensemble HYSPLIT backtrajectories along with the mean trajectory (in red). The ensemble was computed such that the input altitude ranges from bottom of the layer to the top of the layer in discrete altitude increase. The mean trajectory was computed using the trajectory cluster analysis from HYSPLIT. In this particular case, the input altitude ranges from 1323m to 2723m in 50m increments and thus, the ensemble is made of 29 individual trajectories.

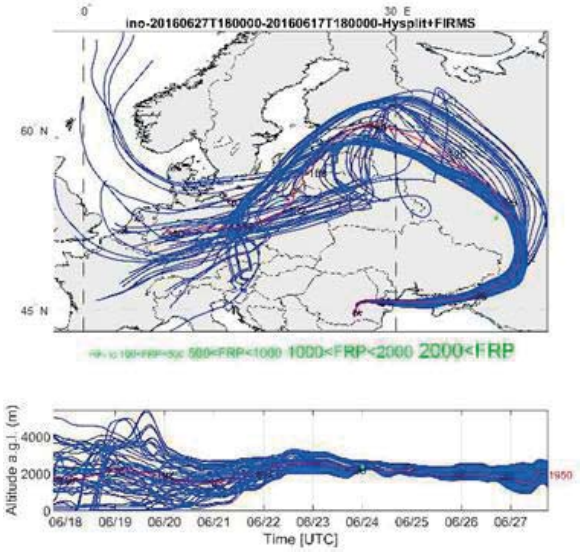

Figure 1. HYSPLIT Ensemble trajectories along with the mean trajectory in red arriving at Magurele at every 50 m between 1323 and 2723m height, 27 June 2016, 1800UTC. The lower plot shows the altitudes of the air mass a.g.l. The location of the fires is shown in green.

The mean trajectory was used to assess if the layers are of biomass burning origin using FIRMS database. The injection height for each fire was computed following Amiridis et al. (2010). Thus, two fires were found to reach the air-mass altitudes (~ 96h back), where the injection heights were 2403m and 4118m, corresponding to air-mass altitudes at 2365m and 2399m. The two fires were detected three times. Thus, at 24 June 2016, 00:00 (air-mass coordinates at 41.048N, 52.708E), the first fire was identified at 39.6375N and 52.5489E where the time of the fire (according to MODIS) was recorded at 23:58 on 23 June 2016 (FRP=53.7MW). One hour backwards (air-mass coordinates at 40.903N and 52.873E), the same fire is observed along with another (39.5806N, 52.5493E, FRP=13.5MW). The time of the fires according to MODIS is 23:58 on 23 June 2016. The land cover corresponding to the two fires are shown in the following table. The preponderant contributions to the fires are deciduous broadleaf forest and evergreen needleleaf forest for the first fire and urban for the second fire. The 'predominant vegetation type' (PVT) is the one for which the coverage percentage is > 50 %. Conversely, the PVT is labelled as mixed. For the current example, PVT is labelled as mixed. The overall predominant vegetation (OPVT) type is taken as the most frequent value of all PVTs. In this example, OPTV is mixed. The lidar measurements were taken around 18:34 on 27 June 2016 and the aerosol pollution layer was between 1083m and 3243m. The lidar intensive parameters are shown in Table 2. CRLR (LR@532/LR@355) is smaller than 1 while EAE=1.45. According to the values of CRLR (<1) and EAE (>1.4), the smoke is labelled fresh (Nicolae et al., 2018). PDR has a low value which characterizes the smoke particles as almost spherical.

Table 1. Vegetation type.

		FireI	FireII
#	Vegetation type	%	%
1	Water	0	0
2	Grasses or cereal	14	12
3	Shrubs	0	0
4	broadleaf crops	0	0
5	savannah	11	5
6	evergreen broadleaf forest	0	0
7	deciduous broadleaf forest	41	22
8	evergreen needleleaf forest	32	21
9	deciduous needleleaf forest	0	0
10	unvegetated	0	0
11	urban	2	40

Table 2. Lidar intensive parameters.

LR@355 [sr]	63±0.6
LR@532 [sr]	41±2.5
CRLR	0.65
EAE	1.45±0.15
BAE@355/532	0.37±0.04
BAE@532/1064	1.6±0.03
CRBAE	4.3
PDR@532 [%]	2.4±0.1

The results for entire dataset will be presented during conference. It is expected to find some relationships between IPs, fires' FRP and vegetation type..

Challenges

Current challenges we try to address:

- Do we have enough and reliable lidar data to draw thorough conclusions?
- Which is the best method to compute the mean trajectory for an ensemble trajectory? How do we define the ensemble?
- Establish a method to characterize the "mixed smoke" events and thus the main type of the burnt vegetation.

Acknowledgements

This work is supported by the Romanian National contracts 18N/08.02.2019, 19PFE/17.10.2018, PN-III-P2-2.1-PED-2019-1816.

References

Adam et al., Biomass burning events measured by lidars in EARLINET – Part 1: Data analysis methodology, *Atmos. Chem. Phys*., 20, 13905–13927, 2020 (a).

Adam et al., Biomass burning recorded by lidar in relationship with vegetation type, *ELC 2020*, S03P036, 2020 (b).

Amiridis et al., Smoke injection heights from agricultural burning in Eastern Europe as seen by CALIPSO, *Atmos. Chem. Phys*., 10, 11567–11576, 2010.

Solomos et al., Modeling and remote sensing of an indirect Pyro-Cb formation and biomass transport from Portugal wildfires towards Europe, *Atmos. Environ*., 206, 303-315, 2019.

Nicolae et al., A neural network aerosol-typing algorithm based on lidar data, *Atmos. Chem. Phys*., 18, 14511–14537, https://doi.org/10.5194/acp-18-14511-2018, 2018.

A Laboratory Instrument for Optical Atmospheric Aerosols Characterization by linear depolarization ratio

D. Bolaños-Marín, M. Hoyos-Restrepo , E. Montilla-Rosero
emontill@eafit.edu.co
Universidad EAFIT, Cra. 49 No. 7S-50, Medellín, Colombia

Introduction

Atmospheric aerosols and their interactions with clouds persist as a primary source of uncertainty in the Earth's radiative budget (IPCC, 2013). Lidar measurements of aerosol optical properties provide valuable information for improving our understanding of the global climate system (Wu et al., 2020); specifically, the particle linear depolarization ratio (δ_p), defined by the ratio of perpendicular to parallel backscattering intensity with respect to the polarization plane of the emitted laser, has been utilized to determine the aerosol type because it is a measure of nonsphericity of these particles (Belegante et al. 2018). Most common studies of aerosol characterization by δ_p use in situ or remote sensing measurements; however, few works using laboratory conditions whose data might be useful as reference values for Lidar measurements have been conducted (Järvinen, et al., 2016; Sakai et al., 2010).

In addition, due to the impact of aerosols on the air quality of cities and the lack of specific information from inter-Andean urban valleys as Aburrá valley (Gómez-Comba, 2017, Henao et al., 2020), in this work, we present an implementation of a laboratory instrument to measure δ_p from backscattered light under controlled laboratory conditions of relative humidity (RH%), aerosol concentration, particle size distribution (PSD) and chemical composition. Two types of particles were used to test the instrument: Calcium carbonate ($CaCO_3$) that is highly concentrated in the Aburrá Valley (AMVA, 2019), and Saharan dust as reference aerosol. The experimental results of δ_p were compared with theoretical results retrieved by MOPSMAP software (Gasteiger et al., 2018).

Results and discussion

We designed and constructed the laboratory instrument illustrated in Figure 1; every component is described below:

1. Chamber, C: 15cmx15cmx20cm, 5 mm thick, stainless steel vessel. The inside of the chamber was painted matte black to avoid stray light scattered by the wall.
2. Fluidizer, F: Generator of aerosols made of glass of 1,5 mm thick. Its geometry allows converting powder into aerosols (Ding et al., 2015). Using clean and dry air (DAC) and air pump (DH) at 13 L/min, the particles produced have a modal radius less than 3,0 μm.
3. RH% control system: An On-Off closed-loop control algorithm was carried out. Humidify method was based on air transport from a water vessel (H) using a vacuum pump; dehumidification uses reverse way.
4. Optical system: For the emission of continuous laser light at 532 nm to the chamber (45º mirror M1) and the collection of backscattered light (two lenses L1 and L2 as a refractive telescope configured to focus light from the chamber geometrical center). Collected light passes through a polarized beam splitter (PBS) and, finally, PMT1 and PMT2 detect the signals.
5. Signal processing: PMT's signals (CH1 and CH2, respectively) were sent to a processor through an oscilloscope. Then, acquisition data, filtering, and analysis codes were carried out.

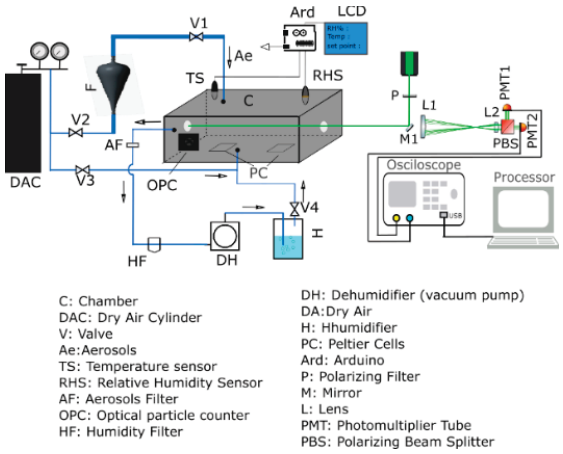

Figure 1. Experimental setup to measure backscatter linear depolarization ratio

To calculate δ_p from the instrument measurements, first, clean and dry air is to put into the chamber to measure background backscattering signals (named $Bg_\perp, Bg_\parallel$), after, aerosols are introduced into the chamber; thus, the background plus aerosol backscattered light is obtained: $I_{\parallel total} = I_{\parallel ae} + Bg_\parallel$, $I_{\perp total} = I_{\perp ae} + Bg_\perp$. Finally, the particle linear depolarization ratio is obtained:

$$\delta_p = \frac{(I_{\perp total} - Bg_\perp)C}{(I_{\parallel total} - Bg_\parallel)} = \frac{I_{\perp ae}}{I_{\parallel ae}} \quad (1)$$

where C=1 is the calibration parameter according to the Delta90 calibration method (Volker, 2016). Figure 2 shows PM2.5 concentration, backscattering signals, and δ_p values during the time of experiment for $CaCO_3$ at around fix RH% value. A direct relationship between concentration and intensity of backscattering signal is observed when the concentration exceeds 200 $\mu g/cm^3$ from t=50s. δ_p high values were obtained ($\delta_p^{average}$=0.76 ± 0.13) for RH ranged between 50% and 54% due to the birefringence property and the irregular shape of the particles.

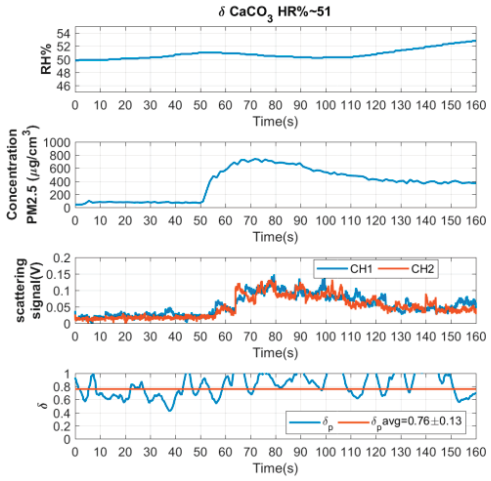

Figure 2. Measurements results for $CaCO_3$

Moreover, the Table 1 shows the relationship between increasing RH%, particle size, and δ_p values. These results suggest hygroscopic particles due to modal radius increased whereas δ_p decreased, indicating a close behavior to spherical particles. For Saharan dust particles, an average value of δ_p of 0.30±0.04 was obtained even with varying RH% values between 30% and 99%. This value is comparable with values reported using Lidar measurements δ_p~0.32 (Liu, 2008).

Table 1. Relationship between air RH%, particle size and δ_p for $CaCO_3$

RH%	Modal radius(μm)	δ_p
$30 < RH < 70$	$r = 2.0$	$0.65 + 0.17$
~70	$r = 2.1$	0.54 ± 0.13
~80	$r = 2.5$	$0.28 + 0.09$
~90	$r = 3.0$	0.3 ± 0.01
~99	$r = 5.0$	$0.1 + 0.01$

Using MOSMAP software, we retrieved for Saharan dust a value of $\delta_{p-simulated} = 0.29$; it matches the experimental value and provides an error of 1.7%. For $CaCO_3$, $\delta_{p-simulated} = 0.532$ was obtained; the difference of 12% is due to simulation assumes a single refractive index and isotropic material, while $CaCO_3$ is birefringent and anisotropic.

Challenges

Could this experiment be reproducible, uptaking aerosols directly from the atmosphere? Could this instrument help characterize the depolarizing property of a large number of know aerosols under laboratory conditions?

Acknowledgements

This work was supported by the EAFIT project 828-000059 Despolarización por aerosoles. The authors thank CEAMA group for their valuable contributions.

References

AMVA, Área metropolitana Valle de Aburrá. Inventario de emisiones atmosféricas, 2019

Belegante, L., et al. Experimental techniques for the calibration of lidar depolarization channels in EARLINET, Atmos. Meas. Tech., 11, 1119–1141.

Ding et al., A system to assess the stability of airborne nanoparticle. Journal of Aerosol Science. pp. 99-108, 2015.

Freudenthaler V., About the effects of polarising optics on lidar signals and the Δ90 calibration, A.M.T, 9, 4181–4255, 2016.

Gasteiger et al., MOPSMAP v1.0: a versatile tool for the modeling of aerosol optical properties, Geosci. Model Dev, 2018.

Gómez-Comba, Contaminación del aire en medellín por PM10 y PM2.5 y sus efectos en la salud, Universidad Militar Nueva Granada., 2017.

Henao J.J. et al., Sub-kilometer dispersion simulation of a CO tracer for an inter-Andean urban valley, atmospheric Pollution Research, 11, 5, 2020.

Järvinen et al., Laboratory investigations of mineral dust near-backscattering depolarization ratios, Journal of Quantitative Spectroscopy & Radiative Transfer, 2016.

Liu et al., CALIPSO lidar observations of the optical properties of Saharan dust: a case study of long-range transport, 2008.

Sakai T. et al., Backscattering linear depolarization ratio measurements of mineral, sea-salt, and ammonium sulfate particles simulated in a laboratory chamber Applied Optics, pp. 4441-4449, 2010.

Wu, M., et al.: Understanding processes that control dust spatial distributions with global climate models and satellite observations, A.C.P, 20, 13835–13855, 2020.

Height-resolved optical and microphysical properties of aged smoke plumes as retrieved from GRASP using both polarized Micro-Pulse Lidar and Sun/sky photometer measurements

M.-Á. López-Cayuela[1], M. Herrera[2], C. Córdoba-Jabonero[1], D. Pérez-Ramírez[3,4], C. V. Carvajal-Pérez[1], O. Dubovik[2], J. L. Guerrero-Rascado[3,4]
lopezcma@inta.es
(1)Instituto Nacional de Técnica Aeroespacial (INTA), Torrejón de Ardoz, 28850-Madrid, Spain
(2) University of Lille, CNRS – LOA, 59000-Lille, France
(3) Andalusian Institute for Earth System Research (IISTA-CEAMA), 18006-Granada, Spain
(4) University of Granada (UGR), 18071-Granada, Spain

Introduction

Biomass burning aerosol particles highly influence the Earth's climate via both direct and indirect radiative effects (Myhre et al., 2013). Wildfires yearly emit to the atmosphere around 40-59% and 60-85% of the global emissions of black and organic carbon aerosols, respectively. For the direct effect of biomass burning, the total radiative forcing is close to zero due to the opposite warming (light absorption) and cooling (light scattering) effects induced by black and organic carbon, respectively. On the indirect effect, smoke particles can act as both cloud condensation and ice nuclei. Moreover, smoke plumes can travel thousands of kilometres away from their sources, being their chemical, physical and morphological properties modified. At this point, lidar systems represent a valuable instrumentation for monitoring and characterization of the smoke plumes.

In this work, we combine polarized Micro-Pulse Lidar (P-MPL) and Sun/sky photometer measurements with the GRASP code (Dubovik et al., 2014) to derive the columnar and vertical aerosol optical and microphysical properties, and their error estimates, of long-range transport for smoke particles. Ten smoke cases are evaluated, corresponding to the arrival of Canadian smoke plumes over El Arenosillo/Huelva station (SW Iberian Peninsula, 37.1ºN 6.7ºW, 59 m a.s.l) on 7-8 September 2017 (Sicard et al., 2019). This station is both an AERONET and MPLNET site.

The GRASP columnar-derived microphysical and optical properties, i.e. particle volume size distribution (VSD, $\mu m^3\ \mu m^{-2}$), total volume concentration (VC, $\mu m^3\ \mu m^{-2}$), effective radius (Reff, µm), single scattering albedo (SSA) and real and imaginary refractive index (RRI, IRI), are compared with AERONET L2.0 V3 data. The GRASP vertically-resolved particle backscatter coefficients (β_p, $Mm^{-1}\ sr^{-1}$) and particle volume concentrations (VC, $\mu m^3\ cm^{-3}$) are compared with those derived using other lidar-based methods. To quantify the expected discrepancies between different methodologies the following statistical proxies are used (López-Cayuela et al., 2021): both the slope (*m*) and the correlation coefficient (*r*) of the linear regression forced to zero, the mean Fractional Bias (MFB), and the relative differences, including the total occurrence (χ, %) for both the columnar and the vertically-resolved variables, whose relative differences are within a particular acceptable confidence interval.

Results and discussion

Figure 1a and 1b shows the columnar VC and Reff, respectively, derived from GRASP and AERONET, considering the ten smoke cases. For both microphysical properties, the four proxies fulfil the acceptable confidence conditions. A high correlation is found, and the slope is close to 1 but showing slight overestimation of Reff. For illustration, Figure 1c shows the VSD for one particular case (marked with a red circle in Figs. 1a and 1b).

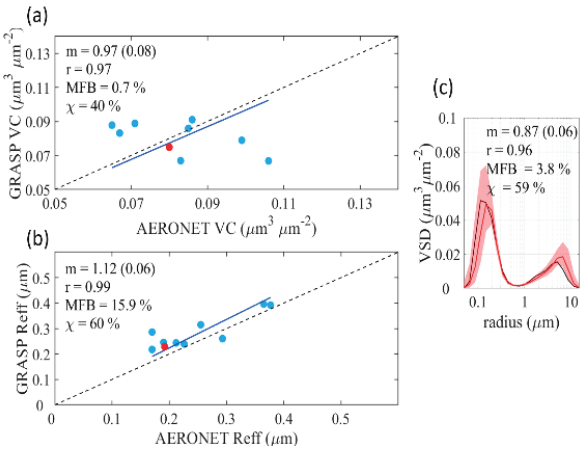

Figure 1. Comparison between GRASP and AERONET: (a) the columnar total volume concentration (VC) and (b) the total effective radius (Reff); (c) the volume size distribution (VSD) for the selected particular case (marked in red in (a) and (b)).Statistical proxies are shown in each panel.

Overall GRASP-derived VSD are slightly displaced towards larger size radii when compared with AERONET retrievals. Comparisons also

reveal moderate χ values (47±16%, on average) that corroborate the discrepancies observed in Reff. However, GRASP highlights the two particle modes and shows a high correlation and low MFB values for all cases, indicating an acceptable confidence in the shape of the VSD (for instance, see Fig. 1c).

For GRASP-derived optical properties, the AERONET criterion for high-quality data is fulfilled for only one case (not shown). Nevertheless, both methodologies show retrieved values typical for long-range transported smoke particles and differences are within the uncertainty intervals.

The height-resolved properties (β_p and VC) derived by GRASP and lidar-based methodology for the selected smoke case (see Fig. 1c) are shown in Figure 2.

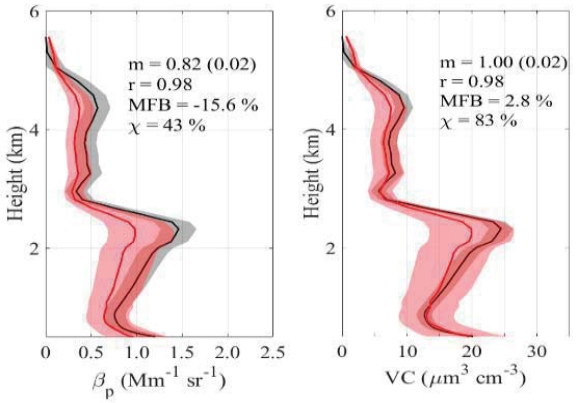

Figure 2. Comparison between GRASP (red) and lidar-derived (black) retrievals for the smoke case shown in Fig. 1c: (Left) the particle backscatter coefficient (β_p), and (Right) the total volume concentration (VC).

Overall all cases fulfil the confidence interval for the four statistical proxies for the β_p profiles. Low absolute MFB and moderately high χ values (|18±10|% and 60±17%, respectively, on average) together with high correlations (> 0.98) indicate a high confidence for the vertical β_p profile. Differences, although within the uncertainty intervals, could be related to the different lidar ratios obtained by both methodologies.

Regarding the VC profiles, good agreements are again found. On average, the ten smoke cases present low MFB and moderately high χ values (|26±15|% and 55±25%, respectively, on average). These results, together with a high correlation (> 0.97), show a high confidence for the vertical VC profiles. Differences obtained could be related to twofold causes: either discrepancies found in the columnar VC values, or the use of specific extinction-to-volume conversion factors (statistically AERONET-derived values for boreal Canadian smoke particles), instead of those retrieved by GRASP.

In general, a good agreement between GRASP and AERONET/lidar-derived microphysical and optical properties is found for aged smoke particles.

Challenges

In order to obtain AERONET high-quality data (L2.0), it is necessary medium/high AOD values (> 0.4 at 440 nm), which could be difficult to reach in the case of long-range transported smoke plumes. The synergy of GRASP methodology using photometer/lidar measurements could serve to obtain both optical and microphysical properties of smoke particles for all AOD ranges with a high degree of confidence. Future works will also incorporate the use of depolarization measurements to distinguish different aerosol types and determine the predominance of non-spherical particles in smoke plumes.

Acknowledgements

This work was funded by the Spanish MICINN (PID2019-104205GB-C21, PID2020-117825GB-C21), and partly by the Spanish MICIU (CGL2017-90884-REDT), the Regional Government of Andalusia (P18-RT-3820) and the Marie Sklodowska-Curie Research Innovation and Staff Exchange (RISE) GRASP-ACE (GA n. 778349). Authors acknowledge the support by the European Union's H2020 research and innovation programme (GA n. 654109, 871115). Authors thanks the use of GRASP inversion algorithm software (http://www.grasp-open.com). Authors also thank the PIs of the AERONET and MPLNET El Arenosillo site and its technical staff for maintenance and operation support. MALC and CVCP are supported by the INTA predoctoral contract programme.

References

Dubovik, O. et al. GRASP: a versatile algorithm for characterizing the atmosphere, 675 SPIE Newsroom, 25, 2014.

López-Cayuela et al., Vertical assessment of the mineral dust optical and microphysical properties as retrieved from the synergy between polarized micro-pulse lidar and sun/sky photometer observations using GRASP code, *Atmos. Res.*, 264(15), 105818, 2021.

Myhre et al. Radiative forcing of the direct aerosol effect from AeroCom Phase II simulations, *Atmos. Chem. Phys.*, 13, 1853–1877, 2013.

Sicard et al., Ground/space, passive/active remote sensing observations coupled with particle dispersion modelling to understand the inter-continental transport of wildfire smoke plumes, *Rem. Sens. Environ.*, 232, 111294, 2019.

CAECENET: Columnar And Vertically-Resolved Aerosol Products In Near-Real-Time Joining Sun/Sky Photometer And Ceilometer Measurement Networks

R. Román[1], *R. González*[1], *A. Cazorla*[2,3], *M. Herreras-Giralda*[4,5], *J.C. Antuña-Sánchez*[1], *C. Toledano*[1]
robertor@goa.uva.es
(1) Grupo de Óptica Atmosférica (GOA), Universidad de Valladolid, Valladolid, Spain
(2) Department of Applied Physics, Universidad de Granada, 18071, Granada, Spain
(3) Andalusian Institute for Earth System Research, IISTA-CEAMA, Granada, Spain
(4) GRASP-SAS, Remote sensing developments, Villeneuve d'Ascq, France
(5) Laboratoire d'Optique Amosphérique, Université des Sciences et Technologies de Lille, Villeneuve d'Ascq, France

Introduction

The knowledge and motinoring of the columnar, but also vertically-resolved, atmospheric aerosol properties is crucial for climate change studies and for other fields like aviation or air quality, among others. Moreover, the knowledge of these properties in near-real-time is important to take quick politic decisions regarding air quality and pollution, and for the demand of information by the general public.

Sun/sky photometers, measuring sky radiance and solar irradiance at different wavelengths, are frequently used to retrieve aerosol properties like aerosol optical depth (AOD) in the atmospheric column. These automatic instruments are used by some worlwide networks, such as AERONET (AErosol RObotic NETwork; Holben et al., 1998) to provide advanced aerosol properties in column in near-real-time. A part of the AERONET photometers is managed by the Group of Atmospheric Physics of the University of Valladolid (GOA-UVa); to this end, CAELIS software tool (Fuertes et al., 2018), which receives photometer data and processes them to generate products like AOD (González et al., 2020), was developed by GOA-UVa

On the other hand, lidars are generally used for the retrieval of vertically-resolved profiles of aerosol properties like aerosol backscattering. In this sense, some networks like EARLINET (Pappalardo et al., 2014) and PollyNET (https://polly.tropos.de) manage multi-wavelength lidar data to provide some aerosol products. However, these lidars are usually expensive and not full automatic, hence there is a scarce of this kind of instruments. A cheaper alternative to lidars are ceilometers and single-wavlelength lidars, which are full automatic measuring continuosly, and the amount of these instruments around the world is much higher. ALC NETWORK (part of E-PROFILE; https://ceilometer.e-profile.eu) and ICENET (Cazorla et al., 2017) are networks providing ceilometer products in near-real-time.

Recently, Román et al. (2018) developed the $GRASP_{pac}$ method, which combines sun/sky photometer and ceilometer measurements into GRASP code (Dubovik et al., 2014) to retrieve sinergetically vertical and columnar aerosol properties. This method can be applied to exploit the high amount of data from collocated sun/sky photometers and ceilometers.

In this framework, the main objective is to develop and establish a system capable to assimilate data from sun/sky photometer and ceilometer networks to apply the $GRASP_{pac}$ method and provide in near-real-time vertically-resolved and columnar aerosol properties. The databases used to this end are from CAELIS for AOD and sky radiances (photometer data) and from ICENET for the ceilometer range corrected signal data. the combination of both databases (CAELIS and ICENET) is what gives the developed system its name: CAECENET.

Results and discussion

CAECENET receives ceilometer data from ICENET for different locations (nowadays 6 spanish locations but increasing). When these data is received, CAECENET calls to CAELIS to look for if any invertible sky scenario (almucantar or hybrid scan) is available for the same time than the ceilometer measurements. In addition, when a photometer sky scenario is received on CAELIS, CAECENET looks for the ceilometer data available. If CAECENET matches the both databases for a given date, and consideres that the measurements were done without clouds (cloud-screening algorithm), then CAECENET prepairs the data and runs GRASP to retrieve aerosol properties. The retrieved data is stored in a mysql database to be accesible.

CAECENET also contains a graphical user interface (CAECENET-viewer) to view and download the data of the retrieved aerosol products. An example of this tool is shown in three screenshots in Figure 1. This tool allows to the user to select one of the CAECENET sites and the time period of interest. The shown example of Figure 1 is for the site of Granada, Spain, at 21st July 2016, but a longer period could be chosen.

The retrievals showing low convergence, with a inversion residual above a threshold chosen by the user as input (Max Residual, see Figure 1), are rejected by CAECENET-viewer and not shown. This tool allows the download of all data products in a .txt file for the chosen period at the selected site and avoiding the non-convergent retrievals; it is just pushing the download data buttom at the bottom-right corner (see Figure 1).

In addition, CAECENET-viewer allows to represent on the screen the different retrieved aerosol properties choosing between three categories: Microphisical properties (upper panel), optical column properties (middle panel) and vertical profile properties (bottom panel).

The first category, Microphysical properties, includes (chosing the tab) columnar volume size distribution, aerosol sphere fraction, and the parameters of the bilog-normal size distribution (fine, coarse and total modes). The second one, optical column, plots the AOD (fine, coarse and total modes), the single scattering albedo, real and imaginary parts of refractive indices, lidar ratio, and asymetry parameter, all at several wavelengths (Figure 1b). Last category, vertical profile, display profiles of aerosol properties like volume concentration, extinction, backscattering, absorption and scattering, all for total, fine and coarse modes (Figure 1c).

The shown example of Figure 1 indicates the presence of coarse particles at Granada at 21st July 2021 that dissapeared at the afternoon, being the AOD near to 1.0 in the morning. These coarse particles reached Granada mainly in an aerosol layer located from 2 km to 3 km asl, with a maximum peak concetration above 350 $\mu m^3/cm^3$.

Challenges

CAECENET has been developed with the aim to provide in near-real-time aerosol properties at column but also with vertical resolution joining different measurements from different networks. It includes tools like CAECENET-viewer to download and display the aerosol products.

It is expected to increase the number of sites and instruments in CAECENET and we encourage to other researchers to participate in this initiative.

Acknowledgements

The authors acknowledge the "Ministerio de Ciencia, Innovación e Universidades" the support obtained with the ePOLAAR (RTI2018-097864-B-I00) project, and the "Junta de Castilla y León" for the AEROCyL (VA227P20) project. The authors acknowledge the use of GRASP inversion algorithm software (https://www.grasp-open.com).

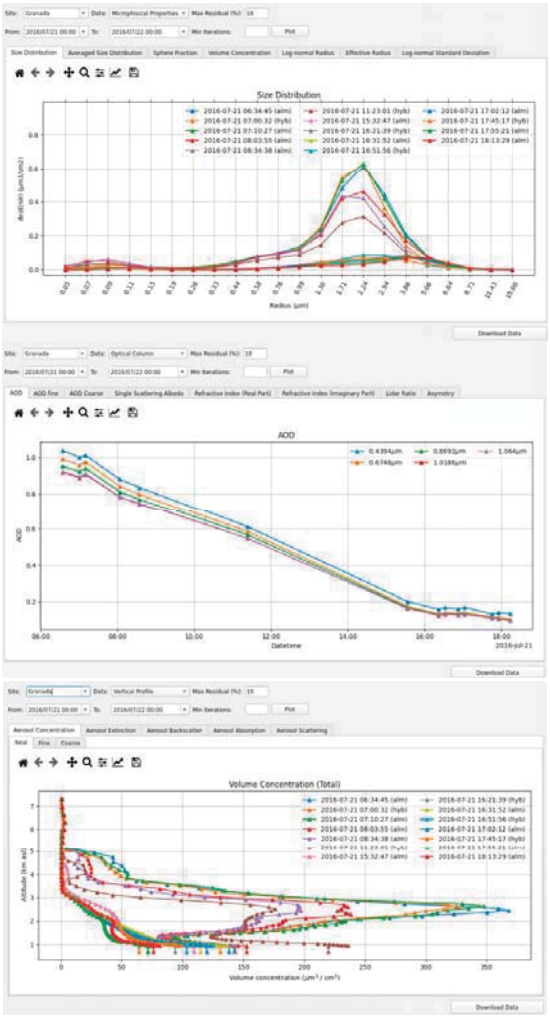

Figure 1. Screenshots of CAECENET-viewer tool showing the retrieved Microphisical properties (upper panel), optical column properties (middle panel) and vertical profile properties (bottom panel) of the CAECENET products for Granada along 21st July 2016.

References

Cazorla et al., Near-real-time processing of a ceilometer network assisted with sun-photometer data: monitoring a dust outbreak over the Iberian Peninsula, *Atmos. Chem. Phys*, 17(19), 11861-11876, 2017.

Dubovik et al., GRASP: a versatile algorithm for characterizing the atmosphere, *SPIE Newsroom*, 25(10.1117), 2-1201408, 2014.

Fuertes et al., CÆLIS: Software for assimilation, management and processing data of an atmospheric measurement network, *Geosci. Instrum. Methods Data Syst.*, 7(1), 67-81, 2018.

González et al., Daytime and nighttime aerosol optical depth implementation in CÆLIS, *Geosci. Instrum. Methods Data Syst.*, 9(2), 417-433, 2020.

Román et al., Retrieval of aerosol profiles combining sunphotometer and ceilometer measurements in GRASP code, *Atmos. Res.*, 204, 161-177, 2018.

Vertical profiles of aerosol properties retrieved at La Palma, Canary Islands, during the Cumbre-Vieja volcano eruption in September-October 2021

***R. Román*[1]**, *R. González*[1], *J.C. Antuña-Sánchez*[1], *A. Barreto*[2], *P. Martín*[1], *C. Toledano*[1], *R. Ramos*[2], *A. Cazorla*[3,4], *S. Herrero-Anta*[1], *D. Mateos*[1], *O. García*[2], *D. González-Fernández*[1], *R. Carracedo*[1], *M. Herreras-Giralda*[5,6], *V. Carreño*[2], *A. Calle*[1], *V.E. Cachorro*[1], *E. Cuevas*[2], *A.M. de Frutos*[1]

robertor@goa.uva.es

(1) Grupo de Óptica Atmosférica (GOA), Universidad de Valladolid, Valladolid, Spain

(2) Izaña Atmospheric Research Center, Meteorological State Agency of Spain (AEMET), Spain.

(3) Department of Applied Physics, Universidad de Granada, 18071, Granada, Spain

(4) Andalusian Institute for Earth System Research, IISTA-CEAMA, Granada, Spain

(5) GRASP-SAS, Remote sensing developments, Villeneuve d'Ascq, France

(6) Laboratoire d'Optique Amosphérique, Université des Sciences et Technologies de Lille, Villeneuve d'Ascq, France

Introduction

The Cumbre-Vieja volcano, located at La Palma Island (Canary Islands, Spain), erupted on September 19, 2021. This kind of events usually emits a big aerosol load to the atmosphere, mainly sulfate particles. The height at which these aerosols are injected is crucial, since they can reach the stratosphere, which implies a long lifetime of these particles in the atmosphere and a greater impact on the climate. In addition, the amount and radiative properties of these aerosols is also important, since the impact of these aerosols over climate depend on these properties.

The Group of Atmospheric Optics of the University of Valladolid (GOA-UVa), in collaboration with the Spanish Meteorology Agency (AEMet), installed a sun/sky/moon AERONET photometer (CE318-T *Cimel Electronique*) and a ceilometer (CHM15k *Lufft*) near to the volcano (about 14-15 km at Southside). The main objective of this joint effort between AEMet and GOA-UVa was to be able to monitor the column and vertically-resolved aerosol properties derived from the Cumbre-Vieja volcano.

The photometer is within AERONET, and its data is received and managed by CAELIS system (*González et al.*, 2020), which processes the measured data and provides aerosol optical depth (AOD) and sky radiances at several wavelengths. The ceilometer is within the Iberian Ceilometer Network (ICENET; *Cazorla et al.*, 2017), measuring the range corrected signal (RCS) at 1064 nm with a vertical resolution of 15 m. All these data (AOD, sky radiances and RCS) from CAELIS and ICENET are assimilated by CAECENET (*Román et al.*, 2021), a system that combines these photometer and ceilometer data to retrieve columnar and vertically-resolved aerosol properties in near-real-time following the method proposed by *Román et al.* (2018) using GRASP code (*Dubovik et al.*, 2014).

The main objective of this work is to show the profiles of some aerosol properties obtained by CAECENET during the first weeks after the Cumbre-Vieja eruption at La Palma.

Results and discussion

Photometer at La Palma started its measurements on 21st September 2021, but the ceilometer arrives the island on 30th September 2021, hence CAECENET products are only available since this last date.

Figure 1 shows the aerosol volume concentration profiles at La Palma, from CAECENET, until 16th October 2021. On the 1st of October a thin aerosol layer can be observed, centred at 5 km asl, in the only one retrieved profile of that day. The Angström Exponent was about 0.4, hence, it is likely that coarse volcanic ash was emitted at this height. In the next two days (2nd and 3rd October) a thin aerosol layer, that was going down from 5.5 to 4.5 km asl, was detected with maximum volume concentrations close to 100 $\mu m^3/cm^3$ and to 200 $\mu m^3/cm^3$ on 2nd and 3rd October, respectively. Both days presented also low Angström Exponent values, indicating the predominance of coarse particles.

Two aerosol layers centred around 3.5 and 1.5 km asl are observed for the afternoon on 6th October, also with the predominance of coarse particles but with volume concentrations below 40 $\mu m^3/cm^3$. In the next days, 7th and 8th October, two aerosol layers can be identified between 1.0 and 3.5 km asl, but with low aerosol volume concetration values (most of them below 30 $\mu m^3/cm^3$) and with Angström values above 1.0 indicating no clear predominance of coarse particles.

The volume concentration on 14th and 15th October presented high values, reaching concentrations around 200 $\mu m^3/cm^3$ near to 1 km asl; the mean volume concentration value was about 150 $\mu m^3/cm^3$ for both days at that layer. A couple of thin aerosol layers around 2.5 and 3.5 km asl on 14th October, which origin could be the volcanic eruption. Fine particles were predominant both days, with high Angström Exponent values.

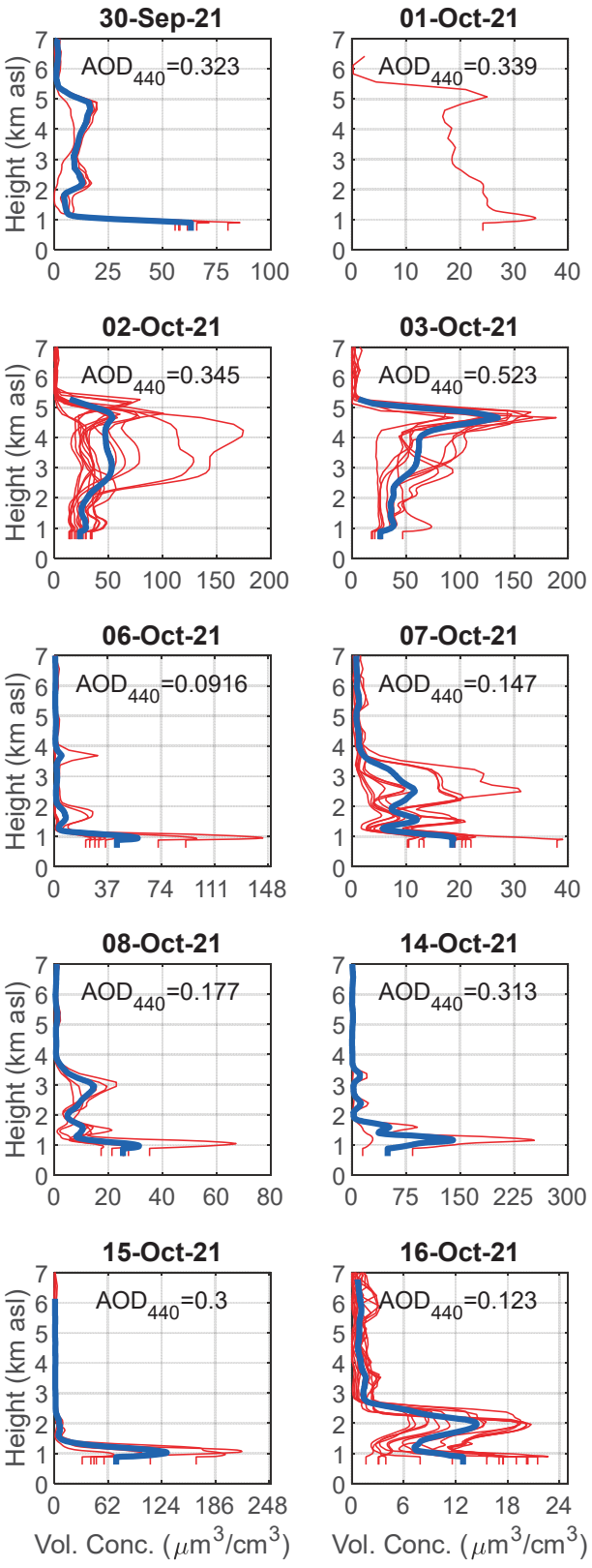

Figure 1. Vertical profiles of aerosol volume concentration (Vol. Conc.) at La Palma (Spain) for 10 days between 30th September 2021 and 16th October 2021. Blue line represents the daily average profile obtained from all availables profiles in each day. Daily average of AOD at 440 nm for each inversion is added in each panel.

Challenges

The aerosol layers observed in this work may have their origin in sources other than those of the volcano; for example, it is known that there were intrusions of Saharan dust during the period analyzed. A more detailed study based on backtrajectories and additional instrumentation will be done to better identification of the aerosol layers of volcanic origin and thus characterize them through the values obtained.

This work shows that a joint effort between scientific groups and institutions can achieve scientific results of interest in near-real-time under extreme situations like a volcanic eruption. The coordination between GOA-UVa and AEMet for the deployment of the instrumentation has been crucial as the coordination between CAELIS and ICENET to provide the data to CAECENET. Aerosol profiles monitoring will continue at least until the eruption ends.

Acknowledgements

The authors acknowledge the "Ministerio de Ciencia, Innovación e Universidades" the support obtained with the ePOLAAR (RTI2018-097864-B-I00) project, and the "Junta de Castilla y León" for the AEROCyL (VA227P20) project. The authors acknowledge the use of GRASP inversion algorithm software (https://www.grasp-open.com). The authors especially thank the important efforts made by AEMet staff to operate and maintain the instrumentation in La Palma.

References

Cazorla et al., Near-real-time processing of a ceilometer network assisted with sun-photometer data: monitoring a dust outbreak over the Iberian Peninsula, *Atmos. Chem. Phys*, 17(19), 11861-11876, 2017.

Dubovik et al., GRASP: a versatile algorithm for characterizing the atmosphere, *SPIE Newsroom*, 25(10.1117), 2-1201408, 2014.

González et al., Daytime and nighttime aerosol optical depth implementation in CÆLIS, *Geosci. Instrum. Methods Data Syst.*, 9(2), 417-433, 2020.

Román et al., Retrieval of aerosol profiles combining sunphotometer and ceilometer measurements in GRASP code, *Atmos. Res.*, 204, 161-177, 2018.

Román et al., CAECENET: Columnar And Vertically-Resolved Aerosol Products In Near-Real-Time Joining Sun/Sky Photometer And Ceilometer Measurement Networks, *European Lidar Conference 2021*, Granada, 2021.

Pollen characterization using AERONET, lidar and Burkard data

M. C. Gatou[1], *E. Giannakaki*[1], *X. Shang*[2], *S. Bohlmann* [2], *V. Gouliaditis, M. Komppula*[2]
margat@phys.uoa.gr
(1) Department of Environmental Physics and Meteorology, University of Athens, Athens, Greece
(2) Finnish Meteorological Institute, Atmospheric Research Centre of Eastern Finland ,70211, Kuopio, Finland

Introduction

One type of biogenic particles is pollen, which show a great diversity among its grains shapes and sizes[1]. More than 1000 active pollen monitoring stations in the world are built to monitor pollen concentrations at ground level using in situ instruments[2] .Recently an increasing interest in pollen has arisen in the aerosol lidar community. since non-spherical pollen grains can generate strong depolarization and thus can be recognizable by lidars. To our knowledge, AERONET data have never been used to characterize the optical properties of pollen.

In this study we investigate the potential of pollen recognition using AERONET data.

Methodology

In this study lidar data will be compared with AERONET observations during a four-month pollen campaign from May to August 2016 at the station in Vehmasmäki (62°44'N, 27°33'E), in Eastern Finland. During the campaign a Hirst type volumetric air sampler was used at ground level which enables identification of pollen types and concentration microscopically with a 2 h time resolution. The Kuopio station is also equipped with a ground-based multi-wavelength Raman polarization lidar PollyXT [3], AERONET data were available at Kuopio station nearby (62.892N, 27.634E).

In this study we utilize night-time profiles of extinction and backscatter coefficients at 355 and 532 nm, which are derived independently using elastic and inelastic Raman-shifted wavelengths (387 and 607 nm), based on the Raman inversion [4].The ratio of extinction-to-backscatter coefficient is called the lidar ratio (LR), which is considered an important parameter to separate particle types.

Cross-polarization and total polarization channels of the PollyXT allow the retrieval of the volume linear depolarization ratio (VDR) and particle linear depolarization ratio (PDR) at 532 nm, which provide information on the shape of the scattering particles

AERONET sun/sky radiometers measure direct solar radiation and sky radiation. These measurements allow the estimation of the elements F11,λ(r, n) and F22,λ(r, n) of the Müller scattering matrix, from which aeronet lidar ratio can be computed as:

$$S_\lambda^p = \frac{4\pi}{\omega_\lambda F_{11,\lambda}(r,n,180°)}$$

,where ω_λ the single-scattering albedo.

The calculation of the particle linear depolarization ratio is also possible using the elements F11,λ(r, n) and F22,λ(r, n) as below:

$$\delta_\lambda^p = \frac{1 - F_{22,\lambda}(r,n,180°)/F_{11,\lambda}(r,n,180°)}{1 + F_{22,\lambda}(r,n,180°)/F_{11,\lambda}(r,n,180°)}$$

Results and discussion

During the campaign twenty types of pollen were observed. While the surrounding forest is mixed in terms of the tree species, the pollination periods of the four different dominant pollen types are distinct, as can be seen from the Burkard-observed number concentration of specific pollen types shown in Fig. 1a. The dominant pollen types identified are shown in Table 1, along with each intense pollen period (IPP).

According to lidar studies during the campaign, lidar ratios at both 355 and 532 nm ranged from 55 to 70 sr for all pollen types, while depolarization ratio was found to be enhanced, ranging from 14-25% when the most abundant pollen type where less spherical (e.g. spruce or pine pollen). The depolarization ratio at 532 nm of pure pollen particles was assessed, resulting to 24 ± 3 % and 36 ± 5 % for birch and pine pollen, respectively with a depolarization ratio at 355 nm 17 % and 30% respectively[5],[6].

In the Figure 1 (b-f) we present the timeseries of lidar ratio at 440nm (b), depolarization ratio at 440nm (c), aerosol optical depth at 440nm (d), Angstrom Exponent between 440 and 870nm (e) and single scattering albedo at 440 nm (f).

The highest values of depolarization ratio (18%±3), indicating non spherical particles, was found for the IPP3. According to Burkard measurements this period is mostly referred to pine pollen particles. Lidar ratio does not seem to vary a lot among the different IPPs, with relatively higher values during IPP2 and late IPP4. A large variation of Angstrom exponent and single scattering albedo was found within the same pollen period indicating either the mixing of absorbing urban particles or possible different sizes and of pollen absorbance capability of the same pollen type.

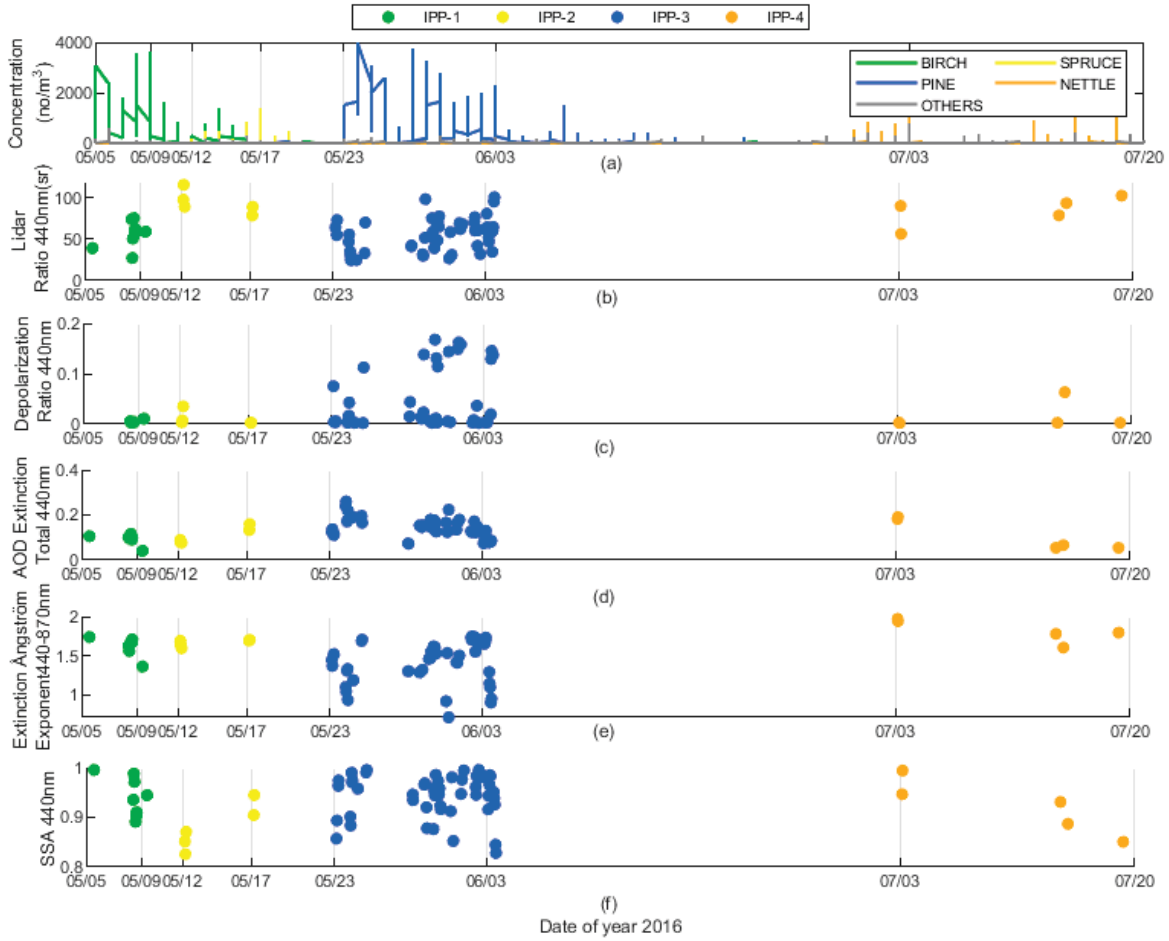

Figure 1. the timeseries of the variation of Lidar ratio 440nm, Depolarization Ratio 440nm, AOD440nm, Angstrom Exponent 440-870nm from AERONET products and pollen concentration (2-hour average) measured by the Burkard sampler, throughout the 4 intense pollination periods (IPPs)

Table 1a. The 4 intense pollen types and the respective pollination periods(IPP's)[a]
[a]

	Period	Pollen Type
IPP1	05.5-09.5	Birch
IPP2	12.05-17.05	Birch and Spruce
IPP3	23.05-25.05 28.05-03.06	Pine
IPP4	01.07-03.07 14.07-18.07 24.07-04.08	Nettle

Acknowledgements

The research work was supported by the Hellenic Foundation for Research and Innovation (H.F.R.I.) under the "First Call for H.F.R.I. Research Projects to support Faculty members and Researchers and the procurement of high-cost research equipment grant" (Project Number:16645).

References

[1] Després, et.al.(2012). Primary biological aerosol particles in the atmosphere: a review. Tellus B: Chemical and Physical Meteorology, 64(1), 15598.

[2]Giesecke, et.al.(2010).From early pollen trapping experiments to the Pollen Monitoring Archaeobotany,Programme. Vegetation History19(4),247-258.

[3]Engelmann, R., et.al. (2016). The automated multiwavelength Raman polarization and water-vapor lidar Polly XT: the neXT generation. Atmospheric Measurement Techniques, 9(4), 1767-1784.

[4] Ansmann, et.al. (1992). Independent measurement of extinction and backscatter profiles in cirrus clouds by using a combined Raman elastic-backscatter lidar. Applied optics, 31(33), 7113-7131.

[5]Bohlmann, et.al. Detection and characterization of birch pollen in the atmosphere using a multiwavelength Raman polarization lidar and Hirst-type pollen sampler in Finland 2019 Atmospheric Chemistry and Physics , Vol. 19, No. 23 p. 14559-14569.

[6]Shang, X.,et..al. (2020). Optical characterization of pure pollen types using a multi-wavelength Raman polarization lidar. Atmospheric Chemistry and Physics, 20(23), 15323-15339.